



Universidade do Minho

I3Bs - Instituto de Investigação em Biomateriais,
Biodegradáveis e Biomiméticos

Cristiana Rodrigues de Carvalho

**Combinatorial approaches for the development
of conduits for guided peripheral nerve
regeneration**

Combinatorial approaches for the development
of conduits for guided peripheral nerve
regeneration

Cristiana Rodrigues de Carvalho

UMinho | 2019



julho de 2019



Universidade do Minho

I3Bs - Instituto de Investigação em Biomateriais,
Biodegradáveis e Biomiméticos

Cristiana Rodrigues de Carvalho

**Combinatorial approaches for the development
of conduits for guided peripheral nerve
regeneration**

Tese de Doutoramento em Engenharia de Tecidos, Medicina
Regenerativa e Células Estaminais

Trabalho efetuado sob a orientação do

Doutor Joaquim Miguel Antunes Correia de Oliveira

e do

Professor Doutor Rui Luís Gonçalves dos Reis

DIREITOS DE AUTOR E CONDIÇÕES DE UTILIZAÇÃO DO TRABALHO POR TERCEIROS

Este é um trabalho académico que pode ser utilizado por terceiros desde que respeitadas as regras e boas práticas internacionalmente aceites, no que concerne aos direitos de autor e direitos conexos.

Assim, o presente trabalho pode ser utilizado nos termos previstos na licença abaixo indicada.

Caso o utilizador necessite de permissão para poder fazer um uso do trabalho em condições não previstas no licenciamento indicado, deverá contactar o autor, através do RepositóriUM da Universidade do Minho.

Licença concedida aos utilizadores deste trabalho



Atribuição
CC BY

<https://creativecommons.org/licenses/by/4.0/>

ACKNOWLEDGMENTS

The journey and preparation of this thesis was most definitely one of the hardest things I have done. As such, and since “no Man is an island”, it would not have been possible without the help and support of a few people. First, none of this would be possible without the support of Prof. Rui Reis. He gave me the opportunity to join this research group and to thrive and prosper along the years. It was an honor to develop and to be able to defend my PhD thesis at the European Institute of Excellence for Tissue Engineering and Regenerative Medicine, under his supervision and leadership. My PhD grant from Norte2020 was also the result of Prof. Rui Reis efforts and hard work along the years. Thank you for preparing me for this competitive world. Second, but not less important, I would like to acknowledge Dr. Joaquim Miguel Oliveira. To him I must thank the fact that I finish my PhD in first place. In less good times where giving up would be my choice, his words of wisdom made me continue. For that I am grateful and that is a special characteristic I would like to have myself in future work experiences.

I would also like to thank the co-authors in this thesis and my colleagues currently working with me, always trying to improve my work. A special thanks to Joana Silva-Correia, who was always a helping hand, especially regarding the writing and correction of manuscripts. Her inputs were extremely valuable. I have spent many years in this institute and friendship is something I am proud of having achieved inside these walls. We shared good, sad and hysterical moments together. “3Bs Pistolada”, thank you for making every single day at work worth it.

Finally, to the four people in my personal life who make everything happen and run smoothly: My dad, my king, my rock, my everything. No words are needed because you know that without you, I would not be half the person I am today. I know everything will be alright in the end, simply because you exist. My mom, for being there, for the wise advices and for being available every minute of every day. Thank you for such unconditional love and for every supportive word whenever needed. My twin sister, my other half. The one that knows my deepest thoughts by just looking at me, the one that will be with me no matter what. João, my lab partner and my life partner. His love, patience, dedication and support were the key in the last years of my PhD. His good mood cheers me up every single day. We met here at 3Bs as PhD students, but our journey will last much longer than this one.

Finally, I acknowledge the financial support from Biohybrid project (EU-FP7-Health-2011-collaborative project 278612, Biohybrid - Templates for peripheral nerve regeneration) and my PhD Scholarship from Horizonte Norte2020 (Norte-08-5369-FSE-000037).

STATEMENT OF INTEGRITY

I hereby declare having conducted this academic work with integrity. I confirm that I have not used plagiarism or any form of undue use of information or falsification of results along the process leading to its elaboration.

I further declare that I have fully acknowledged the Code of Ethical Conduct of the University of Minho.

ABSTRACT

Combinatorial approaches for the development of conduits for guided peripheral nerve regeneration

Regeneration, reconstruction and repair of peripheral nerve injuries (PNIs) are among the most complex and demanding challenges in the field of regenerative medicine. As a promising alternative to the “gold standard” autologous nerve grafts, tissue-engineered nerve guidance conduits (NGCs) have been extensively studied. However, in order to be able to produce an adequate NGC, the basic principles of neuro-biology must be known and followed. Also, great efforts have been made in terms of pre-clinical and clinical applications of engineered biomaterials for peripheral nerve regeneration. Furthermore, nanotechnology approaches have propelled nerve regenerative strategies. These themes are the focus of Section 1, in **Chapters I, II and III**.

This PhD project has focused mainly on researching, developing and testing natural and biodegradable biomaterials using several fabrication methods to obtain the NGCs (**Chapter IV**). The first explored biomaterial was chitosan, in **Chapter V**, where the suitability of chitosan membranes with three different low degrees of acetylation was evaluated. Furthermore, to enhance the membranes' cell adhesion and angiogenic properties, extracted human hair keratin was combined to the previous described membranes (**Chapter VI**). In **Chapter VII**, chitosan NGCs which are currently being used in in the clinical setting (Reaxon®), were used in combination with different gellan gum luminal fillers, mimicking the native Bands of Büngner. In **Chapter VIII**, a ground-breaking silk fibroin (SF) fabrication method for NGCs was established. SF NGCs were produced using a novel technology that comprises a horseradish peroxidase-mediated crosslinking system. Such innovative processing method resulted in the filling of an international patent. The excellent outcomes demonstrated by the enzymatically-crosslinked method lead to an original research paper (**Chapter IX**). In line with the previous work, and because of its resourcefulness, a step forward was given, and a state-of-the-art study was performed, comprising the production of enzymatically-crosslinked SF NGCs capable of incorporating and delivering different neurotrophic factors. The developed NGCs restored the functional activity and enhanced neovascularization in the regenerated nerves, revealing comparable results to the autograft (**Chapter X**). In summary, the presented outcomes contributed to improve the actual state-of-art in what regards peripheral nerve regeneration, providing promising and versatile alternatives by using different types of natural-based biomaterials and approaches (**Chapter XI**).

Keywords: Biomaterials, Conduits, Chitosan, Gellan Gum, Silk Fibroin, Peripheral Nerve

RESUMO

Abordagens combinatórias para o desenvolvimento de tubos para regeneração guiada do nervo periférico

A regeneração, reconstrução e reparação das lesões do nervo periférico encontram-se entre os desafios mais exigentes e complexos na área da Medicina Regenerativa. Como tratamento alternativo aos enxertos de nervo autólogo, Estruturas tubulares e protetoras do nervo produzidos, através de técnicas de Engenharia de Tecidos têm sido extensivamente estudados. Para além disso, grandes esforços têm sido feitos em termos de aplicações clínicas e pré-clínicas de biomateriais para a regeneração do nervo periférico. Abordagens nanotecnológicas têm também impulsionado o avanço nesta área. Estes temas são abordados na Secção 1, nos **Capítulos I, II e III**.

Este projeto de Doutoramento focou-se principalmente na investigação, desenvolvimento e testes laboratoriais de várias formulações de biomateriais, combinados com diferentes técnicas de fabrico (**Capítulo IV**) de estruturas tubulares, usando apenas polímeros biodegradáveis conjugados com outras funcionalizações físicas ou biológicas. O quitosano foi o primeiro material investigado, no **Capítulo V e VI**, onde foram estudadas diferentes membranas de quitosano, assim como a melhoria das propriedades biológicas e angiogénicas destas, através da adição de queratina extraída de cabelo humano. No **Capítulo VII**, tubos de quitosano atualmente usados em Humanos (Reaxon®) foram combinados com diferentes formulações de Gellan Gum, produzidos para preencher o lúmen dos tubos, mimetizando assim as bandas de Bungner. No **Capítulo VIII**, um inovador método de produção de tubos condutores à base da Fibroína da Seda foi desenvolvido, resultando no registo de uma patente internacional. Esta metodologia envolve o uso de um sistema de reticulação enzimática com base na enzima peroxidase e o peróxido de hidrogénio (oxidante). Os excelentes resultados demonstrados através deste sistema de produção de tubos originaram um artigo original (**Capítulo IX**). Seguindo a mesma linha de trabalho, e devido à versatilidade da técnica, estudos inovadores foram desenvolvidos, onde fatores neurotróficos foram incorporados nos tubos de Fibroína da Seda, com o objetivo de restaurar a funcionalidade motora assim como a re-vascularização dos nervos regenerados (**Capítulo X**). Em suma, os resultados apresentados nesta tese indicam a versatilidade dos diferentes biomateriais e formulações testadas, assim como das diferentes técnicas, contribuindo deste modo para melhorar o atual estado da arte no que diz respeito à regeneração do nervo periférico (**Capítulo XI**).

Palavras Chave: Biomateriais, Fibroína da Seda, Gellan Gum, Quitosano, Nervo Periférico

TABLE OF CONTENTS

| | |
|---|-----------|
| ACKNOWLEDGMENTS..... | III |
| STATEMENT OF INTEGRITY..... | IV |
| ABSTRACT..... | V |
| RESUMO..... | VI |
| TABLE OF CONTENTS..... | VII |
| LIST OF ABBREVIATIONS..... | XIV |
| LIST OF EQUATIONS..... | XXI |
| LIST OF FIGURES..... | XXII |
| LIST OF SUPPLEMENTARY FIGURES..... | XXXVIII |
| LIST OF TABLES..... | XLI |
| LIST OF SUPPLEMENTARY TABLES..... | XLIII |
| SHORT CURRICULUM VITAE..... | XLIV |
| LIST OF PUBLICATIONS..... | XLV |
| INTRODUCTION TO THE THESIS FORMAT..... | XLVIII |
| SECTION 1..... | 1 |
| CHAPTER I - FUNDAMENTALS AND CURRENT STRATEGIES FOR PERIPHERAL NERVE REPAIR AND REGENERATION: | 3 |
| Abstract..... | 3 |
| I-1. Introduction..... | 4 |
| I-1.1. Organization of the Nervous System..... | 5 |
| I-1.2. General Overview of Peripheral Nerve Injuries..... | 7 |
| I-1.3. Degeneration and Regeneration following PNIs..... | 9 |
| I-1.4. Strategies for Nerve repair..... | 12 |
| I-2. Conclusions..... | 35 |
| I-3. Acknowledgments..... | 36 |
| I-4. References..... | 36 |
| CHAPTER II - MODERN TRENDS FOR PERIPHERAL NERVE REPAIR AND REGENERATION: BEYOND THE HOLLOW NERVE GUIDANCE CONDUIT: | 46 |
| Abstract..... | 46 |
| II-1. Introduction..... | 47 |
| II-1.1. Insights on nerve injury and repair..... | 48 |
| II-1.2. Neuroplasticity..... | 49 |
| II-1.3. Tissue Engineering and Regenerative Medicine Concepts for PNR..... | 51 |
| II-1.4. Approaches for nerve repair..... | 54 |
| II-1.5. A biomaterials-based approach for NGCs..... | 56 |
| II-1.6. Growth Factors (GFs) as molecular therapies..... | 67 |
| II-1.7. Gradients of growth factors (GFs)..... | 71 |

| | | |
|-----------------------|--|------------|
| II-1.8. | Other biological cues | 73 |
| II-1.9. | Cell-based therapies | 76 |
| II-1.10. | Clinical trials in the scope of PNR..... | 82 |
| II-2. | Conclusions..... | 91 |
| II-3. | Acknowledgments..... | 92 |
| II-4. | References | 92 |
| CHAPTER III - | NANOTECHNOLOGY IN PERIPHERAL NERVE REPAIR AND RECONSTRUCTION¹..... | 105 |
| Abstract..... | | 105 |
| III-1. | Introduction | 106 |
| III-2. | PNIs: Fundamentals, current treatment options and challenges | 109 |
| III-3. | Nanotechnology approaches for functionalization of tubular conduits | 117 |
| III-3.1. | Carbon nanomaterials | 119 |
| III-3.2. | Nanoparticles | 136 |
| III-3.3. | Nanofibers..... | 160 |
| III-3.4. | Topographic cues at micro- and nano-scale | 170 |
| III-4. | Nanotheranostics and imaging | 174 |
| III-4.1. | Nanotheranostics toxicity | 181 |
| III-5. | Final remarks and future perspectives..... | 182 |
| III-6. | Acknowledgments..... | 184 |
| III-7. | References | 184 |
| SECTION 2..... | | 199 |
| CHAPTER IV - | MATERIALS AND METHODS | 201 |
| Overview..... | | 201 |
| IV-1. | Materials | 202 |
| IV-1.1. | Chitosan | 202 |
| IV-1.2. | Gellan Gum | 205 |
| IV-1.3. | Silk fibroin (SF) | 208 |
| IV-1.4. | Keratin | 211 |
| IV-1.5. | Neurotrophic factors (NTFs)..... | 214 |
| IV-2. | Reagents | 216 |
| IV-3. | Methodologies for processing of biomaterials: overview | 216 |
| IV-3.1. | Membranes | 216 |
| IV-3.2. | Freeze-dried hydrogels..... | 217 |
| IV-3.3. | Tubular conduits..... | 219 |
| IV-4. | Production of different materials for PNR..... | 220 |
| IV-4.1. | Production of chitosan-based biomaterials: membranes and conduits..... | 220 |
| IV-4.2. | Production of freeze-dried hair keratin | 221 |
| IV-4.3. | Production of Freeze-dried GG hydrogels | 222 |
| IV-4.4. | Production of enzymatically crosslinked SF NGCs..... | 224 |

| | | |
|--|---|------------|
| IV-5. | Physicochemical Characterization | 228 |
| IV-5.1. | Surface morphology and microstructure evaluation..... | 228 |
| IV-5.2. | Chemical analysis..... | 235 |
| IV-5.3. | Mechanical properties..... | 238 |
| IV-5.4. | Water uptake ratio | 242 |
| IV-5.5. | Weight loss profile | 244 |
| IV-5.6. | <i>In vitro</i> mineralization | 246 |
| IV-5.7. | Molecular permeability tests | 247 |
| IV-6. | <i>In vitro</i> biological tests | 248 |
| IV-6.1. | Cell sources | 248 |
| IV-6.2. | Cryopreservation..... | 252 |
| IV-6.3. | Cell seeding procedures..... | 252 |
| IV-6.4. | <i>In vitro</i> cellular permeability assay..... | 254 |
| IV-6.5. | Metabolic activity and cell viability examination | 255 |
| IV-6.6. | Cell proliferation quantification | 257 |
| IV-6.7. | Cellular cytoskeleton morphology study..... | 258 |
| IV-6.8. | Enzyme-linked Immunosorbent Assay (ELISA) | 259 |
| IV-6.9. | Immunocytochemistry | 260 |
| IV-7. | <i>In vivo</i> studies..... | 261 |
| IV-7.1. | Chick chorioallantoic membrane (CAM) assay | 262 |
| IV-7.2. | Subcutaneous implantation..... | 263 |
| IV-7.3. | <i>In vivo</i> study using rat model of sciatic nerve defect..... | 265 |
| IV-7.4. | Explants characterization | 267 |
| IV-8. | Statistical analysis | 275 |
| IV-9. | References | 276 |
| SECTION 3..... | | 287 |
| EXPERIMENTAL STUDIES..... | | 287 |
| CHAPTER V - INVESTIGATION OF CELL ADHESION IN CHITOSAN MEMBRANES FOR PERIPHERAL NERVE | | |
| REGENERATION: | | 289 |
| Abstract..... | | 289 |
| V-1. | Graphical abstract | 290 |
| V-2. | Introduction | 290 |
| V-3. | Experimental section..... | 292 |
| V-3.1. | Materials | 292 |
| V-3.2. | Methods | 292 |
| V-3.3. | Statistical analyses | 298 |
| V-4. | Results..... | 299 |
| V-4.1. | Physicochemical and Surface Characterization of Membranes | 299 |
| V-4.2. | Biological characterization..... | 306 |

| | | |
|---|---|------------|
| V-5. | Discussion..... | 307 |
| V-6. | Conclusion | 317 |
| V-7. | Acknowledgments..... | 318 |
| V-8. | References | 318 |
| V-9. | Supplementary Data | 322 |
| CHAPTER VI - ENHANCED BIOLOGICAL PERFORMANCE OF CHITOSAN/KERATIN MEMBRANES FOR PERIPHERAL NERVE APPLICATIONS¹..... | | 324 |
| | Abstract..... | 324 |
| VI-1. | Graphical abstract | 325 |
| VI-2. | Introduction | 325 |
| VI-3. | Experimental section..... | 328 |
| VI-3.1. | Materials | 328 |
| VI-3.2. | Manufacturing of CHT powder..... | 328 |
| VI-3.3. | Extraction of keratin from human hair | 328 |
| VI-3.4. | Preparation of CHT and CHT/keratin membranes | 329 |
| VI-3.5. | Physicochemical characterization of CHT and CHT/keratin membranes | 329 |
| VI-3.6. | <i>In vitro</i> biological studies..... | 332 |
| VI-3.7. | <i>In vivo</i> angiogenesis evaluation..... | 335 |
| VI-3.8. | Statistical analysis | 336 |
| VI-4. | Results | 337 |
| VI-4.1. | Physicochemical Characterization | 337 |
| VI-4.2. | <i>Biological In vitro</i> studies | 342 |
| VI-4.3. | <i>In vivo</i> angiogenic assay..... | 346 |
| VI-5. | Discussion..... | 349 |
| VI-6. | Conclusions..... | 352 |
| VI-7. | Acknowledgements..... | 353 |
| VI-8. | References | 353 |
| CHAPTER VII - GELLAN GUM-BASED LUMINAL FILLERS FOR PERIPHERAL NERVE REGENERATION. AN <i>IN VIVO</i> STUDY IN THE RAT SCIATIC NERVE REPAIR MODEL¹..... | | 358 |
| | Abstract..... | 358 |
| VII-1. | Graphical abstract | 359 |
| VII-2. | Introduction | 359 |
| VII-3. | Materials and Methods | 361 |
| VII-3.1. | Production of biomedical systems | 361 |
| VII-3.2. | Physicochemical characterization..... | 362 |
| VII-3.3. | Biological <i>in vitro</i> assays | 364 |
| VII-3.4. | <i>In vivo</i> study | 365 |
| VII-3.5. | Statistical analysis | 370 |
| VII-4. | Results | 371 |

| | | |
|--|---|------------|
| VII-4.1. | Physicochemical characterization | 371 |
| VII-4.2. | Biological <i>in vitro</i> assays | 374 |
| VII-4.3. | <i>In vivo</i> studies..... | 374 |
| VII-5. | Discussion..... | 385 |
| VII-6. | Conclusions..... | 391 |
| VII-7. | Acknowledgments..... | 392 |
| VII-8. | References | 393 |
| VII-9. | Supplementary data..... | 396 |
| CHAPTER VIII - PATENT - NERVE GUIDANCE CONDUITS DERIVED FROM SILK FIBROIN HYDROGELS: METHODS OF PRODUCTION AND USES THEREOF¹ | | 406 |
| Abstract..... | | 406 |
| VIII-1. | Technical field | 407 |
| VIII-2. | Background | 407 |
| VIII-3. | General description..... | 409 |
| VIII-4. | Detailed description | 415 |
| VIII-5. | Claims..... | 422 |
| VIII-6. | List of Figures..... | 425 |
| CHAPTER IX - TUNABLE ENZYMATICALLY CROSS-LINKED SILK FIBROIN TUBULAR CONDUITS FOR GUIDED TISSUE REGENERATION¹ | | 437 |
| Abstract..... | | 437 |
| IX-1. | Graphical abstract | 438 |
| IX-2. | Introduction | 438 |
| IX-3. | Experimental Section | 441 |
| IX-3.1. | Materials | 441 |
| IX-3.2. | SF Purification | 442 |
| IX-3.3. | Preparation of SF Conduits | 442 |
| IX-3.4. | Structure Evaluation by Stereomicroscope..... | 443 |
| IX-3.5. | Micro-computed tomography..... | 443 |
| IX-3.6. | Microstructure evaluation by scanning electron microscopy (SEM) | 443 |
| IX-3.7. | Fourier transform infrared (FTIR) spectroscopy | 443 |
| IX-3.8. | Mechanical properties..... | 443 |
| IX-3.9. | <i>In vitro</i> weight loss and water uptake profiles..... | 444 |
| IX-3.10. | Bioactivity test in Simulated Body Fluid (SBF)..... | 445 |
| IX-3.11. | <i>In vitro</i> molecular permeability assay | 445 |
| IX-3.12. | Cell culture of immortalized human Schwann cells and immortalized human skin fibroblasts (BJ) | 445 |
| IX-3.13. | Cellular direct seeding in SF conduits and quantitative and qualitative viability evaluations | 446 |
| IX-3.14. | <i>In vitro</i> cellular permeability assay (using a modified Boyden chamber) | 446 |
| IX-3.15. | <i>In vivo</i> implantation of SF conduits..... | 447 |
| IX-3.16. | Statistical analyses | 448 |

| | | |
|--|--|------------|
| IX-4. | Results and Discussion | 449 |
| IX-4.1. | Production of TCs using an enzymatically cross-linking approach | 449 |
| IX-4.2. | Macro- and micro-structure of the TCs..... | 450 |
| IX-4.3. | Chemical structure of the TCs | 453 |
| IX-4.4. | Mechanical properties of the TCs | 453 |
| IX-4.5. | Physico-chemical <i>in vitro</i> characterization of the TCs | 454 |
| IX-4.6. | Molecular and cellular permeability of the TCs..... | 458 |
| IX-4.7. | <i>In vitro</i> and <i>in vivo</i> biological properties of the TCs..... | 460 |
| IX-5. | Conclusion | 464 |
| IX-6. | Acknowledgments..... | 466 |
| IX-7. | References | 466 |
| IX-8. | Supplementary Data | 469 |
| CHAPTER X- ENGINEERING SILK FIBROIN-BASED NERVE CONDUIT WITH NEUROTROPHIC FACTORS FOR PROXIMAL PROTECTION AND VASCULARIZATION AFTER PERIPHERAL NERVE INJURY¹ | | 474 |
| Abstract..... | | 474 |
| X-1. | Graphical abstract | 475 |
| X-2. | Introduction | 475 |
| X-3. | Materials and Methods | 478 |
| X-3.1. | Materials | 478 |
| X-3.2. | Preparation of silk fibroin conduits | 478 |
| X-3.3. | Physical characterization of the conduits | 479 |
| X-3.4. | Incorporation of NTFs | 479 |
| X-3.5. | Determination of NTFs' loading efficiency in eSF conduits | 480 |
| X-3.6. | <i>In vitro</i> release of NTFs from the nerve conduits | 481 |
| X-3.7. | <i>In vitro</i> isolation and culturing of DRGs for NTFs bioactivity assay | 481 |
| X-3.8. | Immunocytochemistry | 482 |
| X-3.9. | Image acquisition and data analysis..... | 482 |
| X-3.10. | <i>In vivo</i> study using rat model of sciatic nerve defect..... | 482 |
| X-3.11. | Statistical analysis | 485 |
| X-4. | Results | 485 |
| X-4.1. | Production and physical characterization of silk fibroin conduits | 485 |
| X-4.2. | Neurotrophic factors loading efficiency | 486 |
| X-4.3. | <i>In vitro</i> release of NTFs from silk conduit..... | 488 |
| X-4.4. | NTFs bioactivity assay with DRGs | 490 |
| X-4.5. | <i>In vivo</i> study | 491 |
| X-5. | Discussion..... | 496 |
| X-6. | Conclusions..... | 501 |
| X-7. | Acknowledgments..... | 501 |
| X-8. | References | 502 |

| | |
|--|------------|
| X-9. Supplementary Data | 505 |
| SECTION 4..... | 510 |
| CONCLUSIONS AND FUTURE PERSPECTIVES..... | 510 |
| CHAPTER XI - GENERAL CONCLUSIONS AND FUTURE PERSPECTIVES..... | 512 |
| XI-1. General conclusions | 512 |
| XI-2. Future research directions | 517 |

LIST OF ABBREVIATIONS

A

α – Alpha
AB – Alamar blue
Abs – Absorbance
ADSCs – Adipose-derived stem cells
AFM – Atomic force microscopy
Ag – Silver
AgNPs – Silver nanoparticles
ANG – Autologous nerve graft
ANOVA – Analysis of variance
APPACDM – The Portuguese Association of Parents and Friends of Mentally Disabled Citizens
ASCs – Adipose tissue derived stromal cells
ATR – Attenuated total reflectance
ATR – FTIR - Attenuated total reflectance fourier transform infrared spectroscopy
Au – Gold
AuNPs – Gold nanoparticles
AuNRs – Gold nanorods
AUTOGs – Autologous nerve graft

B

β – Beta
 β -sheet – Beta-sheet
BDNF – Brain-derived neurotrophic factor
bFGF – Basic fibroblast growth factor
BMSCs – Bone marrow derived mesenchymal stromal cells
Br⁻ – Bromide ion
BSA – Bovine serum albumin

C

C1X – 3 mm into proximal side of the conduit
Ca²⁺ – Calcium ions
Calcein-AM – Calcein-Acetoxy-methyl
CAM – Chick chorioallantoic membrane
CaTiO₃ – Calcium titanate
CFF – fiber-film coated
CH – Close from the head
CHT – Chitosan
CH₂I₂ – Diiodomethane
Cl⁻ – Chloride ion
cm – centimeter
cm⁻¹ – Reciprocal wavelength centimeters
CMAPs – compound muscle action potentials
CNF – Carbon nanofibers
CNS – Central nervous system
CNT – Carbon nanotubes
CNTF – Ciliary neurotrophic factor
CO₂ – Carbon dioxide
Cp – Heat capacity
CTB – Cholera toxin subunit B

D

°C – Degree Celsius
d – Days
Da – Dalton
DA – Degree of acetylation
DA I – 1 % Degree of acetylation
DA II – 2 % Degree of acetylation
DA III – 5 % Degree of acetylation
DAPI – 4',6-diamidino-2-phenylindole
DGAV – Direcção Geral de Alimentação e Veterinária
DIV – Days *in vitro*
DMA – Dynamic mechanical analysis
DMEM – Dulbecco's modified Eagle's medium
DMSO – Dimethylsulfoxide
DNA – Deoxyribonucleic acid
DRG – Dorsal root ganglia
DSC – Differential scanning calorimeter
2D – 2-Dimensions
3D – 3-Dimensions

E

E – Young modulus
e.g. – For example, from latin *exempli gratia*
E' – Elastic modulus
ECCC – European collection of cell cultures
ECGS – Endothelial cell growth supplement
ECM – Extracellular matrix
EDS – Energy dispersive spectroscopy
EDTA – Ethylenediaminetetraacetic acid
EGFP – Green fluorescent protein
ELISA – Enzyme-linked immunosorbent Assay
EMEM – Eagle's Minimum Essential Medium
Eq – Equation
EO – Ethylene oxide gas
ES – Electrical stimulation
ESB – European society for biomaterials
et al. – And others
Ex/Em – Excitation/Emission

F

FBS – Fetal bovine serum
FDA – Food and drug administration
FDMP – Freeze-dried more porous
FGF-2 – Fibroblast growth factor
FH – Far from the head
Fig. – Figure
FITC – Fluorescein isothiocyanate
19F MRI – Fluorinated magnetic resonance imaging
FND – functionalized nanodiamonds
FTIR – Fourier transform infrared spectroscopy

G

g – grams

G' – Storage modulus
 G'' – Loss modulus
GDNF – Glial-derived neurotrophic factor
GFAP – Glial fibrillary acidic protein
GFs – Growth factors
GG – Gellan gum
GO – Graphene oxidized
GOF – Graphene oxidized foam
GTR – Guided tissue regeneration

H

H – Hours
HACNT – Horizontally aligned carbon nanotubes
H&E – Hematoxylin–eosin
 H_2O_2 – Hydrogen peroxide
HA – Hyaluronic acid
HA-GG – High acyl gellan gum
HBMSCs – Human bone marrow derived mesenchymal stromal cells
HCl – Hydrochloric acid
 HCO_3^{2-} – Bicarbonate ion
hEnSCs – Human endometrial stem cells
 HPO_4 – Hydrogen phosphate
hNSCs – Human neural stem cells
HRP – Horseradish peroxidase
HUCMSCs – Human umbilical-cord mesenchymal stem cells
Hz – Hertz

I

i.e. – “In other words”, from latin *id est*
IL – Interleukin
iPSCs – Induced pluripotent stem cells
iSC – Immortalized Schwann cells

K

K^+ – Potassium ion
KBr – Potassium bromide
kDa – Kilodalton
kg – Kilogram
kN – kilonewton
kPa – Kilo pascal
kV – Kilovolt

L

L – Liters
L929 – Murine fibroblast cell line
LA-GG – Low acyl gellan gum
LiBr – Lithium bromide
LT – Long-term

M

m – meter
M – Molar

mA – Milliampere
MA-GG – Methacrylated gellan gum
MBP – Myelin basic protein
MCP-1 – Monocyte chemoattractant protein 1
MeCbl – Methyl cobalamin
MEM – Minimum Essential Medium
Mg – milligram
Mg²⁺ – Magnesium ion
MenSCs – Human menstrual MSCs
MHH – Hannover medical school
mi – Initial weight
MIRB – Molday ION Rhodamine B
Micro-CT – Micro computed tomography
Min – minute
miRNA – MicroRNAs
mL – Milliliter
mm – Millimeter
mM – Millimolar
Mf – Final mass
M_w – Medium molecular weight
Mw – Wet mass
MNPs – Magnetic nanoparticles
Mol – Mole
MPa – megapascal
MRI – Magnetic resonance image
MSCs – Mesenchymal derived stromal cells
MSCs – Mesenchymal stem cells
mw – Wet weight
MWCO – Molecular weight cut off
MWCNTs – Multi-walled carbon nanotubes
µm – micrometer
6MP – 6-mercaptopurine

N

n – Number of samples
N/A – Not applicable, Not available
Na⁺ – Sodium ion
NaCl – Sodium chloride
NCD – Nanocrystalline diamond
ND – Nanodiamonds
NaOH – Sodium hydroxide
NECL1 – Nectin-like molecule 1
NF-200 – Neurofilament 200
NGC – Nerve guidance conduits
NGF – Nerve growth factor
NIH3T3 – Fibroblast cell line
NJCBM – New Jersey Center for Biomaterials
Nm – Nanometer
NPs – Nanoparticles
NSCs – Neural stem cells
NT3 – Neurotrophin-3
NT4 – Neurotrophin-4
NTFs – Neurotrophic factors

O

O₂ – Oxigen
O-CCH – Orientated collagen-chitosan
OECs – Olfactory ensheathing cells
OWRK – Owens, Went, Rabel and Kaelble
OxPVA – Oxidized PVA

P

p – Statistical level of significance
Pa – Pascal
PA – Polyaniline
PAM – polyacrylamide
PAMAM – Poly(amidoamine)
PBS – Phosphate buffer saline
PCL – Polycaprolactone
PDLLA – Poly(D,L-lactic acid)
PDMS – Polydimethylsiloxane
PEDOT – Doped-poly(3,4-ethylenedioxythiophene)
PEG – Poly (ethylene glycol)
PELA – Polyethylene glycol-co-polylactic acid
PFC – Perfluorocarbon
PGA – Polyglycolide acid
PGFs – Phosphate glass microfibers
pH – Potential hydrogenionic
PHB – Polyhydroxybutyrate
PHBV – Polyhydroxybutyrate-co-hydroxyvalerate
PI – Propidium iodide
PL – Plantar muscles
PLA – Polylactic acid
PLCL – Poly(L-lactide-co- ϵ -caprolactone)
PLGA – Polylactic-co-glycolic
PLLA – Poly(L-lactic acid)
PN – Peripheral Nerve
PNIs – Peripheral nerve injuries
PNS – Peripheral nervous system
PNW – protectant nerve wraps
PNX – 3 mm from proximal end of the conduit
PPy – Polypyrrole
PO – Protein Zero
% – Percentage

R

Ra – Average surface roughness
RAR β – Neuronal retinoic acid receptor β
Ref. – Reference
RGC – Retinal ganglion cells
RGD – Arginine-glycine-aspartic acid (Arg-Gly-Asp)
RM – Regenerative medicine
RNA – Ribonucleic acid
RFU – Relative fluorescence units
ROS – Reactive oxygen species

Rpm – Rotations per minute
Rq – Root mean square from average flat surface
RT – Room temperature
RT-PCR – Real time polymerase chain reaction
RTKs – Receptor tyrosine kinase

S

SCBL – Schwann cell basal lamina
SBF – Simulated body fluid
SCs – Schwann cells
SD – Standard deviation
SDS – Sodium dodecyl sulfate
SE – Surface energy
SEM – Scanning electron microscopy
SF – Silk fibroin
SH-SY5Y – Neuroblastoma cell line
SiO₂-NPs – Silica nanoparticles
SPIONs – Superparamagnetic iron oxide nanoparticles
S-S – Disulfide bonds
ST – Short-term
SWCNTs – Single-walled carbon nanotubes
SKPCs – Skin-derived precursor cells

T

θ – Teta
TA – Anterior tibial muscles
Tan δ – Loss factor
TC – Tubular conduit
TC 1 – TC freeze-dried after freezing at -80 °C
TC 2 – TC dried in an oven at 50 °C for 3 days
TC 3 – TC kept in a permanent hydrated stat
TCPs – Tissue culture polystyrene
TE – Tissue engineering
TERM – Tissue engineering and regenerative medicine
TG – Glass transition
TMCSH – Thiolated trimethyl chitosan
TMB – 3,3',5,5'-Tetramethylbenzidine
TNF – Tumor necrosis factor

U

U – Units
UV – Ultraviolet

V

V – Volume
(v/v) – Percentage of volume/volume
VCA – Vascularized composite tissue allotransplantation
VEGF – Vascular endothelial growth factor

X

XRD – X-ray diffraction
µg/mL – Microgram per milliliter

μL – Microliter

W

(w/v) – Percentage of weight/volume

WL – Weight loss

WU – Water uptake

%wt. – Percentage of weight

θ Water – Water contact angle

λ – Wavelength

Z

ZN – Zinc

ZnNPs – Zinc nanoparticles

LIST OF EQUATIONS

Equation IV-1 - Equation for the determination of percentage of water uptake244

Equation IV-2 - Equation for the determination of percentage of weight loss245

Equation V-1 - Equation for the determination of weight loss295

Equation V-2 - Equation for the determination of water uptake295

Equation VI-1 - Equation for the determination of weight loss.332

Equation VI-2 - Equation for the determination of water uptake.332

Equation VII-1 - Equation for the determination of percentage of water uptake363

Equation VII-2 - Equation for the determination of percentage of weight loss.....363

Equation IX-1 - Equation for the determination of percentage of water uptake444

Equation IX-2 - Equation for the determination of percentage of weight loss.....444

Equation X-1 - Equation for the determination the NTF loading efficiency.....480

LIST OF FIGURES

Figure I-1 - Schematic representation of nervous system anatomy in the human body. The nervous system is divided in CNS (in blue) and PNS (green). A) The PNS is composed of several pairs of nerves, which transmit signals between afferent sensory neurons and efferent motor neurons to the CNS; B) CNS, composed of the brain and spinal cord, which has connections to PNS. In CNS, interneurons receive information from the periphery; C) A peripheral nerve contains many nerve fibers that are held together by connective tissue and bundled into nerve fascicles. The entire nerve is enclosed by connective tissue called epineurium. Individual fascicles are delineated by perineurium. Endoneurium surrounds each nerve fiber; and D) Each neuron is composed of a cell body, known as Soma, which contains dendrites. The axon, elongating from the cell body may present myelin sheaths. The spaces between the myelin sheaths are Nodes of Ranvier. In the end of the neuron there is an axon terminal, which releases neurotransmitters from one neuron to another.6

Figure I-2 - A) Progression of Wallerian Degeneration: I) A single axon with enwrapping myelinating Schwann cells suffers a traumatic injury; II) The axon breaks and the distal stump undergoes cellular changes. Distal to the injury, there is a destruction of the remaining intact axon and disintegration of myelin cover, leaving debris behind. Macrophages and Schwann cells, which turned to a pro-regenerative phenotype, accumulate at the lesion site and scavenge the debris; III) Schwann cells aligns in the Bands of Bungner. These tubes provide a permissive growth environment and guide extending axons towards distal targets; IV) If the axon is able to traverse the injury gap, the distal target becomes re-energated and the neuron becomes fully functional; and B) The growth cone is a large actin-supported extension of a regenerating neurite pursuing its corresponding synaptic target. It is responsible for the migration and path finding during neurite extension, in which the lamellipodia and filopodia interact with the adjacent matrix.11

Figure I-3 - Strategies for nerve repair. In the case of a significant nerve gap formation where end-to-end coaptation is not possible, nerve grafts or engineered NGCs are required to serve as a bridge between the nerve stumps and to support axonal regrowth. In the case of grafts, they can be from the patient her/himself, known as the autografts. Allografts and xenografts are also a possibility. As an alternative, if the option falls in the NGCs, those can be nerves harvested from the body, which undergo a process of decellularization to avoid immunological reactions, maintaining the ECM for physical support. NGCs can also be manufactured and engineered with biological or synthetic materials, as well as a combination of both.14

Figure I-4 - Promising results obtained with synthetic polymers applied to PNR. A) A non-woven polylactic acid (PLA) tube. Scale bar: 1 mm; B) SEM images of the PLLA multi-channel conduits cross-section using different magnification. Scale bar: 500, 100 and 10 μm , from top to bottom; C) Scanning electron micrograph of double-walled microsphere following incorporation into PCL nerve guides; and D) Gross appearance of disk-shaped and tubular scaffolds made of OxPVA. A), B), C), and D) were reprinted with from (87),(89), (96) and (99), respectively.20

Figure I-5 - Promising results obtained with natural-origin polymers applied to PNR. A) Example of an enzymatically crosslinked SF nerve guidance conduit developed and patented by Carvalho *et al.* (79) for application in PNR. The developed NGC presents outstanding mechanical properties, with kinking-resistant capacity and suturability, as can be seen by the images (in that row); (B) Images of a 5 % of degree of acetylation chitosan membrane, which can be

further used as a NGC by rolling-up or in a different strategy, as a luminal filler; C) 5 % degree of acetylation chitosan membrane incorporating human hair keratin, developed at our research institute; and D) Confocal laser microscopy showing macro-porous alginate fibers incorporating gelatin particle porogens. Scale bars: 500 μm23

Figure I-6 - Promising results obtained with natural-origin polymers applied to PNR. A) SEM micrographs of transverse section of the oriented collagen-chitosan filler /PCL sheath scaffold and magnification of the interior of the conduit; B) SEM micrograph of the aligned fibrin hydrogel nanofiber and its magnification. Below, a DRGs where the neurites align along the aligned fibers; C) Transversal cryosections of hyaluronic acid conduits cultured for 10 days with Schwann cells in their lumen, after staining with Harris' hematoxylin, Alcian blue, and picosirius red; and D) Longitudinal section of injured nerve treated with PBS (at left) or Laminin (at right), stained with antibodies recognizing NF-h (α -RT97, green). The bar graph illustrates significantly increased axon diameter (μm) with laminin treatment. A), B), C) and D) were reprinted with the permission from (165), (168), (174) and (172), respectively.33

Figure I-7 - Patient-specific and 3D printing technologies will allow improving the treatment given to patients in the future. A) 3D printed complex nerve pathways from 3D scanned bifurcating nerves. Reprinted with permission from (200). B) Imaging of a 3D model of median nerve, for further precise reconstruction. Reprinted with permission from (201), Copyright © 2015, Macmillan Publishers Limited.34

Figure II-1- Basic anatomy of a peripheral nerve. A connective tissue layer, endoneurium, involves the individual axons. An arrangement of axons, designed fascicles, is surrounded by the perineurium, and groups of fascicles are separated by the epineurium. External to this layer is the blood supply derived from major arteries and the latter is involved by the mesoneurium Reprinted with the permission from © 2017 The Author(s). Licensee IntechOpen.48

Figure II-2 - Schematic representation of injury and regenerative process involved in peripheral nerves. (A) Represents the intact nerve, with myelin enwrapping healthy axons; (B) The moment where an injury occurs, instantaneous tissue damage happens at the injury site. After a few hours, macrophages gather at the lesion; (C) The normal Wallerian degeneration process starts roughly one day after the initial trauma and axons start to disintegrate; (D) Enrolment of Galectin-3 macrophages, which contribute to myelin degradation and removal of myelin debris; and (E) The typical degradation of the distal nerve end happens with the participation of the Galectin-3 macrophages and Schwann cells. These cellular components scavenge deteriorated myelin and axonal matter. After the clearance of the debris, Schwann cells proliferate and align, forming the Bungers bands, for future guiding of the regenerating axons. Reprinted with permission from (24), Copyright©2011 Rotshenker; licensee BioMed Central Ltd.50

Figure II-3 - Scheme representing the neuroplasticity that occurs throughout the CNS after PNIs. A) Healthy peripheral nerve being subjected to an injury. Immediately after the trauma, the functionality of the nerve is affected, and the correct neurotransmission is interrupted. Neuroplasticity that occurs in the CNS following PNI is thought to occur through several mechanisms, with two of the most prominent theories being: B) Unmasking of existing synaptic connections. In this process, there is the unmasking of neural paths which were not normally used for a specific purpose, and new neural paths are activated when the normally used system fails; and C) Sprouting of new nerve terminals, where there is collateral sprouting from intact healthy cellular components to a denervated region, in an attempt to reestablish the neuronal connection.52

Figure II-4 - The classic TE model, where a triad of components interact with each other: scaffolds, cells and biological molecules. Overall, it includes the combination of living cells isolated from the patient donor tissue and expanded in culture, with a natural, synthetic, or bioartificial matrix or scaffold. Together with the addition of biological stimuli such as growth factors, a 3D living construct that is structurally, mechanically, and functionally equal to a tissue. The engineered construct can be implanted in the patient in order to restore the damaged tissue.....53

Figure II-5 - Strategies for nerve repair. In the case of a significant nerve gap formation where end-to-end coaptation is not possible, nerve grafts or TE NGCS are required to serve as a bridge between the nerve stumps, to protect the gap and to support axonal regrowth. The diverse option available among grafts and nerve conduits can be seen in the scheme. When considering grafts, they might be autologous, from the same species (allografts) or from different species (xenografts). For the NGCs, they can be biological but previously decellularized conduits, or TE NGCS, made of different materials, such as natural, synthetic, or a combination of both.....56

Figure II-6 - Five different phases of nerve regeneration inside a hollow NGC. The phase corresponds to the sequenced phases of Wallerian degeneration and resulting regeneration mechanism. Phase I corresponds to the fluid phase, where the conduit is filled with plasma exudate containing neurotrophic factors and ECM molecules. This phase takes place a few hours after injury. Phase II corresponds to the matrix formation, where fibrin cables are formed along the gap around one week after injury. Phase III is the cellular phase, where Schwann cells invade the gap, migrate and proliferate. They tend to align along the fibrin cable, forming the Bands of Bungner. Phase IV is axonal phase, which occurs around 2 weeks after injury. The re-growing immature axons use the biological cues provided by Schwann cells to reach their distal targets. Phase V corresponds to the myelin phase. At this time, around 3 weeks post-injury, Schwann cells shift to a myelinating phenotype and produce myelin which is wrapped around each axon, forming the mature myelinated axons.....59

Figure II-7 - Due to the incapacity of hollow NGCs to bridge larger nerve gaps, various filler materials and designs have been developed to enhance the performance of NGCs. A) The initial strategy consisted of simple hollow NGCs; When considering luminal fillers, experiments suggested that the regenerating axons prefer aligned features rather than random orientation. Therefore, many of the approaches focus on obtaining an anisotropic topography. With this strategy in mind, many types of luminal matrices are considered: B) Micro- or nano- filaments resembling the structure of endoneurial tubes; C) Micro/nano groove-patterns; D) Magnetically aligned fibrils or cells; E) Micro-channel filling; F) Unidirectionally freeze-dried; G) Another strategy consist in inserting permissive hydrogels as luminal fillers, being a soft support to regenerative axons; and H) One branch of PNR research also focuses on the controlled delivery of growth factors. That can be achieved, for instance, using crescent gradients of growth factors from the proximal to the distal sites, acting as a biochemical cue and attracting regenerating neurons to reach the final target.61

Figure II-8 - Anisotropic guiding cues have been successfully produced as NGCs luminal fillers. A) Transverse and longitudinal Micro-CT sections of the hollow conduit; AII) Transverse and longitudinal Micro-CT sections of the oriented chitosan-gelatin cryogel as luminal filler; BI) DRG explants seeded on the longitudinal sections of the directionally orientated collagen-chitosan filler, where neurites align in the matrix; BII) 3D reconstruction of axonal regeneration and Schwann cell migration on the orientated collagen-chitosan filler; CI) Schematic drawing of the peripheral nerve

structure; CII) SEM micrograph of the produced silk fibroin NGC fabricated incorporating microchannels, which looks like the depicted schematic; Scale bar 200 μm ; DI) DRG explants seeded in 0.25 % volume of the anisogel, presenting isotropic structure, in which neurites do not orient; DII) DRGs explants seeded in 1 % anisogel in which neurites decide to orient; E) Representative images of DRG explants neurites cultured on random patterns achieved with nanoimprinting lithography with metallic stampers made of three different spacings: EI) on a flat surface; EII) On a Blu-Ray disc spacing; EIII) On a digital video disc spacing; and EIV) On a compact disc spacing. Scale bar: 200 μm . Figures have been reprinted and adapted from: A) (128), B) (104), C) (129), D) (130), and E) (131).67

Figure II-9 - Different strategies for incorporation and delivery of GFs from NGCs. One of the simplest approaches is based on simply blending the NTFs on the polymer, with or without further crosslinking of the polymer. Microspheres containing NTFs can also be blended in the polymer. At the surface, NTFs can be found just after an adsorption process or conjugated with other molecules for stronger entrapment or covalent links. When considering the delivery of NTFs from the lumen, several approaches can be followed, such as using engineered cells, nanofibers or hydrogels capable of loading and releasing the NTFs.69

Figure II-10 - Proof of concept regarding the fabrication of a silk fibroin NGCs incorporating a gradient of GFs. A) Schematic of a NGC incorporating two different concentrations of GFs in the wall of the conduit. In principle, the gradient of GFs increases from proximal to the distal, therefore attracting the growing axons to reach their distal target. B) Stereomicrograph of a silk fibroin NGC presenting a gradient along the walls. The orange color represents the chosen Concentration 1, followed by the white color, representing Concentration 2. As it can be assessed, there is no separation in the conduit between the different concentrations, as the conduit is totally uniform. Scale bar: 1000 μm73

Figure II-11 - Schematic on some known mechanisms of how miRNAs can intrinsically control and impact peripheral nerve injury and regeneration. After an injury, the myelin and axons degrade, and Schwann cells dedifferentiate. As these phenomena happen, the molecular regulators (*e.g.* miRNA-221, miRNA 222, and Let-7) can influence neurite outgrowth and modulate phenotypic changes in Schwann cells, as well as their myelinating capacity, among others.76

Figure III-1 - Nanotechnology applied to peripheral nerve regeneration and reconstruction. Carbon nanomaterials, nanoparticles, nanofibers, nano-topographic cues and theranostics and nano-imaging are some of the areas in nanomedicine that should be explored in order to improve tissue bifunctionality.108

Figure III-2 - Schematic representation of the anatomy of peripheral nerve and degeneration and regeneration after an injury. A) Scheme of peripheral nerve anatomy); B) Degeneration and regeneration after peripheral nerve injury. (I) Normal neuron; (II) Wallerian degeneration. Schwann cells proliferate, and macrophages invade the distal nerve segment and phagocytosis of degrading materials; (III) Schwann cells in the distal end align in bands of Bungner; and (IV) Axonal re-joining with distal end and organs; and C) Axonal sprouts advance entrenched with aligned Schwann cells. Reprinted and adapted from A) [351]; B) [18]; C) [14].110

Figure III-3 - General phenomena impairing peripheral nerve regeneration, such as inflammation, excessive scar tissue or lack of vascularization. A) Macrophage plasticity in tissue repair, where M1 pro-inflammatory macrophages can change phenotype into M2 pro-regenerative macrophages; B) After injury, fibroblasts that are attracted to the injury site deposit excessive collagen that leads to perineural adhesions and intraneural fibrosis; and C) Macrophage-

induced blood vessels guide Schwann cell to cross the nerve gap. Reprinted and adapted from A) [67]; B) [320]; C) [76].....116

Figure III-4 - Carbon nanomaterials structure and their application of in peripheral nerve regeneration. A) (I) Single and multi-walled carbon nanotubes schematic structure. (II) Nanodiamond schematic structure; B) Schematic representation of the aligned PGF bundle interfaced with carbon nanotubes for neurite outgrowth; C) DRGs neurite outgrowth can be promoted by 50 mV/mm electrical stimulation or inclusion of 20 µg/mL SWCNTs. The occurrence of both has a synergistic effect; D) Fluorescent nanodiamonds internalized into dissociated neurons. Confocal image of dissociated mouse cortical neurons cultured in the presence of 20 µg/mL fluorescent Nanodiamonds, stained with Alexa Fluor 488-conjugated concanavalin-A and DAPI. Reprinted and adapted from A) (I) [352] and (II) [151]; B) [89]; C) [115]; D) [158].....125

Figure III-5 - Magnetic nanoparticles applied to peripheral nerve regeneration. A) MNPs bind to the injured nerve and a magnetic field is applied, creating mechanical tension. This stimulates nerve regeneration in the direction forced by the magnetic field. This physical guidance is envisioned to direct more efficiently the regeneration of the injured nerve from the proximal toward the distal stump; B) Schwann cells-astrocytes confrontation assay. Magnetized Schwann cells (in green) and astrocytes (in red) were seeded in parallel stripes and were allowed to migrate and intermingle for 1 week under applied magnetic field; C) NGF gradients generated by MNPs are able to direct the growth of extending neurites from chick DRGs. (I) NGF-cNPs directed the extension of neurites from DRG. (II) Control cNPs had no effect on the directional outgrowth of extending neurites, and respective polar histograms (below); and D) Sagittal and axial MRI of experimental animals receiving MSCs in sciatic nerve gap. Animals were implanted with MSC-loaded nerve conduits and MRI images were taken at different time points post-implantation. Arrows indicate the visible location of Fe₃O₄ NPs-labeled cells. Scale bar: 1 mm. Reprinted and adapted from A) [183]; B) [185]; C) [191]; D) [188].....143

Figure III-6 - The effect of other nanoparticles in peripheral nerve regeneration. A) The use of gold nanoparticles in PNR: examples of epifluorescence images of NG108-15 neuronal cells cultured with Au, PSS/Au, and SiO₂/Au NRs and labeled with β-III tubulin (red) and DAPI (blue). The effect of PSS/Au and SiO₂/Au NRs on the percentage of neurons with neurites is evident; and B) Doxycycline-inducible GDNF expression and respective regeneration scenarios in the distal sciatic nerves of experimental 3 weeks' time point. Continuous GDNF expression (dox+/+) causes some axons to avoid the regenerative path; time-restricted GDNF expression (dox+/-) leads to unobstructed and profuse regeneration; White arrows indicate the direction of axonal regeneration (proximal to distal). Total magnification: 100x. Reprinted and adapted from A) [193]; B) [225].....155

Figure III-7 - The use of exosomes in peripheral nerve regeneration. A) Representative transmission electron micrographs of Schwann cell-derived exosomes in DRG axons, after staining exosomes with p75^{NTR}-gold labeling on their surface; B) Axonal regeneration of DRGs after vehicle (Ctrl) or exosome (Exo) treatment for 5 days. DRGs are stained for acetylated tubulin (Ac-Tub, green), Phalloidin-Rhodamine (Phall, red) and nuclei (DAPI, blue). Scale bar: 50 µm. Reprinted and adapted from [256]159

Figure III-8 - The application of nanofibers in peripheral nerve regeneration. A) Schematic representation of the electrospinning process; B) DRG axon outgrowth after fluorescent staining with β-tubulin (green) and DAPI (blue), when cultured on (I) Matrigel® coated coverslips without NGF (negative control conditions; (II) Matrigel® coated

coverslips with 50 ng of NGF/mL in medium (positive control conditions); (III) DRGs seeded on 300 nm fibers; (IV) DRGs seeded on 600 nm fibers; (V) DRGs seeded on 1000 nm fibers; and (VI) DGRs seeded on 1300 nm fibers. Scale bar: 20 μ m; C) Representative images of DRGs cultured for 5 days on aligned and random scaffolds in the presence or absence of microspheres. Samples without microspheres were supplemented with 50 ng/mL of NGF. Aligned fibers direct neurite outgrowth. Scale bar: 250 μ m; D) Use of PPY/PLCL combined with electrical stimulation in peripheral nerve regeneration. (I) The animal operation procedure immediately after 15 mm conduit implantation; (II) Circle electrode implantation; (III) Harvested regenerated nerve at 8 weeks post-implantation; and (IV) 8 weeks post-implantation histological section of the electrode contact site stained with H&E (white arrows indicate the electrode contact site). Reprinted and adapted from A) [276]; B) [281]; C) [291]; D) [297].165

Figure III-9 - The influence of nano-scaled topographic cues on cellular behavior. A) Focal adhesion establishment by stimulating PC12 contacting nanogratings with increasing ridge width. EGFP fluorescent signal in PC12 cells differentiating on nanogratings with a ridge width corresponding to (I) 500nm; (II) 750 nm; (III) 1000 nm; (IV) 1250 nm; (V) 1500 nm; and (VI) 1500 nm. White arrows indicate the direction of the nanografting. Scale bar: 10 μ m; and B) (I) Leech neurons growing atop control substrates pre-coated with concanavalin-A. No preferable growth direction can be detected; and (II) Leech neurons growing on nano-patterned substrates pre-coated with concanavalin-A. Pattern ridges of 25 nm in height. The neuronal branches attach to the ridges and the whole growth pattern is aligned according to the topographic cues. Reprinted and adapted from A) [309]; B) [312].174

Figure III-10 - The application of theranostics and nanoimaging in peripheral nerve regeneration. A) Images of SPION-labeled GFP-dADSCs sciatic nerve. (I) MR images of operated sciatic nerve 28 d after transplantation; (II) Photograph of nerve that has been transplanted with GFP-dADSCs; (III) Fluorescent images of the nerve that has been transplanted with GFP-dADSCs; (IV) Positive control of I; (V) Positive control of II and (VI) Positive control of III. White arrows point to the regenerated sciatic nerve; B) *In vivo* and *ex vivo* $^{19}\text{F}/^1\text{H}$ MRI of experimental autoimmune encephalomyelitis rat shows ^{19}F signal arising from the spinal cord and adjacent vertebral bone marrow, representing accumulation of inflammatory phagocytes; C) Perfluorocarbon nanoemulsion, which is phagocytosed by inflammatory cells, was used in a rat pain model. The nanoemulsion is a near-infrared (NIR) lipophilic fluorescence tracer. The images demonstrate that in live rats, NIR fluorescence is concentrated around the affected sciatic nerve or in the area where incision was made, both reporting the site of macrophages location; and D) *In vivo* ^{19}F MRI performed 5 days after induced nerve injury. In each rat, the fluorine marker uptaken by macrophages could be exclusively found in the left affected thigh, to where macrophages migrated. Two small bilateral “hot spots” are illustrated close to the spine which represent draining lymph nodes where marked macrophages also accumulate; and Reprinted and adapted from A) [336]; B) [337]; C) [338] D) [339].180

Figure IV-1 - Chemical structure of chitin, chitosan and protonated chitosan polymer.203

Figure IV-2 - Chemical structure of native (acetylated) and deacetylated gellan gum. Reprinted with permission from [57].206

Figure IV-3 - Silk cocoons purification process. *Bombyx mori* silk cocoons give origin to purified SF after sericin extraction through degumming procedure. Scale bar of the cocoon: 1 cm.209

Figure IV-4 - Schematic illustration of the natural SF protein composition. (A) H-L complex formation. (B) H-chains organizing themselves together into β -sheet structures. (C) β -sheet structures linked by amorphous domains.....211

| | |
|---|-----|
| Figure IV-5 - Structure of intermediate filament, micro and macro fibril and hair, represented in a cross-section of hair; B) Representative images of keratin extraction steps. Reprinted with permission from [125]. | 213 |
| Figure IV-6 - NTFs used in this thesis, NGF and GDNF. | 215 |
| Figure IV-7 - Prospect of developing novel tubulization strategies for transected nerves based on chitosan membranes, after rolling the membranes to form NGCs. Scale bar: 3 mm. | 217 |
| Figure IV-8 - Schematic representation of hydrogel and freeze-dried hydrogel polymeric network microstructure, which favors cell adhesion. Reprinted with permission from [168]. | 218 |
| Figure IV-9 - Different aspects of the formulations throughout the production process: A) Scheme of a scaffold with the intended microstructure of vertically aligned channels; B) Hydrogel obtained after the ionic PBS cross-linking; C) Hydrogel punched with branched wires to display longitudinal porous channels; D) Freeze-dried hydrogel; E) Re-hydrated freeze-dried hydrogel resembling the initial scheme. Scale bar: 1 mm. | 223 |
| Figure IV-10 - Production of freeze-dried hydrogel filling for chitosan NGC. 2 mm hydrogel-free segments were left at each extreme of the conduit, for nerve insertion and suture purposes. Scale bar: 2 mm. | 224 |
| Figure IV-11 - Concentrated aqueous SF solution in a 50 mL Falcon. Scale bar: 1.5 cm. | 225 |
| Figure IV-12 - Micropipettes Gilson M100 and M1000, specifically designed for hydrogel use. Scale bar: 1 cm. | 225 |
| Figure IV-13 - Scheme representing the fabrication methodology of enzymatically crosslinked SF NGCs in Chapters VIII and IX. | 226 |
| Figure IV-14 - Scheme representing the two different techniques to incorporate NTFs, which are highlighted in (i) and (ii), as the Crosslinking method and the Absorption method, respectively. This methodology was used in Chapter X. | 228 |
| Figure IV-15 - Stereomicroscope from Zeiss, used for macroscopic evaluation of samples in this thesis. Scale bar: 5 cm. | 229 |
| Figure IV-16 - SEM with EDS analyzer. The SEM (JSM-6010 LV, JEOL, Japan) instrument is equipped with the low vacuum mode as a standard feature. The low vacuum mode allows non-conductive specimens to be observed and analyzed without conductive coating. This SEM is equipped with an energy dispersive spectroscope (EDS). Scale bar: 10 cm. | 230 |
| Figure IV-17 - Micro computed tomography for non-destructive 3D analysis of bulk structure of scaffolds. Output is the general structure as a 3D model with micrometer resolution, more importantly the subsequent analysis can yield information in relation to pore size, pore distribution and pore interconnectivity in 3D. Scale bar: 10 cm. | 231 |
| Figure IV-18 - The AFM is able to acquire images of flat surfaces that can encode the surface topography, mechanical response, among other properties. The equipment presents a series of accessories that allows the acquisition of data in liquids and air. In the case of liquids, it is also possible to control the temperature of the experiments. Scale bar: 10 cm. | 233 |
| Figure IV-19 - Interfacial tension at the 3-phase contact line. (a) Contact angle on a solid surface and (b) Vectorial equilibrium for a drop resting on a solid surface to balance three forces (contact angle forces): the interfacial tensions between, | |

| | |
|--|-----|
| solid and liquid (γ_{sl}), solid and vapour (γ_{sv}), and liquid and vapour (γ_{lv}), resulting in Young's equation $\gamma_{sv} = \gamma_{sl} + \gamma_{lv} \cos \theta$ used measure what is referred to as surface energy. | 234 |
| Figure IV-20 - The contact angle Goniometer allows the measurement of static and dynamic contact angles on a thermostated sample stage. Surface energy of solids and liquids surface tension can be calculated. Scale bar: 10 cm.... | 235 |
| Figure IV-21 - D8 ADVANCE Twin with DAVINCI Design - The intelligent beam path components of the D8 ADVANCE with DAVINCI design provide true plug-in play functionality requiring minimum or even no user intervention. Featuring automatic and tool-free switching of the diffraction geometry without the need for complex adjustments, the D8 ADVANCE Twin with DAVINCI design broadens the analytical capabilities for a wide community of X-ray diffraction users Scale bar: 10 cm..... | 236 |
| Figure IV-22 - The Fourier transform infrared (FTIR) spectrometer is used as a standard chemical characterization technique. The samples can be analyzed as films, KBr discs, powder or liquids. The available methodologies comprise transmittance, specular reflectance, diffuse reflectance and attenuated total reflectance (ATR). Scale bar: 10 cm... | 237 |
| Figure IV-23 - Differential scanning calorimetry is a thermal analysis technique that detects the temperatures and heat flows caused by changes in heat capacity or by endothermic and exothermic processes of materials as a function of time and temperature. Scale bar: 10 cm..... | 238 |
| Figure IV-24 - Universal mechanical testing machine (INSTRON 5540) capable to perform tensile, compression and flexural tests. A high range of specimens, including compact biomaterials, acellular and cell-seeded scaffolds, native tissue samples (e.g. bone or cartilage) and tissue engineered constructs can be tested. Tests can be performed under temperature control (using an environmental chamber) or with the samples immersed into a solution. Scale bar: 10 cm. | 240 |
| Figure IV-25 - Enzymatically crosslinked SF conduits being tested in tensile mode with Instron equipment. Scale bar: 10 mm. | 240 |
| Figure IV-26 - DMA with environmental control. The testing can be done to analyses the influence of frequency of applied force and solution conditions (Temperature, pH, ionic strength etc.), and how the mechanical properties change over time (e.g. caused by degradation or mineralization within the bulk of the sample). Scale bar: 10 cm. | 241 |
| Figure IV-27 - In-house developed kinking and suturability tests performed in the produced enzymatically crosslinked SF NGCs. Scale bar: 10 mm. | 242 |
| Figure IV-28 - Illustrative image of the specimens immersed into the SBF solution. | 247 |
| Figure IV-29 - Scheme illustrating the molecular permeability to be achieved in NGCs. | 248 |
| Figure IV-30 - Scheme depicting DRG isolation. Scale bar: 1 cm. | 252 |
| Figure IV-31 - Scheme representing the setup of the <i>in vitro</i> cellular permeability assay. A) Fluoroblock insert; B) Representative scheme of the components involved in the assay inside a well plate; C) In case of cellular migration, those are quantifiable on the other side of the membrane. | 255 |
| Figure IV-32 - Scheme depicting how CyQuant® Cell Proliferation kit works. | 258 |

| | |
|--|-----|
| Figure IV-33 - Scheme of the methodology used in the NTF release and quantification assay by ELISA. | 259 |
| Figure IV-34 - Scheme representing the steps in the <i>in vivo</i> CAM assay. | 263 |
| Figure IV-35 - Animal and sample distribution for <i>in vivo</i> subcutaneous assay. | 264 |
| Figure IV-36 - Scheme of the nerve cutting tool used in the <i>in vivo</i> study, to precisely hold and cut the sciatic nerve during surgery. Tools were 3D-printed using poly (lactic acid) and consisted of a hook with an inner diameter of 2.5 mm and a scalpel alignment groove 700 μm in width. | 267 |
| Figure IV-37 - Transparent NGCs can offer the opportunity to assess parameters related to regeneration, such as inflammation or the presence of a nerve cable, at the moment of explant. Scale bar: 3 mm. | 268 |
| Figure IV-38 - Scheme of cross-section histological cutting for the 3 weeks timepoint samples in Chapter VII. | 269 |
| Figure IV-39 - Scheme for histological cut of the enzymatically crosslinked SF NGC after explant in Chapter X. | 269 |
| Figure V-1 - Surface characterization of chitosan membranes (i – DA I; ii – DA II; iii – DA III). A) Scanning Electron Microscopy micrographs. Scale bar 5 μm ; Magnification 5,000 \times ; B) Atomic Force Microscope three dimensional images of chitosan membranes under simulated physiological conditions by previous 2 hours immersion of samples in PBS. 5 μm \times 5 μm scan area; Contact mode. | 299 |
| Figure V-2 - Physicochemical characterization of chitosan membranes (i – DA I; ii – DA II; iii – DA III). A) Fourier Transforming Infrared Spectroscopy analysis. 32 scans with resolution of 4 cm^{-1} , corresponding to the 4000-400 cm^{-1} spectra region. B) X-ray diffraction patterns of the studied chitosan membranes. Fixed incidence angle of 1 $^\circ$ between the incident X-rays and specimen plane. C) Differential Scanning Calorimetry thermograms of chitosan membranes. Second heating cycle, ranging from 0 $^\circ\text{C}$ to 350 $^\circ\text{C}$ at a rate of 1 $^\circ\text{C}/\text{minute}$. D) Mechanical properties analysis of chitosan membranes. Storage modulus (E) and loss factor ($\tan \delta$) of the three studied chitosan membranes measured as a function of frequency. Studies performed at room temperature. | 302 |
| Figure V-3 - Weight loss and water uptake of chitosan membranes at 37 $^\circ\text{C}$ for different time periods; A) Weight loss of studied chitosan membrane formulations after storage in PBS; B) Weight loss of studied chitosan membrane formulations after storage in PBS with 13 mg/L of lysozyme; C) Water uptake of samples after storage in PBS. The data represents the mean for each timepoint \pm standard deviation. | 304 |
| Figure V-4 - Scanning Electron Microscopy micrographs of chitosan membranes (i – DA I; ii – DA II; iii – DA III). A) Micrographs of dry unmodified surface; and B) Micrographs of dry membranes after 30 days in PBS in the presence of 13 mg/L of lysozyme. Scale bar: 5 μm | 305 |
| Figure V-5 - Scanning Electron Microscopy and EDS analysis of chitosan membranes after 1 and 30 days in SBF: A) DA I after 1 day in SBF; B) DA II after 1 day in SBF; C) DA III after 1 day in SBF; D) DA I after 30 days in SBF; E) DA II after 30 days in SBF; and F) DA III after 30 days in SBF. Scale bar: 5 μm | 306 |
| Figure V-6 - Viability live/dead assay of cell lines after 1, 3 and 7 days after direct seeding on chitosan membranes. Live cells stained with Calcein (green color) and dead cells stained with propidium iodide (red color). A) L929 cell line viability on chitosan films; and B) Schwann cell line viability on chitosan films. Scale bar: 200 μm | 308 |

Figure V-7 - *In vitro* cell culture studies: A) Metabolic activity of L929 cells seeded on chitosan films determined by Alamar Blue after 1, 3 and 7 days; B) Metabolic activity of Schwann cells seeded on chitosan films determined by Alamar Blue after 1, 3 and 7 days; C) Proliferation of L929 cells seeded on chitosan films determined by CyQUANT® Cell Proliferation Assay Kit after 1, 3 and 7 days; and D) Proliferation of Schwann cells seeded on chitosan films determined by CyQUANT® Cell Proliferation Assay Kit after 1, 3 and 7 days.309

Figure V-8 - Phalloidin/DAPI staining of cell lines after 1 (i), 3 (ii) and 7 (iii) days after direct seeding on chitosan membranes. A) L929 cell line morphology on chitosan films; and B) Schwann cell line morphology on chitosan films. Scale bar: 50 μm312

Figure VI-1 - Macro and microphotographs of the developed CHT and CHT/keratin membranes revealing its surface topography. A) Photographs of the membranes taken by stereomicroscope:i) smooth surface of CHT membrane, ii) rough surface of CHT/keratin membrane, iii) comparison between CHT and CHT/keratin membranes; B) SEM microphotographs of the developed membranes:i-ii) CHT membrane, iii-iv) CHT/keratin membrane; C) AFM three dimensional images of developed membranes, 10 μm \times 10 μm scan area, contact mode of the i) CHT and ii) CHT/keratin; D) Quantitative information regarding the average roughness (Ra) and root mean square roughness (Rq) of the i) CHT and ii) CHT/keratin membranes. Two-tailed Mann Whitney Test was used ($p < 0.05$) and statistically significant differences were represented by *** ($p < 0.001$). Scale bars: A) 500 μm ; B) 500 μm (i and iii) and 50 μm (ii and iv).338

Figure VI-2 - Physicochemical characterization of CHT and CHT/keratin membranes. A) FTIR spectra of the produced membranes and keratin powder. Arrows point to specific and characteristic peaks of each component, which are also visible in the final blending membrane; B) XRD pattern of the produced membranes. In the upper right side (green line), at a different scale, is the XRD pattern of keratin powder; C) Dynamic mechanical analysis of the membranes. Storage modulus (E' , black lines) and loss factor ($\tan \delta$, blue lines) of samples measured as a function of frequency; D) Differential Scanning Calorimetry thermograms of developed membranes. Arrows point to specific and characteristic peaks of each component, which are also visible in the final blending membrane; E) Percentage of weight loss of the developed membranes after incubation in PBS for different periods of time. The data represents the mean for each timepoint \pm standard deviation; F) Percentage of water uptake of the developed membranes after incubation in PBS for different periods of time. The data represents the mean for each timepoint \pm standard deviation.343

Figure VI-3 - Short term cytotoxicity and qualitative adhesion study of L929 fibroblasts. A) Metabolic activity of L929 fibroblasts incubated with leachables from CHT and CHT/keratin developed membranes. Kruskal-Wallis test was performed followed by Dunn's multiple comparison test, $p < 0.05$; B) Fluorescence photomicrographs of qualitative adhesion study where L929 fibroblasts were seeded on CHT and CHT/keratin membranes and compared to the positive control (TCPs). Cells were subjected to DAPI/phalloidin staining after fixation. Scale bar: 50 μm345

Figure VI-4 - Metabolic viability and cellular cytoskeleton morphology of BJ fibroblasts, Schwann cells and endothelial cells when seeded on CHT and CHT/keratin membranes, at 1, 3 and 7 days of culturing. At left, graphical representation of the quantification of metabolic activity of each cell type up to 7 days of culturing. On the right, fluorescence micrographs of DAPI/Phalloidin stained cells, up to 7 days of culturing. Scale bar: 50 μm346

Figure VI-5 - Angiogenic response of the CHT-based membranes evaluated in the CAM assay. (A) Ex ovo quantification of the macroscopic blood vessels converging to the implanted CHT and CHT/Keratin membranes and to the positive control Filter paper, after 4 days of implantation. The mean number of convergent blood vessels results from the counts of three independent observers of a minimum of 19 discs per implant. Statistical analysis was performed using one-way analysis of variance followed by Tukey's post-test. Symbols denote significant differences for *p < 0.05, **p < 0.01 and ****p<0,0001. (B) In ovo and ex ovo stereomicroscopy photographs of the CAM with the implanted materials after 4 days of implantation and light microscopy representative images of the respective 4 μm-sagittal CAM sections stained with H&E and lectin. The black arrows indicate infiltrated chick endothelial cells and the white arrows indicate the tendential migration of the erythrocytes and micro-vessels to the proximity of the CHT/keratin membranes.348

Figure VI-6 - The developed CHT/keratin membrane exhibited superior characteristics when compared to simple CHT membranes, both on a physico-chemical as well as on a biological level. When envisioned to be applied in Peripheral Nerve Regeneration, different strategies can be used according to the severity of nerve injury. PNW should be used when the nerve is injured but the cable is intact. NGC must be used the nerve is severed and the result is a non-suturable gap. At last, a luminal filler must be added to a NGC when the nerve cable cannot regenerate on its own due to the excessive long gap formed, and an extra guiding path is necessary for the nerve to reach the proximal side.352

Figure VII-1 - Macro- and microstructure evaluation of the developed formulations. The first row of images corresponds to the different aspects of the formulations throughout the production process: A) Scheme of a scaffold with the intended microstructure of vertically aligned channels; B) Hydrogel obtained after the ionic PBS crosslinking; C) Hydrogel punched with branched wires to display longitudinal porous channels; D) Freeze-dried hydrogel; E) Re-hydrated freeze-dried hydrogel resembling the initial scheme. The second row of images corresponds to SEM micrographs of the freeze-dried formulations: F) Surface cross-section of the scaffold; G) Longitudinal cut of the scaffold. White arrows point to the aligned channels made by the punching (right), which differ from the random network porosity (left); H) Longitudinal section of a chitosan NGC (arrows pointing to the wall of it) filled with GG freeze-dried hydrogel and I) Cross-section of the chitosan NGC (arrows pointing to its wall) filled with GG freeze-dried hydrogels. The third row of images reveals the structure of the biomaterials after Micro-CT 3D reconstructions: J) 3D reconstructions of freeze-dried GG networks; K) 3D reconstructions of final NGCs constructs. As the aspect of all the studied formulations was very similar, the previously presented images are representative of all of them. Scale bars: 1 mm.....372

Figure VII-2 - Percentage of water uptake and weight loss of the developed GG freeze-dried hydrogels. The graphics represent the water uptake and weight loss values corresponding to all the studied formulations along the 30 days of study. The evaluations were performed at 37 °C.....373

Figure VII-3 - Biocompatibility of GG formulations with immortalized Schwann cells (iSCs) *in vitro*. A) Metabolic activity of iSCs seeded on freeze-dried hydrogels formulations after up to 7 days; determination by Alamar Blue; n =3. B) Representative Live/Dead qualitative assay images after direct iSC seeding on freeze-dried hydrogels formulations after up to 7 days; determination by Calcein AM (green fluorescence) and propidium iodide (red fluorescence). Scale bars: 200 μm.375

Figure VII-4 - Micro-computed tomography (micro-CT) evaluation of the explants 12 weeks after surgery and correlation to a corresponding H&E stained histological section. For each sample, different characterization images are displayed in a panel, from left to right: 3D micro-CT reconstruction image, corresponding histograms concerning three areas of the conduit (top, middle and bottom), 2D micro-CT reconstructions (longitudinal sections in vertical and horizontal images and cross section in quadratic box image) and histological sections (H&E staining) in the upper left part of each panel. Notice that in the case of the NGCs just lumen area was selected as a Region of Interest (ROI) for the 3D reconstruction, thus excluding the chitosan tubes from the analysis. All samples were covered with parafilm to avoid water evaporation. A) Positive control where the autologous nerve graft is visible involved by parafilm. B) The representative NGC60:40 sample shows no signs of cellular or tissue ingrowth the NGC or the central GG matrix; C) The representative NGC50:50 sample shows some tissue inside the NGC/ the GG matrix (indicated by the black arrows); D) The representative NGC25:75 shows some tissue ingrowth (indicated by the white arrows). Scale bar: 500 μm380

Figure VII-5 - Representative photomicrographs of the studied formulations after hematoxylin-eosin (H&E) staining. Schematic representation of the cross-sections positioning (top row, example NGC is placed on scale paper with 1mm intersections). Row 2-4: H&E stained cross-sections corresponding to chitosan hollow NGCs (positive control for the ST study) and NGCs filled with different GG freeze-dried formulations (NGC60:40, NGC50:50, NGC25:75) explanted 3 weeks after reconstruction. Black arrows point to regenerated tissue in the respective cross-sections. Asterisks are placed where residual GG is visible inside the NGCs. Scale bars: 200 μm382

Figure VII-6 - Representative photomicrographs of histologically stained NGCs with GG fillings 6 and 12 weeks after reconstruction. Longitudinal sections for each sample after H&E staining can be seen at left and respective immunohistochemistry staining's for NF200, ED1 and DAPI at right. A) Positive control (Hollow conduit at 6 weeks (ST study) and autologous nerve graft (LT study) at 12 weeks. B) NGC60:40 sample; C) NGC50:50; D) NGC25:75. Proximal nerve end is on the top and distal nerve end is on the bottom. Asterisks mark the visible GG in light pink. Scale bars: 500 μm384

Figure VII-7 - Detection of neovascularization in the implanted formulations. Representative photomicrographs of immunohistologically stained sections correspondent to the studied formulations. Stains were performed for the detection of CD31 (green) and CD34 (red) after 3, 6- and 12-weeks post-reconstruction. Photomicrographs correspond to the central zone of the conduits. A) Positive control (at 3 and 6 weeks is a hollow NGC and at 12 weeks is an ANG; B) NGC60:40; C) NGC50:50; D) NGC25:75; Scale bars: 50 μm385

Figure VII-8 - Representative photomicrographs of myelinated axons visualized in distal peripheral nerve segments 12 weeks after reconstruction. High resolution images of representative semithin sections, stained with Toluidine blue, of nerve samples from a (A) healthy sciatic nerve and (B) regenerated through an ANG; (C+D) NGC50:50 conduit, and (E+F) NGC25:75 conduit. Scale bars: 20 μm386

Figure VIII-1 - Schematic representation of the processing method of a tubular conduit/ nerve guidance conduit of silk fibroin.....425

Figure VIII-2 - Schematic representation of embodiment of a tubular conduit/nerve guidance conduit of silk fibroin after production. Scale bar of A), B) and C): 5 mm; Scale bar of D) and E): 3 cm.....425

| | |
|--|-----|
| Figure VIII-3 - Schematic representation of possible methods for obtain the tubular conduit described in the present disclosure..... | 426 |
| Figure VIII-4 - Schematic representation of kinking resistance ability of thick wall conduits. Scale bar: 7mm..... | 426 |
| Figure VIII-5 - Schematic representation of SEM micrographs revealing the increased porosity achieved by reducing silk concentration from 16 % to 8 %. The cross-section is specially affected, with high interconnectivity from the inner to the outer walls of the conduit. Scale bar: 5 μ m (top micrographs) and 50 μ m (bottom micrographs)..... | 427 |
| Figure VIII-6 - Schematic representation of: A) Stereomicroscope pictures of the different silk conduits obtained with different drying methods; B) SEM micrographs of the different silk conduits obtained with different drying methods that lead to different micro-structure and porosity. Scale bar: 500 μ m (first row); 100 μ m (second row); 5 μ m (third row). | 428 |
| Figure VIII-7 - Schematic representation of: A) 3D micro-CT reconstruction of thick and thin wall conduits obtained used different sized molds; B) SEM micrographs of the mentioned conduits, where wall thickness varies; C) Stereomicroscope images of thick and thin wall conduits, in hydrated and dry state. Scale bar: B) top row: 500 μ m; B) middle row: 100 μ m; B) bottom row: 5 μ m. | 429 |
| Figure VIII-8 - Schematic representation of silk conduits containing gradients of bioactive molecules. A) Scheme of desired prototypes containing three different and increasing concentrations, from proximal to distal sites; B) Fabrication of a silk conduit (hydrogel step) with three different zones, that correspond to different growth factor concentrations; C) Different concentrations interface of obtained silk conduit. Scale bar: 200 μ m. | 430 |
| Figure VIII-9 - Schematic representation of a simple hydrated silk conduit (white) when compared to a conductive silk/polypyrrole conduit (black). Scale bar: 500 μ m. | 430 |
| Figure VIII-10 - Schematic representation of a silk conduit when incorporating just 1% of hair keratin in the silk polymeric solution, cellular adhesion increased, which is proved qualitatively by Live/dead assay as well as quantitatively, by Alamar blue assay; (1 % FD Keratin = freeze-dried conduit containing 1 % keratin). Scale bar: 50 μ m. | 431 |
| Figure VIII-11 - Schematic representation of the degradation profiles of several silk fibroin conduits formulations in the presence of 0.2 U/mL of protease for 30 days. By varying only the method of drying, weight loss <i>in vivo</i> and <i>in vitro</i> will be modified; (FD = freeze-dried; AD = air dried at 50 °C; Eth = Directly from ethanol; FDMP= Freeze-dried more porous..... | 432 |
| Figure VIII-12 - SEM micrographs and respective EDS spectra of the silk conduits after 30 days in Simulated Body Fluid. Scale bar: 10 μ m..... | 432 |
| Figure VIII-13 - Schematic representation of mechanical properties of some embodiment of the silk conduits: Tensile stress and Tensile modulus; (FD = freeze dried; AD = air dried at 50 °C; Eth = Directly from ethanol; FDMP= Freeze dried more porous). Scale bar: 1 cm..... | 433 |
| Figure VIII-14 - Differences in the silk fibroin conduits permeability of a 4 kDa molecule due to the method of drying and due to the thickness of the conduit's wall. Scale bar: 1 mm. | 433 |
| Figure VIII-15 - Schematic representation of: A) Results of Alamar Blue cellular density quantification and Live/dead qualitative assay after Schwann cells were seeded in all formulations of thick wall tubes after 7 days. B) Results of | |

| | |
|--|-----|
| Alamar Blue cellular density quantification and Live/dead qualitative assay after BJ skin fibroblasts were seeded in all formulations of thick wall tubes after 7 days. Scale bar: 50 μm | 434 |
| Figure VIII-16 - Schematic representation of: Longitudinal view of thick and thin wall conduits after 4 weeks <i>in vivo</i> subcutaneous implantation in mice. Scale bar: 2000 μm | 435 |
| Figure IX-1 - Scheme of the steps involved in the methodology developed to produce silk fibroin TCs. An intermediate step mediated by enzymatic crosslink allows to obtain a silk fibroin hydrogel inside the mold. As a final step, three different processing methods were explored: freeze-drying after freezing at -80 $^{\circ}\text{C}$ (TC 1), drying in an oven at 50 $^{\circ}\text{C}$ (TC 2) or simply leaving them in a hydrated state without ever extracting the solvent (TC 3). | 451 |
| Figure IX-2 - Macro and microphotographs of the developed silk conduits. A and B) Macrophotographs taken by stereomicroscopy (top) and SEM microphotographs (bottom) of the thick and thin silk conduits, respectively. At right, micro-CT reconstruction of the conduits. For thickness comparison, the TC 3 was left to dry at room temperature (RT). C) Representative SEM microphotographs corresponding to the external, internal and cross-section microstructure of the thick conduits (TC 1 and TC 2). The TC 3 was not suitable for SEM microstructure evaluation. Scale bar: A and B) 2 mm (top), 500 μm (bottom). Micro-CT 3D reconstruction: 1 mm. | 452 |
| Figure IX-3 - Mechanical properties and kinking resistance of the developed silk-based conduits. A and B) Strain (%) as a function of Tensile Stress (MPa) applied in thick and thin conduits. C) Tensile Modulus of thin and thick conduits, according to the methodology (TC 1, TC 2 and TC 3). Quantitative data is presented as mean \pm sd (n=5), where *p < 0.05, **p < 0.01. D and E) Kinking tests performed on thick and thin conduits after bending to 50 $^{\circ}$. Thick conduit revealed to resist bending, with no occlusion of the lumen at this degree, whereas thin conduits did not resist, showing occlusion of the lumen. | 455 |
| Figure IX-4 - <i>In vitro</i> weight loss, water uptake and bioactivity evaluation of the developed silk fibroin-based conduits. A and B) Weight loss of the different thick and thin conduits, respectively, performed by immersion in a PBS protease XIV solution (0.2 U/mL) up to 30 days. C and D) Water uptake profile of the thick and thin conduits, respectively, in a PBS solution up to 30 days. E) Bioactivity assay for the thick silk conduits where results are shown as EDS spectra and SEM microphotographs. The SEM images of the conduits external surface revealed the presence or absence of cauliflower crystals. The results show the absence of an apatite layer in TC 1 and TC 3 but revealed the presence of such crystals in the surface of TC 2. Quantitative data is presented as mean \pm sd (n=3). | 457 |
| Figure IX-5 - Molecular and cellular permeability evaluation of the developed silk-based conduits. A) Graphical representation of the desirable permeability behavior: the conduit wall should allow molecular exchange but not non-neuronal cellular infiltration; B and C) Cumulative release percentage of FITC-labeled Dextran (4 kDa) across the thick and thin conduit walls, respectively, up to 48 hours of study; D) Graphical representation of the Modified Boyden chamber, where the cell-laden conduits were placed on top of an insert, which was immersed in a 0 % FBS medium. Meanwhile, a 40 % FBS-containing medium acts as a chemo-attractant in the bottom; E and F) Fluorescence quantification of BJ fibroblasts (labelled with Cell Tracker) that were able to migrate through the thick and thin conduits wall, respectively, in the modified Boyden chamber, and comparison with the positive control; G) DAPI/Phalloidin staining performed in the bottom of the chamber reveals that cells were not able to migrate through the conduit wall. Quantitative data is presented as mean \pm sd ((B-C) n=3 and (E-F) n=9). # indicates significant differences (p < 0.05) comparing TC 1 with | |

TC 2; indicates significant differences ($p < 0.05$) comparing TC 2 with TC 3; * and ** indicates significant differences ($p < 0.05$ and $p < 0.01$) comparing to the positive control. Scale bar: 100 μm460

Figure IX-6 - Quantitative and qualitative evaluation of Schwann cells viability when cultured *in vitro* in the surface of the silk-based conduits. A and B) Determination of cell number by Alamar Blue assay in thick and thin conduits, respectively, after 1, 3 and 7 days of culturing (top) and respective Live/Dead staining (bottom). C) Quantitative determination of the effect of the wall thickness on Schwann cell proliferation, after 1, 3 and 7 days of culturing in the different conduits (TC 1, TC 2, TC 3). Quantitative data is presented as mean \pm sd ($n=3$), where * $p < 0.05$, ** $p < 0.01$, *** $p < 0.001$. Scale bar: 200 μm461

Figure IX-7 - Biocompatibility evaluation for the developed silk-based conduits. The results were obtained after subcutaneous implantation in CD-1 Albino mice. A) Macroscopic aspect of the conduits at the moment of explantation (after 8 weeks), revealing high vascularization and no signs of material rejection. B) H&E-stained longitudinal sections after 4 and 8 weeks of implantation. Asterisks show cellular infiltration only until the point of anastomosis and not through the conduits walls. Black arrows point to fissures verified in the freeze-dried conduits' structure, which reveal the beginning of the degradation process. C) Higher magnification of the H&E-stained longitudinal sections, where black arrows point to fissures in the freeze-dried conduits' structure and white arrows point to the thin fibrotic capsule formed around the conduits. Scale bar: A) 1 cm, B) 1 mm, C) 200 μm (top), 500 μm (bottom).463

Figure IX-8 - Representative scheme of the easy tunability of the developed silk-based TCs. By simply changing the final processing step or the diameter of the inner mold, conduits with diverse characteristics are obtained. Therefore, apart from peripheral nerve regeneration, these conduits can be envisioned for many other clinical and guided tissue regeneration applications, where tubulization is also required.465

Figure X-1 - Schematic representation of the methodology used to produce the SF conduits. The methodology allows fabricating the enzymatically crosslinked SF NGCs following a method previously developed by Carvalho *et al.*(3, 33) which takes advantage of the presence of tyrosine groups in SF that are known to form a covalently-crosslinked hydrogel. The two different techniques used to incorporate NTFs into the eSF conduits are highlighted in: (i) Crosslinking method, and (ii) Absorption method.; BI) SEM micrographs of eSF conduit where the wall thickness is $\approx 700 \mu\text{m}$ and the lumen has a diameter of $\approx 5 \text{ mm}$; BII) SEM micrograph of eSF conduit surface where the external pore size is in the range of 3-6 μm . Conduits were cut to a total length of 14 mm for all assays. Scale bars: BI) 500 μm and BII) 5 μm487

Figure X-2 - A) Scheme of the methodology used in the NTF release assay. Scale bar: 5 mm. B) ELISA quantification of the NTFs released from the eSF conduit, considering the different methods of incorporation, NTFs used and concentration. BI) Daily amount of GDNF released from eSF conduits within 5 days; BII) Cumulative amount of released GDNF within 50 days; BIII) Daily amount of NGF released from eSF conduits within 5 days; BIV) Cumulative amount of released NGF within 50 days. Results were represented as mean \pm SD ($n=3$). For multiple comparisons, * symbol indicates the comparison of GDNF/A2 or NGF/A2 and crosslinked formulations, # symbol regards comparison of GDNF/A4 or NGF/A4 and crosslinked formulations. Statistically significant differences were represented by */# ($p < 0.5$), **/## ($p < 0.01$), and ***/### ($p < 0.001$).489

Figure X-3 - A) Scheme of the methodology used in the bioactivity assay *in vitro*, which is similar to the methodology used for ELISA quantification. B) Representative confocal fluorescent images of DRGs stained with Neurofilament 200 (in green) after being treated with GDNF released from eSF conduits. C) Quantification of different parameters related to the DRGs neurite outgrowth, such as neurite length, cellular migration from DRG body and percentage of field coverage after being in contact with GDNF releasing eSF conduits. D) Representative confocal fluorescent images of DRGs stained with Neurofilament 200 (in green) after being treated with NGF released from eSF conduits. E) Quantification of different parameters related to the DRGs neurite outgrowth, such as neurite length, cellular migration from DRG body and percentage of field coverage after being in contact with NGF releasing eSF conduits. Statistically significant differences were represented by * ($p < 0.5$), ** ($p < 0.01$), and *** ($p < 0.001$). Scale bar: B and D) 500 μm492

Figure X-4 - Impact of the different GDNF or NGF formulations on DRGs percentage of field coverage (which reflects both the length and density of neurite outgrowth). A) When considering the 4 $\mu\text{g}/\text{mL}$ concentration, there is a significant statistical difference between GDNF/A₄ and NGF/A₄ treated DRGs in terms of percentage of field coverage. Statistically significant differences were represented by * ($p < 0.5$), ** ($p < 0.01$), and *** ($p < 0.001$); B) Representative confocal fluorescent images of DRGs stained with Neurofilament 200 (in green) and Hoechst (in blue) after being treated with GDNF/A₄ or NGF/A₄ Scale bar: 500 μm493

Figure X-5 - Assessment of the *in vivo* performance of the NTF-loaded eSF conduits in a sciatic defect model: A) Implantation of the different study groups: autograft, eSF and GDNF/A₄. B) Immediately after animal sacrifice, the percentage of muscle weight loss was determined. C) Quantitative measurements of the longitudinal sectional nerve area. Measurements were made in the middle of the conduit (since the proximal area was cut for histomorphometric analyses, the measurement was performed 7 mm from the distal stump). D) Representative photomicrographs of the longitudinal sections of implanted autograft, eSF and GDNF/A₄ after hematoxylin-eosin (H&E) staining. E) Representative photograph showing the difference in the regenerated nerve cable thickness. Statistically significant differences were represented by * ($p < 0.5$), ** ($p < 0.01$), and *** ($p < 0.001$). Scale bars: A) 500 μm ; D): 500 μm ; E) 250 μm (left) and 500 μm (right).....495

Figure X-6 - A) Schematic representation of the cross- and longitudinal sections positioning for histological analysis. B) Quantitative evaluation of myelinated axons in the proximal area (PNX), where statistically significant differences were represented by * ($p < 0.5$), ** ($p < 0.01$), and *** ($p < 0.001$). C) Light microscopy representative images of semi-thin nerve cross-sections in the PNX cross-section area, after osmium tetroxide and toluidine blue staining. On the right, close-up images of each *in vivo* study groups. Scale bar: 20 μm496

LIST OF SUPPLEMENTARY FIGURES

- Supplementary Figure V-1 - 3D micro-CT reconstruction of the membrane serving as a guiding luminal filler. In this specific reconstruction, the chitosan tube is composed of DA III membrane and there is a Z shaped DA I membrane inside the tube, showing its flexibility. Scale bar: 2 mm.322
- Supplementary Figure V-2 - Stereomicroscope image of the DA III membranes wrapped to easily form a tubular device. Scale bar: 1 mm.322
- Supplementary Figure VII-1 - Scatter plot depicting the median and range of the amplitude ratios of evocable compound action potentials recorded 12 weeks after nerve reconstruction in the tibialis anterior muscle of control group (AUTOG) and experimental groups (NGC25:75, NGC50:50, NGC60:40) animals. While all animal of the control group displayed motor recovery, only single animals of the experimental groups did so. Nerve reconstruction with NGC60:40 did not allow for recordable muscle reinnervation in any case.396
- Supplementary Figure VII-2 - Appearance of the studied formulations 3 weeks after reconstruction. A+B) Regenerated tissue bridge grown through hollow control NGCs. Black arrows point to the tissue cables located inside the NGC. C) Sample from the NGC50:50 group. White arrows point to the border of the infiltrated GG freeze-dried hydrogel. D) Sample from the NGC25:75 group. White arrows point to the border of the infiltrated GG freeze-dried hydrogel. The NGCs are still enclosed by a thin layer of connective tissue that has formed around them. The specimens were placed on glass plates on top of scale-papers with 1 mm intersections. Scale bar: 3 mm.397
- Supplementary Figure VII-3 - Appearance of the studied formulations through the microsurgery microscope 6 weeks after reconstruction. A) Regenerated nerve tissue grown through an hollow control NGC. Black arrows delineate the tissue bridge that has formed between the nerve ends. B+C) Samples from the NGC60:40 group. There is no presence of ingrown tissue within the GG residues indicated by the asterisk and delineated by white arrows. D+E) Samples from the NGC50:50 group. Black arrows in D) delineate ingrown tissue in the proximal part of the NGC, which is thin and free of surrounding GG residues. White arrows in E) point to the border of an empty GG freeze-dried hydrogel scaffold. The asterisk marks the GG material, while the black arrows signal the infiltrated blood supply in close vicinity to the nerve ends. F+G) Samples from the NGC25:75 group. Black arrows indicate the presence of ingrown tissue. Arrow heads point to a border of the tissue and asterisks indicate residues of freeze-dried GG hydrogel scaffold. Eventually small vessels can be seen along or inside the GG freeze-dried hydrogel scaffolds. The connective tissue that has formed around the NGCs has been removed. The specimens were placed on glass plates on top of scale-papers with 1mm intersections. Scale bar: 3 mm.398
- Supplementary Figure VII-4 - Aspects of nerve implants with electrodiagnostically proven muscle reinnervation at the moment of explantation after 12 weeks in vivo (view through the microsurgery microscope). The connective tissue that has formed around the NGCs has not been removed. Black arrow heads point to the distal nerve segment further processed for nerve morphometry. The specimens have been placed on a glass plate on top of scale-paper with 1mm intersections. A) Autologous nerve graft, black arrows point to the suture line. B-C) Samples from the NGC50:50 group. Black arrows indicate the presence of tissue most likely grown through Gellan Gum scaffolds. Both specimens were affiliated with a positive evaluation for functional recovery. D-F) Samples from the NGC25:75 group: Black

arrows indicate the presence of tissue most likely grown partially through and partially along the Gellan Gum hydrogel matrix. White arrow in F) points to a whitish area not clearly indicating if the GG scaffolds contains ingrown tissue or not. Samples shown in D and F were affiliated with positive evaluation for functional recovery while sample shown in E was not. Scale bar: 3 cm.399

Supplementary Figure IX-1 - SEM analysis of the TC 1 formulation cross-section. The micrographs confirm the porosity obtained, where the exterior wall presents higher pore size when compared to the interior wall. Scale bar: 50 μm ..469

Supplementary Figure IX-2 - SEM analysis of the modified TC 1, *i.e.* conduit produced by freeze-drying after a slower freezing step. The micrographs reveal the exterior and interior walls, as well as the cross-section microstructure of the conduits obtained after a slower freezing process (0 $^{\circ}\text{C}$ followed by -20 $^{\circ}\text{C}$), showing high porosity as compared to the conventional TC 1. The freezing was performed previously to the freeze-drying. This type of conduits would be required in the case of more severe injuries, where bigger gaps need to be treated. The modified treatment of the conduits was done merely as a proof-of-concept, to demonstrate the versatility of the developed tubes.....469

Supplementary Figure IX-3 - FTIR spectra of the different silk fibroin thick TCs (TC 1, TC 2 and TC 3). Similar spectra were obtained regardless of the thickness of the wall (thin conduits data not shown). The spectra show characteristic peaks at 1627 cm^{-1} (amide I), 1520 cm^{-1} (amide II) and 1262 cm^{-1} (amide III).....470

Supplementary Figure IX-4 - Apparatus used for universal mechanical testing machine (Instron) for tensile tests in the developed TCs. Both TC ends were hold with a grip.....470

Supplementary Figure IX-5 - Calcein-AM staining demonstrating the presence of viable cells (capable of migrating) adhered to the interior surface of both thick and thin conduits. The images were taken at the end of the cellular permeability assay (after 48 hours). Scale bar: 200 μm471

Supplementary Figure IX-6 - Weight loss macroscopic observation of the TCs under the effect of Protease XIV solution after 30 days. A) Macroscopic degradation of thick conduits. B) Macroscopic degradation of thin conduits. The TC 1 and TC 2 remained with fragile walls, but the integrity of the conduits was maintained, whereas the TC 3 disintegrated into fragments. Scale bar: 10 mm.471

Supplementary Figure IX-7 - Weight of the developed TCs measured from the moment of production to up to 6 months, revealing the weight stability, with no statistically significant differences along time. The TC 1 and TC 2 were kept in a dry state and the TC 3 was kept in ethanol. This assay demonstrated that the developed TCs are sustainable as off-the-shelf products, allowing storage for several months prior to their use.472

Supplementary Figure X-1 - Photograph and scheme of the nerve cutting tool used in the *in vivo* study, designed to precisely hold and cut the sciatic nerve during surgery. Tools were 3D-printed using poly(lactic acid) and consisted of a hook with an inner diameter of 2.5 mm and a scalpel alignment groove 700 μm in width. Scale bar: 5 mm.505

Supplementary Figure X-2 - Representative SEM micrographs of the SF NGCs microstructure: A) overall aspect of the conduit; B) outer surface of the conduit; C) inner surface of the conduit. Scale bars: A) 500 μm ; B) 5 μm ; C) 5 μm505

Supplementary Figure X-3 - Qualitative vascularization assessment in the *in vivo* study groups in the middle conduit section (C1X) after Toluidine Blue staining: A) Autograft; B) SF; C) GDNF/A⁺. Scale bar: 20 μm506

Supplementary Figure X-4 - Vascularization assessment by quantification of blood vessels in the middle conduit area (C1X). Statistically significant differences were represented by * ($p < 0.5$), ** ($p < 0.01$), and *** ($p < 0.001$)......507

Supplementary Figure X-5 - Influence of cellular components on neurite outgrowth. Representative confocal images of DRGs stained with Neurofilament 200 (green) and DAPI (blue). Cellular migration from the DRG body will influence neurite length, possibly due to biochemical cues formed by laminin secretion. Scale bar: 500 μm507

Supplementary Figure X-6 - Classical neuron structure found within confocal fluorescent images of DRGs after 5 days in culture. Nuclei of Schwann cells (DAPI staining, in blue) can be seen enwrapping long axon (Neurofilament 200 staining, green). In the end, marked by a red circle, a terminal button or axon terminal can be seen. Scale bar: 50 μm508

LIST OF TABLES

| | |
|--|-----|
| Table I-1 - Seddon (30) and Sunderland (31) classification of PNIs. | 8 |
| Table I-2 - Design criteria for the development of NGCs. | 15 |
| Table I-3 - Approved NGCs used in the clinical setting. | 16 |
| Table I-4 - Relevant and recent published works focused on the fabrication of NGC with synthetic biomaterials. | 21 |
| Table I-5 - Relevant and recent published works focused on the fabrication of NGC with natural biomaterials. | 27 |
| Table I-6 - Relevant and recent published works focused on the fabrication of NGC with endogenous biomaterials. | 31 |
| Table II-1 - The use of GFs and their effect on CNS and PNS (189). | 76 |
| Table II-2 - Cell-based therapies for PNR. | 84 |
| Table II-3 - Clinical trials in the scope of PNR being carried in different countries and with different strategies. | 87 |
| Table III-1 - Seddon and Sunderland classifications of nerve injuries according to the pathophysiology of the nerve | 111 |
| Table III-2 - Phenomena prejudicing peripheral nerve regeneration. | 118 |
| Table III-3 - The use of carbon nanotubes applied to peripheral nerve regeneration. | 121 |
| Table III-4 - The use of graphene applied to peripheral nerve regeneration. | 128 |
| Table III-5 - The use of nanodiamonds applied to peripheral nerve regeneration | 134 |
| Table III-6 - The use of inorganic nanoparticles applied to peripheral nerve regeneration. | 138 |
| Table III-7 - The use of organic nanoparticles applied to peripheral nerve regeneration. | 149 |
| Table III-8 - Exosomes in scope of peripheral nerve regeneration. | 158 |
| Table III-9 - The use of nanofibers applied to peripheral nerve regeneration. | 162 |
| Table III-10 - Nano-scale topographic cues applied to peripheral nerve regeneration | 172 |
| Table III-11 - Theranostics and nanoimaging applied to peripheral nerve regeneration. | 179 |
| Table IV-1 - Recent published reports of chitosan formulations for different applications in TE. | 205 |
| Table IV-2 - Recent published reports of chitosan formulations for different applications in TE. | 207 |
| Table IV-3 - Comparative data on amino acid composition of <i>B. mori</i> , <i>N. edulis</i> and <i>N. clavipes</i> silks. Reprinted with permission from (81). | 208 |
| Table IV-4 - Recent published reports of SF formulations for different applications in TE. | 210 |
| Table IV-5 - Recent published reports of keratin formulations for different applications in TE. | 214 |
| Table IV-6 - Gellan Gum formulations and designations. This table presents the nomenclature utilized to designate the different formulations studied during this experimental work, on both in vitro and in vivo characterizations. | 223 |

| | |
|---|-----|
| Table IV-7 - Samples obtained after combining the different incorporation methods, different NTFs and different concentrations for <i>in vitro</i> assays. | 227 |
| Table IV-8 - Ionic concentrations present in the SBF, used for the bioactivity assay, as proposed by Kokubo <i>et al.</i> (220). ... | 246 |
| Table IV-9 - ELISA procedure summary, which was valid for GDNF and NGF. | 260 |
| Table IV-10 - Antibodies used for immunocytochemistry of <i>in vitro</i> samples. | 261 |
| Table IV-11 - Correlation between the different samples that were tested in this <i>in vivo</i> subcutaneous assay. | 264 |
| Table IV-12 - Antibodies used for immunohistochemistry of <i>in vivo</i> samples in Chapter VII. | 272 |
| Table V-1 - General characteristics of the chitosan used on the preparation of each one of the studied membranes. Surface characterization of the chitosan membranes: Mean Roughness (\pm standard deviation) in dry and wet state measured by Atomic Force Microscope analysis and water contact angle, surface energy and its components calculated by the OWRK method. | 300 |
| Table VI-1 - Contact angles (θ), dispersive (γ_d) and polar (γ_p) components and surface energy (γ) of the CHT-based membranes calculated by the OWRK equation. | 340 |
| Table VII-1 - Gellan Gum formulations and designations. This table presents the nomenclature utilized to designate the different formulations studied during this experimental work. | 362 |
| Table VII-2 - Evaluation of functional motor recovery. This table presents the percentages, as well as animals per group, with evocable compound muscle action potentials (CMAPs) recordable from the tibialis anterior muscle or plantar interosseous muscle. The measurements were performed 4, 6 and 12 weeks after nerve reconstruction surgery. Varying animal numbers displayed for CMAP recording from tibialis anterior and plantar muscles, respectively, are related to eventual temporary suspension of animals from plantar recordings upon occurrence of signs of minimal autotomy. | 376 |
| Table VIII-1 - Commercially available nerve guides and wraps. Apart from Avance, Qigel and RevolNerve, all other listed nerve devices are FDA approved. | 418 |
| Table VIII-2 - Relation between drying method and pore size. | 420 |
| Table IX-1 - Silk fibroin conduits according to the processing method used as final step. The table presents the nomenclature utilized to designate the different TCs studied during this work. | 450 |
| Table IX-2 - EDS results revealing the elemental composition and their relative abundance present in the surface of TC 1, TC 2 and TC 3. The bioactivity assay was performed in Simulated Body Fluid. %Wt. stands for percentage by weight and σ stands for standard deviation. | 457 |
| Table X-1 - Samples produced for <i>in vitro</i> assays by means of using the crosslinking and adsorption methods, different NTFs (<i>i.e.</i> , GDNF and NGF), and different NTFs concentrations (<i>i.e.</i> , 2 and 4 $\mu\text{g/mL}$). | 480 |
| Table X-2 - NTFs loading efficiency in the eSF conduits produced by crosslinking and adsorption methods. | 487 |
| Table X-3 - Pinch test results indicating the level of regenerated nerves within the conduit. | 494 |

LIST OF SUPPLEMENTARY TABLES

Supplementary Table VII-1 - Micro-CT analysis of freeze-dried hydrogels for *in vitro* assays: Quantification of mean pore size, trabecular thickness and % of porosity from n=3 samples each400

Supplementary Table VII-2 - Micro-CT analysis of nerve guidance conduits with different gellan gum freeze-dried hydrogels as fillers, similar to those prepared for evaluation *in vivo*: Quantification of mean pore size, trabecular thickness and % of porosity from n=3 samples each.400

Supplementary Table VII-3 - 3 weeks' time point general evaluation.401

Supplementary Table VII-4 - 6 weeks' time point general evaluation.402

Supplementary Table VII-5 - 12 weeks' time point general evaluation. NGC25:75 only present 5 samples because 2 animals from this group had to be sacrificed due to severe autotomy.403

Supplementary Table X-1 - Quantification of DRGs neurite outgrowth parameters in the presence of GDNF releasing SF conduits and respective controls.508

Supplementary Table X-2 - Quantification of DRGs neurite outgrowth parameters in the presence of NGF releasing SF conduits and respective controls.509

SHORT CURRICULUM VITAE

Cristiana Rodrigues de Carvalho was born on the 25th of January 1988, in Braga, Portugal. She is currently a PhD student at 3B's Research Group - I3Bs, Research Institute on Biomaterials, Biodegradables and Biomimetics, at University of Minho, Headquarters of the European Institute of Excellence on Tissue Engineering and Regenerative Medicine at Avepark, Caldas das Taipas, Guimarães, Portugal. This is a research unit that has been classified by the Foundation of Science and Technology (FCT) as excellent and is part of the Portuguese Associate Laboratory ICVS/3B's.

She graduated the Integrated Master in Pharmaceutical Sciences at Faculty of Pharmacy, University of Porto, Portugal with a final grade of 15 (0-20), in 2012. During these 5 years, she had the opportunity to integrate a research project in the Bromatology Lab. That allowed her to take her first steps in the scientific research and participate in IJUP 2010 (Encontro de Investigação Jovem da Universidade do Porto) and to participate in international conferences with poster presentations in a very young age. Also, in her last year, she had the opportunity to do a three-month internship at the World Health Organization Headquarters, in Geneva, Switzerland. That gave her great insights into the Public Health field and the opportunity to work closely with global leaders in public health.

In 2014, she started pursuing her PhD at 3B's Research Group, at University of Minho, Portugal, under the supervision of Dr. Joaquim Miguel Oliveira and Professor Rui L. Reis. For six months, in the first year of her PhD, she was a visiting student at Institute of Neuroanatomy and Cell Biology, Hannover Hospital, Hannover, Germany in the scope of the Biohybrid project, of which she was an active member. In her stay, she studied the role of Gellan Gum as a Nerve Guidance Conduit luminal filler and participated in an extensive *in vivo* study under the supervision of Dr. Kirsten Haastert-Talini. In 2018 she had the great opportunity to spend 7 months in New Jersey Center for Biomaterials, New Jersey, USA, under the direct supervision of renown scientist Prof. Joachim Kohn. In that scope, she was awarded a FLAD scholarship (Fundação Luso-Americana para o Desenvolvimento – Proj. 29/2018) to be able to carry her investigation abroad.

Scientifically, Cristiana has contributed to the field of biomaterials and peripheral nerve regeneration so far with 7 peer-reviewed papers in international journals as first-author, 1 in co-authorship and 1 book chapter, in a total of 9 publications. Furthermore, she is the inventor of 2 filled international patents and participated in international conferences with 4 oral communications, and 6 poster communications.

LIST OF PUBLICATIONS

The work performed under the scope of this PhD thesis resulted in the publications listed below.

INTERNATIONAL PUBLICATIONS IN SCIENTIFIC PEER-REVIEWED JOURNALS

1. **Carvalho CR**, López-Cebral R, Silva-Correia J, Silva JM, Mano JF, Silva TH, Freier T, Reis RL, Oliveira JM, Investigation of cell adhesion in chitosan membranes for peripheral nerve regeneration. *Materials Science and Engineering: C*. 2017;71:1122-3. doi: 10.1016/j.msec.2016.11.100
2. **Carvalho CR**, Costa JB, Costa L, Silva-Correia J, Pina S, Moay ZK, Ng KW, Reis RL and Oliveira JM, Enhanced biological performance of chitosan/keratin membranes for peripheral nerve applications (Submitted).
3. **Carvalho CR**, Wrobel S, Meyer C, Brandenberger C, Cengiz IF, López-Cebral R, Silva-Correia J, Ronchi G, Reis RL, Grothe C, Oliveira JM, Haastert-Talini K. The potential of gellan gum-based luminal fillers for peripheral nerve regeneration: An *in vivo* study in rat sciatic nerve repair model. *Biomaterials Science*. 2018; 1059-1075. doi: 10.1039/c7bm01101f.
4. **Carvalho CR**, Costa JB, Morais AS, López-Cebral R, Silva-Correia J, Reis RL and Oliveira JM, Tunable Enzymatically Crosslinked Silk Fibroin Tubular Conduits for Guided Tissue Regeneration. *Advanced Healthcare Materials*. 2018. e1800186. doi: 10.1002
5. **Carvalho CR**, Chang W, Reis RL, Oliveira JM, Kohn J. Engineering Silk Fibroin-Based Nerve Conduit with Neurotrophic Factors for Proximal Protection and Vascularization After Peripheral Nerve Injury. (Submitted)
6. **Carvalho CR**, Silva-Correia J, Oliveira JM, Reis RL, Nanotechnology in Peripheral Nerve Repair and Reconstruction. *Advanced Drug Delivery Reviews*. 2019. 10.1016/j.addr.2019.01.006
7. **Carvalho CR**, Oliveira JM, Reis RL, Modern trends for peripheral nerve repair and regeneration: Beyond the hollow nerve guidance conduit (Submitted)

AS CO-AUTHOR

1. Carvalho MR, Caballero D, Maia R, **Carvalho CR**, Reis RL, Oliveira JM. Targeting colorectal cancer using highly specific peptide-modified dendrimer nanoparticles (Submitted)

BOOK CHAPTERS

1. **Carvalho CR**, Oliveira JM, Reis RL. Fundamentals and current strategies for peripheral nerve repair and regeneration. Editors: Heung Jae Chun, Antonella Motta, Rui L. Reis, Gilson Khang, in *Advances in Experimental Medicine and Biology (AEMB) Series*, Springer Nature, 2019.

PATENTS

1. **Carvalho CR**, Costa JB, Ribeiro V, Silva-Correia J, Oliveira JM, Reis RL. Nerve guidance conduits derived from silk fibroin hydrogels: methods of production and uses thereof.
 - Request N. °: PCT/IB2017/054708
 - Priorities: PT 109562 (01.08.2016)
 - WIPO N°: WO18025186
2. **Carvalho MR**, Caballero D, **Carvalho CR**, Costa JB, Ribeiro V, Oliveira JM, Kundu SC, Reis RL. Implantable silk hydrogel microfluidic platform, methods of production and uses thereof.

CONFERENCE ORAL PRESENTATIONS

1. **Oral Presentation:** “Chitosan nanofibers for guided peripheral nerve regeneration” **Cristiana R. Carvalho**, Albino Martins, Nuno M. Neves, Joaquim M. Oliveira, Rui L. Reis, 2nd International Symposium Peripheral Nerve Regeneration – Torino, Italy 2014
2. **Oral presentation:** “Chitosan Films with Low Degrees of Acetylation for Peripheral Nerve Regeneration” **Cristiana R. Carvalho**, Joaquim M. Oliveira, Rui L. Reis, 11th Frontiers in Biomedical Polymers Symposium - Riva Del Garda, Italy 2015
3. **Oral presentation:** “Delivery of Neurotrophic factors in a Silk-based Nerve Conduit for Peripheral Nerve Repair”, **Cristiana R. Carvalho**, Wei Chang, Joana Silva-Correia, Rui L. Reis, Joaquim M. Oliveira, Joachim Kohn, Society for Biomaterials Annual Meeting and Exposition – Seattle, USA, 2019
4. **Oral Presentation:** “Neurotrophic Factor Loaded in Enzymatically-Crosslinked Silk Fibroin Conduits for Peripheral Nerve Regeneration”, **Cristiana R. Carvalho**, Wei Chang, Joana Silva-Correia, Rui L. Reis, Joaquim M. Oliveira, Joachim Kohn, TERMIS European Meeting – Rhodes, Greece, 2019

CONFERENCE POSTERS

1. **Poster communication:** "Chitosan films with varying degrees of acetylation for application in peripheral nerve regeneration" Cristiana R. Carvalho*, Rita López-Cebral, Joana Silva-Correia, Tiago H. Silva, Thomas Frier, Joaquim M. Oliveira, Rui L. Reis, TermStem 2013, Porto, Portugal, 2014
2. **Poster Communication:** "Application of keratin/chitosan conduits for Peripheral Nerve Regeneration" Cristiana. R. Carvalho, José. P. Gonçalves, Rui L. Reis, Joaquim. M. Oliveira, TermStem, Porto, Portugal 2014
3. **Poster Communication:** "Keratin/chitosan as novel grafts for peripheral nerve regeneration", Cristiana. R. Carvalho, José. P. Gonçalves, Rui L. Reis, Joaquim. M. Oliveira, Termis EU meeting, Genova, Italy 2014, DOI: 10.1002/term.1932
4. **Poster Communication:** "Biodegradable scaffolds for peripheral nerve regeneration" Cristiana R. Carvalho*, J. Silva-Correia, A. Martins, Nuno M. Neves, Joaquim M. Oliveira, Rui L. Reis, Meeting ICVS/3Bs, Braga, Portugal 2013
5. **Poster Communication:** "Chitosan nanofibers as scaffolds for peripheral nerve regeneration" Cristiana R. Carvalho*, A. Martins, Nuno M. Neves, Joaquim M. Oliveira, Rui L. Reis, TermStem Porto, Portugal 2013, DOI:10.1002/term.1822
6. **Poster communication:** "Future trends in peripheral nerve repair and regeneration: what comes after the hollow nerve guidance conduit?" Cristiana R. Carvalho*, Joaquim M. Oliveira, Rui L. Reis, FoReCaST 2019, Porto, Portugal, 2019

AWARDED GRANTS

1. Horizonte Norte2020 PhD scholarship (Norte-08-5369-FSE-000037)
2. FLAD scholarship (Proj. 29/2018)

INTRODUCTION TO THE THESIS FORMAT

The present thesis is divided into four main sections (1 to 4) containing eleven chapters (I to XI). This structure was adopted to allow a proper organization of the data presented in the various chapters.

A general introduction (Section 1) can be found divided in three different chapters: **Chapters I, II and III**). An overall Materials and Methods section is represented in Section 2, Chapter IV). Section 3, in which **Chapters V to X** can be found, focuses on the experimental studies and results obtained in the context of this thesis, as well as their discussion. To finalize, Section 4 (Chapter XI) completes this thesis with concluding remarks and future perspectives.

The main body of the thesis is based on a series of publications published in international journals or submitted for publication. Each individual chapter is presented in a manuscript form, *i.e.* abstract, introduction, experimental section, results and discussion, conclusion, and Acknowledgments. A list of relevant references is also provided as a subsection within each chapter. The contents of each part and chapter are described below in more detail.

Section 1 – General introduction

Chapter I – Fundamentals and current strategies for peripheral nerve repair and regeneration:

This chapter provides a general introduction to the natural mechanisms of injury and nerve regeneration, vital to understand the processes involved in axonal regeneration. It also describes the latest advances in the Tissue Engineering strategies for NGCs production based on natural-origin and synthetic biomaterials.

Chapter II – Modern trends for peripheral nerve repair and regeneration: Beyond the hollow nerve guidance conduit: This chapter reviews the current reports dealing with the several features that can be used to improve peripheral nerve regeneration (PNR), ranging from the simple use of hollow NGCs, to tissue engineered intraluminal fillers, or to even more advanced strategies, comprising the molecular and gene therapies as well as cell-based therapies, in order to move beyond the hollow NGC.

Chapter III – Nanotechnology in peripheral nerve repair and reconstruction: Nanotechnology-based therapies are now being considered for the repair and reconstruction of peripheral nerves, having the power to deliver bioactive molecules in a controlled manner, to tune cellular behavior, and ultimately guide tissue regeneration in an effective manner.

Section 2 – Detailed description of experimental materials and methodologies

Chapter IV – Materials and Methods: A list of the materials used and methods applied to obtain the results described further on is provided, being the basis to the whole work described in this thesis.

Section 3 – Experimental work regarding the biomaterials approach to peripheral nerve regeneration

Chapter V - Investigation of cell adhesion in chitosan membranes for peripheral nerve regeneration: This chapter describes the production and the great deal of characterization of three different chitosan membranes, with very similar degrees of acetylation. The results obtained during this work permitted to select the formulation with the greatest potential for further exploitation with PNR purposes.

Chapter VI - Enhanced biological performance of chitosan/keratin novel biomaterials for peripheral nerve applications: This chapter describes the addition of freeze-dried hair keratin to chitosan membranes, and how this simple step improved the membranes physicochemical and biological properties, including the crucial phenomena of vascularization for PNR.

Chapter VII - The potential of gellan gum-based luminal fillers for peripheral nerve regeneration: An in vivo study in rat sciatic nerve repair model: This chapter described the innovative use of the biomaterial Gellan Gum as luminal filler for NGCs made from chitosan with a 5 % degree of acetylation. The experimental work focused on *in vitro* and *in vivo* techniques. The engineered constructs should remodel the structural support given to regenerating axons by the so-called bands of Büngner.

Chapter VIII – Patent: Nerve guidance conduits derived from silk fibroin hydrogels: methods of production and uses thereof: This chapter relates to a patent describing silk fibroin tubular conduit and the innovative methodology that allowed their obtaining. It also focuses on silk fibroin tubular conduit respective uses.

Chapter IX – Tunable Enzymatically Crosslinked Silk Fibroin Tubular Conduits for Guided Tissue Regeneration: This chapter describes the new methodology to produce enzymatically-crosslinked silk fibroin NGCs, which takes advantage of the tyrosine groups present in the structure of silk fibroin that are known to form a covalently-crosslinked hydrogel. The conduits were extensively characterized in order to demonstrate its application in several TE areas, but with particular interest in PNR.

Chapter X – Delivery of Neurotrophic factors in a Silk-based Nerve Conduit for Peripheral Nerve Repair: This chapter describes enzymatically crosslinked silk fibroin-based conduits capable of being used as a platform for the controlled delivery of neurotrophic factors. *In vitro* and *in vivo* experiments performed demonstrated that SF NGCs loaded with NTFs could promote proximal neuronal protection, and motor nerve reinnervation, which were all absent in the plain silk fibroin conduit that mimic the current marketed nerve conduits

Section 4 – Concluding remarks

Chapter XI – General Conclusions and Future Perspectives: The final section of the thesis presents the general conclusions and implications, current limitations and potential of the work described for biomaterials in peripheral nerve regeneration. After years working with several biomaterials and studying their application on nerve regeneration, new opinions or perspectives arise, such as critiques to the work. Furthermore, plenty of ideas and suggestions are given to continue such work.

SECTION 1

General introduction

Chapter I

Fundamentals and current strategies for peripheral nerve repair and regeneration

**Fundamentals and current strategies for peripheral
nerve repair and regeneration¹**

ABSTRACT

A body of evidence indicates that peripheral nerves have an extraordinary yet limited capacity to regenerate after an injury. Peripheral nerve injuries have confounded professionals in this field, from neuroscientists to neurologists, plastic surgeons, and the scientific community. Despite all the efforts, full functional recovery is still seldom. The inadequate results attained with the “gold standard” autograft procedure still encourage a dynamic and energetic research around the world for establishing good performing tissue engineered alternative grafts. Resourcing to nerve guidance conduits, a variety of methods have been experimentally used to bridge peripheral nerve gaps of limited size, up to 30-40 mm in length, in humans. Herein, we aim to summarize the fundamentals related to peripheral nerve anatomy and overview the challenges and scientific evidences related to peripheral nerve injury and repair mechanisms. The most relevant reports dealing with the use of both synthetic and natural-based biomaterials used in tissue engineering strategies when treatment of nerve injuries is envisioned are also discussed in depth, along with the state-of-the-art approaches in this field.

Keywords: peripheral nerve injury, regeneration, biomaterials, neurotrophic factors, cell-based therapy

¹This chapter is based on the following publication: [Carvalho CR, Oliveira JM, Reis RL](#). Fundamentals and current strategies for peripheral nerve repair and regeneration. Editors: Heung Jae Chun, Antonella Motta, Rui L. Reis, Gilson Khang, in *Advances in Experimental Medicine and Biology (AEMB) Series*, Springer Nature, 2019.

I-1. INTRODUCTION

The most significant advances in peripheral nerve repair and regeneration have been achieved over the last years with the improvement of technological tools. However, the study of nerve and its regenerative potential initiated in earlier times, possibly in the ancient Greek period (1). Nevertheless, the establishment of the basic notions and modern concepts of nerve repair and regeneration were only developed in the twentieth century with the emergence of the neurosurgery field (2).

Peripheral nerve injuries (PNIs) usually involve sensory and motor neurons and frequently result in axonal loss and demyelination, depending on the severity of the injury. Under ideal conditions, regeneration of a nerve cable is followed by remyelination, thus allowing a certain degree of sensory and functional recovery to be achieved. In the clinics, PNIs repair is based on the knowledge of physiological regenerative processes (3). However, if no additional strategies are used, functional recovery following an injury remains incomplete. In order to address this tissue regeneration and improve clinical outcomes, the contribution of multidisciplinary fields is required. Interestingly, tissue engineering (TE) has allowed to take impressive steps towards the improvement of functional outcomes, by means of combining areas such as reconstructive microsurgery, transplantation and biomaterials (4). Furthermore, the basic triad of TE has an important role in successful nerve regeneration, as the goal remains to develop and fabricate novel nerve guidance conduits (NGCs) built from a particular biomaterial, capable of housing cells and deliver biological and physical molecular cues, enhancing and guiding nerve regeneration (5). As tubulization and the use of NGCs remains the base for nerve repair, the choice of adequate type(s) of biomaterials is the pillar to achieve the so desired regeneration (6). In fact, it has been confirmed experimentally that engineered NGCs may also lead to effective nerve repair, that was earlier thought to only be restorable using autograft (7).

The topics related to the anatomy of the nervous system as well as on the innate mechanisms related to the natural attempts of tissue regeneration are addressed herein. A comprehensive overview of the biomaterial's approaches being pursuit in nerve regeneration can also be found. Pre-clinical studies comprising natural, synthetic and endogenous biomaterials have also been extensively explored. Additionally, strategies to achieve nerve repair as well as challenges that need to be overcome are highlighted.

I-1.1. Organization of the Nervous System

In the case of an injury, in order to make an initial assessment/diagnosis and proceed with the appropriate treatment, it is imperative to have plain knowledge of nervous system anatomy. The nervous system is the instrument through which organized vertebrates keep in touch with its internal structures and external surroundings, reacting to changes and adapting to them. This system has a fundamental role in behavior control and can be divided in the central nervous system (CNS) and peripheral nervous system (PNS) (8). The CNS, composed of the brain and its caudal prolongation, the spinal cord, is connected to the periphery by the PNS (9). During the embryonic development known as ontogenesis, the CNS emerges from the neural plate of the ectoderm that molds into the neural groove, from which the neural tube results. Subsequently, the neural tube is restructured and gives origin to brain and spinal cord. This phenomenon is known as neurulation. Two bands of tissue called the neural crest will give origin to the forthcoming PNS that run along the neural tube. These are multi-potent progenitor cells that later form the PNS (10).

At an anatomical level, the CNS consists of the brain and the spinal cord, being both enclosed by three types of meninges (11). The PNS consists of cranial nerves, spinal nerves and their roots and branches, peripheral nerves, and neuromuscular junctions, in a total of 43 pairs of sensory and motor nerves (12). Bundles of axons in the PNS are referred to as nerves. These are composed of more than just nervous tissue. They have connective tissue participating in their structure, as well as blood vessels supplying the tissues with nourishment. A neuron consists of a cell body, known as Soma, which gives out extensions in PNS, called axons. These are crucial for targeting distant tissues and organs. Axons are coated with myelin sheath membranes, formed by Schwann cells.

Anatomically, each individual axon is firstly protected by a myelin sheath and sheltered by a first layer of collagen and elastic elements, the endoneurium. A group of endoneurium protects axon groups into nerve fascicles, which are sheathed by the perineurium, mainly composed of connective tissue. Finally, several fascicles are gathered together by the epineurium. In the outer layer, the mesoneurium can be found, which also comprises blood vessels supplying oxygen and nutrients to the nerve. Any break or defect in this stratified structure fallouts in a programmed and permanent cell death, unless rapidly and meticulously reestablished (13). Besides myelinated nerve fibers, the PNS contains unmyelinated fibers, with the majority found in the cutaneous nerve, the dorsal roots, and some muscle nerves. **Figure I-1** shows the schematic representation of CNS and PNS in the human body, as well as detailed anatomy of peripheral nerves and neurons.

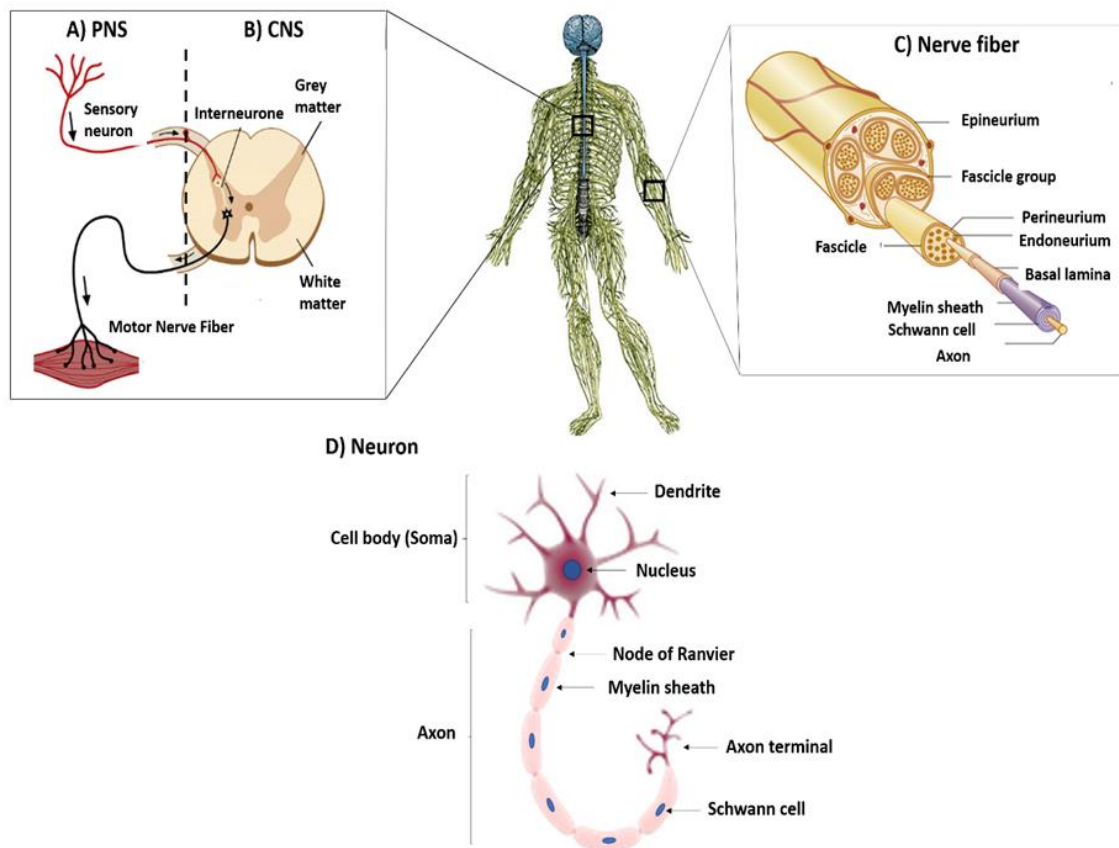


Figure I-1 - Schematic representation of nervous system anatomy in the human body. The nervous system is divided in CNS (in blue) and PNS (green). A) The PNS is composed of several pairs of nerves, which transmit signals between afferent sensory neurons and efferent motor neurons to the CNS; B) CNS, composed of the brain and spinal cord, which has connections to PNS. In CNS, interneurons receive information from the periphery; C) A peripheral nerve contains many nerve fibers that are held together by connective tissue and bundled into nerve fascicles. The entire nerve is enclosed by connective tissue called epineurium. Individual fascicles are delineated by perineurium. Endoneurium surrounds each nerve fiber; and D) Each neuron is composed of a cell body, known as Soma, which contains dendrites. The axon, elongating from the cell body may present myelin sheaths. The spaces between the myelin sheaths are Nodes of Ranvier. In the end of the neuron there is an axon terminal, which releases neurotransmitters from one neuron to another.

Myelin is a constant in both PNS and CNS. Myelin found on neurons in the PNS is formed by Schwann cells while myelin found in the CNS is generated by oligodendrocytes. However, one striking difference can be pointed. In one hand, oligodendrocytes and Schwann cells are often compared to each other in terms of function. However, the biggest difference among the two resides in their ability to repair neurons after nerve damage, as Schwann cells promote nerve regeneration and repair, whereas oligodendrocytes inhibit neuron repair after an injury (14).

In terms of purpose, the primary function of the CNS is integration. Conversely, the PNS is mainly a receptor and effector organ that connects the CNS to every part of the body by cranial and spinal

nerves, and associated ganglia. This connection is made by sensory and motor neurons that conduct impulses to the CNS or the periphery, respectively (15).

I-1.2. General Overview of Peripheral Nerve Injuries

Neurological defects are among the most demanding clinical situations despite decades of research in the neurological field (16). The reason for this relies in the complexity of the nervous system functions, structure and anatomy, which makes it more challenging to treat as compared to other tissues in the human body (17). Opposing to the CNS, the PNS is not protected by a hard bone layer or by the blood-brain barrier, making it much more disposed to traumatism or any kind of injuries (18). Therefore, PNIs are considered a huge clinical burden, being the incidence 1 in 1,000 individuals per year (19). The estimated numbers of PNIs range from 300,000 and 360,000 cases per year for Europe and the USA, respectively (20). In fact, PNIs are associated to \$150 billion health-care expenses per year in the USA alone (15). These costs are underestimated, since “bed-days” and lack of productivity also account for monetary losses, worldwide. It has been assessed that 25 % of patients suffering from traumatic injuries and undergo surgery do not return to work 1.5 years after the intervention. This scenario tends to worsen with the increasing world population and respective average lifespan. Considering those, an additional number of injuries tend to appear and consequently a high number of treatments and surgeries will be required to allow the restoration of the damaged nerves (21).

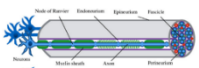
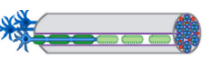
Although the CNS is vastly protected and therefore less prone to injuries, it has a limited ability to regenerate because of the succeeding scar tissue development which can be created by a vast range of cell types, such as fibroblasts, neuroglia, monocytes, and endothelial cells (22). In contrast, PNIs are considerably more common, but the peripheral nerves have a greater regeneration potential as compared to the nerves of CNS. This is because PNS glial cells, Schwann cells, adjust to a regenerative phenotype and have the capacity of triggering neuronal regenerative processes, although usually slow and in a partial manner (23). The regeneration process, however, is dependent on certain factors, such as the lesion size and the quality of the affected nerve, the person’s health status (*e.g.* diabetic or non-diabetic), age, and most importantly, the time period from injury to surgical reconstruction. In the case of lengthy time without repair, the distal nerve end and target tissues and organs are chronically denervated, becoming chronically axotomized, which leads to neurons undergoing apoptosis (24).



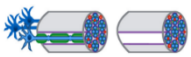
Given to their exposure, peripheral nerve damages can be caused by many types of events, such as traumatic injuries, complications on surgeries, congenital defects and war wounds. Concerning the traumatic injuries, they can also vary significantly and include tearing injuries, crushing or smashing,

ischemia, and less prevalent types of injury such as thermal, electric shock and radiation (25). Compression neuropathies are also ubiquitous among nerve injuries. For instance, carpal tunnel syndrome, the most common compression type of injury, affects 4 % of the overall population (26). A vast range of diseases can also be the root cause of PNIs, as is the case of diabetic peripheral neuropathies (27, 28). Most of these traumatic events cause neuronal death, demyelination, and axonal degeneration resulting in persistent complaints, such as impaired sensory and motor nerve functionality and radiating neuropathic pain. Disorders concerning the PNS usually have overwhelming and life-disturbing impacts on patients' daily functions and habits, which are not usually regarded as significant. There is a substantial lack of consideration of the impact of injury on social and emotional wellbeing, despite their importance to patients. There is, in fact, a strong correlation between PNIs and pain and depression in those patients (29).

Due to the great variety of peripheral nerve traumas, there was a categorization of nerve injuries in main domains, as an attempt to systematize them for the medical and scientific community. Several degrees of injury to peripheral nerves are detailed in **Table I-1**, which were firstly described by Seddon (30), and later by Sunderland (31). The Seddon classification is divided into three categories according to the gravity of the injury: i) neurapraxia, ii) axonotmesis, and iii) neurotmesis. By its turn, Sunderland classification comprises five different categories: first, second, third, fourth and fifth degree. Seddon classification is more straightforward and therefore the most used. Neurapraxia is the least severe type of injury and it is not associated with long-term impairments and consequences. The second level, axonotmesis, is related to axon and myelin discontinuity or disruption. The most severe type, neurotmesis, involves the complete disconnection of the nerve, where a gap is formed.

Table I-1 - Seddon (30) and Sunderland (31) classification of PNIs.

| Seddon and Sunderland classification | Process | Sunderland scheme of nerve injury | Neurological deficits | Degree of recovery |
|--------------------------------------|--|---|-----------------------|--------------------|
| Neurapraxia I | Local myelin damage usually secondary to compression |  | Neuritis, paresthesia | Full recovery |
| Axonotmesis II, III, IV | Axon severed but endoneurium intact (optimal circumstances for regeneration) |  | Paresthesia | Full recovery |

| | | | | |
|-------------------------|--|---|---------------------------|---|
| | Axon discontinuity, endoneurial tube discontinuity, perineurium and fascicular arrangement preserved |  | Paresthesia, dysesthesia | Wallerian degeneration, recovery incomplete |
| | Loss of continuity of axons, endoneurial tubes, perineurium and fasciculi; epineurium intact |  | Dysesthesia, neuroma | Wallerian degeneration, recovery incomplete |
| Neurotmesis V | Complete physiologic disruption of entire nerve trunk |  | Intractable pain, neuroma | Wallerian degeneration, recovery incomplete |

I-1.3. Degeneration and Regeneration following PNIs

Immediately after injury, the regeneration process of peripheral nerves runs in sequenced phases and different events occur at different levels on the injury site encompassing both proximal and distal sites (**Figure I-2A**) (32). In the proximal position, separated axons and cell bodies degenerate via a programmed cell death pathway called chromatolysis (33). In the distal injury end, a process called Wallerian degeneration occurs 24 to 48 hours after injury and all nerve components, including the distal axons and adjacent myelin starts to degenerate (34). The goal of that phenomenon is related to the clearance of undesired debris. Schwann cells phagocytize axonal and myelin debris, until only empty endoneurial tubes remain. Normal nerve function depends on such type of cells, which are the myelinating glial cells of the PNS (35, 36). After debris removal, Schwann cells fill the empty endoneurial tubes and organize in characteristic bands or tubes of Bungner, and by this mean supporting the re-growth of axons. Not only Schwann cells have a crucial role, but also macrophages are recruited to the area releasing growth factors and cytokines. The release of cytokines will stimulate Schwann cells and fibroblast proliferation and are responsible for the axonal regeneration process (37). Ahead in the process, in the proximal injury end, a growth cone emerges following the path formed by the band of Bungner, which is of fundamental importance for the advance of the regenerating axon (38). The growth cone can be seen in **Figure I-2B** (39). In optimal conditions, axonal regeneration is very slow, occurring at a rate of approximately 1 mm/day and demanding at least more than one year for muscle re-innervation and initial functional recovery (40).

I-1.3.1. The role of Schwann cells in injury response

Schwann cells are among the first active components after nerve injury. Finding their embryologic origin in the neural crest, Schwann cells have the capacity to proliferate, produce and deliver neurotrophic factors, modulate the immune response, myelinate axons, migrate and adjust their shape and phenotype. This makes them the perfect cells towards intervening in neural repair (41). Although the degeneration of axons in the distal nerve end starts roughly 2 days after injury, activity of Schwann cells can be distinguished before that, within hours of injury, where Schwann cells undergo a phenotypic change (14). This phenotypic change will support PNR in several ways. Firstly, they dedifferentiate by means of acquiring a non-myelinating and immature Schwann cells stage phenotype. That stage is characterized by an up-regulation of L1, NCAM, p75NTR, and glial fibrillary acidic protein (GFAP). On the other hand, myelin-associated genes are down-regulated, which comprise myelin transcription factor Egr2, organizational and mechanical supporting proteins as such as Protein 0 (P0), myelin basic protein (MBP) and myelin associated glycoprotein (42).

There is also an up-regulation and secretion of a beneficial group of trophic factors, such as nerve growth factor (NGF), brain-derived neurotrophic factor (BDNF), ciliary neurotrophic factor (CNTF), basic fibroblast growth factor (bFGF), vascular endothelial growth factor (VEGF) and pleiotrophin (43). Furthermore, the expression of cytokines capable of recruiting macrophages is also up-regulated, which include tumor necrosis factor (TNF)- α , LIF, interleukin (IL)-1 α , IL-1 β , and monocyte chemoattractant protein 1 (MCP-1). Schwann cells activate a cell-intrinsic myelin breakdown process, which will destroy myelin by an autophagy process, roughly at the 5th day after injury (23).

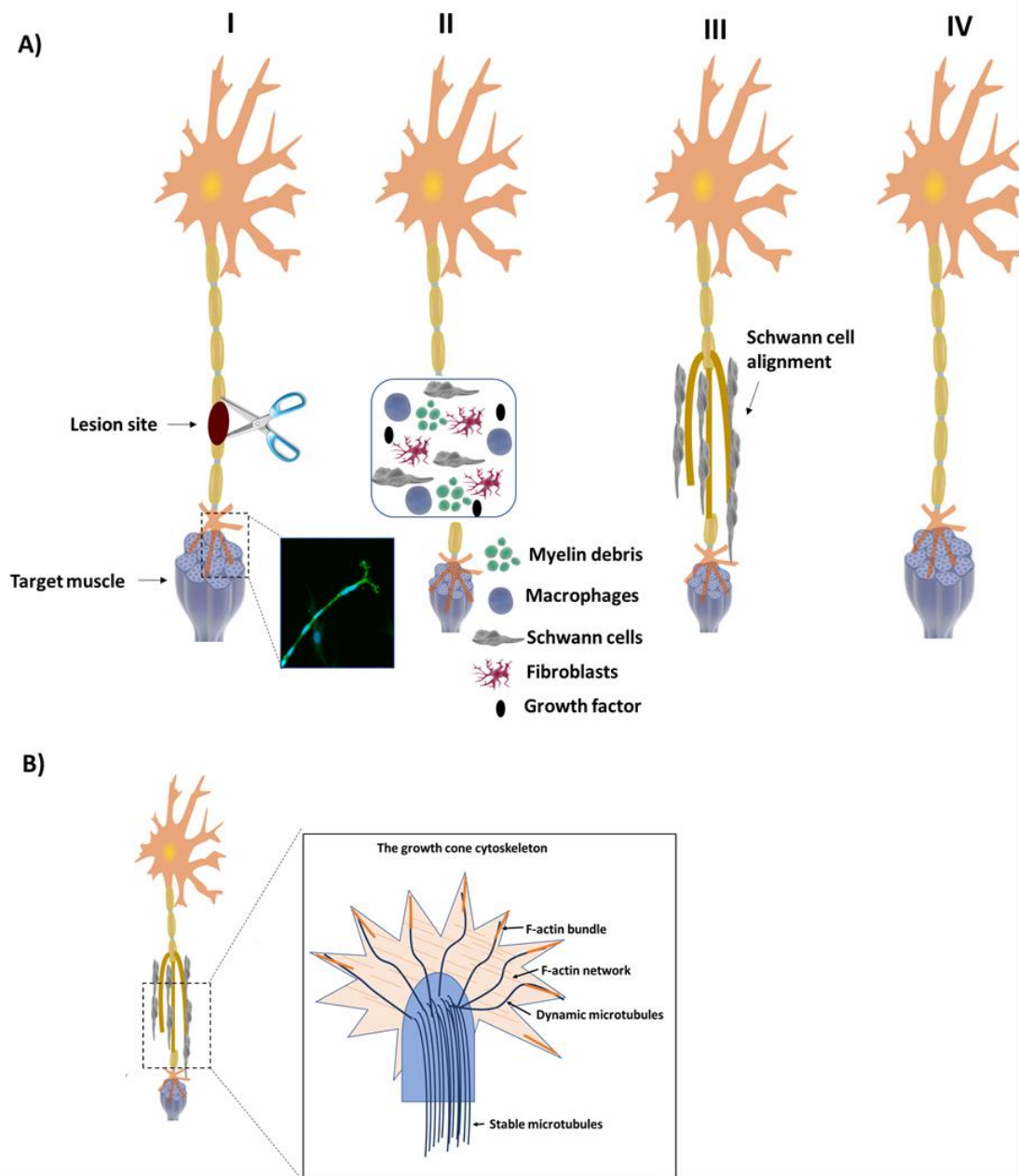


Figure I-2 - A) Progression of Wallerian Degeneration: I) A single axon with enwrapping myelinating Schwann cells suffers a traumatic injury; II) The axon breaks and the distal stump undergoes cellular changes. Distal to the injury, there is a destruction of the remaining intact axon and disintegration of myelin cover, leaving debris behind. Macrophages and Schwann cells, which turned to a pro-regenerative phenotype, accumulate at the lesion site and scavenge the debris; III) Schwann cells aligns in the Bands of Bungner. These tubes provide a permissive growth environment and guide extending axons towards distal targets; IV) If the axon is able to traverse the injury gap, the distal target becomes re-nerved and the neuron becomes fully functional; and B) The growth cone is a large actin-supported extension of a regenerating neurite pursuing its corresponding synaptic target. It is responsible for the migration and path finding during neurite extension, in which the lamellipodia and filopodia interact with the adjacent matrix.

This is a key process intimately related to increasing the regenerative potential after injury. In fact, elimination of degenerated myelin is fundamental for repair since PNS myelin holds molecules that inhibit regeneration of severed axons, namely the myelin associated glycoprotein (44). At last, Schwann cells response to injury also includes the formation of regeneration tracks, known as Bands of Bungner. For that, Schwann cells adopt the elongated spindle-shape morphology and line up in columns. To perform such task, they express a variety of adhesion molecules on their surface, such as N-cadherin, L1 and N-CAM. Extracellular matrix (ECM) molecules are also secreted, such as laminin and fibronectin. All the secreted molecules are considered guidance-promoting signaling molecules, important not only during early development, but also to create a microenvironment that mediates axon regrowth and guidance, allowing axons to reconnect with their target tissues (45).

Overall, Schwann cells acquire a pro-regenerative phenotype, capable of promoting nerve repair, when there is a conversion of myelin-Schwann cells to repair-Schwann cells. The single protein capable of this transformation is c-Jun, which is rapidly up-regulated in the distal nerve end Schwann cells after injury (46).

I-1.4. Strategies for Nerve repair

Clinically, the straight-forward technique to repair minor nerve defects is the end-to-end suture (47). However, this technique is circumscribed to a maximum gap length ranging from 5 mm to 20 mm, depending on the nerve, since the suture must be done without creating excessive tension in the nerve ends. When the nerve gap length makes end-to-end suture unfeasible, peripheral nerve grafts are the gold standard treatment for nerve restoration. In a technique that dates to Philipeux and Vulpian in 1817 (48), the insertion of a graft section provides a physical and biological scaffolding, over which axonal outgrowth occurs. Grafts can be autologous, known as autografts, or allografts. The use of autografts has inherent disadvantages, such as donor site morbidity and reduced availability (49). For allografts, the tissue is harvested from another donor, which can increase the risk of disease transmission and immunological response. However, related to allografts, a recent and promising alternative for patients who have exhausted all reconstructive methods is the vascularized composite tissue allotransplantation (VCA) (50). Furthermore, tacrolimus, one of the immunosuppressant drugs that will accompany the patients for a life-time when subjected to this procedure, has shown to have positive effects in PNR (51).

However, despite those seemingly good chances of recovery with grafts, incomplete recuperation from PNIs usually can lead to multiple negative consequences, which comprise numbness of affected

members, chronic pain, diminishing of sensory and/or motor function and a disturbing permanent disability of the patients (52). It is a fact that these outcomes are unsatisfactory for the demands of today's patient lives, since only 25 % of patients regain proper motor function, and less than 3 % recuperate sensation in a full extent (53).

Decellularized nerve conduits are another possibility for nerve repair (54). In order to avoid the need of immunosuppressive drugs associated to allografts requirements, which make the patient more prone to acquire infection and tumors, the decellularized nerve conduits can eliminate the cellular components that cause immunogenic reactions. However, the native ECM is conserved, along with the basal lamina, the guiding mechanical cues for axonal growth is maintained. Several methods can be used to decellularize nerves, among them, physical methods such as lyophilization (55), direct pressure, and agitation (56). Chemical methods have also been attempted and include digestion with alkaline or acidic solutions (57), detergents (58), together with the action of enzymes such as trypsin and endonucleases (59). Various studies support the hypothesis that decellularized grafts are among the best options for nerve repair, since they can bridge more than 10-20 mm long gaps in rats (60, 61). However, as concluded by the authors who performed a 10-year review of the use of allografts for PNR (54), further research is desirable in order to improve and standardize preparation protocols, including recellularization, advance their effectiveness, therefore being able to substitute the current gold standard, especially in the repair of long nerve defects. For these reasons, increasing efforts have been made over the last decades in the search for effective alternatives to autografts. Surgical treatment strategies in the case of PNI can be seen in **Figure I-3**.

In an attempt to overcome the limitations of nerve grafting as well as the unsatisfactory outcomes, TE approaches focusing on the development of innovative biocompatible artificial nerve devices to assist innate regeneration processes to re-establish the peripheral nerve have also been reported (62, 63). TE strategies have been a widely travelled alternative to bridge the nerve gap and throughout the years many types of NGCs were proposed, being some of them already approved by the Food and Drug Administration (FDA) (64, 65). Since mature neurons are not susceptible to mitosis phenomena, it is crucial to support the re-growth of the existing cell bodies, providing both a protective environment and guiding paths. In this way, it is possible to direct axons from the proximal to the distal site, permitting the proper linking of the damaged synapses connections. In brief, the protection of the injury site and performance as a guidance substrate are the two main reasons why tubulization is used in PNIs.

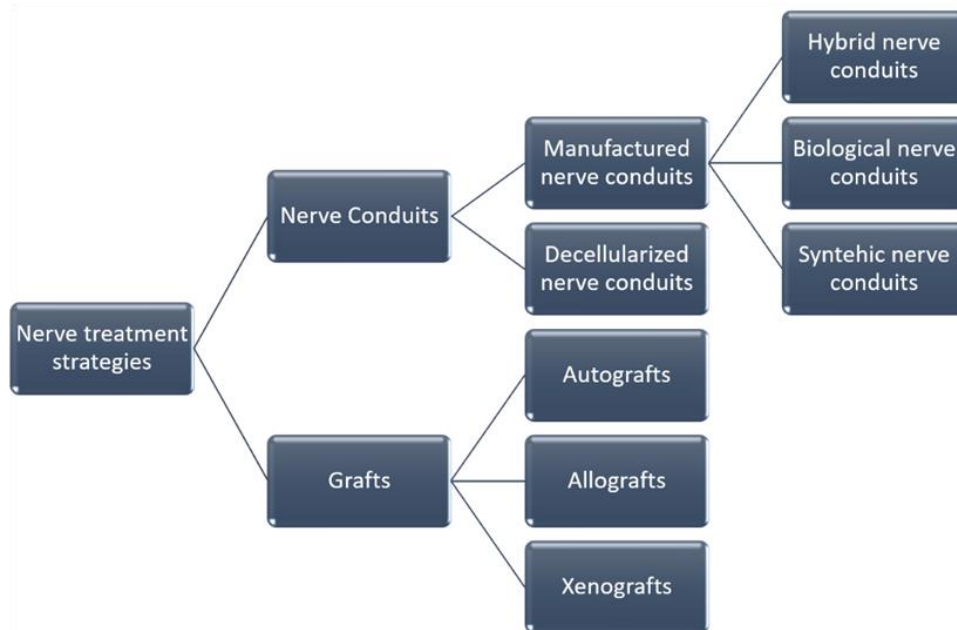


Figure I-3 - Strategies for nerve repair. In the case of a significant nerve gap formation where end-to-end coaptation is not possible, nerve grafts or engineered NGCs are required to serve as a bridge between the nerve stumps and to support axonal regrowth. In the case of grafts, they can be from the patient her/himself, known as the autografts. Allografts and xenografts are also a possibility. As an alternative, if the option falls in the NGCs, those can be nerves harvested from the body, which undergo a process of decellularization to avoid immunological reactions, maintaining the ECM for physical support. NGCs can also be manufactured and engineered with biological or synthetic materials, as well as a combination of both.

Engineering a NGC should aim at facilitating cellular spreading and growth of damaged nerve tissues in 3-dimensions (3D) (66). In addition, it is crucially important that the material envisioned to be used to construct the NGC is cytocompatible and has pronounced biomechanical properties, and suturability. If an engineered NGC does not present a proper cytocompatibility, it may not contribute to the growth of damaged nerves, but would instead be the reason of acute inflammation and even infection (67). It must exhibit good biocompatibility with low inflammatory and immunogenic reactions (68). It must also be biodegradable, and ideally degrade in the same rate as nerve regenerates. Otherwise, a quick degradation might trigger an inflammatory response (66, 69). Regarding the mechanical properties, the NGC should provide sufficient mechanical strength to prevent the NGC rupture during the patient's movements and physically support neural tissue regeneration. The parameters to be considered for the design of NGCs are summarized in **Table I-2** (70-78).

Table I-2 - Design criteria for the development of NGCs.

| Ideal properties of NGCs | Detailed description |
|---------------------------------|---|
| Biocompatibility | Must be well incorporated in surrounding tissues and not cause inflammatory response (70); |
| Degradation | Degradation rate should match nerve regeneration rate (71); |
| Porosity | NGC must allow nutrient and oxygen exchange, limiting scar tissue infiltration (72); |
| Anisotropy | The NGC conduit itself or the luminal filler should be aligned to provide directional guidance (73); |
| Adequate protein release | NGC or the luminal filler should provide sustained release of growth factors (74); |
| Physical fit | Adequate internal diameter not to compress the growing nerve (75); |
| Cellular support | Must allow the adhesion and proliferation of relevant cell types, such as Schwann cells and endothelial cells (76); |
| Electrically conducting | Capable of propagating electrical signals (77); |
| Vascularization | The NGC must allow the vascularization to occur inside the NGCs, to nourish the regenerating tissue (78); |
| Calcification | The implantable NGC must not calcify <i>in vivo</i> (79); |
| Suturability | The NGC must withstand a suture being pulled out without breaking the biomaterial (80). |

Concurrently, the NGC should have appropriate elasticity to be able to lessen tensions in the damaged area (67). Two other major features that NGCs must possess are related to the suturability, where the suture thread cannot be pulled out of the material when in physical stress (81). The second feature relates to the ability of a medical device to not calcify when implanted *in vivo*. Such characteristic must be previously tested and avoided at all costs, since calcification of a conduit would hinder regeneration in a great extent. In fact, Carvalho *et al.* (79) recently reported on a silk fibroin NGC that would or not calcify, according to the method of solvent removal and final surface properties.

Furthermore, the materials used to construct NGCs should prevent the penetration of fibroblasts that will lead to the formation of glial scar tissue around the implant, which could reduce the healing chances (82). The permeability of a conduit is also an important parameter to consider in the NGC design as both nutrients and oxygen must diffuse into the site of regeneration. Otherwise, cells inside the conduit, especially if it is a long conduit, will be under a deleterious ischemic environment which can result in cellular hypoxia and lack of proper nutrients. Ideally, electrical conductivity would be preferred for a NGC used in neural TE in order to mimic the electrical properties of nerves and at the same time excite the neuron communication (83). In brief, an ideal NGC should be biocompatible, biodegradable, flexible, kink-resistant, compliant, easy suturable, porous, neuroconductive and with

suitable surface and overall mechanical properties (75). Furthermore, the developed NGC should allow vascularization to occur in the lumen and avoid calcification *in vivo*.

In the early use of NGCs made of synthetic materials, they were mainly composed by silicon tubes and could only repair injuries up to 10 mm. Some disadvantages on the use of that conduits included total lack of biodegradability, which led to inflammation and chronic foreign body reaction, as well as lack of swelling capacity, which would compress the nerve, thus hindering the regeneration process (84). In order to overcome such difficulties, biodegradable NGCs have been proposed, some of which are FDA-approved and being currently used in the clinical setting (65). The FDA approved NGCs can be seen in **Table I-3** (65).

Table I-3 - Approved NGCs used in the clinical setting.

| Product name | Company | Biomaterial composition | Degradation time |
|-------------------------------|--|---|------------------|
| Neuragen® | Integra Neurosciences, NJ, USA | Collagen type I | 36-48 months |
| NeuraWrap™ | Integra Neurosciences, NJ, USA | Collagen type I | 36-48 months |
| Neuromend™ | Collagen Matrix, Inc, NJ, USA | Collagen type I | 4-8 months |
| Neuromatrix/Neuroflex™ | Collagen Matrix, Inc, NJ, USA | Collagen type I | 4-8 months |
| Neurotube® | Synovis Micro Companies Alliance, AL, USA | Polyglycolic acid (PGA) | 6-12 months |
| Neurolac™ | Polyganics Inc, Netherlands | Poly(D,L-lactide-co-ε-caprolactone (PLCL) | 16 months |
| Salubridge/Salutunnel™ | Salumetica LLC, GA, USA | Polyvinyl alcohol (PVA) | Non-degradable |
| Axoguard® | Cook Biotech Products, IN, USA | Porcine small intestinal submucosa matrix | N/A |
| Avance® | AxoGen Corporation, USA | Human nerve allograft | N/A |

I-1.4.1. Biomaterials

I-1.4.1.1 *Synthetic biomaterials*

Regarding the synthetic materials, these are still considered very promising since the majority of the FDA-approved NGCs are composed of materials such as Neurotube (polyglycolide acid, PGA) and Neurolac (poly(L-lactide-co-ε-caprolactone, PLCL). Other synthetic materials widely used in PNR are polylactic acid (PLA), polylactic-co-glycolic (PLGA), polycaprolactone (PCL), and polyhydroxybutyrate

(PHB). In brief, synthetic nerve conduits provide higher degree of controllability, better mechanical properties, and poor bioactivity as compared to their natural equivalents (65). Moreover, these materials are known for low inflammatory response and effortless processing, which means they can be processed in a variety of forms, to enhance nervous tissue growth. However, in spite of the referred positive characteristics of synthetic polymers, a few disadvantages are also reported (85). The main negative aspects are related to suboptimal biodegradation and possible toxic biodegradation byproducts. These drawbacks block their extended use in the clinics (86). **Figure I-4** shows some promising results considering synthetic biomaterials applied to PNR. From **Table I-4**, it is also possible to find the most recent and relevant reports considering the use of synthetic biomaterials in PNR (87-99).

PLA

PLA has been used as a nerve conduit material in a few studies. Matsumine *et al.* (87) developed a biodegradable nerve conduit with PLA non-woven fabric and evaluated its nerve regeneration promoting effect. The conduit made of randomly connected PLA fibers demonstrated a comparable ability as the autograft to induce PNR in the buccal branch of a 7 mm facial nerve defect. Another author developed a biodegradable multi-layer microbraided PLA fiber-reinforced conduit with outstanding mechanical properties, which revealed to be a promising tool for neuro-regeneration (88).

PLLA

PLLA is the crystalline form of PLA. In a study by Zeng *et al.* (89), several topographies were achieved in the PLLA conduit using low-pressure injection molding and thermal-induced phase separation, including a nano-fibrous microstructure, micro-spherical pores and nano-fibrous pore walls and a ladder-like microstructure. Of all the topographies experimented, the nano-fibrous microstructure allowed the differentiation of neural stem cells (NSCs) into neurons. Also paying a lot of attention to the inner structure of the NGC, others have developed a conduit that consists of a porous poly(D,L-lactic acid) (PDLLA) tubular support structure with a micropatterned inner lumen pre-seeded with Schwann cells (90). Such device delivered physical, chemical and biological guidance cues.

PGA

The use of PGA is not very common in PNR field. However, of the clinically available NGCs, PGA has the most rapid degradation rate and it is FDA-approved (Neurotube®). When testing Neurotube® for facial nerve repair, it was found to be an effective substitute to autologous nerve grafts. However, the

authors reported a few limitations to this NGC, which consist in the fact that it can only be used with gaps of less than 30 mm, it is quite costly and intolerance cases have been reported (92). When compared to other FDA-approved conduits, Neurotube® achieved the poorest result in terms of nerve regeneration (91).

PLGA

PLGA is one of the most attractive synthetic polymers and broadly used in PNR. This FDA-approved material gives rise to very low inflammatory responses, and its degradation can be easily controlled by altering the ratio of its monomer components. Additionally, PLGA scaffolds have the unique ability of adhering to Schwann cells and directing their growth (100). A recent study focused on producing a laminin-coated and yarn-encapsulated PLGA NGC (93). The PLGA fiber yarns were fabricated through a double-nozzle electrospinning system and then the PLGA fibrous outer layer was collected using a general electrospinning method. The conduit demonstrated adequate mechanical properties as well as promising potential in promoting Schwann cells proliferation and migration. In another study also focused on different topographies (101), it was developed a hybrid-structured nerve conduit which consists of a PLGA microfibrillar bundle wrapped in a micro/nanostructured PLGA membrane. This device demonstrated high capability for guiding nerve cells and promoting cell migration. Many other studies using PLGA were developed, inclusively with conduits capable of releasing NTFs or other neuroprotective molecules such as salidroside and Nectin-like molecule 1 (NECL1) (94, 102, 103).

PCL

PCL is one of the most used polymers in TE (104). It has been broadly applied in bone (105), cartilage (106), cancer defects (107), and drug delivery applications (108). It is a biodegradable semi crystalline linear polyester produced by ring-opening polymerisation of ϵ -caprolactone with a low melting point of around 60 °C. For the mentioned biodegradable polyesters mentioned so far, *in vivo* degradation rate is in the order PCL < PLA < PGA. Due to PCL's very low *in vivo* degradation rate and high drug permeability, it has been found to be useful in long-term implantable delivery devices (109). Bearing in mind that polymeric bioabsorbable conduits can be used as drug delivery systems, Salmoria *et al.* (110) produced PCL conduits by melt extrusion technique, which were loaded with ibuprofen. PCL is also a very attractive polymer for the rapidly emerging and recently popular 3D printing technology. In a study recently published by Lee *et al.* (95), combination of stereolithography and electrospinning techniques allowed to fabricate a novel 3D biomimetic PCL neural scaffold with tunable porous

structure and embedded aligned fibers. The results indicated that PCL fibers greatly increased the average neurite length and directed neurite extension of primary cortical neurons along the fiber. Quite often, polyesters are blended with other components to make composite NGCs which allows to improve their mechanical properties and control the general features of the NGCs in more detail (96, 111-114).

PU

Created by a water-born process, PU has recently been applied as the base material for the construction of a novel NGC (97). The NGC was built through the freeze-drying technique and presented an asymmetric microporous structure that allowed bridging a 10-mm gap in rat sciatic nerve. The results, in terms of nerve regeneration, were remarkable. Inclusive, based on functional recovery and histology findings, the efficacy of PU NGC was superior to that of commercial conduit Neurotube®, to which it was compared. Recently, an antioxidant-PU conduit was developed using the electrospinning technique by Singh *et al.* (98) and further filled with an aligned chitosan-gelatin cryogel filler. The *in vitro* cellular tests with dorsal root ganglia (DRGs) cultures showed the aligned growth and cellular migration along the pores, indicating that both the outer part of the conduit as well as the luminal filling are potentially appropriate for PNR.

PVA

PVA is another synthetic polymer used in the construction of NGCs. It is water soluble but non-degradable, being considered non-resorbable. There is currently FDA-approved NGCs made of PVA hydrogels, named SaluBridge™ and SaluTunnel™. However, such devices have not been validated with accessible pre-clinical or clinical studies. It can also be stated that the utilization of nonabsorbable conduits has declined with the crescent use of absorbable synthetic grafts (115). To improve that, Stocco *et al.* (99) recently manufactured a conduit made of a patented and novel biodegradable hydrogel, oxidized PVA (OxPVA). An *in vitro* and *in vivo* battery of tests revealed that OxPVA scaffolds performed very similarly to the autograft group.

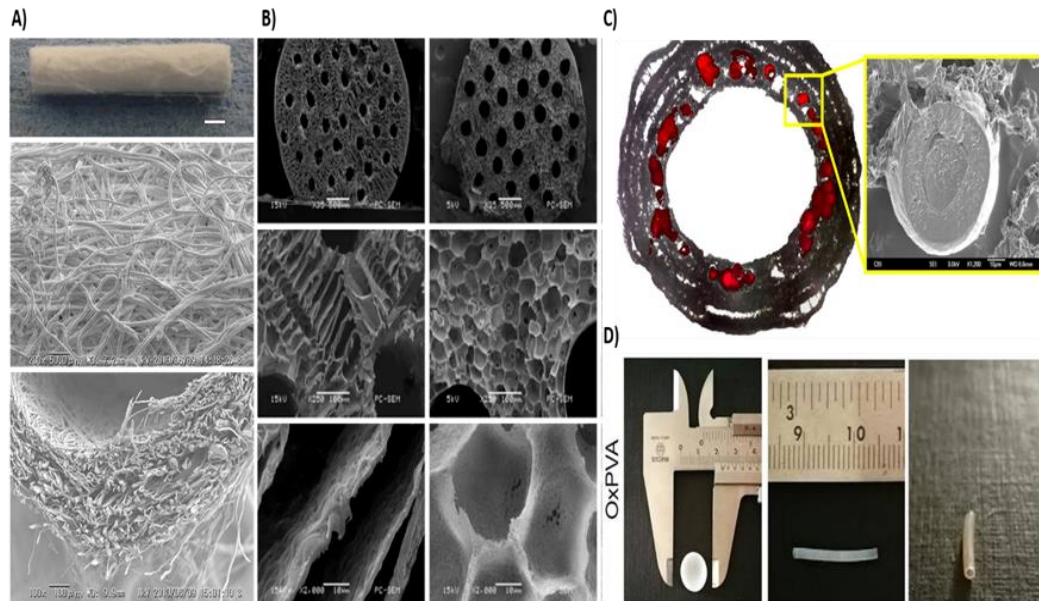


Figure I-4 - Promising results obtained with synthetic polymers applied to PNR. A) A non-woven poly(lactic acid) (PLA) tube. Scale bar: 1 mm; B) SEM images of the PLLA multi-channel conduits cross-section using different magnification. Scale bar: 500, 100 and 10 μm , from top to bottom; C) Scanning electron micrograph of double-walled microsphere following incorporation into PCL nerve guides; and D) Gross appearance of disk-shaped and tubular scaffolds made of OxPVA. A), B), C), and D) were reprinted with from (87), (89), (96) and (99), respectively.

I-1.4.1.2 *Natural-origin Biomaterials*

Natural-origin biopolymers used for the fabrication of NGCs typically have regenerative bioactivity along with appropriate mechanical properties. Natural biomaterials allow for improved communications between cellular components and the scaffold is also an advantage since cells must be stimulated to proliferate, benefiting tissue regeneration (116). However, some restrictions are associated to natural-origin biomaterials, such as the batch to batch disparities (117). In the section below, interesting and recent reports using natural-origin biomaterials for PNR applications, from proteins (*e.g.*, silk fibroin and keratin) to polysaccharides (*e.g.*, chitosan and alginate) will be reviewed. **Figure I-5** shows some promising results obtained with natural-origin biomaterials, in particular, using silk fibroin, chitosan and alginate polymers. The significant works considering the use of natural-origin biomaterials in PNR are summarized in **Table I-5** (118-129).

Table I-4 - Relevant and recent published works focused on the fabrication of NGC with synthetic biomaterials.

| Conduit material | Fabrication method | Location, defect size, model | Outcomes | Year, reference |
|------------------|--|---|--|-----------------|
| PLA | Non-woven material, melt blown process | Facial nerve, 7 mm gap, rat | Comparable ability to induce PNR as autologous nerve graft. | 2014, (87) |
| | Multi-layer, micro-braided, fiber-reinforced conduit | Sciatic nerve, 10 mm gap, rat | Successful regeneration with cables bridging the gap. | 2009, (88) |
| PLLA | Low-pressure injection molding and thermal-induced phase separation technique, 33 inner channel NGC | <i>In vitro</i> assays with NSCs | 81.1 % of NCSs differentiated into neurons. | 2014, (89) |
| | Porous PLLA conduit achieved by dipping method, with micropatterned inner lumen by ion etching. Pre-seeded with Schwann cells | Sciatic nerve, 10 mm gap, rat | Presence of Schwann cells did not affect results, speed of functional recovery was enhanced. | 2004, (90) |
| PGA | Neurotube® is fabricated to form a knitted or woven tubular device | Segmental nerve defect, 10 mm gap, rat | Exhibited the poorest results for functional motor recovery in the rat model in comparison to other FDA-approved conduits. | 2009, (91) |
| | | Facial nerve, 10–30 mm gap, humans | Valid solution for this kind of defect in emergency. Associated to some limitation such as high cost and possible intolerance. | 2005, (92) |
| PLGA | PLGA fibrous outer layer produced by electrospinning and containing laminin coated yarns obtained by double-nozzle electrospinning | <i>In vitro</i> assays with Schwann cells | Significant higher proliferation and elongation of Schwann cells along the inner yarns. | 2017, (93) |
| | Two concentric biodegradable PLGA tubes enclosing a NGF reservoir. Solvent casting method | Sciatic nerve, 15 mm gap, rat | Optimal release levels of NGF; Improved muscle weight, myelinated nerve growth, and higher target connection. | 2017, (94) |
| PCL | 3D printed conduit embedded with electrospun aligned nanofibers | <i>In vitro</i> assays with NSCs and primary cortical neurons | Increased average neurite length and directed neurite extension along the fiber. | 2017, (95) |
| | PCL conduits were fabricated by dipping and incorporate double-walled PLGA/PLA microspheres encapsulating GDNF | Sciatic nerve, 15 mm gap, rat | GDNF increased tissue formation within the nerve guide lumen and promoted the migration and proliferation of Schwann cells. | 2010, (96) |
| PU | Mold casting followed by freeze-drying, producing a porous scaffold | Sciatic nerve, 10 mm gap, rat | Significantly greater efficacy of the PU conduit when compared to the commercial Neurotube®. | 2017, (97) |
| | Electrospun Antioxidant-PU conduit filled with freeze-dried aligned chitosan-gelatin cryogel | <i>In vitro</i> study with neuro 2a, C2C12 and DRGs. | DRGs demonstrated aligned growth of the neurites along the pores of the cryogel inside the NGCs. | 2018, (98) |

| | | | | |
|------------|--------------------------------------|------------------------------|--|------------|
| PVA | SaluBridge™, implantable wrap | N/A | No manuscripts have been published regarding this NGC. | N/A |
| | Dipping technique of OxaPVA hydrogel | Sciatic nerve, 5 mm gap, rat | Axon density in the middle of the conduit significantly higher as compared to autograft. | 2018, (99) |

Silk fibroin

Silk fibroin (SF) is a fibrous protein with remarkable mechanical properties produced by silkworms and spiders (130). Silk polymers consist of repetitive protein sequences and provide structural roles in nature, such as cocoon formation, nest building and web creation (131). With very low immunological response, capacity to be transformed in diverse shapes and matrices, tunable degradation as well as easily chemically modified, SF has the potential to impact the clinical needs in terms of nerve regeneration (132). Beyond PNR, SF has been extensively applied in the TERM field with very distinctive applications (133-135).

Carvalho *et al.* (79) produced tunable enzymatically cross-linked SF NGCs, resorting to tyrosine groups present in silk structure that are known for allowing the formation of a covalently cross-linked hydrogel. The fact that the process involves an enzymatic crosslinking allows tuning several parameters in the final conduit, *i.e.* from its mechanical properties to porosity or biological properties.

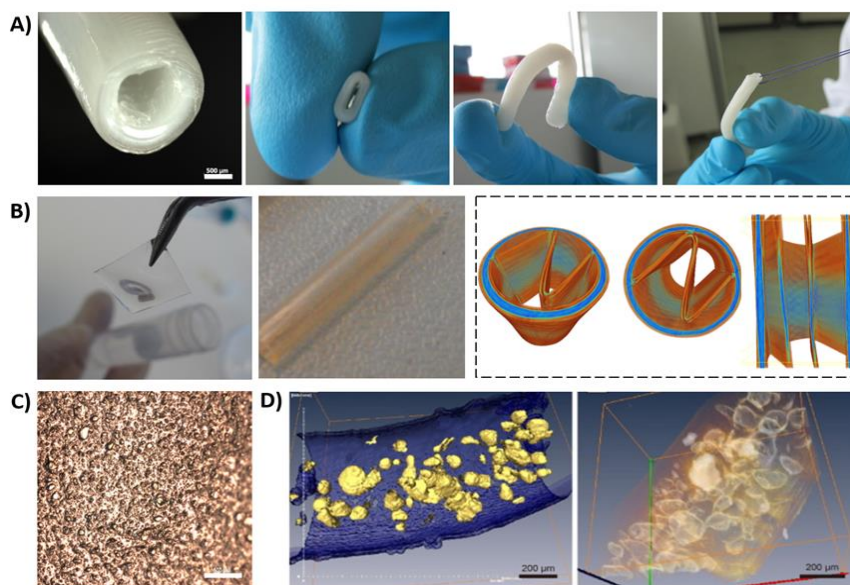


Figure I-5 - Promising results obtained with natural-origin polymers applied to PNR. A) Example of an enzymatically crosslinked SF nerve guidance conduit developed and patented by Carvalho *et al.* (79) for application in PNR. The developed NGC presents outstanding mechanical properties, with kinking-resistant capacity and suturability, as can be seen by the images (in that row); (B) Images of a 5 % of degree of acetylation chitosan membrane, which can be further used as a NGC by rolling-up or in a different strategy, as a luminal filler; (C) 5 % degree of acetylation chitosan membrane incorporating human hair keratin, developed at our research institute; and D) Confocal laser microscopy showing macroporous alginate fibers incorporating gelatin particle porogens. Scale bars: 500 µm.

One of the advantages of SF relies on the ability to be processed in a variety of shapes. Dinis *et al.* (136) developed a 3D multi-channel SF conduit through electrospinning system encompassing approximately 12 multi-channel guides of different sizes inside the main conduit, mimicking the native structure of the nerve endoneurium, perineurium, and epineurium. In fact, due to the outstanding properties that several silk NGC have demonstrated after decades of research, there is an active clinical trial (NCT03673449) with SilkBridge. Such device is a biocompatible SF-based matrix that aims at attracting the patients' native cells to regenerate the nerve, *i.e.* without the need to add cellular components previous to the implantation. The SilkBridge is also being used in digital nerve defects.

Keratin

Keratin protein has been recognized as biomaterial with high potential due to its excellent bioactivity and biocompatibility (137). Lately, the hair keratin has gained much attention (138, 139), not only because of its properties, but because the follicle itself is a bizarrely proliferative organelle that illustrates an extremely arranged regenerative process. Also, the fact that it is potent naturally derived biomaterial, is human-derived and possesses cellular interaction sites making it an attractive protein in TE applications (140).

So far, little has been done concerning the application of hair keratin to PNR. All *in vivo* work done with keratin in the scope of PNR has been developed under the supervision of the scientist Van Dyke at the Wake Forest University (122-124, 141).

Chitin and Chitosan

Chitin and chitosan are two of the most popular natural biopolymers in the TE field, as well as in the area of nerve repair (142). Chitin is a natural biopolymer normally present in the exoskeletons of arthropods and the shells of crustaceans, being the main sources, in fact, the marine crustaceans such as shrimp and crabs. It is a linear homopolymer composed of N-acetyl-D-glucosamine units that form beta-(1-4)-linkages. The most abundant polysaccharide in nature is cellulose, immediately followed by chitin (143). On the other hand, chitosan is obtained through the partial deacetylation of chitin. It is a polysaccharide composed of D-glucosamine and N-acetyl-D-glucosamine units linked through beta-(1-4)-glycosidic bonds. Soluble in acidic aqueous media, chitosan, is finding applications in many areas, such as food, cosmetics and biomedical fields (144).

It has early been proved that chitin and chitosan-based scaffold can allow the attachment, migration, and proliferation of Schwann cells as well as of DRGs, two of main players in the nerve regeneration process (145-148). Furthermore, chitosan biomaterials encourage the aligned orientation of Schwann cell and growing axons (149-151), which is a relevant phenomenon in the process of Wallerian degeneration and consequent regeneration. Additionally, chitosan-based NGCs are easily handled, and transparency facilitates surgical manipulation and suturing of the nerve stumps. Due to the recognized potential of chitosan, a chitosan-based nerve conduit under the name Reaxon® Nerve Guide manufactured by Medovent GmbH (Mainz, Germany), in accordance with the international standard DIN EN ISO 13485, was launched in the market in 2014. These conduits were thoroughly investigated in a report by Haastert-Talini *et al.* (152), where the referred conduits combined several pre-requisites for a clinical acceptance; and the tube with a degree of acetylation of 5 % was considered as the most supportive for peripheral nerve regeneration to bridge a 10 mm gap. That conduits were used in a critical sized nerve gap (64) and in type 2 diabetic Goto-Kakizaki rats (153), confirming their good *in vivo* performance.

Alginate

Alginate is a broadly used bioresorbable polysaccharide in the food industry, wound management or in the TE field. It is a block co-polymer consisting of beta-d-mannuronic acid and alpha-l-guluronic acid, extracted from brown seaweed (154). It is considered a biocompatible material which has no inhibitory effect on cell proliferation *in vitro* and induces reduced foreign body reaction when implanted in tissues *in vivo* (155). It has been described that calcium ions induce specific associations between alginate chains, consequently forming hydrogels (156). Using such mechanism, previous studies (157, 158) have shown the possibility to use alginates applied to PNR. Namely, a decomposable freeze-dried alginate gel covered by PGA mesh was employed in a 50 mm gap in a cat sciatic nerve model with positive results (157). The same authors later examined the interaction between regenerating axons, Schwann cells and the implanted alginate gel (158), showing that alginate gel provides a good environment for axon outgrowth and Schwann cell migration. In another study (128), macro-porous alginate fibres encapsulating primary DRGs were produced by wet spinning an alginate solution containing dispersed gelatine particles. Marked neurite outgrowth was evident over 150 µm, indicating that pores and channels created within the alginate were providing a favourable environment for

neurite development. Other studies have focused on using alginate as NGCs luminal fillers, with promising results (159-161).

I-1.4.1.3 *Endogenous Biomaterials/ ECM proteins*

Still among the natural-origin biomaterials, ECM endogenous proteins such as collagen, fibrin, laminin, and hyaluronic acid (HA) have been highly investigated, since they naturally exist in the human body. ECM is a highly organized 3D structure that occupies the intercellular space, providing a physical support to tissue. It fundamentally acts as a natural scaffold by delivering a matrix, where cells can arrange within the connective tissue. Besides delivering the physical support, ECM also provides the chemical setting for adequate cellular behavior in terms of survival, differentiation and overall fate. Furthermore, Schwann cells express specific integrins, such as $\alpha_1\beta_1$, $\alpha_2\beta_1$, $\alpha_6\beta_1$, $\alpha_6\beta_4$, $\alpha_5\beta_1$, $\alpha V\beta_3$, that connect to ECM and encourage myelination through their interaction with the basal lamina (162). The important interaction between ECM molecules and the nervous system can also be inferred from the fact that laminin, fibronectin and collagen are effectively used as coatings of tissue culture plastics to enhance Schwann cell and DRGs responses, such as adhesion and migration (163). A few recent publications related to the use of endogenous biomaterials applied to PNR can be found in **Table I-6** (164-174). Furthermore, **Figure I-6** summarizes the promising results making use of endogenous biomaterials applied to PNR.

Collagen

Collagen is, within the ECM, probably the major organizational and structural protein of hard and soft tissues. It provides strength, mechanical stability, structural integrity and plays a crucial biological role in a variety of tissues and organs including, bone, cartilage, tendon, skin, and cornea (175). To achieve that, collagen is extremely dynamic, undergoing constant modifications to deliver proper physiologic functions (131). Although collagen offers structure to our bodies, protecting and supporting the soft tissues, collagen is a relatively simple protein, containing a triple-helical structure and the presence of 4-hydroxyproline. Up to this date, 28 collagen types have been acknowledged. The types I, II, III, and V constitutes the essential part of collagen in bone, cartilage, tendon, skin, and muscle. Collagen can be extracted and purified from a variety of sources, typically from bovine and porcine sources. However, in recent years new sources are being exploited, such as marine-origin residues (176).

Table I-5 - Relevant and recent published works focused on the fabrication of NGC with natural biomaterials.

| Conduit material | Fabrication method | Defect size, location, model | Outcomes | Year, references |
|-------------------|--|--|--|------------------|
| Silk fibroin (SF) | Simple spider silk fibers, from <i>Nephilia edulis</i> species | <i>In vitro</i> study, co-culture of ADSCs and Schwann cells | Spider silk fibers represent a suitable NGC filler due to cells migration and elongation along the fibers. | 2018, (118) |
| | SF and PLLA conduit fabricated by electrospinning | 10 mm gap, sciatic nerve defect, rat | The presence of silk augments VEGF secretion, therefore increasing neo-angiogenesis and stimulating nerve regeneration. | 2018, (119) |
| | SF conduit with aligned SF filaments in the interior | 10 mm gap, sciatic nerve defect, rat | FluoroGold retrograde tracing and histological investigation, SF conduits were able to promote nerve regeneration with results approaching those provoked by the positive control autografts. | 2018, (120) |
| | Adsorption of gold nanoparticles onto SF fibres and electrospinning | 10 mm gap, sciatic nerve defect, rat | Nerve conduction velocity as well as the compound muscle action potential was improved due to the presence of conductive gold nanoparticles. | 2018, (121) |
| Keratin | Human hair keratin hydrogel was injected in a FDA-approved conduit | 4 mm gap, tibial nerve defect, mice | Robust nerve regeneration response, in part through activation of Schwann cells. Results similar to autograft. | 2008, (122) |
| | Neuragen® collagen conduit filled with keratin hydrogel | 10 mm gap, median nerve defect, <i>Macaca fascicularis</i> | Confirms earlier findings in studies using rodents; Represents off the shelf alternative to autograft. | 2014, (123) |
| | Double wall PCL containing GDNF-microspheres with a keratin hydrogel | 10 mm gap, sciatic nerve defect, rat | Significant increased density of both Schwann cells and axons, resulting in the better quality of the regenerated nerve through the conduit with keratin. | 2012, (124) |
| Chitosan | Chitosan nerve guides from Reaxon® with a longitudinal chitosan film as a filler | 15 mm gap, sciatic nerve defect, diabetic rat | Supported robust axonal regeneration and functional recovery in healthy animals but also demonstrated to be beneficial for the regeneration process in diabetic rats with relevant blood glucose levels. | 2016, (125) |
| | Chitosan film enhanced with MSCs | 10 mm gap, sciatic nerve defect, rat | Chitosan film enhanced with MSCs improved functional, electrophysiological and histomorphometry recovery of transected sciatic nerves. | 2018, (126) |
| | Chitosan membranes with different degrees of acetylation | Schwann cell and fibroblast <i>in vitro</i> assays | % of acetylation were found to favor Schwann cells invasion and proliferation, presenting at the same time low fibroblast | 2017, (127) |

| | | | | |
|-----------------|--|--|---|-------------|
| | | | adhesion. | |
| | Combination of MSCs with a chitosan film | 10 mm gap, sciatic nerve defect, rat | MSCs were useful for the injury because of the release of several neurotrophic factors as well as the synergistic effect of chitosan accelerating wound healing by promoting an anti-inflammatory effect. | 2018, (127) |
| Alginate | Macroporous alginate fibers produced with a syringe pump | <i>In vitro</i> assays with DRGs | Encapsulation of primary DRGs in macro-porous alginate fibers resulted in marked neurite outgrowth over 150 μm . | 2017, (128) |
| | 3D bioprinting of alginate scaffolds conjugated with single or dual RGD and YIGSR motifs | <i>In vitro</i> assays with Schwann cells and DRGs | Printability, mechanical stability, and neurite outgrowth were assessed with promising results to be used as luminal filler. | 2019, (129) |

The fact that collagen is considered low immunogenic and has good permeability, biocompatibility, and biodegradability make it a great component for TE scaffolding strategies (177). Collagen use in PNR approaches is also extensively accepted, as the protein often exhibits cell-binding domains for aiding neuronal and glial cells attachment and migration. In fact, three collagen conduits are commercially available on the market: The FDA-approved NeuraGen® and NeuroFlex®, which are both made of type I collagen and RevolNerve®, which is made of type I and type III collagens from porcine skin. In a pioneering strategy, Neuromaix® containing collagen-based micro-structured 3D longitudinal guidance channels is capable of providing mechanical support to sprouting DRGs axons and can offer a shielding niche for nerve cells (178).

Fibrin

In the human body, fibrin is an integral part of the clotting cascade. When the coagulation cascade is triggered after an injury, thrombin activates soluble plasma protein fibrinogen, resulting in the formation of an insoluble fibrin milieu. Fibrin is a protein involved in the formation of the blood clot (179). It has found application as a sealant glue in neurosurgery for decades, without any reported complications (180). Furthermore, fibrin plays a critical part in PNR, where longitudinally oriented fibrin cables are formed spontaneously shortly after injury, as a part of the nerve regeneration process, with the intent to direct migration and proliferation of Schwann cells. In fact, the use of fibrin to repair ilioinguinal nerve has shown to have some neuroprotective effect in the injured nerve, where less fibrosis and collagen deposition were found (181).

Fibronectin

Fibronectin, one of the most complex and intriguing proteins, is an abundant soluble constituent of plasma and other body fluids and part of the insoluble ECM. It also mediates a wide variety of cellular interactions with the ECM and plays important roles in cell adhesion, migration, growth and differentiation (182). After extensive characterization, it was found that fibronectin expresses the RGD motif, related to cell adhesion. However, fibronectin has an extensive variety of practical functions other than associate with cell surfaces through integrins. It binds to several biologically important molecules that include heparin, collagen and fibrin. The potential of including fibronectin for PNR was firstly realized when Whitworth *et al.* (183) reported a new nerve conduit material consisting of orientated strands of the cell adhesive fibronectin. In a

10 mm nerve defect in rat, the developed NGC produced the highest rate and amount of axonal regeneration, comparable to the one obtained for autografts. Furthermore, increased expression of fibronectin can be found in damaged peripheral nerve during Wallerian degeneration (184).

Laminin

Laminin is a glycoprotein naturally occurring in nerves. It is a component of ECM that plays a decisive part in cell-recognition, and therefore influences cell migration, differentiation and axonal growth (185). Laminin can also be perceived as a fundamental guiding cue, since the growth cone of regenerating axons is attracted to laminin (186). To make PHBV aligned nanofibers more attractive to neuronal components (187), laminin was adsorbed via electrostatic interactions. Containing both topographic and chemical cues suited for Schwann cell alignment and elongation, the developed NGC was implanted in a critical sized nerve defect in rat, with 12 mm gap and proved to be suitable for such an application. Laminin was also added to collagen gels in a gradient of concentrations with interesting effects (188). For collagen gels without laminin, a typical bimodal response of neurite outgrowth was observed, with increased growth at lower concentrations of collagen gel. However, in the presence of higher laminin concentrations, the growth became independent of the gel stiffness.

Hyaluronic acid (HA)

HA is a linear, anionic and non-sulphated glycosaminoglycan that composes the ECM of all living tissues. Being a very versatile polymer, it finds applications in diverse areas. Furthermore, different molecular weights have an impact on the biological performances, being a highly tunable and adaptable polysaccharide (189). Its use is widely spread in TE applications due to its biocompatibility, biodegradability and chemical modification easiness. HA is also a very versatile biomaterial, which can be prepared in the form of hydrogels, sponges, cryogels, and injectable hydrogels (190). Additionally, HA degradation products seem to exert a positive effect in diverse TE areas, as they encourage wound healing, tissue restoration, and vascularization (191). The injection of HA in a nerve defect has proved to be beneficial for nerve regeneration, since HA groups showed an increase in myelinated axon counts, as well as an increase in retrograde flow, necessary for the regenerative process (192). Furthermore, the advantage of including HA also resides in the fact that it can reduce scar formation after nerve injury (193).

Table I-6 - Relevant and recent published works focused on the fabrication of NGC with endogenous biomaterials.

| Conduit material | Fabrication method | Defect size, location, model | Outcomes | Year, references |
|----------------------|--|--|--|------------------|
| Collagen | Oriented collagen tubes with adsorbed bFGF | 15 mm, sciatic nerve defect, rat | The presence of bFGF revealed to be beneficial in terms of functional recovery. | 2017, (164) |
| | Blend of collagen and chitosan as luminal filler in a PCL conduit | 15 mm, sciatic nerve defect, rat | Axonal regeneration and Schwann cell migration, inclusively inducing comparable functional recovery to that of the autograft control group. | 2018, (165) |
| Fibrin | Micro-suturing with fibrin glue coaptation | 10 mm, sciatic nerve defect, rat | Reduced the operating time and increase the regeneration distance as well as increasing the arborizing axons. | 2013, (166) |
| | Epineural repair with fibrin-glue embedded ADSCs | 10 mm, sciatic nerve defect, rat | Embedding cellular components in the fibrin glue enhanced regeneration, as immunolabeled cells could be found at the neuronal repair site and near intraneuronal vessels indicating an active participation of ADSCs in the process of nerve angiogenesis. | 2016, (167) |
| | 3D hierarchically aligned fibrin nanofiber hydrogel through electrospinning and molecular self-assembly and placed it inside chitosan conduits | 10 mm, sciatic nerve defect, rat | <i>In vitro</i> , directional cell adhesion and migration of Schwann cells and DRGs was detected. <i>In vivo</i> , results showed that the developed NGC performed similarly to the autologous nerve graft. | 2017, (168) |
| Fibronectin | Chitosan conduit enriched with fibronectin | 15 mm, sciatic nerve defect, rat | Fibronectin-enriched scaffolds increased muscle reinnervation and the number of myelinated fiber. | 2017,(170) |
| | Schwann cells embedded in a matrix of alginate/ fibronectin | 10 mm, sciatic nerve defect, rat | Synergistic effect when both Schwann cells and fibronectin were combined with alginate. | 2003, (169) |
| Laminin | Laminin incorporated PLCL nanofibers were produced by electrospinning | <i>In vitro</i> studies with neonatal Schwann cells | Schwann cells expressed bi- and tri-polar elongations due to the presence of laminin. | 2014, (171) |
| | Direct injection of laminin in a peroneal nerve crush | Nerve crush defect, rat | Increased axon presence, larger axon diameter, accelerated axon growth and maturity and advanced motor function recovery. | 2019, (172) |
| Hyaluronic acid (HA) | Electrospinning of a blending of HA in PCL | <i>In vitro</i> cells tests with SH-SY5Y human neuroblastoma cell line | PCL/HA 95:5 exhibit the most balanced properties to meet the required specifications for neural cells. | 2016, (173) |

| | | | | |
|--|--|--|---|-------------|
| | Single-channel tubular conduits based on hyaluronic acid (HA) with and without poly-L-lactide acid fibers in their lumen were fabricated | <i>In vitro</i> tests with Schwann cells | impeded the leakage of the cells seeded in their interior and made them impervious to cell invasion from the exterior, while allowing transport of nutrients and other molecules needed for cell endurance. The NGC interior tubular surface was completely covered with Schwann cells. | 2016, (174) |
|--|--|--|---|-------------|

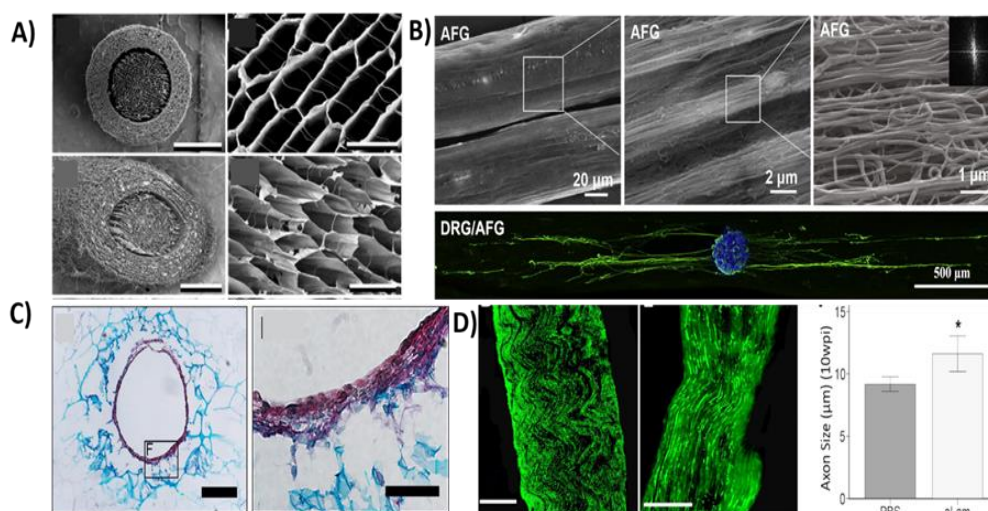


Figure I-6 - Promising results obtained with natural-origin polymers applied to PNR. A) SEM micrographs of transverse section of the oriented collagen-chitosan filler /PCL sheath scaffold and magnification of the interior of the conduit; B) SEM micrograph of the aligned fibrin hydrogel nanofiber and its magnification. Below, a DRGs where the neurites align along the aligned fibers; C) Transversal cryosections of hyaluronic acid conduits cultured for 10 days with Schwann cells in their lumen, after staining with Harris' hematoxylin, Alcian blue, and picosirius red; and D) Longitudinal section of injured nerve treated with PBS (at left) or Laminin (at right), stained with antibodies recognizing NF-h (α -RT97, green). The bar graph illustrates significantly increased axon diameter (μm) with laminin treatment. A), B), C) and D) were reprinted with the permission from (165), (168), (174) and (172), respectively.

I-1.4.2. The possibility of patient-specific nerve repair and NGCs

Personalized TE and regenerative strategies propose a possible solution for contemporary untreatable injuries or illnesses. The use of TE triad offers the possibility of interminable combinations of cells, scaffolds and growth factors, suggesting endless possibilities to customize diagnostic tools, biomedical devices, as well as the final treatments (194). Huge efforts are being carried in laboratories throughout the world to personalize the clinical care, catalyzing major advances in the techniques that allow the treatment of serious injuries and chronic diseases (195). The customization and individualization of medical care carries huge advantages for the patients and the health care systems as well. Targeting the treatments to a specific damage of a patient is critical due to innate discrepancies in patient anatomies, injury shapes and gravity, as well as individual genetic and proteomic features (196). The benefit is clear for the patient, *i.e.* a tailor-made treatment according to its own organism features. For the hospitals and healthcare

systems, the fact that a treatment is 100 % suited for that specific patient and will not fail, will save time and budget.

Peripheral nerves are tissues with different geometries and shapes, which vary anatomically according to the location within the body. But more importantly, the same nerve may vary from person to person with age, according to their medical condition or type of injury (197). Furthermore, the process of nerve regeneration and repair itself is a complex biological phenomenon, with vast singularities, that requires an equilibrium at a molecular, cellular and tissue level (198). Overall, many advantages are envisioned when using 3D printing for nerve repair and regeneration: (1) fabrication of personalized NGC, (2) concomitant assembly of luminal fillers inside NGCs, (3) 3D bioprinting of cells within a bioink or into the NGCs, and (4) establishment of growth factor gradients or pathways (199).

Only recently the hypothesis of patient-specific strategies in nerve regeneration has risen with the development of the 3D-printing technology (200). This was further permitted by the combination of 3D imaging machineries and 3D printing methods. Johnson *et al.* (200) successfully established the combination of 3D imaging and 3D printing for the design and fabrication of anatomically biomimetic truly patient-specific nerve regeneration strategy. It allowed the fabrication of NGCs with complex anatomical structures and inner biofunctionalization with neurotrophic factors, to create a sensory and a motor pathway (Figure I-7A).

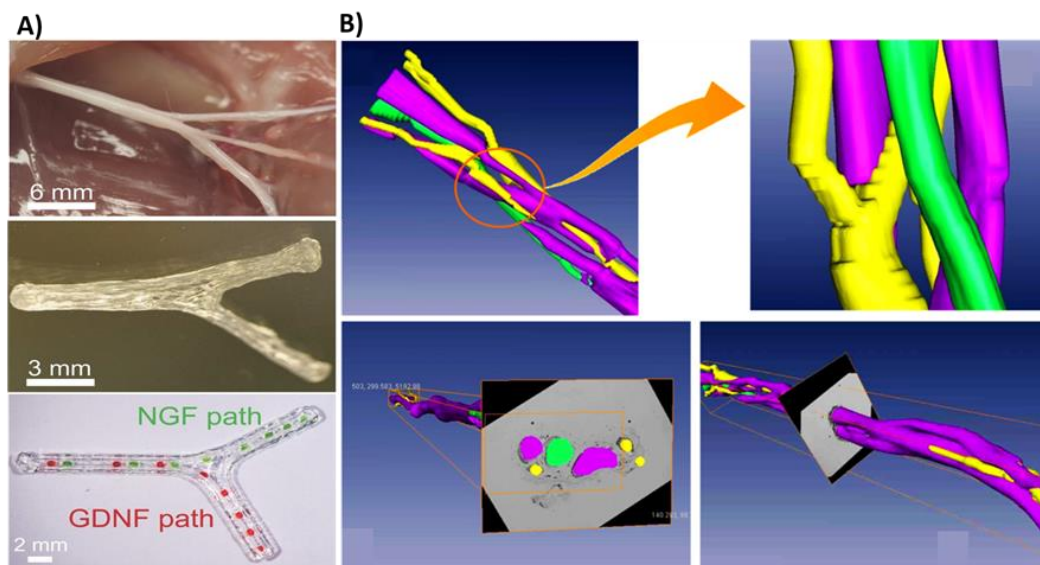


Figure I-7 - Patient-specific and 3D printing technologies will allow improving the treatment given to patients in the future. A) 3D printed complex nerve pathways from 3D scanned bifurcating nerves. Reprinted with permission from (200). B) Imaging of a 3D model of median nerve, for further precise

reconstruction. Reprinted with permission from (201), Copyright © 2015, Macmillan Publishers Limited.

Hu *et al.* (202) explored the 3D-printing technology to prepare a bio-conduit with designer structures for PNR, where the chosen polymer, cryoGelMA gel, was cellularized with ADSCs. When implanted in a 10 mm rat sciatic nerve defect, the results were very similar to the autograft in terms of functional recovery. Tao *et al.* (203) were able to 3D-print an hydrogel conduit with customized size, shape and structure, providing a physical microenvironment for axonal elongation, where the nanoparticles sustained release a drug to facilitate the nerve regeneration. Zohng *et al.* (201) described the key technology of 3D peripheral nerve fascicle reconstruction. First, a 3D virtual model of internal fascicles was obtained and successfully applied for 3D reconstruction for the median nerve (**Figure I-7B**). Exceptional technologies are emerging every day, and 3D printing promises to revolutionize the patient-specific healthcare, namely in PNR.

I-2. CONCLUSIONS

The complex anatomy and physiology of the PNS makes nerve's injury very problematic and extremely difficult to repair. The full recovery is challenging because of the loss of native cues, formation of scar tissue, lack of proper vascularization, and inflammation. The diverse treatments used for nerve repair such as coaptation suturing, grafts, and conduits pose several limitations when trying to recuperate full functionality. Therefore, the development of new NGCs requires a clever combination of the following strategies: (i) the development of new polymer or combination of polymers for better integration with neural native tissue, (ii) additional of topographical structures to intensify neurite alignment and growth, and (iii) biological cues such as growth factors or cellular components.

In what regards the biomaterial choice, there are numerous options to capitalize on different properties of each material. Although many exist and can be used, natural materials are known to be better integrated by host tissue when compared to synthetic ones, more promptly instigating the regenerative mechanisms. The biomaterial availability and cost are also essential parameters to consider. Therefore, and in the author's opinion, SF is probably one of the most versatile biomaterials. It can be processed in a variety of ways and maintain outstanding mechanical properties/suturability and is considered non-immunogenic, with cheap and easy access as well as natural distribution. This biomaterial can be used to fabricate the conduit itself,

as well as anisotropic filling scaffolds in the lumen, in order to be able to treat larger nerve gaps. In addition, several fabrication methods can be used for this biomaterial, including the crosslinking of the tyrosine groups with an enzymatic mediated system or functionalization with growth factors and other molecules of interest. In this context, conductive materials can also be used to intensify the needed neurological transmission and communication.

A brief mention must also be made to the potential of 3D printing for patient-specific nerve reconstructions. The rising of this technology allows to closely reproduce features of the native peripheral nerve, with the aim of possibly replace autologous nerve grafts. Therefore, the current and future bio-imaging modalities allied with detailed printing will permit the production of patient-specific nerve conduits, revolutionizing the field. As the scientific community makes advances on the fundamental knowledge related to the biological mechanisms behind nerve injury and repair, engineers are able to integrate that knowledge in more complex designs, to better mimic natural nerve regeneration and patient specificity in respect to anatomy and biology requirements.

I-3. ACKNOWLEDGMENTS

This work was supported by Cristiana Carvalho PhD scholarship (Norte-08-5369-FSE-000037). J. M. Oliveira also thanks the FCT for the funds provided under the program Investigador FCT 2015 (IF/01285/2015). The authors are also thankful to the FCT funded project NanoOptoNerv (ref. PTDC/NAN-MAT/29936/2017).

I-4. REFERENCES

1. Battiston B, Papalia I, Tos P, Geuna S. Chapter 1: Peripheral nerve repair and regeneration research: a historical note. *International review of neurobiology*. 2009;87:1-7.
2. Belen D, Aciduman A, Er U. History of peripheral nerve repair: may the procedure have been practiced in Hippocratic School? *Surgical neurology*. 2009;72(2):190-3; discussion 3-4.
3. Wu D, Murashov AK. Molecular mechanisms of peripheral nerve regeneration: emerging roles of microRNAs. *Frontiers in physiology*. 2013;4:55-.
4. Geuna S, Tos P, Battiston B. Emerging issues in peripheral nerve repair. *Neural regeneration research*. 2012;7(29):2267-72.
5. Zhang P-X, Han N, Kou Y-H, Zhu Q-T, Liu X-L, Quan D-P, et al. Tissue engineering for the repair of peripheral nerve injury. *Neural Regeneration Research*. 2019;14(1):51-8.
6. Siemionow M, Bozkurt M, Zor F. Regeneration and repair of peripheral nerves with different biomaterials: review. *Microsurgery*. 2010;30(7):574-88.
7. Pixley SK, Hopkins TM, Little KJ, Hom DB. Evaluation of peripheral nerve regeneration through biomaterial conduits via micro-CT imaging. *Laryngoscope investigative otolaryngology*. 2016;1(6):185-90.

8. Herculano-Houzel S. Chapter 1 - Brain Evolution. In: Mai JK, Paxinos G, editors. *The Human Nervous System (Third Edition)*. San Diego: Academic Press; 2012. p. 2-13.
9. Balaji S, Kumar R, Sripriya R, Kakkar P, Ramesh DV, Reddy PNK, et al. Preparation and comparative characterization of keratin–chitosan and keratin–gelatin composite scaffolds for tissue engineering applications. *Materials Science and Engineering: C*. 2012;32(4):975-82.
10. Lobko PI, Ladutjko SI, Bogdanova MI, Golubeva WP. Ganglia formation of the peripheral nervous system. *Acta anatomica*. 1979;103(4):395-9.
11. Payne SL, Ballios BG, Baumann MD, Cooke MJ, Shoichet MS. Chapter 68 - Central Nervous System. In: Atala A, Lanza R, Mikos AG, Nerem R, editors. *Principles of Regenerative Medicine (Third Edition)*. Boston: Academic Press; 2019. p. 1199-221.
12. Birch R, Birch R, Birch R, Birch R. *The Peripheral Nervous System: Anatomy and Function. Peripheral Nerve Injuries: A Clinical Guide*. London: Springer London; 2013. p. 1-67.
13. Fricker M, Tolkovsky AM, Borutaite V, Coleman M, Brown GC. Neuronal Cell Death. *Physiological reviews*. 2018;98(2):813-80.
14. Rotshenker S. Wallerian degeneration: the innate-immune response to traumatic nerve injury. *J Neuroinflammation*. 2011;8:109.
15. Grinsell D, Keating CP. Peripheral Nerve Reconstruction after Injury: A Review of Clinical and Experimental Therapies. *BioMed Research International*. 2014;2014:13.
16. López-Cebal R, Silva-Correia J, Reis RL, Silva TH, Oliveira JM. Peripheral Nerve Injury: Current Challenges, Conventional Treatment Approaches, and New Trends in Biomaterials-Based Regenerative Strategies. *ACS Biomaterials Science & Engineering*. 2017;3(12):3098-122.
17. Gaudin R, Knipfer C, Henningsen A, Smeets R, Heiland M, Hadlock T. Approaches to Peripheral Nerve Repair: Generations of Biomaterial Conduits Yielding to Replacing Autologous Nerve Grafts in Craniomaxillofacial Surgery. *Biomed Res Int*. 2016;2016:3856262-.
18. Rosso G, Liashkovich I, Gess B, Young P, Kun A, Shahin V. Unravelling crucial biomechanical resilience of myelinated peripheral nerve fibres provided by the Schwann cell basal lamina and PMP22. *Scientific Reports*. 2014;4:7286.
19. Zhu S, Ge J, Wang Y, Qi F, Ma T, Wang M, et al. A synthetic oxygen carrier-olfactory ensheathing cell composition system for the promotion of sciatic nerve regeneration. *Biomaterials*. 2014;35(5):1450-61.
20. Shoichet MS, Midha R. Peripheral nerve regeneration through guidance tubes AU - Belkas, Jason S. *Neurological Research*. 2004;26(2):151-60.
21. Jaquet JB, Luijsterburg AJ, Kalmijn S, Kuypers PD, Hofman A, Hovius SE. Median, ulnar, and combined median-ulnar nerve injuries: functional outcome and return to productivity. *The Journal of trauma*. 2001;51(4):687-92.
22. Kawano H, Kimura-Kuroda J, Komuta Y, Yoshioka N, Li HP, Kawamura K, et al. Role of the lesion scar in the response to damage and repair of the central nervous system. *Cell and tissue research*. 2012;349(1):169-80.
23. Jessen KR, Mirsky R. The repair Schwann cell and its function in regenerating nerves. *J Physiol*. 2016;594(13):3521-31.
24. Dahlin LB. Chapter Seven - The Role of Timing in Nerve Reconstruction. In: Geuna S, Perroteau I, Tos P, Battiston B, editors. *International review of neurobiology*. 109: Academic Press; 2013. p. 151-64.
25. Robinson LR. Traumatic injury to peripheral nerves. *Muscle & nerve*. 2000;23(6):863-73.
26. Ghasemi-Rad M, Nosair E, Vegh A, Mohammadi A, Akkad A, Lasha E, et al. A handy review of carpal tunnel syndrome: From anatomy to diagnosis and treatment. *World journal of radiology*. 2014;6(6):284-300.
27. Plastaras CT, Chhatre A, Kotcharian AS. Perioperative upper extremity peripheral nerve traction injuries. *The Orthopedic clinics of North America*. 2014;45(1):47-53.
28. Won JC, Park TS. Recent Advances in Diagnostic Strategies for Diabetic Peripheral Neuropathy. 2016;31(2):230-8.
29. Wojtkiewicz DM, Saunders J, Domeshek L, Novak CB, Kaskutas V, Mackinnon SE. Social impact of peripheral nerve injuries. *Hand (N Y)*. 2015;10(2):161-7.
30. SEDDON HJ. THREE TYPES OF NERVE INJURY. *Brain : a journal of neurology*. 1943;66(4):237-88.
31. Sunderland S. A classification of peripheral nerve injuries producing loss of function. *Brain : a journal of neurology*. 1951;74(4):491-516.
32. DeFrancesco-Lisowitz A, Lindborg JA, Niemi JP, Zigmund RE. The neuroimmunology of degeneration and regeneration in the peripheral nervous system. *Neuroscience*. 2015;302:174-203.
33. Kiryu-Seo S, Kiyama H. The nuclear events guiding successful nerve regeneration. *Frontiers in molecular neuroscience*. 2011;4:53.

34. Conforti L, Gilley J, Coleman MP. Wallerian degeneration: an emerging axon death pathway linking injury and disease. *Nature reviews Neuroscience*. 2014;15(6):394-409.
35. Namgung U. The role of Schwann cell-axon interaction in peripheral nerve regeneration. *Cells, tissues, organs*. 2014;200(1):6-12.
36. Jessen KR, Mirsky R, Lloyd AC. Schwann Cells: Development and Role in Nerve Repair. *Cold Spring Harbor perspectives in biology*. 2015;7(7):a020487.
37. Chen P, Piao X, Bonaldo P. Role of macrophages in Wallerian degeneration and axonal regeneration after peripheral nerve injury. *Acta neuropathologica*. 2015;130(5):605-18.
38. Bearce EA, Erdogan B, Lowery LA. TIPsy tour guides: how microtubule plus-end tracking proteins (+TIPs) facilitate axon guidance. *Frontiers in cellular neuroscience*. 2015;9:241.
39. Steketee MB, Oboudiyat C, Daneman R, Trakhtenberg E, Lamoureux P, Weinstein JE, et al. Regulation of intrinsic axon growth ability at retinal ganglion cell growth cones. *Investigative ophthalmology & visual science*. 2014;55(7):4369-77.
40. Fu SY, Gordon T. The cellular and molecular basis of peripheral nerve regeneration. *Molecular neurobiology*. 1997;14(1-2):67-116.
41. Bhatheja K, Field J. Schwann cells: Origins and role in axonal maintenance and regeneration. *The International Journal of Biochemistry & Cell Biology*. 2006;38(12):1995-9.
42. Jessen KR, Mirsky R. Negative regulation of myelination: relevance for development, injury, and demyelinating disease. *Glia*. 2008;56(14):1552-65.
43. Brushart TM, Aspalter M, Griffin JW, Redett R, Hameed H, Zhou C, et al. Schwann cell phenotype is regulated by axon modality and central-peripheral location, and persists in vitro. *Experimental neurology*. 2013;247:272-81.
44. McKerracher L, David S, Jackson DL, Kottis V, Dunn RJ, Braun PE. Identification of myelin-associated glycoprotein as a major myelin-derived inhibitor of neurite growth. *Neuron*. 1994;13(4):805-11.
45. Namgung U. The Role of Schwann Cell-Axon Interaction in Peripheral Nerve Regeneration 2015.
46. Arthur-Farraj PJ, Latouche M, Wilton DK, Quintes S, Chabrol E, Banerjee A, et al. c-Jun reprograms Schwann cells of injured nerves to generate a repair cell essential for regeneration. *Neuron*. 2012;75(4):633-47.
47. Dahlin LB. Techniques of peripheral nerve repair. *Scandinavian journal of surgery : SJS : official organ for the Finnish Surgical Society and the Scandinavian Surgical Society*. 2008;97(4):310-6.
48. Dellon ES, Dellon AL. The first nerve graft, Vulpian, and the nineteenth century neural regeneration controversy. *The Journal of hand surgery*. 1993;18(2):369-72.
49. Isaacs J. Treatment of acute peripheral nerve injuries: current concepts. *The Journal of hand surgery*. 2010;35(3):491-7; quiz 8.
50. Suchyta MA, Sabbagh MD, Morsy M, Mardini S, Moran SL. Advances in peripheral nerve regeneration as it relates to VCA. *Vascularized Composite Allotransplantation*. 2016;3(1-2):75-88.
51. Fries CA, Tuder DW, Davis MR. Preclinical Models in Vascularized Composite Allotransplantation. *Current Transplantation Reports*. 2015;2(3):284-9.
52. Vale TA, Symmonds M, Polydefkis M, Byrnes K, Rice ASC, Themistocleous AC, et al. Chronic non-freezing cold injury results in neuropathic pain due to a sensory neuropathy. *Brain : a journal of neurology*. 2017;140(10):2557-69.
53. Archibald SJ, Shefner J, Krarup C, Madison RD. Monkey median nerve repaired by nerve graft or collagen nerve guide tube. *The Journal of neuroscience : the official journal of the Society for Neuroscience*. 1995;15(5 Pt 2):4109-23.
54. Lovati AB, D'Arrigo D, Odella S, Tos P, Geuna S, Raimondo S. Nerve Repair Using Decellularized Nerve Grafts in Rat Models. A Review of the Literature. *Front Cell Neurosci*. 2018;12:427-.
55. Gulati AK. Evaluation of acellular and cellular nerve grafts in repair of rat peripheral nerve. *Journal of neurosurgery*. 1988;68(1):117-23.
56. Freytes DO, Badylak SF, Webster TJ, Geddes LA, Rundell AE. Biaxial strength of multilaminated extracellular matrix scaffolds. *Biomaterials*. 2004;25(12):2353-61.
57. De Filippo RE, Yoo JJ, Atala A. Urethral replacement using cell seeded tubularized collagen matrices. *The Journal of urology*. 2002;168(4 Pt 2):1789-92; discussion 92-3.
58. Woods T, Gratzner PF. Effectiveness of three extraction techniques in the development of a decellularized bone-anterior cruciate ligament-bone graft. *Biomaterials*. 2005;26(35):7339-49.
59. Gamba PG, Conconi MT, Lo Piccolo R, Zara G, Spinazzi R, Parnigotto PP. Experimental abdominal wall defect repaired with acellular matrix. *Pediatric surgery international*. 2002;18(5-6):327-31.

60. Kim BS, Yoo JJ, Atala A. Peripheral nerve regeneration using acellular nerve grafts. *Journal of biomedical materials research Part A*. 2004;68(2):201-9.
61. Lin CH, Hsia K, Ma H, Lee H, Lu JH. In Vivo Performance of Decellularized Vascular Grafts: A Review Article. *International journal of molecular sciences*. 2018;19(7).
62. Wang EW, Zhang J, Huang JH. Repairing peripheral nerve injury using tissue engineering techniques. *Neural regeneration research*. 2015;10(9):1393-4.
63. Chang W, Shah MB, Lee P, Yu X. Tissue-engineered spiral nerve guidance conduit for peripheral nerve regeneration. *Acta biomaterialia*. 2018;73:302-11.
64. Gonzalez-Perez F, Cobianchi S, Geuna S, Barwig C, Freier T, Udina E, et al. Tubulization with chitosan guides for the repair of long gap peripheral nerve injury in the rat. *Microsurgery*. 2015;35(4):300-8.
65. Kehoe S, Zhang XF, Boyd D. FDA approved guidance conduits and wraps for peripheral nerve injury: A review of materials and efficacy. *Injury*. 2012;43(5):553-72.
66. de Ruitter GCW, Malessy MJA, Yaszemski MJ, Windebank AJ, Spinner RJ. Designing ideal conduits for peripheral nerve repair. *Neurosurgical focus*. 2009;26(2):E5-E.
67. Bueno FR, Shah SB. Implications of tensile loading for the tissue engineering of nerves. *Tissue engineering Part B, Reviews*. 2008;14(3):219-33.
68. Gu X, Ding F, Williams DF. Neural tissue engineering options for peripheral nerve regeneration. *Biomaterials*. 2014;35(24):6143-56.
69. de Luca AC, Lacour SP, Raffoul W, di Summa PG. Extracellular matrix components in peripheral nerve repair: how to affect neural cellular response and nerve regeneration? *Neural Regeneration Research*. 2014;9(22):1943-8.
70. Chen Y-S, Chang J-Y, Cheng C-Y, Tsai F-J, Yao C-H, Liu B-S. An in vivo evaluation of a biodegradable genipin-cross-linked gelatin peripheral nerve guide conduit material. *Biomaterials*. 2005;26(18):3911-8.
71. Yang Y, Zhao Y, Gu Y, Yan X, Liu J, Ding F, et al. Degradation behaviors of nerve guidance conduits made up of silk fibroin in vitro and in vivo. *Polymer Degradation and Stability*. 2009;94(12):2213-20.
72. Wang ML, Rivlin M, Graham JG, Beredjikian PK. Peripheral nerve injury, scarring, and recovery. *Connective Tissue Research*. 2019;60(1):3-9.
73. Huang C, Ouyang Y, Niu H, He N, Ke Q, Jin X, et al. Nerve Guidance Conduits from Aligned Nanofibers: Improvement of Nerve Regeneration through Longitudinal Nanogrooves on a Fiber Surface. *ACS Applied Materials & Interfaces*. 2015;7(13):7189-96.
74. Liu C, Wang C, Zhao Q, Li X, Xu F, Yao X, et al. Incorporation and release of dual growth factors for nerve tissue engineering using nanofibrous bicomponent scaffolds. *Biomedical Materials*. 2018;13(4):044107.
75. Ruitter GCWd, Malessy MJA, Yaszemski MJ, Windebank AJ, Spinner RJ. Designing ideal conduits for peripheral nerve repair. 2009;26(2):E5.
76. Cattin AL, Burden JJ, Van Emmenis L, Mackenzie FE, Hoving JJ, Garcia Calavia N, et al. Macrophage-Induced Blood Vessels Guide Schwann Cell-Mediated Regeneration of Peripheral Nerves. *Cell*. 2015;162(5):1127-39.
77. Zhao Y-H, Niu C-M, Shi J-Q, Wang Y-Y, Yang Y-M, Wang H-B. Novel conductive polypyrrole/silk fibroin scaffold for neural tissue repair. *Neural Regeneration Research*. 2018;13(8):1455-64.
78. Muangsanit P, Shipley RJ, Phillips JB. Vascularization Strategies for Peripheral Nerve Tissue Engineering. *Anat Rec (Hoboken)*. 2018;301(10):1657-67.
79. Carvalho CR, Costa JB, da Silva Morais A, Lopez-Cebal R, Silva-Correia J, Reis RL, et al. Tunable Enzymatically Cross-Linked Silk Fibroin Tubular Conduits for Guided Tissue Regeneration. *Advanced healthcare materials*. 2018;7(17):e1800186.
80. Giannessi E, Coli A, Stornelli MR, Miragliotta V, Pirone A, Lenzi C, et al. An autologously generated platelet-rich plasma suturable membrane may enhance peripheral nerve regeneration after neurotomy in an acute injury model of sciatic nerve neurotmesis. *Journal of reconstructive microsurgery*. 2014;30(9):617-26.
81. Belanger K, Schlatter G, Hébraud A, Marin F, Testelin S, Dakpé S, et al. A multi-layered nerve guidance conduit design adapted to facilitate surgical implantation. *Health Science Reports*. 2018;1(12):e86.
82. Menorca RMG, Fussell TS, Elfar JC. Peripheral Nerve Trauma: Mechanisms of Injury and Recovery. *Hand clinics*. 2013;29(3):317-30.
83. Subramanian A, Krishnan UM, Sethuraman S. Development of biomaterial scaffold for nerve tissue engineering: Biomaterial mediated neural regeneration. *Journal of biomedical science*. 2009;16(1):108-.
84. Stang F, Keilhoff G, Fansa H. Biocompatibility of Different Nerve Tubes. *Materials*. 2009;2(4):1480.
85. Muheremu A, Ao Q. Past, Present, and Future of Nerve Conduits in the Treatment of Peripheral Nerve Injury. *Biomed Res Int*. 2015;2015:237507-.

86. Nardo T, Carmagnola I, Ruini F, Caddeo S, Calzone S, Chiono V, et al. Chapter 65 - Synthetic Biomaterial for Regenerative Medicine Applications. In: Orlando G, Remuzzi G, Williams DF, editors. *Kidney Transplantation, Bioengineering and Regeneration*: Academic Press; 2017. p. 901-21.
87. Matsumine H, Sasaki R, Yamato M, Okano T, Sakurai H. A polylactic acid non-woven nerve conduit for facial nerve regeneration in rats. *Journal of Tissue Engineering and Regenerative Medicine*. 2014;8(6):454-62.
88. Lu MC, Huang YT, Lin JH, Yao CH, Lou CW, Tsai CC, et al. Evaluation of a multi-layer microbraided polylactic acid fiber-reinforced conduit for peripheral nerve regeneration. *Journal of materials science Materials in medicine*. 2009;20(5):1175-80.
89. Zeng C-G, Xiong Y, Xie G, Dong P, Quan D. Fabrication and evaluation of PLLA multichannel conduits with nanofibrous microstructure for the differentiation of NSCs in vitro. *Tissue engineering Part A*. 2014;20(5-6):1038-48.
90. Rutkowski GE, Miller CA, Jeftinija S, Mallapragada SK. Synergistic effects of micropatterned biodegradable conduits and Schwann cells on sciatic nerve regeneration. *Journal of neural engineering*. 2004;1(3):151-7.
91. Shin RH, Friedrich PF, Crum BA, Bishop AT, Shin AY. Treatment of a segmental nerve defect in the rat with use of bioabsorbable synthetic nerve conduits: a comparison of commercially available conduits. *The Journal of bone and joint surgery American volume*. 2009;91(9):2194-204.
92. Navissano M, Malan F, Carnino R, Battiston B. Neurotube® for facial nerve repair. *Microsurgery*. 2005;25(4):268-71.
93. Wu T, Li D, Wang Y, Sun B, Li D, Morsi Y, et al. Laminin-coated nerve guidance conduits based on poly(l-lactide-co-glycolide) fibers and yarns for promoting Schwann cells' proliferation and migration. *Journal of Materials Chemistry B*. 2017;5(17):3186-94.
94. Labroo P, Shea J, Edwards K, Ho S, Davis B, Sant H, et al. Novel drug delivering conduit for peripheral nerve regeneration. *Journal of neural engineering*. 2017;14(6):066011.
95. Lee SJ, Nowicki M, Harris B, Zhang LG. Fabrication of a Highly Aligned Neural Scaffold via a Table Top Stereolithography 3D Printing and Electrospinning<sup/>. *Tissue Eng Part A*. 2017;23(11-12):491-502.
96. Kokai LE, Ghaznavi AM, Marra KG. Incorporation of double-walled microspheres into polymer nerve guides for the sustained delivery of glial cell line-derived neurotrophic factor. *Biomaterials*. 2010;31(8):2313-22.
97. Hsu S-h, Chang W-C, Yen C-T. Novel flexible nerve conduits made of water-based biodegradable polyurethane for peripheral nerve regeneration. *Journal of Biomedical Materials Research Part A*. 2017;105(5):1383-92.
98. Singh A, Shiekh PA, Das M, Seppala J, Kumar A. Aligned Chitosan-Gelatin Cryogel-Filled Polyurethane Nerve Guidance Channel for Neural Tissue Engineering: Fabrication, Characterization, and In Vitro Evaluation. *Biomacromolecules*. 2018.
99. Stocco E, Barbon S, Lora L, Grandi F, Sartore L, Tiengo C, et al. Partially oxidized polyvinyl alcohol conduit for peripheral nerve regeneration. *Scientific reports*. 2018;8(1):604.
100. Wan H, Li DZ, Yang F, Li JH, Wang SG, Wang ZC. [Research about schwann cells and PLGA implanted to rat transected spinal cord]. *Zhonghua wai ke za zhi [Chinese journal of surgery]*. 2007;45(12):843-6.
101. Peng S-W, Li C-W, Chiu I-M, Wang G-J. Nerve guidance conduit with a hybrid structure of a PLGA microfibrillar bundle wrapped in a micro/nanostructured membrane. *International journal of nanomedicine*. 2017;12:421-32.
102. Liu H, Lv P, Zhu Y, Wu H, Zhang K, Xu F, et al. Salidroside promotes peripheral nerve regeneration based on tissue engineering strategy using Schwann cells and PLGA: in vitro and in vivo. *Sci Rep*. 2017;7:39869.
103. Xu F, Zhang K, Lv P, Lu R, Zheng L, Zhao J. NECL1 coated PLGA as favorable conduits for repair of injured peripheral nerve. *Materials Science and Engineering: C*. 2017;70:1132-40.
104. Tanir TE, Kiziltay A, Hasirci V, Hasirci N. PCL and PCL-based materials in biomedical applications AU - Malikmammadov, Elbay. *Journal of Biomaterials Science, Polymer Edition*. 2018;29(7-9):863-93.
105. Wang W, Huang B, Byun JJ, Bartolo P. Assessment of PCL/carbon material scaffolds for bone regeneration. *Journal of the mechanical behavior of biomedical materials*. 2019;93:52-60.
106. Fu N, Liao J, Lin S, Sun K, Tian T, Zhu B, et al. PCL-PEG-PCL film promotes cartilage regeneration in vivo. *Cell proliferation*. 2016;49(6):729-39.
107. Bala Balakrishnan P, Gardella L, Forouharshad M, Pellegrino T, Monticelli O. Star poly(ϵ -caprolactone)-based electrospun fibers as biocompatible scaffold for doxorubicin with prolonged drug release activity. *Colloids and Surfaces B: Biointerfaces*. 2018;161:488-96.
108. Gossen P, Witzigmann D, Sieber S, Huwyler J. PEG-PCL-based nanomedicines: A biodegradable drug delivery system and its application. *Journal of controlled release : official journal of the Controlled Release Society*. 2017;260:46-60.

109. Pathak VM, Navneet. Review on the current status of polymer degradation: a microbial approach. *Bioresources and Bioprocessing*. 2017;4(1):15.
110. Salmoria GV, Paggi RA, Castro F, Roesler CRM, Moterle D, Kanis LA. Development of PCL/Ibuprofen Tubes for Peripheral Nerve Regeneration. *Procedia CIRP*. 2016;49:193-8.
111. Mobasser A, Faroni A, Minogue BM, Downes S, Terenghi G, Reid AJ. Polymer scaffolds with preferential parallel grooves enhance nerve regeneration. *Tissue Eng Part A*. 2015;21(5-6):1152-62.
112. Zhang XF, Coughlan A, O'Shea H, Towler MR, Kehoe S, Boyd D. Experimental composite guidance conduits for peripheral nerve repair: An evaluation of ion release. *Materials Science and Engineering: C*. 2012;32(6):1654-63.
113. Jing W, Ao Q, Wang L, Huang Z, Cai Q, Chen G, et al. Constructing conductive conduit with conductive fibrous infilling for peripheral nerve regeneration. *Chemical Engineering Journal*. 2018;345:566-77.
114. Sun B, Zhou Z, Li D, Wu T, Zheng H, Liu J, et al. Polypyrrole-coated poly(l-lactic acid-co-ε-caprolactone)/silk fibroin nanofibrous nerve guidance conduit induced nerve regeneration in rat. *Materials Science and Engineering: C*. 2019;94:190-9.
115. Du J, Chen H, Qing L, Yang X, Jia X. Biomimetic neural scaffolds: a crucial step towards optimal peripheral nerve regeneration. *Biomater Sci*. 2018;6(6):1299-311.
116. Pfister LA, Papaloizos M, Merkle HP, Gander B. Hydrogel nerve conduits produced from alginate/chitosan complexes. *Journal of Biomedical Materials Research Part A*. 2007;80A(4):932-7.
117. Wang ZZ, Sakiyama-Elbert SE. Matrices, scaffolds & carriers for cell delivery in nerve regeneration. *Experimental Neurology*. 2018.
118. Resch A, Wolf S, Mann A, Weiss T, Stetco AL, Radtke C. Co-Culturing Human Adipose Derived Stem Cells and Schwann Cells on Spider Silk-A New Approach as Prerequisite for Enhanced Nerve Regeneration. *International journal of molecular sciences*. 2018;20(1).
119. Wang C, Jia Y, Yang W, Zhang C, Zhang K, Chai Y. Silk fibroin enhances peripheral nerve regeneration by improving vascularization within nerve conduits. *Journal of biomedical materials research Part A*. 2018;106(7):2070-7.
120. Yang Y, Ding F, Wu J, Hu W, Liu W, Liu J, et al. Development and evaluation of silk fibroin-based nerve grafts used for peripheral nerve regeneration. *Biomaterials*. 2007;28(36):5526-35.
121. Das S, Sharma M, Saharia D, Sarma KK, Sarma MG, Borthakur BB, et al. In vivo studies of silk based gold nano-composite conduits for functional peripheral nerve regeneration. *Biomaterials*. 2015;62:66-75.
122. Sierpinski P, Garrett J, Ma J, Apel P, Klorig D, Smith T, et al. The use of keratin biomaterials derived from human hair for the promotion of rapid regeneration of peripheral nerves. *Biomaterials*. 2008;29(1):118-28.
123. Pace LA, Plate JF, Mannava S, Barnwell JC, Koman LA, Li Z, et al. A human hair keratin hydrogel scaffold enhances median nerve regeneration in nonhuman primates: an electrophysiological and histological study. *Tissue Eng Part A*. 2014;20(3-4):507-17.
124. Lin YC, Ramadan M, Van Dyke M, Kokai LE, Philips BJ, Rubin JP, et al. Keratin gel filler for peripheral nerve repair in a rodent sciatic nerve injury model. *Plastic and reconstructive surgery*. 2012;129(1):67-78.
125. Meyer C, Stenberg L, Gonzalez-Perez F, Wrobel S, Ronchi G, Udina E, et al. Chitosan-film enhanced chitosan nerve guides for long-distance regeneration of peripheral nerves. *Biomaterials*. 2016;76:33-51.
126. Moattari M, Kouchesfehiani HM, Kaka G, Sadraie SH, Naghdi M, Mansouri K. Chitosan-film associated with mesenchymal stem cells enhanced regeneration of peripheral nerves: A rat sciatic nerve model. *Journal of chemical neuroanatomy*. 2018;88:46-54.
127. Carvalho CR, Lopez-Cebral R, Silva-Correia J, Silva JM, Mano JF, Silva TH, et al. Investigation of cell adhesion in chitosan membranes for peripheral nerve regeneration. *Materials science & engineering C, Materials for biological applications*. 2017;71:1122-34.
128. Lin SC-Y, Wang Y, Wertheim DF, Coombes AGA. Production and in vitro evaluation of macroporous, cell-encapsulating alginate fibres for nerve repair. *Materials Science and Engineering: C*. 2017;73:653-64.
129. Sarker MD, Naghieh S, McInnes AD, Ning L, Schreyer D, Chen X. Bio-fabrication of peptide-modified alginate scaffolds: Printability, mechanical stability and neurite outgrowth assessments. *Bioprinting*. 2019:e00045.
130. Mondal M. The silk proteins, sericin and fibroin in silkworm, *Bombyx mori* Linn., - a review. *Caspian Journal of Environmental Sciences*. 2007;5(2):63-76.
131. Jastrzebska K, Kucharczyk K, Florczak A, Dondajewska E, Mackiewicz A, Dams-Kozłowska H. Silk as an innovative biomaterial for cancer therapy. *Reports of Practical Oncology & Radiotherapy*. 2015;20(2):87-98.
132. Vepari C, Kaplan DL. Silk as a Biomaterial. *Progress in polymer science*. 2007;32(8-9):991-1007.
133. Costa JB, Silva-Correia J, Oliveira JM, Reis RL. Fast Setting Silk Fibroin Bioink for Bioprinting of Patient-Specific Memory-Shape Implants. *Advanced healthcare materials*. 2017;6(22).

134. Ribeiro VP, Silva-Correia J, Goncalves C, Pina S, Radhouani H, Montonen T, et al. Rapidly responsive silk fibroin hydrogels as an artificial matrix for the programmed tumor cells death. *PLoS one*. 2018;13(4):e0194441.
135. Carvalho MR, Maia FR, Vieira S, Reis RL, Oliveira JM. Microfluidics: Tuning Enzymatically Crosslinked Silk Fibroin Hydrogel Properties for the Development of a Colorectal Cancer Extravasation 3D Model on a Chip (Global Challenges 5-6/2018). *Global Challenges*. 2018;2(5-6):1870164.
136. Dinis TM, Elia R, Vidal G, Dermigny Q, Denoed C, Kaplan DL, et al. 3D multi-channel bi-functionalized silk electrospun conduits for peripheral nerve regeneration. *Journal of the mechanical behavior of biomedical materials*. 2015;41:43-55.
137. Ng KW. Human hair keratin templates for biomedical applications. *Frontiers in Bioengineering and Biotechnology*.
138. Ko J, Nguyen LTH, Surendran A, Tan BY, Ng KW, Leong WL. Human Hair Keratin for Biocompatible Flexible and Transient Electronic Devices. *ACS Applied Materials & Interfaces*. 2017;9(49):43004-12.
139. Yue K, Liu Y, Byambaa B, Singh V, Liu W, Li X, et al. Visible light crosslinkable human hair keratin hydrogels. *Bioeng Transl Med*. 2018;3(1):37-48.
140. Lee H, Noh K, Lee SC, Kwon I-K, Han D-W, Lee I-S, et al. Human hair keratin and its-based biomaterials for biomedical applications. *Tissue Engineering and Regenerative Medicine*. 2014;11(4):255-65.
141. Apel PJ, Garrett JP, Sierpinski P, Ma J, Atala A, Smith TL, et al. Peripheral nerve regeneration using a keratin-based scaffold: long-term functional and histological outcomes in a mouse model. *J Hand Surg Am*. 2008;33(9):1541-7.
142. Bak M, Gutkowska ON, Wagner E, Gosk J. The role of chitin and chitosan in peripheral nerve reconstruction. *Polimery w medycynie*. 2017;47(1):43-7.
143. Muzzarelli RAA. CHAPTER 1 - ENZYMIC SYNTHESIS OF CHITIN AND CHITOSAN. In: Muzzarelli RAA, editor. *Chitin*; Pergamon; 1977. p. 5-44.
144. Rinaudo M. Chitin and chitosan: Properties and applications. *Progress in Polymer Science*. 2006;31(7):603-32.
145. Freier T, Montenegro R, Shan Koh H, Shoichet MS. Chitin-based tubes for tissue engineering in the nervous system. *Biomaterials*. 2005;26(22):4624-32.
146. Martin-Lopez E, Nieto-Diaz M, Nieto-Sampedro M. Differential adhesiveness and neurite-promoting activity for neural cells of chitosan, gelatin, and poly-L-lysine films. *Journal of biomaterials applications*. 2012;26(7):791-809.
147. Wenling C, Duohui J, Jiamou L, Yandao G, Nanming Z, Xiufang Z. Effects of the degree of deacetylation on the physicochemical properties and Schwann cell affinity of chitosan films. *Journal of biomaterials applications*. 2005;20(2):157-77.
148. Wrobel S, Serra SC, Ribeiro-Samy S, Sousa N, Heimann C, Barwig C, et al. In vitro evaluation of cell-seeded chitosan films for peripheral nerve tissue engineering. *Tissue Eng Part A*. 2014;20(17-18):2339-49.
149. Cooper A, Bhattarai N, Zhang M. Fabrication and cellular compatibility of aligned chitosan–PCL fibers for nerve tissue regeneration. *Carbohydrate Polymers*. 2011;85(1):149-56.
150. Gnani S, Fornasari BE, Tonda-Turo C, Laurano R, Zanetti M, Ciardelli G, et al. In vitro evaluation of gelatin and chitosan electrospun fibres as an artificial guide in peripheral nerve repair: a comparative study. *Journal of Tissue Engineering and Regenerative Medicine*. 2018;12(2):e679-e94.
151. Wang W, Itoh S, Konno K, Kikkawa T, Ichinose S, Sakai K, et al. Effects of Schwann cell alignment along the oriented electrospun chitosan nanofibers on nerve regeneration. *Journal of biomedical materials research Part A*. 2009;91(4):994-1005.
152. Haastert-Talini K, Geuna S, Dahlin LB, Meyer C, Stenberg L, Freier T, et al. Chitosan tubes of varying degrees of acetylation for bridging peripheral nerve defects. *Biomaterials*. 2013;34(38):9886-904.
153. Stenberg L, Kodama A, Lindwall-Blom C, Dahlin LB. Nerve regeneration in chitosan conduits and in autologous nerve grafts in healthy and in type 2 diabetic Goto-Kakizaki rats. *The European journal of neuroscience*. 2016;43(3):463-73.
154. Lee KY, Mooney DJ. Alginate: properties and biomedical applications. *Prog Polym Sci*. 2012;37(1):106-26.
155. Suzuki Y, Tanihara M, Nishimura Y, Suzuki K, Yamawaki Y, Kudo H, et al. In vivo evaluation of a novel alginate dressing. *Journal of biomedical materials research*. 1999;48(4):522-7.
156. Ochbaum G, Davidovich-Pinhas M, Bitton R. Tuning the mechanical properties of alginate–peptide hydrogels. *Soft Matter*. 2018;14(21):4364-73.
157. Suzuki Y, Tanihara M, Ohnishi K, Suzuki K, Endo K, Nishimura Y. Cat peripheral nerve regeneration across 50 mm gap repaired with a novel nerve guide composed of freeze-dried alginate gel. *Neuroscience letters*. 1999;259(2):75-8.

158. Hashimoto T, Suzuki Y, Kitada M, Kataoka K, Wu S, Suzuki K, et al. Peripheral nerve regeneration through alginate gel: analysis of early outgrowth and late increase in diameter of regenerating axons. *Experimental Brain Research*. 2002;146(3):356-68.
159. Quigley AF, Bulluss KJ, Kyratzis IL, Gilmore K, Mysore T, Schirmer KS, et al. Engineering a multimodal nerve conduit for repair of injured peripheral nerve. *Journal of neural engineering*. 2013;10(1):016008.
160. Naghieh S, Sarker MD, Abelseh E, Chen X. Indirect 3D bioprinting and characterization of alginate scaffolds for potential nerve tissue engineering applications. *Journal of the mechanical behavior of biomedical materials*. 2019;93:183-93.
161. Wu H, Liu J, Fang Q, Xiao B, Wan Y. Establishment of nerve growth factor gradients on aligned chitosan-poly(lactide /alginate fibers for neural tissue engineering applications. *Colloids and Surfaces B: Biointerfaces*. 2017;160:598-609.
162. de Luca AC, Lacour SP, Raffoul W, di Summa PG. Extracellular matrix components in peripheral nerve repair: how to affect neural cellular response and nerve regeneration? *Neural regeneration research*. 2014;9(22):1943-8.
163. Klein S, Prantl L, Vykoukal J, Loibl M, Felthaus O. Differential Effects of Coating Materials on Viability and Migration of Schwann Cells. *Materials (Basel, Switzerland)*. 2016;9(3):150.
164. Fujimaki H, Uchida K, Inoue G, Miyagi M, Nemoto N, Saku T, et al. Oriented collagen tubes combined with basic fibroblast growth factor promote peripheral nerve regeneration in a 15 mm sciatic nerve defect rat model. *Journal of biomedical materials research Part A*. 2017;105(1):8-14.
165. Huang L, Zhu L, Shi X, Xia B, Liu Z, Zhu S, et al. A compound scaffold with uniform longitudinally oriented guidance cues and a porous sheath promotes peripheral nerve regeneration in vivo. *Acta Biomaterialia*. 2018;68:223-36.
166. Bhandari PS. Use of fibrin glue in the repair of brachial plexus and peripheral nerve injuries. *The Indian Journal of Neurotrauma*. 2013;10(1):30-2.
167. Reichenberger MA, Mueller W, Hartmann J, Diehm Y, Lass U, Koellensperger E, et al. ADSCs in a fibrin matrix enhance nerve regeneration after epineural suturing in a rat model. *Microsurgery*. 2016;36(6):491-500.
168. Du J, Liu J, Yao S, Mao H, Peng J, Sun X, et al. Prompt peripheral nerve regeneration induced by a hierarchically aligned fibrin nanofiber hydrogel. *Acta Biomater*. 2017;55:296-309.
169. Mosahebi A, Wiberg M, Terenghi G. Addition of fibronectin to alginate matrix improves peripheral nerve regeneration in tissue-engineered conduits. *Tissue engineering*. 2003;9(2):209-18.
170. Gonzalez-Perez F, Cobianchi S, Heimann C, Phillips JB, Udina E, Navarro X. Stabilization, Rolling, and Addition of Other Extracellular Matrix Proteins to Collagen Hydrogels Improve Regeneration in Chitosan Guides for Long Peripheral Nerve Gaps in Rats. *Neurosurgery*. 2017;80(3):465-74.
171. Kijeńska E, Prabhakaran MP, Swieszkowski W, Kurzydłowski KJ, Ramakrishna S. Interaction of Schwann cells with laminin encapsulated PLCL core-shell nanofibers for nerve tissue engineering. *European Polymer Journal*. 2014;50:30-8.
172. Haggerty AE, Bening MR, Pherribo G, Dauer EA, Oudega M. Laminin polymer treatment accelerates repair of the crushed peripheral nerve in adult rats. *Acta Biomaterialia*. 2019;86:185-93.
173. Entekhabi E, Haghbin Nazarpak M, Moztarzadeh F, Sadeghi A. Design and manufacture of neural tissue engineering scaffolds using hyaluronic acid and polycaprolactone nanofibers with controlled porosity. *Materials Science and Engineering: C*. 2016;69:380-7.
174. Vilariño-Feltrer G, Martínez-Ramos C, Monleón-de-la-Fuente A, Vallés-Lluch A, Moratal D, Barcia Albacar JA, et al. Schwann-cell cylinders grown inside hyaluronic-acid tubular scaffolds with gradient porosity. *Acta Biomaterialia*. 2016;30:199-211.
175. Khan R, Khan MH. Use of collagen as a biomaterial: An update. *J Indian Soc Periodontol*. 2013;17(4):539-42.
176. Silva TH, Moreira-Silva J, Marques ALP, Domingues A, Bayon Y, Reis RL. Marine origin collagens and its potential applications. *Marine drugs*. 2014;12(12):5881-901.
177. Dong C, Lv Y. Application of Collagen Scaffold in Tissue Engineering: Recent Advances and New Perspectives. *Polymers*. 2016;8(2):42.
178. Bozkurt A, Claeys KG, Schradling S, Rodler JV, Altinova H, Schulz JB, et al. Clinical and biometrical 12-month follow-up in patients after reconstruction of the sural nerve biopsy defect by the collagen-based nerve guide Neuromaix. *European journal of medical research*. 2017;22(1):34.
179. Litvinov RI, Weisel JW. What Is the Biological and Clinical Relevance of Fibrin? *Seminars in thrombosis and hemostasis*. 2016;42(4):333-43.

180. Esposito F, Angileri FF, Kruse P, Cavallo LM, Solari D, Esposito V, et al. Fibrin Sealants in Dura Sealing: A Systematic Literature Review. *PLoS One*. 2016;11(4):e0151533-e.
181. Olcucuoglu E, Kulacoglu H, Ensari CO, Yavuz A, Albayrak A, Ergul Z, et al. Fibrin sealant effects on the ilioinguinal nerve. *Journal of investigative surgery : the official journal of the Academy of Surgical Research*. 2011;24(6):267-72.
182. Pankov R, Yamada KM. Fibronectin at a glance. *Journal of Cell Science*. 2002;115(20):3861-3.
183. Whitworth IH, Brown RA, Doré C, Green CJ, Terenghi G. Orientated mats of fibronectin as a conduit material for use in peripheral nerve repair. *The Journal of Hand Surgery: British & European Volume*. 1995;20(4):429-36.
184. Chen YS, Hsieh CL, Tsai CC, Chen TH, Cheng WC, Hu CL, et al. Peripheral nerve regeneration using silicone rubber chambers filled with collagen, laminin and fibronectin. *Biomaterials*. 2000;21(15):1541-7.
185. Liang S, Crutcher KA. Neuronal migration on laminin in vitro. *Brain research Developmental brain research*. 1992;66(1):127-32.
186. Adams DN, Kao EY, Hypolite CL, Distefano MD, Hu WS, Letourneau PC. Growth cones turn and migrate up an immobilized gradient of the laminin IKVAV peptide. *Journal of neurobiology*. 2005;62(1):134-47.
187. Zhang XF, Liu HX, Ortiz LS, Xiao ZD, Huang NP. Laminin-modified and aligned poly(3-hydroxybutyrate-co-3-hydroxyvalerate)/polyethylene oxide nanofibrous nerve conduits promote peripheral nerve regeneration. *J Tissue Eng Regen Med*. 2018;12(1):e627-e36.
188. Swindle-Reilly KE, Papke JB, Kutosky HP, Throm A, Hammer JA, Harkins AB, et al. The impact of laminin on 3D neurite extension in collagen gels. *Journal of neural engineering*. 2012;9(4):046007.
189. Zamboni F, Vieira S, Reis RL, Miguel Oliveira J, Collins MN. The potential of hyaluronic acid in immunoprotection and immunomodulation: Chemistry, processing and function. *Progress in Materials Science*. 2018;97:97-122.
190. Chircov C, Grumezescu AM, Bejenaru LE. Hyaluronic acid-based scaffolds for tissue engineering. *Romanian journal of morphology and embryology = Revue roumaine de morphologie et embryologie*. 2018;59(1):71-6.
191. Huang L, Wang Y, Liu H, Huang J. Local injection of high-molecular hyaluronan promotes wound healing in old rats by increasing angiogenesis. *Oncotarget*. 2017;9(9):8241-52.
192. Wang KK, Nemeth IR, Seckel BR, Chakalis-Haley DP, Swann DA, Kuo JW, et al. Hyaluronic acid enhances peripheral nerve regeneration in vivo. *Microsurgery*. 1998;18(4):270-5.
193. Ikeda K, Yamauchi D, Osamura N, Hagiwara N, Tomita K. Hyaluronic acid prevents peripheral nerve adhesion. *British Journal of Plastic Surgery*. 2003;56(4):342-7.
194. Murphy SV, Atala A. 3D bioprinting of tissues and organs. *Nature biotechnology*. 2014;32(8):773-85.
195. Hamburg MA, Collins FS. The path to personalized medicine. *The New England journal of medicine*. 2010;363(4):301-4.
196. Rengier F, Mehndiratta A, von Tengg-Kobligk H, Zechmann CM, Unterhinninghofen R, Kauczor HU, et al. 3D printing based on imaging data: review of medical applications. *International journal of computer assisted radiology and surgery*. 2010;5(4):335-41.
197. Schmidt CE, Leach JB. Neural tissue engineering: strategies for repair and regeneration. *Annual review of biomedical engineering*. 2003;5:293-347.
198. Ji XM, Wang SS, Cai XD, Wang XH, Liu QY, Wang P, et al. Novel miRNA, miR-sc14, promotes Schwann cell proliferation and migration. *Neural Regen Res*. 2019;14(9):1651-6.
199. Petcu EB, Midha R, McColl E, Popa-Wagner A, Chirila TV, Dalton PD. 3D printing strategies for peripheral nerve regeneration. *Biofabrication*. 2018;10(3):032001.
200. Johnson BN, Lancaster KZ, Zhen G, He J, Gupta MK, Kong YL, et al. 3D Printed Anatomical Nerve Regeneration Pathways. *Advanced Functional Materials*. 2015;25(39):6205-17.
201. Zhong Y, Wang L, Dong J, Zhang Y, Luo P, Qi J, et al. Three-dimensional Reconstruction of Peripheral Nerve Internal Fascicular Groups. *Scientific reports*. 2015;5:17168-.
202. Hu Y, Wu Y, Gou Z, Tao J, Zhang J, Liu Q, et al. 3D-engineering of Cellularized Conduits for Peripheral Nerve Regeneration. *Scientific Reports*. 2016;6:32184.
203. Tao J, Zhang J, Du T, Xu X, Deng X, Chen S, et al. Rapid 3D printing of functional nanoparticle-enhanced conduits for effective nerve repair. *Acta biomaterialia*. 2019;90:49-59.

Chapter II

Modern trends for peripheral nerve repair and regeneration: Beyond the hollow nerve guidance conduit

Chapter II

Modern trends for peripheral nerve repair and regeneration: Beyond the hollow nerve guidance conduit[†]

ABSTRACT

Peripheral nerve repair and regeneration remains among the greatest challenges in tissue engineering and regenerative medicine. Even though peripheral nerve injuries (PNIs) are capable of some degree of regeneration, frail recovery is seen even when the best microsurgical technique is applied. PNIs are known to be very incapacitating for the patient, due to the loss of motor and sensory functions. Since there is no optimal solution for tackling this problem up to this day, the evolution in the field is constant, with innovative designs of advanced nerve guidance conduits (NGCs) being reported every day. As a basic concept, a NGC should act as a physical barrier from the external environment, concomitantly acting as physical guidance for the regenerative axons across the gap lesion. NGCs should also be able to retain the naturally released nerve growth factors secreted by the damaged nerve stumps, as well as reducing the invasion of scar tissue-forming fibroblasts to the injury site. Based on the neurobiological knowledge related to the events that succeed after a nerve injury, neuronal subsistence is subjected to the existence of an ideal environment of growth factors, hormones, cytokines, and extracellular matrix (ECM) factors. Therefore, it is known that multifunctional NGCs fabricated through combinatorial approaches are needed to improve the functional and clinical outcomes after PNIs. The present work overviews the current reports dealing with the several features that can be used to improve peripheral nerve regeneration (PNR), ranging from the simple use of hollow NGCs to tissue engineered intraluminal fillers, or to even more advanced strategies, comprising the molecular and gene therapies as well as cell-based therapies.

Keywords: Peripheral nerve, tissue engineering, biomaterials, nerve guidance conduit

[†]This chapter is based on the following publication: [Carvalho CR, Oliveira JM, Reis RL](#). Modern trends for peripheral nerve repair and regeneration: Beyond the hollow nerve guidance conduits (Submitted).

II-1. INTRODUCTION

Insights of neuronal injury and repair date back to early times, namely to Galen in the second century AD (1). The research on this topic has been rising ever since and several nerve repair techniques have evolved throughout the years. Despite this fact, the status of peripheral nerve injuries (PNIs) and peripheral nerve regeneration (PNR) has always been in the shadow of the neurosurgery field. It is regarded as less significant when compared to areas such as central nervous system (CNS) disorders, which are seen as more prominent, tougher, trickier, and therefore perceived as a more distinguished and notable field. The main reason appointed to this is based on the word “peripheral” itself, as it suggests lesser relevance and difficulty. Furthermore, to increase this fallacy, several forged ideas increase the devaluation of this field, such as the idea that PNIs are irreversible, that peripheral nerves do not have any capacity to regenerate, and the results of peripheral nerve surgery are insignificant to the patient (2). However, although peripheral nerve repair is not a life-saving surgery, it has been proved that it is a life-changing surgery, with infinite benefits in the patient's quality of life. Also, since most patients with PNIs fit in the working-age population, peripheral nerve repair also has substantial socioeconomic implications (3). After decades of investigation, it is becoming progressively clear that peripheral nerve repair is not a “peripheral” area and the full attention by the part of clinicians and scientists is needed to overcome this public-health hazard.

Peripheral nerves provide the path for all types of axons (*e.g.* motor, sensory and vegetative axons) belonging to the peripheral nervous system (PNS). Injuries to these nerves are common conditions, due to their unprotected and superficial position throughout the human body. Depending on the injury, an extensive array of symptoms and outcomes are possible. They will be contingent on the severity, type of trauma, age, and type of nerves involved. Although much awareness and information already exist on the natural mechanisms of injury and regeneration, effective regenerative treatments that ensure complete functional and sensory recovery are rare.

Herein, we aim to summarize the necessary concepts to fully understand the phenomena of PNIs and regeneration, which pose complex and demanding challenges in tissue engineering and regenerative medicine (TERM).

II-1.1. Insights on nerve injury and repair

The phenomena and the principles of PNIs and repair have been established and kept constant in the past 50 years (4). Therefore, most scientific community categorizes the injuries according to Seddon (5) and Sunderland (6) classification, which are mainly differentiated by the degree of anatomical and pathophysiological changes that can occur in the nerve trunk. These classifications also allow to better define a course of treatment (7). To deep understand the phenomena of nerve injury and repair, the basic anatomy of peripheral nerves must be known (**Figure II-1**). Axons are set together and myelinated by enwrapping Schwann cells to form nerve bundles. Furthermore, fibroblasts exist dispersed through nerve bundles, together with blood vessels that sustain the nervous tissue alive (8). In the case of physical nerve injury, where the anatomy of the nerve is interrupted, both retrograde and anterograde phenomena can trigger apoptotic cell death (9). Capable of spontaneous regeneration, peripheral nerve axonotmesis can result in functional recovery within a few weeks. On the other hand, in the case of neurotmesis, which are severe injury with loss of nerve mass resulting in a gap, spontaneous regeneration cannot be attained, unless the gap has a maximum of 10 mm (10).

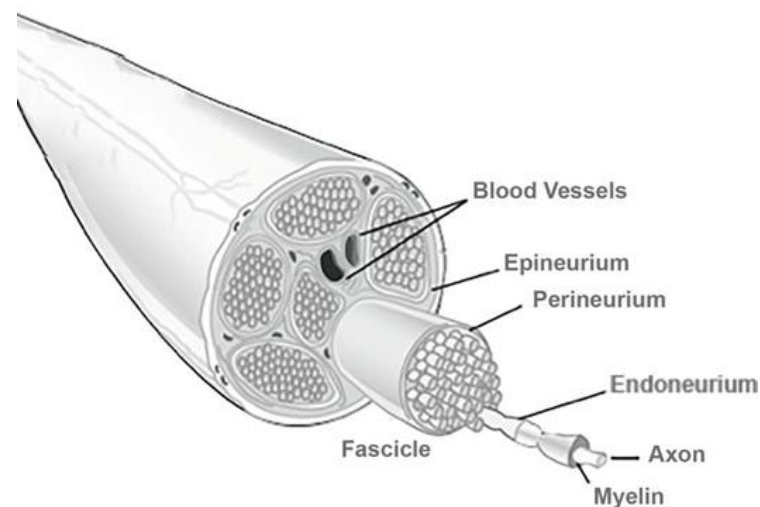


Figure II-1- Basic anatomy of a peripheral nerve. A connective tissue layer, endoneurium, involves the individual axons. An arrangement of axons, designed fascicles, is surrounded by the perineurium, and groups of fascicles are separated by the epineurium. External to this layer is the blood supply derived from major arteries and the latter is involved by the mesoneurium Reprinted with the permission from © 2017 The Author(s). Licensee IntechOpen.

After the injury, the process of Wallerian degeneration starts immediately (11). In brief, nerve stumps distal to the injury site will experience cellular variations despite the fact that the cells themselves were not injured in the first place. Axons starts to collapse, Schwann cells discard their

ensheathing myelin and macrophages are recruited. The later are employed to remove degenerated axons and myelin debris, along with Schwann cells (12). Furthermore, after a few days, Schwann cells de-differentiate owing to their lost connection with axons, starting a vigorous proliferation. Galectin-3 is known to play a key role in activating myelin phagocytosis by macrophages and further promotes Schwann cells to scavenge myelin, thus having a major importance in the degeneration process (13). Both types of Schwann cells, the pre-existent and the recently produced Schwann cells, align together to form the bands of Bungner, which are highly aligned tubes formed by the basal lamina of the Schwann cells. These bands are key topographical cues responsible for guiding the axon and their growth cones, from the proximal to the distal site, across the gap. In optimal conditions, the growth cones can extend at a rate of 1-3 mm a day (14). Overall, Schwann cells affect PNR in three distinct manners: i) proliferation, ii) formation of bands of Bungner, and iii) secretion of adequate growth factors (GF) (15).

Figure II-2 depicts the process of injury and regeneration of peripheral nerves.

II-1.2. Neuroplasticity

Neuroplasticity plays a chief role in PNI patients and how their recovery therapy is carried. Briefly, the term neuroplasticity refers to the ability of the neuronal system to change (16). It is now recognized that the brain is not a hard-wired unchanged circuit, but an adaptative system that may experience injury-induced changes. Research in this field has already proved and continues to deepen the available information regarding the interplay between the CNS and PNS throughout an entire lifespan (17). Animal experiments have recognized that plasticity within the somatosensory cortex begins immediately following peripheral nerve transection (18). More recently, resorting to advanced imaging techniques, many reports established that a PNIs are linked to quantifiable structural changes in the human brains (19-21). For instance, the persistent and chronic pain often present in PNI patients' leads to physical changes in the brain, such as insula thickness (22). In another example, functional magnetic resonance image (fMRI) has shown that patients who had neuromuscular interventions control the reconstructed muscle with different parts of the brain when compared to the healthy muscle (23).

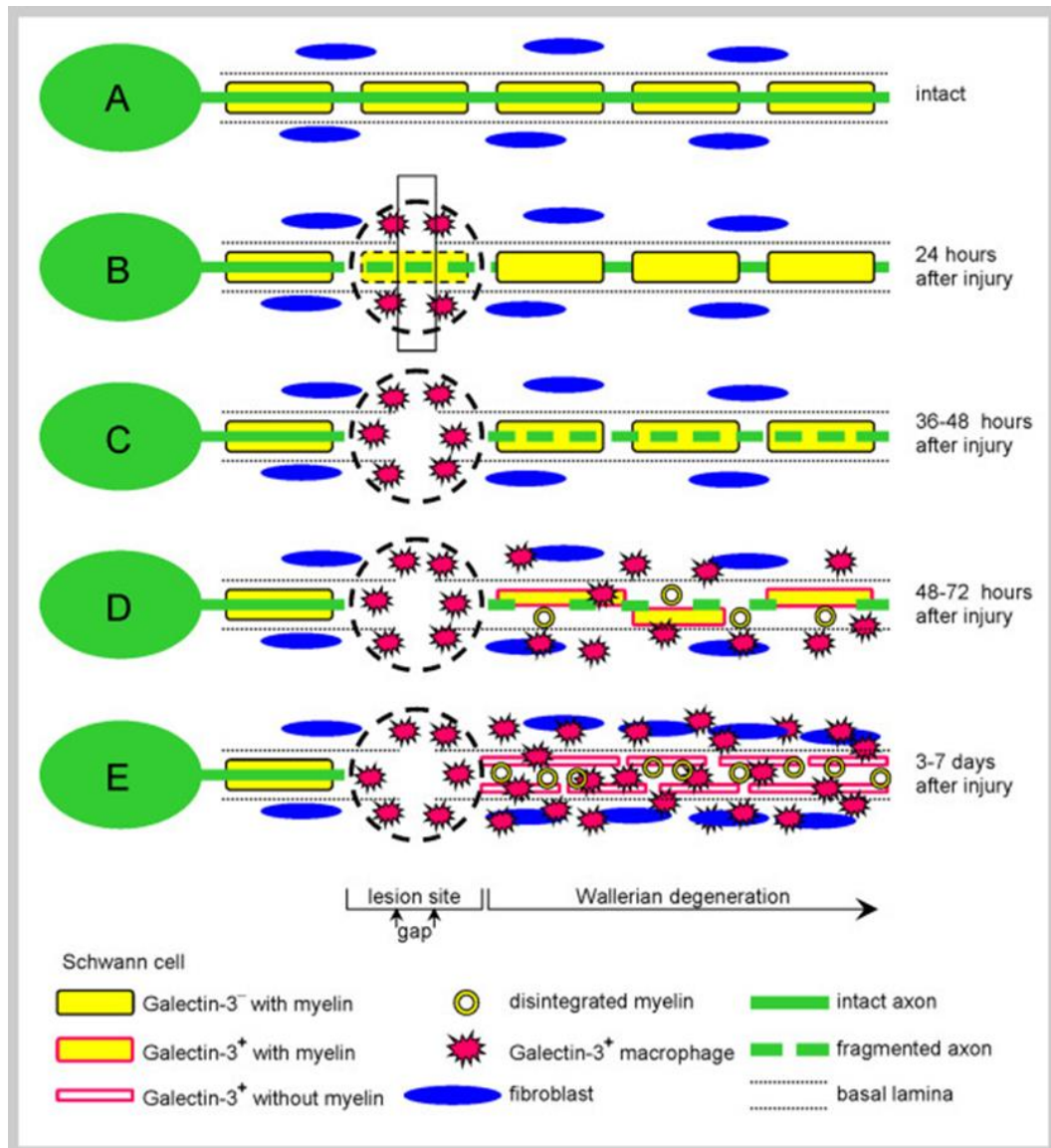


Figure II-2 - Schematic representation of injury and regenerative process involved in peripheral nerves. (A) Represents the intact nerve, with myelin enwrapping healthy axons; (B) The moment where an injury occurs, instantaneous tissue damage happens at the injury site. After a few hours, macrophages gather at the lesion; (C) The normal Wallerian degeneration process starts roughly one day after the initial trauma and axons start to disintegrate; (D) Enrolment of Galectin-3 macrophages, which contribute to myelin degradation and removal of myelin debris; and (E) The typical degradation of the distal nerve end happens with the participation of the Galectin-3 macrophages and Schwann cells. These cellular components scavenge deteriorated myelin and axonal matter. After the clearance of the debris, Schwann cells proliferate and align, forming the Bunge's bands, for future guiding of the regenerating axons. Reprinted with permission from (24), Copyright©2011 Rotshenker; licensee BioMed Central Ltd.

After peripheral nerve transection and surgical repair, it has also been noticed that both grey and white matter suffer from structural abnormalities in several cortical areas as well as thinner cortex, revealing the functional plasticity (17). The literature concentrates mainly on measurable parameters

and the progress of modern non-invasive neuroimaging techniques to scrutinize brain plasticity in humans. Among the first category, nerve conduction studies, quantitative sensory testing and neuronal responsiveness to stimulus are evaluated (25). Related to neuroimaging, fMRI is capable of measuring white/grey matter volume, density and integrity, as well as cortical thickness (26). Not only physical changes can be detected, but psychological and emotional traits can also be recognized, such as depression or the phenomena of catastrophizing pain (27). Maladaptive neuroplasticity also occurs very often. Chronic neuropathic pain is the result of pain-related changes as the answer to the injury (28). Although not fully understood, it is suspected that neuroplasticity arises from deficient and incomplete nerve regeneration, to which the brain must physically adapt. Cortical changes following PNIs include topographic restructuring of the somatosensory and motor cortices, which will be long lasting.

Overall, the importance of this specific field relies on the fact that understanding peripheral and central changes that contribute to the patient recovery may lead to the advance of new therapeutic approaches, including tailoring of timing and rehabilitation policies (25). A scheme representing neuroplasticity can be seen in **Figure II-3**.

II-1.3. Tissue Engineering and Regenerative Medicine Concepts for PNR

Tissue engineering (TE) is a crucial instrument in the field of regenerative medicine (RM), which has been the subject of dynamic scientific research for three decades (29). TE and RM terms can be used separately and interchangeably. However, both terms have been globally referred to as TERM (30). TERM approaches have triggered tremendous interest and revolutionized the present and future of medicine and surgery (31). TERM tactics exist in a variety of human tissues and organs. The pivotal point is that these strategies bring new therapeutic possibilities, not only to general population, but also to young patients and high-level athletes, allowing the restoration of biological functions and rehabilitation.

Overall, TERM strategies assist in the re-establishment, support, regeneration or replacement of injured tissues and organs (32). Traumatic offense, oncological resection, congenital malformations, or progressively degenerative diseases result on tissues and organs that need replacement. Allied to that, there is the fact that the shortage of donor organs is a problematic that is growing given the aging and increasing population.

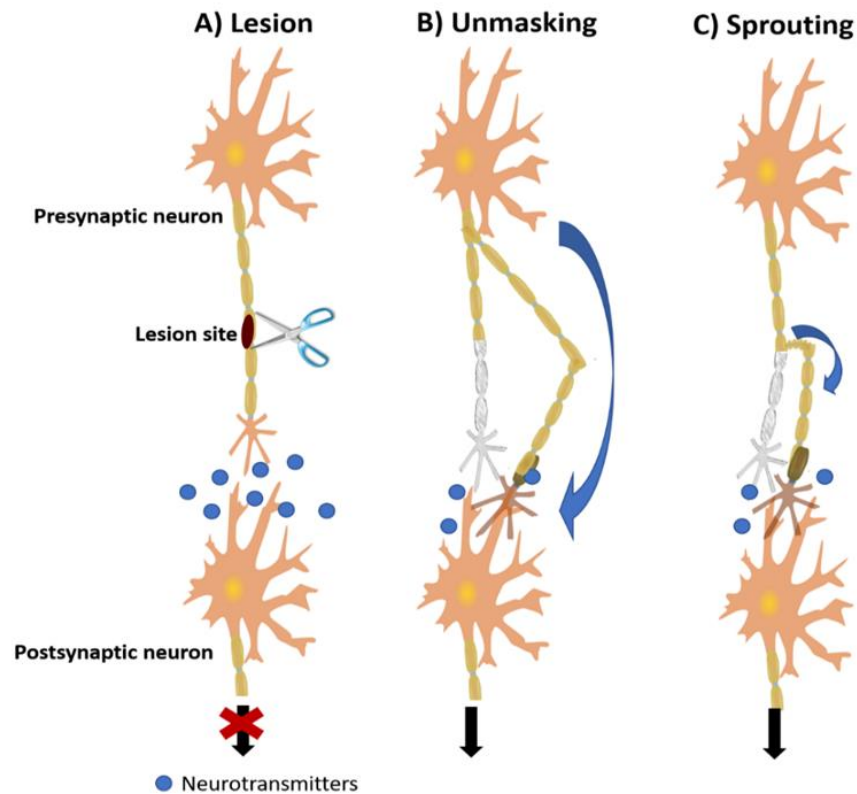


Figure II-3 - Scheme representing the neuroplasticity that occurs throughout the CNS after PNIs. A) Healthy peripheral nerve being subjected to an injury. Immediately after the trauma, the functionality of the nerve is affected, and the correct neurotransmission is interrupted. Neuroplasticity that occurs in the CNS following PNI is thought to occur through several mechanisms, with two of the most prominent theories being: B) Unmasking of existing synaptic connections. In this process, there is the unmasking of neural paths which were not normally used for a specific purpose, and new neural paths are activated when the normally used system fails; and C) Sprouting of new nerve terminals, where there is collateral sprouting from intact healthy cellular components to a denervated region, in an attempt to reestablish the neuronal connection.

TERM strategies propose to apply the ideologies of cell transplantation, material science, nanotechnology and bioengineering to fabricate biological substitutes of the damaged organs, eliminating the need and the wait of a transplant. Given that definition, the ideologies of TERM make it the subject of great hope and interest from a whole community, from patients to academia, industry and medical community. It represents the opportunity to cure several un-curable diseases and to deliver innovative solutions for medical problems in the future. Since its start, TE and now TERM, have been relying on three pillars: i) scaffolds, ii) cells, and iii) growth factors (GF) (29). The basic strategies used in TERM approaches can be seen in **Figure II-4**.

Scaffolds are biodegradable and porous 3-dimensional (3D) templates, which main role is to mimic the Extracellular Matrix (ECM) when they are first implanted. The native functions of ECM comprise

important signaling and regulatory functions as well as contributing to the physical and mechanical integrity of the injured tissue. Therefore, one important area of TERM is to develop smart scaffolds that closely recapitulate the native properties of ECM. Consequently, structural proteins such as collagen, laminin, elastin, and fibronectin have been used as matrices for TERM (33).

By its turn, cells will perform as the biological trigger that will contribute to tissue regeneration. They will secrete biological factors and produce ECM, stimulating endogenous regeneration. Traditionally, differentiated cells harvested from the native tissue were used. Nevertheless, with the increasing knowledge and development of the stem cell field, the advantages of using such cells made it common to use stem cell-based therapies (34).

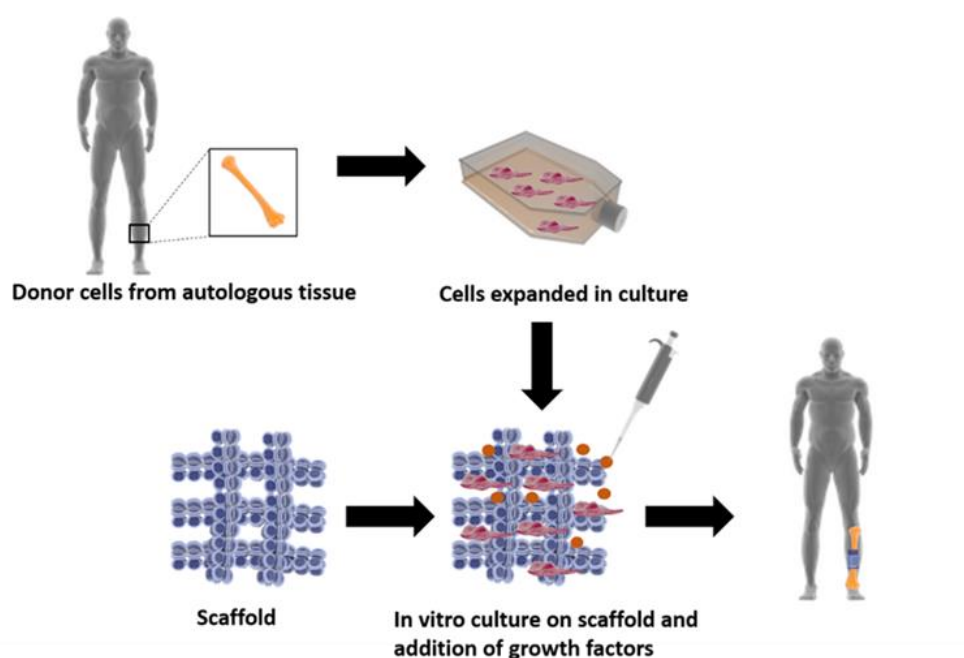


Figure II-4 - The classic TE model, where a triad of components interact with each other: scaffolds, cells and biological molecules. Overall, it includes the combination of living cells isolated from the patient donor tissue and expanded in culture, with a natural, synthetic, or bioartificial matrix or scaffold. Together with the addition of biological stimuli such as growth factors, a 3D living construct that is structurally, mechanically, and functionally equal to a tissue. The engineered construct can be implanted in the patient in order to restore the damaged tissue.

Finally, GF or other biological stimuli are fundamentally relevant in the process of tissue regeneration (35), as they initiate and induce processes such as cell differentiation and vascularization. Their use is inspired in the physiological events seen in the “wound healing cascade”, where a variety of GF is released and creates microenvironments suitable for tissue formation and repair. However, for the GF to be effective, there should be a release of multiple therapeutic agents at an optimized ratio,

physiological dose and in a specific spatiotemporal pattern (35). As consequence, many studies focus on the application of biomaterials-based approaches that allow for controlled spatial presentation and release kinetics of key biological cues treatments (36, 37).

To achieve the ambitioned regeneration, several strategies can be used. One of them is the use of acellular matrices, composed only of smart biomaterials. They can either be prepared by manufacturing artificial scaffolds or by preparing acellular materials after decellularization of tissues (38). Cellular components can also be added and advanced medicinal therapeutic products (ATMPS) are obtained (39). For instance, Hu *et al.* (39) used a 3D-printing technology to manufacture a bio-conduit. It consisted of a cryo-polymerized gelatin methacryloyl gel cellularized with adipose-derived stem cells (ADSCs). In a different approach, Dai *et al.* co-cultured Schwann cells and dental pulp stem cells on poly(d,l-lactide) (PLA) NGCs to test their efficacy in repairing a 15 mm long critical gap defect of rat sciatic nerve. Such strategy consists in the implantation of already cellularized constructs, offering a ground-breaking alternative to cure or treat diverse injuries or diseases.

In both strategies, acellular or cellular materials, the biomaterial transformed in a scaffold must provide mechanical support, shape, and proper architecture for neo-tissue construction *in vitro* or *in vivo* as seeded cells expand and organize (32, 40). Another TERM strategy focuses on the use of cells alone, without the use of biomaterials, in which cells organize by self-organization and self-assembly (41). Altogether, regardless of the strategy followed, TERM aims at the formation of new tissue for the reconstruction of the human body, resulting in substantial therapeutic benefits for patients for whom there are not currently any clinically effective therapies. TE has applications in almost every tissue of the human body which can get diseased, from bone (42), cartilage (43), tendon (44), cardiac tissue (45), pancreas (46), cornea (47), vascular system (48), CNS (49) and PNS (50). However, regrettably, TERM strategies are not yet delivering significant progress in terms of clinical outcomes and commercialization, as there has not been a substantial translation from the bench to the clinics. This applies specifically to the case of PNR. Despite intensive research and plentiful approaches that have been published, none have achieved the desired results.

II-1.4. Approaches for nerve repair

For the complete nerve repair process, surgeons, as well their competence on microsurgical technique, are needed as the crucial link between the technological innovations developed in the labs

and the final clinical treatment (51). For the standard treatment of minor injuries and small gaps (severe axonotmesis and neurotmesis injuries), the direct nerve repair with epineural end-to-end suturing is the optimal option. Nevertheless, that is only possible when the coaptation is done in a tension-free manner and allow re-constructing the original vasculature (52). Briefly, the surgeon must perform a fascicular alignment and matching between the nerve bundles in the two stumps, as well as epineural blood vessels (53). Fibrin glue is increasingly becoming an alternative to the sutures (54). When the injured area is larger than 5 mm and there is a wider portion without nerve mass, a direct repair cannot be performed promptly, and the use of grafts is necessary (55, 56). The “gold-standard” treatment in such cases is the autologous nerve graft, as it is the solution that still provides the best functional and sensory outcomes. However, besides not guaranteeing full recovery, only about 50 % of the patients achieve an acceptable degree of regaining functions (57). This process carries many other disadvantages such as donor site morbidity, insufficient donor nerve availability, and the need for extra operative procedures. Allografts or xenografts are other possible alternatives, but the possible immune rejection as well as the need for heavy use of immunosuppressors can limit their application (58).

The drawbacks of the previously mentioned clinical options may create the opportunity for the development and use of TE NGCs. Therefore, recent research is focused on the development of engineered “nerve guides” or NGCs. A NGC is a tubular structure made of biological or synthetic materials designed to bridge the gap of a sectioned or severed nerve. They were conceived to physically guide the growing axons across the lesion, guiding, and directing the emergent axons from the proximal to the distal stump. The two other fundamental tasks of NGCs are allowing the creation of a favorable milieu for optimal regeneration, by means of concentrating the released GF, preventing the excessive infiltration of fibroblasts and consequent formation of scar tissue, and allowing the migration of Schwann cells. This approach is usually reserved for gap defects between 1.5 and 10 mm (59). **Figure II-5** represents a scheme of all nerve repair options available in the clinical setting.

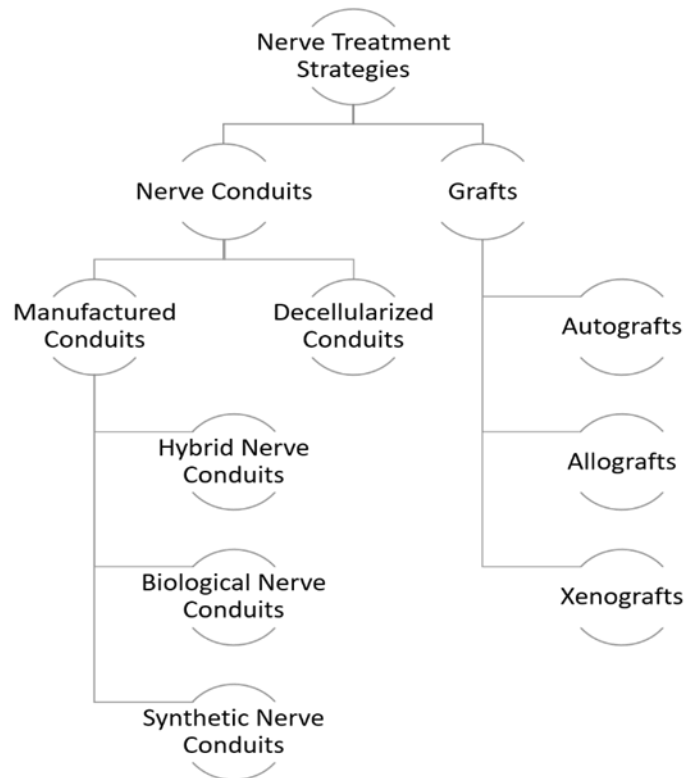


Figure II-5 - Strategies for nerve repair. In the case of a significant nerve gap formation where end-to-end coaptation is not possible, nerve grafts or TE NGCS are required to serve as a bridge between the nerve stumps, to protect the gap and to support axonal regrowth. The diverse option available among grafts and nerve conduits can be seen in the scheme. When considering grafts, they might be autologous, from the same species (allografts) or from different species (xenografts). For the NGCs, they can be biological but previously decellularized conduits, or TE NGCS, made of different materials, such as natural, synthetic, or a combination of both.

II-1.5. A biomaterials-based approach for NGCs

According to the American National Institute of Health, a biomaterial is described as “any substance or combination of substances, other than drugs, synthetic or natural in origin, which can be used for any period of time, which augments or replaces partially or totally any tissue, organ or function of the body, in order to maintain or improve the quality of life of the individual” (60). The first choice for the development of any TE NGC relies on the choice of the biomaterials to be used. The biomaterials field is being incessantly developed, bringing unquestionable advantages to the peripheral nerve research and regeneration field. The use of a 3D network acting as a supporting and protecting matrix is the basic approach in PNR, allowing for guided tissue regeneration. Biomaterials to be used in this field must match a few significant requirements, such as biocompatibility, biodegradability,

permeability, biochemical properties, and surface properties, as well as size (length and width) necessities (61).

In what concerns the synthetic materials, they are still thought as very promising materials for PNR. As a matter of fact, most FDA-approved NGCs are composed of synthetic materials, such as Neurotube (polyglycolide acid, PGA) and Neurolac (poly(L-lactide-co- ϵ -caprolactone, PLCL) (62). However, the use of synthetic materials goes beyond that, and a brief literature review reveals that other synthetic materials widely used in PNR are PLA (63), polylactic-co-glycolic (PLGA) (64), polycaprolactone (PCL) (65) and polyhydroxybutyrate (PHB) (66). The success of synthetic biomaterials for the construction of NGCs relies on the fact that they provide higher degree of controllability, and better mechanical properties compared to their natural equivalents (67). On the other hand, the use of natural-origin biopolymers can offer other advantages, such as having regenerative bioactivity. Furthermore, natural-origin biomaterials allow for improved inter-relation between cellular components and the scaffold, refining tissue regeneration (68). The downside of these biomaterials is based on the fact that present batch to batch discrepancies (69).

ECM endogenous proteins such as collagen, fibrin, laminin, and hyaluronic acid (HA) can be categorized as natural-origin biomaterials. These have been extremely investigated, since they naturally belong in the Human body and are consequently considered the “perfect” biomaterials. These biomaterials tend to act as natural scaffolding by delivering a matrix where cells can assemble within the connective tissue (70).

II-1.5.1. The first concept: Regeneration within a hollow conduit

The application of hollow conduits for nerve repair was first projected in 1881, where a hollow bone was used to bridge the nerve gap in a dog model, nevertheless with poor results (71). The hollow tubulization technique aims to isolate the regenerating axons from scar tissue, protect the regenerating nerve against compression by the surrounding tissue, longitudinally guide the regenerating tissue and condense the growth factors secreted by Schwann cells between the nerve stumps (72). Nowadays, we possess extensive knowledge about Wallerian degeneration and the natural mechanisms of repair (24). Taking this information in consideration, all the evidence points to the advantages related to the addition of luminal fillers to NGCs. Despite that fact, the extensive usage of hollow NGCs remains the common practice in clinical settings, due to their extensive FDA-approval.

The use of hollow NGCs has already proved to be advantageous in some situations, as they can prevent the permeation of fibroblasts and enable the buildup of neurotrophic factors (NTFs), which lead to regenerating cues. Furthermore, it has been proved that hollow conduits prevent neuroma and scar formation, ineffective axon sprouting and fibroblast intrusion. Taking advantage of the initially used impermeable silicon conduits, Williams *et al.* (73) described the different stages of regeneration inside a hollow NGC, in a 10 mm rat sciatic nerve gap. It follows five different phases and can be seen in **Figure II-6**. Briefly, the first phase is the fluid phase, where the conduit is filled with fluid containing NTFs, around 12 hours after the injury. Within the first week, the second phase arises (the matrix phase), where the fibrin cable is formed. It follows the third phase, where the cellular migration starts to occur. Here, the cellular components migrate through the fibrin matrix. The axonal phase is phase four, where the first axons are visible migrating from the proximal nerve end, as early as 2 weeks after the injury. The final phase is the myelination phase, occurring around week 4 after injury (74). However, it is known that single hollow NGCs may lead to incomplete reinnervation. This is due to axon dispersal or poly-innervation of different targets by the axons of the same neuron. Single hollow lumen NGCs are thus recommended for small lesions (up to 10 mm gap) in the sensory nerves (75).

In 2014, however, there was a breakthrough regarding this subject. The first conduit integrating a luminal filler component and acting as 3D guiding and supporting scaffold was FDA-approved. NeuraGen 3D Nerve Guide Matrix® is composed by collagen I, whereas the luminal filler is comprised of collagen I and glycosaminoglycan chondroitin-6-sulfate, with aligned porosity acting as a topographical cue for regenerating axons. *In vivo* studies demonstrated a significantly improved regeneration as compared to the hollow conduit (76).

Hollow cylindrical tubes can be fabricated by several techniques, such as melting extrusion, injection molding, physical film rolling, crosslinking, braiding, and electrospinning methods (77). In the past decades, numerous NGCs made of both synthetic and natural biomaterials have been described. However, one must keep in mind that although hollow conduits do not fully solve the obstacles faced in the clinics, they are subject to a wider clinical acceptance when compared to more complex types of conduits, associated to a better performance.

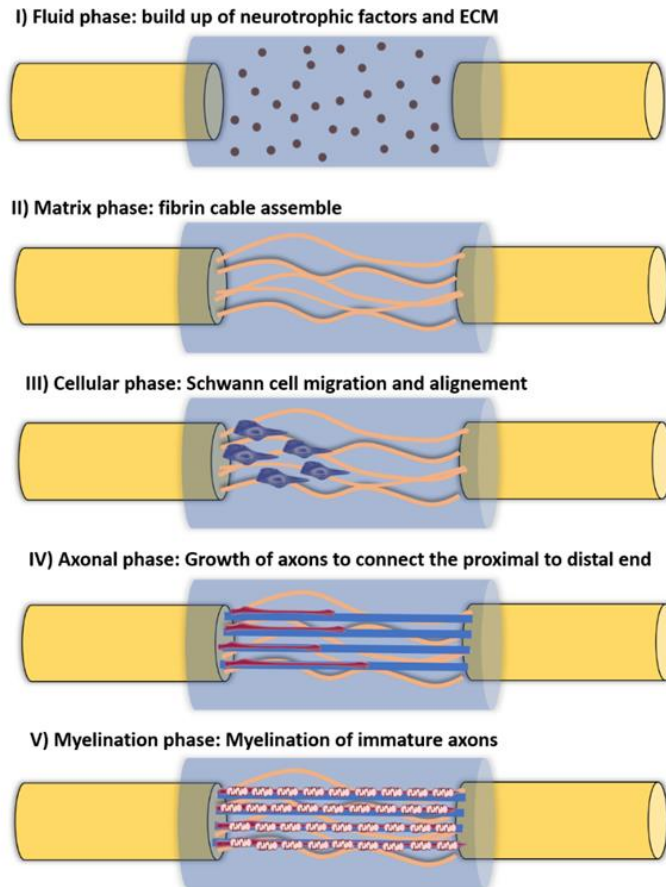


Figure II-6 - Five different phases of nerve regeneration inside a hollow NGC. The phase corresponds to the sequenced phases of Wallerian degeneration and resulting regeneration mechanism. Phase I corresponds to the fluid phase, where the conduit is filled with plasma exudate containing neurotrophic factors and ECM molecules. This phase takes place a few hours after injury. Phase II corresponds to the matrix formation, where fibrin cables are formed along the gap around one week after injury. Phase III is the cellular phase, where Schwann cells invade the gap, migrate and proliferate. They tend to align along the fibrin cable, forming the Bands of Bungner. Phase IV is axonal phase, which occurs around 2 weeks after injury. The re-growing immature axons use the biological cues provided by Schwann cells to reach their distal targets. Phase V corresponds to the myelin phase. At this time, around 3 weeks post-injury, Schwann cells shift to a myelinating phenotype and produce myelin which is wrapped around each axon, forming the mature myelinated axons.

II-1.5.2. Intraluminal guidance structures, a third dimension

Not only the type of biomaterial used in the NGC is important, but its architecture is also a relevant feature (78). The reason for inadequate regeneration when using hollow NGCs may be credited to the lack or inadequate formation of ECM components to guide the growing axons. Succinctly, in longer gaps, the formation of the fibrin cable is compromised. Therefore, Schwann cells are incapable of aligning through the injury site, diminishing the formation of the Bands of Bungner, the indispensable

topographical guidance structures for re-growing axons (79). Hence, to control the scattering of the axons inside the hollow conduits, many approaches focus on filling the lumen with a diversity of shapes, with the objective of being biomimetic and looked at as alternatives to autografts.

In one hand, an empty lumen has the advantage of allowing free space for nerve regeneration, so that the axons may selectively re-innervate the appropriate target. On the other hand, a lumen filled with any type of topographical and biological cues can provide a supporting structure that favors cells ingrowths, guidance and correct targeting (80, 81). In fact, regenerating axons develop distal tip expansions called growth cones that explore and recognize growth and guidance cues within the surrounding milieu, through their filopodia and lamellipodia, at a nanoscale range (82). Thus, the architecture of the NGC's interior is expected to be a crucial factor in order to achieve an effective axon growth across the gap. This may be the reason why single hollow NGCs are limited to 10 mm nerve gaps. Topographical cues may alter cell shape and act together with biochemical environmental cues. However, the mechanism of cellular response to topographical cues is yet to be fully elucidated (83).

A variety of strategies have been explored by scientists in order to attempt to replace the support and guidance provided by the natural ECM tissue cable. NGCs have been filled with all kinds of materials (84), such as hydrogels (85), nanofibers (86) or membranes (87), among others. Some of the most relevant adopted strategies to go beyond a hollow NGC can be seen in the depicted scheme in **Figure II-7**. Furthermore, conventional and rapid prototyping techniques have been used to prepare the inner fillers for NGCs. The main conventional techniques used in the field of peripheral nerve TE include electrospinning (88), poro-leaching (89), freeze-drying (90), and solvent- or thermally- induced phase separation (91). Instead, rapid prototyping techniques are a family of emerging software-driven procedures allowing the controlled layer-by-layer fabrication of scaffolds which have been on the rise due to their outstanding capacities , namely the 3D printing and bioprinting (92).

The anisotropic architecture of the substratum has also demonstrated to be an important feature of native nerve tissue and in the process of Wallerian degeneration. An extensive number of reports advocate that topographical guiding cues are, similar to those delivered by the guiding basal lamina microchannels, indispensable for a nerve scaffold to orient axonal regeneration in a nerve gap (93). In fact, as early as 1934, it has been shown that the oriented structure of clotted blood plasma can serve as tracks for guiding DRG axon growth (94). Aligned structures, with parallel linear grooves, pores or fibers have been shown to promote neurite outgrowth in PNR (95). This alignment induces cell migration and organization along the nerve on a preferred direction, from the proximal to the distal

stump (96). With intensive research in this field, it is now known that aligned topographical cues enhanced neurite outgrowth by activating mTOR pathway (83). From the molecular point of view, mTOR gene expression is at its peak between 48 and 72 hours after positioning of the cells, which coincides with the commencement of rapid and aligned neurite outgrowth. Thus, this study showed that mTOR levels significantly increased by patterned topography.

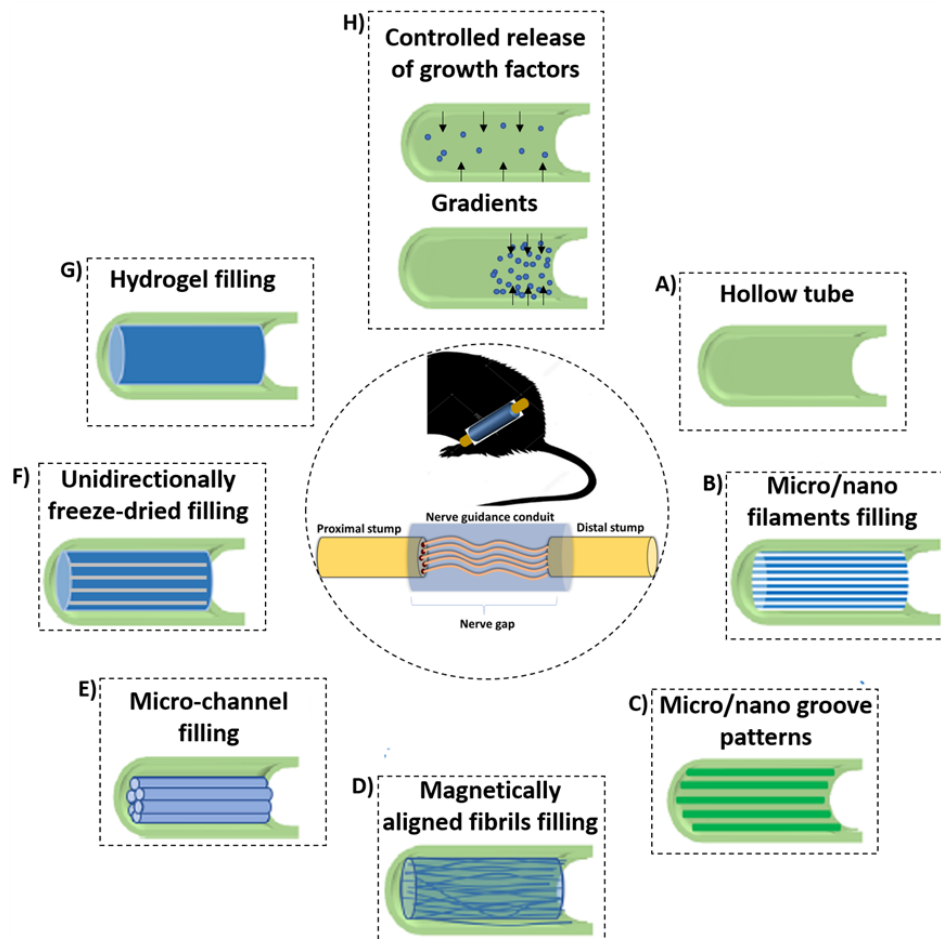


Figure II-7 - Due to the incapacity of hollow NGCs to bridge larger nerve gaps, various filler materials and designs have been developed to enhance the performance of NGCs. A) The initial strategy consisted of simple hollow NGCs; When considering luminal fillers, experiments suggested that the regenerating axons prefer aligned features rather than random orientation. Therefore, many of the approaches focus on obtaining an anisotropic topography. With this strategy in mind, many types of luminal matrices are considered: B) Micro- or nano-filaments resembling the structure of endoneurial tubes; C) Micro/nano groove-patterns; D) Magnetically aligned fibrils or cells; E) Micro-channel filling; F) Unidirectionally freeze-dried; G) Another strategy consist in inserting permissive hydrogels as luminal fillers, being a soft support to regenerative axons; and H) One branch of PNR research also focuses on the controlled delivery of growth factors. That can be achieved, for instance, using crescent gradients of growth factors from the proximal to the distal sites, acting as a biochemical cue and attracting regenerating neurons to reach the final target.

II-1.5.2.1 Hydrogel fillings

Considering hydrogel fillings, polysaccharides, ECM molecules, proteins, and peptides have been used to prepare hydrogel matrices to be placed in the lumen of hollow NGCs. However, reports on the successful nerve regeneration through the use of hydrogels have been contradictory. For instance, self-assembling peptide RADA16-Mix in the form a 3D hydrogel presented to be a suitable environment for sciatic nerve regeneration, when functionalized with IKVAV and RGDs. This hydrogel was injected inside an electrospun PLLA NGC (97). In this specific study, when implanted in a rat, the nerves migrated right through the RADA 16-Mix hydrogel toward the distal position. Furthermore, RADA 16-Mix hydrogel induced more axons regeneration and Schwann cells immigration, resulting in better functional recovery as determined by the gait-stance duration percentage and the formation of new neuromuscular junction structures. In another study where peptides were combined with hydrogels (98), a tubular conduit was filled with synthetic matrix BD™ PuraMatrix™ peptide hydrogel and cultured with Schwann cells. The peptide matrix contains amino-acids which under physiological conditions self-assemble to form a fibrous 3D hydrogel structure. This device was tested *in vivo* on a 10 mm sciatic nerve defect in adult rats. After extensive characterization and several timepoints analyzed, it was found that the addition of the Schwann cells to the BD hydrogel significantly increases the distance of axonal regeneration in short-term experiments but fails to endure long-term neuronal regeneration and muscle recovery. Du *et al.* (99) developed a 3D fibrin hydrogel that proved to be an instructive microenvironment by mimicking the native fibrin cable inside the NGC. In this study, the developed fibrin hydrogel with hierarchically aligned topography presented low elasticity (~1.5 kPa) that is similar to nerve ECM and to the native fibrin cable. After an *in vivo* study in a 10 mm defect model in rat, it was established that the hydrogel provided a beneficial microenvironment to support Schwann cell cable formation and accelerate axonal regrowth with improved motor functional recovery.

Human air keratin hydrogel was also studied (100). The purpose of that study was to investigate PNR using a keratin biomaterial hydrogel as a luminal filler inside a bioabsorbable collagen conduit in a nonhuman primate nerve injury model, in a 10 mm gap. The results were encouraging in terms of nerve regeneration.

On the other hand, NVR-Gel (81) or Gellan Gum (101) placed inside chitosan NGC obviously impaired axonal outgrowth. In the first study, Cora *et al.* reconstructed a critical length nerve defect (15 mm) with chitosan NGCs filled with NVR-Gel. While autologous nerve grafts did guarantee for functional

sensory and motor regeneration in 100 % of the animals, the presence of NVR-Gel into the chitosan nerve guides obviously impaired sufficient axonal outgrowth, physically blocking the regenerated nerves. The same happened to Carvalho *et al.* (101). In this study, different Gellan Gum formulations were injected inside the same chitosan conduits in a 10 mm sciatic nerve defect in rats. After 3, 6, and 12 weeks, functional and histomorphological *in vivo* assays showed that it did not lead to enhanced nerve regeneration, comparing with hollow nerve guidance channels. That was due to excessive density of the filler material.

Therefore, it can be concluded that incorrect positioning, non-uniform distribution or excessive density of intraluminal hydrogel fillers might result in regeneration failure, at least at short time of implantation. Therefore, *in vivo* studies to assess the efficiency of hydrogels as lumen fillers of NGCs functionality at long term (*e.g.* 6 to 12 months) are needed, in future.

II-1.5.2.2 *Freeze-dried anisotropic cues*

Topographical cues are influential regulators of the rate and directionality of neurite regeneration (83). One way to achieve an anisotropic 3D matrix is with controlled freeze-dried technique. More specifically, freeze-casting is a manufacturing method that allows the production of porous matrices containing a controlled and highly hierarchical architecture, which can be done with a variety of polymers (102). Since this is a rather well known and simple approach, it has been widely applied to PNR. Singh *et al.* (103) developed an antioxidant polyurethane NGC filled with aligned chitosan-gelatin cryogel filler. Only tested *in vitro*, neonatal DRGs and Schwann cells were seeded on the aligned scaffolds, which resulted in earlier migration and alignment to form “Bands of Bungner”-like structures. Following a stage-wise strategy, Huang *et al.* (104) produced an directionally freezing oriented collagen-chitosan filler in a porous electrospun PCL conduit. The NGC was optimized to have blend of collagen/chitosan (1:1) as filler and a wall thickness of 400 μm . Such features allowed the NGC to protect regenerating axons from compression stress while providing enough space for regenerating nerves. Furthermore, the anisotropic inner structure allowed Schwann cells and axons from DRGs to extend and migrate parallelly, in a significantly higher rate as compared to a non-anisotropic substrate. Manoukian *et al.* (105) took it a step further, and included interconnected longitudinally-aligned pores in a biodegradable chitosan NGC reinforced with drug-loaded halloysite nanotubes. The chitosan conduit allowed the sustained delivery of 4-Aminopyridine, a potassium-channel blocker, that has the capacity to

modulate prolonged nerve action potentials and strongly promoted neurotransmitters release. The aligned and interconnected pores allowed for longitudinal and horizontal migration of Schwann cells. Furthermore, 4-Aminopyridine delivery resulted in significant, dose-dependent upregulation of critical trophic factors, namely nerve growth factor (NGF), myelin protein zero, and brain derived neurotrophic factor (BDNF). Also, it promoted nerve impulse conduction, being an attractive strategy for nerve repair and regeneration.

II-1.5.2.3 *Multichannel*

In order to promote guided nerve tissue regeneration, multichannel NGCs have been used as permissive pathways for axon growth. Microchannels offer topographical and physical cues within the microchannels of an endoneurium tube, as they imitate and attempt to replace the basal lamina microchannels present in autografts. PLLA nerve conduits, in which each channel diameter ranges 200 μm , showed positive physicochemical characteristics as well as promising neuron oriented differentiation (106). In another study, Xu *et al.* (107) describe and tested a novel nerve-guiding collagen-chitosan scaffold with inner dimensions resembling the basal lamina microchannels of normal nerves. The scaffold presented several structural advantages, such as including longitudinally orientated microchannels and extensive interconnected pores between the parallel microchannels. When implanted *in vivo*, the device achieved nerve regeneration and functional recovery equivalent to that of an autograft. PLLA electrospun nerve guides with microchannels were produced by Frost *et al.* (108). The conduits walls were covered with fibers for topical guidance and were further evaluated in the rat model of 10 mm sciatic nerve defect. Furthermore, in selected groups, cell transplant derived from autologous stromal vascular fraction was added. The results indicate that tailor-made electrospun nerve guides support axonal regeneration *in vivo*, and can act as vehicles for co-transplanted cells

Using SF biomaterial, Dinis *et al.* (109) produced a system containing a high density of aligned and longitudinally oriented microchannels mimicking the fascicles of nerve. Constructed by electrospun SF and capable of incorporating and delivering GFs, the biomimetic multi-channeled functionalized nerve guides displayed a mechanical behavior comparable to that of rat sciatic nerve. This study suggests that the nerve's native epineurium and perineurium are responsible for the nerve tensile strength.

II-1.5.2.4 *Unidirectionally aligned micro- or nano-filaments*

Unidirectionally aligned micro- or nano-filaments inside NGCs support axonal growth cones in recognizing and responding to the microenvironment and stimulating them to follow the path to the distal stump. Furthermore, such structures can allow increasing the available surface area to volume ratio, thus potentially enhancing cellular adhesion and proliferation. In one of the first studies of this kind, Matsumoto *et al.* (110) added laminin coated fibers as NGC luminal filler, to bridge a 80 mm gap in a canine peroneal nerve model, however with poor outcomes. Quigley *et al.* (111) developed an advanced and multi-modal conduit where aligned PLGA fibers are contained within the lumen of a knitted PLA sheath coated with electrospun PLA nanofibers. To provide further support, the PLGA fibers are standing on an alginate hydrogel impregnated with several NTFs. The aligned PLGA fibers were remarkably helpful in guiding the growing axons. The fibers formulations was precisely chosen to encourage either axonal outgrowth or Schwann cell growth (75:25 for axons; 85:15 for Schwann cells). Furthermore, axonal outgrowths were found into and beyond the conduit and most of the repaired axons were myelinated. Such type of strategy has been explored in numerous studies, with variable outcomes (112-114). What they have in common is that the addition of such filaments clearly extends the regeneration limits when compared to hollow NGCs.

Later, studies were focused on the more suitable diameter of fibers as well as the density of fibers inside the NGC, in order to achieve the best possible outcomes (115-117). Regarding the first parameter, the use of fibers in the “nanometer” scale proved to provide the best outcomes, elevating electrospinning as the technique of choice (115, 116). Regarding the density of the fibers, lower densities increase the ability to bridge a critical nerve gap (118). Similar to what was found in the case of hydrogels, higher densities and occlusion of the lumen tend to lead to inhibition of regenerating nerves.

II-1.5.2.5 *Magnetically aligned cells and fibers*

Magnetically aligned cells and fibers also have valuable effects in PNR. In one of the first studies of its kind, Ceballos *et al.* (119) was able to magnetically align type I collagen gel, in which it was visible the nerve fascicle formation. In a similar approach, a study conducted by Rose *et al.* (120) where small amounts of superparamagnetic iron oxide nanoparticles (SPIONs) were incorporated inside the microgels, revealed that the SPIONs could be unidirectionally aligned in the presence of a low external

magnetic field. In fact, nerve cells could align when seeded in this hydrogel, which is a relevant achievement. Not only magnetically aligned matrices can be valuable, but also aligned cellular components have been developed. In this context, Phillips *et al.* (121) developed a tethered aligned collagen guidance conduit device. The authors have shown that the aligned portion of the collagen gel provides guidance cues, promoting the outgrowth of highly aligned neuronal processes from dorsal root ganglia (DRG), *in vitro*. *In vivo* studies in a 5 mm defect in rat model showed that the incorporation of magnetically aligned relevant cell types such as Schwann cells and fibroblasts within gels resulted in advanced neural regeneration when compared to the controls.

II-1.5.2.6 *Micro- or nanopatterning*

In terms of micro- or nano-patterned surfaces for PNR, there are two main approaches that can be used: i) micro- or nano-patterned two dimensional surfaces that can be rolled up to form a conduit, and ii) patterned micro or nanomaterials to be used as a filler material in NGCs. A vast selection of studies has used microgrooves to explore the most suitable sizes to encourage axon elongation, having in consideration the cell diameter (122-124). Experimental data advocates that narrow microgrooves (5-10 μm) confines the growth of cells and axon outgrowth compared to wider grooves (20-60 μm). On the other hand, the smaller microgrooves were found to better align axon growth, minimize the number of axon branches per cell, and reduce wrong target reinnervation. Inclusively, longitudinal nanogrooves (200 nm) supported functional recovery of sciatic nerves in rats (122) and enhanced the growth cone attachment and proliferation (125). Mobasseri *et al.* (126) modified the surface topography of PCL/PLA blending films to improve cellular guiding. The sloped walls grooved conduit with 70 μm wall thickness was compared with the current clinical gold standard of autologous nerve graft in the rat 10 mm sciatic nerve gap model.

Huang *et al.* (96) reported that able to exactly position neuronal cell body and direct axon growth by combining surface topography and a cell placement device, creating the prospect of engineering complex tissues. Furthermore, they were able to create an on-site axotomy, studying how the topography can influence the initial regeneration of injured axons. Promising results obtained using anisotropic topographical cues as luminal fillers can be seen in **Figure II-8**. However, the incorporation of luminal fillers, regardless of their kind, is not always successful, as a recent study by Saltzman *et al.* demonstrated (127). This study aimed to compare the performance of a PGA conduit containing

collagen fibers within the conduit, a hollow collagen conduit, and a nerve autograft. The results demonstrated that the nerve repair using the autograft provided superior motor nerve recovery, followed by the hollow collagen conduit and only then the conduit containing luminal filler. Therefore, a wise selection of the luminal filler must be made since each strategy has its pros and cons.

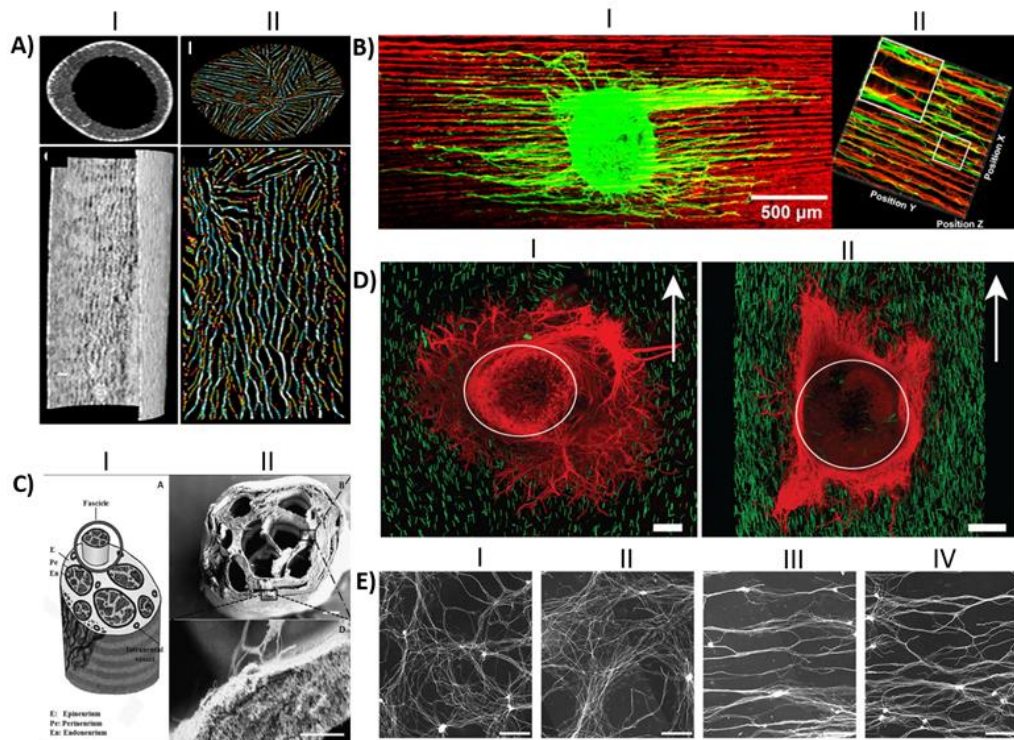


Figure II-8 - Anisotropic guiding cues have been successfully produced as NGCs luminal fillers. A I) Transverse and longitudinal Micro-CT sections of the hollow conduit; A II) Transverse and longitudinal Micro-CT sections of the oriented chitosan-gelatin cryogel as luminal filler; B I) DRG explants seeded on the longitudinal sections of the directionally orientated collagen-chitosan filler, where neurites align in the matrix; B II) 3D reconstruction of axonal regeneration and Schwann cell migration on the orientated collagen-chitosan filler; C I) Schematic drawing of the peripheral nerve structure; C II) SEM micrograph of the produced silk fibroin NGC fabricated incorporating microchannels, which looks like the depicted schematic; Scale bar 200 μ m; D I) DRG explants seeded in 0.25 % volume of the anisogel, presenting isotropic structure, in which neurites do not orient; D II) DRGs explants seeded in 1 % anisogel in which neurites decide to orient; E) Representative images of DRG explant neurites cultured on random patterns achieved with nanoimprinting lithography with metallic stampers made of three different spacings: E I) on a flat surface; E II) On a Blu-Ray disc spacing; E III) On a digital video disc spacing; and E IV) On a compact disc spacing. Scale bar: 200 μ m. Figures have been reprinted and adapted from: A) (128), B) (104), C) (129), D) (130), and E) (131).

II-1.6. Growth Factors (GFs) as molecular therapies

Apart from the use of suitable NGCs and fillers, the creation of a more biologically appealing microenvironment is of high importance in PNR. Nerve GFs are molecules that are naturally released in

the processes of injury and result in enhanced nerve regeneration. Therefore, it is important to mimic their release, which is vital for nerve growth, differentiation and expansion. (132). However, the artificial administration of GFs as a therapy is difficult task to accomplish because of their high biological activity, which obliges to administer extremely small doses. Pleiotropic effects and short biological half-life are also other common constraints (133). The fiasco of GF delivery may be credited to poor release kinetics, as several delivery systems unveil an elevated initial burst release (134). In an attempt to progress in terms of releasing profile, delivery systems that allow adjusting the release kinetics are being investigated (135). The use of biodegradable biomaterials is advantageous in this specific case, since they can act as vehicles for GF delivery, allowing to manipulate specific biomaterials parameters to attain the desired rate of sustained release. Physical crosslinking (136), chemical immobilization (137), polymer coating (136), and nanoparticles (138) are some of the strategies that are being used **(Figure II-9)**.

The various GFs have diverse actions in the nerve, as they can enhance functional regeneration, support axonal elongation, and Schwann cell migration, by means of acting as neuroprotective components through receptor-mediated activation of specific pathways. GFs regularly used to aid in PNR can be seen in **Table II-1**. NTFs normally used to improve nerve regeneration primarily belong to three separate groups (139): the neurotrophins, the glial-cell-line-derived neurotrophic factor family ligands, and the neuropoietic cytokines. The first group, neurotrophins, include NGF, BDNF, neurotrophin-3 (NT3) and neurotrophin-4 (NT4) (140). The second group includes the very glial cell derived neurotrophic factor (GDNF) and the ciliary neurotrophic factor (CNTF) (141). Although they belong to distinct families, all above-mentioned GFs have affinity to different Receptor Tyrosine Kinase (RTKs) on cells, which are trans-membrane proteins that will activate a cascade of events after substrate binding, activating determined cellular responses (142). Furthermore, RTKs are known to be retrograde transported from the extremities back to cell body, where they will once again activate transcription and translation of proteins, initiating signaling pathways to enhance neuronal growth and survival (143). The GFs of the neurotrophin family are structurally and functionally related peptides with active functions in both CNS and PNS, in particular, they mediate the effective survival and differentiation of several neuronal related cell populations.

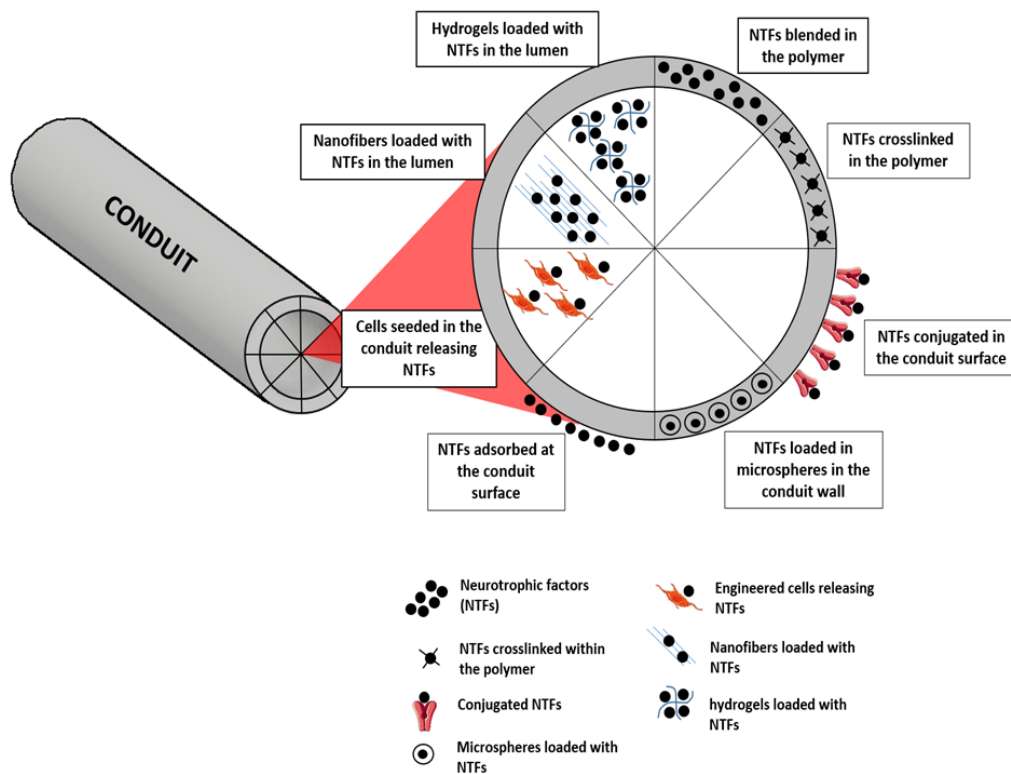


Figure II-9 - Different strategies for incorporation and delivery of GFs from NGCs. One of the simplest approaches is based on simply blending the NTFs on the polymer, with or without further crosslinking of the polymer. Microspheres containing NTFs can also be blended in the polymer. At the surface, NTFs can be found just after an adsorption process or conjugated with other molecules for stronger entrapment or covalent links. When considering the delivery of NTFs from the lumen, several approaches can be followed, such as using engineered cells, nanofibers or hydrogels capable of loading and releasing the NTFs.

II-1.6.1. NGF

NGF, the classical member of this family and therefore abundantly characterized, is largely used both *in vivo* and *in vitro*. Its action is limited to a few neuronal cell populations, namely supporting the outgrowth and survival of peripheral sympathetic and neural crest-derived sensory neurons (144). Recently, Bin Xia *et al.* (145) developed a nanofibrous scaffold loaded with vascular endothelial growth factor (VEGF) and NGF. Although VEGF was only released within the first days, NGF could be continuously released for up to 1 month. The dual-delivery scaffold could enhance the neural differentiation of induced pluripotent stem cells-derived neural crest stem cells (iPSCs-NCSCs), *in vitro*. Additionally, the nanofibrous scaffold was implanted in a critical length defect in rat with positive effects in the both regeneration and vascularization. In addition, recent investigation has revealed that NGF has various effects on inflammatory conditions, beyond the described effects on neuronal cell function.

(146). NGF effects can be either pro-inflammatory or anti-inflammatory (147). This is explained by the fact that NGF is part of an endogenous mechanism that may have both effects: as it activates immune responses, it also triggers pathways necessary to inhibit the inflammatory response, reducing tissue injury. However, and since NGF also appears to have a role in the activation of sodium channels and those correlate to the maintenance of inflammatory pain states, the presence of up-regulated NGF is associated to inflamed tissues (148).

II-1.6.2. BDNF

In peripheral nerves, BDNF is synthesized by Schwann cells, motor neurons, and a specific subgroup of DRG neurons. The up to now known BDNF effects are restricted to certain sub-populations of neurons, including sensory dorsal root ganglion neurons and induction of neurite outgrowth of neurons (149). It has been recently found that BDNF also exerts its effect through stimulation of Schwann cells to produce pro-regenerative cytokines (150). Another study (151) suggested that BDNF may not only stimulate a faster PNR but also significantly can reduce the neuropathic pain, in the rat model.

II-1.6.3. NT-3

NT-3 has overlapping neurotrophic activity with NGF, however studies suggest it has a broader specificity as compared to NGF and BDNF (152). Studies show the reinnervation of motor target tissues is also related to the presence of NT-3 and its physiological effects (153). Few reports have been published regarding this growth factor. One of the most recent focuses on the use of NT-3 to overcome Charcot–Marie–Tooth neuropathies, which are a heterogeneous group of peripheral nerve disorders (154). In these disorders, Schwann cells are affected. However, continued treatment with NT-3 is not feasible due to its short half-life and nonexistence in the market. In a way to overcome this problem, Sahenk *et al.* (154) hypothesized that the delivery of NT-3 via gene therapy with an adeno-associated virus. With such strategy and therapy, measurable NT-3 secretion levels were found in blood, in quantities enough to provide improvement in motor function, histopathology, and electrophysiology of peripheral nerves.

II-1.6.4. GDNF

GDNF has an important role in the case of degenerative diseases, such as Huntington's and Parkinson's, as it has been found that GDNF encourages survival of damaged midbrain dopaminergic neurons (155). GDNF has also been used to target sensory neurons in order to alleviate pain in cases of chronic denervation (156, 157). Due to the difficulty to attain the right dosage of released GDNF, most of the recent strategies using GDNF applied to PNR are focused on cellular or gene based-therapies (158, 159). In this scope, Shakhbazou *et al.* (158) described a proof of concept report where engineered Schwann cells using dendrimers or lentiviral transduction with the vector providing doxycycline-regulated GDNF expression were used. Injection of GDNF-modified cells into the injured peripheral nerve followed by time-restricted administration of doxycycline demonstrated that GDNF expression in Schwann cells can also be controlled locally in the peripheral nerves of the experimental animals. Using a similar strategy, Hsu *et al.* created a Cre/loxP-based hybrid baculovirus vector which enabled intracellular formation of episomal DNA minicircle for effective transduction of rat adipose-derived stem cells (ADSCs) and prolonged expression of functional GDNF. The implantation of such system into sciatic nerve transection site in rats significantly improved the nerve repair, as it was verified enhanced functional recovery, nerve reinnervation, electrophysiological functionality, axon regeneration, myelination and increased angiogenesis.

II-1.7. Gradients of growth factors (GFs)

An advanced and upgraded strategy can be considered using NGCs and GFs, which is the use of a GF gradient along with a NGC device. GFs gradient at the surface of the conduit aims at promoting contact guidance along the structure, maintaining the controlled release properties (160). This technique is based on the fact that the growth cone at the tip of the axon has path-finding ability, aiming at crossing the gap in a precise direction, correctly reaching the distal target. At the same time which is increasing the speed of such phenomena, what is called growth cone chemotaxis (161). Axons extend in search of their appropriate targets, often over long distances with the assistance of growth cones detecting and following molecular gradients (162).

Many studies have been focusing on this strategy of immobilized concentration gradients, either on films or NGCs, with different approaches (160, 163-165). More recently, Uz *et al.* developed a PLLA porous film, that besides having longitudinal surface micropatterns, also presents a gradient of NGF. As

a result, the NGF surface gradient provided initial fast release from the film surface and facilitated directional neurite outgrowth of PC12 along with the longitudinal micropatterns. With this double strategy, significant control over the simultaneous controlled release of neurotrophic factors as well as the guided and directed neurite outgrowth in PC12 cells was achieved. In another study (166), Sun *et al.* introduced exogenous cells secreting GFs capable of spatial distribution along the conduit. Instead of using a normal cellular density and distribution along the conduit, the authors used encapsulated bone marrow MSCs (BMSCs) capable of producing high levels of BDNF. In fact, in the conduits with stem cells encapsulated within the central third area possessed markedly different cell distribution and retention over 6 weeks *in vivo*, compared to standard cell lumen injection. Such a construct promoted Schwann cell migration from the center to the distal end. In another interesting and combinatorial approach, Chang *et al.* (167) developed a natural biodegradable multi-channeled scaffold characterized by aligned electrospun nanofibers and neurotrophic gradient to guide axon outgrowth. For the gradient, the authors followed two strategies: the NGF was simply blended with gelatin and BDNF was encapsulated in nanoparticles further embedded in gelatin hydrogel. The gelatin scaffold was divided into five regions from A1–A5 (low concentration to high concentration, from proximal to distal site). Their strategy promoted intense nerve regeneration in a 15 mm sciatic nerve defect in a rabbit model. Our group has also been developing a GF gradient strategy, by fabricating silk fibroin NGCs containing GF gradients in its walls, as can be seen in **Figure II-10**. However, unlike Tang *et al.* (160), who simply used soaking and coating techniques in the silk fibroin conduits, our group's strategy is based on gradually entrapping the GFs in the conduit's wall. This is achieved by enzymatically crosslinking the polymer, mediated by a horseradish peroxidase/hydrogen peroxide reaction.

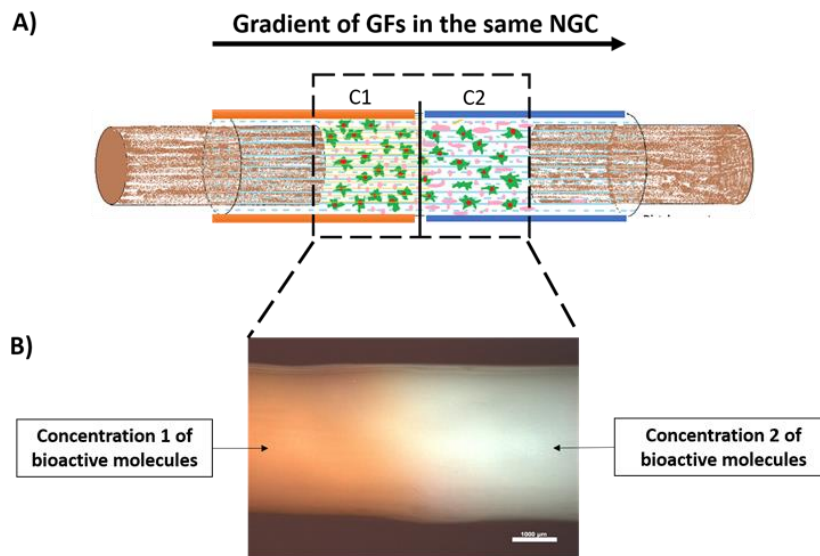


Figure II-10 - Proof of concept regarding the fabrication of a silk fibroin NGCs incorporating a gradient of GFs. A) Schematic of a NGC incorporating two different concentrations of GFs in the wall of the conduit. In principle, the gradient of GFs increases from proximal to the distal, therefore attracting the growing axons to reach their distal target. B) Stereomicrograph of a silk fibroin NGC presenting a gradient along the walls. The orange color represents the chosen Concentration 1, followed by the white color, representing Concentration 2. As it can be assessed, there is no separation in the conduit between the different concentrations, as the conduit is totally uniform. Scale bar: 1000 μm .

II-1.8. Other biological cues

II-1.8.1. VEGF

Not only the three major groups of neurotrophins exerts positive effects on neuronal regeneration. One such growth factor is VEGF. As aforementioned, peripheral nerves consist of several bundles of axon fibers and blood vessels surrounded by the connective tissue. Furthermore, it has been noticed by scientists that the vascular and the nervous system show similar anatomical structures, revealing a strong interconnection between both systems (168). Besides that, ischemia and oxygen deficiency occur in the injured nerve, as well as the destruction of the blood-nerve barrier. Despite the top most position of VEGF as a pro-angiogenetic factor, a collection of reports focuses the attention on VEGF activity on its neurotrophic and neuroprotective effect, both *in vitro* (169) and *in vivo* (170). The administration of VEGF can result in earlier functional improvement of the sciatic nerve when compared to the controls, since higher nerve neo-vascularization leads to improved nerve morphology (171). More recently, it also was discovered through *in vitro* assays that the addition of VEGF to primary Schwann

cells promotes their migration, a major process in the promotion of neurite outgrowth (172). Interestingly, VEGF-B has been tested on injured nerves despite its lack of angiogenic activity, but because of its neuroprotective effect, making VEGF-B a suitable therapeutic target to treat nerve injury (173, 174).

II-1.8.2. Hepatocyte growth factor (HGF)

In a work developed by Ko *et al.* (175), hepatocyte growth factor (HGF) has been recently found to be up-regulated, resulting in a higher expression of the referred HGF after a PNI, both at the injury and distal sites. The authors tested this specific growth factor, with known angiogenic activity and anti-inflammatory activity (176) in a model of PNI in mice. After the injury, not only HGF was highly expressed, but its receptor, c-met, was also found to be upregulated almost exclusively in Schwann cells. In addition, exogenous administration of HGF at the injury site led to an increase of the myelin thickness and axon diameter in injured nerves. To further prove this fact, when mice were treated with a c-met inhibitor, the opposite happened, as myelin thickness and axon regrowth were diminished, indicating that the positive effect of HGF was hindered. In line with this findings, Boldyreva *et al.* (177) also studied the effect of HGF in PNR. Gene therapy with HGF-bearing plasmid (pC4W-hHGF) led to the repair of nerve morphometry and functional recovery comparable to the autograft (positive control). Moreover, in HGF-treated mice, histological analysis showed a three-fold increase in axon number in nerve portion located distal to the lesion site compared to control, indicating great potential in keeping a healthy distal target. Besides confirming the potential of the application of HGF in cases of PNI, gene-therapy itself proved to be effective and advantageous. In addition to confirmed beneficial effects in PNR, literature has revealed that this growth factor exerts neurotrophic effect in motor, sensory, and parasympathetic neurons in addition to mitogenic, morphogenic, angiogenic, antiapoptotic, antifibrotic, and anti-inflammatory effect on various tissues and cells (178).

II-1.8.3. MicroRNA

Minor endogenous non-coding RNA molecules that act as regulators of gene expression after transcription are called microRNAs (miRNA). There are approximately 23 of these molecules, that negatively regulate the expression of a wide variety of genes (179). The role of miRNAs may go overlooked. However, at a post-transcriptional phase, it is projected that miRNAs regulate around 60 %

of the total human genes, therefore playing critical roles in physiological and pathological processes, such as cell differentiation, proliferation, migration, apoptosis, and morphogenesis (46). Related to nerve injury and regeneration, studies have been shown that miRNA play an important role in neuronal disease, as it has been reported that a global deregulation of miRNAs occurs in transected sciatic nerve axons (180). More specifically, it was found through *in vivo* and *in vitro* studies that the removal of Dicer (a crucial molecule in biogenesis of miRNA) disturbs the creation of Dicer-dependent miRNAs, consequently impeding PNR. Such findings confirmed the importance of Dicer-dependent miRNA pathway for effective repair of nerve injuries (181). Bremer *et al.* (182) showed that several miRNAs, including miRNA-34a, miRNA-146, miRNA-30a, miRNA-195, miRNA-140, miRNA-27b, and miRNA-204, were upregulated upon myelination in Dicer mutant mice. On the other hand, Gokey *et al.* (183) revealed that 225 miRNAs were expressed during peripheral myelination by miRNA profiling. By its turn, miRNA-106a, miRNA-20b, miRNA-338, miRNA-92b, miRNA-19b, miRNA-363, miRNA-350, miRNA-17, and miRNA-340 regulated Sox10, which regulates myelin genes, and do have a direct impact on myelination.

The importance of miRNA is also supported by the fact that Schwann cells proliferation and migration are controlled by let-7 through targeting NGF, *in vitro* and *in vivo*. The decrease of let-7d encouraged Schwann cells to intensify NGF production, leading to axon regrowth (184). As mentioned, let-7 miRNAs are highly abundant during myelination, and their levels are inversely correlated to the expression of lin28, which is an antagonist of let-7 buildup. Small amounts of let-7 miRNAs are the consequence of continuous expression of Lin28B, which lead to poor Schwann cell myelination (185). The influence of miRNAs was also verified on neurite outgrowth from DRGs after nerve injury. In one hand, miRNA-21 promoted neurite outgrowth by directly downregulating Sprouty2 expression (186). On the other hand, miRNA-222 targeting PTEN promoted neurite outgrowth. In contrast, the Robo2 expression can be inhibited by blocking the miRNA-145, subsequently reducing neurite outgrowth (187). The knowledge about the mechanisms involved and controlled by miRNAs offers the opportunity to explore potential new therapies, at a molecular level. Some of the mechanisms and miRNAs involved in PNR can be seen in **Figure II-11**.

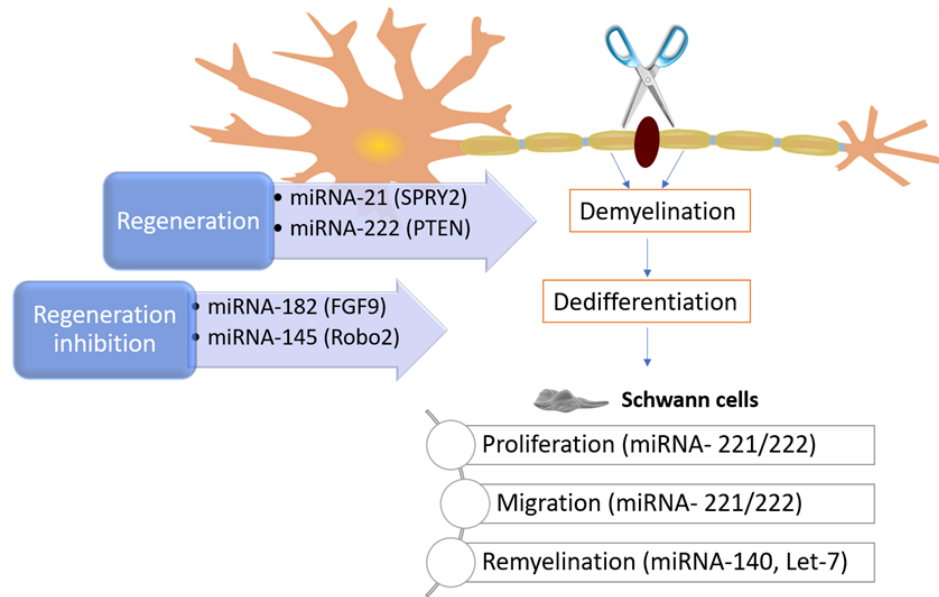


Figure II-11 - Schematic on some known mechanisms of how miRNAs can intrinsically control and impact peripheral nerve injury and regeneration. After an injury, the myelin and axons degrade, and Schwann cells dedifferentiate. As these phenomena happen, the molecular regulators (*e.g.* miRNA-221, miRNA 222, and Let-7) can influence neurite outgrowth and modulate phenotypic changes in Schwann cells, as well as their myelinating capacity, among others.

II-1.9. Cell-based therapies

The importance of cells as crucial actors in the regenerative process is evident. Consequently, cell-based therapy in PNIs has become an important and evidenced intervention which improves the functional clinical outcome (188). Many approaches can be followed, from primary Schwann cells, neural stem cells, embryonic stem cells, bone marrow stromal cells (BMSCs) and tissue engineered cellular components. Some of the most recent and relevant published reports, where cell-therapies are an important tool for PNR, regarding the use of several cell types can be seen in **Table II-2**.

Table II-1 - The use of GFs and their effect on CNS and PNS (189).

| Neurotrophic factor | Neural response | Receptor and action |
|---------------------|---|---|
| NGF | Sensory neuron survival Sensory neuron outgrowth Spinal cord regeneration | TrkA/p75, receptors expressed in sympathetic/peripheral sensory neurons (Schwann cells upregulate NGF and p75 in response to PNS injury); Involved in survival signaling and neurite outgrowth; |
| GDNF | Motor neuron survival Motor neuron outgrowth Sensory neuron survival | GFRA/Ret, receptors expressed in sensory/motor neurons, GDNF primarily produced by Schwann cells in development and plays an important role in sensory regeneration; |

| | | |
|--------------|--|---|
| BDNF | Motor neuron survival Motor neuron outgrowth Sensory neuron outgrowth | TrkB, BDNF mRNA upregulated in distal nerve stump after sciatic nerve transection; positive modulation of peripheral nerve myelination; |
| CNTF | Motor neuron survival Motor neuron outgrowth Spinal cord regeneration | CNTFR, present in peripheral nerves and myelinating Schwann cells; promotes survival of motor neurons; |
| NT-3 | Motor neuron survival Motor neuron outgrowth Sensory neuron outgrowth Spinal cord regeneration | TrkC, NT-3 mRNA downregulated in distal nerve stump after sciatic nerve transection; negative modulation of peripheral nerve myelination; |
| NT4/5 | Motor neuron survival Motor neuron outgrowth Sensory neuron survival | TrkB, plays a role in survival of adult sensory neurons; |
| FGF-2 | Motor neuron survival Motor neuron outgrowth Sensory neuron survival Spinal cord regeneration Peripheral nerve regeneration | FGFR1-3 plays a role in regeneration of motor and sensory neurons, as well as in myelination. |

II-1.9.1. Schwann cells

Schwann cells play a critical part of the Wallerian Degeneration. The high number of Schwann cells after an injury, seventeen times more than seen in the uninjured nerve, proves they are activated, and their presence is beneficial in case of injury (189). Therefore, many therapies are based in the transplantation of autologous or allogenic Schwann cells. Once expanded and harvested, Schwann cells will help in PNR after introduced in the NGC, which can be attained by a variety of methods: direct injection of a cellular suspension to the lumen, (190), suspension within an intraluminal hydrogel (191), distributed along intraluminal guidance structures (87) or released from the luminal (192). It has been considered that autograft is the goldstandard of PNR and autologous Schwann cells are the gold standard of cellular-based therapies (193). However, the use of Schwann cells comes with a few shortcomings such as the difficulty of harvest, the slow expansion in culture and a high immunogenicity, thus requiring further immune suppression strategies to be considered. Due to these drawbacks, the attention shifted to the use of undifferentiated stem cells, which can differentiate into several cell types in the presence of specific drugs/growth factors.

Stem cells can be obtained from numerous sources, but most studies focus on the use of both BMSCs (194) and ADSCs (195). For TE purposes, they have ideal properties such as differentiating in

multiple lineages, being simply extracted, proliferating quickly in culture, having cheap maintenance and above all, do not raise ethical issues (196).

II-1.9.2. BMSCs

BMSCs are one of the most important types of stem cells. Their primary function is to support hematopoiesis in the stromal compartment of bone marrow, from where they are withdrawn with a simple process of aspiration, after which they are easily expanded (197). Many studies have focused on learning the mechanisms through which BMSCs are beneficial for PNR (198-200). Xu *et al.* (201) developed an *in vitro* study in 2011 which demonstrated that a co-culture of BMSCs and DRGs explants stimulated neurite outgrowth and neuronal cell survival through the production of wide list of secretory proteins, including bFGF, NGF, CNTF and BDNF. Also, by means of using a co-culture system of DRGs and BMSCs in a trans-well, it was found that the presence of DRGs helped maintain the stemness of BMSCs through the AMPK/mTOR signaling (202).

II-1.9.3. ADSCs

ADSCs isolated from adipose tissue are one of the most used stem cells. Many *in vitro* and *in vivo* studies have confirmed the ability of ADSCs to promote nerve regeneration, in both undifferentiated (203) and differentiated (204) conditions. Concerning undifferentiated ADSCs, the main concern is related to the possible differentiation that cells may undergo when implanted, originating non-desirable phenotypes, such as adipocytes. In fact, nerve regeneration may be delayed due to fat obstructing NGCs (205). In respect to Schwann cell-like differentiated ADSCs, they were found to express a variety of intrinsic neurotrophic factors, namely NGF, BDNF, GDNF, and NT4 (206). Many *in vivo* studies seem to show beneficial effects when applying either undifferentiated or differentiated ADSCs in the nerve injury site, as can also be seen in **Table II-2**.

II-1.9.4. Human umbilical-cord stem cells (HUCMSCs)

Human umbilical-cord mesenchymal stem cells (HUCMSCs) are also becoming very popular in TE and more specifically in PNR purposes. These cells display exceptional characteristics to be use in TE approaches, such as multilineage potential, immunomodulatory aptitude, effortless isolation, and fast

proliferation (207). Besides, fourteen different neurotrophic factors related to enhance PNR are secreted by HUCMSCs (208). These factors stimulate neuronal survival, vascularization, upregulation of cell binding integrins, delivery of anti-inflammatory molecules, and increased survival and proliferation of Schwann cells. Thus, HUCMSCs paracrine effects probably lead to the efficacy of those cells in the treatment of nerve injuries (209).

II-1.9.5. Olfactory ensheathing cells

Still not widely recognized by the scientific community, Schwann cells and olfactory ensheathing cells (OECs) are two types of glial cells that play pivotal roles in restoring function after nerve injury within the PNS. OECs have similar capacities to Schwann cells, as they can reduce scar formation and promote regeneration (210). As a component of both PNS and CNS, reports on the use of OEC have mostly been focused on the CNS and insufficient assays have addressed their worth for PNI. One of the mechanisms by which OECs assist in PNR, is that they are responsible for creating an environment conducive to neuron growth and axon regeneration by producing neurotrophins, such as NGF, BDNF, NT-3, NT-4/5, BDNF, and GDNF (211). However, unlike Schwann cells, OECs are not capable of producing cytokines that attract macrophages (212).

II-1.9.6. NSCs

NSCs have also been used for PNR. Isolated, among others sources, from the adult striatum, they have the remarkable ability to divide, proliferate, and experience multi-lineage differentiation *in vitro* (213). This fact eliminates the pre-conceived theory that neural tissues cannot regenerate (196). Several studies have proved the capability of NSCs to differentiate into Schwann cell-like phenotypes, being positively marked for anti-S100 and anti-p75 and being capable of producing a myelin sheath (214, 215).

II-1.9.7. SKPCs

The dermis in the skin comprises neural crest related precursor cells, namely the skin-derived precursor cells (SKPCs). They can be differentiated into neural crest cell types with the features of neurons and Schwann cells, to find their application in the PNS (216). For such, SKPCs are cultured in

medium enriched with neural crest cues such as neuregulins, after which SKPCs morphology switches to Schwann cells-like. These cells are capable of inducing myelin proteins transcriptions when in contact with neurites (216).

II-1.9.8. Genetically modified cells

Genetically modified cells have been extensively used in the scope of TE strategies, inclusively for PNR. To be applied in the PNS, modifications are carried out in primary Schwann cells. However, the use of genetically engineered MSCs is also common (188). Genome editing is a remarkable expertise in which therapeutic and interesting genes are inserted in specific cells with the goal of reprogramming the cells to express or inhibit certain genes of interest. The main objective of gene alteration in this field is reprogramming cells to over-release GFs, migratory and adhesive molecules as well as inhibiting undesired or negative effect-related genes (217).

In what concerns the molecular biology tools used to genetically modify cells, Herpes and recombinant virus are the typical used vectors in TE, as they are associated to high yields. However, it has been recently discovered that AAV-PHP.eB and AAV-PHP.S derived from adeno-associated viruses are efficient capsids capable of transduction of the PNS cells with better outcome than traditional viruses (218). One basic purpose of genetically modification of Schwann cells is for them to produce green fluorescent protein (EGFP), in order to follow their fate and track their role in nerve repair and myelination. Many studies use this methodology (219-221). With the intuit of overexpressing a specific GF, Timmer *et al.*(222) implanted a silicon tube filled with Matrigel with enclosed transfected Schwann cells to overexpress fibroblast growth factor (FGF-2). The transfected cell group showed a significant intensification in the number of myelinated axons as compared to the control group. To surpass the “candy store effect,” Marquardt *et al.* (223), used Schwann cells that were previously transduced with a tetracycline-inducible GDNF expressing lentiviral vector. Consequently, it allowed the expression of GDNF to be temporally controlled by doxycycline administration. Their hypothesis was correct, since the results demonstrated that the use of modified Schwann cells increased axonal regeneration and muscle mass recovery, whereas delivery for too short a time arrests extending axons, while prolonged expression entraps axons. In another study by De la Rosa *et al.* (224), MSCs were genetically modified to hyper-secrete various GFs, such as BDNF, GDNF and NGF. In this work, besides the genetic modification with lentiviral vectors, trans-differentiation of the same cells was carried out to obtain

Schwann cell-like cells. Also, within the PNS, the intracochlear infusion of GFs via mini-osmotic pump has been shown to prevent deafness-induced spiral ganglion neuron degeneration. However, it is associated with high incidence of infection within the cochlea, making this technique unsuitable for GF administration in a clinical setting. Therefore, Pettingill *et al.* (247) used gene-based therapy as an alternative. In this study the authors used Schwann cells genetically modified to over-express the BDNF or NT-3. The results suggest that that this therapy was useful in enhancing survival of spiral ganglion neurons.

However, in 2015, Huang *et al.* (248) made the incredible discovery that by genetically modifying Schwann cells to overexpress c-Jun, a component of the AP-1 transcription factor, it would effectively upregulate the expression and secretion of multiple GFs, including NGF, GDNF, BDNF, artemin and leukemia inhibitory factor. A single modification capable of altering the whole process of nerve regeneration and myelination is a potential therapy, that has shown outstanding results.

II-1.9.9. Cell-Carriers

Other than the cell types used, the manner they are incorporated in the NGCs is fundamental for their successful application. The most common approach to deliver cells within a NGC includes the presence of an hydrogel matrix in the lumen of the NGCs, acting as a support material for the transplanted cells (81, 249, 250). A study from 2004 focused on evaluating the effect of fibrin hydrogels for transplanted cells (251). Schwann cells were implanted into PCL NGCs as a non-structured cell suspension or embedded in a 3D matrix. The results revealed that the fibrin/Schwann cells matrix as luminal fillers enhanced the quantity and the quality of PNR through the PCL conduits. This was evident when compared to NGCs that did not have the 3D matrix in their lumen. This points to the fact that hydrogels for cellular encapsulation mimic the neural ECM composition, therefore enhancing cell survival and viability (252). Still, while the incorporation method facilitates the formation of high cell density within the scaffold, direct cell seeding method helps to minimize cell damage by means of avoiding possible harsh fabrication condition and chemical processes such as crosslinking. Furthermore, the 3D bioprinting technique is currently very popular, since it can incorporate and position cells in a specific manner within the scaffold and might therefore mimic the native structure of the damaged tissue. More specifically, 3D bioprinting represents the option of having a cell carrier

which precisely controls the spatiotemporal placement of cells. However, despite all the possible advantages, shear induced cell damage is a chief limitation of the technique (253).

II-1.10. Clinical trials in the scope of PNR

Millions of pre-clinical studies have been carried by the scientific community along the last decades and have proven the value of innovative therapies and discoveries in the case of PNR. The proof are the several hundreds of reports that have been published in the niche of this scientific area. In one hand, these do not correlate to the very scarce clinical trials associated to PNR, found in the platform ClinicalTrials.Gov. On the other hand, even though a few clinical trials have found and reported in this review (**Table II-3**), these clearly outnumber the strategies and policies currently available in the clinics for the patients. Such facts are a worrying reason, since no real effort seems to be being made to take the diverse explored alternatives to the actual patients in need. However, after a brief research in the ClinicalTrials.Gov platform, a few categories could easily be found related to strategies that are, or have been, tested in humans in attempts to treat PNIs. Electrical stimulation (ES) is the first category analyzed. It is not uncommon to find studies assessing the benefits of ES, since peripheral nerve tissue has been shown to accelerate axonal regeneration after ES in the case of an injury. Undoubtedly, PNS relies on electrical activity to carry its basic functions and pre-clinical studies have unquestionably shown its usefulness (254-256). In this scope, different tactics are being tested in humans, *e.g.* ES pre-operatively (NCT03205124), extra-corporal ES after nerve coaptation (NCT03147313) or immediately after surgery NCT02403661.

The second category analyzed focuses on testing TE NGCs made of different biomaterials and in different sized gaps. Collagen, in the form of a collagen wrap (NCT03875833) or the recently developed Neuramaix (NCT01884376) can be found within this category, as well as a novel silk fibroin NGC (NCT03673449). Furthermore, hydrophilic polymers such as polyethylene glycol have been tested as part of a combination therapy to assist in axonal fusion technique (NCT02359825). In terms of endogenous biomaterials, a clinical trial assessing if AxoGuard implant made of small intestine submucosa ECM decreases disabilities after neck dissections is also currently on going (NCT03941327). A novel synthetic polymer NGC under the name 'Polynerve' is also being tested in humans (NCT02970864). Polynerve comprises a co-polymer of PCL and PLA that has the form of a cylinder containing an internal lumen with detailed micro-grooved architecture.

This last feature also represents an improvement, since NGCs containing any kind of luminal features are rarely found in the phase of clinical trials.

Three clinical trials focusing on the use of allografts have also been found. The first represents a combination of strategies. It conjugates an allograft with a Bone Marrow Aspirate, as source of stem cells, to enhance regeneration (NCT03964129). The second clinical trial is focused on the general use of Avance Nerve Graft, intended to evaluate the general outcomes in a real-life clinical setting (NCT01526681). Using the same allograft, Avance Nerve Graft is being specifically tested in patients who underwent robotic assisted prostatectomy for treatment of prostate cancer (NCT00953277). The administration of drugs has been one of the most explored areas in terms of PNR clinical trials. Tesamorelin (NCT03150511), Nicotinamide Riboside (NCT03912220), Tacrolimus (NCT00950391), anti-inflammatory drug GW406381 (NCT00279032), Capsaicin Patch (NCT02228928), topical lidocaine (NCT01112748) and oxcarbazepine for the treatment of chronic pain (NCT01302275) are the adjuvant therapies that have been tested, attempting to reduce some of the symptoms related to PNR.

Regarding cell-therapy, there are numerous pre-clinical reports confirming that cell-based therapy is effective in the treatment of PNI and that it is a promising branch of the PNS regenerative medicine field (81, 257). Only one real study carried out in the scope of PNR could be found, in which autologous Schwann cells harvested from the sural nerve are transplanted along sural nerve autografts (NCT02510079). The other cell-based therapy studies that were found relate to the use of cells applied to CNS injuries. Briefly, autologous Schwann cells or autologous Bone Marrow Stromal Cells were injected in subjects with spinal cord injury (NCT01739023) and (NCT01909154), respectively.

Further high-quality research must be done in order to correctly transfer pre-clinical studies into clinical studies in humans, following their translation to the clinics. However, the fact that a variety of strategies mentioned along this review, *e.g.* luminal guidance structures or cell-based therapies has reached this level in the ladder of clinical acceptance is already thrilling. It means the whole field of PNR is slowly moving to alternatives beyond the hollow NGCs

Table II-2 - Cell-based therapies for PNR.

| Cell type | Defect size, location, animal model | Outcomes | Year, reference |
|---|---|---|-----------------|
| Schwann cells | 15 mm, sciatic nerve, rat | Schwann cells overexpressing FGF-2 in a chitosan conduit supported the early regenerative process; | 2016, (87) |
| | 5 mm, bilateral cavernous nerves, rat | Simple Schwann cells or GDNF-transduced Schwann cells grafts led to 75 % and 94 % success rate, respectively, compared to the 25 % of autografts; | 2016, (225) |
| | <i>In vitro</i> , micro-patterned surface fabricated by laser ablation with NGF | When co-culturing with Schwann cells, NSCs differentiated into neuronal cells with robust expression of β III tubulin and microtubule-associated protein-2; | 2017, (226) |
| | 5 mm, laryngeal nerve, rat | Laminin-chitosan-PLGA NGC combined with Schwann and NSC promoted significantly higher nerve regeneration when compared to acellular grafts; | 2018, (64) |
| | <i>In vitro</i> co-culture of Schwann cells and DRGs | Schwann cells in co-culture with DRGs promoted longer neurite extension and formation of myelin around DRG neurites; | 2018, (227) |
| Bone Marrow stem cells (BMSCs) | 20 mm autograft, sciatic nerve, rat | BMSCs can differentiate into Schwann cell-like phenotype and myelinate axons, also expressing neuronal markers such as GFAP and S100; | 2011, (228) |
| | 10 mm, sciatic nerve, rat | Tropomyosin receptor kinase A overexpression enhanced the efficacy of BMSCs on PNR and improved functional recover; | 2017, (229) |
| | Contusion injury of the spinal cord, rat | Intravenous delivered BMSCs exosomes tend to migrate into the injury site, where they exert their beneficial effects; | 2018, (230) |
| Undifferentiated adipose derived stem cells (ADSCs) | 10 mm, sciatic nerve, rat | Number and diameter of the myelinated fibers were significantly higher in the case of silicone NGC loaded with ADSCs; | 2009, (231) |
| | 6 mm, sciatic nerve, rat | Decreased muscular atrophy and enhanced PNR when PCL conduits were loaded with ADSCs; | 2013, (232) |
| | Blunted injury, sciatic nerve, mouse | Transplanted ADSCs did not differentiate into Schwann cells but promoted PNR, since they encouraged axon regeneration, formation of myelin and restoration of denervated muscle atrophy; | 2016, (233) |
| | 15 mm, sciatic nerve, rat | ADSCs injected directly in the muscles connected to the damaged nerve were found to have increased presence of IL -10 and Ki67, which helped in delaying the onset of muscular atrophy; | 2019, (234) |
| Differentiated adipose derived stem cells (ADSCs) | 10 mm, sciatic nerve, rat | Schwann cell-like differentiated ADSCs were found to express neurotrophic factors, namely NGF, BDNF, glial-GDNF, and NT4. The same study also reported an increase of anti-apoptotic m-RNA of Bcl-2 as well as a decrease of pro-apoptotic m-RNA Bax and caspase-3, which | 2011, (206) |

| | | | |
|---|---|--|-------------|
| | | lead to a neuroprotective state; | |
| Human umbilical-cord stem cells, (HUCMSCs) | 10 mm, sciatic nerve, rat | HUCMSCs increased the expression of neurotrophic and angiogenic factors, which led to a more favorable environment for nerve regeneration; | 2017, (235) |
| | 10 mm, sciatic nerve, rat | Wharton jelly-derived stem cells, in addition to an injection of dexamethasone resulted in advanced regeneration compared to the autograft; | 2018, (236) |
| Olfactory ensheathing cells, (OECs) | 8 mm, sciatic nerve, rat | PLLA NGC seeded with OEC encouraged nerve regeneration similarly to the autograft group; | 2015, (237) |
| | <i>In vitro</i> , to test how OECs promote neurite outgrowth of cortical neurons in an inhibitory scar-like culture model | It was found that OECs enhanced neurite elongation through direct contact and alignment of neuronal and OEC processes in scar-like cultures; | 2015, (238) |
| | 5 mm, facial nerve, rat | OECs transplanted within the NGC improved regeneration of transected facial nerve, with large numbers of myelinated nerve fibers, crude fibers, larger myelin thickness and volume in the transplanted graft; | 2018, (239) |
| Neural stem cells (NSCs) | Intra-orbital crush, optic nerve, mouse | Intravitreally grafted NSCs differentiated into astrocytes that survived in the host eyes, stably expressed CNTF and significantly attenuated the loss of the axotomized retinal ganglion. The CNTF-secreting NSCs also induced long-distance regrowth of the lesioned retinal ganglion axons; | 2014, (240) |
| | 3 mm, sciatic nerve, mouse | The addition of IL12p80 together with NSCs in NGCs improved motor function recovery, promoted nerve regeneration and increases the diameter of newly regenerated nerve up to 4.5 fold. | 2017, (241) |
| Skin-derived precursors (SKPs) | 10 mm, sciatic nerve, miniature pigs | SKPs transplantation showed better in vivo nerve regeneration potential than in the non-cell transplantation control group, with increasing expression of S100 and P75NGFR; | 2011, (242) |
| | Cutaneous nerve regeneration, 1 × 1.5 cm ² circular island of skin, mouse | SKPs were found to be neurotropic toward injured nerves. They had a full capacity to differentiate into Schwann cells and promote axon regeneration. SKPs revealed to be an active participant in cutaneous nerve homeostasis; | 2012, (243) |
| | 15 mm, sciatic nerve, rat | The addition of Schwann cell – like SKPs increased sciatic nerve functional index, peak amplitudes, nerve conduction velocities, number of myelinated fibers, and decreased muscle atrophy; | 2016, (244) |
| Genetically modified cells | 10 mm, sciatic nerve, rat | The transfected cells secreted GDNF at higher rate which enabled better survival of motor neurons when compared to controls. Furthermore, there was an enhanced expression of GDNF mRNA; | 2006, (245) |
| | 15 mm, sciatic nerve, rat | FGF-2 overexpressing Schwann cells were seeded in a chitosan film inside a chitosan conduit, which enhanced nerve regeneration; | 2016, (81) |
| | End-to-end suture, sciatic nerve, rat | GDNF-expressing ADSCs revealed a robust expression of GDNF throughout time, where regeneration of nerve was significantly improved as evidenced by enhanced functional recovery, | 2017, (159) |

| | | | |
|--|---------------------------|---|-------------|
| | | nerve reinnervation, Schwann cell migration and proliferation, axon regeneration, myelination and angiogenesis; | |
| | 10 mm, sciatic nerve, rat | KLF7-transfected Schwann cells enhanced motor and sensory axonal regeneration. Myelinated fibers were also significantly higher; | 2017, (246) |

Table II-3 - Clinical trials in the scope of PNR being carried in different countries and with different strategies.

| Strategy or technology used | Name of the clinical trial study | ClinicalTrials.gov Identifier | Sponsors and Locations | Specifics of the study |
|---|---|-------------------------------|---|--|
| Electrical stimulation | The Effect of Pre-operative Electrical Stimulation on Peripheral Nerve Regeneration | NCT03205124 | University of Alberta | Patients randomized to this group will receive 1 hour of continuous electrical stimulation three days prior to scheduled surgical date; |
| | Electrical Stimulation to Enhance Peripheral Nerve Regeneration | NCT02403661 | University of Alberta | The goal is to test the possible benefit of electrical stimulation of the injured nerve following surgery; |
| | Extra-corporal Shock Wave Treatment to Improve Nerve Regeneration | NCT03147313 | Meidling Trauma Hospital, Lorenz Böhler Trauma Hospital | This study evaluates the impact of extracorporeal shock wave treatment after microsurgical coaptation of finger nerves; |
| TE NGC or other biomaterial approaches | Mid-term Effect Observation of Biodegradable Conduit Small Gap Tubulization Repairing Peripheral Nerve Injury | NCT03359330 | Peking University People's Hospital | The biodegradable conduit small gap tubulization are used to repair the nerve. Their nerve functional recovery conditions are clinically observed according to the standard score methods; |
| | Prospective Analysis of Effect of Collagen Wrap Conduit on Radial and Ulnar Nerve Function Following Radial/Ulnar Forearm Free Flap Harvest | NCT03875833 | The University of Texas Health Science Center | Determination whether collagen nerve conduits placed on exposed radial and ulnar nerves during radial and ulnar forearm free flap harvests will reduce the occurrence and degree of sensory nerve deficit; |
| | Evaluate the Reconstruction of Digital Nerve Defects in Humans Using an Implanted Silk Nerve Guide | NCT03673449 | UniversitätsSpital Zürich, Recruiting, Zürich | Ascertain the feasibility and safety of the procedure using SilkBridge - a biocompatible silk fibroin-based scaffold - for the regeneration of sensory nerve fibres and follow it up together with the reinnervation of the target organs; |
| | Clinical Study for the Treatment of Peripheral Nerve Defects with Neuromaix (PeRepair) | NCT01884376 | RWTH Aachen University | The aim of this study is the development and initial clinical application of the nerve guide Neuromaix in humans to provide evidence for the safety and performance of the device; |

| | | | | |
|-------------------|--|-------------|---|--|
| | A Phase I Trial of a Novel Synthetic Polymer Nerve Conduit 'Polynerve' in Participants with Sensory Digital Nerve Injury (UMANC) | NCT02970864 | University of Manchester | Participants found to have a nerve gap of at least 5 mm and no greater than 20mm will undergo repair with the Polynerve. Participants will be followed up regularly, observed for device-related complications and to assess the return of sensory innervation; |
| | Preliminary Evaluation of the Clinical Safety and Effectiveness of the Bionic Nerve Scaffold | NCT03780855 | Xijing Hospital | The objective of the study is to preliminarily evaluate the clinical safety and effectiveness of the bionic nerve scaffold with longitudinally oriented microchannels; |
| | Performance Study of an Artificial Nerve Guide (Reaxon® Nerve Guide) to Treat Digital Nerve Lesions | NCT02459015 | Medovent GmbH, Several hospitals in Germany | The purpose of this clinical investigation is to confirm the medium- and long-term safety and performance of the chitosan-based nerve guide (Reaxon® Nerve Guide) in comparison to an autologous nerve graft to bridge nerve defects in the finger; |
| | Chitosan Nerv Tube for Primary Repair of Traumatic Sensory Nerve Lesions of the Hand (CNT) | NCT02372669 | BG Unfallklinik, Several hospitals in Germany | The objective of this study is to evaluate whether the additional use of a nerve tube in primary microsurgical repair of traumatic sensory nerve lesions of the hand has an effect on convalescence and functional results; |
| | Nerve Repair Using Hydrophilic Polymers to Promote Immediate Fusion of Severed Axons and Swift Return of Function | NCT02359825 | Vanderbilt University, Vanderbilt University Medical Center | The investigators propose testing the efficacy and safety of a combination therapy: polyethylene glycol (PEG) assisted axonal fusion technique to repair peripheral nerve injuries in humans; |
| | Do AxoGuard Implants Decrease Shoulder Disability After Neck Dissections? | NCT03941327 | University of Mississippi Medical Center | A porcine collagen implant will be used to make a protective sheath around the participant's exposed spinal accessory nerve during surgery. This will be performed by physically wrapping the exposed nerve with the implant and suturing the ends together; |
| Allografts | Bone Marrow Aspirate Concentrate (BMAC) Nerve Allograft Study | NCT03964129 | Brooke Army Medical Center | This study is a prospective, multi-center, proof of principle, phase I human safety study evaluating the sequential treatments of the Avance Nerve Graft, a commercially available decellularized processed peripheral nerve allograft, with autologous Bone Marrow Aspirate Concentrate (BMAC), a source of stem cells; |
| | A Comparative Post-Marketing Study of Commercially Available Peripheral Nerve Gap Repair Options (CHANGE) | NCT00948025 | Axogen Corporation, Several locations across the USA | This study is a comparison of sensory recovery outcomes from the use of AVANCE and hollow tube conduits for peripheral nerve gap repairs in the hand; |

| | | | | |
|--------------------------------|--|-------------|---|---|
| | Study of Nerve Reconstruction Using AVANCE in Subjects Who Undergo Robotic Assisted Prostatectomy for Treatment of Prostate Cancer | NCT00953277 | Axogen Corporation, Vanderbilt University | The purpose of this study is to determine if it is technically feasible to repair nerves that are injured as part of a planned surgical removal of the prostate and the surrounding tissue in subjects with prostate cancer; |
| Other grafts | Muscle-in-vein Conduits for Digital Nerve Reconstruction | NCT01958632 | BG Trauma Center Tuebingen | The actual study should provide a first direct comparison between results after reconstruction of sensory nerves of the hand using muscle-in-vein conduits to the standard methods of nerve transplantation and direct nerve suture; |
| Administration of drugs | Safety and Efficacy Study of Neovasculgen (PI-VEGF165) in Patients with Peripheral Nerve Injury | NCT02352649 | Human Stem Cell Institute, Russia | The purpose of this study is to determine safety and efficacy of Neovasculgen for regeneration of peripheral nerve. Neovasculgen is the permitted in Russian Federation angiogenic medication that induce growth of new vessels and included in a complex therapy for patients with peripheral arterial diseases in Russia; |
| | Tesamorelin to Improve Functional Outcomes After Peripheral Nerve Injury | NCT03150511 | Johns Hopkins University | The aim of this clinical trial is to assess the efficacy of tesamorelin as a therapy for peripheral nerve injuries. The investigators hypothesize that treatment with tesamorelin will allow for faster and greater recovery of motor and sensory function following surgical repair of injured peripheral nerves; |
| | Evaluation of Nicotinamide Riboside in Prevention of Small Fiber Axon Degeneration and Promotion of Nerve Regeneration | NCT03912220 | Johns Hopkins University | This study will evaluate the effects of a nutritional supplement called nicotinamide riboside in preventing small fiber nerve degeneration that is experimentally induced by applying capsaicin to skin in otherwise healthy study participants; |
| | Enhancement of Functional Recovery After Peripheral Nerve Injury with Tacrolimus | NCT00950391 | Washington University School of Medicine | The objective of this study is to explore the ability of tacrolimus to benefit the treatment of patients with peripheral nerve injury; |
| | GW406381 In Patients with Peripheral Nerve Injury | NCT00279032 | GlaxoSmithKline, United Kingdom | The findings from preclinical animal models confirm the peripheral anti-inflammatory/analgesic activity of GW406381 and also suggest contribution of a central site of action to the anti-hyperalgesic efficacy that may not be shared by other COX-2 inhibitors; |
| | Study of Capsaicin Patch for the Management of Peripheral Neuropathic Pain | NCT02228928 | Samyang Biopharmaceuticals Corporation | The goal is to test the efficacy and safety of the low concentration [0.65 % (50 µg/cm ²) and 1.25 % (100 µg/cm ²)] capsaicin patches and compared them to conventional 0.075 % capsaicin cream and placebo patch in patients suffering from peripheral |

| | | | | |
|-----------------------------|---|-------------|---|---|
| | | | | neuropathy; |
| | Topical Lidocaine: Predictors of Response in Peripheral Nerve Injury | NCT01112748 | Danish Pain Research Center | The primary purpose is to study the predictive value of preserved nociceptors and large afferent fibers and dynamic mechanical allodynia on the effect of lidocaine patch; |
| | Oxcarbazepine for the Treatment of Chronic Peripheral Neuropathic Pain (IMIOXC) | NCT01302275 | Danish Pain Research Center and Innovative Medicines Initiative | The purpose of this trial is to determine if the effect of oxcarbazepine on chronic peripheral nerve pain depends on the supposed mechanism of the pain, ie. if oxcarbazepine mainly relieve pain in patients with irritable nerves; |
| Cell-based therapies | Emergent Expanded Access for autologous Human Schwann cells Augmentation of Nerve Autografts After Severe Peripheral Nerve Injury | NCT02510079 | University of Miami | Schwann cells harvested from the sural nerve will be autologously transplanted along sural nerve autografts wrapped in a collagen matrix (Duragen); |
| | Safety of Autologous Human Schwann Cells (ahSC) in Subjects with Subacute SCI | NCT01739023 | The Miami Project to Cure Paralysis, University of Miami | For humans with subacute SCI, we hypothesize that axons might show improved function if myelin repair is induced with the implantation of ahSC; |
| | Safety Study of Local Administration of Autologous Bone Marrow Stromal Cells in Chronic Paraplegia (CME-LEM1) | NCT01909154 | Puerta de Hierro University Hospital | Follow-up of a cohort of patients with chronic spinal cord injury (SCI) who were treated with autologous stromal cells of the bone marrow administrated locally (subarachnoid and intramedullar) by intrathecal microinjection and three months later, by lumbar subarachnoid administration; |

II-2. CONCLUSIONS

PNIs are permanently accompanied by high costs, translated to economical loss in the health care systems. In addition, there is the morbidity and the significant decrease in patient's quality of life. Therefore, improvements in this field are imperative. There is an increasing agreement that further progress in the field of PNR is urgent, and that the success in the area will no longer be dependent on the new and sophisticated microsurgical tools and techniques or simple hollow NGCs. Instead, due to tremendous quality research recently published, the scientific community is realizing that the best way to move forward is with a multi-combinatorial approach, where different disciplines and specialists may reach a new level of innovation. As such, any approach to peripheral nerve regeneration must integrate a comprehensive and multifaceted strategy, mimicking the natural process of nerve injury and regeneration. *In vivo*, a cascade of events takes place where cellular components, growth factors, topographical and biological cues act together and naturally induce a certain degree of regeneration.

Therefore, developed NGCs, their inherent components and consequent activated mechanisms must enable and simplify the host regenerative process and stimulate regeneration, not only at the injury location, but also at both proximal and distal areas of the injury. Only a multi-factorial device will be capable of overcoming inherent obstacles to regeneration, such as denervation atrophy of muscle targets, lack of vascularization and excessive inflammation.

This report focused on reviewing the diverse approaches that can be used in order to go beyond an empty tubular NGCs, similar to those that have been classically used in the clinics. In one hand, it has been proven that to be successful in treating critical gaps (lengthier than 10 mm, in rat), luminal fillers must be added, to encourage the growth cone in its path-finding quest, to reach the distal target. These luminal fillers comprising 3D structures and fabricated in a variety of ways are absolutely needed in the case of more severe injuries. In this scope, the clinical translation of NeuraGen 3D Nerve Guide Matrix® represented a great step towards the change that needed to be seen in this context. Furthermore, the creation of a favorable milieu in the injury site, created with the exogenous delivery of different biological molecules such as neurotrophic factors, other GFs or the presence of pro-regenerative miRNAs, is fundamental for nerve regeneration. In this area, a wide range of factors and delivery strategies can be engineered, maintaining the principle of a timely fashion release.

Finally, tissue engineers have a panoply of cell-based therapies which can be adopted to amend clinical outcomes. Because of stem cells' potential, they have become a source of cells which act as an alternative to Schwann cells in PNR. Either differentiated or undifferentiated, the mechanisms by which they are valuable in the case of PNI were also explored. All of the above-mentioned features can and should be used to tackle the present hurdles of nerve regeneration. Such tools allow the medical community to perform a more precise work both at the diagnostic as well as in the treatment stages. Additionally, only by surpassing these obstacles and enhancing the velocity and quality of regeneration will allow a proper rehabilitation, where a motor and sensor recovery helps patients regain their quality of life.

Overall, it is crucial to understand that a full functional recovery of peripheral nerve injuries is vital for the patient, to improve its mental health, daily performance, morale, general mobility, agility and capability. All the aforementioned technologies, some of which can already be found in the stage of clinical trials, have the power to go beyond the empty NGCs in terms of positive outcomes. Therefore, they should be adopted and adapted to have a future in the clinical setting, so that patient could benefit from them.

II-3. ACKNOWLEDGMENTS

This work was supported by Cristiana Carvalho PhD scholarship (Norte-08-5369-FSE-000037). J. M. Oliveira also thanks the FCT for the funds provided under the program Investigador FCT 2015 (IF/01285/2015). The authors are also thankful to the FCT funded project NanoOptoNerv (ref. PTDC/NAN-MAT/29936/2017).

II-4. REFERENCES

1. Nawabi DH, Jayakumar P, Carlstedt T. Peripheral Nerve Surgery. *Annals of The Royal College of Surgeons of England*. 2006;88(3):327-8.
2. Rasulić L. Peripheral nerve surgery: the road less traveled. *Acta Neurochirurgica*. 2018;160(8):1587-9.
3. Wojtkiewicz DM, Saunders J, Domeshek L, Novak CB, Kaskutas V, Mackinnon SE. Social impact of peripheral nerve injuries. *Hand (N Y)*. 2015;10(2):161-7.
4. Seddon HJ. Peripheral Nerve Injuries. *Glasgow medical journal*. 1943;139(3):61-75.
5. SEDDON HJ. THREE TYPES OF NERVE INJURY. *Brain : a journal of neurology*. 1943;66(4):237-88.
6. Sunderland S. A classification of peripheral nerve injuries producing loss of function. *Brain : a journal of neurology*. 1951;74(4):491-516.

7. Chhabra A, Ahlawat S, Belzberg A, Andreseik G. Peripheral nerve injury grading simplified on MR neurography: As referenced to Seddon and Sunderland classifications. *The Indian journal of radiology & imaging.* 2014;24(3):217-24.
8. Rigoard P, Buffenoir K, Wager M, Bauche S, Giot JP, Robert R, et al. [Anatomy and physiology of the peripheral nerve]. *Neuro-Chirurgie.* 2009;55 Suppl 1:S3-12.
9. Hart AM, Terenghi G, Wiberg M. Neuronal death after peripheral nerve injury and experimental strategies for neuroprotection. *Neurol Res.* 2008;30(10):999-1011.
10. Tamaki T. Bridging long gap peripheral nerve injury using skeletal muscle-derived multipotent stem cells. *Neural regeneration research.* 2014;9(14):1333-6.
11. Rotshenker S. Wallerian degeneration: the innate-immune response to traumatic nerve injury. *Journal of neuroinflammation.* 2011;8:109-.
12. Deumens R, Bozkurt A, Meek MF, Marcus MA, Joosten EA, Weis J, et al. Repairing injured peripheral nerves: Bridging the gap. *Progress in neurobiology.* 2010;92(3):245-76.
13. Pesheva P, Nellen J, Biersack H-J, Probstmeier R. Galectin-3 is differentially expressed during peripheral nerve development: Dependence on the Schwann cell phenotype. *Neuroscience Research Communications.* 2002;30(2):71-82.
14. Griffin JW, Hogan MV, Chhabra AB, Deal DN. Peripheral nerve repair and reconstruction. *The Journal of bone and joint surgery American volume.* 2013;95(23):2144-51.
15. Jessen KR, Mirsky R, Lloyd AC. Schwann Cells: Development and Role in Nerve Repair. *Cold Spring Harbor perspectives in biology.* 7(7):a020487-a.
16. Navarro X, Vivo M, Valero-Cabre A. Neural plasticity after peripheral nerve injury and regeneration. *Progress in neurobiology.* 2007;82(4):163-201.
17. Taylor KS, Anastakis DJ, Davis KD. Cutting your nerve changes your brain. *Brain : a journal of neurology.* 2009;132(Pt 11):3122-33.
18. Wall JT, Kaas JH, Sur M, Nelson RJ, Felleman DJ, Merzenich MM. Functional reorganization in somatosensory cortical areas 3b and 1 of adult monkeys after median nerve repair: possible relationships to sensory recovery in humans. *The Journal of neuroscience : the official journal of the Society for Neuroscience.* 1986;6(1):218-33.
19. Nordmark PF, Ljungberg C, Johansson RS. Structural changes in hand related cortical areas after median nerve injury and repair. *Scientific Reports.* 2018;8(1):4485.
20. Seil FJ. The changeable nervous system: studies on neuroplasticity in cerebellar cultures. *Neurosci Biobehav Rev.* 2014;45:212-32.
21. Makin TR, Bensmaia SJ. Stability of Sensory Topographies in Adult Cortex. *Trends Cogn Sci.* 2017;21(3):195-204.
22. Goswami R, Anastakis DJ, Katz J, Davis KD. A longitudinal study of pain, personality, and brain plasticity following peripheral nerve injury. *Pain.* 2016;157(3):729-39.
23. Chen R, Anastakis DJ, Haywood CT, Mikulis DJ, Manktelow RT. Plasticity of the human motor system following muscle reconstruction: a magnetic stimulation and functional magnetic resonance imaging study. *Clinical neurophysiology : official journal of the International Federation of Clinical Neurophysiology.* 2003;114(12):2434-46.
24. Rotshenker S. Wallerian degeneration: the innate-immune response to traumatic nerve injury. *J Neuroinflammation.* 2011;8:109.
25. Oberman L, Pascual-Leone A. Chapter 4 - Changes in Plasticity Across the Lifespan: Cause of Disease and Target for Intervention. In: Merzenich MM, Nahum M, Van Vleet TM, editors. *Progress in Brain Research.* 207: Elsevier; 2013. p. 91-120.
26. Zatorre RJ, Fields RD, Johansen-Berg H. Plasticity in gray and white: neuroimaging changes in brain structure during learning. *Nature Neuroscience.* 2012;15:528.
27. Fernandez-Munoz JJ, Palacios-Cena M, Cigaran-Mendez M, Ortega-Santiago R, de-la-Llave-Rincon AI, Salom-Moreno J, et al. Pain is Associated to Clinical, Psychological, Physical, and Neurophysiological Variables in Women With Carpal Tunnel Syndrome. *The Clinical journal of pain.* 2016;32(2):122-9.
28. Jensen TS, Finnerup NB. Allodynia and hyperalgesia in neuropathic pain: clinical manifestations and mechanisms. *The Lancet Neurology.* 2014;13(9):924-35.
29. Langer R, Vacanti JP. Tissue engineering. *Science.* 1993;260(5110):920.
30. Furth ME, Atala A, Van Dyke ME. Smart biomaterials design for tissue engineering and regenerative medicine. *Biomaterials.* 2007;28(34):5068-73.
31. Vinatier C, Mrugala D, Jorgensen C, Guicheux J, Noel D. Cartilage engineering: a crucial combination of cells, biomaterials and biofactors. *Trends in biotechnology.* 2009;27(5):307-14.

32. Furth ME, Atala A, Van Dyke ME. Smart biomaterials design for tissue engineering and regenerative medicine. *Biomaterials*. 2007;28(34):5068-73.
33. Bonani W, Singhatanadgige W, Pornanong A, Motta A. Natural Origin Materials for Osteochondral Tissue Engineering. *Advances in experimental medicine and biology*. 2018;1058:3-30.
34. Bajada S, Mazakova I, Richardson JB, Ashammakhi N. Updates on stem cells and their applications in regenerative medicine. *Journal of Tissue Engineering and Regenerative Medicine*. 2008;2(4):169-83.
35. Chen F-M, Zhang M, Wu Z-F. Toward delivery of multiple growth factors in tissue engineering. *Biomaterials*. 2010;31(24):6279-308.
36. Ramburrun P, Kumar P, Choonara YE, Bijukumar D, du Toit LC, Pillay V. A review of bioactive release from nerve conduits as a neurotherapeutic strategy for neuronal growth in peripheral nerve injury. *Biomed Res Int*. 2014;2014:132350-.
37. Lackington WA, Kočí Z, Alekseeva T, Hibbitts AJ, Kneafsey SL, Chen G, et al. Controlling the dose-dependent, synergistic and temporal effects of NGF and GDNF by encapsulation in PLGA microparticles for use in nerve guidance conduits for the repair of large peripheral nerve defects. *Journal of Controlled Release*. 2019;304:51-64.
38. Moore AM, MacEwan M, Santosa KB, Chenard KE, Ray WZ, Hunter DA, et al. Acellular nerve allografts in peripheral nerve regeneration: a comparative study. *Muscle Nerve*. 2011;44(2):221-34.
39. Hu Y, Wu Y, Gou Z, Tao J, Zhang J, Liu Q, et al. 3D-engineering of Cellularized Conduits for Peripheral Nerve Regeneration. *Sci Rep*. 2016;6:32184.
40. Atala A. Tissue engineering and regenerative medicine: concepts for clinical application. *Rejuvenation research*. 2004;7(1):15-31.
41. Shimomura K, Ando W, Fujie H, Hart DA, Yoshikawa H, Nakamura N. Scaffold-free tissue engineering for injured joint surface restoration. *Journal of experimental orthopaedics*. 2018;5(1):2-.
42. Roseti L, Parisi V, Petretta M, Cavallo C, Desando G, Bartolotti I, et al. Scaffolds for Bone Tissue Engineering: State of the art and new perspectives. *Materials Science and Engineering: C*. 2017;78:1246-62.
43. Liu Y, Zhou G, Cao Y. Recent Progress in Cartilage Tissue Engineering—Our Experience and Future Directions. *Engineering*. 2017;3(1):28-35.
44. González-Quevedo D, Martínez-Medina I, Campos A, Campos F, Carriel V. Tissue engineering strategies for the treatment of tendon injuries: a systematic review and meta-analysis of animal models. *Bone & joint research*. 2018;7(4):318-24.
45. Chaudhuri R, Ramachandran M, Moharil P, Harumalani M, Jaiswal AK. Biomaterials and cells for cardiac tissue engineering: Current choices. *Materials Science and Engineering: C*. 2017;79:950-7.
46. Rana TM. Illuminating the silence: understanding the structure and function of small RNAs. *Nature reviews Molecular cell biology*. 2007;8(1):23-36.
47. Sharif R, Priyadarsini S, Rowsey TG, Ma JX, Karamichos D. Corneal Tissue Engineering: An In Vitro Model of the Stromal-nerve Interactions of the Human Cornea. *Journal of visualized experiments : JoVE*. 2018(131).
48. Song HG, Rumma RT, Ozaki CK, Edelman ER, Chen CS. Vascular Tissue Engineering: Progress, Challenges, and Clinical Promise. *Cell stem cell*. 2018;22(3):340-54.
49. Tsintou M, Dalamagkas K, Seifalian AM. Advances in regenerative therapies for spinal cord injury: a biomaterials approach. *Neural regeneration research*. 2015;10(5):726-42.
50. Mobini S, Spearman BS, Lacko CS, Schmidt CE. Recent advances in strategies for peripheral nerve tissue engineering. *Current Opinion in Biomedical Engineering*. 2017;4:134-42.
51. Houschyar KS, Momeni A, Pyles MN, Cha JY, Maan ZN, Duscher D, et al. The Role of Current Techniques and Concepts in Peripheral Nerve Repair. *Plastic Surgery International*. 2016;2016:8.
52. Liao W-C, Chen J-R, Wang Y-J, Tseng G-F. The efficacy of end-to-end and end-to-side nerve repair (neurorrhaphy) in the rat brachial plexus. *J Anat*. 2009;215(5):506-21.
53. Geuna S, Papalia I, Ronchi G, d'Alcontres FS, Natsis K, Papadopoulos NA, et al. The reasons for end-to-side coaptation: how does lateral axon sprouting work? *Neural regeneration research*. 2017;12(4):529-33.
54. Koulaxouzidis G, Reim G, Witzel C. Fibrin glue repair leads to enhanced axonal elongation during early peripheral nerve regeneration in an in vivo mouse model. *Neural regeneration research*. 2015;10(7):1166-71.
55. Paprottka FJ, Wolf P, Harder Y, Kern Y, Paprottka PM, Machens H-G, et al. Sensory recovery outcome after digital nerve repair in relation to different reconstructive techniques: meta-analysis and systematic review. *Plastic surgery international*. 2013;2013:704589-.
56. Xie J, MacEwan MR, Liu W, Jesuraj N, Li X, Hunter D, et al. Nerve guidance conduits based on double-layered scaffolds of electrospun nanofibers for repairing the peripheral nervous system. *ACS Appl Mater Interfaces*. 2014;6(12):9472-80.

57. Lee SK, Wolfe SW. Peripheral nerve injury and repair. *The Journal of the American Academy of Orthopaedic Surgeons*. 2000;8(4):243-52.
58. Etra JW, Shores JT, Sander IB, Brandacher G, Lee WPA. Trauma-induced Rejection in Vascularized Composite Allotransplantation. *Annals of surgery*. 2019.
59. Brunelli GA, Vigasio A, Brunelli GR. Different conduits in peripheral nerve surgery. *Microsurgery*. 1994;15(3):176-8.
60. Williams DF. On the nature of biomaterials. *Biomaterials*. 2009;30(30):5897-909.
61. Subramanian A, Krishnan UM, Sethuraman S. Development of biomaterial scaffold for nerve tissue engineering: Biomaterial mediated neural regeneration. *Journal of biomedical science*. 2009;16(1):108-.
62. Kehoe S, Zhang XF, Boyd D. FDA approved guidance conduits and wraps for peripheral nerve injury: A review of materials and efficacy. *Injury*. 2012;43(5):553-72.
63. Xie F, Li QF, Gu B, Liu K, Shen GX. In vitro and in vivo evaluation of a biodegradable chitosan-PLA composite peripheral nerve guide conduit material. *Microsurgery*. 2008;28(6):471-9.
64. Li Y, Yu Z, Men Y, Chen X, Wang B. Laminin-chitosan-PLGA conduit co-transplanted with Schwann and neural stem cells to repair the injured recurrent laryngeal nerve. *Experimental and therapeutic medicine*. 2018;16(2):1250-8.
65. Jang CH, Lee H, Kim M, Kim G. Effect of polycaprolactone/collagen/hUCS microfiber nerve conduit on facial nerve regeneration. *International journal of biological macromolecules*. 2016;93(Pt B):1575-82.
66. Ozer H, Bozkurt H, Bozkurt G, Demirebilek M. Regenerative potential of chitosan-coated poly-3-hydroxybutyrate conduits seeded with mesenchymal stem cells in a rat sciatic nerve injury model. *The International journal of neuroscience*. 2018;128(9):828-34.
67. Agnew SP, Dumanian GA. Technical Use of Synthetic Conduits for Nerve Repair. *The Journal of Hand Surgery*. 2010;35(5):838-41.
68. Mano JF, Silva GA, Azevedo HS, Malafaya PB, Sousa RA, Silva SS, et al. Natural origin biodegradable systems in tissue engineering and regenerative medicine: present status and some moving trends. *J R Soc Interface*. 2007;4(17):999-1030.
69. Wang ZZ, Sakiyama-Elbert SE. Matrices, scaffolds & carriers for cell delivery in nerve regeneration. *Experimental Neurology*. 2018.
70. Deister C, Aljabari S, Schmidt CE. Effects of collagen 1, fibronectin, laminin and hyaluronic acid concentration in multi-component gels on neurite extension. *Journal of biomaterials science Polymer edition*. 2007;18(8):983-97.
71. FF IJ, Van De Graaf RC, Meek MF. The early history of tubulation in nerve repair. *The Journal of hand surgery, European volume*. 2008;33(5):581-6.
72. Lundborg G, Dahlin LB, Danielsen N, Gelberman RH, Longo FM, Powell HC, et al. Nerve regeneration in silicone chambers: influence of gap length and of distal stump components. *Exp Neurol*. 1982;76(2):361-75.
73. Williams LR, Longo FM, Powell HC, Lundborg G, Varon S. Spatial-temporal progress of peripheral nerve regeneration within a silicone chamber: parameters for a bioassay. *The Journal of comparative neurology*. 1983;218(4):460-70.
74. Shoichet MS, Midha R. Peripheral nerve regeneration through guidance tubes AU - Belkas, Jason S. *Neurological Research*. 2004;26(2):151-60.
75. Du J, Chen H, Qing L, Yang X, Jia X. Biomimetic neural scaffolds: a crucial step towards optimal peripheral nerve regeneration. *Biomater Sci*. 2018;6(6):1299-311.
76. Lee JY, Giusti G, Friedrich PF, Archibald SJ, Kemnitzer JE, Patel J, et al. The effect of collagen nerve conduits filled with collagen-glycosaminoglycan matrix on peripheral motor nerve regeneration in a rat model. *The Journal of bone and joint surgery American volume*. 2012;94(22):2084-91.
77. Sarker M, Naghieh S, McInnes AD, Schreyer DJ, Chen X. Strategic Design and Fabrication of Nerve Guidance Conduits for Peripheral Nerve Regeneration. *Biotechnology Journal*. 2018;13(7):1700635.
78. Mukhatyar VJ, Salmerón-Sánchez M, Rudra S, Mukhopadaya S, Barker TH, Garcia AJ, et al. Role of fibronectin in topographical guidance of neurite extension on electrospun fibers. *Biomaterials*. 2011;32(16):3958-68.
79. Hoffman-Kim D, Mitchel JA, Bellamkonda RV. Topography, cell response, and nerve regeneration. *Annual review of biomedical engineering*. 2010;12:203-31.
80. López-Cebral R, Silva-Correia J, Reis RL, Silva TH, Oliveira JM. Peripheral Nerve Injury: Current Challenges, Conventional Treatment Approaches, and New Trends in Biomaterials-Based Regenerative Strategies. *ACS Biomaterials Science & Engineering*. 2017;3(12):3098-122.
81. Meyer C, Wrobel S, Raimondo S, Rochkind S, Heimann C, Shahar A, et al. Peripheral Nerve Regeneration Through Hydrogel-Enriched Chitosan Conduits Containing Engineered Schwann Cells for Drug Delivery. *Cell transplantation*. 2016;25(1):159-82.

82. Lundborg G. A 25-year perspective of peripheral nerve surgery: evolving neuroscientific concepts and clinical significance. *The Journal of hand surgery*. 2000;25(3):391-414.
83. Thomson SE, Charalambous C, Smith CA, Tsimbouri PM, Dejardin T, Kingham PJ, et al. Microtopographical cues promote peripheral nerve regeneration via transient mTORC2 activation. *Acta biomaterialia*. 2017;60:220-31.
84. Chen MB, Zhang F, Lineaweaver WC. Luminal fillers in nerve conduits for peripheral nerve repair. *Annals of plastic surgery*. 2006;57(4):462-71.
85. Guo Q, Liu C, Hai B, Ma T, Zhang W, Tan J, et al. Chitosan conduits filled with simvastatin/Pluronic F-127 hydrogel promote peripheral nerve regeneration in rats. *Journal of biomedical materials research Part B, Applied biomaterials*. 2017.
86. Zor F, Devenci M, Kilic A, Ozdag MF, Kurt B, Sengezer M, et al. Effect of VEGF gene therapy and hyaluronic acid film sheath on peripheral nerve regeneration. *Microsurgery*. 2014;34(3):209-16.
87. Meyer C, Stenberg L, Gonzalez-Perez F, Wrobel S, Ronchi G, Udina E, et al. Chitosan-film enhanced chitosan nerve guides for long-distance regeneration of peripheral nerves. *Biomaterials*. 2016;76:33-51.
88. Belanger K, Schlatter G, Hébraud A, Marin F, Testelin S, Dakpé S, et al. A multi-layered nerve guidance conduit design adapted to facilitate surgical implantation. *Health science reports*. 2018;1(12):e86-e.
89. Knight E, Przyborski S. Advances in 3D cell culture technologies enabling tissue-like structures to be created in vitro. *J Anat*. 2015;227(6):746-56.
90. Carvalho CR, Costa JB, da Silva Morais A, Lopez-Cebral R, Silva-Correia J, Reis RL, et al. Tunable Enzymatically Cross-Linked Silk Fibroin Tubular Conduits for Guided Tissue Regeneration. *Advanced healthcare materials*. 2018;7(17):e1800186.
91. Liu X, Chen W, Gustafson CT, Miller AL, 2nd, Waletzki BE, Yaszemski MJ, et al. Tunable tissue scaffolds fabricated by in situ crosslink in phase separation system. *RSC advances*. 2015;5(122):100824-33.
92. Petcu EB, Midha R, McColl E, Popa-Wagner A, Chirila TV, Dalton PD. 3D printing strategies for peripheral nerve regeneration. *Biofabrication*. 2018;10(3):032001.
93. Perretta D, Green S. Bridging the Gap in Peripheral Nerve Repair. *Bulletin of the Hospital for Joint Disease (2013)*. 2017;75(1):57-63.
94. Noble J, Munro CA, Prasad VSSV, Midha R. Analysis of Upper and Lower Extremity Peripheral Nerve Injuries in a Population of Patients with Multiple Injuries. *Journal of Trauma and Acute Care Surgery*. 1998;45(1):116-22.
95. Bellamkonda RV. Peripheral nerve regeneration: An opinion on channels, scaffolds and anisotropy. *Biomaterials*. 2006;27(19):3515-8.
96. Huang Y-A, Ho CT, Lin Y-H, Lee C-J, Ho S-M, Li M-C, et al. Nanoimprinted Anisotropic Topography Preferentially Guides Axons and Enhances Nerve Regeneration. *Macromolecular Bioscience*. 2018;18(12):1800335.
97. Wu X, He L, Li W, Li H, Wong W-M, Ramakrishna S, et al. Functional self-assembling peptide nanofiber hydrogel for peripheral nerve regeneration. *Regenerative biomaterials*. 2017;4(1):21-30.
98. McGrath AM, Novikova LN, Novikov LN, Wiberg M. BD™ PuraMatrix™ peptide hydrogel seeded with Schwann cells for peripheral nerve regeneration. *Brain Research Bulletin*. 2010;83(5):207-13.
99. Du J, Liu J, Yao S, Mao H, Peng J, Sun X, et al. Prompt peripheral nerve regeneration induced by a hierarchically aligned fibrin nanofiber hydrogel. *Acta Biomaterialia*. 2017;55:296-309.
100. Pace LA, Plate JF, Mannava S, Barnwell JC, Koman LA, Li Z, et al. A human hair keratin hydrogel scaffold enhances median nerve regeneration in nonhuman primates: an electrophysiological and histological study. *Tissue engineering Part A*. 2014;20(3-4):507-17.
101. Carvalho CR, Wrobel S, Meyer C, Brandenberger C, Cengiz IF, Lopez-Cebral R, et al. Gellan Gum-based luminal fillers for peripheral nerve regeneration: an in vivo study in the rat sciatic nerve repair model. *Biomater Sci*. 2018;6(5):1059-75.
102. Scotti KL, Dunand DC. Freeze casting – A review of processing, microstructure and properties via the open data repository, FreezeCasting.net. *Progress in Materials Science*. 2018;94:243-305.
103. Singh A, Shiekh PA, Das M, Seppala J, Kumar A. Aligned Chitosan-Gelatin Cryogel-Filled Polyurethane Nerve Guidance Channel for Neural Tissue Engineering: Fabrication, Characterization, and In Vitro Evaluation. *Biomacromolecules*. 2018.
104. Huang L, Zhu L, Shi X, Xia B, Liu Z, Zhu S, et al. A compound scaffold with uniform longitudinally oriented guidance cues and a porous sheath promotes peripheral nerve regeneration in vivo. *Acta biomaterialia*. 2018;68:223-36.
105. Manoukian OS, Arul MR, Rudraiah S, Kalajic I, Kumbar SG. Aligned microchannel polymer-nanotube composites for peripheral nerve regeneration: Small molecule drug delivery. *Journal of Controlled Release*. 2019;296:54-67.

106. Liu S, Sun X, Wang T, Chen S, Zeng C-g, Xie G, et al. Nano-fibrous and ladder-like multi-channel nerve conduits: Degradation and modification by gelatin. *Materials Science and Engineering: C*. 2018;83:130-42.
107. Hu X, Huang J, Ye Z, Xia L, Li M, Lv B, et al. A novel scaffold with longitudinally oriented microchannels promotes peripheral nerve regeneration. *Tissue Eng Part A*. 2009;15(11):3297-308.
108. Frost HK, Andersson T, Johansson S, Englund-Johansson U, Ekström P, Dahlin LB, et al. Electrospun nerve guide conduits have the potential to bridge peripheral nerve injuries in vivo. *Scientific Reports*. 2018;8(1):16716.
109. Dinis TM, Elia R, Vidal G, Dermigny Q, Denoed C, Kaplan DL, et al. 3D multi-channel bi-functionalized silk electrospun conduits for peripheral nerve regeneration. *Journal of the Mechanical Behavior of Biomedical Materials*. 2015;41:43-55.
110. Matsumoto K, Ohnishi K, Kiyotani T, Sekine T, Ueda H, Nakamura T, et al. Peripheral nerve regeneration across an 80-mm gap bridged by a polyglycolic acid (PGA)-collagen tube filled with laminin-coated collagen fibers: a histological and electrophysiological evaluation of regenerated nerves. *Brain research*. 2000;868(2):315-28.
111. Quigley AF, Bulluss KJ, Kyrtzis IL, Gilmore K, Mysore T, Schirmer KS, et al. Engineering a multimodal nerve conduit for repair of injured peripheral nerve. *Journal of neural engineering*. 2013;10(1):016008.
112. Kim YT, Haftel VK, Kumar S, Bellamkonda RV. The role of aligned polymer fiber-based constructs in the bridging of long peripheral nerve gaps. *Biomaterials*. 2008;29(21):3117-27.
113. Yoshii S, Oka M. Collagen filaments as a scaffold for nerve regeneration. *Journal of biomedical materials research*. 2001;56(3):400-5.
114. Yoshii S, Oka M, Shima M, Taniguchi A, Akagi M. Bridging a 30-mm nerve defect using collagen filaments. *Journal of biomedical materials research Part A*. 2003;67(2):467-74.
115. Jiang X, Mi R, Hoke A, Chew SY. Nanofibrous nerve conduit-enhanced peripheral nerve regeneration. *Journal of Tissue Engineering and Regenerative Medicine*. 2014;8(5):377-85.
116. Jia Y, Yang W, Zhang K, Qiu S, Xu J, Wang C, et al. Nanofiber arrangement regulates peripheral nerve regeneration through differential modulation of macrophage phenotypes. *Acta Biomaterialia*. 2019;83:291-301.
117. Xie J, MacEwan MR, Liu W, Jesuraj N, Li X, Hunter D, et al. Nerve Guidance Conduits Based on Double-Layered Scaffolds of Electrospun Nanofibers for Repairing the Peripheral Nervous System. *ACS Applied Materials & Interfaces*. 2014;6(12):9472-80.
118. Ngo TT, Waggoner PJ, Romero AA, Nelson KD, Eberhart RC, Smith GM. Poly(L-Lactide) microfilaments enhance peripheral nerve regeneration across extended nerve lesions. *Journal of neuroscience research*. 2003;72(2):227-38.
119. Ceballos D, Navarro X, Dubey N, Wendelschafer-Crabb G, Kennedy WR, Tranquillo RT. Magnetically aligned collagen gel filling a collagen nerve guide improves peripheral nerve regeneration. *Experimental neurology*. 1999;158(2):290-300.
120. Rose JC, Cámara-Torres M, Rahimi K, Köhler J, Möller M, De Laporte L. Nerve Cells Decide to Orient inside an Injectable Hydrogel with Minimal Structural Guidance. *Nano Letters*. 2017;17(6):3782-91.
121. Phillips JB, Bunting SC, Hall SM, Brown RA. Neural tissue engineering: a self-organizing collagen guidance conduit. *Tissue engineering*. 2005;11(9-10):1611-7.
122. Huang C, Ouyang Y, Niu H, He N, Ke Q, Jin X, et al. Nerve guidance conduits from aligned nanofibers: improvement of nerve regeneration through longitudinal nanogrooves on a fiber surface. *ACS Appl Mater Interfaces*. 2015;7(13):7189-96.
123. Li G, Xue C, Wang H, Yang X, Zhao Y, Zhang L, et al. Spatially featured porous chitosan conduits with micropatterned inner wall and seamless sidewall for bridging peripheral nerve regeneration. *Carbohydrate Polymers*. 2018;194:225-35.
124. Davis B, Wojtalewicz S, Labroo P, Shea J, Sant H, Gale B, et al. Controlled release of FK506 from micropatterned PLGA films: potential for application in peripheral nerve repair. *Neural Regeneration Research*. 2018;13(7):1247-52.
125. Park SJ, Lee BK, Na MH, Kim DS. Melt-spun shaped fibers with enhanced surface effects: fiber fabrication, characterization and application to woven scaffolds. *Acta Biomater*. 2013;9(8):7719-26.
126. Mobasser A, Faroni A, Minogue BM, Downes S, Terenghi G, Reid AJ. Polymer scaffolds with preferential parallel grooves enhance nerve regeneration. *Tissue Eng Part A*. 2015;21(5-6):1152-62.
127. Saltzman EB, Villa JC, Doty SB, Feinberg JH, Lee SK, Wolfe SW. A Comparison Between Two Collagen Nerve Conduits and Nerve Autograft: A Rat Model of Motor Nerve Regeneration. *The Journal of hand surgery*. 2018.
128. Singh A, Shiekh PA, Das M, Seppala J, Kumar A. Aligned Chitosan-Gelatin Cryogel-Filled Polyurethane Nerve Guidance Channel for Neural Tissue Engineering: Fabrication, Characterization, and In Vitro Evaluation. *Biomacromolecules*. 2019;20(2):662-73.

129. Dinis TM, Elia R, Vidal G, Dermigny Q, Denoed C, Kaplan DL, et al. 3D multi-channel bi-functionalized silk electrospun conduits for peripheral nerve regeneration. *Journal of the mechanical behavior of biomedical materials*. 2015;41:43-55.
130. Rose JC, Camara-Torres M, Rahimi K, Kohler J, Moller M, De Laporte L. Nerve Cells Decide to Orient inside an Injectable Hydrogel with Minimal Structural Guidance. *Nano letters*. 2017;17(6):3782-91.
131. Huang YA, Ho CT, Lin YH, Lee CJ, Ho SM, Li MC, et al. Nanoimprinted Anisotropic Topography Preferentially Guides Axons and Enhances Nerve Regeneration. *Macromolecular bioscience*. 2018;18(12):e1800335.
132. Tajdaran K, Chan K, Gordon T, Borschel GH. Matrices, scaffolds, and carriers for protein and molecule delivery in peripheral nerve regeneration. *Experimental Neurology*. 2018.
133. Pfister LA, Papaloizos M, Merkle HP, Gander B. Nerve conduits and growth factor delivery in peripheral nerve repair. *Journal of the Peripheral Nervous System*. 2007;12(2):65-82.
134. Madduri S, Feldman K, Tervoort T, Papaloizos M, Gander B. Collagen nerve conduits releasing the neurotrophic factors GDNF and NGF. *Journal of controlled release : official journal of the Controlled Release Society*. 2010;143(2):168-74.
135. Pfister LA, Papaloizos M, Merkle HP, Gander B. Nerve conduits and growth factor delivery in peripheral nerve repair. *Journal of the peripheral nervous system : JPNS*. 2007;12(2):65-82.
136. Madduri S, di Summa P, Papaloizos M, Kalbermatten D, Gander B. Effect of controlled co-delivery of synergistic neurotrophic factors on early nerve regeneration in rats. *Biomaterials*. 2010;31(32):8402-9.
137. Aebischer P, Salessiotis AN, Winn SR. Basic fibroblast growth factor released from synthetic guidance channels facilitates peripheral nerve regeneration across long nerve gaps. *Journal of neuroscience research*. 1989;23(3):282-9.
138. Giannaccini M, Calatayud MP, Poggetti A, Corbianco S, Novelli M, Paoli M, et al. Magnetic Nanoparticles for Efficient Delivery of Growth Factors: Stimulation of Peripheral Nerve Regeneration. *Advanced healthcare materials*. 2017;6(7).
139. Deister C, Schmidt CE. Optimizing neurotrophic factor combinations for neurite outgrowth. *Journal of neural engineering*. 2006;3(2):172-9.
140. Peleshok J, Saragovi HU. Functional mimetics of neurotrophins and their receptors. *Biochemical Society transactions*. 2006;34(Pt 4):612-7.
141. Rickert U, Grampp S, Wilms H, Spreu J, Knerlich-Lukoschus F, Held-Feindt J, et al. Glial Cell Line-Derived Neurotrophic Factor Family Members Reduce Microglial Activation via Inhibiting p38MAPKs-Mediated Inflammatory Responses. *Journal of neurodegenerative diseases*. 2014;2014:369468.
142. Boyd JG, Gordon T. Neurotrophic factors and their receptors in axonal regeneration and functional recovery after peripheral nerve injury. *Molecular Neurobiology*. 2003;27(3):277-323.
143. Hausott B, Klimaschewski L. Membrane turnover and receptor trafficking in regenerating axons. *The European journal of neuroscience*. 2016;43(3):309-17.
144. Shakhbazou A, Kawasoe J, Hoyng SA, Kumar R, van Minnen J, Verhaagen J, et al. Early regenerative effects of NGF-transduced Schwann cells in peripheral nerve repair. *Molecular and Cellular Neuroscience*. 2012;50(1):103-12.
145. Xia B, Lv Y. Dual-delivery of VEGF and NGF by emulsion electrospun nanofibrous scaffold for peripheral nerve regeneration. *Materials Science and Engineering: C*. 2018;82:253-64.
146. Minnone G, De Benedetti F, Bracci-Laudiero L. NGF and Its Receptors in the Regulation of Inflammatory Response. *International journal of molecular sciences*. 2017;18(5):1028.
147. Mamet J, Lazdunski M, Voilley N. How nerve growth factor drives physiological and inflammatory expressions of acid-sensing ion channel 3 in sensory neurons. *The Journal of biological chemistry*. 2003;278(49):48907-13.
148. Gould HJ, 3rd, Gould TN, England JD, Paul D, Liu ZP, Levinson SR. A possible role for nerve growth factor in the augmentation of sodium channels in models of chronic pain. *Brain research*. 2000;854(1-2):19-29.
149. Verderio C, Bianco F, Blanchard MP, Bergami M, Canossa M, Scarfone E, et al. Cross talk between vestibular neurons and Schwann cells mediates BDNF release and neuronal regeneration. *Brain cell biology*. 2006;35(2-3):187-201.
150. Lin G, Zhang H, Sun F, Lu Z, Reed-Maldonado A, Lee Y-C, et al. Brain-derived neurotrophic factor promotes nerve regeneration by activating the JAK/STAT pathway in Schwann cells. *Translational andrology and urology*. 2016;5(2):167-75.
151. Vögelin E, Baker JM, Gates J, Dixit V, Constantinescu MA, Jones NF. Effects of local continuous release of brain derived neurotrophic factor (BDNF) on peripheral nerve regeneration in a rat model. *Experimental neurology*. 2006;199(2):348-53.

152. Maisonpierre PC, Belluscio L, Squinto S, Ip NY, Furth ME, Lindsay RM, et al. Neurotrophin-3: a neurotrophic factor related to NGF and BDNF. *Science*. 1990;247(4949 Pt 1):1446-51.
153. Sterne GD, Coulton GR, Brown RA, Green CJ, Terenghi G. Neurotrophin-3-enhanced nerve regeneration selectively improves recovery of muscle fibers expressing myosin heavy chains 2b. *The Journal of cell biology*. 1997;139(3):709-15.
154. Sahenk Z, Galloway G, Clark KR, Malik V, Rodino-Klapac LR, Kaspar BK, et al. AAV1.NT-3 gene therapy for charcot-marie-tooth neuropathy. *Molecular therapy : the journal of the American Society of Gene Therapy*. 2014;22(3):511-21.
155. Cheng S, Tereshchenko J, Zimmer V, Vachey G, Pythoud C, Rey M, et al. Therapeutic efficacy of regulable GDNF expression for Huntington's and Parkinson's disease by a high-induction, background-free "GeneSwitch" vector. *Experimental neurology*. 2018;309:79-90.
156. Ding Z, Xu W, Zhang J, Zou W, Guo Q, Huang C, et al. Normalizing GDNF expression in the spinal cord alleviates cutaneous hyperalgesia but not ongoing pain in a rat model of bone cancer pain. *International journal of cancer*. 2017;140(2):411-22.
157. Höke A. Augmenting glial cell-line derived neurotrophic factor signaling to treat painful neuropathies. *Proceedings of the National Academy of Sciences of the United States of America*. 2014;111(6):2060-1.
158. Shakhbazov A, Mohanty C, Shcharbin D, Bryszewska M, Caminade A-M, Majoral J-P, et al. Doxycycline-regulated GDNF expression promotes axonal regeneration and functional recovery in transected peripheral nerve. *Journal of Controlled Release*. 2013;172(3):841-51.
159. Hsu M-N, Liao H-T, Li K-C, Chen H-H, Yen T-C, Makarevich P, et al. Adipose-derived stem cell sheets functionalized by hybrid baculovirus for prolonged GDNF expression and improved nerve regeneration. *Biomaterials*. 2017;140:189-200.
160. Tang S, Zhu J, Xu Y, Xiang AP, Jiang MH, Quan D. The effects of gradients of nerve growth factor immobilized PCLA scaffolds on neurite outgrowth in vitro and peripheral nerve regeneration in rats. *Biomaterials*. 2013;34(29):7086-96.
161. Mai J, Fok L, Gao H, Zhang X, Poo M-m. Axon Initiation and Growth Cone Turning on Bound Protein Gradients. *The Journal of Neuroscience*. 2009;29(23):7450-8.
162. Mortimer D, Fothergill T, Pujic Z, Richards LJ, Goodhill GJ. Growth cone chemotaxis. *Trends in Neurosciences*. 2008;31(2):90-8.
163. Yu LMY, Miller FD, Shoichet MS. The use of immobilized neurotrophins to support neuron survival and guide nerve fiber growth in compartmentalized chambers. *Biomaterials*. 2010;31(27):6987-99.
164. Lin YC, Ramadan M, Hronik-Tupaj M, Kaplan DL, Philips BJ, Sivak W, et al. Spatially controlled delivery of neurotrophic factors in silk fibroin-based nerve conduits for peripheral nerve repair. *Annals of plastic surgery*. 2011;67(2):147-55.
165. Moore K, MacSween M, Shoichet M. Immobilized concentration gradients of neurotrophic factors guide neurite outgrowth of primary neurons in macroporous scaffolds. *Tissue engineering*. 2006;12(2):267-78.
166. Sun AX, Prest TA, Fowler JR, Brick RM, Gloss KM, Li X, et al. Conduits harnessing spatially controlled cell-secreted neurotrophic factors improve peripheral nerve regeneration. *Biomaterials*. 2019;203:86-95.
167. Chang YC, Chen MH, Liao SY, Wu HC, Kuan CH, Sun JS, et al. Multichanneled Nerve Guidance Conduit with Spatial Gradients of Neurotrophic Factors and Oriented Nanotopography for Repairing the Peripheral Nervous System. *ACS Appl Mater Interfaces*. 2017;9(43):37623-36.
168. Andreone BJ, Lacoste B, Gu C. Neuronal and vascular interactions. *Annu Rev Neurosci*. 2015;38:25-46.
169. Sondell M, Sundler F, Kanje M. Vascular endothelial growth factor is a neurotrophic factor which stimulates axonal outgrowth through the flk-1 receptor. *The European journal of neuroscience*. 2000;12(12):4243-54.
170. Hobson MI, Green CJ, Terenghi G. VEGF enhances intraneural angiogenesis and improves nerve regeneration after axotomy. *Journal of anatomy*. 2000;197 Pt 4(Pt 4):591-605.
171. Mohammadi R, Ahsan S, Masoumi M, Amini K. Vascular endothelial growth factor promotes peripheral nerve regeneration after sciatic nerve transection in rat. *Chinese Journal of Traumatology*. 2013;16(6):323-9.
172. Muratori L, Gnani S, Fregnan F, Mancardi A, Raimondo S, Perroteau I, et al. Evaluation of Vascular Endothelial Growth Factor (VEGF) and Its Family Member Expression After Peripheral Nerve Regeneration and Denervation. *The Anatomical Record*. 2018;301(10):1646-56.
173. Guaiquil VH, Pan Z, Karagianni N, Fukuoka S, Alegre G, Rosenblatt MI. VEGF-B selectively regenerates injured peripheral neurons and restores sensory and trophic functions. *Proceedings of the National Academy of Sciences of the United States of America*. 2014;111(48):17272-7.
174. Calvo PM, de la Cruz RR, Pastor AM. Synaptic loss and firing alterations in Axotomized Motoneurons are restored by vascular endothelial growth factor (VEGF) and VEGF-B. *Experimental neurology*. 2018;304:67-81.

175. Ko KR, Lee J, Lee D, Nho B, Kim S. Hepatocyte Growth Factor (HGF) Promotes Peripheral Nerve Regeneration by Activating Repair Schwann Cells. *Scientific Reports*. 2018;8(1):8316.
176. Nakamura T, Mizuno S. The discovery of Hepatocyte Growth Factor (HGF) and its significance for cell biology, life sciences and clinical medicine. *Proceedings of the Japan Academy, Series B*. 2010;86(6):588-610.
177. Boldyreva M A, Bondar IV, Stafeev IS, Makarevich PI, Beloglazova IB, Zubkova ES, et al. Plasmid-based gene therapy with hepatocyte growth factor stimulates peripheral nerve regeneration after traumatic injury. *Biomedicine & Pharmacotherapy*. 2018;101:682-90.
178. Imamura R, Matsumoto K. Hepatocyte growth factor in physiology and infectious diseases. *Cytokine*. 2017;98:97-106.
179. Bartel DP. MicroRNAs: target recognition and regulatory functions. *Cell*. 2009;136(2):215-33.
180. Li S, Liu Q, Wang Y, Gu Y, Liu D, Wang C, et al. Differential gene expression profiling and biological process analysis in proximal nerve segments after sciatic nerve transection. *PLoS one*. 2013;8(2):e57000.
181. Eacker SM, Dawson TM, Dawson VL. Understanding microRNAs in neurodegeneration. *Nature reviews Neuroscience*. 2009;10(12):837-41.
182. Bremer J, O'Connor T, Tiberi C, Rehrauer H, Weis J, Aguzzi A. Ablation of Dicer from murine Schwann cells increases their proliferation while blocking myelination. *PLoS one*. 2010;5(8):e12450.
183. Gokey NG, Srinivasan R, Lopez-Anido C, Krueger C, Svaren J. Developmental regulation of microRNA expression in Schwann cells. *Molecular and cellular biology*. 2012;32(2):558-68.
184. Li S, Wang X, Gu Y, Chen C, Wang Y, Liu J, et al. Let-7 microRNAs regenerate peripheral nerve regeneration by targeting nerve growth factor. *Mol Ther*. 2015;23(3):423-33.
185. Gökbuğet D, Pereira JA, Bachofner S, Marchais A, Ciaudo C, Stoffel M, et al. The Lin28/let-7 axis is critical for myelination in the peripheral nervous system. *Nature Communications*. 2015;6:8584.
186. Strickland IT, Richards L, Holmes FE, Wynick D, Uney JB, Wong LF. Axotomy-induced miR-21 promotes axon growth in adult dorsal root ganglion neurons. *PLoS one*. 2011;6(8):e23423.
187. Zhang HY, Zheng SJ, Zhao JH, Zhao W, Zheng LF, Zhao D, et al. MicroRNAs 144, 145, and 214 are down-regulated in primary neurons responding to sciatic nerve transection. *Brain research*. 2011;1383:62-70.
188. Yousefi F, Lavi Arab F, Nikkha K, Amiri H, Mahmoudi M. Novel approaches using mesenchymal stem cells for curing peripheral nerve injuries. *Life Sciences*. 2019;221:99-108.
189. Evans GR, Brandt K, Katz S, Chauvin P, Otto L, Bogle M, et al. Bioactive poly(L-lactic acid) conduits seeded with Schwann cells for peripheral nerve regeneration. *Biomaterials*. 2002;23(3):841-8.
190. Jesuraj N, B Santosa K, Newton P, Liu Z, Hunter D, E Mackinnon S, et al. A Systematic Evaluation of Schwann Cell Injection into Acellular Cold-Preserved Nerve Grafts 2011. 209-15 p.
191. Cerqueira SR, Lee Y-S, Cornelison RC, Mertz MW, Wachs RA, Schmidt CE, et al. Decellularized peripheral nerve supports Schwann cell transplants and axon growth following spinal cord injury. *Biomaterials*. 2018;177:176-85.
192. Kalbermatten DF, Kingham PJ, Mahay D, Mantovani C, Pettersson J, Raffoul W, et al. Fibrin matrix for suspension of regenerative cells in an artificial nerve conduit. *Journal of Plastic, Reconstructive & Aesthetic Surgery*. 2008;61(6):669-75.
193. Pearse DD, Bastidas J, Izabel SS, Ghosh M. Schwann Cell Transplantation Subdues the Pro-Inflammatory Innate Immune Cell Response after Spinal Cord Injury. *International journal of molecular sciences*. 2018;19(9):2550.
194. Oliveira JT, Mostacada K, de Lima S, Martinez AM. Bone marrow mesenchymal stem cell transplantation for improving nerve regeneration. *International review of neurobiology*. 2013;108:59-77.
195. Zhang R, Rosen JM. The role of undifferentiated adipose-derived stem cells in peripheral nerve repair. *Neural regeneration research*. 2018;13(5):757-63.
196. Wang C, Lu C-F, Peng J, Hu C-D, Wang Y. Roles of neural stem cells in the repair of peripheral nerve injury. *Neural regeneration research*. 2017;12(12):2106-12.
197. Abdallah BM, Kassem M. Human mesenchymal stem cells: from basic biology to clinical applications. *Gene therapy*. 2008;15(2):109-16.
198. Mimura T, Dezawa M, Kanno H, Sawada H, Yamamoto I. Peripheral nerve regeneration by transplantation of bone marrow stromal cell-derived Schwann cells in adult rats. *Journal of neurosurgery*. 2004;101(5):806-12.
199. Hou B, Ye Z, Ji W, Cai M, Ling C, Chen C, et al. Comparison of the Effects of BMSC-derived Schwann Cells and Autologous Schwann Cells on Remyelination Using a Rat Sciatic Nerve Defect Model. *Int J Biol Sci*. 2018;14(13):1910-22.
200. Ishikawa N, Suzuki Y, Dezawa M, Kataoka K, Ohta M, Cho H, et al. Peripheral nerve regeneration by transplantation of BMSC-derived Schwann cells as chitosan gel sponge scaffolds. *Journal of Biomedical Materials Research Part A*. 2009;89A(4):1118-24.

201. Xu W, Zhao Z, Zhao B, Wang Y, Peng J, Zhang L, et al. [Effect of different number of bone marrow mesenchymal stem cells on growth of rat dorsal root ganglia in vitro]. *Zhongguo xiu fu chong jian wai ke za zhi = Zhongguo xiufu chongjian waike zazhi = Chinese journal of reparative and reconstructive surgery*. 2011;25(10):1245-9.
202. Zhang S, Li J, Jiang H, Gao Y, Cheng P, Cao T, et al. Dorsal Root Ganglion Maintains Stemness of Bone Marrow Mesenchymal Stem Cells by Enhancing Autophagy through the AMPK/mTOR Pathway in a Coculture System. *Stem cells international*. 2018;2018:8478953-.
203. Zhang R, Rosen JM. The role of undifferentiated adipose-derived stem cells in peripheral nerve repair. *Neural Regen Res*. 2018;13(5):757-63.
204. Ching RC, Wiberg M, Kingham PJ. Schwann cell-like differentiated adipose stem cells promote neurite outgrowth via secreted exosomes and RNA transfer. *Stem Cell Res Ther*. 2018;9(1):266-.
205. Papalia I, Raimondo S, Ronchi G, Magaouda L, Giacobini-Robecchi MG, Geuna S. Repairing nerve gaps by vein conduits filled with lipoaspirate-derived entire adipose tissue hinders nerve regeneration. *Annals of anatomy = Anatomischer Anzeiger : official organ of the Anatomische Gesellschaft*. 2013;195(3):225-30.
206. Reid AJ, Sun M, Wiberg M, Downes S, Terenghi G, Kingham PJ. Nerve repair with adipose-derived stem cells protects dorsal root ganglia neurons from apoptosis. *Neuroscience*. 2011;199:515-22.
207. Ding DC, Chang YH, Shyu WC, Lin SZ. Human umbilical cord mesenchymal stem cells: a new era for stem cell therapy. *Cell transplantation*. 2015;24(3):339-47.
208. Guo ZY, Sun X, Xu XL, Zhao Q, Peng J, Wang Y. Human umbilical cord mesenchymal stem cells promote peripheral nerve repair via paracrine mechanisms. *Neural Regen Res*. 2015;10(4):651-8.
209. Ma Y, Dong L, Zhou D, Li L, Zhang W, Zhen Y, et al. Extracellular vesicles from human umbilical cord mesenchymal stem cells improve nerve regeneration after sciatic nerve transection in rats. *Journal of Cellular and Molecular Medicine*. 2019;23(4):2822-35.
210. Yao R, Murtaza M, Velasquez JT, Todorovic M, Rayfield A, Ekberg J, et al. Olfactory Ensheathing Cells for Spinal Cord Injury: Sniffing Out the Issues. *Cell transplantation*. 2018;27(6):879-89.
211. Woodhall E, West AK, Chuah MI. Cultured olfactory ensheathing cells express nerve growth factor, brain-derived neurotrophic factor, glia cell line-derived neurotrophic factor and their receptors. *Molecular Brain Research*. 2001;88(1):203-13.
212. Su Z, Yuan Y, Chen J, Cao L, Zhu Y, Gao L, et al. Reactive astrocytes in glial scar attract olfactory ensheathing cells migration by secreted TNF-alpha in spinal cord lesion of rat. *PloS one*. 2009;4(12):e8141.
213. Tang Y, Yu P, Cheng L. Current progress in the derivation and therapeutic application of neural stem cells. *Cell death & disease*. 2017;8(10):e3108.
214. El Seady R, Huisman MA, Lowik CW, Frijns JH. Uncomplicated differentiation of stem cells into bipolar neurons and myelinating glia. *Biochemical and biophysical research communications*. 2008;376(2):358-62.
215. Tong L, Ji L, Wang Z, Tong X, Zhang L, Sun X. Differentiation of neural stem cells into Schwann-like cells in vitro. *Biochemical and biophysical research communications*. 2010;401(4):592-7.
216. McKenzie IA, Biernaskie J, Toma JG, Midha R, Miller FD. Skin-derived precursors generate myelinating Schwann cells for the injured and dysmyelinated nervous system. *The Journal of neuroscience : the official journal of the Society for Neuroscience*. 2006;26(24):6651-60.
217. Jandial R, Singec I, Ames CP, Snyder EY. Genetic modification of neural stem cells. *Molecular therapy : the journal of the American Society of Gene Therapy*. 2008;16(3):450-7.
218. Chan KY, Jang MJ, Yoo BB, Greenbaum A, Ravi N, Wu WL, et al. Engineered AAVs for efficient noninvasive gene delivery to the central and peripheral nervous systems. *Nat Neurosci*. 2017;20(8):1172-9.
219. Schmitte R, Tipold A, Stein VM, Schenk H, Flietsch C, Grothe C, et al. Genetically modified canine Schwann cells—In vitro and in vivo evaluation of their suitability for peripheral nerve tissue engineering. *Journal of Neuroscience Methods*. 2010;186(2):202-8.
220. Deng Y, Kim B, He X, Kim S, Lu C, Wang H, et al. Direct visualization of membrane architecture of myelinating cells in transgenic mice expressing membrane-anchored EGFP. *Genesis*. 2014;52(4):341-9.
221. Zhang M, Jiang MH, Kim D-W, Ahn W, Chung E, Son Y, et al. Comparative Analysis of the Cell Fates of Induced Schwann Cells from Subcutaneous Fat Tissue and Naïve Schwann Cells in the Sciatic Nerve Injury Model. *Biomed Res Int*. 2017;2017:1252851-.
222. Timmer M, Robben S, Muller-Ostermeyer F, Nikkhah G, Grothe C. Axonal regeneration across long gaps in silicone chambers filled with Schwann cells overexpressing high molecular weight FGF-2. *Cell transplantation*. 2003;12(3):265-77.
223. Marquardt LM, Ee X, Iyer N, Hunter D, Mackinnon SE, Wood MD, et al. Finely Tuned Temporal and Spatial Delivery of GDNF Promotes Enhanced Nerve Regeneration in a Long Nerve Defect Model. *Tissue engineering Part A*. 2015;21(23-24):2852-64.

224. Bierlein De la Rosa M, Sharma AD, Mallapragada SK, Sakaguchi DS. Transdifferentiation of brain-derived neurotrophic factor (BDNF)-secreting mesenchymal stem cells significantly enhance BDNF secretion and Schwann cell marker proteins. *Journal of Bioscience and Bioengineering*. 2017;124(5):572-82.
225. May F, Buchner A, Matiasek K, Schlenker B, Stief C, Weidner N. Recovery of erectile function comparing autologous nerve grafts, unseeded conduits, Schwann-cell-seeded guidance tubes and GDNF-overexpressing Schwann cell grafts. *Disease models & mechanisms*. 2016;9(12):1507-11.
226. Yeh CW, Wang LW, Wu HC, Hsieh YK, Wang J, Chen MH, et al. Development of biomimetic micro-patterned device incorporated with neurotrophic gradient and supportive Schwann cells for the applications in neural tissue engineering. *Biofabrication*. 2017;9(1):015024.
227. Wu S, Chen MS, Maurel P, Lee YS, Bunge MB, Arinze TL. Aligned fibrous PVDF-TrFE scaffolds with Schwann cells support neurite extension and myelination in vitro. *Journal of neural engineering*. 2018;15(5):056010.
228. Keilhoff G, Fansa H. Mesenchymal stem cells for peripheral nerve regeneration—A real hope or just an empty promise? *Experimental neurology*. 2011;232(2):110-3.
229. Zheng M, Duan J, He Z, Wang Z, Mu S, Zeng Z, et al. Transplantation of bone marrow stromal stem cells overexpressing tropomyosin receptor kinase A for peripheral nerve repair. *Cytotherapy*. 2017;19(8):916-26.
230. Lankford KL, Arroyo EJ, Nazimek K, Bryniarski K, Askenase PW, Kocsis JD. Intravenously delivered mesenchymal stem cell-derived exosomes target M2-type macrophages in the injured spinal cord. *PLoS one*. 2018;13(1):e0190358.
231. Santiago LY, Clavijo-Alvarez J, Brayfield C, Rubin JP, Marra KG. Delivery of adipose-derived precursor cells for peripheral nerve repair. *Cell transplantation*. 2009;18(2):145-58.
232. Mohammadi R, Azizi S, Amini K. Effects of undifferentiated cultured omental adipose-derived stem cells on peripheral nerve regeneration. *Journal of Surgical Research*. 2013;180(2):e91-e7.
233. Sowa Y, Kishida T, Imura T, Numajiri T, Nishino K, Tabata Y, et al. Adipose-Derived Stem Cells Promote Peripheral Nerve Regeneration In Vivo without Differentiation into Schwann-Like Lineage. *Plast Reconstr Surg*. 2016;137(2):318e-30e.
234. Schilling BK, Schusterman MA, 2nd, Kim DY, Repko A, Klett K, Christ GJ, et al. Adipose-Derived Stem Cells Delay Muscle Atrophy after Peripheral Nerve Injury in the Rodent Model. *Muscle & nerve*. 2019.
235. Shalaby SM, El-Shal AS, Ahmed FE, Shaban SF, Wahdan RA, Kandel WA, et al. Combined Wharton's jelly derived mesenchymal stem cells and nerve guidance conduit: A potential promising therapy for peripheral nerve injuries. *Int J Biochem Cell Biol*. 2017;86:67-76.
236. Moattari F, Kaka G, Mohseni Kouchesfehani H, Sadraie SH, Naghdi M, Mansouri K. Evaluation of dexamethasone treated mesenchymal stem cells for recovery in neurotmesis model of peripheral nerve injury AU - Moattari, Mehrnaz. *Neurological Research*. 2018;40(12):1060-70.
237. Kabiri M, Oraee-Yazdani S, Shafiee A, Hanaee-Ahvaz H, Dodel M, Vaseei M, et al. Neuroregenerative effects of olfactory ensheathing cells transplanted in a multi-layered conductive nanofibrous conduit in peripheral nerve repair in rats. *Journal of biomedical science*. 2015;22(1):35-.
238. Khankan RR, Wanner IB, Phelps PE. Olfactory ensheathing cell-neurite alignment enhances neurite outgrowth in scar-like cultures. *Experimental neurology*. 2015;269:93-101.
239. Li M, Zhu Q, Liu J. Olfactory ensheathing cells in facial nerve regeneration. *Brazilian Journal of Otorhinolaryngology*. 2018.
240. Flachsbarth K, Kruszewski K, Jung G, Jankowiak W, Riecken K, Wagenfeld L, et al. Neural stem cell-based intraocular administration of ciliary neurotrophic factor attenuates the loss of axotomized ganglion cells in adult mice. *Investigative ophthalmology & visual science*. 2014;55(11):7029-39.
241. Lee DC, Chen JH, Hsu TY, Chang LH, Chang H, Chi YH, et al. Neural stem cells promote nerve regeneration through IL12-induced Schwann cell differentiation. *Molecular and cellular neurosciences*. 2017;79:1-11.
242. Park B-W, Kang D-H, Kang E-J, Byun J-H, Lee J-S, Maeng G-H, et al. Peripheral nerve regeneration using autologous porcine skin-derived mesenchymal stem cells. *Journal of Tissue Engineering and Regenerative Medicine*. 2012;6(2):113-24.
243. Chen Z, Pradhan S, Liu C, Le LQ. Skin-derived Precursors as a Source of Progenitors for Cutaneous Nerve Regeneration. *STEM CELLS*. 2012;30(10):2261-70.
244. Wang H, Wu J, Zhang X, Ding L, Zeng Q. Study of synergistic role of allogenic skin-derived precursor differentiated Schwann cells and heregulin-1beta in nerve regeneration with an acellular nerve allograft. *Neurochemistry international*. 2016;97:146-53.
245. Li Q, Ping P, Jiang H, Liu K. Nerve conduit filled with GDNF gene-modified schwann cells enhances regeneration of the peripheral nerve. *Microsurgery*. 2006;26(2):116-21.

246. Wang Y, Li W-y, Jia H, Zhai F-g, Qu W-r, Cheng Y-x, et al. KLF7-transfected Schwann cell graft transplantation promotes sciatic nerve regeneration. *Neuroscience*. 2017;340:319-32.
247. Pettingill LN, Minter RL, Shepherd RK. Schwann cells genetically modified to express neurotrophins promote spiral ganglion neuron survival in vitro. *Neuroscience*. 2008;152(3):821-8.
248. Huang L, Quan X, Liu Z, Ma T, Wu Y, Ge J, et al. c-Jun gene-modified Schwann cells: upregulating multiple neurotrophic factors and promoting neurite outgrowth. *Tissue engineering Part A*. 2015;21(7-8):1409-21.
249. Ma F, Xu F, Li R, Zheng Y, Wang F, wei N, et al. Sustained delivery of glial cell-derived neurotrophic factors in collagen conduits for facial nerve regeneration. *Acta biomaterialia*. 2018;69:146-55.
250. Suri S, Schmidt CE. Cell-laden hydrogel constructs of hyaluronic acid, collagen, and laminin for neural tissue engineering. *Tissue engineering Part A*. 2010;16(5):1703-16.
251. Galla TJ, Vedecnik SV, Halbgewachs J, Steinmann S, Friedrich C, Stark GB. Fibrin/Schwann cell matrix in poly-epsilon-caprolactone conduits enhances guided nerve regeneration. *The International journal of artificial organs*. 2004;27(2):127-36.
252. Georgiou M, Golding JP, Loughlin AJ, Kingham PJ, Phillips JB. Engineered neural tissue with aligned, differentiated adipose-derived stem cells promotes peripheral nerve regeneration across a critical sized defect in rat sciatic nerve. *Biomaterials*. 2015;37:242-51.
253. Naghieh S, Karamooz-Ravari MR, Sarker MD, Karki E, Chen X. Influence of crosslinking on the mechanical behavior of 3D printed alginate scaffolds: Experimental and numerical approaches. *Journal of the Mechanical Behavior of Biomedical Materials*. 2018;80:111-8.
254. MacEwan MR, Gamble P, Stephen M, Ray WZ. Therapeutic electrical stimulation of injured peripheral nerve tissue using implantable thin-film wireless nerve stimulators. *Journal of neurosurgery*. 2018:1-10.
255. Gordon T, English AW. Strategies to promote peripheral nerve regeneration: electrical stimulation and/or exercise. *Eur J Neurosci*. 2016;43(3):336-50.
256. Willand MP, Nguyen MA, Borschel GH, Gordon T. Electrical Stimulation to Promote Peripheral Nerve Regeneration. *Neurorehabilitation and neural repair*. 2016;30(5):490-6.
257. Sayad Fathi S, Zaminy A. Stem cell therapy for nerve injury. *World J Stem Cells*. 2017;9(9):144-51.

Chapter III

Nanotechnology in peripheral nerve repair and reconstruction

Chapter III

Nanotechnology in peripheral nerve repair and reconstruction¹

ABSTRACT

The recent progress in biomaterials science and development of tubular conduits (TCs) still fails in solving the current challenges in the treatment of peripheral nerve injuries (PNIs), in particular when disease-related and long-gap defects need to be addressed. Nanotechnology-based therapies that seemed unreachable in the past are now being considered for the repair and reconstruction of PNIs, having the power to deliver bioactive molecules in a controlled manner, to tune cellular behavior, and ultimately guide tissue regeneration in an effective manner. It also offers opportunities in the imaging field, with a degree of precision never achieved before, which is useful for diagnosis, surgery and in the patient's follow-up. Nanotechnology approaches applied in PNI regeneration and theranostics, emphasizing the ones that are moving from the lab bench to the clinics, are herein overviewed.

Keywords: Peripheral nerve regeneration; nanotechnology; nanomedicine; carbon nanomaterials; nanoparticles; nanofibers; nanoimaging; repair; tubular conduits.

¹This chapter is based on the following publication: [Carvalho CR, Silva-Correia J, Oliveira JM, Reis RL, Nanotechnology in Peripheral Nerve Repair and Reconstruction. *Advanced Drug Delivery Reviews*. 2019. 10.1016/j.addr.2019.01.006.](#)

III-1. INTRODUCTION

Neurological defects are among the most common and demanding clinical situations despite decades of research in the neurological field (1). The reason for this relies in the complexity of the nervous system functions, structure and anatomy, which makes it more challenging to treat as compared to other tissues in the human body (2). The nervous system comprises two components: i) the peripheral nervous system (PNS), and ii) the central nervous system (CNS). The PNS consists of the regions of the nervous system outside the CNS (brain and the spinal cord). The PNS includes cranial nerves, spinal nerves and their roots and branches, peripheral nerves (PNs), and neuromuscular junctions. Opposing to the CNS, the PNS is not protected by a hard bone layer or by the blood-brain barrier, making it much more disposed to traumatism or any kind of injuries (3). Therefore, PN injuries (PNIs) are considered a huge clinical burden, being the incidence 1 in 1,000 individuals per year (4). In fact, PNI is associated to \$150 billion health-care expenses per year in the USA alone (5). These costs are though underestimated, since “bed-days” and lack of productivity also account for monetary losses, worldwide. This scenario tends to worsen with the increasing world population and respective average lifespan. Considering those, an additional number of injuries tend to appear and consequently a high number of treatments and surgeries will be required to allow the restoration of the damaged nerves.

In this scope, nanotechnology and nano-based materials have attracted a significant amount of interest from the scientific and medical community. These types of materials are considered a reliable alternative to tackle the main hurdles in PN regeneration (PNR). Although the CNS is vastly protected and therefore less prone to injuries, it has a limited ability to regenerate because of the succeeding scar tissue development which can be created by a vast range of cell types, such as fibroblasts, neuroglia, monocytes, and endothelial cells (6). In contrast, PNIs are considerably more common, but the PNs have a greater regeneration potential when compared to the nerves of CNS. This is because PNS glial cells, *i.e.* Schwann cells (SCs), tend to adapt to a regenerative phenotype and have the capacity of triggering neuronal regenerative processes, although usually slow and in a partial manner (7). Given to their exposure, PN damages can be caused by many types of events, such as traumatic injuries, complications on surgeries, congenital defects and war wounds. Concerning the traumatic injuries, they can also vary significantly and include penetrating injuries, crush, traction, ischemia, and less common mechanisms such as thermal, electric shock and radiation (8). Another common injury mechanism is

compression, which may involve mechanical deformation, as well as ischemia. A vast range of diseases can also be the root cause of PNIs, as is the case of diabetic peripheral neuropathies (9, 10).

In respect to the type of injury, small and long gaps must also be differentiated. This concerns the severity of the injury, as well as the outcome and the degree of recovery for the patient. In humans, for small gaps, which usually measure less than 30 mm, hollow lumen conduits can be used with rather good outcomes. However, reconstruction of gaps longer than 30 mm still remains a challenge nowadays. Nerve autografts and allografts still remain the clinically available options and the ones that provide the best chances of recovery (11). However, when considering long gaps, most of the barriers to recovery remain unsolved, namely the slow regeneration rates and specificity of target innervation, which means that the distal stump is too far from the proximal. The degeneration of the target end-organ is another obstacle to a proper and functional regeneration (12). Therefore, the challenge presented by long gaps is the reason why innovative nanotechnology-based strategies are sought to be a good technological possibility. **Figure III-1** summarizes the main possible applications of nanotechnology approaches in an attempt to tackle some of the hurdles of PNIs.

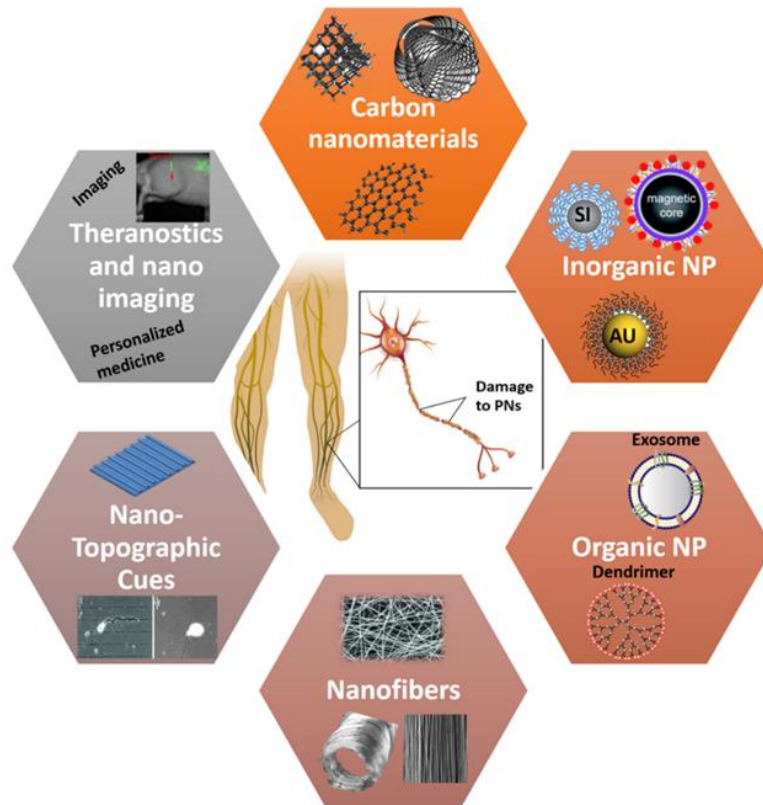


Figure III-1 - Nanotechnology applied to peripheral nerve regeneration and reconstruction. Carbon nanomaterials, nanoparticles, nanofibers, nano-topographic cues and theranostics and nano-imaging are some of the areas in nanomedicine that should be explored in order to improve tissue bifunctionality.

Despite those seemingly good chances of recovery when using autografts, incomplete recuperation from PNIs usually lead to multiple negative consequences, which comprise numbness of affected members, chronic pain, diminishing of sensory and/or motor function and a disturbing permanent disability of the patients. It is a fact that these outcomes are unsatisfactory for the demands of today's patient lives, since only 25 % of patients regain proper motor function and less than 3 % recuperate sensation in a full extent (13). The outcome is a major loss of patient's quality of life, both physically and mentally, and considering the above mentioned facts, it is urgent to visualize PNIs as a worldwide pertinent clinical problem (14). Given the stated importance of PNI, the use of nanotechnology to help address and solve some of the challenges posed to clinical management of PNI is a field worthy to be explored and properly funded, and certainly will growth in the coming years.

III-2. PNIs: FUNDAMENTALS, CURRENT TREATMENT OPTIONS AND CHALLENGES

In order to make a preliminary evaluation, followed by a precise diagnosis and proceeding with the proper treatment of nerve injuries, it is imperative to have plain knowledge of nerve anatomy (**Figure III-2**), as well as the neurobiological mechanisms that occur immediately after injuries. That is of utmost importance, since strategies to improve the outcomes following nerve injuries are often based on such biological mechanisms (15). The PNS is composed of motor and sensory neurons. Their cell bodies can be found within the spinal cord and their elongated cytoplasmic extensions, called axons, link and transmit the signals to the distant corresponding organ (5). **Figure III-2A** schematically represents the anatomy of the peripheral nerve. Anatomically, each individual axon is protected by the endoneurium, a layer of collagen and elastic elements. A group of endoneurium protects axon groups into nerve fascicles, which are sheathed by the perineurium, mainly composed of connective tissue. Finally, several fascicles are gathered together by the epineurium. External to this layer is the mesoneurium, containing the blood supply to the nerve. A fine network of capillaries exists at the endoneurial level (1, 5, 16). Any break or defect in this stratified structure fallouts in a programmed and permanent cell death, unless rapidly and thoroughly reestablished (17, 18).

The several degrees of injury to PNs are detailed in **Table III-1**, which were firstly described by Seddon (19), and later by Sunderland (20). The Seddon classification is divided into three categories according to the gravity of the injury: i) neurapraxia, ii) axonotmesis, and iii) neurotmesis.

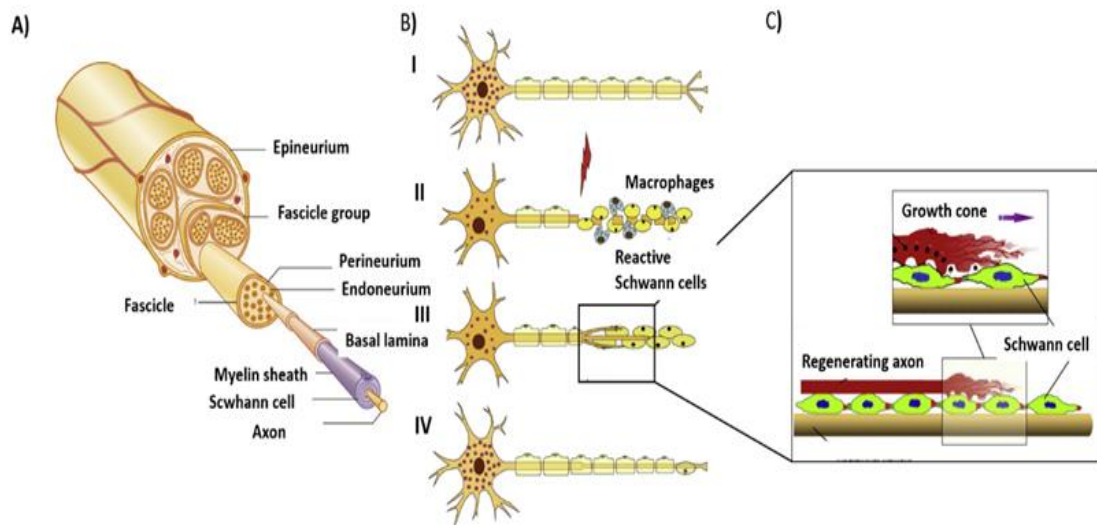


Figure III-2 - Schematic representation of the anatomy of peripheral nerve and degeneration and regeneration after an injury. A) Scheme of peripheral nerve anatomy); B) Degeneration and regeneration after peripheral nerve injury. (I) Normal neuron; (II) Wallerian degeneration. Schwann cells proliferate, and macrophages invade the distal nerve segment and phagocytosis of degrading materials; (III) Schwann cells in the distal end align in bands of Bungner; and (IV) Axonal re-joining with distal end and organs; and C) Axonal sprouts advance entrenched with aligned Schwann cells. Reprinted and adapted from A) [351]; B) [18]; C) [14].

By its turn, Sunderland classification comprises five different categories: first, second, third, fourth and fifth degree. There are also three different types of PNs that should be considered for reconstruction after an injury: i) the motor neuron, ii) the sensory neuron, and iii) the mixed PNs (21). Although all the three types of nerves are essential to carry a normal lifestyle, the motor and the mixed type of nerve are the ones that have major clinical importance in the reestablishment of the movement of the limbs. However, up to date, mostly sensory nerves are involved in the repair strategies due to easier harvesting, and relatively lower donor-site morbidity.

Immediately after injury, the regeneration process of PNs runs in sequenced phases and different phenomena can occur at different levels on the injury site (**Figure III-2B**), encompassing both proximal and distal sites (22). In the proximal position, separated axons and cell bodies degenerate via a programmed cell death pathway called chromatolysis (23). In the distal injury end, a process called Wallerian degeneration occurs at 24 to 48 hours after injury and all nerve components, such as distal axons and adjacent myelin starts to degenerate (24). The goal of that phenomenon is related to the clearance of undesired debris. SCs phagocytize axonal and myelin debris, until only empty endoneurial tubes remain. SCs, which are the ensheathing glial cells of the PNS, are crucial for normal nerve function, nerve repair and constitute 90 % of nucleated cells within PNs (25, 26).

Table III-1 - Seddon and Sunderland classifications of nerve injuries according to the pathophysiology of the nerve

| Seddon classification | Sunderland classification | Process | Degree of recovery |
|-----------------------|---------------------------|---|--|
| Neurapraxia | I | Local myelin damage usually secondary to compression; | Full recovery; |
| Axonotmesis | II | Axon severed but endoneurium intact (optimal circumstances for regeneration); | Full recovery; |
| | III | Axon discontinuity, endoneurial tube discontinuity, perineurium and fascicular arrangement preserved; | Wallerian degeneration, recovery incomplete; |
| | IV | Loss of continuity of axons, endoneurial tubes, perineurium and fasciculi; epineurium intact; | Wallerian degeneration, recovery incomplete; |
| Neurotmesis | V | Complete physiologic disruption of entire nerve trunk: | Wallerian degeneration, recovery incomplete; |

After debris removal, they fill the empty endoneurial tubes and organize in characteristic bands or tubes of Bungner, and by this mean supporting the re-growth of axons. Not only SCs have a crucial role, but also macrophages are recruited to the area releasing growth factors and cytokines. They will stimulate SCs and fibroblast proliferation and are responsible for the axonal regeneration process (27). Ahead in the process, in the proximal injury end, a growth cone emerges following the path formed by the band of Bungner, which is of fundamental importance for the advance of the regenerating axon (**Figure III-2C**) (28).

Considering the current state-of-the-art on nerve pathophysiology, only minor advances in medical and operating techniques have been made in the past years. Epineural repair remains the preferred surgical reconstruction when it is accomplished by direct tension-free suture of both well-vascularized nerve ends (29). Whenever that approach is not possible, due to excessive tension caused by elongating the nerves, and a gap remains, these lesions do not spontaneously regenerate. In such cases, autologous nerve grafts (ANG) become the gold standard treatment for nerve restoration (30). However, ANG cannot guarantee an absolute functional outcome for the patient. Problematic consequences, such as unavailability of appropriate-sized nerves and donor site morbidities, sensibility abnormalities and painful conditions are also frequently associated to this type of approach (30). An alternative option to use in nerve transplantation is cadaveric allografts (31). However, like ANG, there are pros and cons regarding the use of allografts. The selection of the type of graft is based on the patient's needs and typically it involves a systemic immunosuppression therapy in the patient for long periods of time (32).

For these reasons, increasing efforts have been made over the last decades in the search for effective alternatives to ANG. Tissue engineered tubulization has been a widely explored alternative to bridge the nerve gap and throughout the years many types of nerve guidance conduits (NGC) were proposed, being some of them already approved by the Food and Drug Administration (FDA) (33, 34). Since mature neurons are not susceptible to mitosis phenomena, it is crucial to support the re-growth of the existing cell bodies, providing a protective environment and guiding paths. In this way, it is possible to direct axons from the proximal do the distal site, permitting the proper linking of the damaged synapses connections. In brief, the protection of the injury site and performance as a guidance substrate are the two main reasons why tubulization is used in PNI.

In the early use of conduits made of synthetic materials in the clinics, they were mainly composed by silicon tubes and could only repair injuries up to 10 mm. Some disadvantages on the use of that conduits included total lack of biodegradability, which led to inflammation and chronic foreign body reaction, as well as lack of swelling capacity, which would compress the nerve, thus hindering the regeneration process (35). In order to overcome such difficulties, biodegradable nerve guidance conduits have been proposed, some of which are FDA-approved and being currently used in the clinical setting (34). Nevertheless, despite the major advances achieved with the use of silicon conduits, most NGCs are hollow tubes and can only repair short nerve gaps. In 2014, however, there was a breakthrough regarding this subject. The first conduit integrating a luminal filler acting as three dimensional (3D) guiding and supporting scaffold was approved. NeuraGen®3D nerve guide matrix is composed by collagen I, whereas the luminal filler comprised of collagen I and glycosaminoglycan chondroitin-6-sulfate, with aligned porosity acts as a topographical cue for regenerating axons. *In vivo* data demonstrated significantly improved regeneration as compared to an empty conduit (36).

In the past decades, numerous NGC made of both synthetic and natural biomaterials have been described. Regarding the synthetic materials, these are still considered very promising since the majority of the FDA-approved nerve guidance conduits are composed of materials such as polyglycolic acid (PGA), polylactic-co-glycolic (PLGA), polycaprolactone (PCL) (34). Polyhydroxybutyrate (PHB) has been reported to have neuroprotective features and support axons regrowth (37). Among the natural-based biomaterials, polysaccharides such as chitosan (Cht) (38, 39) and alginate (40) have been also considered as promising materials due to their worthy results in the scope of PNR. Still among the natural-origin biomaterials, extracellular matrix (ECM) endogenous proteins such as collagen (41), fibrin

(42), laminin (43, 44), and hyaluronic acid (HA) (45) have been highly investigated, since they all naturally exist in the human body.

Not only the type of biomaterial used in the NGC is important, but its architecture is also an important feature. There is still no consensus in the scientific community on whether the conduit should remain empty (46) or filled with any kind of materials (47), such as hydrogels (48), nanofibers (49) or films (50). An empty lumen has the advantage of allowing free space for nerve regeneration, so that the axons may selectively re-innervate the appropriate target. Conversely, a lumen filled with any type of topographical and biological cues can provide a supporting structure that may favor cells ingrowths and guidance (1, 51). Apart from the use of NGC and fillers, systemic or localized delivery of neurogenic, anti-inflammatory and pro-angiogenic factors should be ideally performed. Among those, cytokines, drugs or stem cell therapies can be considered in order to enhance the neurofunctional outcomes (52). It is important to point out that these strategies work by different mechanisms and distinct biochemical pathways. Therefore, a proper combination of a promising NGC, guiding fillers, with cellular therapy and localized delivery of factors will most definitely match the results usually obtained with ANG. Although PNS has a certain ability to regenerate, other physiopathological phenomena impair nerve regeneration and these are presented as the great challenges that need to be overcome to succeed in PNR. Also, most of the strategies being developed are focused on the specific injury site (53). Other scientific solutions should be sought in order to address problems that emerge after the injury itself and focus on maintaining distal axonal and muscular target integrity. Also, it must be guaranteed the survival of cell bodies in the proximal site, occurrence that remains largely unexplored and would essentially contribute to maintain the natural physiology after injury.

Therefore, other therapies or approaches should be taken in consideration to address simultaneously what happens in the nerve gap itself, but also, upstream and downstream of that location. This is where novel nanotechnologies, including for instance, nanoparticles (NPs), nanoimaging and carbon nanomaterials start to take a key role in cutting-edge approaches that might be able to solve problems that could not be addressed with traditional methods. Taking a closer look to some nanotechnologies, one can immediately understand their potential in PNR. In one hand, the refinement of NGC's technologies lies in the incorporation of nanotechnological techniques. On the other hand, nanotechnological approaches can be used on their own (54). Because of their properties and competences, NPs have an immense broad of applications in PNR. They can not only carry every type of growth factor or biomolecules of interest to the desired place but can also deliver it with the

appropriate kinetics for an optimal result. This has been a problem that scientist have been trying to address for years, since mimicking the natural events by the correct delivery of biological factors is crucial for an efficient regeneration (55). Further than that, they comprise the basic nanoimaging tools, such as MRI (magnetic resonance imaging) allowing visualization techniques never achieved before in the clinics (56). Carbon nanomaterials, such as carbon nanotubes, are another exciting example of multiple-advantageous materials for PNR, encouraging the scientists to achieve goals that take PNR to another level. Since PNS relies on electric conduciveness, not only can they be used for coating electrodes for interfacing neurological prosthesis, but they can simply integrate tubular conduits making them also electrically conductive (57). In addition to providing a permissive substrate for neuronal growth, patterned carbon nanotubes substrates are also able to control the direction of neurite outgrowth and participate in the organization of neural networks, as the misdirection of growing axons is still an intriguing problem for surgeons and scientists.

First of all, engineering a NGC should aim at facilitating cellular spreading and growth of damaged nerve tissues in 3D (58). Other than that, it is crucially important that the material envisioned to be used to construct the NGC is cytocompatible and has pronounced biomechanical properties. If an engineered NGC does not present a proper cytocompatibility, may not contribute to the growth of damaged nerves, but would instead be the reason of acute inflammation and even infection (59). It must exhibit good biocompatibility with low inflammatory and immunogenic reactions (14). It must also be biodegradable, and ideally degrade in the same rate as nerve regenerates. Otherwise, a quick degradation might trigger an inflammatory response (58, 60). Regarding the mechanical properties, the NGC should provide sufficient mechanical strength to prevent the NGC rupture during the patient's movements and physically support neural tissue regeneration. Concurrently, the NGC should have appropriate elasticity to be able to lessen tensions in the damaged area (59). Furthermore, the materials used to construct NGC should prevent the migration of fibroblasts that will lead to the formation of glial scar tissue around the implant, which could reduce the healing chances (61).

The permeability of a conduit is also an important parameter to consider in the TCs design as both nutrients and oxygen must diffuse into the site of regeneration. Otherwise, cells inside the conduit, especially if it is a long conduit, will be under a deleterious ischemic environment which can result in cellular hypoxia and lack of proper nutrients. Ideally, electrical conductivity would be preferred for a NGC used in neural tissue engineering (TE) in order to mimic the electrical properties of nerves and at the same time excite the neuron communication (62). Succinctly, an ideal NGC should be

biocompatible, biodegradable, flexible, compliant, porous, neuroconductive and with suitable surface and mechanical properties. However, even if all these criteria were successfully gathered in a developed NGC, there are some complications that are difficult to avoid and that reduce the chances of regenerative success. This section unfolds some of the most important physiopathological phenomena (e.g. inflammatory response, fibrosis or scar tissue formation, and lack of proper vascularization) that prejudice PNR and should be addressed to achieve a successful nerve recovery as overviewed in **Table III-2**. A schematic of such events can also be seen in **Figure III-3**.

Neuroinflammation is an important phenomenon in nerve degeneration and consequent regeneration and is intrinsically associated with PNIs. It is a lively and active process that changes throughout the sequence of recovery. Both the timing and grade of inflammation will either result in the improvement or obstruction of the regeneration process. This process also significantly varies between individuals, which makes it harder to control (63). The immune system plays a critical role during nerve regeneration and an inflammatory response is always involved after an injury. As SCs release cytokines and chemokines, different immune cell types are recruited to the critical place in the first hours after the traumatic event, including granulocytes (neutrophils and mast cells) and agranulocytes (monocytes/macrophages and lymphocytes) (50, 64). Controlling the inflammation that occurs in the neurodegenerative scene is a highly complex problem that requires patient-specific interventions. Recently, investigations in the area of nanotechnology have been trying to address that problem (65). Considering the neuroinflammation process as something to take advantage of, and by marking macrophages with specific NPs, one could retrieve information about the biodistribution of drugs, treatment efficacy and assessment on possible toxicity in a real-time manner, with consequent improved therapeutic intervention. Along with SCs, macrophages play the most crucial role after an injury, intrinsically connected to Wallerian degeneration. These cells can assume two phenotypes (**Figure III-3A**): i) pro-inflammatory, being designated as M1, and ii) anti-inflammatory/pro-healing, being in this case designated as M2, phenotypes, which change during the course of the injury (66, 67). However, endogenous mechanisms exist that intend to control PNI inflammation, such as the release of cytokine interleukin 10 (IL-10) (68). Also, SCs remyelination of regenerated axons stimulates macrophage removal. Still, these mechanisms are not efficient enough and prolonged or chronic inflammation becomes deleterious and a challenge during PNR (69).

Fibrosis or scar tissue formation around the implant is another expected and natural occurring event after an injury (70). However, depending on its extension, it might be critical for nerve

regeneration since excessive deposition of ECM and consequent remodeling lead to the formation of permanent scars. Fibrosis can hinder regeneration in two ways: i) intraneural fibrosis will prevent the passage of axons from the proximal segment to the distal segment, and ii) extraneural fibrosis limits the physiological movement of nerves during the patients' movement, leading to pain and functional limitation (**Figure III-3B**) (71). Moreover, it was reported that IL-10 supports scar less healing in postnatal tissue, acting as an adjuvant in combating the excessive fibrosis formation that prevents the correct process of regeneration (72).

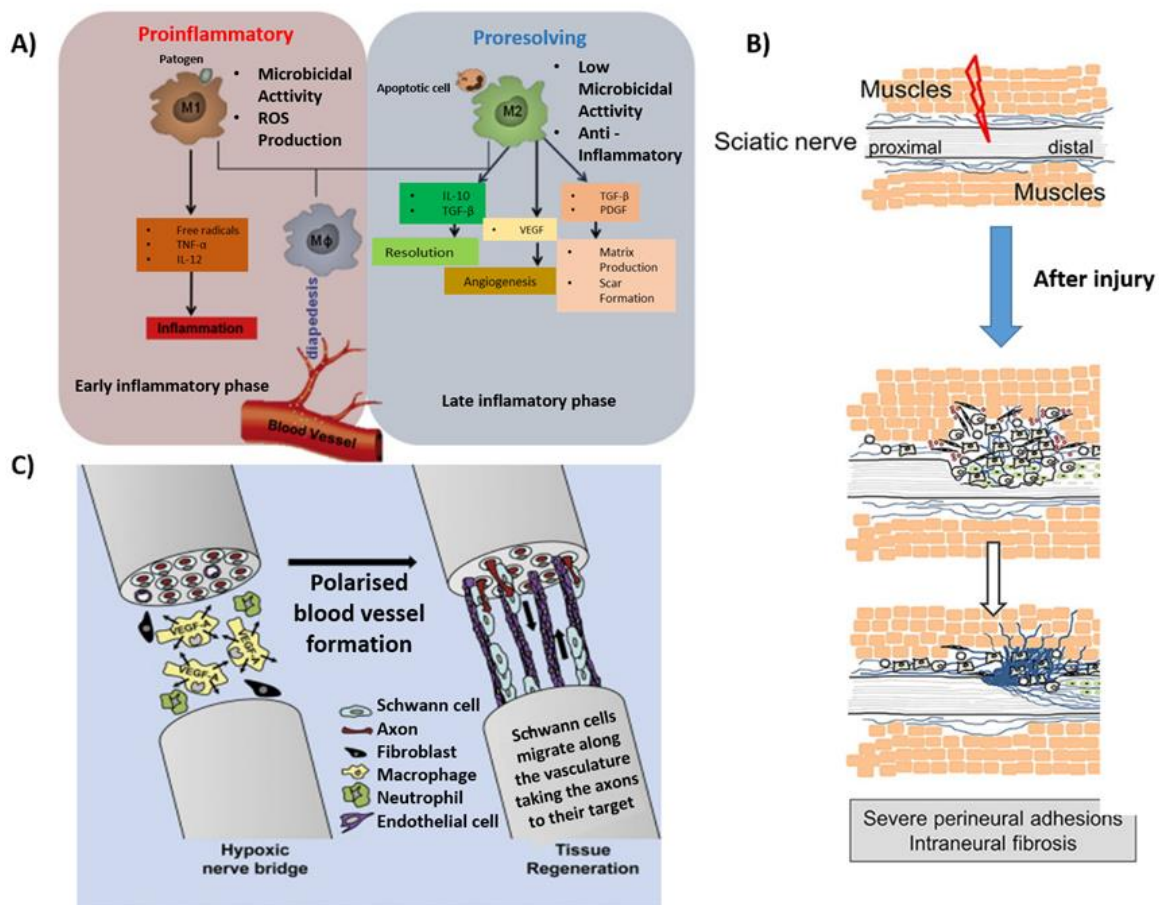


Figure III-3 - General phenomena impairing peripheral nerve regeneration, such as inflammation, excessive scar tissue or lack of vascularization. A) Macrophage plasticity in tissue repair, where M1 pro-inflammatory macrophages can change phenotype into M2 pro-regenerative macrophages; B) After injury, fibroblasts that are attracted to the injury site deposit excessive collagen that leads to perineural adhesions and intraneural fibrosis; and C) Macrophage-induced blood vessels guide Schwann cell to cross the nerve gap. Reprinted and adapted from A) [67]; B) [320]; C) [76].

Lack of proper vascularization, *i.e.* the deficiency of angiogenesis process in the injured site, has lately been considered as one of the main factors limiting nerve regeneration. The relationship between vascularization and neural TE has been recognized as early as 1990 (73). After nerve reconstruction,

the nerve is subjected to ischemic conditions, which potentially alters the regenerative environment and outcome across the bridge or graft (74). Tissues subjected to prolonged ischemia are associated to abundant pathological processes, including cell damage and death, due to the lack of oxygenation and nutrients' supply. This has been considered an explanation for the poor regenerative outcomes of engineered grafts, since a delayed re-vascularization has been observed, in comparison to normal autografts that re-vascularize much faster (75). However, the beginning of the regeneration process (*e.g.* Wallerian degeneration and SCs arrangement in band of Bungner) is initiated by hypoxia (76). Such phenomena are selectively sensed by macrophages that start to secrete vascular endothelial growth factor (VEGF), inducing a polarized vasculature that relieves from hypoxia. SCs then use the blood vessels as physical guiding cues to migrate through the gap and bring regenerating axons along the way (Figure III-3C).

III-3. NANOTECHNOLOGY APPROACHES FOR FUNCTIONALIZATION OF TUBULAR CONDUITS

With the rising application of nanotechnology in every sector of our daily lives, the demand for the development of novel nano-scaled (< 100 nm) approaches is growing at an incredible rate (77). The use of nanotechnology and nano-based materials is widely spread in a variety of sectors, such as healthcare (78), electronics (79), cosmetics (80), agriculture (81) and the continuous improvement and innovation in the field is perceived as an extraordinary opportunity for significantly improve treatment and diagnosis of PNIs (82). Thus, the application of precisely engineered nanomaterials that can be used in all stages of illness: prevention, diagnosis and therapy, including neurological pathologies is now attracting a great deal of attention (83). The ultimate advantage of nanomaterials applied in medicine is based on their ability to interact with biological systems, which takes place at a molecular level with a high degree of specificity. This translates on the ability of such materials to migrate through cell membranes, amplified solubility, steadiness and bioavailability of biomolecules, thereby enhancing their delivery competence (83).

Table III-2 - Phenomena prejudicing peripheral nerve regeneration.

| Phenomena impairing PNR | Related features | Cells/molecules involved |
|--|---|---|
| Inflammatory response | <ul style="list-style-type: none"> - Inflammatory response is always involved after an injury; - Timing and inflammation severity influence regeneration process; - Process varies between individuals; | <ul style="list-style-type: none"> - Macrophages that can be either M1 (anti-inflammatory) or M2 pro-inflammatory - IL10 (anti-inflammatory cytokine) |
| Fibrosis or Scar tissue formation | <ul style="list-style-type: none"> - Intraneural fibrosis will prevent the passage of axons from the proximal segment to the distal segment; - Extra-neural fibrosis limits the physiological movement of nerves during the patients' movement; - Excessive fibrosis results in painful adhesions; | <ul style="list-style-type: none"> - Fibroblasts (fibrotic tissue deposition) - IL-10 (support scar less healing) |
| Lack of vascularization | <ul style="list-style-type: none"> - The relationship between vascularization and neural TE has been recognize as early as 1990; - Lack of vascularization leads to ischemia and consequent cell death by lack of oxygen and nutrients; | <ul style="list-style-type: none"> - VEGF - Macrophages |

Therefore, besides the incorporation of nanomaterials in scaffolds with the aim of boosting their properties, the application of nanomaterials alone can be done for bioimaging (84) and targeted delivery of desired specific molecules into cells (70). Another major advantage of nanomaterials is their nano-roughness resemblance to ECM (85). In this sense, nanomaterials reproduce what happens at a nano-scale level in the human body, being therefore regarded as the ultimate biomimetic materials.

Although, nanotechnology has played a huge role in PNR in recent years, both problems of short and long gaps are being simultaneously addressed by means of developing advanced nanosystems (*e.g.* aligned nanofibers (86, 87) or carbon nanotubes (88-90)) that can act as guiding cues and direct and stimulate the correct re-growth of axons. Advances in nanomedicine field applied to PNR are expected to have a major impact in the patient's recovery and quality of life, since novel therapeutic strategies are evolving and reflecting the interdisciplinary and integrated treatment strategies that bring together nanotechnology and TE (91). Among the variety of available nanomaterials existing and the hundreds of thousands of publications in the area, the most promising works reporting on nanomaterials and offering remarkable advances in the field of PNR were selected and are reviewed herein.

III-3.1. Carbon nanomaterials

Carbon nanomaterials were projected as encouraging candidates for many industrial and technical purposes many decades ago. Worldwide commercial interest in carbon nanomaterials is reflected in its extreme production every year. Diverse commercial products ranging from batteries, motorized components, sporting goods, any kind of structural material and even agricultural products have nanomaterials in their composition now-a-days (92, 93). Only after that initial burst in other areas, their potential for biomedical applications was realized (94). That was due to their great properties that were envisioned as very useful when combined with other biomaterials in TE approaches (95).

Carbon nanostructures were proposed as promising candidates to develop neural scaffolds. When considering neuronal regeneration, electrical stimulation, as well as appropriate electrical conductivity of the applied biomaterials, have been considered one main advantage since the natural PNS is capable of easily transmitting electrical impulses (96, 97). Furthermore, carbon

materials are mainly composed of the very basic element existing in all things, *e.g.* carbon. Currently, the best-known carbon nanostructures belong to four different categories: carbon nanotubes (CNTs), graphene, carbon nanofibers (CNFs), and nanodiamonds (ND). **Figure III-4** depicts some of the most interesting results concerning the section of carbon nanomaterials, which will be discussed in depth.

III-3.1.1. Carbon nanotubes

Carbon nanotubes (CNTs) represent one of the most studied allotropes of carbon. CNTs are sheets of graphite rolled into cylindrical tubes, built from a hexagonal arrangement of sp^2 -hybridized carbon atoms in nano-scale dimensions and were first introduced by Iijima (98). They can be mainly divided in two categories depending on the number of shells: single-walled carbon nanotubes (SWCNTs), with diameter ranging between 0.8-2.0 nm and multi-walled carbon nanotubes (MWCNTs), with diameter ranging from 2.0 and 100 nm. Scheme of such CNTs can be seen in **Figure III-4A1**. There are numerous methods for CNTs production, that mainly include electric discharge (98), laser ablation (99) and chemical vapor deposition (100). Some of the exciting features of CNTs include their extreme mechanical, thermal, magnetic, optical, electrical, surface, and chemical properties. The combination of these characteristics enlarges the range of possible biomedical applications where they can be applied (101). As previously mentioned, besides being in the nano-scale range, the most attractive feature of such materials relies on their ability to display metallic and superconducting electron transport properties. However, original CNTs do not own the necessary solubility for being used in biomedical applications. Therefore, it is critical to functionalize CNTs not only to make them more soluble, but to allow their integration into many organic, inorganic, and biological systems and applications. Two main strategies have been identified to allow the application of CNTs under physiological conditions, which rely on covalent and non-covalent functionalization (102). With such modifications, CNTs can be used in several biomedical applications, such as drug delivery, diagnostics, biosensors, biomedical imaging, as well as TE and regenerative medicine.

The diameter of an individual CNT (1–100 nm, depending on the number of walls) is comparable to that of a single protein complex, such as a microtubule (25 nm diameter), which forms the basic structural element of the neuronal cytoskeleton (103).

Table III-3 - The use of carbon nanotubes applied to peripheral nerve regeneration.

| Type of carbon nanotube | Cell type and/or animal model | Main results | Year, References |
|---|---|--|--------------------------------------|
| MWCNTs | Primary embryonic (E15) rat Motor Neuron | Major neurites are more likely to be oriented parallel to the aligned CNTs; | Roberts <i>et al.</i> , 2014 [112] |
| Nanofibers reinforced with MWCNTs | Schwann cells; sciatic nerve defect in rat | <i>In vitro</i> support of Schwann cell adhesion and elongation and <i>in vivo</i> promotion of sciatic nerve regeneration in rat; | Yu <i>et al.</i> , 2014 [88] |
| Chitosan-aligned MWCNTs composite | HT-22 hippocampal neurons | Improvement of mechanical properties, electrical conductivity and <i>in vitro</i> alignment of hippocampal neurons; | Gupta <i>et al.</i> , 2015 [90] |
| Chitosan-MWCNTs | L929 fibroblasts and mHippoE-18 hippocampal cells | Both SWCNTs and MWCNTs can be incorporated with an electrodeposited phenomenon and cytocompatibility was proved between these materials and cells; | Nawrotek <i>et al.</i> , 2016 [113] |
| Chitin/CNTs nanofibrillar structure | PC12 cells and RCS96 cells | Three different concentrations of CNTs were used, being the one with 5 %wt the most successful one. PC12 and RCS96 cells were used to test the biocompatibility with promising results; | Wu <i>et al.</i> , 2017 [114] |
| CNT-interfaced Phosphate Glass Fibers | PC12 cells, DRGs; sciatic nerve defect in rat | Carbon nanotubes were successfully interfaced on phosphate glass fibers for nerve guidance and then implemented into a 3-D scaffold which possessed physicochemical integrity with good cell viability and neuronal interactions | Ahn <i>et al.</i> , 2015 [89] |
| SWCNTs in collagen type I-10 % Matrigel™ composite hydrogel | DRGs | Presence of SWCNTs was beneficial due to increased electrical conductivity; | Koppes <i>et al.</i> , 2016 [115] |
| Nanocomposite where MWCNTs, were dispersed in a poly-L-lactic acid matrix | SH-SY5Y cells | The combination of the nanocomposite scaffold and such peptides proved to synergistically boost neuronal differentiation of SH-SY5Y; | Scapin <i>et al.</i> , 2015 [116] |
| Poly-PEDOT and MWCNTs coated on the electrode surface | Coated and un-coated electrodes were implanted on rats DRGs | <i>In vivo</i> model involving stimulation of DRGs Coated electrodes revealed healthier neurons after stimulation; | Kolarcik <i>et al.</i> , 2015 [117] |
| Gold-CNTs electrode | Electrode place in rat sciatic nerve | Amongst the several formulations, the electrode made of gold-CNTs has significant lower impedance and dramatically increases the signal recording resolutions; | Xue <i>et al.</i> , 2015 [118] |
| Residual rubber shielded MWCNTs | NIH3T3 fibroblasts and human neuroblastoma cell line, SH-SY5Y | Neuroblastoma cells revealed amplified filopodia growth in comparison to unetched surfaces and silicone rubber; | Tegtmeier <i>et al.</i> , 2016 [119] |
| MWCNTs-PDMS | Schwann cells and DRGS | Two-fold increase in the viability and proliferation of the neural cells and Schwann cells using the PDMS/MWNT sheet; | Kang <i>et al.</i> , 2015 [120] |

However, these carbon nanomaterials have many extraordinary features to be applied in neuronal repair, namely: (1) are chemically stable and inert, being also biocompatible due to their carbon composition; (2) have nano-scale topography mimicking neural tissues (*e.g.* neurites); (3) enable intracellular permeation for delivery of biomolecules; (4) interact with neuronal cells, *i.e.* by means of promoting cell attachment, differentiation and growth by overall supporting neurite elongation and branching being internalized by neuronal cells, as PC12, Schwann or SH-SY5Y and to guide them; (5) enable to expose neuronal cells to different kinds of stimulus, according to the properties of the applied carbons materials; (6) are cell-friendly allowing neuronal cells adhesion and proliferation; and (7) have bulk electrical properties in accordance with native neuronal tissues (101, 104).

The exact role of CNTs in PNR have not been defined yet but is mainly related to enhancing axon growth rates via electrical stimulation and contact guidance cues, as well as providing structural reinforcement of NGCs. Also, CNTs could be used for localized delivery of growth-promoting molecules (105). The first report on the application of CNTs in the field of neuronal research was published in 2000 by Mattson *et al.* (106). In that work, embryonic rat-brain neurons were grown on MWCNTs and it was observed that on unmodified nanotubes, neurons extend only one or two neurites. By its turn, nanotubes coated with the bioactive molecule 4-hydroxynonenal, allowed neurons to develop multiple neurites and display extensive branching. These findings establish for the first time the feasibility of using CNTs as substrates for nerve cell growth.

Ever since, several works have already demonstrated the significant and profound effects of CNTs in PNR, opening the path for further research (105, 107-111). In **Table III-3**, the main uses of CNTs in PNR are summarized (88-90, 112-120). In 2014, Roberts *et al.* (112) have produced horizontally aligned carbon nanotubes (HACNT) on both film substrates and flat glass coverslips. The HACNT substrates were found to support the growth of primary embryonic rat motor neuron for up to eight days in serum-free culture. Importantly, major neurites were more likely to be oriented parallel to the aligned CNTs. In the same year, Yu *et al.* (88) combined the superior properties of MWNTs with collagen/PCL nanofibers produced by electrospinning. The aim was to evaluate the mechanical effects and efficacy of MWNTs on the electrospun nerve conduit, as well as their biocompatibility and toxicology when applied *in vivo*. Their studies revealed that carboxyl MWNTs could greatly alter the nanofibers' physicochemical properties, such as hydrophilicity,

mechanical properties and degradability. The carbon materials were also able to support SCs adhesion and elongation *in vitro*. In *in vivo* studies, MWNT-enhanced collagen/PCL conduits were shown to effectively promote nerve regeneration of sciatic nerve defect in rats and prevent muscle atrophy without promoting body rejection or serious chronic inflammation, evidencing the potential of this biocomposite NGC.

In 2015, Gupta *et al.* (90), achieved the challenging task of aligning MWCNTs in a Cht scaffold, producing an anisotropic conductive MWCNTs-Cht composite scaffold fabricated using electric field alignment technique. Not only the mechanical properties greatly improved with the incorporation of 0.5 %wt. of aligned MWCNTs, but electrical conductivity increased 100,000 times along its direction. When tested *in vitro*, 50–60 % of HT-22 hippocampal neurons were aligned in the MWCNTs alignment direction of the scaffold with increasing viability over time. With the same materials, Nawrotec *et al.* (113) developed a new straightforward method for obtaining Cht–CNT implants enriched with calcium ions in the form of tubular hydrogels. Both SWCNTs as well as MWCNTs can be incorporated by an electrodeposited phenomenon. Additionally, hydroxyapatite was added once it has been proved to increase neuronal growth due to the increase of calcium concentration. L929 fibroblasts and mHippoE-18 hippocampal cells were tested in pro-inflammatory tests to reveal the cytocompatibility of such NGC intended for PNR.

Both Cht and chitin have been proposed as components of composites containing CNTs, despite their poor solubility. Wu *et al.* (114) developed chitin/CNTs composite hydrogels by dispersing CNTs in chitin previously dissolved in sodium hydroxide/urea aqueous system. The resulting hydrogels exhibited nanofibrillar network with outstanding mechanical properties. Three different concentrations of CNTs were used, being the 5 %wt the most successful concentration showing promising results in terms of biocompatibility when using PC12 and RCS96 cells. In the work of Ahn *et al.* (89) aminated CNTs were chemically linked onto the surface of aligned phosphate glass microfibers (PGFs), as shown in **Figure III-4B**. Then, CNT-interfaced PGFs (CNT–PGFs) were successfully placed into 3D poly (l/d-lactic acid) (PLDLA) porous tubes, by wrapping the CNTs-PGFs onto a PLDLA nanofiber mesh and embedding in a porous PLDLA tube afterwards. This composite scaffold, although effective in restoring motor functions as observed by electrophysiological studies, it did not provide better conditions than those of ANG. Koppes *et al.* (115) also envisioned to use SWCNTs to manipulate the bulk electrical properties of a collagen type I-10 % Matrigel™ composite hydrogel. The researchers tested the effect of the

presence and absence of SWCNTs, as well as the beneficial effects of electrical stimulation or the lack of it. In fact, electrical stimulation and SWCNTs-loaded biomaterials resulted in a 7.0-fold increase in outgrowth relative to the unstimulated, nanofiller-free controls, as seen in **Figure III-4C**.

In a more complex approach, Scapin *et al.* (116) developed a nanocomposite scaffold, where MWCNTs were dispersed in a poly-l-lactic acid matrix, contributing to provide electrical cues and mimic neural topography. Furthermore, to mimic guidance cues and the natural neuronal environment, biomimetic peptides reproducing active motifs from L1 and Leucine-rich repeat and immunoglobulin domain-containing protein 1 proteins were incorporated. These peptides control neurite outgrowth, adhesion, myelination and axon guidance. The combination of the nanocomposite scaffold and such peptides proved to synergistically boost neuronal differentiation of SH-SY5Y. Kolarcik *et al.* (117) aimed to construct a neural electrode capable of *in situ* stimulation of the rat dorsal root ganglion (DRG). For that, authors used the conductive polymer poly(3,4-ethylenedioxythiophene) (PEDOT) and MWCNTs, which were coated on the electrode surface and doped with dexamethasone. In fact, results showed that coated microelectrodes have lower *in vitro* and *in vivo* impedance values. Significantly less neuronal damage was observed with coated electrodes as compared to non-coated controls. The inflammatory response with the PEDOT/CNT-coated electrodes was also reduced, demonstrating the advantage of including MWCNTs in such devices.

In field of electrodes for recording PNs signals, Xue *et al.* (118) developed a novel polyimide-based C-shaped neural interface electrode. Amongst the several formulations, the gold-CNTs made electrode had significant lower impedance values and dramatically increased the signal recording resolution, when compared to CNTs-free electrodes. Tegtmeier *et al.* (119) developed an active neural implant by immersing MWCNTs in silicone rubber and re-etching the surface. Since rubber presents toxic substances, residual rubber was reduced to an estimated layer of only 13 nm covering the CNTs and thus securing them to the electrode material. Impedance measurements confirmed the etching success. NIH3T3 fibroblasts and human neuroblastoma SH-SY5Y cell lines were used to prove the adequate biocompatibility of the neural implant. Inclusively, neuroblastoma cells also revealed amplified filopodia growth in comparison to non-etched surfaces and silicone rubber. Kang *et al.* (120) studied the applicability of MWCNTs mixed with polydimethylsiloxane (PDMS) sheet to promote primary neuronal cells proliferation, by

incorporating MWCNTs in PDMS using a simple printing transfer method. The results showed increased mechanical properties and roughness, as well as superior electroconductivity when compared to PDMS sheets alone. The developed material increased adhesion and proliferation of primary DRGs, as well as SCs, in a higher extent when compared to poly-L-lysine (PLL) coated dishes, which are commonly used to increase cellular attachment.

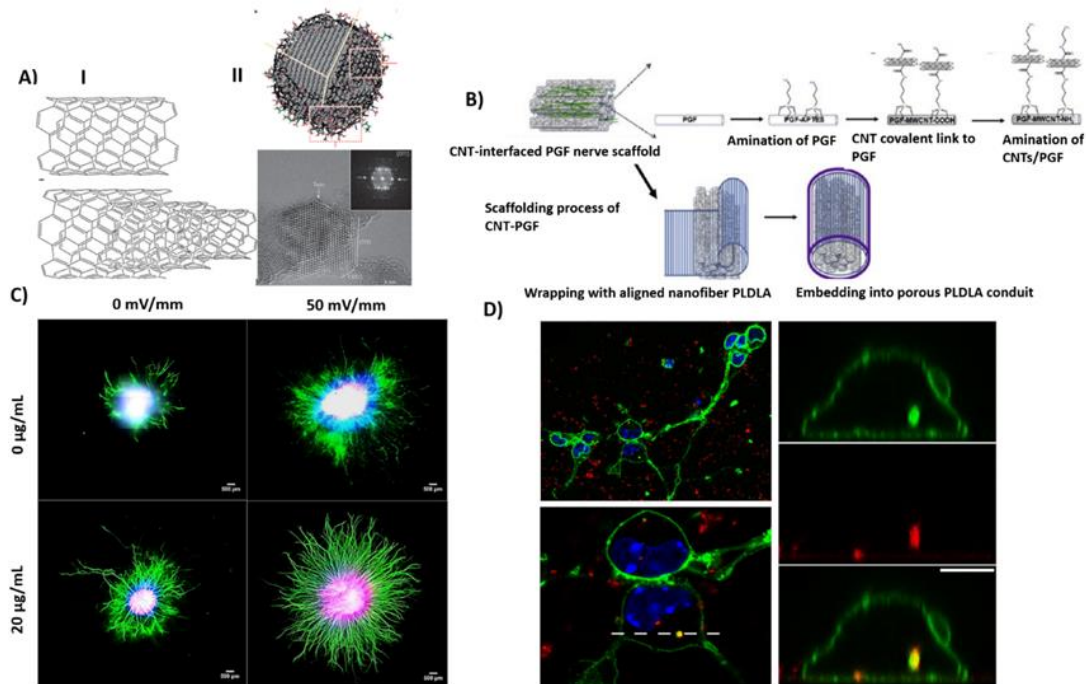


Figure III-4 - Carbon nanomaterials structure and their application of in peripheral nerve regeneration. A) (I) Single and multi-walled carbon nanotubes schematic structure. (II) Nanodiamond schematic structure; B) Schematic representation of the aligned PGF bundle interfaced with carbon nanotubes for neurite outgrowth; C) DRGs neurite outgrowth can be promoted by 50 mV/mm electrical stimulation or inclusion of 20 $\mu\text{g}/\text{mL}$ SWCNTs. The occurrence of both has a synergistic effect; D) Fluorescent nanodiamonds internalized into dissociated neurons. Confocal image of dissociated mouse cortical neurons cultured in the presence of 20 $\mu\text{g}/\text{mL}$ fluorescent Nanodiamonds, stained with Alexa Fluor 488-conjugated concanavalin-A and DAPI. Reprinted and adapted from A) (I) [352] and (II) [151]; B) [89]; C) [115]; D) [158].

The downside of the use of carbon nanomaterials for PNR relies in their toxic nature (121). Their physicochemical properties could make them toxic for living organisms or the environment (122). Mechanisms of toxicity include membrane damage, DNA damage, oxidative stress, changes in mitochondrial activity and altered intracellular metabolic routes (122). CNTs have a highly hydrophobic surface and a non-biodegradable nature that contributes to their reduced biocompatibility, limiting their application in the biomedical field, with growing concerns about

their chronic toxicity (122). Presently, there are controversial results regarding carbon nanomaterials toxicity, as some publication reported that carbon materials are toxic for neuronal-related cells. For instance, MWCNTs seem to inhibit neuronal differentiation of PC12 cells (123) and SH-SY5Y (124). Moreover, Wu *et al.* (125) reported that exposure of DRG cultures to MWCNTs compromises regenerative axonogenesis (125). Additionally, respiratory toxicity is the main concern when carbon nanomaterials are used (126, 127). Nevertheless, many other works report non-toxic effects both in *in vivo* and *in vitro* (88, 114). Meanwhile, it was reported that MWNTs are likely to be a more neural-friendly interface than SWNTs, since they allow for a wider external surface and effective functionalization (128). What is important to state is that before transposing carbon-based nanotechnology to the clinics, scientists must be critical in assessing its possible toxicity.

III-3.1.2. Graphene

Graphene belongs to one of the allotropic forms of carbon. This two-dimensional planar monolayer nanomaterial composed of SP²-bonded carbon atoms is by norm arranged in a honeycomb form with carbon to carbon interatomic length, also possessing a number of amazing mechanical, optical and conductive properties (129). The intensive research on the biological applications of graphene and its derivatives is based on its several fascinating properties, such as high specific surface area (2,630 m²/g), exceptional electric conductivity, thermal conductivity ($\approx 5,000$ W/m/K), mechanical strength (Young's modulus, $\approx 1,100$ GPa), intrinsic biocompatibility, low cost and scalable production, and facile biological/chemical functionalization of graphene oxide (130). In its elementary form, graphene can also be used to aid in PNR. However, due to the fact that the surface of graphene lacks functional groups, it is difficult to dissolve in solvent and can easily agglomerate. Therefore, in many works, graphene oxidized (GO) is used, since its surface is rich in functional groups containing oxygen (131). **Table III-4** overviews the works showing the application of graphene in PNR (132-142).

Li *et al.* (132) developed a GO/polyacrylamide (GO/PAM) composite hydrogel fabricated by in-situ free radical polymerization. The GO/PAM composite hydrogel with 0.4 % GO could effectively enhance the attachment and proliferation of SCs and release higher amounts of growth factors and larger matrix adsorption than other samples with different amounts of GO.

Baniasadi *et al.* (133) were responsible for the development of a porous conductive Cht/gelatin scaffold containing polyaniline/graphene (PA-Graphene) nanocomposite. The effects of PA-Graphene content showed that the electrical conductivity and mechanical properties increased proportionally to the increase in PA-Graphene loading, while the porosity, swelling ratio and *in vitro* biodegradability decreased.

Table III-4 - The use of graphene applied to peripheral nerve regeneration.

| Type of graphene nanomaterial | Cell type or animal model | Main results | Year, References |
|--|---------------------------|---|--|
| Graphene/hydrogel | Schwann cells | GO/PAM composite hydrogel with 0.4 % GO enhanced the attachment and proliferation of Schwann cells; | Li <i>et al.</i> , 2016 [132] |
| Conductive Graphene nanoparticles | Schwann cells | Construct containing 2.5 %wt. of PAG revealed to be the most suitable in terms of Schwann cell adhesion; | Baniasadi <i>et al.</i> , 2016 [133] |
| Graphene-based electrode | MSCs | Differentiation of MSCs into Schwann cell-like phenotypes through an electrical stimulus, without the need of additional chemical growth factors; | Das <i>et al.</i> , 2017 [134] |
| Polypyrrole functionalized graphene (PPy-Graphene) | Retinal ganglion cells | PPy-Graphene based aligned nanofibers were fabricated for guided growth and electrical stimulation of RGCs. Significantly enhanced viability, neurite outgrowth and anti-aging ability of RGCs were observed after electrical stimulation; | Zhao <i>et al.</i> , 2016 [135] |
| GO-coated PLLA electrospun nanofibers | Schwann cells, PC12 cells | The GO coating improved properties of the simply aligned PLLA nanofibrous mesh, including surface roughness and hydrophilicity. Also, it significantly promoted SCs growth and regulated cell orientation, and induced PC12 cells differentiation and neurite growth; | Zhang <i>et al.</i> , 2016 [136] |
| Electrospun graphene-silk fibroin composite | L929 cells, Schwann cells | 10 %wt. of graphene in the nanofibrous mesh was selected as the optimized one, as this specific concentration allowed cell viability and cell attachment; | Zhao <i>et al.</i> , 2017 [137] |
| Electrospun silk fibroin scaffolds coated with reduced GO | PC12 cells | The coating with GO improved the adhesion of cells. The use of SF/GO scaffolds combined with electrical stimulation promoted the differentiation into neural phenotypes more than treatment with NGF; | Aznar-Cervantes <i>et al.</i> , 2017 [138] |
| Hybrid Gr nanosheets-sodium alginate (SA)/polyvinyl alcohol (PVA) (Gr-AP) fibrous scaffold | PC12 cells | Successfully developed hybrid graphene incorporated alginate/PVA fibrous scaffolds in which the best amount of graphene was 1 %wt; | Golafshan <i>et al.</i> , 2017 [139] |
| Graphene oxidized combining with decellularized rat sciatic nerve defect (allograft) | Rat sciatic nerve defect | GO nanomaterial could combine with allogeneic sciatic nerve decellularized scaffold to facilitate nerve regeneration; | Wang <i>et al.</i> , 2017 [140] |
| Graphene oxide foam layers with thicknesses of ~15–50 μm | hNSCs | Rolled GOFs were developed as electrically conductive 3D-scaffolds with desirable large-scales and utilized in directional growth of neural fibers under electrical stimulations; | Akhavan <i>et al.</i> , 2016 [141] |

| | | | |
|---|--------------------------|---|----------------------------------|
| poly(ϵ -caprolactone) tubular prosthesis associated with nanoparticles of carbon and graphene | Rat sciatic nerve defect | Nanocomposite PCL tube enables nerve repair and results in better regeneration; | Assaf <i>et al.</i> , 2017 [142] |
|---|--------------------------|---|----------------------------------|

Overall, the construct containing 2.5 %wt. of PA-Graphene revealed to be the most suitable in terms of SCs adhesion, and therefore the most promising for PNR. Das *et al.* (134) reported for the first time a method that allows the differentiation of mesenchymal stem cells (MSCs) into a SC-like phenotype through electrical stimuli, without the need of additional chemical growth factors. Such differentiation was carried out on a flexible, inkjet-printed graphene interdigitated electrode. This work opened doors to the scalable nano-manufacturing of graphene and graphene-based circuits with complex geometries on virtually any substrate, including flexible and degradable polymers.

Nanofibers are considered a very promising type of scaffold for the integration of graphene. Zhao *et al.* (135) synthesized polypyrrole functionalized graphene (PPy-Graphene) by using for the first time a simplistic but effective polymerization-enhanced ball milling method, which is an environmental-friendly, easy to be controlled and efficient method for preparing functionalized graphene. Such strategy can be envisioned for application as a retinal electronic implant to repair the damage of optic nerve, which is mainly derived from the atrophy, apoptosis or death of retinal ganglion cells (RGCs). Following the polymerization reaction, PPy-Graphene based aligned nanofibers were fabricated and designed to act as guiding cues and permit electrical stimulation of RGCs. This successful approach significantly enhanced viability, neurite outgrowth and anti-aging ability of RGCs after electrical stimulation. Zhang *et al.* (136) also fabricated GO nanosheets with topological structure of aligned nanofibrous for PNR applications. However, these differ from the above since the GO nanosheets were coated onto aligned and aminolyzed poly-L-lactide (PLLA) nanofibrous scaffolds produced by electrospinning. The GO coating improved several properties of the simply aligned PLLA nanofibrous mesh, including surface roughness and hydrophilicity. Further than that, it significantly promoted SCs growth, regulated cell orientation and induced PC12 cells differentiation and neurite growth. Zhao *et al.* (137) were able to obtain graphene/silk fibroin (SF) based nano-membranes acquired by electrospinning technique. Graphene percentage varied from 0 %wt. to 20 %wt., however a concentration of 10 %wt. of graphene in the nanofibrous mesh was selected, since it allowed cell viability and attachment, supporting the survival and growth of SCs with no significant cytotoxic effects. In a similar approach, Aznar-Cervantes *et al.* (138) reported promising results that indicate the potential use of electrospun SF scaffolds coated with reduced GO for neural tissue engineering. The stimulus provided by the reduced GO alone induced a significant differentiation level of PC12 cells to

neuronal-like phenotype, which can even increase by application of electrical stimulation. By this manner, the neurite outgrowth was more pronounced when electric currents are applied to the cell cultures when compared to the traditional treatment with nerve growth factor (NGF).

Golafshan *et al.* (139) developed hybrid graphene incorporated alginate/PVA fibrous scaffolds with varying amounts of graphene (up to 5 %wt.), using an electrospinning approach for engineering nerve tissue. The authors found that the incorporation of 1 %wt. of graphene in the nanosheets enhanced the toughness and strength of the scaffolds by 4- and 3-fold, while tensile modulus did not significantly vary. Moreover, the addition of graphene upon 1 %wt. resulted in a significant reduction in impedance value, meaning higher electrical conductivity, which is advantageous for PNR. Wang *et al.* (140) innovatively prepared GO through improving Hammer's Method and combining it with decellularized scaffold of a sciatic nerve of rats. The GO/decellularized scaffold was used to bridge a 10 mm gap of injured sciatic nerve. Such operation was conducted by using the oscillation mixing method. It has been proved that GO nanomaterial could be associated with allogeneic sciatic nerve decellularized scaffold to induce nerve regeneration. The regeneration parameters evaluated, *i.e.* sciatic nerve action potentials, thickness of myelin sheath, diameter of axon and dominated muscle rehabilitation level, revealed that the regeneration of the nanomaterial group were significantly higher than the blank group.

Graphene foams have successfully been developed and suggested as 3D scaffolds providing an adequate support with the desired topographies for differentiation of cells (143). Akhavan and colleagues, (141) firstly fabricated graphene oxide foam (GOF) layers with thicknesses of $\approx 15\text{--}50\ \mu\text{m}$ and density of ≈ 10 graphene oxide. Then, the GOF layers with desirable scales were rolled to obtain 3D scaffolds with capability of inducing directional proliferation and differentiation of neurons along the main axis of the rolls. After seeding human neural stem cells (hNSCs) and proceeding with electrical stimulation, increased hNSCs proliferation rates and accelerated differentiation into neurons was observed, as compared to the differentiation into glial cells. Assaf *et al.* (142) combined both graphene and carbon NPs to enhance the properties of a tubular conduit made of PCL. Despite the final conduit transparency and adequate mechanical properties, which allowed the correct alignment of the stumps, the gap was not a critical gap presenting only 3 to 4 mm between the nerve ends, therefore not permitting a correct evaluation of the results.

III-3.1.3. Carbon nanofibers

Carbon nanofibers (CNFs) are other type of carbon nanomaterials, such as vapor grown carbon nanofibers (144) and carbonization of polymer based nanofibers produced in the electrospinning process (145) that are manufactured using different methods. These nanofibers are characterized as non-microporous graphitic materials with a high surface area (100–200 m²/g), high purity and tunable surface chemistry (146). They have been investigated for numerous applications due to their unique physical properties, such as high strength, low density, metallic conductivity, tunable morphology, chemical and environmental stabilities, as well as compatibility with organo-chemical modification (147).

Being the less explored carbon nanomaterials, especially for PNR applications, CNFs were developed by Shilpee and colleagues, (148) using electrospinning technique. Their effect on SCs fate was studied when seeded on amorphous carbon substrates, depending on the evolution of intracellular oxidative stress. That results are encouraging, as evidenced that CNFs own a conducting nature and their fibrous structure can provide directional growth to axons, facilitating SCs proliferation and growth. The level of reactive oxygen species was not high enough to induce apoptosis in all the culturing periods tested on carbon fibrous and film substrates. Wei Zhu *et al.* (149) developed novel carbon nanofibrous scaffolds by annealing electrospun mats at elevated temperature, whose graphitic structure generated by annealing rendered superior electrical conductivity. When subjected to electrical stimulation, neural stem cell proliferation was promoted, while an up-regulated neuronal gene expression level and increased expression of microtubule-associated protein 2 were detected, thus demonstrating an improved neuronal differentiation and maturation.

III-3.1.4. Nanodiamonds

Nanodiamonds (NDs) were termed for the first time by researchers in World War II in 1963, as detonation investigations with carbon-based explosives were being implemented and 4-5 nm diamond particles accompanied by graphite and other non- diamond carbon particles were found (150). NDs are an evolving type of carbon nanomaterials which holds a distinctive set of properties, either at a chemical, physical, and biological level. Its generic structure can be

appreciated in **Figure III-4AII**. Above all, they are considered to be completely non-toxic, making them suitable for biomedical applications (151). Such intrinsic physicochemical properties are indispensable and allow designing innovative therapies in several areas of the medical field, such as delivery of therapeutic molecules, and many applications in TE and imaging (152).

In what concerns drug delivery, NDs are promising materials because of their high surface area to volume ratio and surface chemistry, which permits the stocking of molecules in their amine groups, as well as in other polar moieties. The phenomenon occurs by physical adsorption, allowing drugs and other molecules of interest to be non-covalently linked to NDs (151). This simplistic loading process is effective and does not involve the usually hard and time-consuming processes of chemical modification (153). Another major advantage of NDs is that they are promptly internalized by cells but do not undergo an immediate exocytosis. Therefore, bioactive molecules stay within the cell for an improved therapeutic effect (154). Similarly, to other carbon nanomaterials, NDs have also been used as nano-fillers to strengthen the mechanical properties of composite implantable biomaterials.

The number of advantages of NDs increased, as the optical properties of fluorescent NDs (FNDs) allowed their use as imaging probes (155). These properties permit the location of such NPs within living organisms. Finally, the high biocompatibility of NDs when compared to the above mentioned carbon nanomaterials (*e.g.*, SWCNTs, MWCNTs, graphene), translates into a great advantage for NDs and increases the probability of such carbon materials to be translated to the clinical practice (156). Although NDs' mechanical and electrical properties seem suitable for PNR applications, there are not many works publications describing the use of this promising technology. These properties combined with the aforementioned ones, make NDs an encouraging environment for neuronal networks. **Table III-5** summarizes the most relevant reports describing the use of NDs in PNR (157-162). Interestingly, Thalhammer *et al.* (163) first tested a NDs monolayer coating surface to promote the formation of functional neuronal networks, achieving extraordinary results that proved that detonation-derived NDs exhibit encouraging similarity to protein-coated materials in what concerns neuronal cell attachment, neurite outgrowth and functional network formation. Furthermore, cell-autonomous neuronal excitability and functionality of the resulting electrical networks demonstrated the potentiality of this type of coating. More recently, Hopper *et al.* (157) were able to produce amine functionalized NDs, which were studied as substrates for neuronal cell culture.

Table III-5 - The use of nanodiamonds applied to peripheral nerve regeneration

| Type of nanodiamonds | Cell type or animal model | Main results | Year, Reference |
|---|---|---|-----------------------------------|
| Amine functionalized ND | NG108-15 neuroblastoma cells, SCs, DRGs | Amine-terminated surface NDs proved to be a suitable substrate since it promoted neuronal cell adhesion, proliferation and neurite outgrowth; | Hopper <i>et al.</i> , 2014 [157] |
| Fluorescent ND | Hippocampal neurons and DRGs | Fluorescent ND did not induce cytotoxicity in primary neurons from CNS or PNS. However, interfere with neuronal morphogenesis; | Huang <i>et al.</i> , 2014 [158] |
| ND ink | Not applicable | ND solutions can be used instead of proteins and factors that are commonly used for cell guiding patterning; | Tong <i>et al.</i> , 2015 [159] |
| 3D-nanostructured boron doped ND | Spinal cord and hippocampal cell cultures | 3D-nanostructured BDD offers good performances for neural recording and stimulation; | Piret <i>et al.</i> , 2015 [160] |
| Nitrogen included ultra-nanocrystalline diamond | Rat cortical neurons | The fabricated neural interfaces exhibit high efficacy, long-term stability and a healthy neuron/electrode interface; | Tong <i>et al.</i> , 2016 [161] |
| Micro-textured nanocrystalline diamond | Inner-ear neuron of human and mouse origins and ReNcell (a human neural progenitor cell line) | The findings demonstrate that regenerating auditory neurons show a strong affinity to the NCD pillars, and the technique could be used for neural guidance and the creation of new neural networks; | Cai <i>et al.</i> , 2016 [162] |

The obtained results indicated that these functionalized NDs (FND) are beneficial for *in vitro* neural cell culture and can be regarded as possible coatings for *in vivo* neural implants. The NDs were able to support the growth of primary SCs and DRGs neurons with the correct phenotype over three weeks of *in vitro* culturing. In the same year, Huang *et al.* (158) reported for the first time the influence and application of FNDs on the nervous system. Neurons were treated with FNDs particles, which did not induce cytotoxicity in primary neurons from either CNS or PNS. Furthermore, the neuronal uptake of FNDs was confirmed, as seen in **Figure III-4D**.

Nevertheless, it was found that FNDs caused a decrease in neurite length in both CNS and PNS neurons. These outcomes proved that FNDs exhibit low neuronal toxicity but in fact, have the power to interfere with neuronal morphogenesis. This must be considered when the application of FNDs involves the growing of neurites, such as in PNR. In a different approach, Tong *et al.* (159) presented a method for fabricating a diamond platform with the goal to direct neural cell adhesion. Micro-contact printing was used for selective NDs seeding and chemical vapor deposition was conducted subsequently to form NDs patterns. As a result of this work, it was observed that NDs solutions can be used in replacement of proteins and factors that are commonly used for cell patterning with good alignment results.

In the field of neural implants and neuroprostheses, Piret *et al.* (160) aimed at developing a platform that exhibits high capacitance and appropriately contacts with neurons to provoke real neural responses at low voltages. For such, they developed a 3D-nanostructured boron doped NDs platform. This interface allowed neural cell attachment, survival and neurite extension, after experiments with spinal cord and hippocampal cell cultures. Particularly, the platform allowed the detection of low amplitude in the range of 10–20 μV local-field potentials. These properties are found to be extremely valuable for the fabrication of diamond neural interfaces with the predictable long-term steadiness of diamonds at the same time supporting the life of healthy neurons. In the same field, Tong *et al.* (161) reported on a new high capacitance material fabricated using nitrogen - ultra nanocrystalline diamond, which was treated with oxygen plasma, resulting in increased charge injection capacity. Rat cortical neurons were used *in vitro* to measure its biocompatibility. Surface roughness was found to be critical for healthy neuron growth, with best results observed on surfaces with a roughness of approximately 20 nm. Overall, the authors provided a method of producing a ND electrode that is optimized for both high charge injection capacity and neuronal biocompatibility.

In the field of cochlear implants for patients with profound hearing loss due to neuronal deficits, Cai *et al.* (162) developed micro-textured nanocrystalline diamond (NCD) surfaces on cochlear implants electrode arrays, where the surface consisted in micrometer-sized pillars (size $5 \times 5 \mu\text{m}^2$). When using human and murine inner-ear ganglion neurites and a neural progenitor cell line, the results showed that these cells can attach to patterned NCD surfaces without any ECM coating. These findings demonstrated that regenerating auditory neurons have a solid affinity to the NCD pillars and the technique could be used for neural guidance and the creation of new neural networks.

III-3.2. Nanoparticles

In the last years, researchers have been proposing the use of NPs for neural regeneration approaches (164). There are several benefits offered by NPs, such as their small size, physical properties that diverge from the bulk, surface functionalization and chemical stability. They also differ from other nano-sized particles in their electrical charge, magnetic and optical properties (165). These nano-sized biomaterials are mainly envisioned as carriers for targeted and controlled delivery of drugs and other biological molecules such as growth factors, both *in vitro* and *in vivo*. Antibodies, labeling probes, hydrophobic or hydrophilic molecules, DNA and oligonucleotides are other types of molecules that can be linked to NPs, allowing a tailored application for the desired purpose, such as drug delivery or cell tracking and monitoring (166, 167). This versatility is mostly a result of the wide range of approaches that can be used for NPs functionalization. Furthermore, NPs are widely used to enhance the properties of scaffolds, as mechanical properties and degradation rate in several TE applications. When it concerns to neuronal regeneration, NPs can be used with different purposes, as enhancing neuronal differentiation (168), stimulating neuronal regeneration and survival (169), manipulation of neuronal electrical activity (170, 171) or allowing imaging and theranostics (172). NPs will be divided according to their composition in two main categories, inorganic and organic, and the most significant reports overviewed herein.

III-3.2.1. Inorganic NPs

Inorganic nanomaterials are being widely exploited for nerve regeneration applications. Within this field, gold (Au), zinc (Zn), silver (Ag) and silica-based NPs (SiO₂-NPs) are the ones that have been attracting a great deal of attention. **Table III-6** summarizes the most significant works describing the use of inorganic NPs applied in PNR (169, 173-194).

III-3.2.1.1 *Magnetic NPs*

Magnetic elements in the nanometer scale (*e.g.* iron, nickel, cobalt and their oxides), are being used in different biomedical applications (195). One characteristic that is modified when iron becomes a nano-scale material is its magnetism. Reducing the size of iron as a bulk material to the nano-scale level results in superparamagnetic behavior. Superparamagnetic iron NPs (SPIONs) are non-magnetic particles until they are exposed to a strong magnetic field. If the magnetic field is removed, they revert to a non-magnetic state again (177). Several approaches have been using these magnetic NPs (MNPs) in the last few years (196, 197). The main advantages rely on the fact that MNPs-loaded cells can be directed to specific sites in response to an external magnetic field gradient and the possibility of imaging through MRI. **Figure III-5** captures some of the most interesting results related to the use of MNPs applied to PNR. In 2014, Riggio *et al.* (173) developed and validated a non-invasive approach for physical guidance of nerve regeneration based on the synergic use of MNPs allied to the appliance of magnetic fields. These MNPs demonstrated to be able to trigger PC12 differentiation into a neuronal phenotype. Above all, these authors evidenced that mechanical tension created by the MNPs and the magnetic field can induce “stretch growth” of neurites process initiation, as depicted in **Figure III-5A**. Marcus *et al.* (174) studied the interactions of four different types of iron oxide MNPs with PC12 cells and have shown that cell uptake is highly sensitive to the MNPs type and incubation conditions. The researchers demonstrated that uncoated maghemite MNPs led to maximal cellular penetration, thus proposing these particles as efficient candidates for magnetic-based neuronal manipulations. Huang *et al.* (175) developed a way to improve the therapeutic potential of SCs, which consisted in magnetically drive SCs to migrate across the astrocyte-SC boundary to interact with astrocytes (**Figure III-5B**). To achieve that, SCs were firstly magnetized with PLL-coated SPIONs.

Table III-6 - The use of inorganic nanoparticles applied to peripheral nerve regeneration.

| | Type of nanoparticle | Cell type or animal model | Main results | Year, References |
|--------------|---|--|---|--|
| Magnetic NPs | PEI-coated Fe ₃ O ₄ NP | PC12 differentiation | MNPs direct the neurite outgrowth preferentially along the direction imposed by an external magnetic field; | Riggio <i>et al.</i> , 2014 [173] |
| | Maghemite (γ -Fe ₂ O ₃) fluorinated magnetic NP and Magnetite (Fe ₃ O ₄) core particles with different coatings | PC12 cells and SHSY-5Y cells | MNPs control neurite growth orientation of primary neurons along the process of neural network formation; | Marcus <i>et al.</i> , 2016 [174] |
| | SPIONs | SCs and astrocytes | SPION-mediated forces could act as powerful stimulants to enhance the migration of SCs across the astrocyte-SC boundary; | Huang <i>et al.</i> , 2017 [175] |
| | MNP (Fe ₃ O ₄)-chitosan mixture was fabricated into membranes or scaffolds | SCs | Magnetic nanocomposites containing 10 %wt MNPs were able to support SCs adhesion and spreading under magnetic field exposure. Same concentration of MNPs, increased the gene expression and protein secretion of BDNF, GDNF, NT-3, and VEGF; | Liu <i>et al.</i> , 2014 [176] |
| | MNP (Fe ₃ O ₄)-chitosan scaffold (same author as previous) | SCs; rat sciatic nerve defect | The magnetic chitosan scaffold synergized with the magnetic field enhanced the viability of SCs. The same scaffold loaded with SCs in addition to the magnetic field promoted nerve regeneration and functional recovery; | Liu <i>et al.</i> , 2017 [198] |
| | SPIONs | MSCs single cells or spheroids; rat sciatic nerve defect | Compared to MSC single cells, the pristine or BDNF-transfected MSC spheroids significantly promoted the functional recovery of animals; | Tseng <i>et al.</i> , 2014 [178] |
| | Nanohydroxyapatite coated Fe ₃ O ₄ magnetic NP | DRGs | (n-HA) coated Fe ₃ O ₄ can successfully increase cell viability and promote axonal elongation. Also, Netrin-1 axonal guidance cues rise significantly after treatment with n-HA-coated Fe ₃ O ₄ ; | Liu <i>et al.</i> , 2015 [179] |
| | Polyethylenimine -coated (Fe ₃ O ₄) NPs | PC12; zebrafish; rat sciatic nerve defect | MNPs functionalized with NGF and VEGF accelerated the regeneration process and recovery of motor function; | Giannaccini <i>et al.</i> , 2016 [180] |
| | SPIONs | DRGs | NGF releasing PLLA/iron oxide composite-NPs can direct neurite outgrowth and composite-NPs can be positioned by external magnetic field gradients; | Zuidema <i>et al.</i> , 2015 [181] |
| | SPIONs | L929, DRGs | With the aid of SPIONs and a magnetic field, the micro-structure of an hydrogel could be aligned, which in turn aligned the neurites of the | Rose <i>et al.</i> , 2017 [182] |

| | | | DRSs; | |
|---------------------|---|--|--|-------------------------------------|
| Metallic NPs | Gold nanorods | NG108-15 neuronal cells | NG108-15 cells were cultured with both bare and coated Au NRs and then irradiated with 1.2-7.5 W/cm ² at 780 nm, which showed a neurite length increase of up to 25 μ m versus control; | Paviolo <i>et al.</i> , 2013 [183] |
| | Gold nanorods | NG108-15 neuronal cells | When NG108-15 neuronal cells were exposed to the NIR light of 780 nm laser diode, it was found to induce intracellular Ca ²⁺ transients; | Paviolo <i>et al.</i> , 2014 [184] |
| | Polyethylenimine -coated gold-NPs | PC12 cells | Pulsed current stimulation induced neurite outgrowth of PC12 cells to the AuNPs coated surfaces, thus proving the potential of AuNPs as an electrically conductive matrix for nerve regeneration; | Adel <i>et al.</i> , 2017 [185] |
| | Gold-NP adsorbed in electrospun silk fibroin nanofibers | SCs; rat sciatic nerve injury | AuNP-silk fibroin nanofiber noticeably decreases the resistance of an electrically insulating material like silk; | Das <i>et al.</i> , 2015 [186] |
| | AuNPs modified with 6-mercaptopurine (6MP) and a neuron-penetrating peptide | SH-SY5Y cells | Seeded SH-SY5Y cells in a surface coated with 6MP-AuNPs-RDP, are capable of internalizing NP, which led to a significant increase of neurite growth; | Xiao <i>et al.</i> , 2017 [187] |
| | Gold nanoparticles/Polyvinylidene fluoride (PVDF) composite electrospun mat | PC12 cells | Au NPs/PVDF composite nanofibers have the ability to stimulate the growth and adhesion of neuronal cells; | Motamedi <i>et al.</i> , 2017 [188] |
| | Chitosan-zinc oxide nanocomposite conduit | Rat sciatic nerve defect | Chitosan-zinc oxide nanocomposite conduit resulted in acceleration of functional recovery and quantitative morphometric indices of sciatic nerve; | Iman <i>et al.</i> , 2017 [189] |
| | PCL electrospun matrix with variable quantities of zero valent zinc NPs | Human primary fibroblasts and U87 brain glioblastoma cell line | Low concentrations of Zn-NPs promoted neuronal regeneration and showed relatively non-toxic characteristics to fibroblasts; | Aydemir <i>et al.</i> , 2017 [190] |
| | Silver NPs | SH-SY5Y cells | The analysis of single neurite level reveals increased neurite formation and growth, better than on the AuNP and ZnONP substrates or smooth substrates; | Alon <i>et al.</i> , 2014 [169] |
| Silica NPs | SiO ₂ -NPs | Guinea pigs | Significantly greater survival of SGNs in cochleae that received BDNF. supraparticles were well tolerated; | Wise <i>et al.</i> , 2016 [191] |
| | SiO ₂ -NPs encapsulated within a lipid bilayer and modified with the atoxic subunit B of the cholera toxin (CTB) | Motoneuron-like NSC-34 cells and L6 muscle cells | SiO ₂ -NPs functionalized with CTB showed greater motor neuron uptake when compared to unmodified lipid bilayer (60 % vs. 15 %, respectively); | Porrás <i>et al.</i> , 2016 [192] |

| | | | | |
|--|---|--------------------------|---|------------------------------------|
| | Aligned poly lactic- PLGA and PLGA/gelatin nanofibrous scaffolds embedded with mesoporous SiO ₂ -NPs | PC12 | Cellular proliferation on PLGA and PLGA/gelatin with SiO ₂ -NPs were higher than that on the aligned pure PLGA scaffolds; | Mehrasa <i>et al.</i> , 2015 [193] |
| | SiO ₂ -NPs encapsulated with Tetrodoxin | Rat sciatic nerve defect | The proved sustained release properties of hollow SiO ₂ -NPs contributed to the extension of nerve block and enhanced safety by slowing release; | Liu <i>et al.</i> , 2017 [194] |

As a result, magnetized SCs exhibited enhanced migration along the direction of force in the presence of a magnetic field. It was also demonstrated that SPION-mediated forces could act as powerful stimulants to enhance the migration of SCs across the astrocyte-SC boundary, via integrin-mediated mechano-transduction.

Using the same kind of strategy of combining magnetically responsive MNPs and a magnetic field, Liu *et al.* (176) prepared MNPs–Cht/glycerophosphate membranes and scaffolds and explored whether such magnetic nanocomposites would regulate SCs biological activities via application of magnetic fields. It was observed that magnetic nanocomposites containing 10 % MNPs were able to support cell adhesion and spreading and further promote proliferation of SCs under magnetic field exposure. Interestingly, a magnetic field applied through the 10 % MNPs scaffold significantly increased the gene expression and protein secretion of brain-derived neurotrophic factor (BDNF), glial derived neurotrophic factor (GDNF), neurotrophin-3 (NT-3) and VEGF. Later on, the same authors proved that the same scaffolds had modest magnetization and proper degradation rate, making them suitable for cellular distribution and new axon regeneration (198). After loading the scaffold with SCs and exposure to a magnetic field, it was observed a synergistic improvement of nerve regeneration and functional recovery *in vivo*, by increasing the distribution efficiency and viability of SCs.

Tseng *et al.* (178) combined the cell transplantation strategy with the use of spheroids and the incorporation of SPIONs. The authors investigated the effect of the substrate-derived MSC spheroids versus single cells on the regeneration of transected rat sciatic nerve (**Figure III-5D**). This effect was evaluated after injection of Fe₃O₄NPs-labeled MSC spheroids into microporous nerve conduits made of polylactide acid (PLA). With this strategy, MRI could be employed to trace the distribution and migration of these spheroids *in vivo*. Furthermore, authors also delivered BDNF gene to MSC spheroids and evaluated the efficacy of BDNF-transfected spheroids on nerve regeneration across the gap defect, which showed significant functional recovery. Liu *et al.*, (179) explored for the first time the use of hydroxyapatite-coated MNPs to enhance neuronal regeneration in injured nerves. For that purpose, the experiments were carried out on cultured rat DRG neurons and the results showed that n-HA-coated magnetic NPs (Fe₃O₄-n-HA) can effectively increase cell viability and promote axonal elongation. Interestingly, the authors have also demonstrated by Western blot that Netrin-1 axonal guidance cues significantly increase after n-HA-coated magnetic NPs treatment. Gianaccini *et al.* (180) reported on the ability to immobilize

NGF and VEGF on MNPs for controlled release, both *in vitro* and *in vivo*. Bioactivity tests were performed to induce a neuronal-like phenotype in PC12 cells with NGF and neo-angiogenesis in a zebrafish model with VEGF. Afterwards, a neurotmesis of the rat median nerve was made in which the two nerve stumps were sutured to the ends of a synthetic conduit filled with the particles. In conclusion, there was an increase in the stability of growth factor concentration and delivery, mediated by MNPs. Its use is responsible for the enhanced neuroprotective effects of VEGF and NGF in the MNPs group as compared with the control group. Zuidema *et al.* (181) established a composite-NPs to create NGF gradients at specific locations within a tissue culture dish to direct neurite extension. The composite nanoparticle was fabricated by combining NGF-releasing PLLA NPs with iron oxide MNPs, which were manipulated by the administration of an external magnetic field gradient, through the modification of water/oil/water double emulsion technique. NGF-composite-NPs was afterwards combined with aligned PLLA microfibers to create a biomaterial approach that utilizes both topography and chemotropic gradients to direct extending neurites. In brief, the authors have demonstrated that magnetic, NGF releasing PLLA/iron oxide composite-NPs can direct neurite outgrowth and that composite-NPs can be positioned by external magnetic field gradients, and release NGF for up to 6 days. This can be seen in **Figure III-5C**. Also in combination with other materials, namely injectable hydrogels, Rose *et al.* (182) developed the first biomaterial that can achieve *in situ* highly controlled and ordered structures after injection to guide cell and nerve growth. Those are magnetoceptive, anisometric microgels that were applied as building blocks to create a unidirectional structure, with the aid of magnetic fields. For such, microgels were doped with small quantities of SPIONs, allowing alignment by external magnetic fields in the milliTesla order, in which DRGs neurites were stimulated, to grow and align.

III-3.2.1.2 *Other metallic NPs*

Metallic NPs are predominantly striking because of their unique optical properties. Indeed, when metal NPs are irradiated by an external light field, they can generate a resonant coherent oscillation called “localized surface plasmon resonance”, which depends on the NPs shape and aspect ratio (199). With respect to metallic NPs, gold NPs (AuNPs) and gold nanorods (AuNRs) are the most widely explored. The integration of AuNPs in neurological research has the potential

to lead to the discovery of new approaches to treat conditions that medicine and science previously failed to. This perspective arises from their exceptional properties, including optical response, chemical and physical stability, relatively low toxicity, and wide range of possible surface functionalization (200).

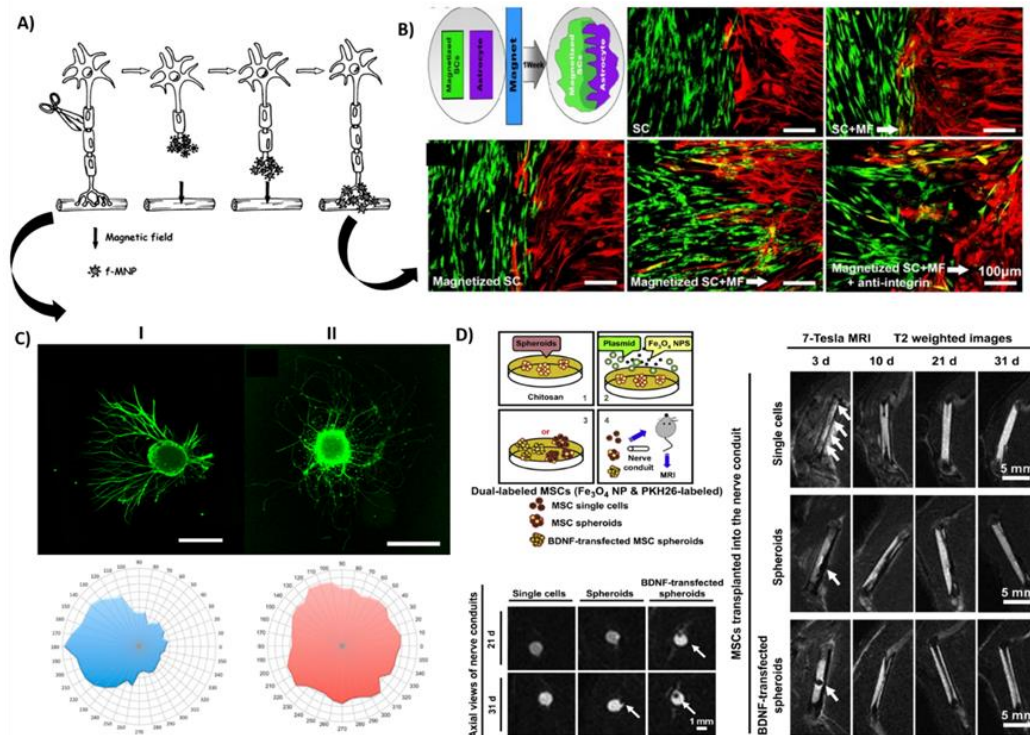


Figure III-5 - Magnetic nanoparticles applied to peripheral nerve regeneration. A) MNPs bind to the injured nerve and a magnetic field is applied, creating mechanical tension. This stimulates nerve regeneration in the direction forced by the magnetic field. This physical guidance is envisioned to direct more efficiently the regeneration of the injured nerve from the proximal toward the distal stump; B) Schwann cells-astrocytes confrontation assay. Magnetized Schwann cells (in green) and astrocytes (in red) were seeded in parallel stripes and were allowed to migrate and intermingle for 1 week under applied magnetic field; C) NGF gradients generated by MNPs are able to direct the growth of extending neurites from chick DRGs. (I) NGF-cNPs directed the extension of neurites from DRG. (II) Control cNPs had no effect on the directional outgrowth of extending neurites, and respective polar histograms (below); and D) Sagittal and axial MRI of experimental animals receiving MSCs in sciatic nerve gap. Animals were implanted with MSC-loaded nerve conduits and MRI images were taken at different time points post-implantation. Arrows indicate the visible location of Fe₃O₄ NPs-labeled cells. Scale bar: 1 mm. Reprinted and adapted from A) [183]; B) [185]; C) [191]; D) [188].

Paviolo and colleagues, (183) revealed a novel and extraordinary application for AuNRs associated with a low power laser exposure of NG108-15 neuronal cells after uptake of such NPs. Surprisingly, when these cells were irradiated with a 780 nm laser (IR or near-IR), the number of

neurons and respective neurites augmented. A scheme of such work can be observed in **Figure III-6A**. Later on, the same authors (184) explored one of the mechanisms of such phenomenon. They described the fabrication of AuNRs that were up-taken by NG108-15 neuronal cells. Cells were then exposed to the near-infrared light of 780 nm laser diode, which was found to induce intracellular Ca^{2+} transients. In order to explain such phenomena, the authors hypothesized that the temporary heating resultant from the light excitation of the localized Surface Plasmon Resonance of the NRs could serve either to generate changes in the cellular membranes capacitance by activating temperature sensitive ion channels in the cell membrane or to diminish the intracellular calcium storage in the organelles.

In a study reported by Adel *et al.* (185) AuNPs were able to induce neurite outgrowth of PC12 cells, after another kind of stimulus to which these particles are sensitive to: pulsed electrical stimulation. The authors firstly evaluate the deposition of 39 nm AuNPs onto polyethyleneimine pre-coated surfaces and then studied the effect of the pulsed electrical stimulation. That study showed that pulsed current stimulation induced neurite outgrowth of PC12 cells adhered to the AuNPs coated surfaces, thus demonstrating the potential use of AuNPs as electrically conductive matrix for nerve regeneration. Being aware that the presence of AuNPs enhances the conductive potential of the materials, Das *et al.* (186) reported on a novel SF-Au nanocomposite conduit which was tested in a neurotmesis grade sciatic nerve injury rat model over a period of eighteen months, after pre-seeded with rat SCs. To produce this scaffold, AuNPs were adsorbed onto silk fibers and further transformed into a nanocomposite sheet by electrospinning. The results show that AuNPs-SF nanofiber noticeably decreases the resistance of an electrically insulating material like silk.

Xiao *et al.* (187) reported on the production of AuNPs modified with 6-mercaptopurine (6MP) and a neuron-penetrating peptide as a neurotrophic agent. The 6MP is an anti-inflammatory drug which has been used to functionalize the surface of AuNPs to form 6MP-modified AuNPs (6MP-AuNPs) through an Au-sulfur bond. Additionally, with the purpose of increasing the neural cell uptake efficiency of 6MP-AuNPs, it was linked to the particle surface to form a 6MP-AuNPs-RDP conjugate. When SH-SY5Y cells were transplanted to a surface coated with 6MP-AuNPs-RDP it was concluded that the conjugate attached to the cell surface and was then internalized into cells, which in turn led to a significant increase of neurite growth. Motamedi *et al.* (188) fabricated and characterized AuNPs/polyvinylidene fluoride composite electrospun

mat with enhanced piezoelectricity in which the Au colloidal NPs were prepared via laser ablation of metallic targets in liquid media. After an extensive physicochemical characterization, the *in vitro* cytocompatibility, as well as the attachment and morphology of PC12 cells cultured on the electrospun composite was evaluated. It was demonstrated that laser ablated AuNPs can be used together with PVDF nanofibers, with proper organizational properties and increased piezoelectricity.

Zn is another metal that can be conjugated with NPs to form electrically conductive matrices. Having in mind that numerous studies have reported that the mechanical and electrical properties of different polymers have improved when Zn oxide NPs are incorporated into polymeric matrices, Iman *et al.* (189) reported the fabrication of a Cht-Zn oxide nanocomposite conduit and its effect on functional recovery of transected PNs. Results of this study indicated that the use of a Cht-Zn oxide nanocomposite seems to have several distinct advantages for the treatment of PNs, because it is inert and does not induce extensive scarring or degeneration after implantation. Also, Aydemir Sezer and colleagues (190) attempted to use for the first time a PCL electrospun matrix with variable quantities of zero valent ZnNPs, aiming at use it as conductive and biodegradable luminal fillers. Human primary fibroblasts and U87 brain glioblastoma cell line were used for evaluation of cytotoxicity, metabolic activity and proliferation. The results showed that low concentrations (5 and 10 %) of ZnNPs were non-toxic to fibroblasts and promoted neuronal regeneration. The fact that electrical conductance became approximately nine times greater in PCL/Zn5 samples than in PCL, and material characterization and mechanical analysis indicated that the material is compatible with soft tissues and is suturable, makes it a great candidate for PNR applications.

Alon *et al.* (169) reported the use of AgNPs as regenerative agents to promote neuronal growth. Neuroblastoma cells were seeded on surfaces coated with AgNPs. The effect on the development of the neurites during the initiation and the elongation growth phases was evaluated, with the observation that AgNPs function as favorable anchoring sites. Indeed, the growth on the AgNPs-coated substrates leads to a significantly enhanced neurite outgrowth with three times more neurites than cells grown on uncoated substrates, and two times more than cells grown on substrates sputtered with a plain homogenous layer of Ag, which thus evidences the benefit of using AgNPs.

III-3.2.1.3 Silica NPs

Moreover, still in the scope of inorganic NPs, SiO₂-NPs play an important role. SiO₂ is known to be biocompatible, with an outstanding chemical permanence and defined properties (201). There are, however, an extensive assortment of SiO₂ nano-formulations that can be applied in biomedical applications, in many different purposes, such as: i) common biomedical imaging and integration as imaging contrast agents, ii) application in ablative technologies, and iii) application in controlled drug delivery. The reasons rely on the fact that SiO₂-NPs can be produced using multiple synthetic techniques that allow to accurately regulate their physical and chemical characteristics (202).

Wise *et al.* (191) was able to improve auditory nerve survival with nano-engineered SiO₂-NPs aiming at delivery of neurotrophic factors. The authors investigated the safety and efficacy of BDNF-SiO₂-NPs as drug delivery system for the cochlea. For that, they bilaterally implanted the system into the basal turn of cochleae in deeply deafened guinea pigs. The results showed a significantly greater survival of spiral ganglion neurons in cochleae that received BDNF-SiO₂-NPs as compared to the contralateral control cochleae. Also, they were well tolerated within the cochlea, with a tissue response that was localized only at the site of implantation in the cochlear base. Gonzales Porras *et al.* (192) described a novel delivery system to motor neurons using mesoporous SiO₂-NPs encapsulated within a lipid bilayer and modified with the non-toxic subunit B of the cholera toxin (CTB). This subunit was described to bind to gangliosides present on neuronal membranes. The aim was to increase the interaction between muscle fibers and motor neurons in case of neuromuscular disorders. It was found that the whole system containing SiO₂-NPs functionalized with CTB showed greater motor neuron uptake when compared to unmodified lipid bilayers, when tested using motoneuron-like NSC-34 cells. By its turn, Mehrasa *et al.* (193) resorted to the electrospinning technique to produce a nanocomposite of aligned PLGA and PLGA/gelatin nanofibrous scaffold embedded with mesoporous SiO₂-NPs. Cultivation of PC12 cells on such scaffolds demonstrated that the introduction of mesoporous SiO₂-NPs into the matrices leads to improved cell attachment and proliferation, as well as longer cellular processes. DAPI staining results indicated that cell proliferation on the PLGA 10 %wt. mesoporous SiO₂-NPs and the PLGA/gelatin/10 %wt. mesoporous SiO₂-NPs scaffolds were outstandingly higher than that on the aligned pure PLGA scaffolds, reaching values of 2.5 and 3 folds, respectively.

Liu *et al.* (194) looked at the problem of anesthetizing PNs for surgeries and other procedures. That is because the drug delivery systems that have been used to prolong the duration of local anesthetic effect are generally thought of as being essentially systems that release local anesthetics in the surrounding area of the nerve. The authors have demonstrated that 28 nm hollow SiO₂-NPs-containing Tetrodotoxin, which is a powerful anesthetic, can penetrate the nerve. This phenomenon contributes to the increase in the number of successful nerve blocks as well as the prolongation of nerve block. The proved sustained release properties of hollow SiO₂-NPs also contributed to the extension of nerve block and enhanced safety by slowing release. The discovery of a system that can penetrate in PNs could be useful in delivering not only local anesthetics, but also a range of other therapeutics.

III-3.2.2. Organic NPs

III-3.2.3. Polymeric NPs

Polymers have been considered appealing materials due to their bulk physical properties, tunable structural design and architecture as well as customized biodegradability (203). There are countless flexible synthesis methods of polymers and the polymer chains allow functionalization with a wide range of molecules. In this regard, the final polymer products can be made of different compositions and properties, envisioning a wide range of applications and strategies. When in the nano-scale, polymer NPs have the amazing capacity of a high drug loading capability (204). **Table III-7** summarizes the relevant reports dealing with the use of organic NPs applied in PNR (205-218).

Cht is one of the most explored polymers in the field of TE and regenerative medicine. To further improve the property of promoting PN regeneration of Cht materials, several authors have prepared and explored such polymer in the form of NPs (219-221). Mili *et al.* (205) prepared the NGF encapsulated Cht NPs (NGF-ChtNPs) by ionotropic gelation method with tripolyphosphate as an ionic cross-linking agent and evaluated the neuronal differentiation potential of canine bone marrow derived mesenchymal stem cells. With a NPs size of 80-90 nm and a NGF loading efficiency of 61 %, the NGF-ChtNPs were found to be cytocompatible to MSC. Furthermore, NGF-ChtNPs can release bioactive NGF with the ability to transdifferentiate mesenchymal stem cells

into neurons. Li *et al.* (2016) produced Chitosan porous hybrid scaffolds with varying amounts of Calcium titanate (CaTiO_3), which is well known for its high dielectric constant, conductivity properties and luminescence. Primary Schwann Cells (SCs) directly cultured onto Chitosan/ CaTiO_3 hybrid scaffolds with a suitable concentration of CaTiO_3 NPs, which was distinguished to be with 5 mg of NPs, could evidently stimulate the attachment, proliferation and biological function maintenance of SCs.

Table III-7 - The use of organic nanoparticles applied to peripheral nerve regeneration.

| | Type of nanoparticle | Cell type or animal model | Main results | Year, References |
|---------------|---|---|--|-----------------------------------|
| | NGF encapsulated chitosan nanoparticles | Canine bone marrow derived MSCs | NGF-CNPs are capable of releasing bioactive NGF with the ability to transdifferentiate mesenchymal stem cells into neurons; | Mili <i>et al.</i> , 2017 [205] |
| | Chitosan porous hybrid scaffolds with varying amounts of Calcium titanate (CaTiO ₃) NP | SCs | 5 mg of NP, could evidently stimulate the attachment, proliferation and biological function maintenance of Schwann cells; | Li <i>et al.</i> , 2017 [206] |
| | Trimethylated chitosan-based NP | Microfluidic based DRG neuron culture | This microfluidic-based neuron culture showed to be of added value in the evaluation of cell–nanoparticle interactions, nanoparticle axonal transport and safety; | Lopes <i>et al.</i> , 2016 [207] |
| | Thiolated trimethyl chitosan(TMCSH) grafted with the non-toxic carboxylic fragment of the tetanus neurotoxin | Mice crush injury nerve model | TMCSH-HC/BDNF NP use stimulated the release and expression of BDNF, which led to a superior functional recovery after injury. Furthermore, there was an improvement in crucial pro-regenerative actions; | Lopes <i>et al.</i> , 2017 [208] |
| | Hyaluronic acid (HA) doped-poly(3,4-ethylenedioxythiophene) (PEDOT-HA) NP into a chitosan/gelatin (Cs/Gel) matrix | PC12 cells | 8 % PEDOT-HA/Cht/Gel scaffold had a higher cell adhesive efficiency and cell viability than the other conductive scaffolds and could support PC12 cells adhesion, survival, and proliferation. Cells in conductive scaffold expressed high synapse growth gene of GAP43 and SYP; | Wang <i>et al.</i> , 2017 [209] |
| Polymeric NPs | PEDOT-HA/PLLA film | PC12 cells | Electrical stimulation of 0.5 mA for 2 hours significantly promoted neurite outgrowth with an average value length of $122 \pm 5 \mu\text{m}$ and enhanced the mRNA expression of GAP43 and SYP in PC12; | Wang <i>et al.</i> , 2017 [210] |
| | Hydroxyapatite nanoparticle-containing collagen type I hydrogel | SCs; sciatic nerve defect in rats | significantly enhanced functional behavior of the rats compared with the collagen hydrogel without NP; | Salehi <i>et al.</i> , 2017 [211] |
| | (NGF)-loaded heparinized cationic solid lipid nanoparticles (NGF-loaded | (NGF-loaded HCSSLNs) effect was studied in induced pluripotent stem cells (iPSCs) | NGF-loaded HCSSLNs can be used for differentiation of iPSCs into neurons and NGF-loaded HCSSLNs with | Kuo <i>et al.</i> , 2017 [212] |

| | | | | |
|-------------------|--|---|---|--|
| | HCSLNs) | | EQ 1 had higher viability of iPSCs than NGF-loaded HCSLNs with SA; | |
| | (Rop)- polyethylene glycol-co-poly(lactic acid) (PELA) NP | Rat postoperative pain model | Analgesic effect for nerve blocking for over 3 days after single administration, compared do the 3h of normal administration; | Wang <i>et al.</i> , 2016 [213] |
| | 3-D biomimetic scaffold, with tunable porous structure and embedded core-shell NP | PC12 cells and primary rat cortical neurons | It was found that 3-D scaffolds with NGF NP greatly increased the neurite outgrowth of PC12 cells and primary cortical neurons; | Lee <i>et al.</i> , 2017 [214] |
| Dendrimers | PAMAM and phosphorus dendrimers | Transgenic cells were next injected into transected and repaired sciatic nerves of isogenic Lewis rats to assess GDNF expression | Cell-based GDNF therapy was shown to increase the extent of axonal regeneration, while controlled deactivation of GDNF effectively prevented trapping of regenerating axons in GDNF-enriched areas, which was associated with improved functional recovery; | Shakhbazau <i>et al.</i> , 2013 [215] |
| | (PAMAM)-NH ₂ dendrimers of fourth generation - pLVTHM/PAMAM nanocomplex | SCs seeded onto GAG matrix | SCs migration into the GAG-matrix tubes separately from proximal and distal ends of transected sciatic nerve; | Shakhbazau <i>et al.</i> , 2014 [216] |
| | PAMAM dendrimers of generation 5 modified with RGD, YIGSR, or IKVAV peptides | Study on the neurite outgrowth of PC12 cells after inducing NGF differentiation | The adhesive peptides were successfully conjugated to PAMAM dendrimer to promote cell-material interaction and subsequently cell attachment; | Maturavongsadit <i>et al.</i> , 2016 [217] |
| | Dendrimers covalently linked to near-infra red cyanine-5 fluorescent dye (D-Cy5) | Injected the molecules both intravitreally and systemically (in the rats) or just systemically (in the monkey) after induction of NAION | Systemic administration of dendrimers allows selectively targeting of the ischemic optic nerve lesion; | Guo <i>et al.</i> , 2016 [218] |

In a very advanced and innovative strategy, Lopes *et al.* (207) explored the use of a microfluidic based DRG neuron culture to test the uptake and transport kinetics of gene carrying trimethylated Chit (TMChit)-based NPs actively targeted to neurons. For such, the NPs surface was functionalized with the nontoxic and neurotropic C-terminal 54 kDa fragment of the Tetanus neurotoxin heavy chain. The purpose was to develop a way of directly deliver any kind of molecules to a relatively inaccessible injection site of PNs and DRG, all of this while mimicking a peripheral *in vivo* route of administration. This microfluidic-based neuron culture showed to be of added value in the evaluation of cell–nanoparticle interactions, namely Chit NPs and PNs. One year later, the same authors (208) explored another interesting way to mediate the targeted delivery of therapeutic genes to DRG neurons, through the development of biocompatible and biodegradable NPs, using the same optimized TMChit-based NPs. They proposed the use of such NPs to mediate targeted gene delivery to peripheral neurons upon a peripheral and minimally invasive intramuscular administration. To do so, they grafted the NPs with the non-toxic carboxylic fragment of the tetanus neurotoxin to allow neuron targeting and were explored to deliver a plasmid DNA encoding for BDNF in a PN injury model. This complex loaded NPs stimulated the release and expression of BDNF, which in turn led to a superior functional recovery after injury. Furthermore, there was an improvement in crucial pro-regenerative actions, like the increased expression of neurofilament and growth-associated protein GAP-43 in the injured nerves as well as significantly higher density of myelinated in the distal stump of injured nerves. Wang *et al.* (209) produced a novel porous conductive scaffold that was prepared by incorporating conductive HA doped with PEDOT (PEDOT-HA) NPs into a Chit/gelatin matrix. As expected, the incorporation of PEDOT-HA into the scaffold increased the electrical and mechanical properties while decreasing the porosity and water absorption. The results revealed that 8 % PEDOT-HA/Chit/Gelatin scaffold had a higher PC12 cell adhesive efficiency and cell viability than the other conductive scaffolds. Furthermore, cells in the scaffold with 8 %wt PEDOT-HA expressed higher synapse growth gene of GAP43 and SYP compared with Chit/Gelatin control group suggesting that 8 % PEDOT-HA/Chit/Gel scaffold is an attractive cell culture conductive substrate which could support neuronal cells survival. In a different approach, but using the identical conductive material, PEDOT, the same authors (210) produced the same kind of NPs, (HA)-doped PEDOT NPs but instead of Chit, prepared PEDOT-HA/PLLA composite films, which were subjected to different current intensity to elucidate on the effect of electrical stimulation on

neurite outgrowth of PC12 cells. Electrical stimulation of 0.5 mA for 2 hours significantly promoted neurite outgrowth with an average value length of $122 \pm 5 \mu\text{m}$. It also enhanced the mRNA expression of growth-associated protein (GAP43) and synaptophysin in PC12 cells as compared with other types of stimulation. These results suggest that PEDOT-HA/PLLA film combined with electrical stimulation may be an attractive candidate for enhancing nerve regeneration.

Moving to another kind of biomaterials as matrix for embedding NPs, Salehi *et al.* (211) aimed to enhance the efficacy of PNR by combining Ha-NPs with the diameter of 212 nm in a collagen type I hydrogel, extracted from rats tails. *In vitro*, primary rat SCs cultivation on the prepared hydrogel demonstrated a significantly higher cell proliferation than the tissue culture plate. *In vivo*, the prepared nanocomposite of collagen hydrogel was administrated on the sciatic nerve crush injury in rats showing significantly enhanced functional behavior when compared to the collagen hydrogel without NPs. In a different approach, Kuo *et al.* (212) were able to produce (NGF)-loaded heparinized cationic solid lipid NPs (NGF-loaded HCSLNs) using heparin-stearic acid conjugate, cacao butter, cholesterol, stearylamine (SA) or esterquat 1 (EQ 1) as reagents. The immunochemical staining of neuronal nuclei revealed that NGF-loaded HCSLNs can be used for differentiation of induced pluripotent stem cells (iPSCs) into neurons and NGF-loaded HCSLNs with EQ 1 had higher viability of iPSCs than NGF-loaded HCSLNs with SA, proving that EQ 1 may be promising formulation to regulate the membrane charge of iPSCs during neuronal differentiation.

Once again addressing the problem of anesthetizing PNs, Wang *et al.* (213) designed a study to develop and test long-acting NPs and observe the analgesic effects for nerve block in a rat postoperative pain model. For such, they developed long-acting anesthetic ropivacaine-NPs using polyethylene glycol-co-polylactic acid (PELA). Having in mind that the analgesic effect of ropivacaine lasts 3–6 hours after intrathecal injection for single use, the ropivacaine-PELA NPs produced an analgesic effect for nerve blocking for over 3 days after single administration. Lee *et al.* (214) used a groundbreaking technique to fabricate 3D biomimetic scaffolds. Stereolithography is a laser-based 3D printing system capable of fabricating aligned micro- and macro-size 3D constructs via a layer by layer assembly method: the scaffolds were in the shape of square grid as the base pattern, creating a 3D porous scaffold with internal pores and channels. To complement this technology, BSA–PLGA NPs and NGF-PLGA NPs were embedded

into the previous matrix. It was found that 3D scaffolds with NGF NPs greatly increased the neurite outgrowth of PC-12 cells and primary cortical neurons. The authors believe that is not only because of the bioactive factor, but also because of the increase of the nano-roughness added by the incorporation of NPs.

These nano-sized molecules have been extensively considered as promising candidates for application as drug-delivery carriers in all biomedical fields. They are highly-branched and symmetrical, branching out from a central core and subdivided into hierarchical branch units, external capping units, with unique structural properties (222). Their important characteristics ascend from their unique and extremely well controlled architecture, size and surface properties as compared to traditional linear polymers. Such characteristics offer dendrimers the exciting possibility of accommodating other molecules in their interior, which characterizes its crucial advantage of acting as non-covalent drug-encapsulating agents (223). These spherical, biocompatible and biodegradable polymeric-based NPs were reported in the late 70s, by Vögtle group, however, they can still be considered as new drug solubilizers (224).

To our knowledge, little has been done with the dendrimer nanotechnology in PNR and repair. On the other hand, there is a vast literature on the use of dendrimers applied in the central nervous system (225-229). Shakhbazau *et al.* (215) reported on proof-of-concept work focused on the application of provisional GDNF expression system in injured PNs. For such, they firstly engineered primary cultured SCs using dendrimers or lentiviral transduction with the vector providing doxycycline-regulated GDNF expression. Transgenic cells were next injected into transected and repaired sciatic nerves of isogenic Lewis rats to assess GDNF expression. With this study, they were able to demonstrate for the first time the genetic modification of SCs with use of dendrimer/plasmid complexes. They have also shown for the first time that dendrimer-driven expression of neurotrophic factors is compatible with doxycycline-regulated system and ensures tight control of GDNF release, as seen in **Figure III-6B**. The same authors, (216) hypothesized that a collagen-glycosaminoglycan matrix could provide a synthetic way to mimic the SC Basal Lamina (SCBL), since SCBL is a particularly potent substrate for neurite promotion. Also, the authors wanted to confirm the compatibility of such matrix with a virus-free genetic engineering approach, as the use of dendrimers. For such, collagen and chondroitin-6-sulfate proteoglycan suspension was dispensed into the collagen conduits, which were tested in a sciatic nerve defect in rats. Their transfection experiments confirmed polyamidoamine (PAMAM)

dendrimers ability to transfect SCs and the penetration of dendrimer complex into the 3D matrix structure.

The 5th generation PAMAM dendrimers were used by Maturavongsadit *et al.* (217) with the goal of enhancing cellular responses, namely the promotion of increased cellular adhesion. The real aim of the work consisted in both assess the possibility of functionalizing the dendrimers with several cell-binding motifs, such as RGD, YIGSR, or IKVAV peptides and determine how it affects cellular responses. The RGD, YIGSR, or IKVAV functionalized PAMAM coated substrate could promote evident neurite outgrowth of PC12 cells on all the peptides-modified PAMAM coated substrates by day 1. Quantitative image analysis of the neurite lengths on all the peptide-modified PAMAM surfaces were in range of 18–20, 50–60, and 90–115 μm on day 1, 2 and 4, respectively, which were significantly higher than the neurite length on the control surfaces. In an attempt to address non-arthritis anterior ischemic-optic neuropathy and knowing that dendrimers should be directed and collected in inflammatory cells upon systemic administration, Guo *et al.* (218) tested the difference between locally and systemic injection of traceable dendrimers covalently linked to near-infra red cyanine-5 fluorescent dye. The results revealed that systemic dendrimer administration provided the best penetration in the optic neuropathy lesion site when injected shortly after induction, leading to the conclusion that systemic administration of dendrimers allows selectively targeting of the ischemic optic nerve lesion.

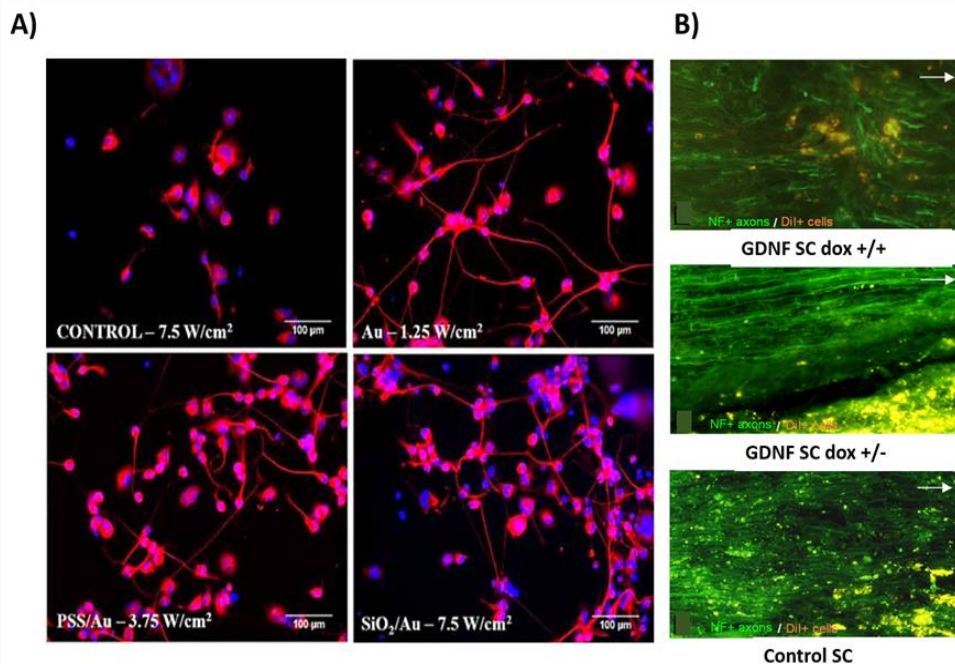


Figure III-6 - The effect of other nanoparticles in peripheral nerve regeneration. A) The use of gold nanoparticles in PNR: examples of epifluorescence images of NG108-15 neuronal cells cultured with Au, PSS/Au, and SiO₂/Au NRs and labeled with β -III tubulin (red) and DAPI (blue). The effect of PSS/Au and SiO₂/Au NRs on the percentage of neurons with neurites is evident; and B) Doxycycline-inducible GDNF expression and respective regeneration scenarios in the distal sciatic nerves of experimental 3 weeks' time point. Continuous GDNF expression (dox+/+) causes some axons to avoid the regenerative path; time-restricted GDNF expression (dox+/-) leads to unobstructed and profuse regeneration; White arrows indicate the direction of axonal regeneration (proximal to distal). Total magnification: 100x. Reprinted and adapted from A) [193]; B) [225].

III-3.2.4. Biologically derived NPs

Intercellular transfer of macromolecules through vesicles, known as exosomes, has become the subject of increasing interest as a novel means for intercellular crosstalk. Exosomes can be considered one kind of NPs. However, unlike the ones mentioned in the sections before, these are biologically derived. By definition, exosomes are small membranous vesicles or nanovesicles with 40 to 100 nm in size, with a density of approximately 1.13–1.19 g/cm³ (230). Regarding their development, exosomes are produced via the internal budding of endosomes to form multivesicular bodies that fuse with the plasma membranes to release exosomes into the surrounding environment. Based on the cell types they are originated from, they contain a wide range of factors, such as proteins, lipids, RNA, mRNA and miRNA (231). These elements that are carried by exosomes can be termed as “cargo” and will be delivered either to the surroundings cells or

taken to have action in more distant cells. With this, it is understandable that depending on the cargo content, different phenomena can happen to the recipient cells, including its DNA reprogramming (232). Not only the cargo will have an impact on the receptor cell, but also the surface membrane of the exosomes contains proteins that act as markers (233). Exosomes are therefore recognized as new form of intercellular communication between cellular components, but without the expected cell-to-cell direct contact. After understanding the way exosomes work, the potential of such NPs can be assumed for drug delivery and other therapies (234).

It is known today that exosomes are deeply involved in neuronal activity, from its protection, degeneration, development and even regeneration. Many studies have shown that CNS components are capable of releasing exosomes (235-237). For instance, studies indicate the release of exosomes by neurons (238), microglia (239), astrocytes (240), oligodendrocytes (241), and neural stem cells (242). However, its role in the PNS has only been showed much more recently. **Figure III-7** embodies some exciting results obtained from research works focused on exosomes. In 2008, Court *et al.*, (243) proved that in damaged PNs, SCs deliver vesicles containing ribosomes into the axon and its contents are then released. Therefore, exosomes can deliver mRNA and ribosomes to injured nerves and promote local protein synthesis which is needed for the process of Wallerian degeneration and consequent regeneration. In this context, the same author (244) has shown that labelled ribosomes in the nerve are derived from the SCs. However, not all exosomes secreted by SCs have positive effects. In fact, SCs have been shown to secrete exosomes containing pathogenic prions *in vitro*, therefore existing the possibility that these pathogens might be released from the PNS to infect the CNS (245). Recent literature on the relation between exosomes and PNR is reviewed and summarized in **Table III-8** (246-250).

In 2013, Lopez-Verrilli *et al.* (246) focused on the regulation of axons by SCs mediated secreted vesicles and studied this means of communication between these two role players of PNS, to support neuronal and axonal regeneration after an injury. The authors explored the hypothesis that exosomes released from SCs would be up taken by axons in a way to regulate intrinsic mechanisms of neuronal regeneration. They have in fact demonstrated, both *in vivo* and *in vitro* that SCs secrete exosomes and that they are selectively internalized by axons. To support their exciting findings, they further proved that SC-secreted exosomes, but not fibroblast-derived ones, markedly increase axonal regeneration. Images regarding this work can be seen in **Figure III-7**. The same authors compared the effect of human menstrual MSCs (MenSCs) mediated by

three different ways: cell–cell contact, by their total secretome or by secretome-derived extracellular vesicles on neuritic outgrowth in primary neuronal cultures (247). As exciting conclusion, they found that the contact of MenSCs with cortical neurons inhibited neurite outgrowth as their total secretome containing exosomes enhanced it. To complete their hypothesis of using exosomes derived from Stem cells, they found that extracellular vesicle fractions showed a distinctive effect. While the exosome-enriched fraction enhanced neurite outgrowth, the micro vesicle-enriched fraction displayed an inhibitory effect, suggesting that exosomes derived from MenSCs could have possible applications in PNR. To address the problem of neuropathic pain and knowing that it is highly likely that miRNA plays some key roles in the formation of pain, Hori *et al.* (248) performed a miRNA array analysis in the DRG of mice with sciatic nerve ligation and investigated the possible changes in DRG-associated miRNAs in exosomes derived from blood serum in mice. They demonstrated that miR-21, miR-431, and miR-511-3p in the DRG gradually increased in an IL-6-dependent manner during the development of neuropathic pain, but only miR-21 in exosomes extracted from blood was secreted in mice with sciatic nerve ligation. With these results, the authors believe that amplified blood exosomal miR-21 after sciatic nerve ligation may be seen as a diagnostic biomarker for neuropathic pain. Still considering the subject of neuropathic pain, Simeoli *et al.* (249) show that DRG neuron cell bodies release extracellular vesicles, including exosomes containing miRs.

Table III-8 - Exosomes in scope of peripheral nerve regeneration.

| Type of nanoparticle | Cell type or animal model | Main results | Year, References |
|---|---|--|---|
| SCs exosomes | SCs, fibroblasts, DRGS, Rat crush injury model | Dedifferentiated SCs secrete nano-vesicles known as exosomes which are specifically internalized by axons. They increase axonal regeneration both <i>in vivo</i> and <i>in vitro</i> ; | Lopez-Verrilli <i>et al.</i> , 2013 [246] |
| MSCs's derived exosomes | Menstrual MSCs Bone Marrow MSCs, umbilical cord MSCs and chorion MSCs | MenSC exosomes showed superior effects on the growth of the longest neurite in cortical neurons; | Lopez-Verrilli <i>et al.</i> , 2016 [247] |
| Exosomes derived from blood serum in mice | Mice and partial sciatic nerve ligation model in rat | demonstrated that miR-21, miR431, and miR-511-3p in the DRG gradually increased in an IL-6-dependent manner during the development of neuropathic pain; | Hori <i>et al.</i> , 2016 [248] |
| DRGs exosomes | DRGs, nerve injury in mice | Up-regulation and release of miR-21 contributed to sensory neuron–macrophage communication after damage to the peripheral nerve; | Simeoli <i>et al.</i> , 2017 [249] |
| NG2+ cells exosomes | NG2+ cells, rat neurons | The release of Retinoic Acid in association with exosomes provided a permissive substrate to neurite outgrowth; | Gonçalves <i>et al.</i> , 2018 [250] |

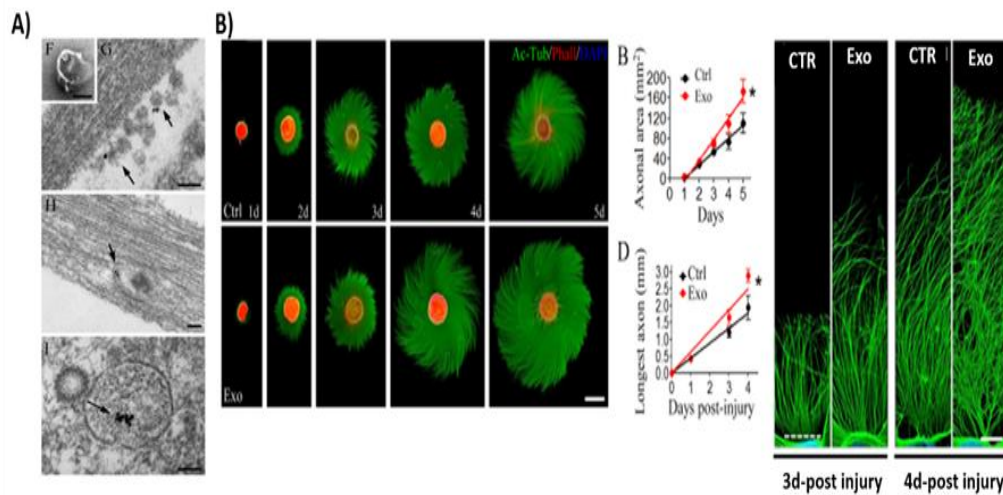


Figure III-7 - The use of exosomes in peripheral nerve regeneration. A) Representative transmission electron micrographs of Schwann cell-derived exosomes in DRG axons, after staining exosomes with p75^{NM}-gold labeling on their surface; B) Axonal regeneration of DRGs after vehicle (Ctrl) or exosome (Exo) treatment for 5 days. DRGs are stained for acetylated tubulin (Ac-Tub, green), Phalloidin-Rhodamine (Phall, red) and nuclei (DAPI, blue). Scale bar: 50 µm. Reprinted and adapted from [256].

They have demonstrated that pure sensory neuron-derived exosomes released by capsaicin are readily phagocytosed by macrophages in which an increase in miR-21-5p expression promotes a pro-inflammatory phenotype. This suggests that upregulation and release of miR-21 contribute to sensory neuron-macrophage communication after damage to the peripheral nerve. Gonçalves *et al.* (250) identified a novel mechanism by which neuronal retinoic acid receptor β (RAR β) activation results in the endogenous synthesis of retinoic acid, which is released in association with exosomes and acts as a positive cue to promote axonal/neurite outgrowth. The excitement of this discovery relies in the fact that their data suggests the possibility of an advantageous therapeutic approach where a RAR β agonist could be used for a much shorter period than the one required for the full regeneration of the axon.

These biologically derived NPs are a promising field in the PNR area. One can envision the use of SCs autologous patient-specific exosomes to enhance nerve regeneration. However, the downside of this is the same as the use of autografts, as one healthy nerve needs to be sacrificed for such (251). However, stem-cells play a major role here, since it is well known that Schwann-like cells can be obtained from both MSCs and Adipose Derived Stem Cells (ACs) and so could their exosomes.

Nevertheless, the above-mentioned studies might result in significant improvements for the patients in the future when the use of exosomes is used in the clinical setting, however that vision is still a step ahead.

III-3.2.5. Toxicity of NPs

Although related to various successful and innovative discoveries, the use of NPs is not completely safe and various reports have been considering this subject (252-255). This is mainly due to the fact that such particles in the nano-size interact directly with cells and lead to the formation of reactive oxygen species, leading to oxidative stress (252). Further cytotoxicity can be found in positively charged NPs, as they have the capacity to interact and induce disruptions in the living cells plasma membranes (256). Especially relevant to the nervous system, are recent studies suggesting the nano-substances can cross the blood–brain barrier. Indeed, When PC12 cells are differentiated, they appear to be even more sensitive to cytotoxicity of NPs (257).

Often, the toxicity is provided not by the NPs themselves, but by the coatings many time used to facilitate the processes in biomedical applications, which is the case of polydimethylamine, found to have cytotoxic effects in cortical neurons isolated from chick embryos (258).

In the end, one must have precaution when using these nano-scale materials, since they can in fact interact with organisms in a cellular lever, especially in the nervous system. However, their benefits for the future of the science and medical community concerning PN treatment and repair are undeniable and many examples of that were described above.

III-3.3. Nanofibers

Nanofibers are fibers with diameters one or two orders of magnitude smaller than conventional fibers that closely mimic the ECM. These fibers have a uniquely large surface area-to-mass ratio and can be usually produced by electrospinning (259) and self-assembly (260) techniques. Electrospinning is a simple and versatile electrodynamic practice in which a polymer solution can be spun by engaging a high potential electric field to obtain nano-scale long fibers, meaning it relies on the electrostatic repulsion between surface charges to continuously draw

nanofibers from a viscoelastic fluid. It includes the quick evaporation of solvent and solidification of droplets to form fibers (261). As the external electrical field is applied, the liquid in the metallic needle is induced to elongate at the tip of the needle and takes on the form of a cone which is extended in the form of a jet. A typical electrospinning apparatus contains four main components: i) a high voltage source (1–30 kV), ii) a metallic needle or capillary, iii) a syringe pump, and iv) a grounded conductive collector, that among many shapes, usually is a simple flat plate or rotating mandrel (262).

An incredible amount of materials can be used for electrospinning, including polymers, ceramics, small molecules, and their combinations (263). Not only different biomaterials can be used, but the final smooth nanofiber meshes can be adapted to create nanofibers with a number of secondary structures, comprising porous, hollow, or core–sheath structures. Therefore, it has been recognized at least for a decade now that nanofibrous scaffolds also offer great potential in the field of neural tissue engineering, as they are able to mimic native tissue tubular structures including axons, microtubules and ion channels (264, 265). Because of the potential related to the use of nanofibrous in PN tissue engineering, many interesting publications have emerged in the last few years. Extraordinary results obtained with reviewed random, aligned and conductive nanofibers can be seen in **Figure III-8**, as well as the electrospinning apparatus (**Figure III-8A**). **Table III-9** summarizes the reports on use of the different nanofibers applied in PN regeneration that will be further discussed (86, 87, 266-282).

III-3.3.1. Random nanofibers

As mentioned before, nanofibrous mats are very successful due to its resemblance to ECM. However, in a study conducted by Gnani *et al.* (266) the influence of the fiber size on explanted cultures of SCs and DRGs was studied after producing micro- or nanofibers made of gelatin by electrospinning. In one hand, nanofibers promoted cell spreading and actin cytoskeleton organization, increasing cellular adhesion and the proliferation rate. On the other hand, both migration rate and motility, quantified by means of carrying out trans-well and time-lapse assays respectively, were greater in cells cultured on micro-fibers. That study clearly indicates that topography of electrospun gelatin fibers can be adjusted to modulate SC and axon organization (**Figure III-8B**).

Table III-9 - The use of nanofibers applied to peripheral nerve regeneration.

| | Type of nanofiber | Cell type or animal model | Main results | Year, Reference |
|---------------------------|--|--|---|-------------------------------------|
| Random nanofibers | Gelatin micro- or nanofibers | SCs and DRGs | The topography of electrospun gelatin fibers can be adjusted to modulate SC and axon organization, since it affects parameters such as motility or cytoskeleton organization; | Gnavi <i>et al.</i> , 2015 [266] |
| | PCL and MeCbl Nanofibers | Cortical neurons; rat sciatic nerve crush injury model | Local administration of MeCbl at PN injury sites promoted nerve regeneration and enhanced functional recovery in a rat sciatic nerve crush injury model; | Suzuki <i>et al.</i> , 2017 [267] |
| | poly (ε-caprolactone)/collagen/nanobioglass (PCL/collagen/NBG) nanofibrous conduits transplanted with hEnSCs | Human endometrial stem cells (hEnSCs) | PCL/collagen/NBG nanofibrous conduit filled with hEnSCs is a suitable strategy to improve nerve regeneration after a nerve transaction in rat; | Mohamadi <i>et al.</i> , 2017 [268] |
| | electrospun PCL porous conduit with O-CCH as a longitudinally oriented microstructure filler | DRG, Schwann cells; rat sciatic nerve defect | Functional results indicated that the CCH/PCL compound scaffold induced comparable functional recovery to that of the autograft group at the end of the study; | Huang <i>et al.</i> , 2017 [269] |
| | Emulsion electrospun poly (L-lactic acid) (PLLA) nanofibrous | Induced pluripotent stem cells-derived neural crest stem cells (iPSCs-NCSCs) | VEGF and NGF in emulsion electrospun nanofibrous scaffold had a synergistic effect on regeneration of vascularized nerve tissue; | Xia <i>et al.</i> , 2018 [270] |
| | PLCL/SF nanofiber sponges | SCs; rat sciatic nerve model | The results demonstrated that nanofibers-sponge containing conduit performed better than the hollow conduit; | Sun <i>et al.</i> , 2017 [271] |
| | PCL and collagen/PCL blends incorporated in a gelatin matrix and inserted in collagen tubes | Rat sciatic nerves defect | When implanted in 15 mm sciatic nerve defect, animals containing collagen/PCL fibers had higher extent of recovery when compared to animals that had received empty implants, but not as good as with autologous nerve transplantation; | Kriebel <i>et al.</i> , 2017 [272] |
| Aligned nanofibers | Randomly oriented and aligned poly (methyl methacrylate) nanofibers | DRGs and SCs | When co-cultured, DRGs and SCs revealed that on aligned nanofibers, neurites and SCs had a higher chance of co-localization than on randomly oriented nanofibers; | Xia <i>et al.</i> , 2014 [273] |
| | Randomly oriented and aligned poly (methyl methacrylate) nanofibers | DRGs and SCs | When co-cultured, DRGs and SCs revealed that on aligned nanofibers, neurites and SCs had a higher chance of co-localization than on randomly oriented nanofibers; | Xia <i>et al.</i> , 2016 [86] |
| | Aligned PHBV nanofiber | Rat sciatic nerve defect | Nanofibers in an aligned orientation favored stem cell growth and | Hu <i>et al.</i> , 2017 [87] |

| | | | | |
|--|---|---|--|--------------------------------------|
| | | | elongation and indicated that the FGF2- <i>miR-218</i> induction approach combined with the (PHBV)-3D nanofiber scaffolds facilitated the nerve regeneration; | |
| | Randomly oriented and aligned poly (L-lactic acid) nanofibrous scaffolds | iPSC-derived neural stem cells | Compared with randomly, the aligned PLLA nanofibers greatly directed neurite outgrowth from the iNSCs and significantly promoted neurite growth along the nanofibrous alignment; | Lin <i>et al.</i> , 2018 [274] |
| | Aligned electrospun polylactic acid (PLLA) microtube array membrane (MTAM) | Co-cultures of rat fetal neural stem cells (NSC) and astrocytes | MTAM is a better co-culture platform than the traditional transwell system; | Tseng <i>et al.</i> , 2017 [275] |
| | Aligned electrospun Methacrylated hyaluronic acid nanofibers | DRGs | DRGs seeded on the scaffolds revealed that the combination of NGF released from the microspheres and the aligned nanofibers significantly enhanced neurite outgrowth; | Whitehead <i>et al.</i> , 2017 [276] |
| | PCL electrospun nanofibers were mixed with gelatin and further embedded in 3D printed hydrogel scaffold | Primary cortical neurons | It was possible to fabricate 3D neural tissue constructs by combining 3D bioprinting and electrospinning techniques and the neurons aligned in the aligned nanofibers; | Lee <i>et al.</i> , 2016 [277] |
| | 3D hierarchically aligned fibrin nanofiber hydrogel (AFG) | SCs, DRGs;Rat sciatic nerve injury | The developed scaffold supports SCs cable formation and axonal regrowth within 2 weeks, with similar results to the autograft after short and long-term studies; | Du <i>et al.</i> , 2017 [278] |
| Nanofibers combined with conductive materials | Polyaniline and silk fibroin (PASF) nanofibers | SCs; sciatic nerve nerve defect | 12 months after implantation it was verified enhanced neuro-regeneration; | Das <i>et al.</i> , 2017 [279] |
| | PPy(lactide acid) conductive fiber-film (CFF) coated with cell-derived extracellular matrix derived from L929 cells (CFF-ECM) | PC12 cells | The combination of ECM-CFF with electrical stimulation could improve the nerve regeneration by encouraging neural-cell adhesion, neurite growth and extension; | Zhou <i>et al.</i> , 2017 [280] |
| | PLA/PPy nanofibrous scaffold | human umbilical cord MCSs, SCs | PLA/PPy nanofibrous scaffold containing 15 % PPy with sustained conductivity and aligned topography. Additionally, the direction of cell elongation on the scaffold was parallel to the direction of fibers; | Zhou <i>et al.</i> , 2016 [281] |
| | Conductive PPy/PLCL conduits were synthesized by polymerizing pyrrole coated on Poly (l-lactic acid-co-ε-caprolactone) | PC12 cells, DRG; Rat sciatic nerve defect | The PPy/PLCL conduits with electrical stimulation showed a similar performance compared with the autograft group, and significantly better than the non-stimulated PPy/PLCL conduit group showing great potential for PN regeneration; | Song <i>et al.</i> , 2016 [282] |

In a noteworthy publication, Suzuki *et al.* (267) hypothesized whether an electrospun nanofiber sheet incorporating methylcobalamin (MeCbl), one of the active forms of vitamin B12 homologues, when delivered locally to the PN injury site, would contribute to promoting nerve regeneration. *In vitro*, cortical neurons were cultured in microfluidic chambers and it was seen that local administration of MeCbl to the axon compartment promoted axonal outgrowth equal to axon and administration of MeCbl. *In vivo*, when wrapping the nanofiber sheet around the PN injury, local administration of MeCbl promoted nerve regeneration and enhanced functional recovery. In another study comprising random nanofibers, Mohamadi and colleagues (268) aimed at evaluating the sciatic nerve regeneration potential in the rat nerve transaction injury model followed by implantation of poly(ϵ -caprolactone)/collagen/nanobioglass (PCL/collagen/NBG) nanofibrous conduits containing human endometrial stem cells (hEnSCs). To do so, the authors first prepared the respective conduit by electrospinning. Afterwards, a fibrin gel containing hEnSCs with a concentration of 1×10^5 cells/mL was injected in the conduits and implanted. After extensive evaluation, the authors demonstrated that hEnSCs grafted inside a PCL/Collagen/NBG conduits have the potential to improve sciatic nerve regeneration, however without knowing the exact roles of hEnSCs in the process. Huang *et al.* (269) combined the stage-wise approach of electrospinning to produce the outer conduit made of random nanofibers with the directionally freezing orientated collagen-chitosan (O-CCH) filler, since incorrect positioning or distribution of intraluminal fillers and consequent incorrect wiring of the regenerating axons might result in regeneration failure. After proper characterization, collagen/chitosan in the reason (1:1) was selected for filler fabrication and a wall thickness of 400 μm was selected for PCL sheath production. 3D-reconstruction further revealed that the O-CCH filler unveiled a longitudinally oriented microstructure with 85 % of pores and the electrospun PCL porous sheath with pore sizes of $6.5 \pm 3.3 \mu\text{m}$ that prevented fibroblast invasion. Overall, *in vitro* and *in vivo* studies up to 12 weeks indicated that the O-CCH/PCL scaffolds could promote axonal regeneration and migration.

Xia *et al.* (270) was able to incorporate VEGF and NGF on the surface and in the core of emulsion random electrospun PLLA nanofibrous scaffold, respectively, which was capable of dual delivery. In this sense, VEGF and NGF had a sequential release pattern, in which most of the VEGF was released in the first few days as it was embedded in the surface of the meshes, but the NGF could be continuously released for more than 1 month, as it was captivated in the

interior of the nanofibers. *In vitro*, the use of such scaffold could enhance the neural differentiation of iPSCs-derived neural crest stem cells (iPSCs-NCSCs).

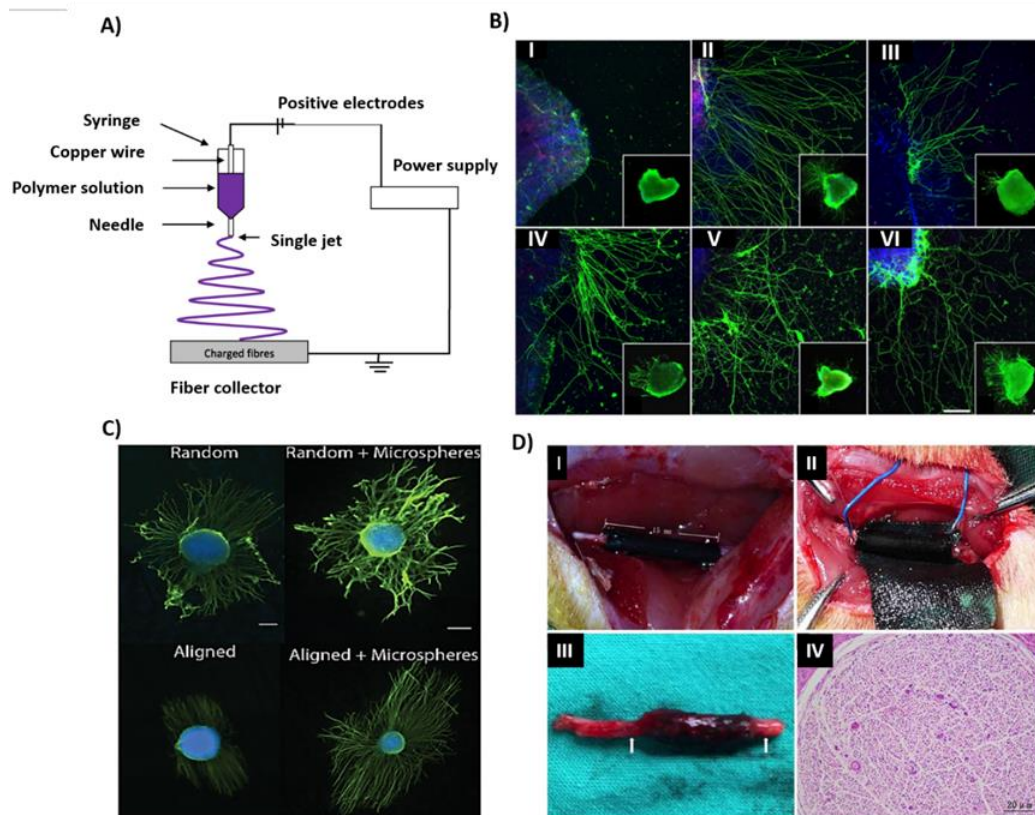


Figure III-8 - The application of nanofibers in peripheral nerve regeneration. A) Schematic representation of the electrospinning process; B) DRG axon outgrowth after fluorescent staining with β -tubulin (green) and DAPI (blue), when cultured on (I) Matrigel® coated coverslips without NGF (negative control conditions); (II) Matrigel® coated coverslips with 50 ng of NGF/mL in medium (positive control conditions); (III) DRGs seeded on 300 nm fibers; (IV) DRGs seeded on 600 nm fibers; (V) DRGs seeded on 1000 nm fibers; and (VI) DRGs seeded on 1300 nm fibers. Scale bar: 20 μ m; C) Representative images of DRGs cultured for 5 days on aligned and random scaffolds in the presence or absence of microspheres. Samples without microspheres were supplemented with 50 ng/mL of NGF. Aligned fibers direct neurite outgrowth. Scale bar: 250 μ m; D) Use of PPY/PLCL combined with electrical stimulation in peripheral nerve regeneration. (I) The animal operation procedure immediately after 15 mm conduit implantation; (II) Circle electrode implantation; (III) Harvested regenerated nerve at 8 weeks post-implantation; and (IV) 8 weeks post-implantation histological section of the electrode contact site stained with H&E (white arrows indicate the electrode contact site). Reprinted and adapted from A) [276]; B) [281]; C) [291]; D) [297].

Additionally, this scaffold was applied to a critical sized defect in rat sciatic nerve model *in vivo*, which revealed a significant improvement of neovascularization as well as nerve healing after 3 months post-operation. Sun *et al.* (271) reversed the previous strategy of using the nanofibers meshes as conduits and used it instead as a filler. Poly (L-lactic acid-co- ϵ -

caprolactone)/SF (PLCL/SF) nanofiber sponges were used as fillers to prepare 3D nanofiber sponges containing conduit. The filler fabricated by electrospinning and subsequent freeze-drying demonstrated abundant macropores, high porosity and superior compressive modulus. *In vitro* cell viability studies indicated that the fabricated conduit could enhance the proliferation of SCs due to the macro-porous structure, since hematoxylin-eosin and immunofluorescence staining confirmed that these cells infiltrated into the nanofiber-sponges. Afterwards, the conduit was implanted in the rat sciatic nerve defect model to evaluate the effect *in vivo*, which in general performed better than the hollow conduit group. Using the same strategy of applying nanofibers as a luminal filler, Kriebel *et al.* (272) developed a cell-free, 3D scaffold for axonal guidance for long-distance nerve repair in which the nanofibers of made of biodegradable PCL and collagen/PCL blends were incorporated in a gelatin matrix and inserted in collagen tubes, in a complex strategy developed earlier by the same author. When implanted in 15 mm sciatic nerve defect, animals containing collagen/PCL fibers had higher extent of recovery (compound muscle action potentials, motor functions of the hind limbs) when compared to animals that had received empty implants, but not as good as with autologous nerve transplantation.

III-3.3.2. Aligned nanofibers

Many works have been focusing on horizontally aligned nanofibers, since in 2006 (283) and 2008 (284) it was proved the high potential of anisotropic topographies for PNR. This is because of the natural formation of the Bands of Bungner after an injury, which are oriented columns of laminin-1 and aligned SC. Regenerating fibers then enter the gap and follow these Bands of Bungner, reaching the distal end of the severed nerve, re-energating the distal target, guided by the horizontal aligned cues. Xia *et al.* (273) aimed at meticulously analyze the specifics of neurite growth of DRGs on randomly oriented and aligned poly(methyl methacrylate) (PMMA) nanofibers and understand the relationship between neurites and nanofibers, as well as the alignment or random orientation of the nanofibers. The authors verified a relationship between neurites and nanofibers, as the neurites of DRGs were in close contact with the substrate nanofibers, and the neurites seemed to follow aligned nanofibers more than randomly oriented nanofibers. Most importantly, when co-cultured, DRGs and SCs revealed that on aligned nanofibers, neurites and SCs had a higher chance of co-localization than on randomly oriented nanofibers, which is of key importance in the process of nerve regeneration. The same authors (86) described aligned

electrospun PMMA nanofibers as a SC-loading scaffold *in vitro*, by monitoring the GFP-containing SCs cultured on nanofibers. They found that aligned nanofibers provided better support for the cells than did non-aligned nanofibers, as relationships between SCs and fibers could clearly be seen. Once again, the co-culture experiment showed on aligned nanofibers both SCs and DRGs adhered and elongated along the axes of the fibers, so they had a higher chance of co-localization is definitely beneficial to ensure the process of myelination.

Hu *et al.* (87) were able to combine biomaterials and stem cells in an approach where neuronal differentiation of stem cells was based on the temporally sequential use of *miR-218* and Fibroblast Growth Factor 2 (FGF2) *in vitro*, (FGF2-*miR-218* induction approach). Furthermore, the authors applied this novel approach in repairing sciatic nerve damage *in vivo*. The neuronally differentiated ASCs were integrated with the 3D aligned nanofibers and implanted in a 10 mm transected rat sciatic nerve defect *in vivo*. The results showed that, compared to randomly aligned nanofibers, the nanofibers in an aligned orientation favored stem cell growth and elongation. Furthermore, FGF2-*miR-218* induction approach combined with the poly(hydroxybutyrate-co-3-hydroxyvalerate) (PHBV) 3D nanofiber scaffolds facilitated nerve regeneration.

In a complex report also involving biomaterials and stem cells, Lin *et al.* (274) used mouse iPSCs generated from mouse embryonic fibroblasts with the non-integrating episomal vectors pCEP4-EO2S-ET2K and pCEP4-miR-302-367 cluster and differentiated them into NSCs as transplanting cells. Electrospinning was then used to fabricate randomly oriented and aligned PLLA nanofibers. Compared with randomly oriented, the aligned PLLA nanofibers greatly directed neurite outgrowth from the iNSCs and significantly promoted neurite growth along the nanofibrous alignment. Tseng *et al.* (275) developed an innovative system where a substrate made of aligned electrospun PLLA microtube array membrane (MTAM) was successfully developed as a cell co-culture platform. Its architecture is based on one-to-one connected, ultrathin, nano-scale fibers that are set in an arrayed creation. To study the co-culture potential, rat fetal NSC and astrocytes were examined by relating the outcome of a typical transwell-based co-culture system and that of MTAM-based co-culture system. Greater cell viability of NSC was detected when cultured in electrospun PLLA MTAM and RT-PCR exposed a robust interaction between astrocytes and NSC confirming that MTAM is clearly a better co-culture platform than the traditional Trans-well system.

Making use of aligned nanofibers, Whitehead *et al.* (276) developed a conduit with all mechanical, chemical, and topographical cues destined for PNR. Methacrylated-HA was electrospun into aligned fibers, with poly-lactic-co-glycolic acid microspheres to deliver NGF. DRG seeded in the scaffolds revealed that the combination of NGF release from the microspheres and the aligned nanofibers significantly increased neurite growth (**Figure III-8C**).

To address some limitations of the regular 3D printing, Lee *et al.* (277) combined stereolithography and electrospinning techniques to fabricate a novel 3D biomimetic neural scaffold with a tunable porous structure and highly aligned nanofibers. PCL nanofibers were mixed with gelatin and further embedded in 3D printed hydrogel scaffold. Then printable hydrogel inks, composed of 40 %wt.

Polyethyleneglycol (PEG), 60 %wt. diacrylate (PEG-DA) and photo-initiator (0.5 %wt. of PEG-DA concentration) covered the electrospun fiber. As expected, the results indicated that 3D printed scaffolds with electrospun fibers significantly improved NSC adhesion when compared to those without the fibers. Notably, the scaffold with PCL/gelatin fibers greatly increased the average neurite length and directed neurite extension of primary cortical neurons along the nanofibers. Du *et al.* (278) was capable of producing a 3D hierarchically aligned fibrin nanofiber hydrogel through electrospinning and molecular self-assembly to resemble the architecture and biological function of the native fibrin cable mentioned before as bands of Bungner. In this produced biomaterial, nanofibers are laid in the surface of the hydrogel. Firstly, *in vitro* assays with SCs and DRGs showed fast and directional cell adhesion and migration, as well as alignment of neurites. Secondly, the aligned hydrogel was then used as a potential intraluminal substrate in a bioengineered chitosan tube to bridge a 10 mm long sciatic nerve gap in rats, revealing a beneficial microenvironment to support SCs cable formation and axonal regrowth within 2 weeks, with similar results to the autograft after short and long-term studies.

III-3.3.3. Nanofibers combined with conductive materials

Das *et al.* (279) synthesized and described for the first time Polyaniline-based (PA) nerve conduits, expressing the safety and efficacy of the conduits in PN injuries. For the production of such conduits, the nanocomposite was synthesized by electrospun a mixture of PA and SF, in which the silk nanofibers were uniformly coated with PA. Subsequently, by means of rolling of the

electrospun sheet over a stainless-steel mandrel, tubular shaped nerve conduits are molded. It was verified that implanted PA-SF conduits seeded with SCs exhibited exceptional nerve conduction velocity, compound muscle action potential, motor unit potential, visible growth of healthy tissue along the nerve gap and thick myelination of axons 12 months after implantation, indicating enhanced neuro-regeneration, when compared to similar electrically conductive conduits. Using PPy as the conductive material to blend in the nanofibers, Zhou and colleagues (280) could enhance neurite adhesion, alignment and elongation of PC12 cells on PPy-PLA conductive fiber-film (CFF) coated with cell-derived ECM derived from L929 cells (CFF-ECM). By combining the developed material with electrical stimulation, it was verified that PC12 cell adhesion rate, neurite-bearing cell rate, neurite alignment rate and neurite length on ECM-CFF were significantly larger than the corresponding values on bare CFF. Using the same materials, PPy and PLA, Zhou *et al.* (281) embedded PPy into PLA nanofibers *via* electrospinning and fabricated a PLA/PPy nanofibrous scaffold. *In vitro* assays with human umbilical cord mesenchymal stem cells as well as SCs proved the scaffolds had good biocompatibility with such cells. Additionally, the direction of cell elongation on the meshes containing 15 %wt PPy proved sustained conductivity and aligned topography. Song *et al.* (282) investigated the abilities of direct current electrical stimulation through electrospinning conductive polymer composites composed of PPy and PLCL (PPY/PLCL) in PN regeneration. PC12 cells and DRGs cells cultured on PPY/PLCL scaffolds were stimulated with 100 mV/cm for 4 hours per day. After that, the median neurite length and cell viability were measured in PC-12 cells and the levels of BDNF, GDNF and NT-3 were analyzed in DRG neurons, revealing that not only the quantity of PC12 cells increased, but also the median neurite length increase significantly after electrical stimulation. Regarding the neurotrophic factors, all of them were up-regulated, which was detected by western blot, RT-PCR and Elisa quantifications. When implanted *in vivo* and after electrical stimulation, the results revealed satisfying functional recovery and equivalent morphological recovery to nerve autografts (**Figure III-8D**).

After this review of the lately published works comprising both random and aligned nanofibers, as well as mixed with conductive polymers, one can easily see the huge potential of these nanotechnologies. This is primarily related with three points: i) its resemblance with ECM, to which PNS cellular components easily adhere, ii) the advantage of this technology that allows to change its architecture to extremely aligned nanofibers, which is of crucial significance in PNR,

as the process of nerve regeneration itself lies in the formation of aligned fibrin cables and ultimately possibly to augment nerve regeneration, and iii) the electrospinning allows the easy incorporation of many kinds of substrates and molecules, such as vitamins, conductive polymers or other polymers that might act as co-adjuvants or stimulants in the process of regeneration.

III-3.4. Topographic cues at micro- and nano-scale

There is now sufficient body of evidence which states that artificial physical cues, such as topography, can have an important impact on the neuronal cell functions (285). In fact, a relatively new theory states that the growth cone guidance follows the “substrate-cytoskeletal coupling” model (286). Accordingly, “growth cones can move forward if they are capable of coupling intracellular motility signals to a fixed extracellular translocation substrate via cell surface adhesion receptors”.

The power of topography and its influence on neuronal cells has been established as early as 1914, when R. G. Harrison first cultured embryonic frog in the threads of a spider web. Surprisingly, he observed that the cells specially stretched along the support given by the threads (287). With the new production techniques of micro- and nano-topographies, new types of cell culture platforms can be established, and the influence of a panoply of topographical cues can be studied in what regards cellular functions, such as cytoskeleton morphology, proliferation or differentiation. However, most of the structures that were studied and had the power to affect axonal growth and alignment were of micro-sizes (288-290). In the field of topography, there are several methods available for the development of patterned biomaterial surfaces, ranging from simple manual scraping to highly controlled manufacture methods. Contact printing, (291) lithography, (292) microfluidic patterning (293) and electrospinning (269) are some of the techniques that allow a more precise and nano-scale physical cues to be achieved. **Table III-10** resumes the use of nano-scaled topographic cues applied in PN regeneration (294-298). **Figure III-9** depicts some of the most interesting achievements related to topographic and neuronal investigations.

In what concerns nanotopography, Ferrari *et al.*(294) studied the neuronal polarity of PC12 cells on cyclic-olefin-copolymer grooves of 350 nm depth and 500 nm groove width with varying ridge width. It was shown that cells would fluctuate from monopolar and bipolar to multipolar

morphology, as the ridges width shifted, as seen in **Figure III-9A**. The same authors (295) described an experience where PC12 cells were in contact with nano-gratings, which are periodic sub-wavelength structures, where there is an alternating of submicron lines of ridges and grooves, with 350 nm depth and with line widths and pitches of 500 nm were fabricated by nanoimprint lithography. Cells were stimulated or co-stimulated with NGF and other neuronal factors like forskolin.

Table III-10 - Nano-scale topographic cues applied to peripheral nerve regeneration

| Type of nanomaterial | Cell type or animal model | Main results | Year, Reference |
|---|--------------------------------------|--|------------------------------------|
| Nanogratings with 350 nm depth and with line widths and pitches of 500 nm were fabricated | PC12 cells | Nanogratings with the smallest ridge size (500 nm) strongly favor bipolar cells and a transition to multipolarity is obtained increasing the ridge width to 1500 nm; | Ferrari <i>et al.</i> , 2011 [294] |
| Nanogratings with 350 nm depth and with line widths and pitches of 500 nm were fabricated | PC12 cells | Topographical guidance in PC12 cells is modulated by the activation of alternative neuronal differentiation pathways; | Ferrari <i>et al.</i> , 2010 [295] |
| X-ray lithography was used to pattern silicon wafers. The resulting period:ridge widths for the six patterned surfaces were as follows; 400:70, 800:250, 1200:400, 1600:650, 2000:850 and 4000:1900 (nm). Groove depths were 600 nm | PC12 cells | It was verified that the scale of substratum features can act supportively with sub-optimal growth factor concentrations acting as chemical cues to stimulate neurite extension; | Folei <i>et al.</i> , 2005 [296] |
| Lines are fabricated by standard photolithography methods | Neurons from adult medicinal leeches | Neuronal processes, which are of micron size, have strong interactions with ridges even as low as 10 nm in which the interactions depend on the ridges' height; | Baranes <i>et al.</i> , 2012 [297] |
| Varying micro and nano-scale geometries: resorcinol-formaldehyde (RF) gel derived carbon films and electrospun nanofibrous (~200 nm diameter) mat and SU-8 (a negative photoresist) derived carbon micro-patterns | Neuroblastoma cells and SCs | The <i>in vitro</i> studies on such carbon scaffolds using neural cells confirm that SCs are more adaptive towards topographic cues than undifferentiated N2a cells; | Mitra <i>et al.</i> , 2013 [298] |

It was found that the presence of Forskolin diminished the phenomena of neurite alignment to the nanogratings which was related to the inhibition of focal adhesion maturation necessary for the alignment to occur.

In a pioneer work, Foley *et al.* (296) addressed the question of which role topography might play in promoting neurogenesis, since the phenomena of contact guidance has been well established before. For that, the authors cultured PC12 cells within an array of NGF concentrations on surfaces with ridge sizes ranging from 70 nm up to 1900 nm. Interestingly, it was found that with sub-optimal or lower concentrations of NGF, the neurogenesis was reinforced by topographic feature size. Also, contact guidance would happen to feature sizes as small as 70 nm. These results propose that topographic features can act compliantly with NGF signaling to regulate the formation and development of neurites. Baranes *et al.* (297) used photolithography to produce matrices with line-pattern ridges in the nano-scale dimension. By using neurons isolated from the CNS of adult leeches, they found that majority of the neuronal processes that approach ridges of 75 nm and higher are affected by the ridge and change their original growth direction, as seen in **Figure III-9B**. Also, there are two parameters that, according to them, must be considered when predicting the probability of a neuronal process to be affected by the ridge: the ridges' height and the neuronal incoming angle, since for low ridges, the larger effective membrane surface due to acute incoming angles compensates the lack of adhesion surface.

CNT can also be considered as a kind of nano-scale surface texture. Megan *et al.* (112) was able to verify that motor neurons grow and align when seeded over thin films of horizontally aligned CNTs. Mitra *et al.* (298) also worked with carbon materials, this time in a study that involved textured carbon substrates which were planned for investigation of neural cell performance and cytocompatibility. Nano-scale geometries in materials like resorcinol-formaldehyde gel derived carbon films and electrospun nanofibrous (200 nm diameter) mat derived carbon micro-patterns were tested with results showing that textural features from 200 nm (carbon fibers) were found to affect neurite outgrowth. Furthermore, regardless of the randomness of carbon nanofibers, they promoted preferential differentiation of N2a cells into neuronal lineage, showing the importance of the nano-scale topography.

With the above reviewed works, it is our feeling that it would be interesting to further explore the lower limit of neuronal sensitivity to nano-scale topographic cues and the resolution of that sensitivity.

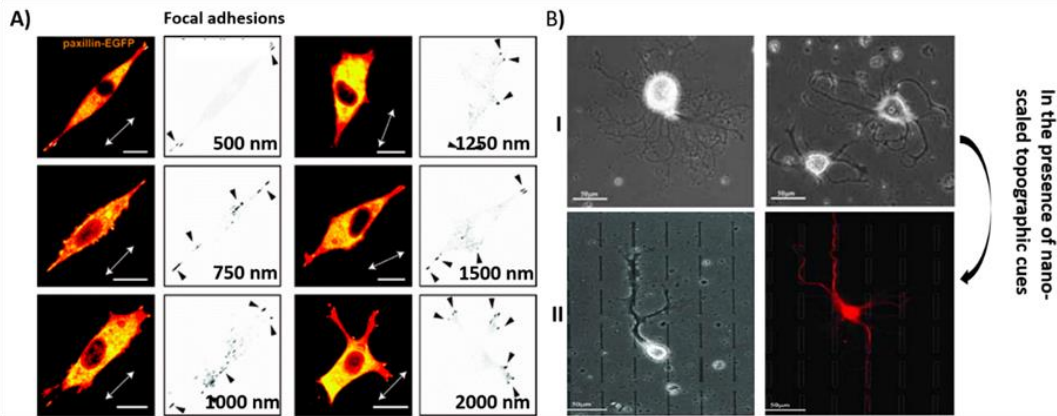


Figure III-9 - The influence of nano-scaled topographic cues on cellular behavior. A) Focal adhesion establishment by stimulating PC12 contacting nanogratings with increasing ridge width. EGFP fluorescent signal in PC12 cells differentiating on nanogratings with a ridge width corresponding to (I) 500nm; (II) 750 nm; (III) 1000 nm; (IV) 1250 nm; (V) 1500 nm; and (VI) 1500 nm. White arrows indicate the direction of the nanografting. Scale bar: 10 μ m; and B) (I) Leech neurons growing atop control substrates pre-coated with concanavalin-A. No preferable growth direction can be detected; and (II) Leech neurons growing on nano-patterned substrates pre-coated with concanavalin-A. Pattern ridges of 25 nm in height. The neuronal branches attach to the ridges and the whole growth pattern is aligned according to the topographic cues. Reprinted and adapted from A) [309]; B) [312].

III-4. NANOTHERANOSTICS AND IMAGING

The concept of theranostics relies in the combination of both therapeutics and diagnostics in one set. It is based in the image-guided therapy and also defining the treatment outcome at an early stage (299). Theranostics should provide a visualization and tracking of imaging-labeled components not only for the diagnosis of the problem, but also possibly assessing the biodistribution of a therapeutic drug during treatment or specific molecular target (300). Up to date, whenever an injury to PN is confirmed in the clinic context, the standard diagnosis is generally based on a fusion of simple clinical examination findings by the physicians and neuro-electrophysiology approaches (301). Consequently, the diagnosis precision is often reduced since the two approaches mentioned before do not provide satisfactory information for the needed surgical repair, which in turn leads to improper treatments and poor outcomes for the patients, which results in life-long disabilities.

The fact that injuries vary according to patient populations, etiologies, age and complexity of the injuries are co-adjutant of this problem. The alarming consequences of PNI are not because of the injury itself, but due of the poor diagnosis and delayed time of medical action (302, 303).

Furthermore, whenever a treatment like surgery is applied, there is a complete lack of monitoring tools and reliable non-invasive strategies to assess the consequent degeneration or axonal regeneration into the distal segment (304). Therefore, there is a pressing medical need for the development of reliable and reproducible, non-invasive imaging strategies (305). Such imaging strategies must have adequate spatial and temporal resolution for the early and exact diagnosis assessment of PNI as well as continued monitoring after treatment (306). Consistent, harmless, noninvasive and reproducible methodologies that aid in the determination of the injury degree and nature are required for the correct diagnosis, for instance to help in finding the exact location where changes in the normal nerve anatomy occurred. Once the diagnosis is correctly made, “regenerative tracking” and longitudinal monitoring of nerve regeneration, followed by treatment with neurotherapeutics holds great promise to achieve well-timed and precise treatments of PNI (307).

A few imaging techniques have been exploited for PNI, both in the scientific and pre-clinical settings, such as optical imaging, positron emission tomography computed tomography, magnetic resonance imaging, high resolution ultrasound and nuclear medicine (303, 308-311). Nevertheless, despite the promising advances in the literature, it remains clinically difficult to apply noninvasive imaging technologies, since most require general improvement to be considered as a standard method (312). Now a days, there are two main methods used for imaging of PNS. The first is ultrasound, thanks to its wide availability and spatial resolution. Its use has clearly established indications and is particularly useful for PNS tumors. MRI is commonly considered as the second-line imaging method, aiming at providing decisive additional information thanks to its excellent contrast resolution. Both technologies are robust and widely spread in the clinic. Also, one has to consider the strong benefit of being able to examine the perineural environment, which cannot be evaluated by clinical examination alone or by electroneuromyography (313).

However, despite the panoplies of imaging methods mentioned before, it has been discussed previously that, in summary, MRI is the one that offers most promising results when in combination with nanotechnology, therefore is considered the best potential tool for PNI. MRI uses a robust magnetic field to generate a magnetization in the tissue, followed by a disruption of magnetization with a brief radio pulse (314). In one hand, the resolution of the standard MRI is within the range of hundreds of microns which goes against the possibility of using it for

visualizing axons which are from 5 to 10 μm . On the other hand, high definition MRI-based imaging techniques are highly specialized, very expensive and logistically restricted, so most often unreachable by patients who need it (315). As a result, nano-systems tactics allied to MRI for molecular and cellular imaging after PNI must be highly considered. Furthermore, these systems that would allow visualizing the true cellular behaviors and molecular complex phenomena that take place after injuries of each patient would gratefully contribute to personalize medicine and provide a patient specific therapy. In our opinion, nanotechnology is the way to address this need. NPs such as iron oxide NPs are an especially useful tool in nano-systems based imaging. They are highly sensitive contrast agents that can be up-taken by cells and their position changed by magnetic fields and located by MRI (316).

Perfluorocarbon (PFC) nanoemulsions are also considered as attractive nano-components as imaging platforms (317). They are highly biologically inert and easily detected by MRI (318). **Table III-11** summarizes the approaches envisioned for nanotheranostics and nanoimaging comprising nanotechnology in the field of PN regeneration (306, 319-324). Also, **Figure III-10** reveals some of the most exciting results obtained in the field of theranostics and nano-imaging. Zheng *et al.* (306) described a molecular and nano-scale imaging methodology, namely molecular and cellular MRI (MCMRI). Based on the fact that there are cellular and molecular changes on the nervous system, both at proximal and distal sites after an injury, the authors hypothesized that *in vivo* PN targets can be imaged using MCMRI with specific probes, based on injured nerve specific proteins as targets. That was achieved by using a molecular antibody fragment conjugated to iron NPs as an MRI probe. The options considered were protein 0 (P0) and PMP 22 kDa as PNs specific target proteins, since the exclusivity of the targets in PNs is the basis of this hypothesis. To be able to get an image, such antibodies fragments were conjugated to ultra-small super paramagnetic iron oxide (USPIOs), which shortens the transverse relaxation of hydrogen proton and influence the imaging signal intensity and enhances the contrast. However, for this hypothesis to be successful, it is essential that the probes have good bio-distribution and are able to surpass the blood-brain barrier and have its deposition done in PNs.

In another study, Ghanouni *et al.* (319) used USPIOs conjugated with MRI to monitor macrophage trafficking, with the purpose of determining whether minocycline modulates macrophage trafficking to the site of PN injury *in vivo* and, in turn, results in altered pain thresholds. In fact, Animals with neuropathic pain in the left hindpaw show increased trafficking

of USPIO-laden macrophages to the site of sciatic nerve injury, which might contribute to the anti-nociceptive effect. Umashankar *et al.* (320) performed a comprehensive examination of rat NSC survival and regenerative function upon labeling with a specific kind of USPIO, named Molday ION Rhodamine B (MIRB), which allows for dual MRI and optical imaging. They observed that both MIRB doses (20 and 50 $\mu\text{g}/\text{mL}$) supported the robust detection of NSCs, over an extended period of time *in vitro* and *in vivo* after transplantation into the striata of host rats, using MRI and fluorescence imaging. However, animals receiving the 50 $\mu\text{g}/\text{mL}$ MIRB-labeled NSCs, had an immune response consisting of an increased number of CD68(+)-activated microglia, which appeared to have phagocytized MIRB particles and cells contributing to an exaggerated MRI signal dropout in the animals. Li *et al.* (321) investigated the feasibility of the use of MRI to noninvasively track the role of ASCs in the repair of PNI *in vivo*. For such, the authors isolated, expanded and differentiated Green fluorescent protein (GFP)-expressing ASCs into SC-like phenotype (GFP-dASCs) at early passages and subsequently labeled with SPIONs. The results showed GFP-dASCs were efficiently labeled with SPIONs, without affecting their viability and proliferation. The labeled cells implanted into the mice sciatic nerve conduit exhibited a significant increase in axonal regeneration compared with the empty conduit and could be detected by MRI. Some images of such results can be seen in **Figure III-10A**. In other approaches, the MRI technique has been mainly used to detect the migration of immune cells in living organisms, which contributes to the adequate understanding of the pathologies (322, 325). Also, the understanding of the neuroinflammation process is of extreme importance, as a comprehensive approach on this parameter will give clues about neuronal regeneration. Also, the process of neuroinflammation changes during the course of the injury and respective restorative pathway. Therefore, it can be used to monitor the variable progress from individual to individual, using MRI as the most promising imaging technique. Fortunately, monocytes and macrophages are key players in the neuroinflammation process and are also extremely reachable to be used as cellular targets, since they usually phagocytose the imaging agents or NPs injected in the blood stream (326). Zhong *et al.* (322) evaluated the ability to noninvasively image and quantitate disease pathology using emerging “hot-spot” ^{19}F MRI methods in an experimental autoimmune encephalomyelitis rat. Once again, PFC nanoemulsion was used and injected intravenously, which labeled predominately monocytes and macrophages *in situ*. Once again, the analysis of

the spin-density weighted ^{19}F MRI data enabled quantification of the apparent macrophage burden in the central and peripheral nervous system and other tissues, as can be seen in **Figure III-10B**.

Table III-11 - Theranostics and nanoimaging applied to peripheral nerve regeneration.

| | Type of nanomaterial | Cell type or animal model | Main result | Year, Reference |
|------------------------------|---|---|--|---------------------------------------|
| PNR imaging with MRI | USPIO labeling protein O (P0) and PMP 22 kDa | Not applicable | The developed MRI probe would allow for imaging the PN targets <i>in vivo</i> ; | Zheng <i>et al.</i> , 2014 [306] |
| | USPIO conjugated with MRI | A model of neuropathic in rat sciatic nerve | Animals with neuropathic pain in the left hind paw show increased trafficking of USPIO-laden macrophages to the site of sciatic nerve injury; | Ghanouni <i>et al.</i> , 2012 [319] |
| | USPIO, Molday ION Rhodamine B (MIRB) | Rat Neural Stem Cells | Although USPIO particles, such as MIRB, may have advantageous labeling and magnetic resonance-sensitive features for NSC tracking, a further examination of their effects might be necessary before they can be used in clinical scenarios of cell-based transplantation due to exaggerated MRI signal dropout in the animals; | Umashankar <i>et al.</i> , 2016 [320] |
| | SPION-labeled cells | GFP-expressing ADSCs; mice sciatic nerve defect | Histological analysis and immunohistochemistry confirmed the axon regeneration firstly revealed by MRI; | Li <i>et al.</i> , 2013 [321] |
| Imaging of neuroinflammation | Perfluorocarbon nanoemulsion, which is phagocytosed by inflammatory cells | Autoimmune encephalomyelitis rat | The <i>in vivo</i> MRI results were confirmed by extremely high-resolution $^{19}\text{F}/^1\text{H}$ magnetic resonance microscopy; | Zhong <i>et al.</i> , 2015 [322] |
| | Perfluorocarbon nanoemulsion, which is phagocytosed by inflammatory cells | Chronic constriction injury in rat | The results demonstrate that the infiltration of immune cells into the sciatic nerve can be visualized in live animals using these methods; | Vasudeva <i>et al.</i> , 2014 [323] |
| | Perfluorocarbon nanoemulsion | Rat sciatic nerve | ^{19}F MRI allows <i>in vivo</i> visualization of inflammation in the peripheral nervous system. Inflammation is detected unambiguously with high spatial resolution. Quantification of the fluorine signal is possible with <i>ex vivo</i> ^{19}F spectroscopy; | Weise <i>et al.</i> , 2011 [324] |

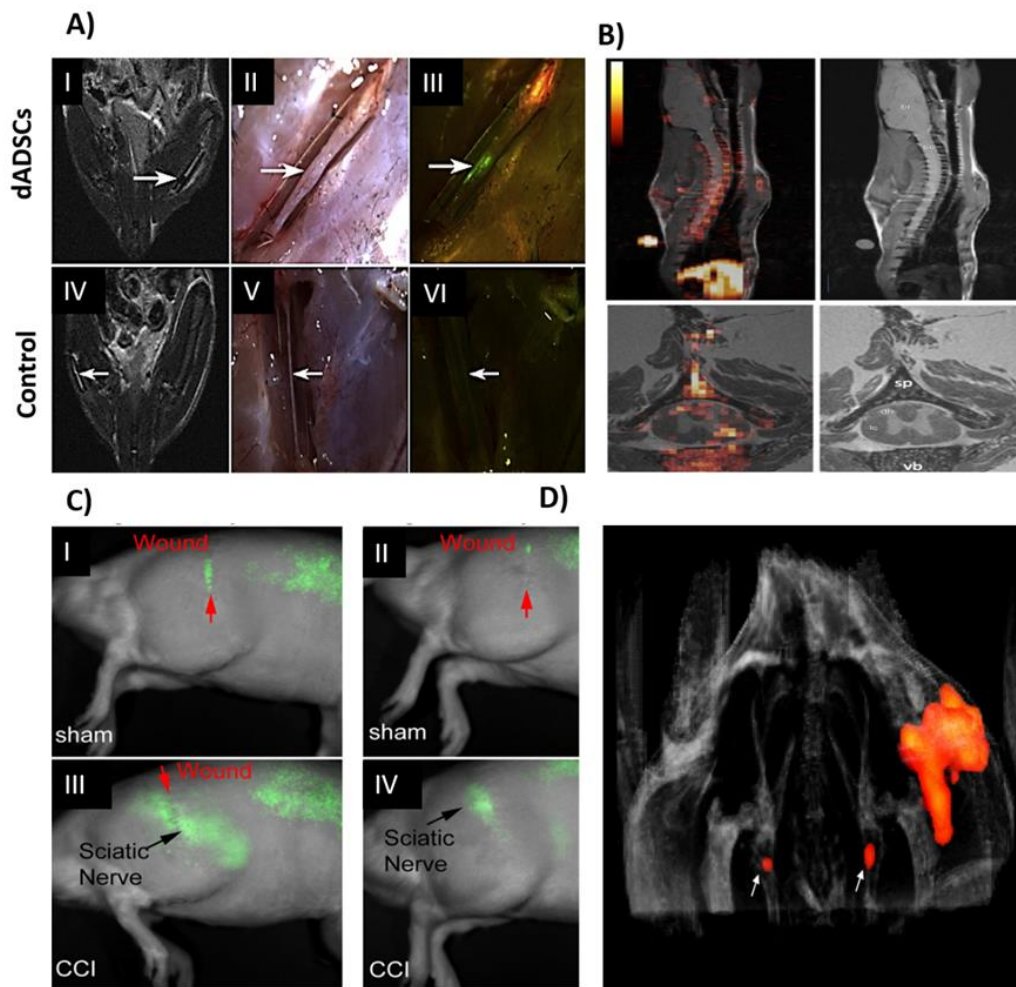


Figure III-10 - The application of theranostics and nanoimaging in peripheral nerve regeneration. A) Images of SPION-labeled GFP-dADSCs sciatic nerve. (I) MR images of operated sciatic nerve 28 d after transplantation; (II) Photograph of nerve that has been transplanted with GFP-dADSCs; (III) Fluorescent images of the nerve that has been transplanted with GFP-dADSCs; (IV) Positive control of I; (V) Positive control of II and (VI) Positive control of III. White arrows point to the regenerated sciatic nerve; B) *In vivo* and *ex vivo* ¹⁹F/¹H MRI of experimental autoimmune encephalomyelitis rat shows ¹⁹F signal arising from the spinal cord and adjacent vertebral bone marrow, representing accumulation of inflammatory phagocytes; C) Perfluorocarbon nanoemulsion, which is phagocytosed by inflammatory cells, was used in a rat pain model. The nanoemulsion is a near-infrared (NIR) lipophilic fluorescence tracer. The images demonstrate that in live rats, NIR fluorescence is concentrated around the affected sciatic nerve or in the area where incision was made, both reporting the site of macrophages location; and D) *In vivo* ¹⁹F MRI performed 5 days after induced nerve injury. In each rat, the fluorine marker uptaken by macrophages could be exclusively found in the left affected thigh, to where macrophages migrated. Two small bilateral “hot spots” are illustrated close to the spine which represent draining lymph nodes where marked macrophages also accumulate; and Reprinted and adapted from A) [336]; B) [337]; C) [338] D) [339].

Vasudeva *et al.* (323) hypothesize that the infiltration of immune cells into the affected sciatic nerve could be monitored *in vivo* by molecular imaging. To test this hypothesis, an

intravenous injection of a novel PFC nanoemulsion, which is phagocytosed by inflammatory cells, was used in a rat chronic constriction injury model in the sciatic nerve. To monitor the events, the nanoemulsion carries two distinct imaging agents, a near-infrared (NIR) lipophilic fluorescence reporter and a ^{19}F MRI (magnetic resonance imaging) tracer. They have demonstrated that NIR fluorescence is concentrated in the area of the affected sciatic nerve as well as the ^{19}F MRI signal, as can be seen in **Figure III-10C**. That was proven to be true when histological examination revealed significant infiltration of CD68 positive macrophages. Weise *et al.* (324) established ^{19}F MRI for cell tracking in the PNS of rats. In their experiment, in order to induce neuroinflammation, lysolecithin was injected directly into the left sciatic nerve which lead to demyelination followed by severe infiltration of monocytes/macrophages. In fact, and as a proof of concept, systemic administration of PFC led to a fluorine signal along the proximal stretch of the affected sciatic nerves in *in vivo* ^{19}F MRI which was not seen on the right healthy side. An *in vivo* ^{19}F MRI performed 5 days after induced nerve injury can be seen in **Figure III-10D**.

Despite the reviewed promising advances, noninvasive imaging of PNI remains in its infancy in the clinic. In this specific field, it is essential that pharmaceutical industries take a leading role so that translation of innovative technologies is accelerated from the bench to the clinics.

III-4.1. Nanotheranostics toxicity

In the nanotheranostics field, PFCs have attracted a great deal of attention in the last decade. Two main factors contribute to the high positive impact of PFCs: (i) the lack of natural endogenous background signal *in vivo* and (ii) the high NMR sensitivity of the ^{19}F atom. These make PFC nanoemulsions ideal agents for cellular and magnetic resonance molecular imaging (327). The wide range of drugs that PFCs can incorporate represent another advantage. Its core is surrounded by a lipid monolayer that can be functionalized to contain various agents for imaging or therapeutic action (328). Despite the high toxicity presented by many drugs of interest, namely anti-tumor drugs, the use of such nanoemulsions can increase the degree of tumor targeting while diminishing its undesired secondary effects (329). Analyzing PFCs toxicity, the tissue clearance time varies based on the chemical compound. These tissue half-lives range from 4 days to 65 days (329). Clearance of PFCs takes place not through

metabolism, but through slow dissolution back into the circulation by the lipid carriers in the structure being, in a last step, removed through expiration (330).

In a study developed by Zhong *et al.* (322). PFCs showed uptake at 24 h primarily in the liver, followed by spleen and lung, with minimal uptake in kidney and heart, with no binding to the brain. Indeed, no negative change was seen in animal body during the time of the study, even with multiple nanoemulsion administrations. At this point of research, all the findings point to the potential of nanoemulsions for accurate organ/cell targeting while imaging at the same time, with no apparent toxicity, being considered one of the greatest advantages in the medical field.

Still in the field of theranostics, iron oxide contrast agents, well known as USPIOs, have been combined with magnetic resonance imaging for cell tracking. There are two main reasons why these nanoparticles need to be coated. The first is related to the fact that iron nanoparticles interact with each other in two forms: magnetically and via van der Waals' interactions, leading the NP to flocculate (331). The second reason is related to their cytotoxicity, as uncoated NP have been shown to have up to a six-fold increase in cytotoxicity compared to dextran-coated iron NP. That cytotoxicity is mainly related to the creation of ROS, reduction of cellular proliferation and induction of cell death (332).

When it comes to USPIOs elimination by the body, they are phagocytosed by the reticuloendothelial system from the blood pool. These nanoparticles are typically taken up by macrophages and phagocytic cells in the liver, bone marrow, and spleen. Afterwards, the lysosomal compartments of macrophages gradually degrade the iron nanoparticles (333).

USPIO's have been reported to have an intrinsic toxicity that can be overcome by means of performing a surface coating with a biocompatible polymer, therefore increasing its potential to be used in the medical practices. Such demonstration has been made in a study by Neuwelt *et al.* (334) where it was concluded that USPIOs agents are a viable a more safe option for patients which cannot use the typical Gadolinium based contrast agent due to chronic kidney disease.

III-5. FINAL REMARKS AND FUTURE PERSPECTIVES

Peripheral nervous injuries are a public-health problem and recent achievements within the nanotechnology area, in particular to what concerns the development of advanced nanomaterials

are expected to revolutionize novel therapies and provide improvements to current diagnostic and treatments. Furthermore, with nanotechnologies, the medical community is able to perform a more precise determination of the extent of the neuronal damage, which enables a better diagnosis, thereby leading to a proper treatment and improvement of the consequent outcomes, instead of just using the old functional evaluation of the damaged nerve.

It is believed that current pre-clinical successes of nanotechnology can and should be adopted and adapted to the science of PNs regeneration and reconstruction. Not only that, but the described technologies should have a future in the clinics, since their benefits are immense. There are several significant PNR challenges which have not been fully addressed yet, despite decades of research. Poor vascularization, guided tissue regeneration, excessive fibrosis and neuroinflammation are some of those hurdles

Carbon nanomaterials, which are characterized by their excellent electrical properties, are of full interest when considering that electrical stimulation is beneficial for PNR. Allied to the fact that it is possible to conjugate other molecules and that carbon nanomaterials can be arranged in specific topographies, the outcomes are overall improved when they are used as neuronal cellular substrates, either alone or in conjugation with other materials.

Nanoparticles have the widest spectrum of benefits, since their purposes are endless: they can be used to just improve any materials' bulk properties, to deliver growth factors in a controlled and dependent manner or be used to label and track cells. This is useful not only to better understand the mechanisms of naturally occurring PNR, but also to provide a permissive and encouraging environment for the regenerative process. Due to the aligned and nano-scaled nature of PNS components, nanofibers and nano-topographic cues are essential as physical cues and provide the guidance that PNs requires for a successful regeneration.

Finally, nanotheranostics and imaging allow to improve not only the diagnostic process, but also the course of treatment after PNIs. Recently developed contrast agents allow clear visualization of PNR phenomena, such as inflammation, pain and the regeneration itself, depending on the targeted cells and contrast agents used. All of the above-mentioned nanotechnologies have a promising role in the clinics, since the outcomes are always improved in their presence. However, at this stage, it is fundamentally important to assess each

nanotechnology safety, efficacy and quality, in order to be able to make that fundamental clinical translation.

The aforementioned sections overviewed the current nanomaterials, strategies and different approaches that scientists have been working on, that gives an insight into the dynamics of damage and regeneration of PNs and their cellular components.

III-6. ACKNOWLEDGMENTS

The authors acknowledge the Portuguese Foundation for Science and Technology (FCT) for the financial support provided to Joaquim M. Oliveira (IF/01285/2015) and Joana Silva-Correia (IF/00115/2015) under the program “Investigador FCT”.

III-7. REFERENCES

1. López-Cebral R, Silva-Correia J, Reis RL, Silva TH, Oliveira JM. Peripheral Nerve Injury: Current Challenges, Conventional Treatment Approaches, and New Trends in Biomaterials-Based Regenerative Strategies. *ACS Biomaterials Science & Engineering*. 2017;3(12):3098-122.
2. Gaudin R, Knipfer C, Henningsen A, Smeets R, Heiland M, Hadlock T. Approaches to Peripheral Nerve Repair: Generations of Biomaterial Conduits Yielding to Replacing Autologous Nerve Grafts in Craniomaxillofacial Surgery. *Biomed Res Int*. 2016;2016:3856262-.
3. Rosso G, Liashkovich I, Gess B, Young P, Kun A, Shahin V. Unravelling crucial biomechanical resilience of myelinated peripheral nerve fibres provided by the Schwann cell basal lamina and PMP22. *Scientific Reports*. 2014;4:7286.
4. Zhu S, Ge J, Wang Y, Qi F, Ma T, Wang M, et al. A synthetic oxygen carrier-olfactory ensheathing cell composition system for the promotion of sciatic nerve regeneration. *Biomaterials*. 2014;35(5):1450-61.
5. Grinsell D, Keating CP. Peripheral Nerve Reconstruction after Injury: A Review of Clinical and Experimental Therapies. *BioMed Research International*. 2014;2014:13.
6. Kawano H, Kimura-Kuroda J, Komuta Y, Yoshioka N, Li HP, Kawamura K, et al. Role of the lesion scar in the response to damage and repair of the central nervous system. *Cell and tissue research*. 2012;349(1):169-80.
7. Geuna S, Raimondo S, Ronchi G, Di Scipio F, Tos P, Czaja K, et al. Chapter 3 Histology of the Peripheral Nerve and Changes Occurring During Nerve Regeneration. *International Review of Neurobiology*. 87: Academic Press; 2009. p. 27-46.
8. Robinson LR. Traumatic injury to peripheral nerves. *Muscle & nerve*. 2000;23(6):863-73.
9. Plastaras CT, Chhatre A, Kotcharian AS. Perioperative upper extremity peripheral nerve traction injuries. *The Orthopedic clinics of North America*. 2014;45(1):47-53.
10. Won JC, Park TS. Recent Advances in Diagnostic Strategies for Diabetic Peripheral Neuropathy. *2016;31(2):230-8*.
11. Vasudevan S, Yan JG, Zhang LL, Matloub HS, Cheng JJ. A rat model for long-gap peripheral nerve reconstruction. *Plastic and reconstructive surgery*. 2013;132(4):871-6.
12. Palispis WA, Gupta R. Surgical repair in humans after traumatic nerve injury provides limited functional neural regeneration in adults. *Experimental neurology*. 2017;290:106-14.
13. Archibald SJ, Shefner J, Krarup C, Madison RD. Monkey median nerve repaired by nerve graft or collagen nerve guide tube. *The Journal of neuroscience : the official journal of the Society for Neuroscience*. 1995;15(5 Pt 2):4109-23.

14. Gu X, Ding F, Williams DF. Neural tissue engineering options for peripheral nerve regeneration. *Biomaterials*. 2014;35(24):6143-56.
15. Yan L, Yao Z, Lin T, Zhu Q, Qi J, Gu L, et al. The role of precisely matching fascicles in the quick recovery of nerve function in long peripheral nerve defects. *Neuroreport*. 2017;28(15):1008-15.
16. Alvites RD, Santos ARC, Varejão ASP, Mauricio ACPdCO. Olfactory Mucosa Mesenchymal Stem Cells and Biomaterials: A New Combination to Regenerative Therapies after Peripheral Nerve Injury. In: Pham PV, editor. *Mesenchymal Stem Cells - Isolation, Characterization and Applications*. Rijeka: InTech; 2017. p. Ch. 05.
17. Mizisin AP, Weerasuriya A. Homeostatic regulation of the endoneurial microenvironment during development, aging and in response to trauma, disease and toxic insult. *Acta Neuropathologica*. 2011;121(3):291-312.
18. Allodi I, Udina E, Navarro X. Specificity of peripheral nerve regeneration: Interactions at the axon level. *Progress in Neurobiology*. 2012;98(1):16-37.
19. SEDDON HJ. THREE TYPES OF NERVE INJURY. *Brain : a journal of neurology*. 1943;66(4):237-88.
20. Sunderland S. A classification of peripheral nerve injuries producing loss of function. *Brain : a journal of neurology*. 1951;74(4):491-516.
21. M.F G, M M, S H, Khan WS. Peripheral Nerve Injury: Principles for Repair and Regeneration. *The Open Orthopaedics Journal*. 2014;8:199-203.
22. DeFrancesco-Lisowitz A, Lindborg JA, Niemi JP, Zigmond RE. The neuroimmunology of degeneration and regeneration in the peripheral nervous system. *Neuroscience*. 2015;302:174-203.
23. Kiryu-Seo S, Kiyama H. The nuclear events guiding successful nerve regeneration. *Frontiers in molecular neuroscience*. 2011;4:53.
24. Conforti L, Gilley J, Coleman MP. Wallerian degeneration: an emerging axon death pathway linking injury and disease. *Nature reviews Neuroscience*. 2014;15(6):394-409.
25. Namgung U. The role of Schwann cell-axon interaction in peripheral nerve regeneration. *Cells, tissues, organs*. 2014;200(1):6-12.
26. Jessen KR, Mirsky R, Lloyd AC. Schwann Cells: Development and Role in Nerve Repair. *Cold Spring Harbor perspectives in biology*. 2015;7(7):a020487.
27. Chen P, Piao X, Bonaldo P. Role of macrophages in Wallerian degeneration and axonal regeneration after peripheral nerve injury. *Acta Neuropathol*. 2015;130(5):605-18.
28. Steketee MB, Oboudiyat C, Daneman R, Trakhtenberg E, Lamoureux P, Weinstein JE, et al. Regulation of intrinsic axon growth ability at retinal ganglion cell growth cones. *Investigative ophthalmology & visual science*. 2014;55(7):4369-77.
29. Saied A, Shekaari MA, Sadeghifar A, Karbalaiekhani A. Introduction of a New Suture Method in Repair of Peripheral Nerves Injured with a Sharp Mechanism. *The archives of bone and joint surgery*. 2015;3(4):254-9.
30. Pindrik J, Belzberg AJ. Peripheral nerve surgery: primer for the imagers. *Neuroimaging clinics of North America*. 2014;24(1):193-210.
31. Elkwood AI, Holland NR, Arbes SM, Rose MI, Kaufman MR, Ashinoff RL, et al. Nerve allograft transplantation for functional restoration of the upper extremity: case series. *The journal of spinal cord medicine*. 2011;34(2):241-7.
32. Fox IK, Mackinnon SE. Experience with Nerve Allograft Transplantation. *Seminars in Plastic Surgery*. 2007;21(4):242-9.
33. Gonzalez-Perez F, Cobianchi S, Geuna S, Barwig C, Freier T, Udina E, et al. Tubulization with chitosan guides for the repair of long gap peripheral nerve injury in the rat. *Microsurgery*. 2015;35(4):300-8.
34. Kehoe S, Zhang XF, Boyd D. FDA approved guidance conduits and wraps for peripheral nerve injury: A review of materials and efficacy. *Injury*. 2012;43(5):553-72.
35. Stang F, Keilhoff G, Fansa H. Biocompatibility of Different Nerve Tubes. *Materials*. 2009;2(4):1480.
36. Lee JY, Giusti G, Friedrich PF, Archibald SJ, Kemnitzer JE, Patel J, et al. The effect of collagen nerve conduits filled with collagen-glycosaminoglycan matrix on peripheral motor nerve regeneration in a rat model. *The Journal of bone and joint surgery American volume*. 2012;94(22):2084-91.
37. Young RC, Wiberg M, Terenghi G. Poly-3-hydroxybutyrate (PHB): a resorbable conduit for long-gap repair in peripheral nerves. *British journal of plastic surgery*. 2002;55(3):235-40.
38. Carvalho CR, López-Cebal R, Silva-Correia J, Silva JM, Mano JF, Silva TH, et al. Investigation of cell adhesion in chitosan membranes for peripheral nerve regeneration. *Materials Science and Engineering: C*. 2017;71(Supplement C):1122-34.

39. Moattari M, Kouchesfehiani HM, Kaka G, Sadraie SH, Naghdi M, Mansouri K. Chitosan-film associated with mesenchymal stem cells enhanced regeneration of peripheral nerves: A rat sciatic nerve model. *Journal of Chemical Neuroanatomy*. 2018;88(Supplement C):46-54.
40. Lin SC-Y, Wang Y, Wertheim DF, Coombes AGA. Production and in vitro evaluation of macroporous, cell-encapsulating alginate fibres for nerve repair. *Materials Science and Engineering: C*. 2017;73(Supplement C):653-64.
41. Huang YA, Ho CT, Lin YH, Lee CJ, Ho SM, Li MC, et al. Nanoimprinted Anisotropic Topography Preferentially Guides Axons and Enhances Nerve Regeneration. *Macromolecular bioscience*. 2018;18(12):e1800335.
42. Reichenberger MA, Mueller W, Hartmann J, Diehm Y, Lass U, Koellensperger E, et al. ADSCs in a fibrin matrix enhance nerve regeneration after epineural suturing in a rat model. *Microsurgery*. 2016;36(6):491-500.
43. Zhang XF, Liu HX, Ortiz LS, Xiao ZD, Huang NP. Laminin-modified and aligned poly(3-hydroxybutyrate-co-3-hydroxyvalerate)/polyethylene oxide nanofibrous nerve conduits promote peripheral nerve regeneration. *Journal of tissue engineering and regenerative medicine*. 2016.
44. Swindle-Reilly KE, Papke JB, Kutosky HP, Throm A, Hammer JA, Harkins AB, et al. The impact of laminin on 3D neurite extension in collagen gels. *Journal of neural engineering*. 2012;9(4):046007.
45. Zor F, Deveci M, Kilic A, Ozdag MF, Kurt B, Sengezer M, et al. Effect of VEGF gene therapy and hyaluronic acid film sheath on peripheral nerve regeneration. *Microsurgery*. 2014;34(3):209-16.
46. Haastert-Talini K, Geuna S, Dahlin LB, Meyer C, Stenberg L, Freier T, et al. Chitosan tubes of varying degrees of acetylation for bridging peripheral nerve defects. *Biomaterials*. 2013;34(38):9886-904.
47. Chen MB, Zhang F, Lineaweaver WC. Luminal fillers in nerve conduits for peripheral nerve repair. *Annals of plastic surgery*. 2006;57(4):462-71.
48. Guo Q, Liu C, Hai B, Ma T, Zhang W, Tan J, et al. Chitosan conduits filled with simvastatin/Pluronic F-127 hydrogel promote peripheral nerve regeneration in rats. *Journal of biomedical materials research Part B, Applied biomaterials*. 2017.
49. Li A, Hokugo A, Yalom A, Berns EJ, Stephanopoulos N, McClendon MT, et al. A bioengineered peripheral nerve construct using aligned peptide amphiphile nanofibers. *Biomaterials*. 2014;35(31):8780-90.
50. Meyer C, Stenberg L, Gonzalez-Perez F, Wrobel S, Ronchi G, Udina E, et al. Chitosan-film enhanced chitosan nerve guides for long-distance regeneration of peripheral nerves. *Biomaterials*. 2016;76:33-51.
51. Meyer C, Wrobel S, Raimondo S, Rochkind S, Heimann C, Shahar A, et al. Peripheral Nerve Regeneration Through Hydrogel-Enriched Chitosan Conduits Containing Engineered Schwann Cells for Drug Delivery. *Cell transplantation*. 2016;25(1):159-82.
52. Glaus SW, Johnson PJ, Mackinnon SE. Clinical strategies to enhance nerve regeneration in composite tissue allotransplantation. *Hand clinics*. 2011;27(4):495-509, ix.
53. Faroni A, Mobasser SA, Kingham PJ, Reid AJ. Peripheral nerve regeneration: experimental strategies and future perspectives. *Advanced drug delivery reviews*. 2015;82-83:160-7.
54. Sedaghati T, Yang SY, Mosahebi A, Alavijeh MS, Seifalian AM. Nerve regeneration with aid of nanotechnology and cellular engineering. *Biotechnology and applied biochemistry*. 2011;58(5):288-300.
55. Paviolo C, Stoddart PR. Metallic nanoparticles for peripheral nerve regeneration: is it a feasible approach? *Neural regeneration research*. 2015;10(7):1065-6.
56. Lee GP, Pernal SP, Shokuhfar T, Engelhard HH. Chapter 16 - Nanoparticles as Therapeutic Agents for Patients With Brain Tumors. In: Newton HB, editor. *Handbook of Brain Tumor Chemotherapy, Molecular Therapeutics, and Immunotherapy (Second Edition)*: Academic Press; 2018. p. 229-46.
57. Oprych KM, Whitby RL, Mikhalovsky SV, Tomlins P, Adu J. Repairing Peripheral Nerves: Is there a Role for Carbon Nanotubes? *Advanced healthcare materials*. 2016;5(11):1253-71.
58. de Ruiter GCW, Malessy MJA, Yaszemski MJ, Windebank AJ, Spinner RJ. Designing ideal conduits for peripheral nerve repair. *Neurosurgical focus*. 2009;26(2):E5-E.
59. Bueno FR, Shah SB. Implications of tensile loading for the tissue engineering of nerves. *Tissue engineering Part B, Reviews*. 2008;14(3):219-33.
60. de Luca AC, Lacour SP, Raffoul W, di Summa PG. Extracellular matrix components in peripheral nerve repair: how to affect neural cellular response and nerve regeneration? *Neural Regeneration Research*. 2014;9(22):1943-8.
61. Menorca RMG, Fussell TS, Elfar JC. Peripheral Nerve Trauma: Mechanisms of Injury and Recovery. *Hand clinics*. 2013;29(3):317-30.
62. Subramanian A, Krishnan UM, Sethuraman S. Development of biomaterial scaffold for nerve tissue engineering: Biomaterial mediated neural regeneration. *Journal of biomedical science*. 2009;16(1):108-.

63. Benga A, Zor F, Korkmaz A, Marinescu B, Gorantla V. The neurochemistry of peripheral nerve regeneration. *Indian Journal of Plastic Surgery : Official Publication of the Association of Plastic Surgeons of India*. 2017;50(1):5-15.
64. Gaudet AD, Popovich PG, Ramer MS. Wallerian degeneration: gaining perspective on inflammatory events after peripheral nerve injury. *Journal of neuroinflammation*. 2011;8:110.
65. Patel SK, Janjic JM. Macrophage targeted theranostics as personalized nanomedicine strategies for inflammatory diseases. *Theranostics*. 2015;5(2):150-72.
66. Stratton JA, Shah PT. Macrophage polarization in nerve injury: do Schwann cells play a role? *Neural Regeneration Research*. 2016;11(1):53-7.
67. Das A, Sinha M, Datta S, Abas M, Chaffee S, Sen CK, et al. Monocyte and macrophage plasticity in tissue repair and regeneration. *The American journal of pathology*. 2015;185(10):2596-606.
68. Siqueira Mietto B, Kroner A. Role of IL-10 in Resolution of Inflammation and Functional Recovery after Peripheral Nerve Injury. 2015;35(50):16431-42.
69. Mietto BS, Mostacada K, Martinez AMB. Neurotrauma and Inflammation: CNS and PNS Responses. *Mediators of Inflammation*. 2015;2015:251204.
70. Yao C, Mengjiao X, Yi G, Keyao T, Weimin W, Jianjun W, et al. Targeted chimera delivery to ovarian cancer cells by heterogeneous gold magnetic nanoparticle. *Nanotechnology*. 2017;28(2):025101.
71. Mathieu L, Adam C, Legagneux J, Bruneval P, Masmejean E. Reduction of neural scarring after peripheral nerve suture: An experimental study about collagen membrane and autologous vein wrapping. *Chirurgie de la Main*. 2012;31(6):311-7.
72. Kieran I, Knock A, Bush J, So K, Metcalfe A, Hobson R, et al. Interleukin-10 reduces scar formation in both animal and human cutaneous wounds: results of two preclinical and phase II randomized control studies. *Wound repair and regeneration : official publication of the Wound Healing Society [and] the European Tissue Repair Society*. 2013;21(3):428-36.
73. Hobson MI, Brown R, Green CJ, Terenghi G. Inter-relationships between angiogenesis and nerve regeneration: a histochemical study. *British journal of plastic surgery*. 1997;50(2):125-31.
74. Farber SJ, Hoben GM, Hunter DA, Yan Y, Johnson PJ, Mackinnon SE, et al. Vascularization is delayed in long nerve constructs compared to nerve grafts. *Muscle & nerve*. 2016;54(2):319-21.
75. Fansa H, Schneider W, Keilhoff G. Revascularization of tissue-engineered nerve grafts and invasion of macrophages. *Tissue engineering*. 2001;7(5):519-24.
76. Cattin A-L, Burden Jemima J, Van Emmenis L, Mackenzie Francesca E, Hoving Julian J, Garcia Calavia N, et al. Macrophage-Induced Blood Vessels Guide Schwann Cell-Mediated Regeneration of Peripheral Nerves. *Cell*. 2015;162(5):1127-39.
77. Lin P-C, Lin S, Wang PC, Sridhar R. Techniques for physicochemical characterization of nanomaterials. *Biotechnology advances*. 2014;32(4):711-26.
78. Kumar S, Ahlawat W, Kumar R, Dilbaghi N. Graphene, carbon nanotubes, zinc oxide and gold as elite nanomaterials for fabrication of biosensors for healthcare. *Biosensors & bioelectronics*. 2015;70:498-503.
79. Secor EB, Hersam MC. Emerging Carbon and Post-Carbon Nanomaterial Inks for Printed Electronics. *The journal of physical chemistry letters*. 2015;6(4):620-6.
80. Katz LM, Dewan K, Bronaugh RL. *Nanotechnology in cosmetics*. Food and chemical toxicology : an international journal published for the British Industrial Biological Research Association. 2015;85:127-37.
81. Noruzi M. Electrospun nanofibres in agriculture and the food industry: a review. *Journal of the science of food and agriculture*. 2016;96(14):4663-78.
82. Saracino GA, Cigognini D, Silva D, Caprini A, Gelain F. Nanomaterials design and tests for neural tissue engineering. *Chemical Society reviews*. 2013;42(1):225-62.
83. Padmanabhan J, Kyriakides TR. Nanomaterials, inflammation, and tissue engineering. *Wiley interdisciplinary reviews Nanomedicine and nanobiotechnology*. 2015;7(3):355-70.
84. Jin C, Fu T, Wang R, Liu H, Zou J, Zhao Z, et al. Fluorinated molecular beacons as functional DNA nanomolecules for cellular imaging. *Chemical Science*. 2017;8(10):7082-6.
85. Cunha C, Panseri S, Antonini S. Emerging nanotechnology approaches in tissue engineering for peripheral nerve regeneration. *Nanomedicine: Nanotechnology, Biology and Medicine*. 2011;7(1):50-9.
86. Xia H, Sun X, Liu D, Zhou Y, Zhong D. Oriented growth of rat Schwann cells on aligned electrospun poly(methyl methacrylate) nanofibers. *Journal of the Neurological Sciences*. 2016;369:88-95.
87. Hu F, Zhang X, Liu H, Xu P, Doulathunnisa, Teng G, et al. Neuronally differentiated adipose-derived stem cells and aligned PHBV nanofiber nerve scaffolds promote sciatic nerve regeneration. *Biochemical and Biophysical Research Communications*. 2017;489(2):171-8.

88. Wenwen Y, Xinquan J, Ming C, Wen Z, Dongxia Y, Yong Z, et al. A novel electrospun nerve conduit enhanced by carbon nanotubes for peripheral nerve regeneration. *Nanotechnology*. 2014;25(16):165102.
89. Ahn H-S, Hwang J-Y, Kim MS, Lee J-Y, Kim J-W, Kim H-S, et al. Carbon-nanotube-interfaced glass fiber scaffold for regeneration of transected sciatic nerve. *Acta Biomaterialia*. 2015;13(Supplement C):324-34.
90. Gupta P, Sharan S, Roy P, Lahiri D. Aligned carbon nanotube reinforced polymeric scaffolds with electrical cues for neural tissue regeneration. *Carbon*. 2015;95(Supplement C):715-24.
91. Chen N, Tian L, He L, Ramakrishna S. Nanobiomaterials for neural regeneration. *Neural Regeneration Research*. 2016;11(9):1372-4.
92. Lee J, Mahendra S, Alvarez PJJ. Nanomaterials in the Construction Industry: A Review of Their Applications and Environmental Health and Safety Considerations. *ACS Nano*. 2010;4(7):3580-90.
93. Shamim N, Sharma VK, editors. *Sustainable Nanotechnology and the Environment: Advances and Achievements*: American Chemical Society; 2013.
94. De Volder MFL, Tawfick SH, Baughman RH, Hart AJ. Carbon Nanotubes: Present and Future Commercial Applications. *Science*. 2013;339(6119):535.
95. Cha C, Shin SR, Annabi N, Dokmeci MR, Khademhosseini A. Carbon-Based Nanomaterials: Multifunctional Materials for Biomedical Engineering. *ACS Nano*. 2013;7(4):2891-7.
96. Chen Y-S. Effects of electrical stimulation on peripheral nerve regeneration. *BioMedicine*. 2011;1(1):33-6.
97. Lee S, Sheshadri S, Xiang Z, Delgado-Martinez I, Xue N, Sun T, et al. Selective stimulation and neural recording on peripheral nerves using flexible split ring electrodes. *Sensors and Actuators B: Chemical*. 2017;242(Supplement C):1165-70.
98. Iijima S. Helical microtubules of graphitic carbon. *Nature*. 1991;354:56-8.
99. Thess A, Lee R, Nikolaev P, Dai H, Petit P, Robert J, et al. Crystalline Ropes of Metallic Carbon Nanotubes. *Science*. 1996;273(5274):483.
100. Zishan HK, Numan AS, Sami SH, Ameer A, El-Shahawi MS. Multi-Walled Carbon Nanotubes Film Sensor for Carbon Mono-Oxide Gas. *Current Nanoscience*. 2012;8(2):274-9.
101. Alshehri R, Ilyas AM, Hasan A, Arnaout A, Ahmed F, Memic A. Carbon Nanotubes in Biomedical Applications: Factors, Mechanisms, and Remedies of Toxicity. *Journal of Medicinal Chemistry*. 2016;59(18):8149-67.
102. Tasis D, Tagmatarchis N, Bianco A, Prato M. Chemistry of Carbon Nanotubes. *Chemical Reviews*. 2006;106(3):1105-36.
103. Fraczek-Szczypta A. Carbon nanomaterials for nerve tissue stimulation and regeneration. *Materials Science and Engineering: C*. 2014;34:35-49.
104. Hopley EL, Salmasi S, Kalaskar DM, Seifalian AM. Carbon nanotubes leading the way forward in new generation 3D tissue engineering. *Biotechnol Adv*. 2014;32(5):1000-14.
105. Matsumoto K, Sato C, Naka Y, Kitazawa A, Whitby RLD, Shimizu N. Neurite outgrowths of neurons with neurotrophin-coated carbon nanotubes. *Journal of Bioscience and Bioengineering*. 2007;103(3):216-20.
106. Mattson MP, Haddon RC, Rao AM. Molecular functionalization of carbon nanotubes and use as substrates for neuronal growth. *Journal of Molecular Neuroscience*. 2000;14(3):175-82.
107. Galvan-Garcia P, Keefer EW, Yang F, Zhang M, Fang S, Zakhidov AA, et al. Robust cell migration and neuronal growth on pristine carbon nanotube sheets and yarns. *Journal of Biomaterials Science, Polymer Edition*. 2007;18(10):1245-61.
108. Hu H, Ni Y, Montana V, Haddon RC, Parpura V. Chemically Functionalized Carbon Nanotubes as Substrates for Neuronal Growth. *Nano Letters*. 2004;4(3):507-11.
109. Lovat V, Pantarotto D, Lagostena L, Cacciari B, Grandolfo M, Righi M, et al. Carbon Nanotube Substrates Boost Neuronal Electrical Signaling. *Nano Letters*. 2005;5(6):1107-10.
110. Gheith MK, Sinani VA, Wicksted JP, Matts RL, Kotov NA. Single-Walled Carbon Nanotube Polyelectrolyte Multilayers and Freestanding Films as a Biocompatible Platform for Neuroprosthetic Implants. *Advanced Materials*. 2005;17(22):2663-70.
111. Huang Y-J, Wu H-C, Tai N-H, Wang T-W. Carbon Nanotube Rope with Electrical Stimulation Promotes the Differentiation and Maturity of Neural Stem Cells. *Small*. 2012;8(18):2869-77.
112. Megan JR, Michelle KL, Mostafa B, Eric RM, Davor C, Joseph MC, et al. Growth of primary motor neurons on horizontally aligned carbon nanotube thin films and striped patterns. *Journal of neural engineering*. 2014;11(3):036013.
113. Nawrotek K, Tylman M, Rudnicka K, Gatkowska J, Balcerzak J. Tubular electrodeposition of chitosan-carbon nanotube implants enriched with calcium ions. *Journal of the Mechanical Behavior of Biomedical Materials*. 2016;60(Supplement C):256-66.

114. Wu S, Duan B, Lu A, Wang Y, Ye Q, Zhang L. Biocompatible chitin/carbon nanotubes composite hydrogels as neuronal growth substrates. *Carbohydrate Polymers*. 2017;174(Supplement C):830-40.
115. Koppes AN, Keating KW, McGregor AL, Koppes RA, Kearns KR, Ziemba AM, et al. Robust neurite extension following exogenous electrical stimulation within single walled carbon nanotube-composite hydrogels. *Acta Biomaterialia*. 2016;39(Supplement C):34-43.
116. Scapin G, Salice P, Tescari S, Menna E, De Filippis V, Filippini F. Enhanced neuronal cell differentiation combining biomimetic peptides and a carbon nanotube-polymer scaffold. *Nanomedicine: Nanotechnology, Biology and Medicine*. 2015;11(3):621-32.
117. Christi LK, Kasey C, Erika R, Ingrid NA, Dennis B, Zhanhong D, et al. Evaluation of poly(3,4-ethylenedioxythiophene)/carbon nanotube neural electrode coatings for stimulation in the dorsal root ganglion. *Journal of neural engineering*. 2015;12(1):016008.
118. Xue N, Sun T, Tsang WM, Delgado-Martinez I, Lee S-H, Sheshadri S, et al. Polymeric C-shaped cuff electrode for recording of peripheral nerve signal. *Sensors and Actuators B: Chemical*. 2015;210(Supplement C):640-8.
119. Tegtmeier K, Aliuos P, Lenarz T, Doll T. Residual rubber shielded multi walled carbon nanotube electrodes for neural interfacing in active medical implants. *Physics in Medicine*. 2016;1(Supplement C):8-19.
120. Kang D-W, Sun F, Choi YJ, Zou F, Cho W-H, Choi B-K, et al. Enhancement of primary neuronal cell proliferation using printing-transferred carbon nanotube sheets. *Journal of Biomedical Materials Research Part A*. 2015;103(5):1746-54.
121. Hurt RH, Monthieux M, Kane A. Toxicology of carbon nanomaterials: Status, trends, and perspectives on the special issue. *Carbon*. 2006;44(6):1028-33.
122. Kong H, Wang L, Zhu Y, Huang Q, Fan C. Culture medium-associated physicochemical insights on the cytotoxicity of carbon nanomaterials. *Chemical research in toxicology*. 2015;28(3):290-5.
123. Meng L, Jiang A, Chen R, Li C-z, Wang L, Qu Y, et al. Inhibitory effects of multiwall carbon nanotubes with high iron impurity on viability and neuronal differentiation in cultured PC12 cells. *Toxicology*. 2013;313(1):49-58.
124. Nurulhuda I, Poh R, Mazatulikhma MZ, Rusop M. 2014.
125. Wu D, Pak ES, Wingard CJ, Murashov AK. Multi-walled carbon nanotubes inhibit regenerative axon growth of dorsal root ganglia neurons of mice. *Neuroscience letters*. 2012;507(1):72-7.
126. Lam C-W, James JT, McCluskey R, Hunter RL. Pulmonary Toxicity of Single-Wall Carbon Nanotubes in Mice 7 and 90 Days After Intratracheal Instillation. *Toxicological Sciences*. 2004;77(1):126-34.
127. Muller J, Huaux F, Lison D. Respiratory toxicity of carbon nanotubes: How worried should we be? *Carbon*. 2006;44(6):1048-56.
128. Gaillard C, Cellot G, Li S, Toma FM, Dumortier H, Spalluto G, et al. Carbon Nanotubes Carrying Cell-Adhesion Peptides do not Interfere with Neuronal Functionality. *Advanced Materials*. 2009;21(28):2903-8.
129. Jiang H. Chemical preparation of graphene-based nanomaterials and their applications in chemical and biological sensors. *Small*. 2011;7(17):2413-27.
130. Kenry, Lee WC, Loh KP, Lim CT. When stem cells meet graphene: Opportunities and challenges in regenerative medicine. *Biomaterials*. 2018;155:236-50.
131. Dave SH, Gong C, Robertson AW, Warner JH, Grossman JC. Chemistry and Structure of Graphene Oxide via Direct Imaging. *ACS Nano*. 2016;10(8):7515-22.
132. Li G, Zhao Y, Zhang L, Gao M, Kong Y, Yang Y. Preparation of graphene oxide/polyacrylamide composite hydrogel and its effect on Schwann cells attachment and proliferation. *Colloids and Surfaces B: Biointerfaces*. 2016;143(Supplement C):547-56.
133. Baniasadi H, Ramazani S.A A, Mashayekhan S. Fabrication and characterization of conductive chitosan/gelatin-based scaffolds for nerve tissue engineering. *International Journal of Biological Macromolecules*. 2015;74(Supplement C):360-6.
134. Das SR, Uz M, Ding S, Lentner MT, Hondred JA, Cargill AA, et al. Electrical Differentiation of Mesenchymal Stem Cells into Schwann-Cell-Like Phenotypes Using Inkjet-Printed Graphene Circuits. *Advanced healthcare materials*. 2017;6(7).
135. Yan L, Zhao B, Liu X, Li X, Zeng C, Shi H, et al. Aligned Nanofibers from Polypyrrole/Graphene as Electrodes for Regeneration of Optic Nerve via Electrical Stimulation. *ACS Applied Materials & Interfaces*. 2016;8(11):6834-40.
136. Zhang K, Zheng H, Liang S, Gao C. Aligned PLLA nanofibrous scaffolds coated with graphene oxide for promoting neural cell growth. *Acta Biomaterialia*. 2016;37(Supplement C):131-42.
137. Zhao Y, Gong J, Niu C, Wei Z, Shi J, Li G, et al. A new electrospun graphene-silk fibroin composite scaffolds for guiding Schwann cells. *Journal of Biomaterials Science, Polymer Edition*. 2017;28(18):2171-85.

138. Aznar-Cervantes S, Pagán A, Martínez JG, Bernabeu-Esclapez A, Otero TF, Meseguer-Olmo L, et al. Electrospun silk fibroin scaffolds coated with reduced graphene promote neurite outgrowth of PC-12 cells under electrical stimulation. *Materials Science and Engineering: C*. 2017;79(Supplement C):315-25.
139. Golafshan N, Kharaziha M, Fathi M. Tough and conductive hybrid graphene-PVA: Alginate fibrous scaffolds for engineering neural construct. *Carbon*. 2017;111(Supplement C):752-63.
140. Wang Q, Chen J, Niu Q, Fu X, Sun X, Tong X. The application of graphene oxidized combining with decellularized scaffold to repair of sciatic nerve injury in rats. *Saudi Pharmaceutical Journal*. 2017;25(4):469-76.
141. Akhavan O, Ghaderi E, Shirazian SA, Rahighi R. Rolled graphene oxide foams as three-dimensional scaffolds for growth of neural fibers using electrical stimulation of stem cells. *Carbon*. 2016;97(Supplement C):71-7.
142. Assaf K, Leal CV, Derami MS, de Rezende Duek EA, Ceragioli HJ, de Oliveira ALR. Sciatic nerve repair using poly(ϵ -caprolactone) tubular prosthesis associated with nanoparticles of carbon and graphene. *Brain and Behavior*. 2017;7(8):e00755-n/a.
143. Krueger E, Chang AN, Brown D, Eixenberger J, Brown R, Rastegar S, et al. Graphene Foam as a Three-Dimensional Platform for Myotube Growth. *ACS Biomaterials Science & Engineering*. 2016;2(8):1234-41.
144. Al-Saleh MH, Sundararaj U. A review of vapor grown carbon nanofiber/polymer conductive composites. *Carbon*. 2009;47(1):2-22.
145. Esrafilzadeh D, Morshed M, Tavanai H. An investigation on the stabilization of special polyacrylonitrile nanofibers as carbon or activated carbon nanofiber precursor. *Synthetic Metals*. 2009;159(3):267-72.
146. Yokoyama A, Sato Y, Nodasaka Y, Yamamoto S, Kawasaki T, Shindoh M, et al. Biological Behavior of Hat-Stacked Carbon Nanofibers in the Subcutaneous Tissue in Rats. *Nano Letters*. 2005;5(1):157-61.
147. Klein KL, Melechko AV, McKnight TE, Retterer ST, Rack PD, Fowlkes JD, et al. Surface characterization and functionalization of carbon nanofibers. *Journal of Applied Physics*. 2008;103(6):061301.
148. Jain S, Webster TJ, Sharma A, Basu B. Intracellular reactive oxidative stress, cell proliferation and apoptosis of Schwann cells on carbon nanofibrous substrates. *Biomaterials*. 2013;34(21):4891-901.
149. Zhu W, Ye T, Lee S-J, Cui H, Miao S, Zhou X, et al. Enhanced neural stem cell functions in conductive annealed carbon nanofibrous scaffolds with electrical stimulation. *Nanomedicine: Nanotechnology, Biology and Medicine*. 2017.
150. Danilenko VV. On the history of the discovery of nanodiamond synthesis. *Physics of the Solid State*. 2004;46(4):595-9.
151. Mochalin VN, Shenderova O, Ho D, Gogotsi Y. The properties and applications of nanodiamonds. *Nature nanotechnology*. 2011;7(1):11-23.
152. Vul AY, Dideikin AT, Aleksenskii AE, Baidakova MV. CHAPTER 2 Detonation Nanodiamonds: Synthesis, Properties and Applications. *Nanodiamond: The Royal Society of Chemistry*; 2014. p. 27-48.
153. Wang X, Low XC, Hou W, Abdullah LN, Toh TB, Mohd Abdul Rashid M, et al. Epirubicin-Adsorbed Nanodiamonds Kill Chemoresistant Hepatic Cancer Stem Cells. *ACS Nano*. 2014;8(12):12151-66.
154. Perevedentseva E, Hong S-F, Huang K-J, Chiang I-T, Lee C-Y, Tseng Y-T, et al. Nanodiamond internalization in cells and the cell uptake mechanism. *Journal of Nanoparticle Research*. 2013;15(8):1834.
155. Hegyi AN, Yablonovitch E. Nanodiamond imaging: a new molecular imaging approach. *Conference proceedings : Annual International Conference of the IEEE Engineering in Medicine and Biology Society IEEE Engineering in Medicine and Biology Society Annual Conference*. 2012;2012:2639-42.
156. Zhu Y, Li J, Li W, Zhang Y, Yang X, Chen N, et al. The Biocompatibility of Nanodiamonds and Their Application in Drug Delivery Systems. *Theranostics*. 2012;2(3):302-12.
157. Hopper AP, Dugan JM, Gill AA, Fox OJ, May PW, Haycock JW, et al. Amine functionalized nanodiamond promotes cellular adhesion, proliferation and neurite outgrowth. *Biomedical materials (Bristol, England)*. 2014;9(4):045009.
158. Huang Y-A, Kao C-W, Liu K-K, Huang H-S, Chiang M-H, Soo C-R, et al. The effect of fluorescent nanodiamonds on neuronal survival and morphogenesis. *Scientific Reports*. 2014;4:6919.
159. Tong W, Fox K, Ganesan K, Prawer S. Design of a Patterned Diamond Substrate for Ordered Neural Cell Adhesion. *Procedia Technology*. 2015;20:206-11.
160. Piret G, Hébert C, Mazellier J-P, Rousseau L, Scorsone E, Cottance M, et al. 3D-nanostructured boron-doped diamond for microelectrode array neural interfacing. *Biomaterials*. 2015;53:173-83.
161. Tong W, Fox K, Zamani A, Turnley AM, Ganesan K, Ahnood A, et al. Optimizing growth and post treatment of diamond for high capacitance neural interfaces. *Biomaterials*. 2016;104:32-42.
162. Cai Y, Edin F, Jin Z, Alexsson A, Gudjonsson O, Liu W, et al. Strategy towards independent electrical stimulation from cochlear implants: Guided auditory neuron growth on topographically modified nanocrystalline diamond. *Acta Biomater*. 2016;31:211-20.

163. Thalhammer A, Edgington RJ, Cingolani LA, Schoepfer R, Jackman RB. The use of nanodiamond monolayer coatings to promote the formation of functional neuronal networks. *Biomaterials*. 2010;31(8):2097-104.
164. Biazar E, Khorasani MT, Zaeifi D. Nanotechnology for peripheral nerve regeneration. *International Journal of Nano Dimension*. 2010;1(1):1-23.
165. Sedaghati T, Seifalian AM. Nanotechnology and bio-functionalisation for peripheral nerve regeneration. *Neural Regen Res*. 2015;10(8):1191-4.
166. Mclaughlin S, Podrebarac J, Ruel M, Suuronen EJ, McNeill B, Alarcon EI. Nano-Engineered Biomaterials for Tissue Regeneration: What Has Been Achieved So Far? *Frontiers in Materials*. 2016;3(27).
167. Nicolas J, Mura S, Brambilla D, Mackiewicz N, Couvreur P. Design, functionalization strategies and biomedical applications of targeted biodegradable/biocompatible polymer-based nanocarriers for drug delivery. *Chemical Society reviews*. 2013;42(3):1147-235.
168. Kim JA, Lee N, Kim BH, Rhee WJ, Yoon S, Hyeon T, et al. Enhancement of neurite outgrowth in PC12 cells by iron oxide nanoparticles. *Biomaterials*. 2011;32(11):2871-7.
169. Alon N, Miroshnikov Y, Perkash N, Nissan I, Gedanken A, Shefi O. Substrates coated with silver nanoparticles as a neuronal regenerative material. *International Journal of Nanomedicine*. 2014;9(Suppl 1):23-31.
170. Liu Z, Ren G, Zhang T, Yang Z. Action potential changes associated with the inhibitory effects on voltage-gated sodium current of hippocampal CA1 neurons by silver nanoparticles. *Toxicology*. 2009;264(3):179-84.
171. Gramowski A, Flossdorf J, Bhattacharya K, Jonas L, Lantow M, Rahman Q, et al. Nanoparticles induce changes of the electrical activity of neuronal networks on microelectrode array neurochips. *Environ Health Perspect*. 2010;118(10):1363-9.
172. Zhang K, Osakada Y, Vrljic M, Chen L, Mudrakola HV, Cui B. Single molecule imaging of NGF axonal transport in microfluidic devices. *Lab on a chip*. 2010;10(19):2566-73.
173. Riggio C, Calatayud MP, Giannaccini M, Sanz B, Torres TE, Fernández-Pacheco R, et al. The orientation of the neuronal growth process can be directed via magnetic nanoparticles under an applied magnetic field. *Nanomedicine: Nanotechnology, Biology and Medicine*. 2014;10(7):1549-58.
174. Marcus M, Karni M, Baranes K, Levy I, Alon N, Margel S, et al. Iron oxide nanoparticles for neuronal cell applications: uptake study and magnetic manipulations. *Journal of Nanobiotechnology*. 2016;14(1):37.
175. Huang L, Xia B, Liu Z, Cao Q, Huang J, Luo Z. Superparamagnetic Iron Oxide Nanoparticle-Mediated Forces Enhance the Migration of Schwann Cells Across the Astrocyte-Schwann Cell Boundary In vitro. *Frontiers in Cellular Neuroscience*. 2017;11:83.
176. Liu Z, Huang L, Liu L, Luo B, Liang M, Sun Z, et al. Activation of Schwann cells in vitro by magnetic nanocomposites via applied magnetic field. *International journal of nanomedicine [Internet]*. 2015 2015; 10:[43-61 pp.]. Available from: <http://europepmc.org/abstract/MED/25565803>.
177. Liu J, Zhang W, Li Y, Zhu H, Qiu R, Song Z, et al. Mechanical manipulation of magnetic nanoparticles by magnetic force microscopy. *Journal of Magnetism and Magnetic Materials*. 2017;443:184-9.
178. Tseng T-C, Hsu S-h. Substrate-mediated nanoparticle/gene delivery to MSC spheroids and their applications in peripheral nerve regeneration. *Biomaterials*. 2014;35(9):2630-41.
179. Liu M, Zhou G, Hou Y, Kuang G, Jia Z, Li P, et al. Effect of nano-hydroxyapatite-coated magnetic nanoparticles on axonal guidance growth of rat dorsal root ganglion neurons. *Journal of biomedical materials research Part A*. 2015;103(9):3066-71.
180. Giannaccini M, Calatayud MP, Poggetti A, Corbianco S, Novelli M, Paoli M, et al. Magnetic Nanoparticles for Efficient Delivery of Growth Factors: Stimulation of Peripheral Nerve Regeneration. *Advanced healthcare materials*. 2017;6(7).
181. Zuidema JM, Provenza C, Caliendo T, Dutz S, Gilbert RJ. Magnetic NGF-Releasing PLLA/Iron Oxide Nanoparticles Direct Extending Neurites and Preferentially Guide Neurites along Aligned Electrospun Microfibers. *ACS Chemical Neuroscience*. 2015;6(11):1781-8.
182. Rose JC, Cámara-Torres M, Rahimi K, Köhler J, Möller M, De Laporte L. Nerve Cells Decide to Orient inside an Injectable Hydrogel with Minimal Structural Guidance. *Nano Letters*. 2017;17(6):3782-91.
183. Paviolo C, Haycock JW, Yong J, Yu A, Stoddart PR, McArthur SL. Laser exposure of gold nanorods can increase neuronal cell outgrowth. *Biotechnology and bioengineering*. 2013;110(8):2277-91.
184. Paviolo C, Haycock JW, Cadusch PJ, McArthur SL, Stoddart PR. Laser exposure of gold nanorods can induce intracellular calcium transients. *Journal of biophotonics*. 2014;7(10):761-5.
185. Adel M, Zahmatkeshan M, Johari B, Kharrazi S, Mehdizadeh M, Bolouri B, et al. Investigating the effects of electrical stimulation via gold nanoparticles on in vitro neurite outgrowth: Perspective to nerve regeneration. *Microelectronic Engineering*. 2017;173:1-5.

186. Das S, Sharma M, Saharia D, Sarma KK, Sarma MG, Borthakur BB, et al. In vivo studies of silk based gold nano-composite conduits for functional peripheral nerve regeneration. *Biomaterials*. 2015;62:66-75.
187. Xiao Y, Zhang E, Fu A. Promotion of SH-SY5Y Cell Growth by Gold Nanoparticles Modified with 6-Mercaptopurine and a Neuron-Penetrating Peptide. *Nanoscale research letters*. 2017;12(1):641.
188. Motamedi AS, Mirzadeh H, Hajiesmaeilbaigi F, Bagheri-Khoulenjani S, Shokrgozar MA. Piezoelectric electrospun nanocomposite comprising Au NPs/PVDF for nerve tissue engineering. *Journal of biomedical materials research Part A*. 2017;105(7):1984-93.
189. Iman M, Araghi M, Panahi Y, Mohammadi R. Effects of Chitosan-Zinc Oxide Nanocomposite Conduit on Transected Sciatic Nerve: An Animal Model Study. *Bulletin of Emergency & Trauma*. 2017;5(4):240-8.
190. Aydemir Sezer U, Ozturk K, Aru B, Yanikkaya Demirel G, Sezer S, Bozkurt MR. Zero valent zinc nanoparticles promote neuroglial cell proliferation: A biodegradable and conductive filler candidate for nerve regeneration. *Journal of materials science Materials in medicine*. 2017;28(1):19.
191. Wise AK, Tan J, Wang Y, Caruso F, Shepherd RK. Improved Auditory Nerve Survival with Nanoengineered Supraparticles for Neurotrophin Delivery into the Deafened Cochlea. *PLoS one*. 2016;11(10):e0164867.
192. Gonzalez Porras MA, Durfee PN, Gregory AM, Sieck GC, Brinker CJ, Mantilla CB. A novel approach for targeted delivery to motoneurons using cholera toxin-B modified protocells. *Journal of Neuroscience Methods*. 2016;273:160-74.
193. Mehrasa M, Asadollahi MA, Ghaedi K, Salehi H, Arpanaei A. Electrospun aligned PLGA and PLGA/gelatin nanofibers embedded with silica nanoparticles for tissue engineering. *Int J Biol Macromol*. 2015;79:687-95.
194. Liu Q, Santamaria CM, Wei T, Zhao C, Ji T, Yang T, et al. Hollow Silica Nanoparticles Penetrate the Peripheral Nerve and Enhance the Nerve Blockade from Tetrodotoxin. *Nano Letters*. 2018;18(1):32-7.
195. Sensenig R, Sapir Y, MacDonald C, Cohen S, Polyak B. Magnetic nanoparticle-based approaches to locally target therapy and enhance tissue regeneration in vivo. *Nanomedicine (London, England)*. 2012;7(9):1425-42.
196. Mahmoudi M, Sant S, Wang B, Laurent S, Sen T. Superparamagnetic iron oxide nanoparticles (SPIONs): development, surface modification and applications in chemotherapy. *Advanced drug delivery reviews*. 2011;63(1-2):24-46.
197. Barrow M, Taylor A, Fuentes-Caparros AM, Sharkey J, Daniels LM, Mandal P, et al. SPIONs for cell labelling and tracking using MRI: magnetite or maghemite? *Biomaterials Science*. 2018;6(1):101-6.
198. Liu Z, Zhu S, Liu L, Ge J, Huang L, Sun Z, et al. A magnetically responsive nanocomposite scaffold combined with Schwann cells promotes sciatic nerve regeneration upon exposure to magnetic field. *Int J Nanomedicine*. 2017;12:7815-32.
199. Ocsoy I, Tasdemir D, Mazicioglu S, Celik C, Kati A, Ulgen F. Biomolecules incorporated metallic nanoparticles synthesis and their biomedical applications. *Materials Letters*. 2018;212:45-50.
200. Ahmad B, Hafeez N, Bashir S, Rauf A, Mujeeb ur R. Phytofabricated gold nanoparticles and their biomedical applications. *Biomedicine & Pharmacotherapy*. 2017;89:414-25.
201. Tang Y, Zhao Y, Wang X, Lin T. Layer-by-layer assembly of silica nanoparticles on 3D fibrous scaffolds: Enhancement of osteoblast cell adhesion, proliferation, and differentiation. *Journal of Biomedical Materials Research Part A*. 2014;102(11):3803-12.
202. Liberman A, Mendez N, Trogler WC, Kummel AC. Synthesis and surface functionalization of silica nanoparticles for nanomedicine. *Surface science reports*. 2014;69(2-3):132-58.
203. Bennet D, Kim S. Polymer Nanoparticles for Smart Drug Delivery. In: Sezer AD, editor. *Application of Nanotechnology in Drug Delivery*. Rijeka: InTech; 2014. p. Ch. 08.
204. Crucho CIC, Barros MT. Polymeric nanoparticles: A study on the preparation variables and characterization methods. *Materials Science and Engineering: C*. 2017;80:771-84.
205. Mili B, Das K, Kumar A, Saxena AC, Singh P, Ghosh S, et al. Preparation of NGF encapsulated chitosan nanoparticles and its evaluation on neuronal differentiation potentiality of canine mesenchymal stem cells. *Journal of Materials Science: Materials in Medicine*. 2017;29(1):4.
206. Li G, Xiao Q, McNaughton R, Han L, Zhang L, Wang Y, et al. Nanoengineered porous chitosan/CaTiO₃ hybrid scaffolds for accelerating Schwann cells growth in peripheral nerve regeneration. *Colloids and Surfaces B: Biointerfaces*. 2017;158:57-67.
207. Lopes CD, Gomes CP, Neto E, Sampaio P, Aguiar P, Pego AP. Microfluidic-based platform to mimic the in vivo peripheral administration of neurotropic nanoparticles. *Nanomedicine (London, England)*. 2016;11(24):3205-21.
208. Lopes CDF, Gonçalves NP, Gomes CP, Saraiva MJ, Pêgo AP. BDNF gene delivery mediated by neuron-targeted nanoparticles is neuroprotective in peripheral nerve injury. *Biomaterials*. 2017;121:83-96.

209. Wang S, Guan S, Zhu Z, Li W, Liu T, Ma X. Hyaluronic acid doped-poly(3,4-ethylenedioxythiophene)/chitosan/gelatin (PEDOT-HA/Cs/Gel) porous conductive scaffold for nerve regeneration. *Materials Science and Engineering: C*. 2017;71:308-16.
210. Wang S, Guan S, Wang J, Liu H, Liu T, Ma X, et al. Fabrication and characterization of conductive poly(3,4-ethylenedioxythiophene) doped with hyaluronic acid/poly(L-lactic acid) composite film for biomedical application. *Journal of Bioscience and Bioengineering*. 2017;123(1):116-25.
211. Salehi M, Naseri-Nosar M, Ebrahimi-Barough S, Nourani M, Vaez A, Farzamfar S, et al. Regeneration of sciatic nerve crush injury by a hydroxyapatite nanoparticle-containing collagen type I hydrogel. *The journal of physiological sciences : JPS*. 2017.
212. Kuo Y-C, Rajesh R. Nerve growth factor-loaded heparinized cationic solid lipid nanoparticles for regulating membrane charge of induced pluripotent stem cells during differentiation. *Materials Science and Engineering: C*. 2017;77:680-9.
213. Wang Z, Huang H, Yang S, Huang S, Guo J, Tang Q, et al. Long-term effect of ropivacaine nanoparticles for sciatic nerve block on postoperative pain in rats. *Int J Nanomedicine*. 2016;11:2081-90.
214. Lee SJ, Zhu W, Heyburn L, Nowicki M, Harris B, Zhang LG. Development of Novel 3-D Printed Scaffolds With Core-Shell Nanoparticles for Nerve Regeneration. *IEEE Transactions on Biomedical Engineering*. 2017;64(2):408-18.
215. Shakhbazou A, Mohanty C, Shcharbin D, Bryszewska M, Caminade A-M, Majoral J-P, et al. Doxycycline-regulated GDNF expression promotes axonal regeneration and functional recovery in transected peripheral nerve. *Journal of Controlled Release*. 2013;172(3):841-51.
216. Shakhbazou A, Archibald SJ, Shcharbin D, Bryszewska M, Midha R. Aligned collagen-GAG matrix as a 3D substrate for Schwann cell migration and dendrimer-based gene delivery. *Journal of materials science Materials in medicine*. 2014;25(8):1979-89.
217. Maturavongsadit P, Bi X, Gado TA, Nie Y-Z, Wang Q. Adhesive peptides conjugated PAMAM dendrimer as a coating polymeric material enhancing cell responses. *Chinese Chemical Letters*. 2016;27(9):1473-8.
218. Guo Y, Johnson MA, Mehrabian Z, Mishra MK, Kannan R, Miller NR, et al. Dendrimers Target the Ischemic Lesion in Rodent and Primate Models of Nonarteritic Anterior Ischemic Optic Neuropathy. *PLoS one*. 2016;11(4):e0154437.
219. Muxika A, Etxabide A, Uranga J, Guerrero P, de la Caba K. Chitosan as a bioactive polymer: Processing, properties and applications. *International Journal of Biological Macromolecules*. 2017;105:1358-68.
220. Sullivan DJ, Cruz-Romero M, Collins T, Cummins E, Kerry JP, Morris MA. Synthesis of monodisperse chitosan nanoparticles. *Food Hydrocolloids*. 2018.
221. Chanphai P, Tajmir-Riahi HA. Encapsulation of testosterone by chitosan nanoparticles. *International Journal of Biological Macromolecules*. 2017;98:535-41.
222. Gorain B, Tekade M, Kesharwani P, Iyer AK, Kalia K, Tekade RK. The use of nanoscaffolds and dendrimers in tissue engineering. *Drug Discovery Today*. 2017;22(4):652-64.
223. Sharma AK, Gothwal A, Kesharwani P, Alsaab H, Iyer AK, Gupta U. Dendrimer nanoarchitectures for cancer diagnosis and anticancer drug delivery. *Drug Discovery Today*. 2017;22(2):314-26.
224. Abbasi E, Aval SF, Akbarzadeh A, Milani M, Nasrabadi HT, Joo SW, et al. Dendrimers: synthesis, applications, and properties. *Nanoscale research letters*. 2014;9(1):247-.
225. Nance E, Zhang F, Mishra MK, Zhang Z, Kambhampati SP, Kannan RM, et al. Nanoscale effects in dendrimer-mediated targeting of neuroinflammation. *Biomaterials*. 2016;101:96-107.
226. Shakhbazou A, Mishra M, Chu T-H, Brideau C, Cummins K, Tsutsui S, et al. Fluorescent Phosphorus Dendrimer as a Spectral Nanosensor for Macrophage Polarization and Fate Tracking in Spinal Cord Injury. *Macromolecular Bioscience*. 2015;15(11):1523-34.
227. Shrestha B, Jiang X, Ge S, Paul D, Chianchiano P, Pachter JS. Spatiotemporal resolution of spinal meningeal and parenchymal inflammation during experimental autoimmune encephalomyelitis. *Neurobiology of Disease*. 2017;108:159-72.
228. Mishra V, Kesharwani P. Dendrimer technologies for brain tumor. *Drug Discovery Today*. 2016;21(5):766-78.
229. Mignani S, Bryszewska M, Zablocka M, Klajnert-Maculewicz B, Cladera J, Shcharbin D, et al. Can dendrimer based nanoparticles fight neurodegenerative diseases? Current situation versus other established approaches. *Progress in Polymer Science*. 2017;64:23-51.
230. Thery C, Boussac M, Veron P, Ricciardi-Castagnoli P, Raposo G, Garin J, et al. Proteomic analysis of dendritic cell-derived exosomes: a secreted subcellular compartment distinct from apoptotic vesicles. *Journal of immunology (Baltimore, Md : 1950)*. 2001;166(12):7309-18.

231. Valadi H, Ekstrom K, Bossios A, Sjostrand M, Lee JJ, Lotvall JO. Exosome-mediated transfer of mRNAs and microRNAs is a novel mechanism of genetic exchange between cells. *Nature cell biology*. 2007;9(6):654-9.
232. Sarko DK, McKinney CE. Exosomes: Origins and Therapeutic Potential for Neurodegenerative Disease. *Frontiers in Neuroscience*. 2017;11:82.
233. Muller G. Microvesicles/exosomes as potential novel biomarkers of metabolic diseases. *Diabetes, metabolic syndrome and obesity : targets and therapy*. 2012;5:247-82.
234. Luan X, Sansanaphongpricha K, Myers I, Chen H, Yuan H, Sun D. Engineering exosomes as refined biological nanoplateforms for drug delivery. *Acta Pharmacologica Sinica*. 2017;38(6):754-63.
235. Skog J, Wurdinger T, van Rijn S, Meijer D, Gainche L, Sena-Estevés M, et al. Glioblastoma microvesicles transport RNA and protein that promote tumor growth and provide diagnostic biomarkers. *Nature cell biology*. 2008;10(12):1470-6.
236. Bianco F, Perrotta C, Novellino L, Francolini M, Riganti L, Menna E, et al. Acid sphingomyelinase activity triggers microparticle release from glial cells. *The EMBO journal*. 2009;28(8):1043-54.
237. Fruhbeis C, Frohlich D, Kramer-Albers EM. Emerging roles of exosomes in neuron-glia communication. *Frontiers in physiology*. 2012;3:119.
238. Faure J, Lachenal G, Court M, Hirrlinger J, Chatellard-Causse C, Blot B, et al. Exosomes are released by cultured cortical neurones. *Molecular and cellular neurosciences*. 2006;31(4):642-8.
239. Potolicchio I, Carven GJ, Xu X, Stipp C, Riese RJ, Stern LJ, et al. Proteomic analysis of microglia-derived exosomes: metabolic role of the aminopeptidase CD13 in neuropeptide catabolism. *Journal of immunology (Baltimore, Md : 1950)*. 2005;175(4):2237-43.
240. Taylor AR, Robinson MB, Gifondorwa DJ, Tytell M, Milligan CE. Regulation of heat shock protein 70 release in astrocytes: role of signaling kinases. *Developmental neurobiology*. 2007;67(13):1815-29.
241. Kramer-Albers EM, Bretz N, Tenzer S, Winterstein C, Mobius W, Berger H, et al. Oligodendrocytes secrete exosomes containing major myelin and stress-protective proteins: Trophic support for axons? *Proteomics Clinical applications*. 2007;1(11):1446-61.
242. Marzesco AM, Janich P, Wilsch-Brauninger M, Dubreuil V, Langenfeld K, Corbeil D, et al. Release of extracellular membrane particles carrying the stem cell marker prominin-1 (CD133) from neural progenitors and other epithelial cells. *Journal of cell science*. 2005;118(Pt 13):2849-58.
243. Court FA, Hendriks WT, MacGillavry HD, Alvarez J, van Minnen J. Schwann cell to axon transfer of ribosomes: toward a novel understanding of the role of glia in the nervous system. *The Journal of neuroscience : the official journal of the Society for Neuroscience*. 2008;28(43):11024-9.
244. Court FA, Midha R, Cisterna BA, Grochmal J, Shakhbazov A, Hendriks WT, et al. Morphological evidence for a transport of ribosomes from Schwann cells to regenerating axons. *Glia*. 2011;59(10):1529-39.
245. Fevrier B, Vilette D, Archer F, Loew D, Faigle W, Vidal M, et al. Cells release prions in association with exosomes. *Proceedings of the National Academy of Sciences of the United States of America*. 2004;101(26):9683-8.
246. Lopez-Verrilli MA, Picou F, Court FA. Schwann cell-derived exosomes enhance axonal regeneration in the peripheral nervous system. *Glia*. 2013;61(11):1795-806.
247. Lopez-Verrilli MA, Caviedes A, Cabrera A, Sandoval S, Wyneken U, Khoury M. Mesenchymal stem cell-derived exosomes from different sources selectively promote neuritic outgrowth. *Neuroscience*. 2016;320:129-39.
248. Hori N, Narita M, Yamashita A, Horiuchi H, Hamada Y, Kondo T, et al. Changes in the expression of IL-6-Mediated MicroRNAs in the dorsal root ganglion under neuropathic pain in mice. *Synapse*. 2016;70(8):317-24.
249. Simeoli R, Montague K. Exosomal cargo including microRNA regulates sensory neuron to macrophage communication after nerve trauma. 2017;8(1):1778.
250. Goncalves MB, Wu Y, Trigo D, Clarke E, Malmqvist T, Grist J, et al. Retinoic acid synthesis by NG2 expressing cells promotes a permissive environment for axonal outgrowth. *Neurobiology of Disease*. 2018;111:70-9.
251. Ching RC, Kingham PJ. The role of exosomes in peripheral nerve regeneration. *Neural Regeneration Research*. 2015;10(5):743-7.
252. Soto K, Garza KM, Murr LE. Cytotoxic effects of aggregated nanomaterials. *Acta Biomaterialia*. 2007;3(3):351-8.
253. Lewinski N, Colvin V, Drezek R. Cytotoxicity of Nanoparticles. *Small*. 2008;4(1):26-49.
254. Li Y-F, Chen C. Fate and Toxicity of Metallic and Metal-Containing Nanoparticles for Biomedical Applications. *Small*. 2011;7(21):2965-80.
255. Wang X, Zhu M, Li J. Biomedical Effects and Nanosafety of Engineered Nanomaterials: Recent Progress. *Chinese Journal of Chemistry*. 2012;30(9):1931-47.

256. Chen J, Hessler JA, Putschakayala K, Panama BK, Khan DP, Hong S, et al. Cationic Nanoparticles Induce Nanoscale Disruption in Living Cell Plasma Membranes. *The Journal of Physical Chemistry B*. 2009;113(32):11179-85.
257. Larner SF, Wang J, Goodman J, Altman MBO, Xin M, Wang KKW. In Vitro Neurotoxicity Resulting from Exposure of Cultured Neural Cells to Several Types of Nanoparticles. *Journal of cell death*. 2017;10:1179670717694523.
258. Rivet CJ, Yuan Y, Borca-Tasciuc D-A, Gilbert RJ. Altering Iron Oxide Nanoparticle Surface Properties Induce Cortical Neuron Cytotoxicity. *Chemical research in toxicology*. 2012;25(1):153-61.
259. Teo WE, Ramakrishna S. A review on electrospinning design and nanofibre assemblies. *Nanotechnology*. 2006;17(14):R89.
260. Xu D, Samways DSK, Dong H. Fabrication of self-assembling nanofibers with optimal cell uptake and therapeutic delivery efficacy. *Bioactive Materials*. 2017;2(4):260-8.
261. Sarbatly R, Krishnaiah D, Kamin Z. A review of polymer nanofibres by electrospinning and their application in oil–water separation for cleaning up marine oil spills. *Marine Pollution Bulletin*. 2016;106(1):8-16.
262. Doshi J, Reneker DH. Electrospinning process and applications of electrospun fibers. *Journal of Electrostatics*. 1995;35(2):151-60.
263. Huang Z-M, Zhang YZ, Kotaki M, Ramakrishna S. A review on polymer nanofibers by electrospinning and their applications in nanocomposites. *Composites Science and Technology*. 2003;63(15):2223-53.
264. Chew SY, Mi R, Hoke A, Leong KW. The effect of the alignment of electrospun fibrous scaffolds on Schwann cell maturation. *Biomaterials*. 2008;29(6):653-61.
265. Olakowska E, Woszczycka-Korczynska I, Jedrzejowska-Szypulka H, Lewin-Kowalik J. Application of nanotubes and nanofibres in nerve repair. A review. *Folia neuropathologica*. 2010;48(4):231-7.
266. Gnani S, Fornasari BE, Tonda-Turo C, Ciardelli G, Zanetti M, Geuna S, et al. The influence of electrospun fibre size on Schwann cell behaviour and axonal outgrowth. *Materials Science and Engineering: C*. 2015;48:620-31.
267. Suzuki K, Tanaka H, Ebara M, Uto K, Matsuoka H, Nishimoto S, et al. Electrospun nanofiber sheets incorporating methylcobalamin promote nerve regeneration and functional recovery in a rat sciatic nerve crush injury model. *Acta Biomaterialia*. 2017;53:250-9.
268. Mohamadi F, Ebrahimi-Barough S, Nourani MR, Mansoori K, Salehi M, Alizadeh AA, et al. Enhanced sciatic nerve regeneration by human endometrial stem cells in an electrospun poly (epsilon-caprolactone)/collagen/NBG nerve conduit in rat. *Artificial cells, nanomedicine, and biotechnology*. 2017:1-13.
269. Huang L, Zhu L, Shi X, Xia B, Liu Z, Zhu S, et al. A compound scaffold with uniform longitudinally oriented guidance cues and a porous sheath promotes peripheral nerve regeneration in vivo. *Acta Biomaterialia*. 2017.
270. Xia B, Lv Y. Dual-delivery of VEGF and NGF by emulsion electrospun nanofibrous scaffold for peripheral nerve regeneration. *Materials Science and Engineering: C*. 2018;82:253-64.
271. Sun B, Zhou Z, Wu T, Chen W, Li D, Zheng H, et al. Development of Nanofiber Sponges-Containing Nerve Guidance Conduit for Peripheral Nerve Regeneration in Vivo. *ACS Applied Materials & Interfaces*. 2017;9(32):26684-96.
272. Kriebel A, Hodde D, Kuenzel T, Engels J, Brook G, Mey J. Cell-free artificial implants of electrospun fibres in a three-dimensional gelatin matrix support sciatic nerve regeneration in vivo. *Journal of tissue engineering and regenerative medicine*. 2017;11(12):3289-304.
273. Xia H, Chen Q, Fang Y, Liu D, Zhong D, Wu H, et al. Directed neurite growth of rat dorsal root ganglion neurons and increased colocalization with Schwann cells on aligned poly(methyl methacrylate) electrospun nanofibers. *Brain Research*. 2014;1565:18-27.
274. Lin C, Liu C, Zhang L, Huang Z, Zhao P, Chen R, et al. Interaction of iPSC-derived neural stem cells on poly(L-lactic acid) nanofibrous scaffolds for possible use in neural tissue engineering. *International journal of molecular medicine*. 2018;41(2):697-708.
275. Tseng VC, Chew CH, Huang WT, Wang YK, Chen KS, Chou SY, et al. An Effective Cell Coculture Platform Based on the Electrospun Microtube Array Membrane for Nerve Regeneration. *Cells, tissues, organs*. 2017;204(3-4):179-90.
276. Whitehead TJ, Avila COC, Sundararaghavan HG. Combining growth factor releasing microspheres within aligned nanofibers enhances neurite outgrowth. *Journal of biomedical materials research Part A*. 2018;106(1):17-25.
277. Lee SJ, Nowicki M, Harris B, Zhang LG. Fabrication of a Highly Aligned Neural Scaffold via a Table Top Stereolithography 3D Printing and Electrospinning(). *Tissue engineering Part A*. 2017;23(11-12):491-502.
278. Du J, Liu J, Yao S, Mao H, Peng J, Sun X, et al. Prompt peripheral nerve regeneration induced by a hierarchically aligned fibrin nanofiber hydrogel. *Acta Biomaterialia*. 2017;55:296-309.

279. Das S, Sharma M, Saharia D, Sarma KK, Muir EM, Bora U. Electrospun silk-polyaniline conduits for functional nerve regeneration in rat sciatic nerve injury model. *Biomedical materials* (Bristol, England). 2017;12(4):045025.
280. Zhou X, Yang A, Huang Z, Yin G, Pu X, Jin J. Enhancement of neurite adhesion, alignment and elongation on conductive polypyrrole-poly(lactide acid) fibers with cell-derived extracellular matrix. *Colloids and surfaces B, Biointerfaces*. 2017;149:217-25.
281. Zhou JF, Wang YG, Cheng L, Wu Z, Sun XD. Preparation of polypyrrole-embedded electrospun poly(lactic acid) nanofibrous scaffolds for nerve tissue engineering. 2016;11(10):1644-52.
282. Song J, Sun B, Liu S, Chen W, Zhang Y, Wang C, et al. Polymerizing Pyrrole Coated Poly (l-lactic acid-copolymerized-caprolactone) (PLCL) Conductive Nanofibrous Conduit Combined with Electric Stimulation for Long-Range Peripheral Nerve Regeneration. *Frontiers in molecular neuroscience*. 2016;9:117.
283. Bellamkonda RV. Peripheral nerve regeneration: An opinion on channels, scaffolds and anisotropy. *Biomaterials*. 2006;27(19):3515-8.
284. Subramanian A, Krishnan UM, Sethuraman S. Fabrication of uniaxially aligned 3D electrospun scaffolds for neural regeneration. *Biomedical materials* (Bristol, England). 2011;6(2):025004.
285. Simitzi C, Ranella A, Stratakis E. Controlling the morphology and outgrowth of nerve and neuroglial cells: The effect of surface topography. *Acta Biomaterialia*. 2017;51:21-52.
286. Suter DM, Forscher P. Substrate-cytoskeletal coupling as a mechanism for the regulation of growth cone motility and guidance. *Journal of neurobiology*. 2000;44(2):97-113.
287. Moore SW, Sheetz MP. Biophysics of substrate interaction: influence on neural motility, differentiation, and repair. *Developmental neurobiology*. 2011;71(11):1090-101.
288. den Braber ET, de Ruijter JE, Ginsel LA, von Recum AF, Jansen JA. Orientation of ECM protein deposition, fibroblast cytoskeleton, and attachment complex components on silicone microgrooved surfaces. *Journal of Biomedical Materials Research*. 1998;40(2):291-300.
289. Mahoney MJ, Chen RR, Tan J, Mark Saltzman W. The influence of microchannels on neurite growth and architecture. *Biomaterials*. 2005;26(7):771-8.
290. Fricke R, Zentis PD, Rajappa LT, Hofmann B, Banzet M, Offenhausser A, et al. Axon guidance of rat cortical neurons by microcontact printed gradients. *Biomaterials*. 2011;32(8):2070-6.
291. Thakur UK, Kim B-G, Park SJ, Baac HW, Lee D, Park HJ. Soft-Contact Printing of Nanoparticle-Based Nanoink for Functional Nanopatterns. *Journal of Nanomaterials*. 2015;2015:6.
292. Wood MA. Colloidal lithography and current fabrication techniques producing in-plane nanotopography for biological applications. *Journal of the Royal Society, Interface*. 2007;4(12):1-17.
293. Andersson H, van den Berg A. Microfabrication and microfluidics for tissue engineering: state of the art and future opportunities. *Lab on a chip*. 2004;4(2):98-103.
294. Ferrari A, Cecchini M, Dhawan A, Micera S, Tonazzini I, Stabile R, et al. Nanotopographic Control of Neuronal Polarity. *Nano Letters*. 2011;11(2):505-11.
295. Ferrari A, Faraci P, Cecchini M, Beltram F. The effect of alternative neuronal differentiation pathways on PC12 cell adhesion and neurite alignment to nanogratings. *Biomaterials*. 2010;31(9):2565-73.
296. Foley JD, Grunwald EW, Nealey PF, Murphy CJ. Cooperative modulation of neurite growth by PC12 cells by topography and nerve growth factor. *Biomaterials*. 2005;26(17):3639-44.
297. Baranes K, Chejanovsky N, Alon N, Sharoni A, Shefi O. Topographic cues of nano-scale height direct neuronal growth pattern. *Biotechnology and bioengineering*. 2012;109(7):1791-7.
298. Mitra J, Jain S, Sharma A, Basu B. Patterned growth and differentiation of neural cells on polymer derived carbon substrates with micro/nano structures in vitro. *Carbon*. 2013;65:140-55.
299. Kalash RS, Lakshmanan VK, Cho C-S, Park I-K. 4.4 - Theranostics A2 - Ebara, Mitsuhiro. *Biomaterials Nanoarchitectonics*: William Andrew Publishing; 2016. p. 197-215.
300. Hassanzadeh P, Atyabi F, Dinarvand R. Application of modelling and nanotechnology-based approaches: The emergence of breakthroughs in theranostics of central nervous system disorders. *Life Sciences*. 2017;182:93-103.
301. Tagliafico A, Altafini L, Garello I, Marchetti A, Gennaro S, Martinoli C. Traumatic neuropathies: spectrum of imaging findings and postoperative assessment. *Seminars in musculoskeletal radiology*. 2010;14(5):512-22.
302. Faroni A, Mobasser SA, Kingham PJ, Reid AJ. Peripheral nerve regeneration: Experimental strategies and future perspectives. *Advanced drug delivery reviews*. 2015;82-83:160-7.
303. Rangavajla G, Mokarram N, Masoodzadehgan N, Pai SB, Bellamkonda RV. Noninvasive imaging of peripheral nerves. *Cells, tissues, organs*. 2014;200(1):69-77.

304. Scheib J, Hoke A. Advances in peripheral nerve regeneration. *Nature reviews Neurology*. 2013;9(12):668-76.
305. Kemp SWP, Cederna PS, Midha R. Comparative outcome measures in peripheral regeneration studies. *Experimental neurology*. 2017;287:348-57.
306. Zheng L, Li K, Han Y, Wei W, Zheng S, Zhang G. In vivo targeted peripheral nerve imaging with a nerve-specific nanoscale magnetic resonance probe. *Medical hypotheses*. 2014;83(5):588-92.
307. Janjic JM, Gorantla VS. Peripheral Nerve Nanoimaging: Monitoring Treatment and Regeneration. *The AAPS journal*. 2017;19(5):1304-16.
308. Maravilla KR, Bowen BC. Imaging of the peripheral nervous system: evaluation of peripheral neuropathy and plexopathy. *AJNR American journal of neuroradiology*. 1998;19(6):1011-23.
309. Stoll G, Bendszus M, Perez J, Pham M. Magnetic resonance imaging of the peripheral nervous system. *Journal of neurology*. 2009;256(7):1043-51.
310. Stoll G, Wilder-Smith E, Bendszus M. Imaging of the peripheral nervous system. *Handbook of clinical neurology*. 2013;115:137-53.
311. Kathirgamanathan A, French J, Foxall GL, Hardman JG, Bedfordth NM. Delineation of distal ulnar nerve anatomy using ultrasound in volunteers to identify an optimum approach for neural blockade. *European journal of anaesthesiology*. 2009;26(1):43-6.
312. Rangavajla G, Mokarram N, Masoodzadehgan N, Pai SB, Bellamkonda RV. Non-Invasive Imaging of Peripheral Nerves. *Cells, tissues, organs*. 2014;200(1):69-77.
313. Ohana M, Moser T, Moussaoui A, Kremer S, Carlier RY, Liverneaux P, et al. Current and future imaging of the peripheral nervous system. *Diagnostic and Interventional Imaging*. 2014;95(1):17-26.
314. Duan X-H, Cheng L-N, Zhang F, Liu J, Guo R-M, Zhong X-M, et al. In vivo MRI monitoring nerve regeneration of acute peripheral nerve traction injury following mesenchymal stem cell transplantation. *European Journal of Radiology*. 2012;81(9):2154-60.
315. Raval SB, Zhao T, Krishnamurthy N, Ibrahim TS, Gorantla VS. Exploring Peripheral Nerve, Macro and Micro-Vasculature Imaging Applications at Ultra-High Field MRI. *Plastic and reconstructive surgery*. 2015;136(4 Suppl):20.
316. Aparicio-Blanco J, Torres-Suárez A-I. Towards tailored management of malignant brain tumors with nanotheranostics. *Acta Biomaterialia*. 2018.
317. Janjic JM, Vasudeva K, Saleem M, Stevens A, Liu L, Patel S, et al. Low-dose NSAIDs reduce pain via macrophage targeted nanoemulsion delivery to neuroinflammation of the sciatic nerve in rat. *Journal of Neuroimmunology*. 2018;318:72-9.
318. Balducci A, Wen Y, Zhang Y, Helfer BM, Hitchens TK, Meng WS, et al. A novel probe for the non-invasive detection of tumor-associated inflammation. *Oncoimmunology*. 2013;2(2):e23034.
319. Ghanouni P, Behera D, Xie J, Chen X, Moseley M, Biswal S. In vivo USPIO magnetic resonance imaging shows that minocycline mitigates macrophage recruitment to a peripheral nerve injury. *Molecular pain*. 2012;8:49.
320. Umashankar A, Corenblum MJ, Ray S, Valdez M, Yoshimaru ES, Trouard TP, et al. Effects of the iron oxide nanoparticle Molday ION Rhodamine B on the viability and regenerative function of neural stem cells: relevance to clinical translation. *Int J Nanomedicine*. 2016;11:1731-48.
321. Li K, Qin J, Wang X, Xu Y, Shen Z, Lu X, et al. Magnetic resonance imaging monitoring dual-labeled stem cells for treatment of mouse nerve injury. *Cytotherapy*. 2013;15(10):1275-85.
322. Zhong J, Narsinh K, Morel PA, Xu H, Ahrens ET. In Vivo Quantification of Inflammation in Experimental Autoimmune Encephalomyelitis Rats Using Fluorine-19 Magnetic Resonance Imaging Reveals Immune Cell Recruitment outside the Nervous System. *PloS one*. 2015;10(10):e0140238.
323. Vasudeva K, Andersen K, Zeyzus-Johns B, Hitchens TK, Patel SK, Balducci A, et al. Imaging neuroinflammation in vivo in a neuropathic pain rat model with near-infrared fluorescence and (1)(9)F magnetic resonance. *PloS one*. 2014;9(2):e90589.
324. Weise G, Basse-Luesebrink TC, Wessig C, Jakob PM, Stoll G. In vivo imaging of inflammation in the peripheral nervous system by 19F MRI. *Experimental neurology*. 2011;229(2):494-501.
325. Hitchens TK, Liu L, Foley LM, Simplaceanu V, Ahrens ET, Ho C. Combining perfluorocarbon and superparamagnetic iron-oxide cell labeling for improved and expanded applications of cellular MRI. *Magnetic resonance in medicine*. 2015;73(1):367-75.
326. Weissleder R, Nahrendorf M, Pittet MJ. Imaging macrophages with nanoparticles. *Nature materials*. 2014;13(2):125-38.
327. Kaneda MM, Caruthers S, Lanza GM, Wickline SA. Perfluorocarbon nanoemulsions for quantitative molecular imaging and targeted therapeutics. *Annals of biomedical engineering*. 2009;37(10):1922-33.

328. Janjic JM, Shao P, Zhang S, Yang X, Patel SK, Bai M. Perfluorocarbon nanoemulsions with fluorescent, colloidal and magnetic properties. *Biomaterials*. 2014;35(18):4958-68.
329. Zhou QL, Chen ZY, Wang YX, Yang F, Lin Y, Liao YY. Ultrasound-mediated local drug and gene delivery using nanocarriers. *BioMed research international*. 2014;2014:963891.
330. Schmieder AH, Caruthers SD, Keupp J, Wickline SA, Lanza GM. Recent Advances in (19)Fluorine Magnetic Resonance Imaging with Perfluorocarbon Emulsions. *Engineering (Beijing, China)*. 2015;1(4):475-89.
331. Moser BA, Steinhardt RC, Esser-Kahn AP. Surface Coating of Nanoparticles Reduces Background Inflammatory Activity while Increasing Particle Uptake and Delivery. *ACS Biomater Sci Eng*. 2017;3(2):206-13.
332. Yu M, Huang S, Yu KJ, Clyne AM. Dextran and polymer polyethylene glycol (PEG) coating reduce both 5 and 30 nm iron oxide nanoparticle cytotoxicity in 2D and 3D cell culture. *Int J Mol Sci*. 2012;13(5):5554-70.
333. Arami H, Khandhar A, Liggitt D, Krishnan KM. In vivo delivery, pharmacokinetics, biodistribution and toxicity of iron oxide nanoparticles. *Chem Soc Rev*. 2015;44(23):8576-607.
334. Neuwelt EA, Hamilton BE, Varallyay CG, Rooney WR, Edelman RD, Jacobs PM, et al. Ultrasmall superparamagnetic iron oxides (USPIOs): a future alternative magnetic resonance (MR) contrast agent for patients at risk for nephrogenic systemic fibrosis (NSF)? *Kidney international*. 2009;75(5):465-74.

SECTION 2

MATERIALS AND METHODS

Chapter IV

Materials and methods

Chapter IV

Materials and methods

OVERVIEW

This chapter aims at providing a comprehensive overview on the experimental procedures behind the results presented in the following Section III, and the respective chapters. Additionally, some considerations found relevant will be made regarding the selection of the materials, membranes, scaffolds and conduits processing methodologies, and the physicochemical and biological characterization techniques used to support the proposed methodologies. With this, it is expected to present a clearer perspective of the developed work in this thesis and how it can be correlated.

IV-1. MATERIALS

European Society for Biomaterials' (ESB), current definition for “biomaterial” is a material intended to interface with biological systems to evaluate, treat, augment or replace any tissue, organ or function of the body (1). Natural biomaterials were considered vital in the conception of this thesis. They frequently contain endogenous domains that stimulate cell adhesion and proliferation, and they do not trigger strong immune responses upon implantation, making them promising for transplant applications (2).

IV-1.1. Chitosan

Chitin is the second most abundant polysaccharide found on the planet, after cellulose (3). It can be found in shells of crustaceans, insects and fungi cellular walls (4). However, its deacetylated form, chitosan, is the one that attracts most of attention. Although discovered as early as 1859 by Rouget, chitin and chitosan remained publicly unknown and scientifically unexplored until the decade of 1950 (5). Only in 1990s chitosan has entered the pharmaceuticals area, as both the scientific community as well as the industry created new and more effective therapeutic systems based on it. Studies regarding chitin and chitosan have been intensified because it was found that these polysaccharides display excellent characteristics to be used in the TE field, having as well important pharmacological properties (6). Overall, chitin-based materials have far-reaching medical utility. Furthermore, intensive research has also allowed to find applications related with agricultural, food, and environmental engineering uses (7).

In one hand, chitin is a linear, high molecular weight, crystalline polysaccharide, theoretically comprised entirely by N-acetylated D-glucosamine units. On the other hand, chitosan, known as poly-(β -1/4)-2-amino-2-deoxy-D-glucopyranose is a hydrophilic polycationic copolymer made of D-glucosamine and N-acetyl-D-glucosamine, which are linked with β (1–4) bonds, as can be seen in **Figure IV-1**. Glucosamine is the predominant repeating unit in its structure (8). Chitosan is obtained industrially by hydrolyzing the amino acetyl groups of chitin by an alkaline treatment. A prompt distinction between chitin and chitosan can be achieved from their solubility. Chitin is soluble in dimethylacetamide in the presence of 5-10 %wt. lithium chloride and other corrosive and mutagenic solvents, being insoluble in low acidic solutions. The complete opposite happens for chitosan (9).

Chitosan chemical features offer chitosan with a unique set of functional properties. The biopolymer main characteristics, such as degradation, mechanical properties or cellular adhesion depend on the molecular weight and degree of acetylation (DA). In its turn, the DA of the chitosan is characterized by the portion of N-acetyl-D-glucosamine units in respect to the total number of units. DA can therefore be used to distinguish chitin from chitosan (10). In one hand, the molecule is named chitin if the DA is high, superior to 30 %. Conversely, it is name chitosan if the DA is low, below 30 %. In what concerns molecular weight, chitosan may vary between 10,000 to 2 million Dalton (11). The accurate determination of the DA is of major importance, especially in the TE field (12). The final features of the developed scaffolds, such as charge density, crystallinity, solubility, as well as chitosan propensity to enzymatic degradability are all dependent on the chitosan DA.

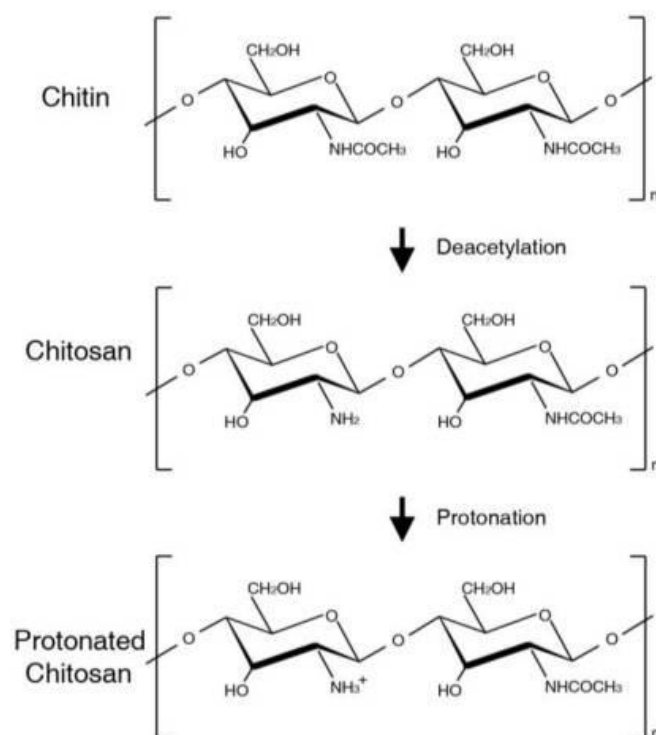


Figure IV-1 - Chemical structure of chitin, chitosan and protonated chitosan polymer.

. Many features make chitosan an attractive polymer for TERM approaches and to be processed as an implantable scaffold(13). It is non-toxic and biocompatible (14), causes no allergic reactions, it is biodegradable (15), has polyelectrolyte properties (16), the presence of reactive functional groups, gel-forming ability (17), high adsorption capacity, complete biodegradability (18), bacteriostatic (19) and fungistatic properties (20) and anti-tumor effects (21, 22).

Chitosan biodegradation is important in biomedical approaches since it may influence cellular behavior and determine tissue neof ormation (15). It can be hydrolyzed by human enzymes, such as lysozyme, mainly produced by macrophages. It acts by breaking the linkage between acetylated units, transforming chitosan into oligosaccharides (18). Another important characteristic of chitosan that makes it suitable for TERM approaches regards the fact that its amino groups become protonated and positively charged once dissolved in acidic media, which happens *in vitro* and *in vivo*, increasing even more chitosan's solubility (23). Due to the cationic nature of chitosan, it networks with anionic glycosaminoglycans, proteoglycans and many other negatively charged molecules, such as cytokines and growth factors. Therefore, scaffolds made of or containing chitosan are expected to carry growth factors more efficiently (24). This implicates that chitosan can recruit and effectively bind to bioactive factors from adjacent surroundings, shielding these factors from degradation and increasing local concentration and efficacy (25). In addition, positively charged chitosan also interrelates with negatively charged ECM components, such as glycosaminoglycans and proteoglycans (26). The cationic asset of chitosan can be inverted by sulfonation, introducing an anionic character (27).

Due to chitosan appropriate characteristics to act as a bioactive system, it has been widely applied in drug delivery. The simple control over the loading and releasing of bioactive agents renders chitosan an appropriate vehicle for drug delivery, which has been widely explored (28). With chitin and chitosan-based materials, diverse types of scaffolds can be fabricated, such as hydrogels (29), microcapsules (30), beads (31), nanoparticles (32), films (33), a variety of 3-dimensional porous structures (34), and fibers at micro- (35) or nanoscale (36). Furthermore, these scaffolds can be modified to yield polymer blends (37), which are formed to grant that the final scaffold will attain the desired structure, chemical and mechanical properties as well as biological performance adequate for a specific tissue.

Another fascinating ability of chitosan relies on its ability to regulate gene expression, which has been documented for bone and cartilage tissue engineering (38). This is an appealing feature, since most cell functions are controlled by gene expression. If performed in the lab, it is often meticulously provided by means of expensive and complex molecular biology techniques. Therefore, the simple use of a biomaterial to regulate biological responses is more convenient and economical.

Since chitosan has favorable biological properties for tissue regeneration, many different applications have been sought, as can be seen in **Table IV-1**. Overall, the current commercial interest in chitin and chitosan polymers rises from the fact that they combine numerous promising characteristics,

as biodegradability, biocompatibility and non-toxicity, making them appreciated and treasured materials for pharmaceutical, biomedical as well as industrial applications. Despite the tremendous potential of chitin and chitosan-based material for clinical applications, most of the studies are in a pre-clinical phase. Scarce chitin and chitosan-based materials, such as dressings designed for wound care, have been successfully transferred from bench to the clinical setting.

Table IV-1 - Recent published reports of chitosan formulations for different applications in TE.

| Type of scaffold | Application | Year, Ref- |
|---|---------------------------|------------|
| Injectable chitosan hydrogel | Bone | 2019, (39) |
| Chitosan hydrogel | Skin/wound healing | 2019, (40) |
| Chitosan-hyaluronic acid hydrogel | Cartilage | 2017, (41) |
| Asymmetric cellularized chitosan film | Tendon | 2018, (42) |
| Chitosan nanoparticles | Cornea | 2018, (43) |
| Chitosan tubes with NT-3-loaded chitosan carriers | Central nervous system | 2019, (44) |
| Chitin/carboxymethyl chitosan tube | Peripheral nervous system | 2019, (45) |
| PLGA nanoparticles coated with chitosan | Oral mucosa | 2018, (46) |
| Chitosan-gelatin bi-layered porous scaffold | Blood vessels | 2017, (47) |
| Chitosan-gelatin porous scaffold | Drug delivery | 2018, (48) |
| Chitosan scaffolds with 200 μ m inter-filaments | 3D printing | 2018, (49) |

The chitosan used in the experimental works comprised in this thesis is highly purified chitosan powder (Ki2Med® LO80+) with 5 % DA, provided by Altakitin S.A. (Lisboa, Portugal). Chitosan powder with 2 % and 1 % DA, respectively, were produced from 5 % DA chitosan by one or two hydrolysis steps in 40 % (v/v) sodium hydroxide for 2 hours at 80 °C (50).

IV-1.2. Gellan Gum

Gellan gum (GG) is an extracellular polysaccharide produced by different bacteria, mainly by the aerobic fermentation process of *Sphingomonas elodea* and *Sphingomonas paucimobilis* (51). It is a linear and anionic polymer composed of repeating units of a tetrasaccharide [D-glucose(β 1 \rightarrow 4) D-glucuronic acid(β 1 \rightarrow 4)D-glucose(β 1 \rightarrow 4)-L-rhamnose(α 1 \rightarrow 3)]_n, as can be seen in **Figure IV-2**. Two acyl substituents, L-glyceryl and acetyl are present at the O-3- linked glucose at the O-2 and O-6 positions, respectively (52). During commercial processing, these substituents are easily lost. Therefore, according to the degree of acyl substitution, GG can be categorized as high acyl (HA) GG and low acyl (LA) GG. Due to these structural differences, HA-GG assumes double helix geometry at a much higher

temperature when compared with LA-GG. The latter can form strong and firm gels, with a brittle structure when compared to HA-GG. This allows to fabricate gels with an assortment of textures, water content and mechanical properties, and to be tuned according with the desired application (53). Since ion-binding sites exist on GG structure, pairs of helices are formed in antiparallel junction zones in the presence of cations, namely divalent cations, Ca^{2+} and Mg^{2+} , or of two monovalent cations, K^+ and Na^+ (54).

GG was initially highly used in the food industry. In fact, it was first introduced into the food application in the year 1988 at Japan. FDA later approved its use in the United States and Europe (55). Its functions as food supplements are mainly as a thickener, binder, and stabilizer. It primarily stabilizes the water-based gels, such as desserts and drinking jellies (56).

Due to their interesting characteristics, many authors have suggested GG as a promising biomaterial for TE in the last years, as it can be considered a soft-tissue mimetic (57). The advantage resides in the fact that GG is able to hold large amounts of water (58) and possess bio-adhesive properties. Additionally, it also permits the encapsulation of cells and drugs to occur in mild conditions. More specifically, gelation process of GG solutions occurs rapidly at $\approx 39^\circ\text{C}$. Thus, the exceptionality of this biomaterial is related to the fact that GG biomaterials can be easily tuned and stabilized in physiologic conditions, by immersion in saline solutions (pH 7.4) or culture media. Other advantage of GG is related to the fact that different processing methods result in different biological properties.

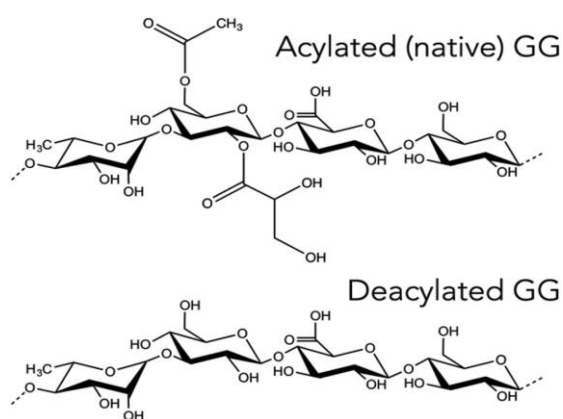


Figure IV-2 - Chemical structure of native (acetylated) and deacetylated gellan gum. Reprinted with permission from [57].

As an example, in the form of hydrogels, different cell types have been shown to not adhere and spread when encapsulated within gels. This feature makes it useful as an anti-adhesion barrier, finding its use in acellular tissues (59). However, when processed to have a porous structure, GG can become cell-

adhesive, allowing the adhesion and proliferation of different cell types (60, 61). Different applications have been sought along the years, as can be seen in **Table II-2**

Table IV-2 - Recent published reports of chitosan formulations for different applications in TE.

| Type of scaffold | Application | Year, Ref. |
|--|---------------------------|------------|
| Calcium-enriched methacrylated GG beads | Bone | 2019, (62) |
| GG composite hydrogels | Cartilage | 2018, (63) |
| GG-based hydrogels | Intervertebral disc | 2015, (64) |
| GG-based hydrogels | Vascular system | 2017, (65) |
| TiO ₂ nanotubes incorporated in GG film | Skin/wound healing | 2018, (66) |
| Peptide modified GG hydrogel | Central nervous system | 2016, (67) |
| GG-based freeze-dried luminal fillers | Peripheral nervous system | 2018, (60) |
| Electroactive Gellan Gum scaffolds | Muscle | 2017, (68) |
| GG sponge | Dental fillings | 2012, (69) |
| Nanocomposite GG-based hydrogels | Drug delivery | 2018, (70) |
| GG-based hydrogels | 3D printing | 2018, (71) |

IV-1.2.1. Methacrilated-GG

Chemical modifications and functionalization of GG have been widely proposed by several authors, as the free carboxylic groups present in GG permit to alter this linear polysaccharide. Although the carboxylic groups are the mostly used, the hydroxyl groups are also prone to be modified. The goal of these strategies is to adjust the final properties of GG gels, according to the final applications (70).

Coutinho *et al.* (72) firstly modified GG with methacrylate groups, in order to overcome the fact that GG could only be crosslinked by physical methods. To surpass that drawback, the authors synthesized GG hydrogels crosslinkable by both physical and chemical mechanisms, being both ionic- and photo-crosslinkable. The protocol involved the addition of methacrylic anhydride to GG solution at 50 °C, in order to synthesize methacrylated-GG with various degrees of methacrylation. In a second approach, Silva-Correia *et al.* (53) projected the methacrylation of GG would ameliorate the solubility of GG, being also capable of obtaining ionic- and photo-crosslinkable materials. For that, the authors started with the dispersion of 1 %wt. LA-GG, to which glycidyl methacrylate was added. After the pH was adjusted to 8.5, it was left to stir for 24 hours.

According to the degree of methacrylation, the developed materials present highly tunable mechanical and degradation profiles, finding its application in a variety of TE approaches.

The HA-GG used in the experimental work in this thesis was bought commercially, under the name of KelcoGelW LT100®, CP Kelco (Atlanta, Georgia, USA), with a molecular weight of 1–2 x 10⁶ Da. MA-GG was kindly supplied by Stematters (Irisbiosciences, Guimarães, Portugal), under the name of Mimsys G®, with a molecular weight of 62.4 kDa.

IV-1.3. Silk fibroin (SF)

Being one of the oldest natural polymers discovered by men, SF has evolved during its history of over 380 million years (73). For centuries, SF has been exploited as a high-quality textile fiber. SF has also been used as a surgical suture material for decades (74). Lately, its use in biomedical applications has exponentially increased, due to silk's highly tailorable properties, biocompatibility (75), biodegradability (76), outstanding mechanical properties (77) and facile chemical modifications (78).

SF is a fibrous protein usually spun into fibers from glands of silk producing arthropods, such as silkworms, spiders and scorpions (79). These fibers are composed of a fibrous protein core, composed of fibroin, with a surrounding glue protein, sericin. More specifically, two parallel fibroin fibers are held together with a layer of sericin on their surfaces. According to the SF origin, its amino acid composition varies, as can be seen in **Table IV-3**. In the experimental works developed in this thesis, SF derived from domesticated mulberry *Bombyx mori* silkworm, which is the most famous member of the family *Bombycidae* (80).

Table IV-3 - Comparative data on amino acid composition of *B. mori*, *N. edulis* and *N. clavipes* silks. Reprinted with permission from (81).

| Amino acid | <i>B. mori</i> | <i>N. edulis</i> | <i>N. clavipes</i> |
|------------|----------------|------------------|--------------------|
| Ala | 30.0 | 24.0 | 22.71 |
| Gly | 42.9 | 38.2 | 49.96 |
| Tyr | 4.8 | 5.2 | 2.99 |
| Ser | 12.2 | 1.7 | 2.24 |
| Asp | 1.9 | 1.5 | 1.06 |
| Arg | 0.5 | 2.3 | 1.76 |
| His | 0.2 | Trace | 0.21 |
| Glu | 1.4 | 12.8 | 11.02 |

| | | | |
|-----|-----|-----|------|
| Lys | 0.4 | 0.3 | 0.10 |
| Val | 2.5 | 0.7 | 0.89 |
| Leu | 0.6 | 2.4 | 4.26 |
| Ile | 0.6 | 0.4 | 0.07 |
| Phe | 0.7 | 0.3 | 0.26 |
| Pro | 0.5 | 9.4 | 2.04 |
| Thr | 0.9 | 0.4 | 0.34 |
| Met | 0.1 | 0.3 | 0.04 |
| Cys | 0.0 | ND | 0.06 |

The use of SF has numerous advantages when compared to other naturally-obtained biomaterials, from allogenic or xenogeneic origins. The main inconveniences of other biomaterials are related to the high risk of infection, poor biocompatibility and complex and expensive processes of isolation and purification. Sericin, with a molecular weight of 20-310 kDa is a protein produced along with silk, currently seen as a trigger of *in vivo* inflammatory responses (82). Therefore, its extraction is required for biomedical applications, in a process entitled degumming. In the case of the *Bombyx mori* SF, this process of purification is routinely established and involves a simple alkali- or enzyme-mediated degumming procedure to extract sericin from the cocoons. Regularly, after the degumming, it is possible to obtain SF at 70 %wt. of the original cocoon mass (excluding the worm weight), which can be seen in **Figure IV-3**.

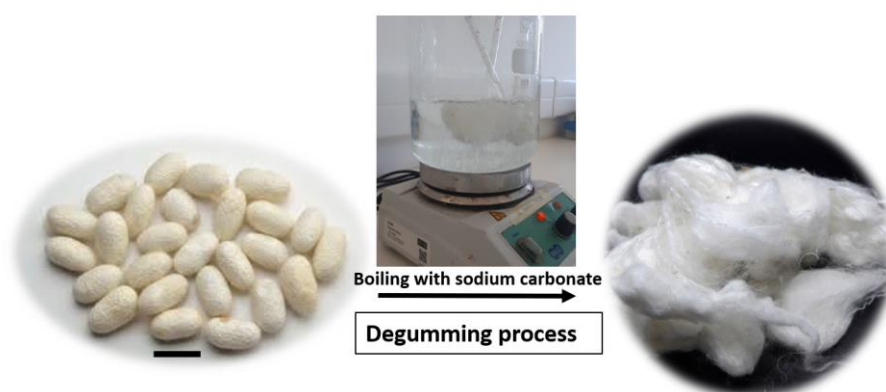


Figure IV-3 - Silk cocoons purification process. *Bombyx mori* silk cocoons give origin to purified SF after sericin extraction through degumming procedure. Scale bar of the cocoon: 1 cm.

However, there is an on-going discussion related to the use of sericin in the scientific field, as other *in vivo* reports contradict the previous report claiming its non-immunogenicity (83).

Related to its chemical structure, SF is formed by heavy (H) and light (L) chains linked by a disulfide bond, with hydrophobic domains of the H-chains interspaced by hydrophilic regions at the L-chains, as can be seen in **Figure IV-4**. The hydrophobic domains contain highly ordered Glycine-X (X being Alanine, Serine, Tyrosine, Valine) repeats that form stacked anti-parallel β -sheets (silk II) of crystalline structure. The hydrophilic regions constitute the amorphous phase of the protein. Processed in a variety of forms, silk-based materials include porous scaffolds (84) and sponges (85), films (86), tubes (87), electrospun (88) or micro-fibers(89), hydrogels (90) and textiles (91). These have been assessed for several TE applications, as it can be seen in **Table IV-4**.

Table IV-4 - Recent published reports of SF formulations for different applications in TE.

| Type of scaffold | Application | Year, Ref. |
|---|---------------------------|-------------|
| Silk fibroin /hydroxyapatite composites | Bone | 2018, (92) |
| SF fiber-chitosan porous composite | Cartilage | 2018, (93) |
| Electrospun SF/collagen scaffold | Vascular system | 2018, (94) |
| REDV peptides/porous SF scaffolds | Skin/wound healing | 2018, (95) |
| Bioactive SF/hyaluronic acid hydrogels | Central nervous system | 2018, (96) |
| Gold nanorods/SF conduits | Peripheral nervous system | 2019, (97) |
| Porous SF scaffolds | Intervertebral disc | 2010, (78) |
| SF porous scaffolds | Dental fillings | 2014, (98) |
| SF nanoparticles | Drug delivery | 2019, (99) |
| Enzymatically crosslinked SF hydrogel | 3D printing | 2017, (100) |
| Electrospun SF | Bladder | 2011, (101) |

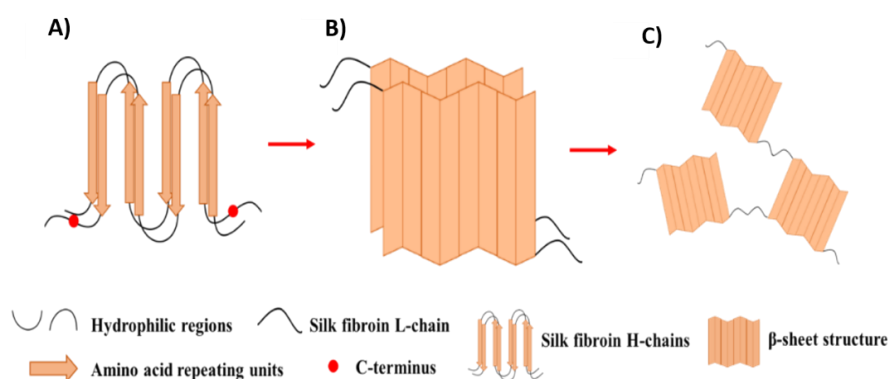


Figure IV-4 - Schematic illustration of the natural SF protein composition. (A) H-L complex formation. (B) H-chains organizing themselves together into β -sheet structures. (C) β -sheet structures linked by amorphous domains.

To be processed in the diverse forms previously mentioned, after the purification or degumming process, SF must be dissolved in concentrated lithium bromide (102), ionic liquids (103), lithium thiocyanate (104) or organic solvent hexafluoroisopropanol. Regarding the final constructs, they naturally shift from an amorphous state to a predominant β -sheet conformation (105). Nevertheless, this naturally occurring process can be briefly controlled by using different chemical and physical methods, including the addition of sodium chloride (106), immersion in alcohol solutions (107), organic solvents, temperature and pH variations (108), ultrasonication (109), or vortex induction (110). Except from hydrogels, most of the SF scaffolds are normally used in biomedical applications after acquiring the β -sheet crystalline structure. It has been demonstrated that such conformation has superior mechanical and biological properties and adequate water insolubility. Therefore, processing SF under mild processing conditions and at room temperature (RT), allows SF-based materials to be prepared in a friendly processing, which favors the incorporation of bioactive proteins, drugs and cells (111).

The SF raw materials used in this thesis were supplied by the Portuguese Association of Parents and Friends of Mentally Disabled Citizens (APPACDM, Castelo Branco, Portugal) and used after purification and dissolution.

IV-1.4. Keratin

Keratin is the name given to a broad category of organizational and structural-based proteins, which mainly exist in human hair, skin and nails. Furthermore, it exists in the feathers, wool, horns and hooves of several animals (112). There have been great developments in the area of keratin extraction, purification and characterization of keratins from their original sources in the past decades, which

permitted a vast progress and expansion in the keratin-based biomaterials field (113). Being highly insoluble, keratin extraction requires the breakage of disulfide bonds avoiding the breaking of peptide bonds. For that, harsh reagents are needed and a process of four steps is required: delipidization, solubilization, dialysis, and freeze-drying, as can be seen in **Figure IV-5**.

The search for protein-based biomaterials for TE applications arose due to their aptitude to mimic ECM that enables cell-cell and cell-matrix communication (114). Adding to this, food industry and other animal related businesses produces millions of tons of keratin waste products, making it readily available. Hair salons and barber shops also produce a surplus of keratin-containing biomass, which is not considered as a resource (115).

Amino acid cysteine is extremely abundant in keratin and the S-S (sulfur-sulfur) bonds present in the cysteine side chain allows a strong crosslink, making these proteins particularly strong and insoluble. In fact, keratin-containing tissues are considered one of the strongest non-mineralized tissue in nature. The cysteine residues also allow the protein to promptly arrange in intermediate filaments (116).

Based on its structure, keratin proteins can be divided in two distinct groups. In one hand, hard keratins can form well-organized arrays of intermediate filaments surrounded by a milieu of cystine-rich proteins, cooperating to obtain the hard and tough construction of epidermal appendages. On the other hand, lightly-packed bundles of intermediate filaments form the soft keratins, granting some resilience to epithelial cells (117). Furthermore, these two types of keratins differ in their amino acid composition. Normally, hard keratins contain a high volume of cysteine, low glycine content, and possess mechanical and physical durability, as the reverse happens for soft keratins (118).

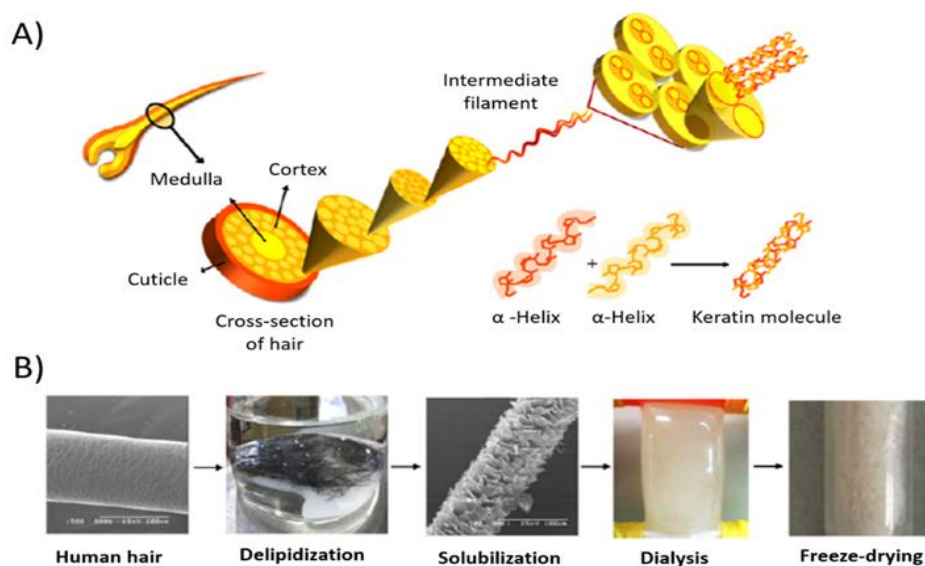


Figure IV-5 - Structure of intermediate filament, micro and macro fibril and hair, represented in a cross-section of hair; B) Representative images of keratin extraction steps. Reprinted with permission from [125].

There are mainly two aspects contributing to the success of keratin in biomedical and TE applications. The first resides in their capability to prompt self-assembly and polymerize, allowing the facile formation of porous scaffolds (119), membranes (120) and hydrogels (121). The second is related to the fact that keratin biomaterials derived from wool and human hair have been shown to possess cell binding motifs, such as leucine-aspartic acid-valine (LDV) and glutamic acid-aspartic acid-serine (EDS) binding residues, which are capable of supporting cellular attachment (122). In addition to integrin-mediated cellular binding, it has been reported that a non-integrin receptor can mediate cell-keratin interactions (123). These molecular findings allow keratin to be successfully used as coating material for cell culture, improving cell adhesion and proliferation (124).

More specifically, in recent years, keratin extracted from human hair has been acknowledged as a powerful biomaterial owing to the fact that it is a human-derived source, therefore reducing possible immunological reactions and increasing its biocompatibility (125). Human hair keratins are classified as hard keratins, entailing 65-96 %wt. of proteins, 1-9 %wt. of lipids, 3 %wt. of melanin, and other negligible compounds (126). Hair keratins are rich in chemical cues, such as growth factors and other signaling molecules involved in the cycles of hair growth. Consequently, it is expected that these factors also play an important role on tissue regeneration, as they do in the highly orchestrated process of hair growth (127).

Related to PNR, several studies with human hair keratin have been conducted in different animal models, from mice (128), rats (129), to rabbits (130) and nonhuman primates (131). Due to the visible success of a keratin hydrogel in promoting nerve repair, a phase I prospective, randomized trial is currently ongoing, entitled “Multicenter Clinical Trial of Keratin Biomaterial for Peripheral Nerve Regeneration” (ADA613738).

Overall, the structural integrity and solubility of keratin as well as its natural biocompatibility, controllable biodegradability, and bioactivity make keratin an ideal medical polymer. As such, biomedical applications using keratins increased over the years and many different applications can be found in literature, in the TE field, as can be seen in **Table IV-5**.

The keratin used in the experimental work presented in this thesis was kindly provided by Prof. Kee Woei Ng from Nanyang Technological University in Singapore.

Table IV-5 - Recent published reports of keratin formulations for different applications in TE.

| Type of scaffold | Application | Year, Ref |
|----------------------------------|---------------------------|-------------|
| Keratin powder wound dressing | Skin/wound healing | 2017, (132) |
| Calcium phosphate coated Keratin | Bone | 2015, (133) |
| Keratin nanoparticles | Central nervous system | 2016, (134) |
| Keratin hydrogel | Peripheral nervous system | 2012, (135) |
| Keratin nanoparticles | Drug delivery | 2018, (136) |
| Solubilized keratin proteins | Hemostatic agent | 2013, (137) |
| Keratin film | Ocular reconstruction | 2015, (138) |
| Electrospun keratin fibers | Cartilage | 2014, (139) |
| Electrospun keratin fibers | Vascular system | 2016, (140) |

IV-1.5. Neurotrophic factors (NTFs)

NTFs are molecules that are naturally released in the process of injury, resulting in nerve regeneration. The various growth factors have diverse actions in the nerve, as they can enhance functional regeneration, support axonal elongation, Schwann cell migration, overall acting as neuroprotective components through receptor-mediated activation of specific pathways (141). NTFs normally used to improve nerve regeneration primarily belong to three separate groups (142): the neurotrophins, the glial-cell-line-derived neurotrophic factor family ligands and the neuropoietic cytokines. The first group, neurotrophins, include NGF, BDNF, NT-3 and NT-4 (143). The second group

includes the very GDNF and CNTF (144). When linked to their specific receptor, which are trans-membrane proteins, they will activate a cascade of events after substrate binding, activating determined cellular responses (145). In **Chapter X**, the two NTFs that were used are NGF and GDNF, as can be seen in **Figure IV-6**.

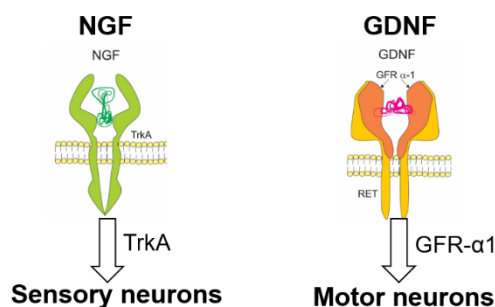


Figure IV-6 - NTFs used in this thesis, NGF and GDNF.

NGF, the classical member of the neurotrophins family and therefore abundantly characterized, is largely used both *in vivo* and *in vitro*. Its action is limited to a few neuronal populations, namely supporting the outgrowth and survival of peripheral sympathetic and neural crest-derived sensory neurons (146).

GDNF has an important role in the case of degenerative diseases, such as Huntington's and Parkinson's, as it has been found that GDNF encourages survival of damaged midbrain dopaminergic neurons (147). GDNF has also been used to target sensory neurons in order to alleviate pain in cases of chronic denervation (148, 149). However, its main function is related to motor neurons.

When using NTFs in TE approaches, it is important to mimic their natural release, which is vital for nerve growth, differentiation and expansion (150). However, the artificial administration of growth factors as a therapy is a difficult task to accomplish because of their high biological activity, which obliges to administer extremely small doses, pleiotropic effects and short biological half-life (151). Therefore, one of the main goals of **Chapter X** was to find an appropriate delivery method for these NTFs. In **Chapter X**, Human recombinant GDNF (cat#450-10-10 µg) and Human recombinant NGF (cat#450-01-100 µg) were purchased from Peprotech (New Jersey, USA) were used

IV-2. REAGENTS

Unless addressed otherwise, all the reagents used in this thesis were purchased from Sigma-Aldrich (St. Louis, MO, USA).

IV-3. METHODOLOGIES FOR PROCESSING OF BIOMATERIALS: OVERVIEW

Regarding the fabrication of the scaffold itself, there is no idyllic methodology or common biomaterial processing that meets all the scaffolding requirements for tissue regeneration. Different tissues, as well as different biomaterials, require specific physical, mechanical and degradation properties (152).

Knowing that the classic TE paradigm relies on a combination of biomaterial scaffolds, cells, and bioactive molecules to orchestrate tissue formation and integration within the host environment (153), biomaterials processing plays a vital role in the regenerative process. TE scaffolds are premeditated to influence the physical, chemical and biological environment surrounding the damaged tissue. The processing method is the key factor that mostly contributes to control all the parameters that will influence its behavior *in vitro* and *in vivo* (154). The different biomaterials used in this thesis were processed in a variety of ways, namely in the form of membranes, freeze-dried hydrogels and conduits.

IV-3.1. Membranes

The use of membranes for guided tissue regeneration was initially considered for bone or periodontal TE strategies (155). This concept was based on using a bioabsorbable or non-resorbable membrane that would mainly behave as a barrier to prevent soft-tissue invasion into the injured area and form a 'chamber' to guide the regeneration process through the desired area (156). The same principle is applied to PNR, where the tubulization purpose is to protect the regenerative tissue from external detrimental factors and mainly direct and physical guide the growing axons (157).

One of the main advantages related to the use of membranes in TE regards the fact that they are easily produced by simple solvent casting technique (158). Parameters such as thickness, porosity and mechanical properties are also easily controlled by the polymer concentration and the quantity of material used. Furthermore, any kind of surface modification is more easily performed on membranes,

which when rolled up and turned in conduits, allow the fabrication of tailor-made peripheral nerve grafts, as can be seen in **Figure IV-7**.



Figure IV-7 - Prospect of developing novel tubulization strategies for transected nerves based on chitosan membranes, after rolling the membranes to form NGCs. Scale bar: 3 mm.

IV-3.2. Freeze-dried hydrogels

Hydrogels have been studied for several TE applications, involving cell encapsulation strategies or drug delivery systems (159). Also, the similarity between the ECM of soft tissue and hydrogels, characterized by high water content viscoelastic polymeric networks, has been sustaining the advancement of hydrogels TERM purposes. For instance, hydrogel systems have been one of the first choices to be used as fillers or combined with cells or bioactive agents in different cartilage or bone regeneration applications (160). In this sense, the injectable hydrogels are attracting much interest (161, 162). Several methodologies have been applied to produce hydrogels, including photopolymerization (163), ionic or thermal gelation (164), and enzymatic reactions (165).

However, despite the attractive characteristics of hydrogels, cellular behavior such as adhesion, proliferation and migration, critical to achieve positive results in TE and which are mediated by receptor–ligand interactions at the cell–material interface, are features that are not displayed by traditional hydrogels. One way to surpass these difficulties is by incorporation of proteins or peptide sequences, that would originate cell-adhesive hydrogels (166). Their production is, however, more complex and more expensive (167). A simple way to overcome this strain is based on subsequent freezing, freeze-drying and rehydration steps, after the formation of the initial hydrogel (168). As it has been established before (168), there are many differences between a freeze-dried hydrogel and the antecedent hydrogel. The advantage of using freeze-dried hydrogels resides in their low water-content, microstructure re-organization, increased pore size and wall thickening, all leading to an augmented cell adhesiveness, when compared to the precursor hydrogel. These further steps allow for a microstructure re-arrangement, which brings benefits for cellular behavior, as can be assessed in **Figure IV-8**.

Furthermore, improved levels of control over the microstructure are achieved following this methodology, allowing to attain soft-tissue equivalents.

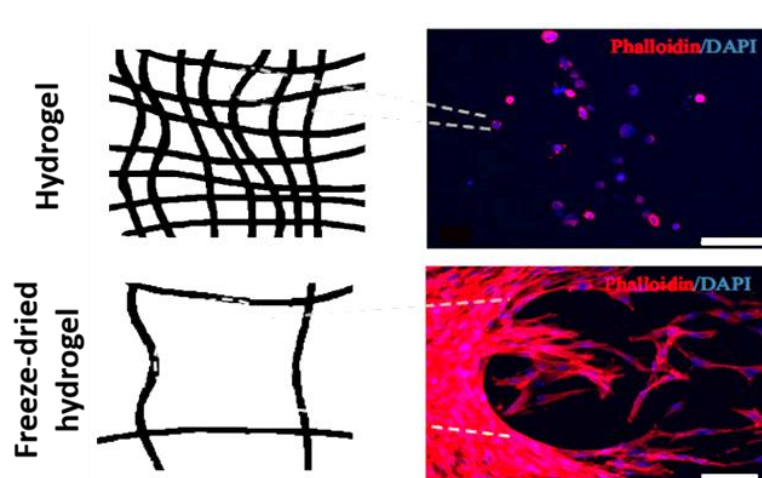


Figure IV-8 - Schematic representation of hydrogel and freeze-dried hydrogel polymeric network microstructure, which favors cell adhesion. Reprinted with permission from [168].

At last, the possibility of having off-the-shelf structures is another major advantage of this methodology.

Regarding GG freeze-dried hydrogels used in this thesis, in **Chapter VII**, they can be formed by two complementary or independent procedures: by temperature decrease and/or by the addition of ions (53). Hence, GG hydrogels are termed thermo-reversible hydrogels as they respond to temperature decrease with a sol-gel transition. In fact, GG has a thermally reversible coil form at high temperatures, which upon temperature decrease down to 37 °C, changes to a double-helix form. Next, a structure composed of anti-parallel double helices is self-assembled to form oriented bundles. These, called junction zones, that link untwined regions of extended helical chains per se, lead to the formation of a 3D network, the hydrogel. In addition, the use of counterions, specifically monovalent or divalent cations, promotes a physical bonding between cations and carboxylate groups of the GG, particularly strong when involving divalent ions, leading to the formation of the 3D reticulated hydrogel. Due to this dual formation mechanism, GG hydrogels have great potential for biomedical applications. They can be crosslinked *in situ* when reaching an *in vivo* environment which is ionic and holds temperatures of 37 °C.

In what concerns SF hydrogels, they have been typically prepared from a conformational transition of the SF protein from random coil to β -sheet, using extreme physical treatments (108-110) or chemical reagents (106). In many cases, these involved long gelation times and harsh preparation

conditions that limited their use as injectable systems. At the same time, these hydrogels showed homogeneous and stable physicochemical properties for hard tissues application, including bone or cartilage (169) as well as soft tissue applications (170).

However, in **Chapters VIII, IX and X**, the purpose of this thesis, was to take advantage from the peroxidase-mediated crosslinked SF hydrogels, and in combination with freeze-drying methodologies create novel SF porous NGCs of controlled conformation and mechanical properties (87). The transformation of a SF solution into an hydrogel, as a middle step of the processing, was crucial to obtain the fine-tuned NGCs. The detailed preparation of GG freeze-dried hydrogels as well as enzymatically crosslinked SF hydrogels which were also freeze-dried can be assessed in **IV-5.3** and **IV-5.4**, respectively.

IV-3.3. Tubular conduits

The development of tubular conduits in the biomedical field is in rapid expansion due to the growing medical need for viable supports that can aid in the guidance of soft and hard tissues regeneration (171, 172). Soft tissue regeneration that would profit from the creation of appropriate conduits includes, among others, vascular regeneration (173) and PNR (174). For PNR tissue regeneration, there is currently a significant clinical need for the development of an alternative substitute to autologous grafts, especially in terms of small diameter conduits. Indeed, no clinically viable small-diameter grafts, synthetic or natural, have been successfully developed so far (175), at least to a point where the outcomes are better than autografts. Hard tissue regeneration includes bone or ligament-to-bone tissue regeneration. In the latter, a graded material system exhibiting a gradual transition from non-mineralized tissue (*e.g.*, tendon or ligament) to mineralized tissue (*e.g.*, bone) is necessary, which is extremely difficult to achieve (176, 177). The fabrication of tubular conduits for tear drainage is an area that is somehow disregarded and could benefit from the development of more effective conduits. In this field, several complications were observed in the use of FDA-approved conduits, such as tube extrusion or obstruction (178, 179).

Many other tissues would also benefit from advances in the field of tubular conduits development and fine-tuning, including the CNS (180), tendon (181), tracheas (182), and ureters (183). Currently, there is a lack of biomanufacturing approaches that can produce reproducible tubular conduits with the desired characteristics for a specific application (184). Although the gross geometry of these devices is

quite similar for soft and hard tissue engineering, the necessary features of conduits (*i.e.*, porosity, size, permeability, bioactivity and mechanical properties) will likely vary considerably according to the tissue of interest. A fine-tuned fabrication of tubular conduits would offer the opportunity to explore the combination of biomaterials and processing techniques to achieve the desired final characteristics and ultimately, an efficient tissue regeneration.

In the particular case of PNR, customized nerve conduits that can offer guidance for the regenerating axons, while the influence of external cellular and humoral factors is minimized, would be the ideal solution for tackling short- and long-gap nerve defects. Due to the shortcomings shown by the conventional methodologies, such as electrospinning or braiding, it was hypothesized to produce tunable SF-based tubular conduits using an enzymatically-mediated crosslinking method. Our research group (185, 186), as well as others, (187, 188) have been previously exploiting the presence of tyrosine groups in SF to obtain enzymatically-crosslinked hydrogels, by using horseradish peroxidase (HRP) as enzyme and hydrogen peroxide (H_2O_2) as substrate. By using the HRP/ H_2O_2 crosslinking method, the initially produced aqueous SF solution can be rapidly transformed into an amorphous and transparent hydrogel with superior stability (189), which can undergo conformational changes under specific conditions. Therefore, in this thesis, in **Chapter VIII** and **IX**, the potential of the developed work to produce innovative NGCs is based on this recently developed class of enzymatically-crosslinked SF hydrogels. Our strategy to develop tube-shape scaffolds with customized properties relies solely on using different final processing steps, which include different methods of solvent extraction and the use of molds with diverse diameters of the inner cylinder. The conduits developed following these processing methods can be modulated in virtually any of its intrinsic characteristics, which cannot be achieved using the previously described conventional methodologies.

IV-4. PRODUCTION OF DIFFERENT MATERIALS FOR PNR

IV-4.1. Production of chitosan-based biomaterials: membranes and conduits

Pandalus borealis shrimp shells served as a source for the certified medical grade chitosan, branded Ki2Med® (Altakitin S.A., Lisboa, Portugal), with a molecular weight of 260 kDa and 5 % of DA. This product was the basis to produce all chitosan materials in this thesis.

In **Chapter V**, chitosan membranes were produced and kindly supplied by the Biohybrid project partner, Medovent GmbH (Mainz, Germany). Briefly, highly purified chitosan powder Ki2Med® with 1 %, 2 %, or 5 % DA, respectively, was dissolved in 0.75 % (v/v) acetic acid to obtain a 1.5 %wt solution, which was filtered and poured into Petri dishes, followed by drying at RT for 72 hours. The resulting membranes were treated with a solution of ammonia in methanol/water, washed once with distilled water and dried for another 24 hours.

In **Chapter VI**, highly purified chitosan powder Ki2Med® with a DA of 5% was dissolved in 0.25 M acetic acid aqueous solution to attain a final concentration of 2% wt. For the samples containing keratin, the freeze-dried keratin powder was added to the previous solution to achieve a 2 %wt. chitosan / 1 %wt. keratin solution. The solutions were stirred overnight and filtered to remove impurities. After casting onto glass petri dishes, samples were dried for at least 5 days at RT. The dried membranes were neutralized in 0.25 N sodium hydroxide and washed every 30 minutes until reaching neutral pH. They were further dried at RT in the respective molds.

In **Chapter VII**, chitosan hollow tubes were kindly supplied by the Biohybrid project partner Medovent GmbH (Mainz, Germany). Conduits were manufactured under ISO 13485 conditions, using the Medical grade chitosan (Ki2Med®, 5 % DA) More specifically, an extrusion process was applied for their obtaining, followed by distinctive washing. The formulations were finally cut into fragments presenting the required length of 14 mm.

All chitosan membranes and conduits in the three mentioned chapters were sterilized with ethylene oxide gas (EO), considered by some authors the most suitable method of sterilization for chitosan materials (190).

IV-4.2. Production of freeze-dried hair keratin

Freeze-dried human hair keratin used in **Chapter VI** was kindly supplied and extracted by Dr. Ng Kee Woei at School of Materials and Science, Nanyang Technological University of Singapore.

Briefly, random human hair samples were obtained from hair salons in Singapore and processed as previously described (191), with minor modifications. After washing the hair samples with soap and ethanol, delipidization was done with a mixture of chloroform and methanol at a ratio of 2:1, for 24 hours. The delipidized hair was thoroughly air-dried to remove the organic solvents and snipped into fragments as small as 1 - 2 mm for keratin extraction. 45 g of the hair fragments was immersed in 1 L

of 0.125 M sodium sulphide solution in deionized water and incubated at 40 °C for 4 hours. The resulting solution was filtered and extensively dialyzed against deionized water using membranes of 10 kDa molecular mass cut-off to remove residual sodium sulphide. The dialyzed solution was subsequently freeze-dried to obtain keratin powder and stored at -20 °C until use. To ensure sterility, the whole process was conducted in a class II biosafety cabinet and all solutions were sterile filtered. Typical yields were calculated to be between 20 % and 40 % by weight percentage. Based on this extraction protocol, the protein fraction obtained was previously shown to contain both monomers of Types 1 and 2 hair keratins in the molecular weight range of 45-60 kDa (192), which retain the typical peptide bond profiles expected of intact proteins (193).

IV-4.3. Production of Freeze-dried GG hydrogels

The methodology used to obtain freeze-dried GG-based hydrogels involves hydrogel preparation, freezing, freeze-drying and final re-hydration with a solvent, usually phosphate buffer saline (PBS) (for *in vitro* assays) or 0.9 % (v/v) sodium chloride (NaCl) (for *in vivo* assays).

In **Chapter VII**, four different GG blending mixtures were prepared with different amounts of HA-GG and MA-GG, as it has been proved that varying the ratios of the two forms of GG produces a wide variety of textures, with different biological and physicochemical features (194).

First, a solution of HA-GG (KelcoGelW LT100 with MW=1–2 x 10⁶ Da, CP Kelco, Atlanta, GA, USA) at 0.7 %wt. was prepared, by dissolving the powder in deionized water under stirring and at 40 °C for 30 minutes, to enable its dissolution and fluidification. Separately, a solution of MA-GG (Mimsys G[®] with MW=62.4 kDa, Stematters, Irisbiosciences, Guimarães, Portugal) at 0.7 %wt. was prepared under stirring, at RT. When the temperature of the HA-GG reached 37 °C, MA-GG solution was added at the pre-defined ratio, continuing the stirring for a few minutes. When visually homogenous, the blending solutions were casted into the desired molds (diameter and height were 6 mm and 10 mm, respectively), self-made from silicon tubing (purchased from Deltalab, Spain) and rapidly mixed with the crosslinking solution containing divalent cations, in this specific case, PBS solution. The blending mixtures were allowed to stabilize in PBS overnight to reach the equilibrium swelling state. The ratios of the blending mixture prepared are described in **Table IV-6**. While gellifying, these hydrogels were punched with a branched (200 µm of diameter linear branches) metallic self-made device (stainless steel), in order to create interior linear porous channels.

After stabilizing in PBS, GG-based hydrogels were frozen for 24 hours at $-80\text{ }^{\circ}\text{C}$ or $-196\text{ }^{\circ}\text{C}$. Frozen GG-based hydrogels were freeze-dried to completely remove all the water. The time of the freeze-drying process was sufficient enough to sublime all the water and was completed for one cycle, at $-80\text{ }^{\circ}\text{C}$, 0 atm and for 4 days (LyoAlfa 10/15, Telstar, Spain). The dried polymeric networks obtained from freeze-drying were then sterilized by OE, packed and stored off-the-shelf prior use, at controlled humidity and temperature conditions. The GG-based dried polymeric networks were re-hydrated at any time with a proper solution. The macroscopic look of the samples during the whole processing can be seen in **Figure IV-9**.

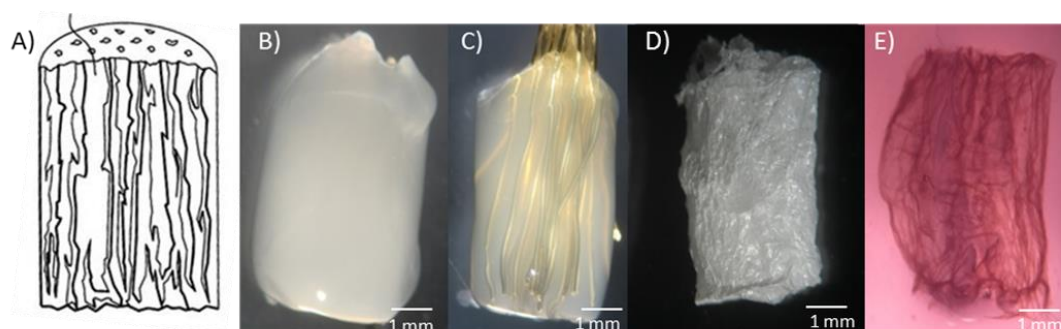


Figure IV-9 - Different aspects of the formulations throughout the production process: A) Scheme of a scaffold with the intended microstructure of vertically aligned channels; B) Hydrogel obtained after the ionic PBS cross-linking; C) Hydrogel punched with branched wires to display longitudinal porous channels; D) Freeze-dried hydrogel; E) Re-hydrated freeze-dried hydrogel resembling the initial scheme. Scale bar: 1 mm.

Table IV-6 - Gellan Gum formulations and designations. This table presents the nomenclature utilized to designate the different formulations studied during this experimental work, on both in vitro and in vivo characterizations.

| Composition | <i>Freeze-dried hydrogel formulation</i> | <i>Freeze-dried hydrogel filling for chitosan NGC</i> |
|-----------------------------------|--|---|
| 60:40 % (v/v) HA-GG : MA-GG | H60:40 | NGC60:40 |
| 50:50 % (v/v) HA-GG : MA-GG | H50:50 | NGC50:50 |
| 25:75 % (v/v) HA-GG : MA-GG | H25:75 | NGC25:75 |
| 0:100 % MA-GG (v/v) HA-GG : MA-GG | H0:100 | x |

IV-4.3.1. Production of Freeze-dried Gellan gum hydrogel filling for chitosan conduits

The blending mixtures mentioned in **Table IV-6** in the *Freeze-dried hydrogel filling for chitosan NGC* column, were prepared using the same methodology described in section IV-5.3. However,

before the stabilization step with PBS, the different formulations were injected inside the chitosan NGCs with the help of a syringe (21G). During this step, it was important to keep 2 mm hydrogel-free segments at each extreme of the tube, for nerve insertion and suture purposes, as can be seen in **Figure IV-10**. The injection of GG blending formulations inside the chitosan conduit was done slowly, in order to avoid to formation of air bubbles. The filled tubes were then immersed in PBS overnight for gelation and stabilization by ionic crosslink, frozen at $-80\text{ }^{\circ}\text{C}$ and freeze-dried.

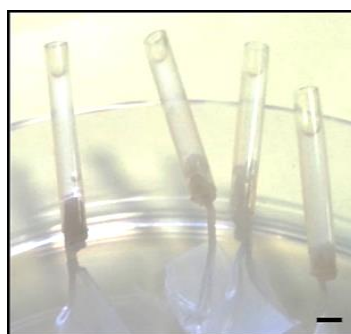


Figure IV-10 - Production of freeze-dried hydrogel filling for chitosan NGC. 2 mm hydrogel-free segments were left at each extreme of the conduit, for nerve insertion and suture purposes. Scale bar: 2 mm.

IV-4.4. Production of enzymatically crosslinked SF NGCs

SF was purified from the *Bombyx mori* cocoons in order to extract the glue-like protein sericin and wax (82). For that, 5 g of cocoons were previously cut and cleaned into several pieces and boiled for 1 hour in 2 L of sodium carbonate solution (0.02 M). Then, the purified SF was washed for 1 hour in 1 L of boiling distilled water, followed by washing in distilled water several times. Afterwards, SF was dried in a flow chamber. In order to obtain aqueous SF solution, 5 g of purified SF were dissolved in 25 mL of lithium bromide solution (9.3 M) at $70\text{ }^{\circ}\text{C}$ for 1 hour (195). The solution was dialyzed in distilled water for 2 days, using a benzoylated dialysis tubing (MWCO: 2 kDa), changing the distilled water at least 3 times per day. It was followed by concentration in a 20 %wt. poly(ethylene glycol) powder (20,000 g/mol) for at least 6 hours (196). The dialysis tubing was carefully washed in distilled water and the solution collected to a 50 mL centrifuge tube (Thermo Fisher Scientific, Waltham, MA, USA) (**Figure IV-11**).

The final concentration of the SF solution was determined by weight measurement. For that, around 500 μL of SF solution were weighted (wet weight) and dried overnight at $70\text{ }^{\circ}\text{C}$ in an oven. Then,

the dry weight of the sample was determined, and the concentration obtained by dividing the dry weight by the wet weight. The SF solution was stored at 4°C until further use.

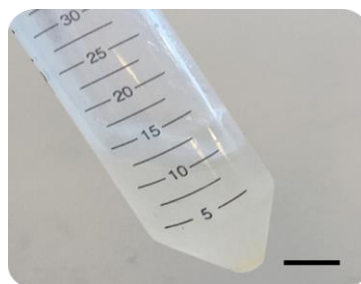


Figure IV-11 - Concentrated aqueous SF solution in a 50 mL Falcon. Scale bar: 1.5 cm.

HRP solution (0.84 mg/mL) and H₂O₂ solution (0.36 %wt.) were both prepared in PBS solution. For the preparation of the SF hydrogel, the SF solutions (pH ~7.0) were diluted into 16 %wt. by PBS. Micropipettes M100 and M1000 (Gilson, Middleton, WI, USA, **Figure IV-12**) and corresponding tips were used for preparing the reaction mixtures. In **Chapters VI, VII** and **VIII**, 1 mL of SF solution was mixed with 100 µL of HRP and 65 µL of H₂O₂ solutions in a 1.5 mL centrifuge tube (Eppendorf, Hamburg, Germany), for the hydrogel formation.



Figure IV-12 - Micropipettes Gilson M100 and M1000, specifically designed for hydrogel use. Scale bar: 1 cm.

The previous blend was then quickly introduced, with a 21G syringe, within the space between two concentric cylinder molds, with different diameters, leading to the formation of thick-wall-conduits and thin-wall-conduits. The system was posteriorly incubated at 37 °C for 30 minutes to achieve the gelation of the solution. After hydrogel crosslinking, a temporary β-sheet is induced with a momentary immersion in liquid nitrogen, which gives rise to a permanent semi-crystalline structure and facilitates the removal from the outer mold. Afterwards, the conduits were immersed in ethanol 70 %(v/v) to

induce permanent β -sheet conformation and remove the inner mold. Although most of the research published so far mentions the use of methanol to induce such conformational change in the SF structure, this is a toxic and harmful substance for the nervous system and thus should be avoided.

In **Chapter IX**, as the final stage of the processing, the obtained hollow NGCs were subjected to three different drying methodologies [37], namely: (TC 1) freeze-drying after freezing at $-80\text{ }^{\circ}\text{C}$, (TC 2) drying in an oven at $50\text{ }^{\circ}\text{C}$ for 3 days, and (TC 3) kept in a permanent hydrated state without ever extracting the solvent. A scheme representing the above-mentioned steps is shown in **Figure IV-13**.

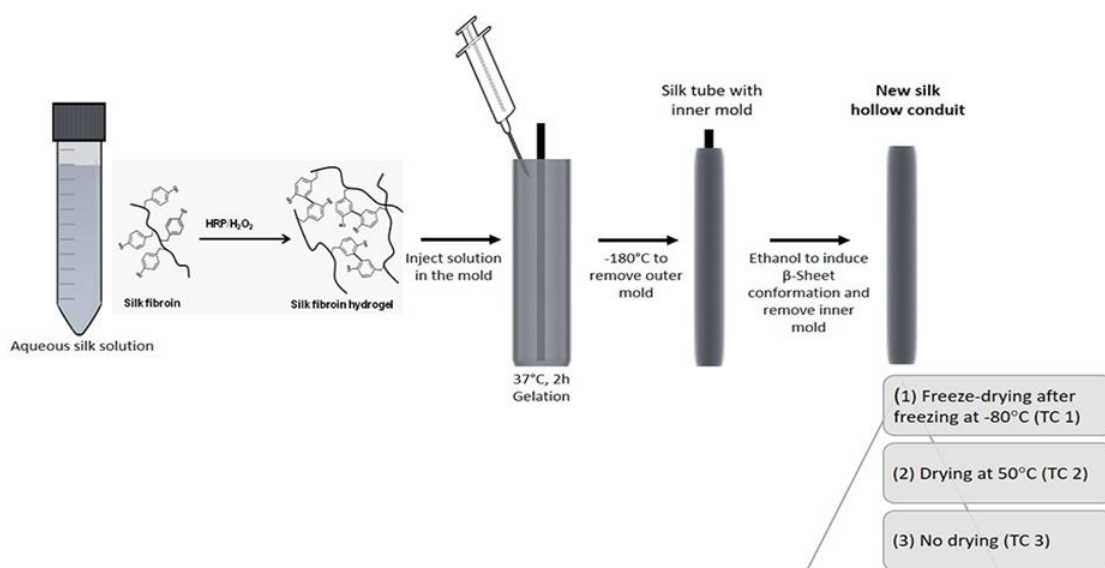


Figure IV-13 - Scheme representing the fabrication methodology of enzymatically crosslinked SF NGCs in Chapters VIII and IX.

IV-4.4.1. Production of enzymatically crosslinked SF NGCs incorporating NTFs

The incorporation of NTFs in the enzymatically crosslinked SF NGCs was performed in **Chapter X**. All the steps involved in the processing of SF, from the purification to the final freeze-drying step, described in **section IV-5.4** are valid for this chapter. Due to the versatility of this production method, it was envisioned the incorporation of different NTFs, in two different manners. Therefore, along the processing, the incorporation of NTFs was achieved via two different methods, which are designated by (i) crosslinking method and (ii) absorption method.

The NTFs were purchased from Peprotech and immediately aliquoted at a concentration of 100 µg/mL. The aliquots were kept frozen at -80 °C until used (Human recombinant GDNF (cat#450-10-10 µg) and Human recombinant NGF (cat#450-01-100 µg)).

For the first method, crosslinking, a NTF solution of 4 µg/mL of NGF or GDNF in PBS was added to 1 mL of 16 % (v/v) aqueous SF solution. As described in the preparation of the conduits, the solution was then mixed with HRP and H₂O₂ allowing the NTFs to be entrapped in the conduits' walls after crosslinking. The processing was then carried out until the end as previously described, finalizing with the freeze-drying step. For the second method, absorption, the conduits' preparation was carried normally and the final lyophilized conduits (made of 1 mL of SF solution) were immersed in 1 mL of a 4 µg/mL or 2 µg/mL of NGF or GDNF solution in PBS, for 3 hours at 37 °C. A second step of lyophilization is necessary for the absorption method. **Figure IV-13** depicts the processing involved in this **Chapter X**.

The NTFs incorporated in the SF conduits by crosslinking and absorption were GDNF and NGF. A table identifying the six produced samples can be seen below (**Table IV-7**).

Table IV-7 - Samples obtained after combining the different incorporation methods, different NTFs and different concentrations for in vitro assays.

| | Crosslinking 4 µg /mL | Absorption 2 µg/mL | Absorption 4 µg/mL |
|-------------|--------------------------|-----------------------|-----------------------|
| GDNF | GDNF/C | GDNF/A ₂ | GDNF/A ₄ |
| NGF | NGF/C | NGF/A ₂ | NGF/A ₄ |

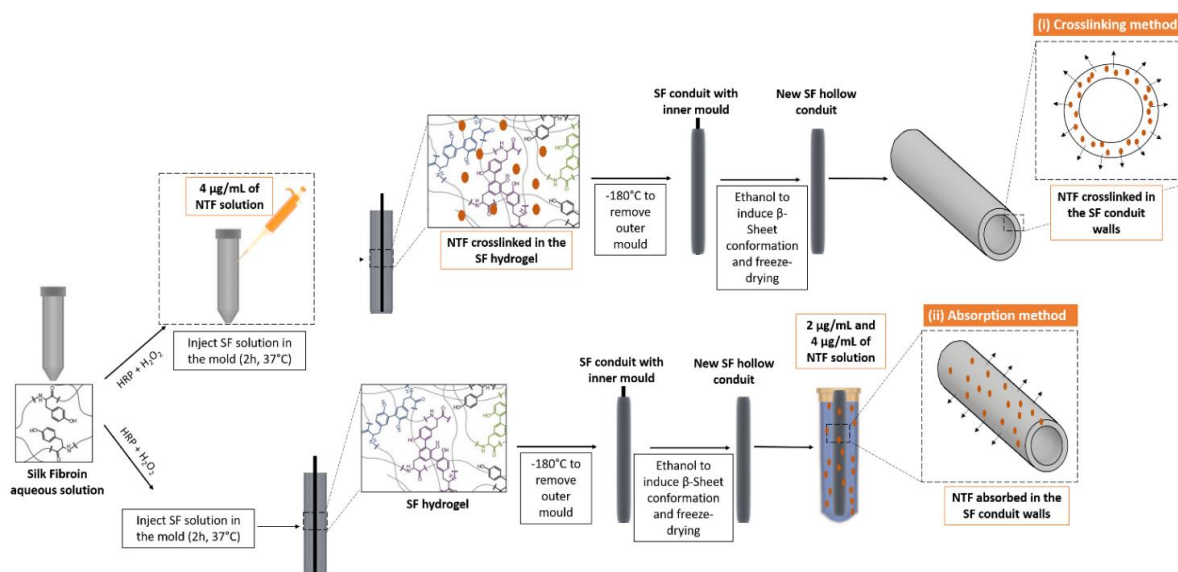


Figure IV-14 - Scheme representing the two different techniques to incorporate NTFs, which are highlighted in (i) and (ii), as the Crosslinking method and the Absorption method, respectively. This methodology was used in Chapter X.

IV-5. PHYSICOCHEMICAL CHARACTERIZATION

IV-5.1. Surface morphology and microstructure evaluation

IV-5.1.1. Structure evaluation by stereomicroscopy

The materials developed under the scope of this thesis were examined under the Stereo Microscope + Lamp (Schott KL 200, model Stemi 1000, Zeiss, Germany) for a macroscopic inspection, which can be seen in **Figure IV-15**. This technique allows for the visualization of the samples with a higher degree of precision and variable light settings. Not reaching the magnification of a microscope, this technique is ideal for the close observation of features in the samples.



Figure IV-15 - Stereomicroscope from Zeiss, used for macroscopic evaluation of samples in this thesis. Scale bar: 5 cm.

IV-5.1.2. Scanning Electron Microscopy (SEM) and Energy Dispersive Spectroscopy (EDS) analysis

Scanning Electron Microscopy (SEM), is an imaging technique that produces images of a sample by scanning the surface with focused beam of electrons. When in contact with the atoms at the sample's surface, the electrons produce several signals containing the collected information (197). Thus, the qualitative information regarding the surface morphology of samples and elemental information can be obtained. In **Chapters V, VI, VII, VIII** and **IX**, the morphology and the microarchitecture of the produced materials, either membranes, freeze-dried GG scaffolds or SF NGCs was observed using the scanning electron microscope (Leica Cambridge S-360, Cambridge, England). Prior to the analysis, samples were sputter-coated with gold (Fisons Instruments, Sputter Coater SC502, England) and the micrographs were taken at an accelerating voltage of 15 kV at different magnifications. The samples were fixed with mutual conductive adhesive tape on aluminum stubs.

Although EDS is a technique for chemical characterization, it will be described in this section, as the equipment itself is coupled with SEM, and EDS does not exist separately from SEM. In what regards the EDS analyzer, it qualitatively calculates the relative percentage of the atomic elements present in a sample, creating an elemental map with the elements' distribution. This technique was used to characterize samples which were subjected to *in vitro* mineralization SBF assay for 30 days. The elemental characterization was performed with an Energy Dispersive Spectrometer (EDS; Pegasus X4M) coupled to the SEM, in three independent areas selected in the membranes and NGCs. This technique was used in **Chapter V, VIII** and **IX**, in order to detect the mineralization phenomena, by the deposition of an apatite layer of calcium and phosphorous ions in the surface of the materials. It is

fundamental to assess that biomaterials to be used in neuronal applications do not calcify under similar conditions to the human body.



Figure IV-16 - SEM with EDS analyzer. The SEM (JSM-6010 LV, JEOL, Japan) instrument is equipped with the low vacuum mode as a standard feature. The low vacuum mode allows non-conductive specimens to be observed and analyzed without conductive coating. This SEM is equipped with an energy dispersive spectroscope (EDS). Scale bar: 10 cm.

IV-5.1.3. Micro-Computed Tomography (Micro-CT)

Micro-CT analysis is a powerful tool used to analyze the microstructure of scaffolds in a 3D perspective. Micro-CT uses X-ray to scan and obtain the 3D reconstruction of samples and reach cross-section information of the object. The obtained data set, when processed by the software, allows to quantify the microstructure data of scaffolds, including pore size, porosity, interconnectivity, pore-wall size, and phase distribution (198, 199). X-ray CT has been used for many years to image biological topographies with different purposes. More recently, X-ray sources with the capability to focus the X-ray beam to 10 μm spot sizes have given rise to X-ray micro-CT, which has dramatically improved spatial resolution relative to traditional X-ray CT

In **Chapter VII**, the architecture of the GG freeze-dried scaffolds for *in vitro* testing, as well as the freeze-dried hydrogel filling in chitosan NGCs for *in vivo* assays were quantitatively and qualitatively evaluated using a high-resolution X-ray microtomography system Skyscan 1072 scanner (Skyscan, Kontich, Belgium), as can be seen in **Figure IV-17**. In more detail, the structure of the samples was acquired by X-ray scanning and 3D-reconstructed. Morphometric parameters, such as porosity, mean

pore size and trabecular thickness, were determined. Data acquisition was carried out using a SkyScan 1072 scanner with a pixel size of 2 μm and an integration time of 1182 ms. The X-ray source was set at 39.4 kV and 244 μA . A total of 500 projections were acquired over a rotation range of 180° , with a rotation step of 0.23° . Datasets were reconstructed using standardized cone-beam reconstruction software (NRecon v. 1.6.6.0, SkyScan). The output format for each sample was bitmap images. The set of images was orientated with DataViewer software (v. 1.4.4, SkyScan) to obtain all the samples in the same axis. A representative dataset of the slices was segmented into binary images with a dynamic threshold of 40–120, which were used for morphometric analysis (CT Analyser, v. 1.12.0.0, SkyScan) and to obtain the 3D models (CT Vox, v. 2.3.0 r810, SkyScan). A minimum number of three specimens were used for each scaffold.

In **Chapter VIII** and **IX**, the SF NGCs were scanned using the same equipment, with a pixel size of 11.31 μm x/y/z and an X-ray source fixed at 41 keV of energy and 215 μA of current. For the NGCs, the pixel size used was 14.71 μm x/y/z and the X-ray source was set at 40 keV and 154 μA . Representative serial images in each data set were transferred into binary images with a dynamic threshold of 60-225 for the NGCs (grey values). Then, the binary images were used for morphometric analysis (CT Analyzer) to build the 3D virtual models of the spacer structures (Data Viewer and CT-Vox). A minimum number of three specimens were used for each scaffold.



Figure IV-17 - Micro computed tomography for non-destructive 3D analysis of bulk structure of scaffolds. Output is the general structure as a 3D model with micrometer resolution, more importantly the subsequent analysis can yield information in relation to pore size, pore distribution and pore interconnectivity in 3D. Scale bar: 10 cm.

IV-5.1.4. Atomic Force Microscopy (AFM)

Atomic Force Microscopy (AFM) technique allows the observation and measurement of the surface

structure of samples with an unprecedented resolution and accuracy. Through this analysis, it is possible to obtain images showing the arrangement of individual atoms in a surface sample, or to see the structure of individual molecules (200). Comparing to the optical or electron microscopes, AFM does not form an image by focusing light or electrons onto a surface. It “feels” the samples surface with a sharp probe or cantilever and builds a map covering the height or topography of the samples surface. The type of images generated by this microscope can reach a magnification greater than 1000 x. On the other hand, from an imaging microscope, only a 2D projection of a samples surface can be reached without any height information included. Furthermore, besides being an imaging tool AFM has several spectroscopic modes that measure other samples properties as nanoscale (201).

In **Chapter V**, the membranes surface roughness was analyzed using a Dimension 3000 Atomic Force Microscope (Digital Instruments, Santa Barbara, CA) as seen in **Figure IV-18**, on a 5 μm \times 5 μm scan area. Contact mode was used with a Multimode (Veeco, USA) connected to a NanoScope III (Veeco, USA) having a contacting silicon nitride nanoprobe (model DNP, Bruker). For this analysis, the membranes were tested under ambient conditions (dry) and after being immersed in Phosphate Buffer Saline (PBS) during 2 h to mimic physiological conditions (wet). The average surface roughness (R_a , nm) corresponding to the membranes in both dry and wet state was measured. All images were fitted to a plan using the 3rd degrees flatten procedure included in the NanoScope software version 4.43r8. The values are presented as mean \pm standard deviation.

In **Chapter VI**, for surface roughness analysis, membranes were analyzed on five spots using TappingMode™ with a MultiMode connected to a NanoScope III (Veeco, USA) with non-contacting silicon nanoprobe (TESP model) purchased from Bruker, Germany. The images (10 μm x 10 μm wide) were fitted to a plane using the first-degree flatten procedure included in the NanoScope software version 4.43r8. The surface roughness was calculated as R_q (root mean square from average flat surface) and R_a (average absolute distance from average flat surface).



Figure IV-18 - The AFM is able to acquire images of flat surfaces that can encode the surface topography, mechanical response, among other properties. The equipment presents a series of accessories that allows the acquisition of data in liquids and air. In the case of liquids, it is also possible to control the temperature of the experiments. Scale bar: 10 cm.

IV-5.1.5. Contact angle and surface energy

Surfaces are crucial for every biological system as they are the first parts to come into contact with cells, as well as being a direct connection between the material and the environment (202). Contact angle is measured as the angle where a liquid interacts with the solid surface. A high contact angle indicates that the surface has low wetting. A low contact angle indicates that the surface is high wetting, meaning that the water droplet spreads out more on the surface. The contact angle depends on several interconnected parameters, such as, surface chemistry, roughness and crystallinity. In terms of surface energy, the calculated surface energy components of the materials surface are used to give a quantitative determination of the magnitude of their hydrophobicity (203). Furthermore, surface energy is a parameter fundamentally related with the ability of a surface to sustain cell adhesion, migration and proliferation (204). It is a valuable and quantifiable tool to distinguish surface properties. A scheme of how water contact angle works can be seen in **Figure IV-19**.

Contact angle (θ) and surface energy (γ) measurements were obtained in **Chapter V** and **VI**, to evaluate the wettability and surface energy of the membranes.

Static contact angle measurements were obtained by the sessile drop method using a standard contact angle apparatus (Model OCA 151) incorporating a high-performance image processing system (DataPhysics Instruments, Germany), as can be seen in **Figure IV-20**. All the measurements were made

at RT and the probe liquids were ultrapure water (as the polar component) and diiodomethane (CH_2I_2 ; 1 mL, HPLC grade, as the non-polar component), added by a motor-driven syringe. Three samples of each condition were used and five measurements were recorded per sample. The average values were recorded after 5 seconds of the drop deposition (settling time). The obtained results from both liquids were used to calculate the surface free energy (γ) according to a method proposed by Owens, Went, Rabel and Kaelble (OWRK) (205, 206), which is particularly indicated for the determination of low energy surfaces (polymers). According to this method the surface tension can be determined into a polar (γ^p) and disperse (γ^d) component, whose contribution to the surface energy calculation, is dependent on the intermolecular attraction that results from a variety of intermolecular forces according to an additive rule.

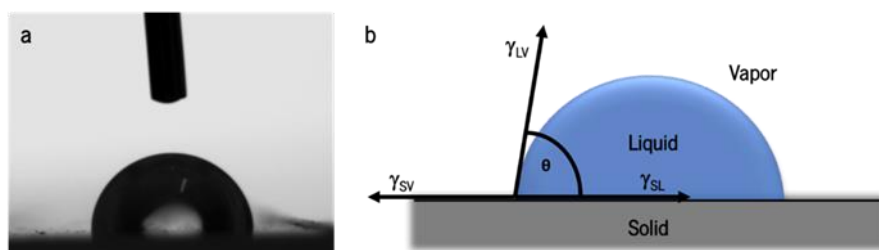


Figure IV-19 - Interfacial tension at the 3-phase contact line. (a) Contact angle on a solid surface and (b) Vectorial equilibrium for a drop resting on a solid surface to balance three forces (contact angle forces): the interfacial tensions between, solid and liquid (γ_{sl}), solid and vapour (γ_{sv}), and liquid and vapour (γ_{lv}), resulting in Young's equation $\gamma_{sv} = \gamma_{sl} + \gamma_{lv} \cos \theta$ used measure what is referred to as surface energy.

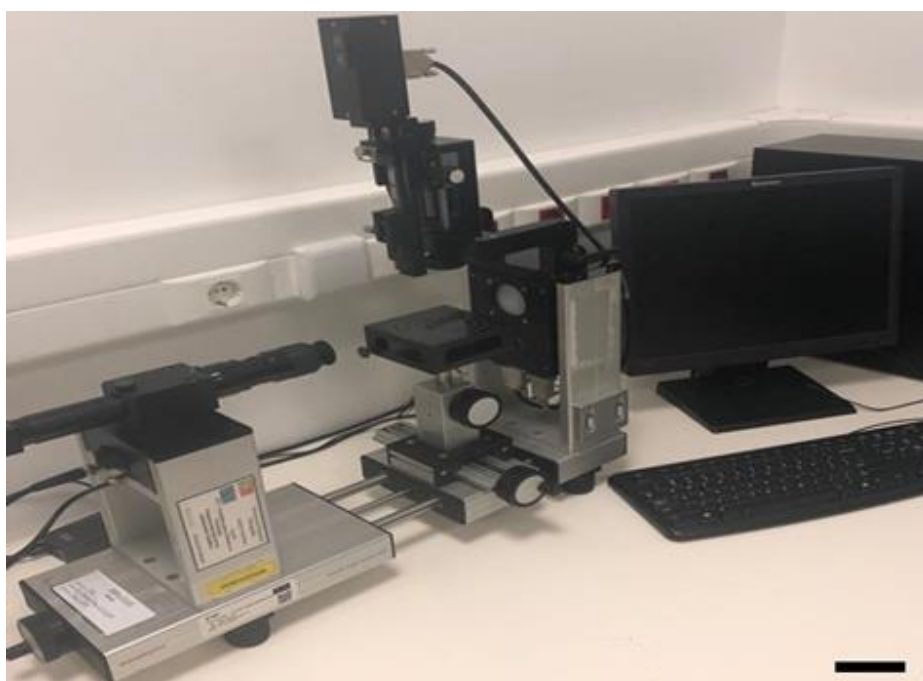


Figure IV-20 - The contact angle Goniometer allows the measurement of static and dynamic contact angles on a thermostated sample stage. Surface energy of solids and liquids surface tension can be calculated. Scale bar: 10 cm.

IV-5.2. Chemical analysis

IV-5.2.1. X-Ray Diffraction (XRD)

X-Ray Diffraction (XRD) is a quick analytical technique that primarily used to sense the crystalline or amorphous structure of materials. The principle of this technique is based on the diffraction of the X-ray radiation into a specific direction, depending on the crystalline atoms or molecules of materials. By measuring the intensity and angles of these signals, it is possible to know the crystallinity and arrangement of the atoms in the crystals (207). **Figure IV-21** depicts the XRD apparatus used.

In **Chapters V**, the diffraction pattern was measured using grazing incidence X-ray diffraction (GIXRD) with a diffractometer (Bruker AXS D8 Advance Discover, Karlsruhe, Germany) operated with accelerating voltage of 40 kV and a current of 40 mA. The GIXRD scans were performed using Cu K α radiation (wavelength = 0.154 nm), keeping a fixed incidence angle of 1° between the incident X-rays and specimen plane, while the detector was revolved between 5° and 40° with respect to the specimen, at a speed of 0.04°/1 second.

In **Chapter VI**, X-ray diffraction patterns of keratin powder, CHT and CHT/keratin membranes were used to determine their crystalline structure. Measurements were performed in a Bruker D8 Advance Davinci diffractometer equipped with Cu K α radiation ($\lambda = 1.547 \text{ \AA}$), produced at 40 kV and 40 mA. The data was collected at room temperature, increment of 0.02°, 2θ range of 5-40° and increment 's acquisition time of 1 second.

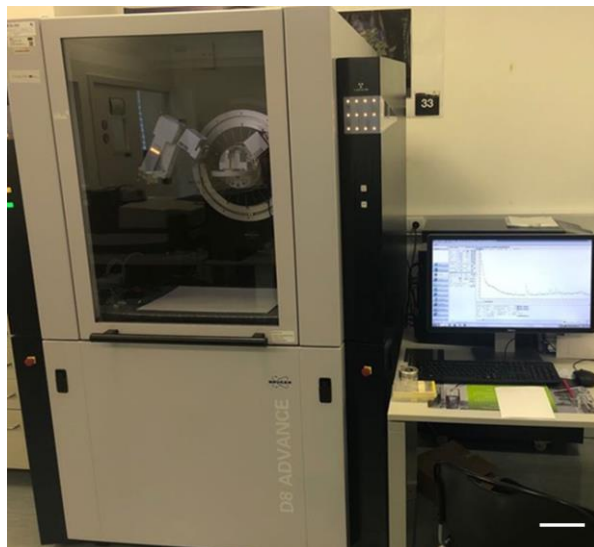


Figure IV-21 - D8 ADVANCE Twin with DAVINCI Design - The intelligent beam path components of the D8 ADVANCE with DAVINCI design provide true plug-in play functionality requiring minimum or even no user intervention. Featuring automatic and tool-free switching of the diffraction geometry without the need for complex adjustments, the D8 ADVANCE Twin with DAVINCI design broadens the analytical capabilities for a wide community of X-ray diffraction users Scale bar: 10 cm.

IV-5.2.2. Fourier Transform Infrared Spectroscopy (FTIR)

Fourier transform infrared (FTIR) spectroscopy is a form of vibrational spectroscopy that is useful in the study of a variety of soil chemical processes. In the mid-infrared range, vibrations arise from many environmentally important molecules such as organic acids, soil organic matter, mineral phases, and oxyanions. Therefore, it is a cost-effective technique that acts as a fingerprint used to identify the chemical groups in materials. Similar chemical groups absorb in the IR at similar frequencies, which enables to screen the ratio of the components in the tested material. Fourier transformation algorithm allied to IR spectroscopy gives a spectrum of IR absorption per frequency/wavelength (208). It is possible to utilize FTIR spectroscopy as a quantitative analytical method and also as a tool to determine bonding mechanisms in solids and on surfaces.

In **Chapter V** and **VI**, the FTIR spectrum of the chitosan membranes was obtained using Shimadzu IRPrestige 21 spectrometer (Shimadzu, Europe). Samples were prepared as potassium bromide pellets at RT. The spectrum was collected by averaging 32 scans with a resolution of 4 cm^{-1} , corresponding to the $4000\text{--}400\text{ cm}^{-1}$ spectra region.

In **Chapter IX**, the NGC conformation and composition information were evaluated by an Attenuated Total Reflectance (ATR) model (IRPrestige-21, Shimadzu, Japan) in a FTIR equipment (Perkin-Elmer 1600 series equipment, CA, USA) equipped with a Germanium crystal, as can be seen in **Figure IV-22**. All spectra were obtained between 4600 and 800 cm^{-1} , at a 4 cm^{-1} resolution for an average of 50 scans.



Figure IV-22 - The Fourier transform infrared (FTIR) spectrometer is used as a standard chemical characterization technique. The samples can be analyzed as films, KBr discs, powder or liquids. The available methodologies comprise transmittance, specular reflectance, diffuse reflectance and attenuated total reflectance (ATR). Scale bar: 10 cm.

IV-5.2.3. Scanning calorimetry analysis (DSC)

Differential scanning calorimeter (DSC) is an important instrument in thermal analysis being useful to understand amorphous and crystalline behavior, eutectic transitions, curing and degree of cure, and many other material's properties used to design, manufacture, and test products. This technique allows to study the material's heat capacity (C_p) as function of the temperature. A sample of known mass is heated or cooled and the changes in its C_p are tracked as changes in the heat flow, which allows the detection of transitions such as melting, glass transitions, among other parameters (209). The DSC experiments were performed using DSC Q100 V9.8 Build 296 apparatus, which can be seen in **Figure IV-23**.

In **Chapter III**, the weighted samples (3.5 – 4 mg sample weight) were covered with a suitable aluminum cover. Both temperature and heat flux were previously calibrated with Indium. All samples were subjected to a first heating cycle, ranging from 0 °C to 200 °C at a rate of 10 °C/minute, an isothermal step of 2 minutes followed by cooling to 0 °C and a second heating cycle, ranging from 0 °C to 350 °C at a rate of 1 °C/minute. The measurements were performed under dry nitrogen

atmosphere, at a flow rate of 50 mL/minute. Only the behavior showed by the membranes during the second heating cycle is presented were placed in aluminum pans and heated at a rate of 10 °C/minute from 20 to 220 °C, cooled to 20 °C and heated at 5 °C/minute until 200 °C. Standard calibrations were performed using indium leads.

In **Chapter IV**, samples with a weight between 3 - 6 mg, were covered with a suitable aluminum cover. Both temperature and heat flux were previously calibrated with Indium. Both samples were subjected to ramp heating ranging from 0 °C to 350 °C at a rate of 5 °C/minute. The measurements were performed under dry nitrogen atmosphere, at a flow rate of 50 mL/minute.

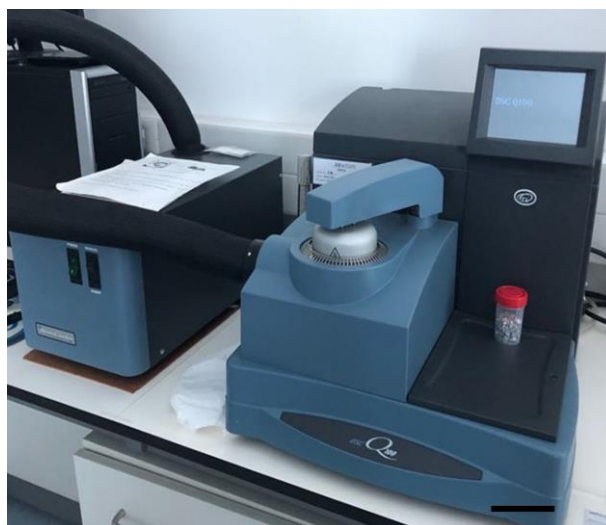


Figure IV-23 - Differential scanning calorimetry is a thermal analysis technique that detects the temperatures and heat flows caused by changes in heat capacity or by endothermic and exothermic processes of materials as a function of time and temperature. Scale bar: 10 cm.

IV-5.3. Mechanical properties

IV-5.3.1. Tensile test

Tensile properties show how the material reacts to forces being applied in tension. Tensile tests are able to show the ability of a material to withstand tensile loads without failure. They can also measure the ability of a material to deform under tensile stresses. Tensile testing is a fundamental materials science and engineering test. Different properties can be directly measured, including ultimate tensile strength, breaking strength and maximum elongation of biomaterials. From these measurements, the Young's modulus can also be determined (210). The importance of determine the elastic and failure properties of scaffold materials to be applied in biological hard-tissues like cartilage,

bone, tendon or ligament or soft-tissues like nerves, is of great clinical importance. These structures should hold sufficient mechanical properties to support tissue regeneration without breaking and understanding their mechanical behavior properties prior *in vivo* implantation will bring a great advantage to anticipate its behavior.

Considering nerve repair, nerve is under tensile load *in situ*, as evidenced by the fact that it retracts when severed. The biological mechanical parameters of tissues comprehend a wide spectrum of values.

In the specific case of artificial nerve grafts, they will have to endure the *in-situ* stress to which peripheral nerves are submitted, while suture holding ability will also be needed. In addition, it is well-known that cells have a specific behavior in response to mechanical stress. The structural organization of peripheral nerves enables them to function while tolerating and adapting to stresses placed upon them by postures and movements of the trunk, head and limbs.

In **Chapter VIII** and **IX**, the tensile properties of the enzymatically crosslinked SF NGCs were determined by performing tensile tests in an Instron 4505 Universal Machine (Instron Corporation, MA, USA) according to the ASTM C749–08 standard method. Instron electromechanical universal testing machines (depicted in **Figure IV-24**) are able to perform tensile, compression, bend, peel, tear, and other mechanical tests on materials. These systems are available in a wide range of sizes, and with several force capacities depending on the testing material and final application. The tensile modulus, ultimate tensile strength and strain at maximum load were measured using a load cell of 1kn was used. All the samples were fixed in each extremity by using a grip. A cross-head speed of 5 mm.min⁻¹ was employed and the samples were stressed until enough force was applied to trigger their rupture. The tensile modulus was determined in the most linear region of the stress/strain curve using the secant method. The test was performed using hydrated samples, in order to mimic physiologic conditions, which were prepared by immersion of the NGCs in PBS solution for 3 days. Five samples of 14 mm in length were analyzed per condition, as can be seen in **Figure IV-25**.

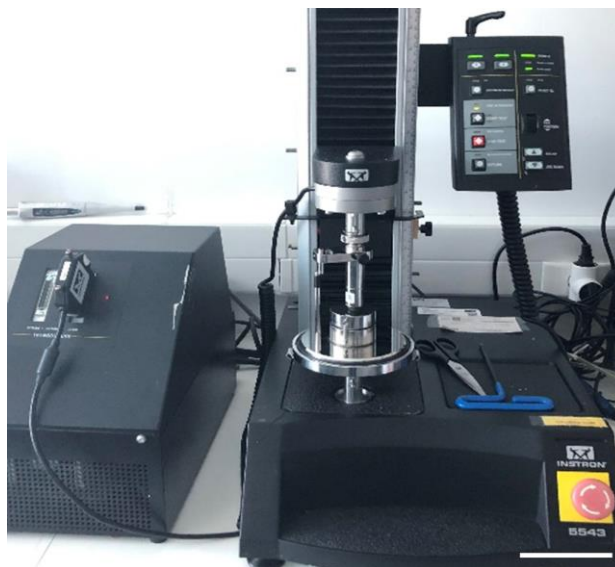


Figure IV-24 - Universal mechanical testing machine (INSTRON 5540) capable to perform tensile, compression and flexural tests. A high range of specimens, including compact biomaterials, acellular and cell-seeded scaffolds, native tissue samples (*e.g.* bone or cartilage) and tissue engineered constructs can be tested. Tests can be performed under temperature control (using an environmental chamber) or with the samples immersed into a solution. Scale bar: 10 cm.



Figure IV-25 - Enzymatically crosslinked SF conduits being tested in tensile mode with Instron equipment. Scale bar: 10 mm.

IV-5.3.2. Dynamic Mechanical Analysis (DMA)

When a scaffold is implanted *in vivo*, it is expected that it will be under constant physical load with different frequencies. Thus, it is important to understand the performance of the scaffolds under dynamic loading, prior to implantation. Dynamic mechanical analysis (DMA), depicted in **Figure IV-26**, is a helpful tool to reveal this information.

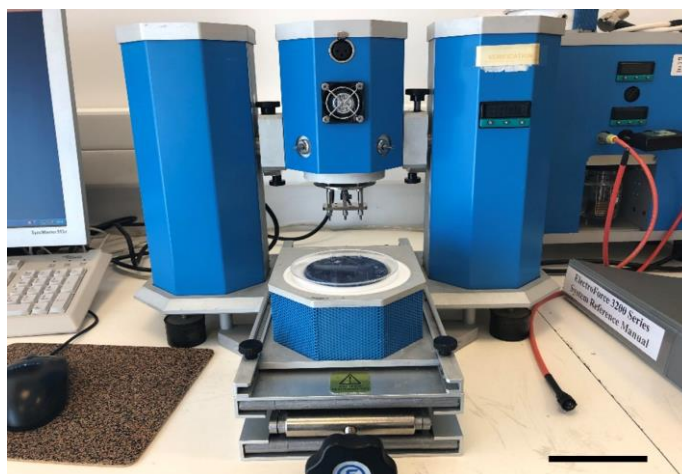


Figure IV-26 - DMA with environmental control. The testing can be done to analyse the influence of frequency of applied force and solution conditions (Temperature, pH, ionic strength etc.), and how the mechanical properties change over time (*e.g.* caused by degradation or mineralization within the bulk of the sample). Scale bar: 10 cm.

Through this technique, the materials' properties are characterized as a function of temperature, time, stress, atmosphere, frequency, or by the combination of these parameters. DMA apparatus works by applying a sinusoidal deformation to a sample of pre-established geometry and size, which can undergo a controlled stress and strain. The deformation of the sample is directly related to its stiffness, measuring the stiffness and damping properties of samples, reported as modulus (E') and tan delta ($\tan \delta$). This modulus can be expressed as storage modulus, which measures the elastic behavior of samples, and loss modulus. The ratio between the loss and storage modulus will give the tan delta that is often called damping factor, measuring the energy dissipation of materials.

In **Chapters V** and **VI**, the viscoelastic measurements were performed using a DMA TRI-TEC8000B model from Triton Technology manufacturer (Lincolnshire, UK), equipped with the tensile mode. All samples were immersed in PBS at least 24 hours before measurement. DMA spectra were obtained during a frequency scan ranging between 0.1 and 15 Hz for all time points. The experiments were performed under constant strain amplitude, corresponding to approximately 2 % of the original height of the sample. Samples were tested under physiological conditions, at 37 °C in the hydrated state, by immersing the samples in PBS solution in a Teflon® reservoir and clamped in the DMA apparatus. Before the analysis, a small pre-load was applied to each sample to ensure that the entire surface of the scaffold was in contact with the compression plates, being the distance between plates equal for all tested samples. In both chapters, chitosan membranes were cut in 10 x 5 mm.

IV-5.3.3. Kinking-resistance and suturability

Kinking and suturability tests were performed in **Chapter VIII** and **IX**. Since NGCs are often placed near flexible body parts such as knees, hips or fingers, it is clinically relevant that they resist to lumen occlusion when subjected to bending forces (211). Kinking tests were done with 3 cm length conduits by bending them up to 50° in a metallic flexible 0.5 mm wire and assessing macroscopically the bending point, as can be seen in **Figure IV-27A**.

Regarding the suturability properties, an engineered conduit must hold structural integrity and stability when a surgeon manipulates and grafts it. More specifically, the resistance of the tubular conduits to sutures is of capital importance when grafting purposes are considered. Suturability tests showed that the developed tubular conduits can withstand a suture thread being pulled in and out of them, thus indicating its appropriateness in terms of suturability (212). The suturability was assessed by means of inserting a 4-0 suture at the place where peripheral nerve suturing would be performed, which is 2 mm from the end of the conduit, considering its long axis and strain to the rupture point, as can be seen in **Figure IV-27B**.

These two assays were performed to assess the suitability of the developed enzymatically crosslinked SF NGCs for implantation near joints and for practical surgical procedures in PNR.

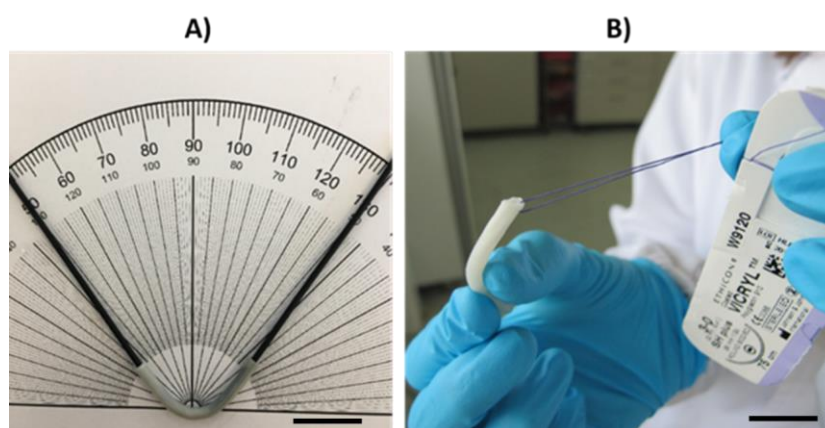


Figure IV-27 - In-house developed kinking and suturability tests performed in the produced enzymatically crosslinked SF NGCs. Scale bar: 10 mm.

IV-5.4. Water uptake ratio

One of the key aspects influencing the effectiveness of materials to be applied in nerve repair is the swelling ability, also known as water uptake ratio. It is critical to guarantee that swelling will not cause

compression phenomena in the implanted scaffold, pressing the nerve or occluding the lumen, which could lead to ineffective nerve functioning and regeneration (213). Still, it is important that the material swells to a certain extent *in vitro*, to be able to integrate the culture medium needed for cell survival, and *in vivo*, to mimic endogenous tissues, which are mainly composed by water ($\approx 60\%$ of the total weight). Furthermore, understanding the behavior of a biomaterial in contact with hydrated medium is of great importance to predict their interactions with the surrounding tissues, especially in terms of adjustability to the defect sites. These parameters are determined, in general, by means of water-uptake studies (214), that in some cases can also address the biodegradability of a material.

The percentage of water uptake, or swelling, was investigated in all developed biomaterials, from **Chapter V** in chitosan membranes, **Chapter VI** in chitosan/keratin membranes, **Chapter VII** for freeze-dried GG hydrogels and in **Chapter VIII and IX**, for enzymatically crosslinked SF NGCs. For that, dry samples of the diverse formulations were initially weighed (initial mass, m_i) and immersed in PBS at 37 °C. The specimens were removed from the solution at pre-determined timepoints and finally weighted (wet mass, m_w).

In more detail, in **Chapter V and VI**, the water uptake assay was performed by means of soaking 1 cm² chitosan and chitosan/keratin membranes in PBS (pH 7.4) for a period up to 30 days, in a water bath set to 37 °C and dynamic condition of 60 rpm (GFL 1086; GFL, Burgwedel, Germany). Before the final measure, the excess of water was removed with filter paper. The timepoints analyzed were 1, 15 and 30 days.

In **Chapter VII**, water uptake of the GG freeze-dried hydrogels was performed by means of soaking the freeze-dried hydrogel scaffolds in PBS (pH 7.4) for a period up to 30 days, in a water bath set to 37 °C and dynamic condition of 60 rpm (GFL 1086; GFL, Burgwedel, Germany). Before the final measure, the excess of water was removed with filter paper. The timepoints analyzed were 1, 7, 14 and 30 days.

In **Chapter VIII and IX**, for the assessment of the water uptake profile of the enzymatically crosslinked SF NGCs, the scaffolds were soaked in in PBS (pH 7.4) for a period up to 30 days, in a water bath set to 37 °C and dynamic condition of 60 rpm (GFL 1086; GFL, Burgwedel, Germany). In the specific case of TC 3, m_i was considered right after the sample was removed from ethanol. Before the final measure, the excess of water was removed with filter paper. The timepoints analyzed were 0.08 (2 hours), 0.16 (4 hours), 0.33 (8 hours), 1, 3, 7, 14, 21 and 30 days.

In all Chapters, water uptake or swelling ratio was determined by using **Equation IV-1**:

Equation IV-1 - Equation for the determination of percentage of water uptake.

$$\text{Water uptake (\%)} = \frac{m_w - m_i}{m_i} \times 100$$

In **Equation IV-1**, m_i is the initial weight of the sample before hydration, and m_w is the weight of the wet sample after removal from the solution at each tested period. Five samples were used for analysis.

IV-5.5. Weight loss profile

Weight loss, also known as degradation of a biomaterial, is an important parameter to consider when the use of a scaffold for PNR is envisioned. The ideal device should remain intact during axon regeneration, and then progressively degrade (215). The main challenge of these biodegradable devices is to have a uniform and homogenous degradation.

When implanted, a biomaterial will be inevitably in the presence of body fluids containing various ECM modulatory enzymes, that in some cases can induce the degradation process of biomaterial. In human body, the enzymes that conduct proteolysis can degrade proteins in high efficiency. Because of that, in **Chapter V, VIII and IX**, the simple hydrolysis of the materials was compared to proteolysis carried out by specific enzymes.

The biodegradability of chitosan in the human body is subjected to the degree of deacetylation and molecular weight. Chitosan can be degraded by enzymes that hydrolyze the bonds among glucosamine–glucosamine, glucosamine–*N*-acetyl-glucosamine and *N*-acetyl-glucosamine–*N*-acetyl-glucosamine units. In human body, chitosan mainly degrades due to the activity of lysozyme (216). The lysozyme concentration in human body is found to be 13 mg/L.

Therefore, in **Chapter V**, weight loss was performed by means of soaking 1 cm² chitosan membranes in PBS enriched with 13 mg/L of lysozyme for 30 days, at 37 °C and dynamic condition (60 rpm) in a water bath. In the weight loss assay, to distinguish weight loss related to enzymatic degradation or simple hydrolysis, samples were also put in PBS without lysozyme for degradation assessment. At predefined time points (1 day, 15 days, 30 days) the degraded samples were extracted, and the excess of water removed with filter paper. To minimize both enzyme loss of activity and

possible changes in the pH, enzyme solution was changed every 3 days. The samples were left to completely dry at RT for a few weeks and finally weighed.

Gellan Gum is known to be degraded by gellanase, which does not exist in the human body (217). Therefore, in order to mimicking physiologic conditions, its degradation is only associated to the hydrolysis phenomena in the presence of PBS overtime. In **Chapter VII**, weight loss studies concerning the GG freeze-dried hydrogels were performed by means of soaking in PBS, at 37 °C and dynamic condition (60 rpm) in a water bath. At predefined time points (1, 7, 14 and 30 days) the degraded samples were extracted, and the excess of water removed with filter paper. The samples were left to completely dry at RT for a few weeks and finally weighed.

Related to SF scaffolds, it is known that some human body enzymes have shown to degrade SF biomaterials at similar levels to those observed in the presence of protease XIV, which is not present in the human body and has no specific function in the chemical or amino acid structure of the protein (218). However, in order to achieve the same functional performance offered by these enzymes, protease XIV was chosen to carry out the degradation studies *in vitro* in **Chapter VIII and IX**. Protease XIV was derived from *Streptomyces griseus* (3.5 U/mg) and prepared at different concentrations by dissolving in PBS solution and each sample was immersed in 5 mL of solution into 5 mL tubes. All the enzyme solutions were refreshed every 24 hours. Samples immersed in PBS solution were used as controls.

The experiments of SF NGCs degradation were conducted at 37 °C and dynamic condition (60 rpm) in a water bath. First, the initial weight of NGCs was determined by immersion in a PBS solution and kept at 37 °C for 24 hours, to reach the maximum swelling. Then, filter paper was used to remove the excess of liquid prior to initial weighing. This was considered our initial weight (m_i). The conduits were then immersed in 5 mL of PBS containing protease XIV solution (0.2 U/mL), which was changed every 24 hours. After 0.08 (2 hours), 0.16 (4 hours), 0.33 (8 hours), 1, 3, 7, 14, 21 and 30 days, the specimens were removed, the excess of liquid eliminated, and final mass determined.

In all Chapters, the weight loss is given by **Equation IV-2**.

Equation IV-2 - Equation for the determination of percentage of weight loss.

$$\text{Weight loss (\%)} = \frac{m_i - m_f}{m_i} \times 100$$

In **Equation IV-2**, m_i is the initial weight of the sample before degradation, and m_f is the dry weight of the sample been degraded for a certain period of time and after drying until constant weight is reached. Three specimens were used for each tested concentration at each time point.

IV-5.6. *In vitro* mineralization

The bone-bonding and calcification ability of a material can be evaluated by examining the apatite formation on the surface of materials immersed in simulated body fluid (SBF) with ions concentrations nearly equal to those of human blood plasma. This is useful for predicting the *in vivo* bioactivity of such materials. In the context of nerve repair and regeneration, the aim of this assay is to discard the possibility of bioactivity occurring in the developed membranes, as this is a completely undesirable phenomenon in the context of PNR.

This assay is performed by immersing the scaffolds in SBF solution up to 1, 15 and 30 days in an oven at 37 °C and dynamic condition (60 rpm), following the method proposed by Tas *et al.* (219) and Kokubo *et al.* (220). Briefly, SBF solution containing ionic concentrations (Na^+ 142.0, K^+ 5.0, Ca^{2+} 2.5, Mg^{2+} 1.5, Cl^- 148.8, HPO_4^- 1.0, HCO_3^{2-} 4.2, SO_4^{2-} 0.5 mM/L, pH 7.4) similar to those of human blood plasma (see Table IV-, was prepared and placed in 50 mL centrifuge tubes for pre-heating at 37 °C. Then, each specimen was transferred to an individual tube and submerged in the SBF solution, as shown in **Figure IV-16**. At each timepoint, the specimens were removed from the SBF solution, washed with distilled water and absorbed in filter paper to remove the excess of surface water. Then, the samples were dried at 37 °C in the oven for 3 days and further analyzed by SEM and EDS.

In **Chapter V**, 1 cm² samples were used, in contraposition to dry membranes, that did not undergo this assay (controls). DA I, DA II and DA III membranes were studied.

In **Chapter VIII and IX**, enzymatically crosslinked SF NGCs with 14 mm in length were used. TC 1, TC 2 and TC 3 were studied.

Table IV-8 - Ionic concentrations present in the SBF, used for the bioactivity assay, as proposed by Kokubo *et al.* (220).

| Ions | Concentration (mM/L) |
|---------------|----------------------|
| Na^+ | 142.0 |
| K^+ | 5.0 |

| | |
|-------------------------------|-------|
| Ca ²⁺ | 2.5 |
| Mg ²⁺ | 1.5 |
| Cl ⁻ | 148.8 |
| HPO ₄ ⁻ | 1.0 |
| HCO ₃ ⁻ | 4.2 |
| SO ₄ ²⁻ | 0.5 |

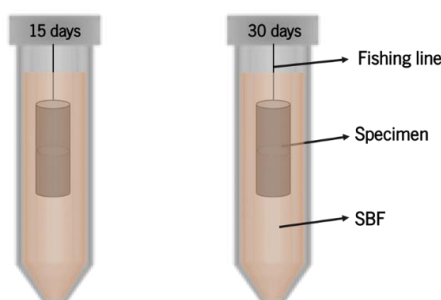


Figure IV-28 - Illustrative image of the specimens immersed into the SBF solution.

IV-5.7. Molecular permeability tests

The permeability of a NGC wall plays a key role in the regenerative process (221). More specifically, a conduit should be protein permeable, in order to allow the exchange of nutrients and oxygen, for cellular survival and regeneration. In this sense, molecular permeability assays of the conduit wall were designed and performed. The principle behind this assay is that if the wall is permeable to FITC-labeled Dextran (4 kDa), it will also allow the exchange of nutrients (glucose ~ 180 Da) and oxygen, as seen in Figure IV-29. In Chapter IX, in order to assess the molecular permeability of the developed SF NGC walls, an assay based on the fluorometric properties of fluorescein isothiocyanate–dextran (FITC-labeled Dextran, 4 kDa) molecule was designed. More specifically, conduits of 14 mm in length were immersed in a PBS solution for 24 hours to reach the maximum swelling, and then the excess of liquid was rapidly removed with filter paper. Each conduit was filled with 10 μ L of FITC-labeled Dextran solution (1 mg/mL in PBS) and both conduit ends were sealed. Each loaded conduit was kept in individual vials with 1 mL of PBS at 37 °C for up to 48 hours. Aliquots of 300 μ L were withdrawn from the vial at predetermined time periods and replenished by fresh PBS. The amount of FITC-labeled Dextran that got to the PBS release medium after crossing the conduit wall

was determined with the help of a microplate reader (FL 600, Bio-Tek Instruments, USA) at a 520 nm emission wavelength (480 nm excitation wavelength), and independent calibration curves. A total of 5 replicates per condition (TC 1, TC 2 and TC 3) were studied. Data is presented as average \pm standard deviation of the cumulative percentage of dextran release.

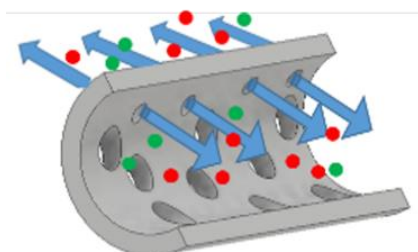


Figure IV-29 - Scheme illustrating the molecular permeability to be achieved in NGCs.

IV-6. *IN VITRO* BIOLOGICAL TESTS

In this thesis, all cell-based models were used in a cell-scaffold approaches for different TE strategies. For that, the cell sources and all the aspects related to the cell culture procedures are herein described.

IV-6.1. Cell sources

Most of the cellular work performed in this thesis was carried out using cell lines. Cells lines are immortalized cells that present the ability to proliferate indefinitely either due to a random mutation or due to a programmed modification. Cell lines are useful models for doing research, because they provide reliability in experimental results due to the possibility to obtain large amounts of cells for prolonged use (222). L929 cell line is the usual choice in many standard tests, such as material biocompatibility testing, drug cytotoxicity testing and cell biology studies.

Furthermore, since this thesis was developed in the context of PNR, immortalized Schwann cells were abundantly used.

IV-6.1.1. L929 cell line

A L929 cell line from mouse lung fibroblasts, (European Collection of Cell Cultures (ECCC), UK) was cultured in low glucose Dulbecco's modified Eagle's medium (DMEM), supplemented with 44 mM of sodium bicarbonate, 10 % (v/v) of fetal bovine serum (FBS; Biochrom, Berlin, Germany), and 1 % (v/v) of antibiotic/antimycotic solution (prepared with 10,000 units/mL penicillin G sodium, 10.000 µg/mL streptomycin sulfate, and 25 µg/mL amphotericin B as Fungizone (R) in 0.85 % wt. saline; Gibco®, Life Technologies, Carlsbad, CA, USA). The L929 cells were incubated in an atmosphere containing 5 % CO₂ at 37 °C, and the medium changed every 2-3 days. Cells were routinely trypsinized (0.25 % (v/v) trypsin–EDTA solution; Life Technologies, Carlsbad, CA, USA) for 2-3 minutes at 37 °C, centrifuged at 300 g for 5 minutes (Eppendorf 5810R centrifuge equipped with an A-4-62 rotor), and re-suspended at a density of 1 x 10⁶ cells in T150 cell culture flasks (BD Biosciences, Enzifarma, Porto, Portugal). These cells can be used until passage 50. L929 cell line was used in **Chapter V and Chapter VI**.

IV-6.1.2. Immortalized Rat Schwann Cells

Immortalized Rat Schwann cells were kindly supplied by Hannover Medical School, (Hannover, Germany) (223), where they were kept in a stock (2×10⁶ cells/mL, in 1.5 mL cryovials, in a cryotank). They were cultured in low glucose DMEM supplemented with 10 % (v/v) fetal calf serum, 1 % (v/v) of antibiotic/antimycotic solution (prepared with 10,000 units/mL penicillin G sodium, 10.000 µg/mL streptomycin sulfate, and 25 µg/mL amphotericin B as Fungizone (R) in 0.85 % wt. saline; Gibco®, Life Technologies, Carlsbad, CA, USA), 1 mM or 1 % (v/v) sodium pyruvate, and 2 mM or 1 % (v/v) L-glutamine (all from PAA Laboratories, GmbH). Schwann cells were incubated in an atmosphere containing 5 % CO₂ at 37 °C, and the medium changed every 2-3 days. Cells were routinely trypsinized (0.25 % (v/v) trypsin–EDTA solution; Life Technologies, Carlsbad, CA, USA) for 2 - 3 minutes at 37 °C, centrifuged at 300 g for 5 minutes (Eppendorf 5810R centrifuge equipped with an A-4-62 rotor), and re-suspended at a density of 1 x 10⁶ cells in T150 cell culture flasks (BD Biosciences, Enzifarma, Porto, Portugal). These cells were used in **Chapter VII**.

IV-6.1.3. Immortalized Human Schwann Cells

Immortalized Human Schwann cells (sNF96.2, ATCC) derived from human neurofibromatosis type 1 were purchased from ATCC. They were used between passage 3 and 20 and cultured at 37 °C and 5 % CO₂ in High Glucose DMEM supplemented with 44 mM of sodium bicarbonate, 10 % (v/v) of FBS (Biochrom, Berlin, Germany), and 1% (v/v) of antibiotic/antimycotic solution (prepared with 10,000 units/mL penicillin G sodium, 10.000 µg/mL streptomycin sulfate, and 25 µg/mL amphotericin B as Fungizone (R) in 0.85 %wt. saline; Gibco®, Life Technologies, Carlsbad, CA, USA) were incubated in an atmosphere containing 5 % CO₂ at 37 °C, and the medium changed every 2 - 3 days. Cells were routinely trypsinized (0.25 % (v/v) trypsin–EDTA solution; Life Technologies, Carlsbad, CA, USA) for 2 - 3 minutes at 37 °C, centrifuged at 200 g for 4 minutes (Eppendorf 5810R centrifuge equipped with an A-4-62 rotor), and re-suspended at a density of 1 x 10⁶ cells in T150 cell culture flasks (BD Biosciences, Enzifarma, Porto, Portugal). These cells were used in **Chapter V, VI, VIII, IX.**

IV-6.1.4. Immortalized Endothelial cells

HPMEC-ST1.6R endothelial cells are human pulmonary microvascular endothelial cells. They were kindly provided by ICVS/3Bs lab partners, where they were successfully immortalized. This cell line has been used to study the angiogenic process *in vitro* (224). The cells were cultured in M199 medium supplemented with 20 % (v/v) FBS (Biochrom, Berlin, Germany), 2 mM Glutamax (Life Technologies 1 % (v/v) of antibiotic/antimycotic solution (prepared with 10,000 units/mL penicillin G sodium, 10.000 µg/mL streptomycin sulfate, and 25 µg/mL amphotericin B as Fungizone (R) in 0.85 %wt. saline; Gibco®, Life Technologies, Carlsbad, CA, USA), 50 µg/mL of heparin, 25 µg/mL of endothelial cell growth supplement (ECGS,; Becton Dickinson). They were incubated at 37 °C in a humidified 5 % CO₂ atmosphere. HPMECST1.6R were used at passages 30–32. Medium was changed twice a week until cell reached 90 % confluence. Cells were routinely trypsinized (0.25 % (v/v) trypsin–EDTA solution; Life Technologies, Carlsbad, CA, USA) for 2 - 3 minutes at 37 °C, centrifuged at 300 g for 5 minutes (Eppendorf 5810R centrifuge equipped with an A-4-62 rotor), and re-suspended at a density of 1 x 10⁶ cells in T150 cell culture flasks (BD Biosciences, Enzifarma, Porto, Portugal). These cells were used in **Chapter VI.**

IV-6.1.5. BJ Fibroblasts

BJ fibroblasts (BJ, CRL-2522, ATCC) derived from normal human skin were purchased from ATCC. They were used between passage 3 and 10 and cultured at 37 °C and 5 % CO₂ in Eagle's Minimum Essential Medium (EMEM), supplemented with 44 mM of sodium bicarbonate, 10 % (v/v) of fetal bovine serum (FBS; Biochrom, Berlin, Germany), and 1 % (v/v) of antibiotic/antimycotic solution (prepared with 10,000 units/mL penicillin G sodium, 10.000 µg/mL streptomycin sulfate, and 25 µg/mL amphotericin B as Fungizone (R) in 0.85 %wt. saline; Gibco®, Life Technologies, Carlsbad, CA, USA) were incubated in an atmosphere containing 5 % CO₂ at 37 °C, and the medium changed every 2 - 3 days. Cells were routinely trypsinized (0.25 % (v/v) trypsin-EDTA solution; Life Technologies, Carlsbad, CA, USA) for 2-3 minutes at 37 °C, centrifuged at 300 g for 5 minutes (Eppendorf 5810R centrifuge equipped with an A-4-62 rotor), and re-suspended at a density of 1 x 10⁶ cells in T150 cell culture flasks (BD Biosciences, Enzifarma, Porto, Portugal). These cells were used in **Chapter VI, VIII, IX.**

IV-6.1.6. Isolation of neonatal rat dorsal root ganglia (DRGs)

Dorsal root ganglia (DRG) are structures located in the intervertebral foramina of the spinal column, containing the sensory neuronal cells innervating the peripheral organs. When dissociated, they can be used as a suitable *in vitro* model for the study of nerve regeneration (225). **In Chapter X**, DRGs explants were isolated from neonatal rat pups (considered neonatal from day 1 to day 5). Once the pups were sacrificed, they were cleaned using ethanol and the procedure was done under a stereomicroscope. Using sharp scissors, the spinal column was excised taking extra care of the confined organs and blood vessels. The spinal column was moved to a sterile Petri Dish with sterile cold PBS. The spinal column was divided in half along the longitudinal axis using sterile and sharp surgical scissors to expose the cord tissue. Using fine forceps, gently remove all the cord tissue, paying attention to not pull and remove the DRG roots. This way, the DRG and roots will be exposed within the vertebral canals, still encased in the column, as can be seen in **Figure IV-30.**

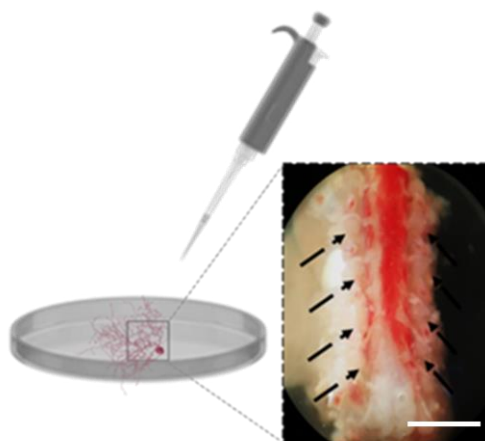


Figure IV-30 - Scheme depicting DRG isolation. Scale bar: 1 cm.

They were further cleaned with dissecting forceps to remove the tails and excessive connective tissue. After cutting the DRGs in halves, they were immediately seeded on Matrigel® coated wells. The Matrigel® coating was done at least 3 hours before the DRGs seeding, using cold Matrigel (4 °C) and allowing it to polymerize at 37 °C. The DRGs were kept in regular DMEM supplemented with 10 % (v/v) FBS and 1 % (v/v) Penicillin/Streptomycin for the first 24 hours, allowing cellular attachment.

IV-6.2. Cryopreservation

The cryopreservation of the cells used in this thesis was performed using a Statebourne Biosystem 24 cryogenic tank (Statebourne Cryogenics Ltd., UK). Briefly, cell suspensions of 1×10^6 cells/mL were prepared in a cryopreservation solution, consisting of 10 % (v/v) DMSO - Dimethyl Sulfoxide (N182, VWR, Radnor, PA, USA) in FBS, and transferred into 1.5 mL cryovials (479-6841, VWR, Radnor, PA, USA). Then, cell suspensions were gently cooled down, first at -20 °C for at least 2 hours and then moved to -80 °C freezer for a minimum period of 12 hours. The cryovials were subsequently stored at -176 °C in the gas nitrogen phase of the cryogenic tank.

IV-6.3. Cell seeding procedures

IV-6.3.1. Seeding in membranes

In **Chapter V**, membrane samples of 1 cm² were used to analyze the behavior of L929 mouse lung fibroblasts on passage 31 and human immortalized Schwann cells on passage 20. These cells

were seeded separately in 24-well cell culture plates, at a density of 3,000 cells/membrane for metabolic activity assay and 6,000 cells/membrane for proliferation assay, due to the different sensibility of each kit. In all the experiments, samples were appropriately washed with PBS and analyzed after 1, 3 and 7 days in culture.

In **Chapter VI**, for the Alamar Blue (AB) assay, BJ fibroblasts, immortalized Schwann Cells and HPMEC-ST1.6R endothelial cells were seeded separately in 1 cm² chitosan and chitosan/keratin membranes placed in the bottom of 24-well cell culture plates, at a density of 15,000 cells/membrane. Samples were analyzed at 1, 3 and 7 days.

IV-6.3.2. Seeding in freeze-dried hydrogel scaffolds

In **Chapter VII**, immortalized rat Schwann cells were directly seeded (500,000 cells/scaffold) on top of the GG freeze-dried hydrogels. Each scaffold was put in a well, in a 24-well plate.

IV-6.3.3. Seeding in SF conduits

In **Chapter VIII and IX**, for the cellular seeding intended for analysis of biological behavior, conduits with 14 mm of length were cut longitudinally and used in halves. Both BJ fibroblasts and immortalized Human Schwann cells were separately seeded in the internal and concave surface of dry conduits, at a density of 10,000 cells/conduit.

However, in **Chapter IX**, the cellular seeding performed to assess the *in vitro* cellular permeability assay was firstly optimized. It was set to 8,000 cells/conduit.

IV-6.3.4. Seeding of DRGs

Due to already described autofluorescence of SF material (226), it was not feasible to directly seed DRGs in the concave conduit wall and proceed with the necessary immunostaining. In **Chapter X**, in a way to contour that, the NTF-loaded SF conduits were put in Eppendorfs, immersed in 1 mL of complete DMEM and incubated at 37 °C at a shaking velocity of 60 rpm, producing a NTF enriched media, denominated as conditioned media. At the same time, DRGs were seeded on a 24-well plate coated Matrigel®. Every 24 hours, the conditioned media from the Eppendorfs was transferred to the well-plate containing the DRGs and replaced with fresh media.

IV-6.4. *In vitro* cellular permeability assay

Permeability is a key characteristic when designing a new NGC. In one hand, permeability is necessary for nutrients and oxygen to diffuse into the site of regeneration before the tube becomes vascularized. However, excessive cellular permeability negatively influences nerve regeneration, as surrounding collagen-depositing fibroblasts permeation tend to contribute to excessive and harmful formation of scar tissue (227).

With that in mind, a cell migration assay was designed to verify the cellular permeability of the SF NGCs to BJ fibroblasts, in **Chapter IX**. A Scheme of such assay can be seen in **Figure IV-31**. HTS Corning FluoroBlok™ Cell Culture Inserts (24 well) with an 8 µm pore size (Becton Dickinson, USA) were used. For direct cellular seeding, conduits with 4 mm in length were cut longitudinally (to fit the insert) and used in halves. First, BJ fibroblasts were pre-labelled with Cell Tracker Red (Invitrogen, CA, USA) for 30 minutes (5 mM), and then seeded directly in the internal and concave surface of the conduit (cell density was optimized 8000 cells/conduit). Briefly, Cell Tracker probes freely pass through cell membranes and once inside the cell they are transformed into cell-impermeable reaction products well retained in living cells through several generations, but not transferred to adjacent cells in a population.

Cellular adhesion was allowed to occur in a normal non-adherent 24 well plate for 3 hours, using a serum free medium. Cell-laden constructs were then moved to the upper chamber of the HTS Corning FluoroBlok Cell Culture Inserts, making sure the external and convex surface of the conduit was in contact with the insert surface. In the upper chamber where the construct was placed, MEM serum-free medium was added (500 µL). In the lower chamber, MEM medium supplemented with 40 % (v/v) FBS was added (500 µl), in order to serve as a chemoattractant gradient. As a positive control, the same cellular density was directly seeded in the upper chamber. At different time points (0, 6, 24 and 48 hours), fluorescence intensity from the bottom (basal side) was measured using a microplate spectrofluorometer (FL 600, Bio-Tek Instruments) in area-scan bottom-reading mode, at excitation/emission wavelengths of 553/570 nm. Results are presented as the increment in relative fluorescence units (RFU) in relation to the time point 0 hours (when cell-laden constructs were put in the FluoroBlok Cell Culture Inserts). Fluorescence images of cells that migrated through the conduit wall were collected using an inverted fluorescence microscope (model TCS SP8, Leica, Germany). After the last time point (48 hours), cells that migrated through the conduit wall were fixed with formalin (10 %

(v/v)) (Sigma, Germany) and stained with phalloidin (Molecular Probes, Invitrogen, USA) and 4,6-diamidino-2-phenylindole dilactate (DAPI blue, Molecular Probes), following suppliers' protocol. To evaluate if cells were viable and capable of migrating throughout the assay, the cells in the conduit were subjected to Calcein AM staining after the last time point (48 hours).

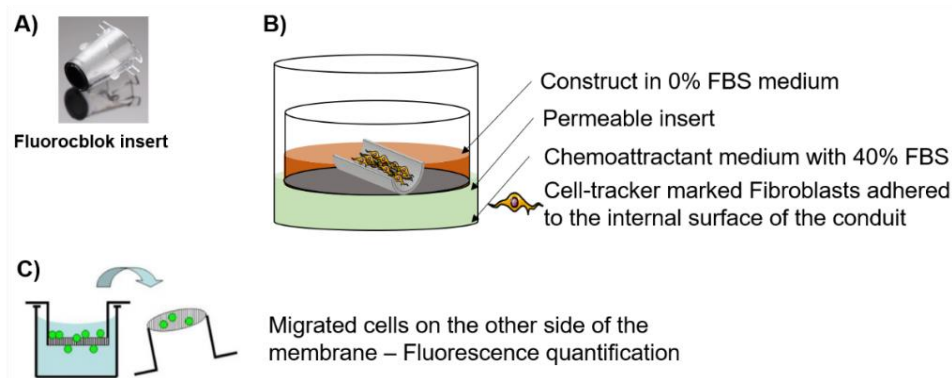


Figure IV-31 - Scheme representing the setup of the *in vitro* cellular permeability assay. A) Fluoroblok insert; B) Representative scheme of the components involved in the assay inside a well plate; C) In case of cellular migration, those are quantifiable on the other side of the membrane.

IV-6.5. Metabolic activity and cell viability examination

IV-6.5.1. Alamar blue (AB) assay

AB assay was used to evaluate the metabolic activity of cells. AB is a cell viability reagent that functions by using the reducing power of living cells to quantitatively measure their metabolic activity. When cells are metabolically active, they maintain a reducing environment within the cytosol. Resazurin, is the active ingredient of AlamarBlue® reagent, blue in color, non-toxic and cell permeable. Upon within the cells, resazurin is reduced to resorufin, a compound that is red in color and highly fluorescent. Viable cells continuously convert resazurin to resorufin, increasing the overall fluorescence and color of the media surrounding the cells (228).

In **Chapters V and VI**, an AB working solution containing 10 % (v/v) AlamarBlue® (BioRad, Hercules, CA, USA) solution and 90 % (v/v) culture medium was prepared and protected from light. In **Chapter VII, VIII and IX**, an AB working solution containing 20 % (v/v) AlamarBlue® (BioRad, Hercules, CA, USA) solution and 80 % (v/v) culture medium was prepared and protected from light. The difference in AB concentration was firstly optimized. 10 % (v/v) of reagent is enough for 2D-cultures,

which is the case of membranes (**Chapters V and VI**), and 20 % (v/v) of reagent is used in 3D scaffolds or NGCs (**Chapter VII, VIII and IX**).

At each pre-determined time-point, the materials were washed with PBS solution and transferred to new culture plates. Then, the 2D membranes were immersed in 300 μ L Alamar blue working solution, whereas the 3D GG scaffolds or NGC were supplemented with 500 μ L/construct. The culture plates were kept in the dark, at 37 °C in the CO₂ incubator for 4 hours. The reacted AlamarBlue® was transferred to white opaque 96-well plates and read in a microplate reader (Synergy HT, BioTek, Instruments, USA) using 100 μ L supernatant per well, at an excitation wavelength of 530/25 nm and at an emission wavelength of 590/535 nm. Meanwhile, the constructs were washed with PBS solution and returned to the wells in the original culture plates, supplemented with the corresponding culture medium. Three specimens of each group were tested at each time-point. Three independent experiments were performed. The metabolic activity values were calculated by normalization with the mean fluorescence value obtained for the controls (Tissue culture polystyrene; TCPs) with and without cells.

IV-6.5.2. Live/Dead staining assay for cell viability

Calcein acetoxymethyl (Calcein-AM)/Propidium iodide (PI) staining is a method for visualization of cell viability and cell death, especially used when cells are cultured in an environment that absorbs visible light. Calcein-AM/PI staining is a method for the visualization of live and death cells. In this method, cells are incubated with Calcein-AM, which is a non-fluorescent and cell-permeant derivative of calcein, transported through the cellular membrane. When the intracellular esterases of living cells remove the acetomethoxy group, this probe became green fluorescent. However, it stays non-fluorescent when the acetoxymethyl ester is intact because of the non-active esterases of dead cells. The specific visualization of dead cells can be performed by incubation with fluorescent (PI), which shows enhanced fluorescence when binding with high affinity to DNA. Contrary to calcein-AM, PI does not permeant the cellular membrane, it binds to the cytoplasmic DNA when the cellular membrane of dead cells is disrupted (229).

In **Chapter V**, the qualitative viability of L929 fibroblasts and immortalized Human Schwann cells seeded over the DA I, DA II and DA III membranes was evaluated after 1, 3 and 7 days of culture. Each seeded membrane was washed with PBS and immersed in 1 mL of culture medium supplemented with

1 μg Calcein AM and 2 μg PI. These immersions lasted for 15 minutes, at 37 °C, in the dark, after which the samples were washed with PBS and analyzed.

In **Chapter VII**, the qualitative viability of immortalized rat Schwann cells was assessed after 1, 5 and 7 days *in vitro*. Each scaffold was washed with PBS and immersed in 1 mL of culture medium supplemented with 2 μg Calcein AM and 4 μg PI (Life Technologies, CA, USA). These immersions lasted for 2 hours, at 37 °C, after which the samples were thoroughly washed with PBS and analyzed.

In **Chapter VIII** and **IX**, the qualitative viability of immortalized Human Schwann cells and BJ fibroblasts within SF NGCs was followed with a Live/Dead assay evaluated after 1, 3 and 7 days of culture. Briefly, cell-laden conduits were washed three times with PBS and incubated for 30 minutes, at 37 °C in the dark, with 1 mL of culture medium supplemented with 1 μg of Calcein AM and 2 μg of PI. Before observation, the samples were washed with PBS to eliminate excessive background.

The analyses of all the samples were carried out in a transmitted and reflected light microscope (Calcein AM excitation/emission wavelength of 495/515 nm; PI excitation/emission wavelength of 495/635 nm). Images were acquired using the Zen microscope processing software, connected to the digital camera AxioCam MR3. A Z-stack function was used to combine images at different depths into one final image.

IV-6.6. Cell proliferation quantification

CyQuant® Cell Proliferation (Life Technologies, USA) assay was used to quantify cellular proliferation in **Chapter V**. This is a fluorescence-based method to quantify cells through the measurement of DNA. This assay is based on the interaction of a dye that fluoresces upon binding to DNA. DNA content is determined by comparison with a predetermined DNA standard curve and the fluorescence intensity is proportional to the DNA content within the sample. The CyQUANT® Cell Proliferation Assay, unlike other cell proliferation quantification kits, does not require cell lysis, long incubations, radioactivity, or removal of stain from cells. After 1, 3 and 7 days, membranes seeded with cells were washed with PBS, placed in new wells and culture medium incorporating 0.4 % (v/v) of CyQUANT® Direct nucleic acid stain and 2 % (v/v) of CyQUANT®. Direct background suppressor was added to the wells. The samples were incubated for 2 hours at 37 °C, in 5 % CO₂ atmosphere. The fluorescence intensity of each sample was measured using a fluorescence microplate. Fluorescence

was read at an excitation wavelength of 480 nm and emission wavelength of 520, in the microplate reader. A scheme of how this kit works can be seen in **Figure IV-32**.

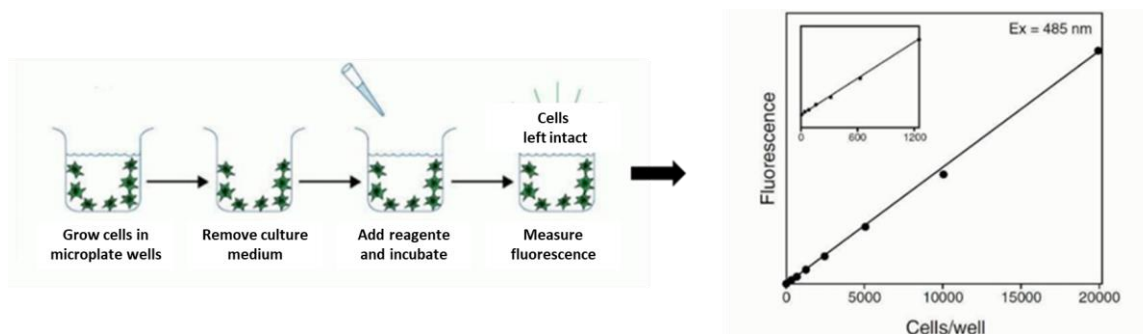


Figure IV-32 - Scheme depicting how CyQuant® Cell Proliferation kit works.

IV-6.7. Cellular cytoskeleton morphology study

DAPI (4,6-diaminidino-2-phenylindole-dilactate fluorescent dye) and phalloidin - (Tetramethyl rhodamine B isothiocyanate fluorescent dye) were used in the assay to qualitatively analyze cellular morphology and proceed with cytoskeletal qualitative evaluation.

Phalloidin is a staining method to visualize the cytoskeleton of cells. It is a rigid bicyclic heptapeptide lethal toxin which binds and stabilizes actin filaments (F-actin) and prevents the depolymerization of actin fibers. Visualization of actin can be attained by means of incubating previously fixed cells with fluorescent Phalloidin. On the other hand, DAPI binds strongly to adenine–thymine rich regions in DNA, found in the nuclei.

In **Chapter V** and **VI**, at each timepoint (1, 3 and 7 days of culture) samples were washed with PBS after culture media removal and fixed in 10 % (v/v) formalin for 1 hour. Afterwards, formalin was removed by PBS washing and 1 mL of PBS containing 2 μ L of phalloidin (10 mg/mL) was added to the systems, leaving them to react for 40 minutes at RT. After extensively washing with PBS, nuclei were simultaneously counter-stained with DAPI. 1 mL of PBS containing 1 μ L of DAPI (20 mg/mL) was incorporated in the systems and left to react for 10 minutes. The dye was removed by washing with PBS. Finally, the samples were analyzed using a transmitted and reflected light microscope (Axio Imager Z1m, Zeiss, Jena, Germany) with the filters 594 nm (phalloidin), and 405 nm (DAPI).

IV-6.8. Enzyme-linked Immunosorbent Assay (ELISA)

Enzyme-linked Immunosorbent Assay (ELISA) is a method for detection and quantification of specific antigens. The principle of this technique relies on antigen-antibody binding, as the antigen is quantified using a solid-phase enzyme immunoassay. A primary antibody of interest is attached to the surface of a multi well-plate and then the sample (antigen) is added and binds to the antibody. Following, a secondary antibody is added to the well, an enzyme is added to bind the antibody and, finally, a substrate for the enzyme is added. The color change is measured using a spectrometer and the antigen concentration is determined by comparison to a standard curve (230).

In **Chapter X**, the quantification of released GDNF and NGF from the SF NGCs was evaluated. The brief scheme of the assay can be seen in **Figure IV-33**.

Briefly, each conduit, the size of 14 mm in length, was incubated in 1 mL of release medium (1 %wt. bovine serum albumin (BSA) in PBS, at 37 °C, with shaking at 60 rpm, for 50 days. The supernatant was collected and substituted with 1 mL of fresh release medium every 24 hours. Released NTF from the conduits was frozen at -80 °C until analysis. The supernatant containing NTFs was measured according to the manufacturer's instructions. The absorbance was measured at 450 nm using a plate reader (Tecan, park 10M, Männedorf Switzerland). The NTFs concentration was determined by comparing the reading to the obtained standard curve after normalization. A more detailed protocol of the ELISA protocol of both GDNF and NGF molecules can be found in **Table IV-9**.

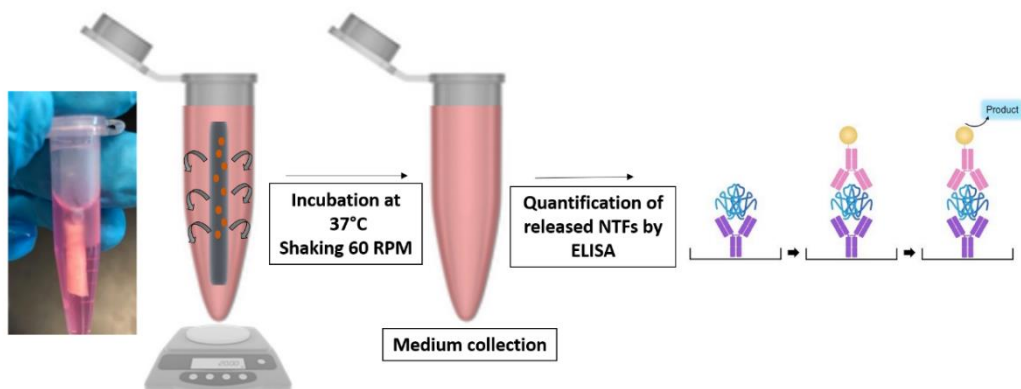


Figure IV-33 - Scheme of the methodology used in the NTF release and quantification assay by ELISA.

Table IV-9 - ELISA procedure summary, which was valid for GDNF and NGF.

| | GDNF | NGF |
|--|--|--|
| Capture antibody | 100 μ L, overnight incubation, at 4 °C, washing, | 100 μ L, overnight incubation, at 4 °C, washing, |
| Blocking | 300 μ L of BSA 1 %wt, at RT, 1 hour, washing, | 300 μ L of BSA 1 %wt, at RT, 1 hour, washing, |
| Sample/Standard | 100 μ L, 2 hours incubation, at RT washing, | 100 μ L, 2 hours incubation, at RT, washing, |
| Biotinylated detection antibody | 100 μ L, 2 hours incubation, at RT washing, | 100 μ L, 2 hours incubation, at RT washing, |
| Streptavidine-HRP | 100 μ L, incubation for 20 min, at RT, dark, washing, | 100 μ L, incubation for 20 min, at RT, dark, washing, |
| TMB one-step Substrate | 100 μ L, incubation for 20 min, at RT, dark, no washing, | 100 μ L, incubation for 20 min, at RT, dark, no washing, |
| Reaction Stop Solution | 50 μ L, no washing, | 50 μ L, no washing, |
| Absorbance | 540 nm | 540 nm |
| Sensitivity | 2000 pg/mL | 2000 pg/mL |

IV-6.9. Immunocytochemistry

Immunocytochemistry is a method for detection and visualization of specific antigens in cells. The principle of this technique relies in the specific binding of a primary antibody to an antigen, followed by binding of a fluorescent-labeled secondary antibody to the primary antibody and visualization under a fluorescence microscope (231). This procedure involves some preliminary steps after cell culturing, including cell fixation, cell membrane permeabilization, enables the antibodies to enter the cells when searching for intracellular antigens, and a blocking step that blocks unspecific bindings of antibodies. These steps are intercalated with washing steps to remove unbound antibodies.

In **Chapter X**, immunocytochemistry techniques were used to allow the visualization of DRGs. After 5 days of incubation, DRGs and cells were fixed with 4 % (v/v) paraformaldehyde for 30 minutes. DRGs were washed and treated with Triton 0.2 % (v/v) in PBS for 10 minutes for permeabilization purposes.

The next step consists in adding blocking buffer comprising 3 %wt. BSA at RT for 30 minutes. The primary antibody was added next, diluted in 1 % (v/v) BSA in PBS for 1 hour at RT (1:150, Monoclonal Anti-Neurofilament 200, produced in mouse). After washing with PBS, the secondary antibody was immediately added and left for 1 hour at RT, protected from light (1:500, Alexa Fluor® 488 goat anti-mouse). The last step consisted in nuclei staining, in which Hoechst staining was applied for 5 minutes in the dark (1:5000). The antibodies used for immunocytochemistry can be found in **Table I-10**.

The stained DRGs were analyzed using the confocal laser microscope (Leica, Wetzlar, Germany). Confocal images were acquired by confocal and mounted together to fit in a black square (with the exact same size in all images) so that it would be possible to do image analysis and comparable quantifications. Confocal microscopy is based on the same principle as the fluorescence microscope, but it has a special pinhole in the detector system that eliminates out-of-focus (background).

Table IV-10 - Antibodies used for immunocytochemistry of *in vitro* samples.

| Antibody | Type | Reference | Host | Dilution | Clonality/Reactivity |
|------------------------|-----------|-----------|-------|----------|----------------------|
| Anti-Neurofilament 200 | Primary | N5389 | Mouse | 1:150 | Monoclonal rat |
| Alexa Fluor® 488 | Secondary | A21202 | Goat | 1:200 | Mouse |

IV-7. *IN VIVO* STUDIES

Several *in vivo* studies were performed in this thesis, according to the rules of the respective country or university. Animal manipulation for *in vivo* studies was performed only by qualified personnel and following the Principle of the 3Rs.

In **Chapter VII**, all animal experiments followed the rules of the EU Directive 2010/63/EU for animal experiments and were permitted by the animal care committee of Lower-Saxony, Germany: Nds. Landesamt für Verbraucherschutz und Lebensmittelsicherheit Dezernat 33/Tierschutz, reference number 33.12 42502-04-12/0816.

In **Chapter IX**, the maintenance and study of animals were carried out in accordance to the Ethics Committee of University of Minho and approved by the Portuguese Licensing Authority (DGV-DSSPA). All

animal protocols were conducted in accordance with the Portuguese legislation (Portaria no1005/92) and international standards on animal welfare as defined by the EC Directive 2010/63/EU.

In **Chapter X**, all experiments were conducted under an approved protocol of the Rutgers Animal Care and Facilities Committee and the Institutional Animal Care and Use Committee (IACUC), United States of America.

IV-7.1. Chick chorioallantoic membrane (CAM) assay

The basic principle of the chick chorioallantoic membrane (CAM) assay relies on providing a non-innervated rapidly growing vascular bed, which can serve as a surrogate blood supply for organ culture, and hence a platform for TE biomaterial testing (232). More specifically, it is a minimally invasive in vivo assay for angiogenesis studies. CAM is composed of a multilayer epithelium, including the ectoderm at the air interface, mesoderm or stroma and endoderm at the interface with the allantoic sac. This membrane contains ECM proteins, such as, fibronectin, laminin, collagen type I and integrins, and the presence of such proteins mimics the physiological cancer environment. For that reason, CAM assay have been widely used to study tumor cell invasion and angiogenesis. The highly-vascularized nature of the CAM greatly promotes efficiency for materials grafting, high reproducibility, simplicity and cost effectiveness, being an attractive and well established model for studying angiogenesis and cell invasion (233).

In **Chapter VI**, CAM assay was performed to evaluate the angiogenic potential of the chitosan and chitosan/keratin membranes. All the membranes were previous hydrated in PBS for 24 hours and cut with a 4 mm² round punch for CAM implantation. The scaffolds were sterilized by EO and all the procedures were performed in aseptic conditions, in a sterile vertical laminar airflow cabinet to minimize contaminations. Gelatin sponges with 9 mm diameter and 3 mm height were prepared from sterile Cutanplast® sponge (Mascia Brunelli S.p.a., Milan, Italy) and used as negative control for angiogenesis. Filter paper was used as the positive control. A total number of 120 white fertilized chicken eggs (Pintobar, Amares, Portugal) were incubated at 37 °C (Laboratory Incubator model B8420; Termaks, Bergen, Norway) for 3 days for embryonic growth. A small hole was created in the pointed end of the eggs to allow dissociation of the CAM from the shell membrane. Then, a circular window was made into the eggshell, in order to evaluate embryo viability and access the CAM. The shell opening was sealed with transparent tape (50 x 30 mm, Staples) to prevent dehydration and the eggs

were returned to the incubator at 37 °C until implantation of the scaffolds. After 10 days of embryonic development, the sterile membranes were implanted into the CAM and the shell windows were again sealed with transparent tape for incubation until day 14. Afterwards, the embryos and their membranes were fixed *in ovo*, using 4 % (v/v) paraformaldehyde (PFA; Merck, Berlin, Germany) solution onto the CAM surface, for 10 minutes at -80 °C in an ultra-low freezer. The implanted specimens and adjacent CAM region were dissected using surgical forces and scissors and transferred to 6-well culture plates in 4 % (v/v) PFA for analysis. *Ex ovo* images were acquired using the AxioVision imaging software (release 4.8; Zeiss, Jena, Germany) connected to an AxioCAM ICc1 digital camera (Zeiss, Jena, Germany) attached to a stereomicroscope (Stemi 2000-C; Zeiss, Jena, Germany). A minimum number of 18 samples were tested for each group. Three independent CAM experiments were performed.

A scheme representing the CAM assay can be seen in **Figure IV-34**.

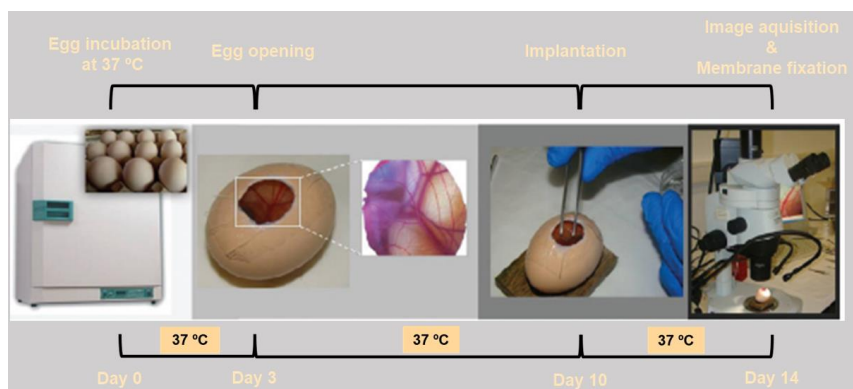


Figure IV-34 - Scheme representing the steps in the *in vivo* CAM assay.

IV-7.2. Subcutaneous implantation

The main goal of a subcutaneous *in vivo* assay is to assess a new biomaterials biocompatibility, to verify the normal foreign body response, abnormal signs of inflammation or poor vascularization that arise as consequence of the implantation. The animal's immune response to the implant will predict the suitability of the biomaterial for further studies (234).

In **Chapter IX**, enzymatically crosslinked SF NGCs of different wall thickness and dried in different ways (TC 1, TC 2 and TC 3) were tested for the *in vivo* biological performance as well as their general behavior *in vivo*, by subcutaneous implantation in Hsd:ICR (CD-1®) mice. The conduits were 14 mm in length. The results were evaluated after 4 and 8 weeks. 5 weeks old mice were used in the studies, always manipulated in aseptic conditions.

For each timepoint, six mice with an average weight of 25-30 g were used for the implantation of the different SF conduits. Each mouse was anesthetized by intraperitoneal injection of ketamine (25 mg/kg) and medetomidine (0.15 mL/kg) for anesthesia, cephalexin (15 mg/kg) as antibiotic, and bupivacaine and pethidine (5-10 mg/kg) as analgesic. The hair of the mice was shaved in the area of implantation and disinfected with 70 % (v/v) ethanol and iodine. In each mouse, four skin incisions (1 cm length) were made in the dorsal midline, two close from the head (CH) and two far from the head (FH). Afterwards, sterile conduits were implanted subcutaneously into the four different positioned pockets and then the skin was sutured. Four replicates of each condition (thick and thin TC 1, TC 2 and TC 3) were implanted. The scheme of animals and samples distribution can be seen in **Figure IV-35**, so that each sample would be placed in a different pocket in every different animal. **Table IV-11** refers to the different samples that were tested in this specific assay. After each time-point, the mice were euthanized by injection of overdose pentobarbital sodium (250 mg/kg) and the implanted materials, together with the surrounding tissue, were then retrieved. For histological analysis, the explants were fixed with 10 % (v/v) formalin solution for at least 2 days at RT, dehydrated through increasing series of ethanol concentrations (from 30 % up to 100 % (v/v)) and transferred to histological cassettes for immersion in paraffin.

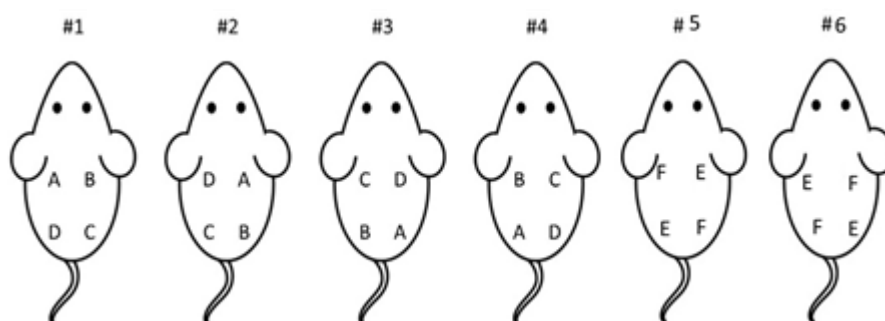


Figure IV-35 - Animal and sample distribution for *in vivo* subcutaneous assay.

Table IV-11 - Correlation between the different samples that were tested in this *in vivo* subcutaneous assay.

| Letter in the animal | Correspondent sample |
|----------------------|----------------------|
| A | TC 1 Thick wall |
| B | TC 2 Thick wall |
| C | TC 3 Thick wall |
| D | TC 1 Thin wall |

| | |
|---|----------------|
| E | TC 2 Thin wall |
| F | TC 3 Thin wall |

IV-7.3. *In vivo* study using rat model of sciatic nerve defect

Translation of the new therapeutic approaches to the patient always requires a final pre-clinical step using *in vivo* reliable animal models. Furthermore, an *in vivo* study where a true nerve lesion is repaired with the developed biomaterials tools, reveals its real potential, as well as drawbacks to be improved.

In **Chapter VII**, the effectiveness of the developed chitosan tubes filled with GG freeze-dried hydrogels as PNR guidance conduits (NGC60:40, NGC50:50 and NGC25:75) was tested in a 10 mm rat sciatic nerve defect, using nearly 70 specimens). Samples for histological analysis were collected after both short-term (ST, 3 and 6 weeks) and long-term (LT, 12 weeks) observation periods. For the ST studies, 4 animals were selected for the implantation of each NGC formulation. Hollow chitosan tubes served as positive controls (235). For LT studies, 7 animals were studied per NGC formulation and 7 animals receiving an autologous nerve graft served as controls. This *in vivo* study was performed in Hannover Medical School (MHH, Hannover, Germany).

Female Wistar rats (225 to 250 g) were kept in groups of four animals under standard conditions (room temperature 22 ± 2 °C; humidity 55 ± 5 %; light–dark cycle 14 hours/10 hours), with food and water *ad libitum*. For surgical procedures, animals were anesthetized by an intraperitoneal injection of chloral hydrate (370 mg/kg of body weight). NGCs with a length of 14 mm were saturated for 30 minutes in 0.9 % (v/v) NaCl prior to implantation. Animals were placed on a thermostatic blanket throughout the surgical procedures and postoperative periods. Aseptic conditions were observed. After exposure of the sciatic nerve, it was transected at a constant point (6 mm from the exit of the gluteus muscle) for the removal of 5 mm of the distal end. Once the PNI was caused, NGCs were implanted to bridge a 10 mm nerve defect. NGCs were connected by a single 9-0 suture (9-0, EH7981G, Ethilon, Ethicon, Scotland) to the respective nerve end. Alternatively, autologous nerve grafts were implanted. Therefore, a 10 mm nerve segment was excised from the same nerve (proximal transection again at 6 mm from the exit of the gluteus muscle), reversed and 180° turned along its longitudinal axis, and sutured back into the nerve with three 9-0 sutures at each end. Postoperative analgesia was guaranteed

by intramuscular injection of buprenorphine (0.045 mg/kg of body weight, Buprenovet®; Bayer Pharmaceuticals, Leverkusen, Germany).

In **Chapter X**, the regenerative potential of the developed NTF loaded SF conduits was investigated *in vivo* on a 10 mm rat sciatic nerve gap. This study was conducted at New Jersey Center for Biomaterials, Rutgers University, New Jersey, United States.

In a total of fifteen animals, five animals were distributed in three experimental groups (n=5). More specifically, the experimental groups include the following: 1) Autograft; 2) eSF and 3) GDNF/A₄. The reversed autograft was considered the positive control and the plain silk conduit was considered the negative control, in order to assess the NTF incorporation beneficial effects. The degree of regeneration was assessed 6 weeks after implantation surgery.

In more detail, male Lewis rats weighing 250–300 g (Charles River Labs, USA) were anesthetized with isoflurane inhalation (1-5 % isoflurane in 100 % (v/v) O₂) via an appropriate face mask, which was kept throughout the surgical procedure for anesthesia maintenance. Animals were kept on a heated pad entirely until they recovered from anesthesia. Before the surgery, Buprenorphine (for analgesic purposes, 0.05 mg/kg) and Baytril (for antibiotic purposes, 5mg/kg) were administered subcutaneously. After shaving the surgical site on the left limb, local anesthesia (Bupivacaine, diluted to 0.25 % (v/v), 2.5 mg/kg) was also administered where the incision would be made. The shaved area was then cleaned by scrubbing three pairs of alternating applications of chlorhexidine followed by 70 % (v/v) isopropyl alcohol in circular motions.

Nerve cutting tools were printed from poly (lactic acid) on a Monoprice fused deposition modeling printer. Tools had a hook with an inner diameter of 2.5 mm and a scalpel alignment groove 700 µm in width. Tools had a beveled tip and a model specific dimensions to allow for minimal tissue damage while exposing and sectioning the nerve. Printed tools were cleaned in ethanol, individually packed and surgically sterilized with ethylene oxide. A scheme of a nerve cutting tool can be seen in **Figure IV-36**. For the conduits' groups, a 5 mm section of the sciatic nerve was removed with the aid of the nerve cutting tool, and the nerve stumps were allowed to retract to form a 10 mm gap. Sterile conduits (14 mm in length) were first hydrated for 10 minutes with sterile saline and then sutured to the nerve stumps using two 9-0 epineurial sutures on each end, maintaining the 10 mm gap between the stumps. In that process, nerve stumps were secured approximately 1 mm into each end of the conduit. In the case of autografts, a 10 mm segment of nerve was removed, reversed, and sutured back in the gap using 9-0 sutures on each end. Both muscular and skin tissues were sutured in layers using absorbable 5-0 sutures. For post-operative analgesia, buprenorphine SR (1 mg/kg) was

administered 8 hours after the surgery. Six weeks after reconstruction, rats were deeply anesthetized using the same method. SF conduits with repaired nerve stumps and the autografts on the experimental side were harvested, as well as a segment of uninjured nerve on the contralateral side. Still under general anesthesia, animals were euthanized by carbon dioxide asphyxiation.

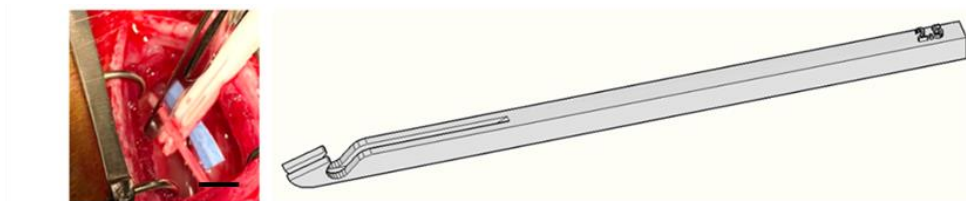


Figure IV-36 - Scheme of the nerve cutting tool used in the *in vivo* study, to precisely hold and cut the sciatic nerve during surgery. Tools were 3D-printed using poly (lactic acid) and consisted of a hook with an inner diameter of 2.5 mm and a scalpel alignment groove 700 μm in width.

IV-7.4. Explants characterization

IV-7.4.1. Macroscopic inspection of the reconstructed nerves

In **Chapter VII**, the regenerated sciatic nerves were exposed and inspected with the help of a microsurgery microscope. Because chitosan tubes are transparent, it offered the possibility to assess some degree of regeneration, nerve cable thickness, as well vascularization or excessive inflammatory response. One example of macroscopic inspection of the explanted chitosan tube 12 weeks after reconstruction can be seen in **Figure IV-37**.

In **Chapter X**, a macroscopic inspection was also performed to the surgical site only, since the enzymatically crosslinked SF NGCs are not transparent and do not allow a direct visualization of its interior. However, no inflammation was detected in animal, at the moment of the explant.

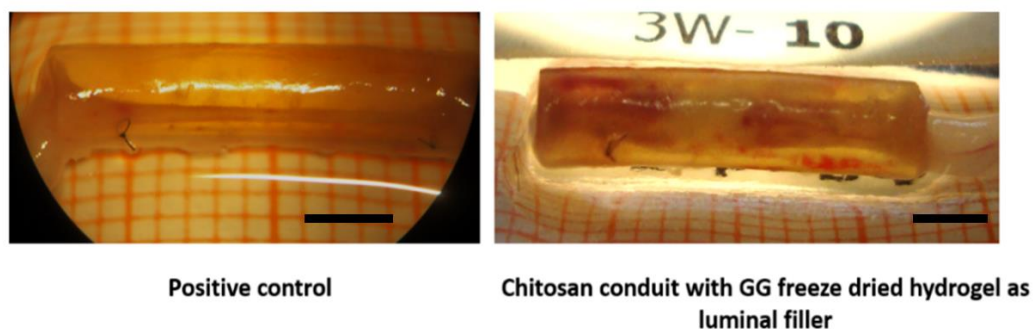


Figure IV-37 - Transparent NGCs can offer the opportunity to assess parameters related to regeneration, such as inflammation or the presence of a nerve cable, at the moment of explant. Scale bar: 3 mm.

IV-7.4.2. Analysis of blood vessels convergence

In **Chapter VI**, as a result of the CAM assay, a semi-quantitative method was used to evaluate the total number of macroscopic blood vessels converging toward the implanted chitosan and chitosan/keratin membranes. This method has been previously described by Ribatti *et al.* (236) for the quantification of angiogenesis in the CAM of chicken eggs, using gelatin sponges as implanted materials. In this thesis, the *ex ovo* images of the explants obtained after 14 days of embryonic development, were processed according to Silva-Correia *et al.* (237) and a new method based on the work of Nowak-Sliwinska *et al.* (238). Both methods of imaging processing were automated in macro files for analysis at the ImageJ software program (US National Institutes of Health) and compared. The magnification of the stereomicroscope images was kept constant (7x), as well as, the image-processed area (1000 x 1000 pixels). The total number of blood vessels converging toward the implants was counted blindly for each egg by three independent observers.

IV-7.4.3. Histological examination

In **Chapter VI**, histological analysis was performed to the explants after CAM assay and subcutaneous implantation in mice. The collected explants were sectioned with 3.5 - 4.0 μm thick in a microtome and processed for histological analysis. Representative sections of the explants were stained with hematoxylin–eosin (H&E) following standard protocol. Briefly, selected slides were subjected to H&E staining. Briefly, samples were deparaffinized in xylol, hydrated through decreasing ethanol series (100 %, 96 %, 70 % and 50 % (v/v) of alcohol) and finally washed in distilled water. After immersion in

hematoxylin, samples were rinsed in running soft tap water. Samples were then immersed in an 80 % (v/v) alcohol solution and briefly in the eosin staining. Slides were dehydrated through 96 % (v/v) ethanol, absolute ethanol and finally cleared in xylol and mounted with Moviol (Calbiochem, Germany, No. 475904).

In **Chapter VII**, the 3 weeks timepoint was cut in cross-sections, as can be seen in **Figure II-38**. For both LT timepoints, 6 weeks and 12 weeks, longitudinal sections were produced in order to harvest the complete length of the GG material and eventually regrown tissue along the 10 mm nerve gap. As soon as the complete length of the material was visible in one section, a series of 24 sections (7 μm thickness) was produced and two sections per slide were collected. Selected slides were subjected to H&E staining, which the same as followed for **Chapter VI**.

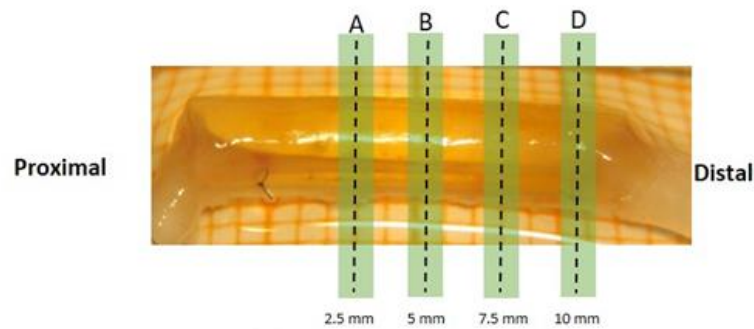


Figure IV-38 - Scheme of cross-section histological cutting for the 3 weeks timepoint samples in Chapter VII.

In **Chapter X**, the histological cuts were done by cross-sectioning the proximal site (PNX location) and 3 mm into the conduit (C1X), but longitudinally for the rest of the conduit. The scheme of histological cutting can be seen in **Figure IV-39**.

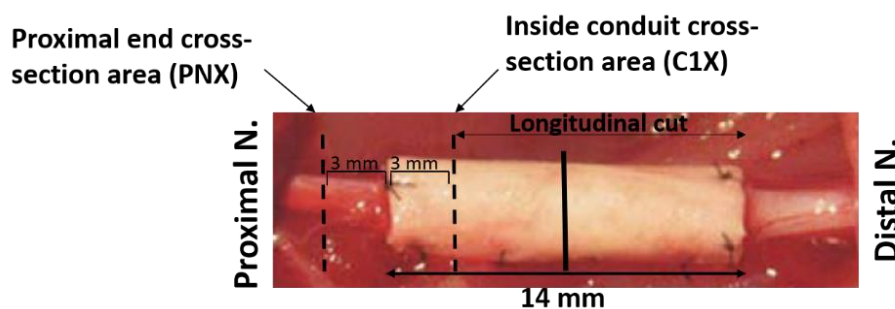


Figure IV-39 - Scheme for histological cut of the enzymatically crosslinked SF NGC after explant in Chapter X.

IV-7.4.4. Immunohistochemistry

IV-7.4.4.1 *Immunohistochemistry for lectin (CAM assay)*

In **Chapter VI**, representative CAM sections of 4.0 μm thick were used for immunohistochemical detection of the endothelial cells marker SNA-lectin (Vector Laboratories, Burlingame, CA, USA). Sambucus Nigra Lectin (SNA, EBL) has been used to identify vascular beds in chick CAMs. It specifically binds to the endothelial cells that surround and infiltrate the CAM implants, being useful for angiogenesis assays (237). Briefly, after paraffin dewaxing and rehydration, sections were submitted to a heat-induced antigen retrieval using 10 mmol/L sodium citrate buffer (Merck, Berlin, Germany) pH 6, for 20 minutes at 98 °C in the water bath. Sections were incubated with 50 μL of 3 % (v/v) H_2O_2 for 10 minutes at RT, in order to inactivate block tissue endogenous peroxidase activity, which may induce a high and non-specific background when using HRP conjugated antibodies. After soaking in PBS solution, sections were incubated in protein blocking solution (Ultra V block), from the UltraVision Detection System kit (Lab Vision, Thermo Scientific, CA, USA), for 10 minutes at RT. Afterwards, 50 μL of SNA-lectin (Vector Laboratories, Burlingame, CA, USA; dilution 1:750 in Ultra V block) were added to each section and incubated for 10 minutes at RT. Sections were then washed with PBS solution and incubated in streptavidin-peroxidase complex, from the UltraVision Detection System kit, for 10 minutes at RT. A 3,3'-diaminobenzidine (DAB) solution was prepared using the Peroxidase Substrate Kit – DAB* (Vector Laboratories, Burlingame, CA, USA) and incubated for 2-3 minutes at RT. Sections were washed for 5 minutes in running water, to completely remove the DAB solution, and counterstained with Gill-2 hematoxylin (Merck, Berlin, Germany; dilution 1:2 in distilled water) solution. After washing with distilled water, sections were dehydrated and mounted in Entelan. Slides were observed under transmitted microscopy, using the transmitted and reflected light microscope. Images were acquired using the Zen microscope processing software, connected to the digital camera AxioCam MRc5.

*DAB Solution: 5 mL of distilled water, 2 drops of buffer stock solution, 4 drops of DAB stock solution, 2 drops of H_2O_2 .

IV-7.4.4.2 *Immunohistochemistry for detection of axonal regeneration and immunological reaction*

In **Chapter VII**, immunohistology was performed over sections that were consecutive to the ones processed for H&E staining. A double staining was performed to detect neurofilaments (NF-200) and activated macrophages (ED-1). Nuclear counterstaining was obtained with DAPI. For such, slides were

deparaffinized and immersed in an antigen retrieval solution (citrate buffer, 10 mM, pH 6.0 + 0.05 % (v/v) Tween 20), heated at 90 °C for 30 minutes and left to cool down for another 30 minutes in distilled water. Afterwards, they were incubated in a blocking solution (PBS + 5 %wt. milk powder + 0.5 % (v/v) Triton X-100) prior to incubation with a primary mouse anti-rat ED-1 antibody (1:1000 diluted in blocking solution, MCA 275R Serotec, UK) at 4 °C overnight. The next day the sections were washed with PBS (3×) before being incubated with an Alexa 555-conjugated secondary goat-anti-mouse antibody (1:1000 diluted in blocking solution, Invitrogen, Germany) for 1 hour at room temperature (RT). After incubation with the secondary antibody, sections were further washed with PBS (3×) and a second blocking step was performed for 20 minutes. Overnight incubation at 4 °C with a primary rabbit anti-rat NF-200 antibody (1:200 diluted in blocking solution, N4142, Sigma Aldrich, Germany) was done following the previously described steps. The samples were washed with PBS (3×) and incubated with an Alexa 488-conjugated secondary goat-anti rabbit antibody (1:1000 diluted in blocking solution, Invitrogen, Germany) for 1 hour at RT. The double-labelled sections were afterwards counterstained with the nuclear dye (DAPI, 1:2000 diluted in PBS, Sigma, Germany) for 5 minutes at RT, and finally mounted with Moviol (Calbiochem, Germany, No. 475904).

IV-7.4.4.3 *Nerve histology for the detection of neovascularization*

In **Chapter VII**, immunohistology was performed over sections to detect neo-vascularization or angiogenesis. Blind-coded sections from each segment were deparaffinized and immersed in an antigen retrieval solution (citrate buffer, 10 mM, pH 6.0 + 0.05% (v/v) Tween 20), heated at 90 °C for 30 minutes and left to cool down for another 30 minutes in distilled water. Slides were posteriorly immersed in a blocking solution (3 %wt. BSA in PBS) prior to incubation with a primary goat anti-Mouse/Rat CD31/PECAM-1 antibody (AF3628, R&D Systems, UK) (15 µg/ mL diluted in 1 %wt. BSA in PBS) at 4 °C overnight. The next day the corresponding sections were washed with PBS (3×) before being incubated with an Alexa 488-conjugated secondary rabbit anti-goat antibody (1:500 in 1 %wt. BSA in PBS) for 1 hour at RT. After incubation with the secondary antibody, sections were further washed with PBS (3×) and a second blocking step was done for 20 minutes. This was followed by overnight incubation (4 °C) with a primary rabbit anti-mouse CD34 antibody (1:2500 diluted in 1 %wt. BSA in PBS), Abcam, Cambridge, UK). After washing with PBS (3×), incubation with an Alexa Fluor 594 donkey anti-rabbit IgG secondary antibody (1:500 diluted in 1 %wt. BSA in PBS), Molecular Probes, Oregon, United States) was performed for 1 hour at RT. Sections were finally counterstained with the nuclear

dye (DAPI, 1:2000 diluted in PBS, Sigma, Germany) for 5 minutes at RT and then mounted with PermaFluor (Thermo Fisher Scientific, UK). Since for the 3 weeks' time point the samples were cut into cross-sections, the example photo belongs to an area around 5 mm after the proximal nerve end. Results were qualitatively analyzed using a transmitted and reflected light microscope (Axio Imager Z1m, Zeiss, Jena, Germany). All the antibodies used for immunohistochemistry in **Chapter VII** can be seen in **Table IV-12**.

Table IV-12 - Antibodies used for immunohistochemistry of *in vivo* samples in Chapter VII.

| Antibody | Type | Reference | Host | Dilution | Clonality/Reactivity |
|---------------------|-----------|-------------------------|--------|----------|-------------------------|
| ED1 | Primary | MCA 275R, Serotec | Mouse | 1:1000 | Monoclonal Rat |
| NF200 | Primary | N4142, Sigma Aldrich | Rabbit | 1:200 | Polyclonal Rat |
| CD31/PECAM-1 | Primary | AF3628, R&D Systems | Goat | 1:50 | Monoclonal mouse/rat |
| CD34 | Primary | Ab81289, Abcam | Rabbit | 1:2500 | Monoclonal Mouse |
| Alexa 555 | Secondary | A-21422, Invitrogen | Goat | 1:1000 | Polyclonal Mouse |
| Alexa 488 | Secondary | A-11008, Invitrogen | Goat | 1:1000 | Polyclonal Rabbit |
| Alexa 488 | Secondary | A-11078, Invitrogen | Rabbit | 1:500 | Polyclonal Goat |

IV-7.4.5. Evaluation of functional recovery

In **Chapter VII**, electrodiagnostic recordings were done to evaluate functional recovery. Evoked compound muscle action potentials (CMAPs) from the anterior tibial muscles (TA) and the plantar muscles (PL) were performed. During the 12-week study period two sessions of non-invasive (week 4 and week 8 post-surgery) measurements and one final session of invasive (12 weeks post-surgery) measurements were carried out. The investigators performing the tests were blinded for the general implantation conditions and the formulation type of the implanted tubes. In brief, a portable electrodiagnostic device (Keypoint Portable; Medtronic Functional Diagnostics A/S, Denmark) was used to stimulate the sciatic nerve and to record the evoked CMAPs. In the non-invasive setting, the sciatic nerve was stimulated with single electrical pulses (100 μ s duration and supramaximal intensity) delivered by monopolar needles (30G, diameter 0.3 mm, length 10 mm; Natus Europe GmbH, Planegg, Germany), percutaneously placed at the sciatic notch (proximal stimulation) or at the popliteal fossa (distal stimulation). The active recording electrode was located in the respective muscle belly, the reference electrode in the tip of the second toe and the ground needle electrode was inserted in the skin at the flank. In the invasive setting, the sciatic nerves at both the injured and non-injured sides were consecutively exposed. With the help of a bipolar steel hook electrode, the sciatic nerves were directly stimulated proximal and distal to the transplants. Single electrical pulses (100 ms duration) with gradually increased intensity (not exceeding 8 mA) were applied in order to evaluate the threshold and maximal CMAP. The recording electrodes were placed as described before. Whenever a CMAP could be evoked, the signal was recorded and the signal amplitude of the negative CMAP peak analyzed. Amplitude ratio values were obtained using CMAP signals evoked and recorded from the contralateral healthy side of the animal. If no evoked CMAP was detected, a 0.00 value was noted down.

IV-7.4.6. *In vivo* micro-CT evaluation of the explants

In an advanced form of micro-CT, an *in-vivo* micro-CT scanner is able to offer a large field-of-view (80 mm) with high resolution (5 μ m), being a versatile scanner for the in-vivo X-ray micro computed-tomography imaging of mice, rats, and extremities of larger animals up to small rabbits.

In **Chapter VII**, the explants were scanned using a high-resolution micro-CT device, VivaCT 80 (Scanco Medical AG, Brüttisellen, Switzerland). 250 projections with a resolution of 1024 \times 1024 pixels were obtained in each scan with an integration time of 200 ms. Images with an isotropic pixel size of

31.2 μm were obtained at 45 kV, 177 μA and 8 W. The acquired images were reconstructed to obtain 2D image datasets in μCT Evaluation Program V6.5 (Scanco Medical AG, Brüttisellen, Switzerland). Using the CT Analyser software V1.15.4.0 (Bruker micro-CT, Belgium) the regions of interest were defined on the 2D images of the explants that were viewed in 3D and 2D all planes on DataViewer V1.5.3.6 (Bruker micro-CT, Belgium).

IV-7.4.7. Pinch test

The pinch test is a fast, cheap and immediate-response technique to assess if there is sensory reinnervation from the injured nerve to the pinched area before euthanizing the animals.

In **Chapter X**, a pinch test was performed in a way to assess sensory functional recovery. Before euthanizing the animals, the distal nerve segment was pinched with a pair of forceps to determine any reflex of the ipsilateral side, which is marked positive when there is a reflex of the paw. Three evaluations were performed in each reconstructed nerve.

IV-7.4.8. Gastrocnemius muscle harvest and weight ratio

The analysis of the weight of the gastrocnemius muscle is extremely important as it is an indicator of motor reinnervation and motor fibers survival. The main goal with our TE approaches is that the muscle weight loss or atrophy are significantly avoided, which is critical for functional recovery.

In **Chapter VII**, upon harvest of the nerve tissue, the gastrocnemius muscles were collected. The fresh muscle weight from the ipsilateral lesioned side was then compared to the weight measured from contralateral healthy muscles to calculate the muscle weight ratio ($[\text{g}]$ ipsilateral/ $[\text{g}]$ contralateral). However, these results are not shown in the respective publication.

In **Chapter X**, upon nerve harvest and after animal sacrifice, the gastrocnemius muscle of both hind limbs (operated side and contralateral healthy side) were immediately harvested by exposing the musculature via a knee to ankle longitudinal skin incision. The muscles were harvested from origin to insertion and weighed with an electronic balance in order to be able to determine the muscle atrophy resultant from muscle denervation. Results are expressed as the percentage of the left side (reconstructed with SF conduits) to the non-operated contralateral side, as a mean of the five samples per condition (mean \pm SD).

IV-7.4.9. Nerve morphometry analysis

In Chapter VII, nerve tissue segments 5 mm in length were harvested directly distal to the sutures connecting the implants with the distal nerve end and processed for nerve morphometry. Segments taken from the contralateral healthy nerve at a similar height served as controls. Therefore, fixation was performed in Karnovsky fixans (2 % (v/v) PFA, 2.5 % (v/v) glutaraldehyde in 0.2 M sodium cacodylate buffer, pH 7.3, for 24 hours) prior to rinsing the samples 3 times with 0.1 M sodium cacodylate buffer containing 7.5 %wt. sucrose. Post-fixation was performed in 1 % (v/v) OsO₄ for 1.5 hours followed by myelin staining for 24 hours in 1 %wt. potassium dichromate, 24 hours in 25 % (v/v) ethanol and 24 hours in hematoxylin (0.5 % in 70 % (v/v) ethanol), according to a modified Schultze protocol. After dehydration, the samples were embedded in epoxy resin. 1 µm (semithin) cross-sections were cut with glass knives (Ultramikrotome System, 2128 Ultratome®, LKB, Bromma, Sweden) and mounted on uncoated glass slides. Toluidine blue staining was then performed to further enhance the myelin staining (239). For quantitative analysis, those samples were chosen that were obtained from animals with electrodiagnostically proved reinnervation of the tibialis anterior muscle 12 weeks after surgery.

In Chapter X, immediately after the harvest, both reconstructed nerves and healthy contralateral nerves were subjected to *in-situ* fixation by immersing in 4% (v/v) paraformaldehyde. The nerve was then harvested and processed as described previously (240). The explant was embedded in epoxy resin and 1 µm thick sections (semithin) were obtained and stained with osmium tetroxide following by 1 % (v/v) toluidine blue.

IV-8. STATISTICAL ANALYSIS

GraphPad Prism 5.0 software (GraphPad Software, La Jolla, CA, USA) was used to perform the statistical analysis in all chapters of this thesis. Statistical significance was set to *p<0.05, **p<0.01, ***p<0.001.

In Chapter V, all the performed tests were conducted in triplicate and the obtained data points are presented as mean ± standard deviation (SD). One-way analysis of variance (ANOVA) was used to establish statistical differences between the different DA of chitosan membranes.

In Chapter VI, all the numerical results were presented as mean ± SD. At least 3 specimens were used in each condition. For AFM data analysis, Two-tailed Mann Whitney Test was used. Results from *in*

in vitro tests were analyzed for normality of data distribution by the Shapiro-Wilk normality test followed by Kruskal Wallis test in order to compare the results from the different groups.

In **Chapter VII**, all quantitative physicochemical and biological *in vitro* experiments were run in triplicates, and the results are expressed as the mean \pm SD. Regarding the Alamar Blue assay, normality of the data distribution was tested by using the Shapiro–Wilk normality test. Afterwards, a Kruskal–Wallis test was performed in order to compare the different groups, followed by Dunn’s multiple comparison test. No statistical analysis was performed on the data obtained during functional evaluation of nerve recovery since $n \leq 3$ of the NGC groups demonstrated functional recovery and the numbers were too few for statistical analysis. The results of the morphometric analysis are given in terms of the mean \pm SD for healthy nerve samples, AUTOG and NGC25:75, while for less than 3 animals per group (NGC50:50) the single values are presented.

In **Chapter VIII** and **IX**, all the numerical results (mechanical analysis and molecular permeability assay) were presented as mean \pm SD. At least three specimens were used in each condition. For biological assays (quantitative and qualitative viability evaluation and *in vitro* cellular permeability assay), three independent experiments were performed, and three samples were analyzed per group in each culturing time. First, a Shapiro-Wilk test was used to ascertain about the data normality. Subsequently, a Kruskal-Wallis test was performed followed by Dunn’s multiple comparison test. For the analysis of Tensile Modulus results, a Two-tailed Mann Whitney Test was used.

In **Chapter X**, numerical data was represented as mean \pm SD. At least 3 specimens were used in each condition. For ELISA quantification analysis, a Shapiro-Wilk test was used to ascertain about the data normality. Subsequently, a Kruskal-Wallis test was performed followed by Dunn's Multiple comparison test. The biological experiments were repeated three independent times. For *in vitro* and *in vivo* image analysis, a Two-tailed Mann Whitney Test was used.

IV-9. REFERENCES

1. O'Brien FJ. Biomaterials & scaffolds for tissue engineering. *Materials Today*. 2011;14(3):88-95.
2. Lee EJ, Kasper FK, Mikos AG. Biomaterials for tissue engineering. *Annals of biomedical engineering*. 2014;42(2):323-37.
3. Jayakumar R, Chennazhi KP, Srinivasan S, Nair SV, Furuike T, Tamura H. Chitin scaffolds in tissue engineering. *International journal of molecular sciences*. 2011;12(3):1876-87.
4. Yang T-L. Chitin-based materials in tissue engineering: applications in soft tissue and epithelial organ. *International journal of molecular sciences*. 2011;12(3):1936-63.

5. Raafat D, Sahl H-G. Chitosan and its antimicrobial potential—a critical literature survey. *Microbial biotechnology*. 2009;2(2):186-201.
6. Ahsan SM, Thomas M, Reddy KK, Sooraparaju SG, Asthana A, Bhatnagar I. Chitosan as biomaterial in drug delivery and tissue engineering. *International journal of biological macromolecules*. 2018;110:97-109.
7. Shahidi F, Abuzaytoun R. Chitin, Chitosan, and Co-Products: Chemistry, Production, Applications, and Health Effects. *Advances in Food and Nutrition Research*. 49: Academic Press; 2005. p. 93-135.
8. Islam S, Bhuiyan MAR, Islam MN. Chitin and Chitosan: Structure, Properties and Applications in Biomedical Engineering. *Journal of Polymers and the Environment*. 2017;25(3):854-66.
9. Roberts GAF. Solubility and Solution Behaviour of Chitin and Chitosan. *Chitin Chemistry*. London: Macmillan Education UK; 1992. p. 274-329.
10. Chatelet C, Damour O, Domard A. Influence of the degree of acetylation on some biological properties of chitosan films. *Biomaterials*. 2001;22(3):261-8.
11. Lizardi-Mendoza J, Argüelles Monal WM, Goycoolea Valencia FM. Chapter 1 - Chemical Characteristics and Functional Properties of Chitosan. In: Bautista-Baños S, Romanazzi G, Jiménez-Aparicio A, editors. *Chitosan in the Preservation of Agricultural Commodities*. San Diego: Academic Press; 2016. p. 3-31.
12. Dos Santos ZM, Caroni AL, Pereira MR, da Silva DR, Fonseca JL. Determination of deacetylation degree of chitosan: a comparison between conductometric titration and CHN elemental analysis. *Carbohydrate research*. 2009;344(18):2591-5.
13. Yin R, He J, Bai M, Huang C, Wang K, Zhang H, et al. Engineering synthetic artificial pancreas using chitosan hydrogels integrated with glucose-responsive microspheres for insulin delivery. *Materials science & engineering C, Materials for biological applications*. 2019;96:374-82.
14. VandeVord PJ, Matthew HW, DeSilva SP, Mayton L, Wu B, Wooley PH. Evaluation of the biocompatibility of a chitosan scaffold in mice. *Journal of biomedical materials research*. 2002;59(3):585-90.
15. Yan J, Chen R, Zhang H, Bryers JD. Injectable Biodegradable Chitosan-Alginate 3D Porous Gel Scaffold for mRNA Vaccine Delivery. *Macromolecular bioscience*. 2019;19(2):e1800242.
16. Luo Y, Wang Q. Recent development of chitosan-based polyelectrolyte complexes with natural polysaccharides for drug delivery. *International journal of biological macromolecules*. 2014;64C:353-67.
17. Cho MH, Kim KS, Ahn HH, Kim MS, Kim SH, Khang G, et al. Chitosan gel as an in situ-forming scaffold for rat bone marrow mesenchymal stem cells in vivo. *Tissue Eng Part A*. 2008;14(6):1099-108.
18. Ren D, Yi H, Wang W, Ma X. The enzymatic degradation and swelling properties of chitosan matrices with different degrees of N-acetylation. *Carbohydr Res*. 2005;340(15):2403-10.
19. Zheng L-Y, Zhu J-F. Study on antimicrobial activity of chitosan with different molecular weights. *Carbohydr Polym*. 2003;54(4):527-30.
20. Chatterjee S, Guha AK. A study on biochemical changes during cultivation of *Rhizopus oryzae* in deproteinized whey medium in relation to chitosan production. *Lett Appl Microbiol*. 2014;59(2):155-60.
21. Ignatova M, Kalinov K, Manolova N, Toshkova R, Rashkov I, Alexandrov M. Quaternized chitosan-coated nanofibrous implants loaded with gossypol prepared by electrospinning and their efficacy against Graffi myeloid tumor. *J Biomater Sci Polym Ed*. 2014;25(3):287-306.
22. Xu X, Li Y, Shen Y, Guo S. Synthesis and in vitro cellular evaluation of novel anti-tumor norcantharidin-conjugated chitosan derivatives. *International journal of biological macromolecules*. 2013;62:418-25.
23. Fu Y, Xiao C. A facile physical approach to make chitosan soluble in acid-free water. *International journal of biological macromolecules*. 2017;103:575-80.
24. Venkatesan J, Anil S, Kim SK, Shim MS. Chitosan as a vehicle for growth factor delivery: Various preparations and their applications in bone tissue regeneration. *International journal of biological macromolecules*. 2017;104(Pt B):1383-97.
25. Masuoka K, Ishihara M, Asazuma T, Hattori H, Matsui T, Takase B, et al. The interaction of chitosan with fibroblast growth factor-2 and its protection from inactivation. *Biomaterials*. 2005;26(16):3277-84.
26. Mi FL, Shyu SS, Peng CK, Wu YB, Sung HW, Wang PS, et al. Fabrication of chondroitin sulfate-chitosan composite artificial extracellular matrix for stabilization of fibroblast growth factor. *Journal of biomedical materials research Part A*. 2006;76(1):1-15.
27. Lv S, Liu J, Zhou Q, Huang L, Sun T. Synthesis of Modified Chitosan Superplasticizer by Amidation and Sulfonation and Its Application Performance and Working Mechanism. *Industrial & Engineering Chemistry Research*. 2014;53(10):3908-16.
28. Ali A, Ahmed S. A review on chitosan and its nanocomposites in drug delivery. *International Journal of Biological Macromolecules*. 2018;109:273-86.
29. Hamedi H, Moradi S, Hudson SM, Tonelli AE. Chitosan based hydrogels and their applications for drug delivery in wound dressings: A review. *Carbohydrate Polymers*. 2018;199:445-60.

30. Cui X, Guan X, Zhong S, Chen J, Zhu H, Li Z, et al. Multi-stimuli responsive smart chitosan-based microcapsules for targeted drug delivery and triggered drug release. *Ultrasonics sonochemistry*. 2017;38:145-53.
31. Marques Neto JdO, Bellato CR, Milagres JL, Pessoa KD, Alvarenga ESd. Preparation and evaluation of chitosan beads immobilized with Iron(III) for the removal of As(III) and As(V) from water. *Journal of the Brazilian Chemical Society*. 2013;24:121-32.
32. Ribeiro MC, Corrêa VLR, da Silva FKL, de Oliveira Neto JR, Casas AA, de Menezes LB, et al. Improving peptide quantification in chitosan nanoparticles. *International Journal of Biological Macromolecules*. 2018;119:32-6.
33. Cui L, Gao S, Song X, Huang L, Dong H, Liu J, et al. Preparation and characterization of chitosan membranes. *RSC Advances*. 2018;8(50):28433-9.
34. Xu Y, Xia D, Han J, Yuan S, Lin H, Zhao C. Design and fabrication of porous chitosan scaffolds with tunable structures and mechanical properties. *Carbohydrate Polymers*. 2017;177:210-6.
35. Albanna MZ, Bou-Akl TH, Blowytsky O, Walters HL, Matthew HWT. Chitosan fibers with improved biological and mechanical properties for tissue engineering applications. *Journal of the Mechanical Behavior of Biomedical Materials*. 2013;20:217-26.
36. Elsabee MZ, Naguib HF, Morsi RE. Chitosan based nanofibers, review. *Materials Science and Engineering: C*. 2012;32(7):1711-26.
37. Oliveira PN, Montebault A, Sudre G, Alcouffe P, Marcon L, Gehan H, et al. Self-crosslinked fibrous collagen/chitosan blends: Processing, properties evaluation and monitoring of degradation by bi-fluorescence imaging. *International Journal of Biological Macromolecules*. 2019.
38. Lahiji A, Sohrabi A, Hungerford DS, Frondoza CG. Chitosan supports the expression of extracellular matrix proteins in human osteoblasts and chondrocytes. *Journal of biomedical materials research*. 2000;51(4):586-95.
39. Saekhor K, Udomsinprasert W, Honsawek S, Tachaboonyakiat W. Preparation of an injectable modified chitosan-based hydrogel approaching for bone tissue engineering. *International Journal of Biological Macromolecules*. 2019;123:167-73.
40. Cardoso AM, de Oliveira EG, Coradini K, Bruinsmann FA, Aguirre T, Lorenzoni R, et al. Chitosan hydrogels containing nanoencapsulated phenytoin for cutaneous use: Skin permeation/penetration and efficacy in wound healing. *Materials Science and Engineering: C*. 2019;96:205-17.
41. Mohan N, Mohanan PV, Sabareeswaran A, Nair P. Chitosan-hyaluronic acid hydrogel for cartilage repair. *International Journal of Biological Macromolecules*. 2017;104:1936-45.
42. Chen E, Yang L, Ye C, Zhang W, Ran J, Xue D, et al. An asymmetric chitosan scaffold for tendon tissue engineering: In vitro and in vivo evaluation with rat tendon stem/progenitor cells. *Acta Biomaterialia*. 2018;73:377-87.
43. Zahir-Jouzani F, Mahbod M, Soleimani M, Vakhshiteh F, Arefian E, Shahosseini S, et al. Chitosan and thiolated chitosan: Novel therapeutic approach for preventing corneal haze after chemical injuries. *Carbohydrate Polymers*. 2018;179:42-9.
44. Oudega M, Hao P, Shang J, Haggerty AE, Wang Z, Sun J, et al. Validation study of neurotrophin-3-releasing chitosan facilitation of neural tissue generation in the severely injured adult rat spinal cord. *Experimental Neurology*. 2019;312:51-62.
45. Jiang Z, Song Y, Qiao J, Yang Y, Zhang W, Liu W, et al. Rat sciatic nerve regeneration across a 10-mm defect bridged by a chitin/CM-chitosan artificial nerve graft. *International Journal of Biological Macromolecules*. 2019;129:997-1005.
46. Takeuchi I, Kamiki Y, Makino K. Therapeutic efficacy of rebamipide-loaded PLGA nanoparticles coated with chitosan in a mouse model for oral mucositis induced by cancer chemotherapy. *Colloids and Surfaces B: Biointerfaces*. 2018;167:468-73.
47. Badhe RV, Bijukumar D, Chejara DR, Mabrouk M, Choonara YE, Kumar P, et al. A composite chitosan-gelatin bi-layered, biomimetic macroporous scaffold for blood vessel tissue engineering. *Carbohydrate Polymers*. 2017;157:1215-25.
48. Azizian S, Hadjizadeh A, Niknejad H. Chitosan-gelatin porous scaffold incorporated with Chitosan nanoparticles for growth factor delivery in tissue engineering. *Carbohydrate Polymers*. 2018;202:315-22.
49. Intini C, Elviri L, Cabral J, Mros S, Bergonzi C, Bianchera A, et al. 3D-printed chitosan-based scaffolds: An in vitro study of human skin cell growth and an in-vivo wound healing evaluation in experimental diabetes in rats. *Carbohydrate Polymers*. 2018;199:593-602.
50. Carvalho CR, Lopez-Cebral R, Silva-Correia J, Silva JM, Mano JF, Silva TH, et al. Investigation of cell adhesion in chitosan membranes for peripheral nerve regeneration. *Materials science & engineering C, Materials for biological applications*. 2017;71:1122-34.
51. Bajaj IB, Saudagar PS, Singhal RS, Pandey A. Statistical approach to optimization of fermentative production of gellan gum from *Sphingomonas paucimobilis* ATCC 31461. *J Biosci Bioeng*. 2006;102(3):150-6.
52. Xu Z, Li Z, Jiang S, Bratlie KM. Chemically Modified Gellan Gum Hydrogels with Tunable Properties for Use as Tissue Engineering Scaffolds. *ACS Omega*. 2018;3(6):6998-7007.

53. Silva-Correia J, Oliveira JM, Caridade SG, Oliveira JT, Sousa RA, Mano JF, et al. Gellan gum-based hydrogels for intervertebral disc tissue-engineering applications. *Journal of tissue engineering and regenerative medicine*. 2011;5(6):e97-107.
54. Koivisto JT, Joki T, Parraga JE, Paakkonen R, Yla-Outinen L, Salonen L, et al. Bioamine-crosslinked gellan gum hydrogel for neural tissue engineering. *Biomedical materials (Bristol, England)*. 2017;12(2):025014.
55. Gulati AK. Evaluation of acellular and cellular nerve grafts in repair of rat peripheral nerve. *J Neurosurg*. 1988;68(1):117-23.
56. Jindal N, Singh Khattar J. Chapter 4 - Microbial Polysaccharides in Food Industry. In: Grumezescu AM, Holban AM, editors. *Biopolymers for Food Design*: Academic Press; 2018. p. 95-123.
57. Stevens LR, Gilmore KJ, Wallace GG, in het Panhuis M. Tissue engineering with gellan gum. *Biomaterials Science*. 2016;4(9):1276-90.
58. Mao R, Tang J, Swanson BG. Water holding capacity and microstructure of gellan gels. *Carbohydrate Polymers*. 2001;46(4):365-71.
59. Silva-Correia J, Miranda-Goncalves V, Salgado AJ, Sousa N, Oliveira JM, Reis RM, et al. Angiogenic potential of gellan-gum-based hydrogels for application in nucleus pulposus regeneration: in vivo study. *Tissue engineering Part A*. 2012;18(11-12):1203-12.
60. Carvalho CR, Wrobel S, Meyer C, Brandenberger C, Cengiz IF, Lopez-Cebal R, et al. Gellan Gum-based luminal fillers for peripheral nerve regeneration: an in vivo study in the rat sciatic nerve repair model. *Biomater Sci*. 2018;6(5):1059-75.
61. da Silva LP, Cerqueira MT, Sousa RA, Reis RL, Correlo VM, Marques AP. Engineering cell-adhesive gellan gum spongy-like hydrogels for regenerative medicine purposes. *Acta biomaterialia*. 2014;10(11):4787-97.
62. Vieira S, da Silva Morais A, Garet E, Silva-Correia J, Reis RL, González-Fernández Á, et al. Self-mineralizing Ca-enriched methacrylated gellan gum beads for bone tissue engineering. *Acta Biomaterialia*. 2019.
63. Bonifacio MA, Cometa S, Cochis A, Gentile P, Ferreira AM, Azzimonti B, et al. Antibacterial effectiveness meets improved mechanical properties: Manuka honey/gellan gum composite hydrogels for cartilage repair. *Carbohydrate Polymers*. 2018;198:462-72.
64. Khang G, Lee SK, Kim HN, Silva-Correia J, Gomes ME, Viegas CA, et al. Biological evaluation of intervertebral disc cells in different formulations of gellan gum-based hydrogels. *Journal of tissue engineering and regenerative medicine*. 2015;9(3):265-75.
65. Natori T, Fujiyoshi M, Uchida M, Abe N, Kanaki T, Fukumoto Y, et al. Growth arrest of vascular smooth muscle cells in suspension culture using low-acyl gellan gum. *In vitro cellular & developmental biology Animal*. 2017;53(3):191-8.
66. Ismail NA, Mat Amin KA, Razali MH. Novel gellan gum incorporated TiO₂ nanotubes film for skin tissue engineering. *Materials Letters*. 2018;228:116-20.
67. Gomes ED, Mendes SS, Leite-Almeida H, Gimble JM, Tam RY, Shoichet MS, et al. Combination of a peptide-modified gellan gum hydrogel with cell therapy in a lumbar spinal cord injury animal model. *Biomaterials*. 2016;105:38-51.
68. Berti FV, Srisuk P, da Silva LP, Marques AP, Reis RL, Correlo VM. (*) Synthesis and Characterization of Electroactive Gellan Gum Spongy-Like Hydrogels for Skeletal Muscle Tissue Engineering Applications. *Tissue Eng Part A*. 2017;23(17-18):968-79.
69. Chang SJ, Huang Y-T, Yang S-C, Kuo S-M, Lee M-W. In vitro properties of gellan gum sponge as the dental filling to maintain alveolar space. *Carbohydrate Polymers*. 2012;88(2):684-9.
70. Pacelli S, Paolicelli P, Dreesen I, Kobayashi S, Vitalone A, Casadei MA. Injectable and photocross-linkable gels based on gellan gum methacrylate: A new tool for biomedical application. *International journal of biological macromolecules*. 2015;72:1335-42.
71. Wu D, Yu Y, Tan J, Huang L, Luo B, Lu L, et al. 3D bioprinting of gellan gum and poly (ethylene glycol) diacrylate based hydrogels to produce human-scale constructs with high-fidelity. *Materials & Design*. 2018;160:486-95.
72. Coutinho DF, Sant SV, Shin H, Oliveira JT, Gomes ME, Neves NM, et al. Modified Gellan Gum hydrogels with tunable physical and mechanical properties. *Biomaterials*. 2010;31(29):7494-502.
73. Yang M, Shuai Y, He W, Min S, Zhu L. Preparation of porous scaffolds from silk fibroin extracted from the silk gland of *Bombyx mori* (B. mori). *Int J Mol Sci*. 2012;13(6):7762-75.
74. Thilagavathi G, Viju S. 11 - Silk as a suture material. In: Basu A, editor. *Advances in Silk Science and Technology*: Woodhead Publishing; 2015. p. 219-32.
75. Xie H, Wang J, He Y, Gu Z, Xu J, Li L, et al. Biocompatibility and safety evaluation of a silk fibroin-doped calcium polyphosphate scaffold copolymer in vitro and in vivo. *RSC advances*. 2017;7(73):46036-44.
76. Cao Y, Wang B. Biodegradation of silk biomaterials. *International journal of molecular sciences*. 2009;10(4):1514-24.
77. Koh L-D, Cheng Y, Teng C-P, Khin Y-W, Loh X-J, Tee S-Y, et al. Structures, mechanical properties and applications of silk fibroin materials. *Prog Polym Sci*. 2015;46:86-110.

78. Ghnenis AB, Czaikowski RE, Zhang ZJ, Bushman JS. Toluidine Blue Staining of Resin-Embedded Sections for Evaluation of Peripheral Nerve Morphology. *Journal of visualized experiments : JoVE*. 2018(137).
79. Melke J, Midha S, Ghosh S, Ito K, Hofmann S. Silk fibroin as biomaterial for bone tissue engineering. *Acta biomaterialia*. 2016;31:1-16.
80. Valluzzi R, Winkler S, Wilson D, Kaplan DL. Silk: molecular organization and control of assembly. *Philosophical transactions of the Royal Society of London Series B, Biological sciences*. 2002;357(1418):165-7.
81. Fu C, Shao Z, Fritz V. Animal silks: their structures, properties and artificial production. *Chemical Communications*. 2009(43):6515-29.
82. Du N, Yang Z, Liu XY, Li Y, Xu HY. Structural Origin of the Strain-Hardening of Spider Silk. *Advanced Functional Materials*. 2011;21(4):772-8.
83. Mandal BB, Priya AS, Kundu SC. Novel silk sericin/gelatin 3-D scaffolds and 2-D films: Fabrication and characterization for potential tissue engineering applications. *Acta biomaterialia*. 2009;5(8):3007-20.
84. Zeng C, Yang Q, Zhu M, Du L, Zhang J, Ma X, et al. Silk fibroin porous scaffolds for nucleus pulposus tissue engineering. *Mater Sci Eng C Mater Biol Appl*. 2014;37:232-40.
85. Panda D, Konar S, Bajpai SK, Arockiarajan A. Synthesis and viscoelastic characterization of microstructurally aligned Silk fibroin sponges. *J Mech Behav Biomed Mater*. 2017;71:362-71.
86. Jackman SL, Chen CH, Chettih SN, Neufeld SQ, Drew IR, Agba CK, et al. Silk Fibroin Films Facilitate Single-Step Targeted Expression of Optogenetic Proteins. *Cell Rep*. 2018;22(12):3351-61.
87. Carvalho CR, Costa JB, da Silva Morais A, Lopez-Cebral R, Silva-Correia J, Reis RL, et al. Tunable Enzymatically Cross-Linked Silk Fibroin Tubular Conduits for Guided Tissue Regeneration. *Advanced healthcare materials*. 2018;7(17):e1800186.
88. Fang Y, Xu L, Wang M. High-Throughput Preparation of Silk Fibroin Nanofibers by Modified Bubble-Electrospinning. *Nanomaterials (Basel, Switzerland)*. 2018;8(7):471.
89. Zhang X, Jia C, Qiao X, Liu T, Sun K. Silk fibroin microfibers and chitosan modified poly (glycerol sebacate) composite scaffolds for skin tissue engineering. *Polymer Testing*. 2017;62:88-95.
90. Ribeiro VP, Silva-Correia J, Gonçalves C, Pina S, Radhouani H, Montonen T, et al. Rapidly responsive silk fibroin hydrogels as an artificial matrix for the programmed tumor cells death. *PloS one*. 2018;13(4):e0194441-e.
91. Ribeiro VP, Silva-Correia J, Nascimento AI, da Silva Morais A, Marques AP, Ribeiro AS, et al. Silk-based anisotropical 3D biotextiles for bone regeneration. *Biomaterials*. 2017;123:92-106.
92. Farokhi M, Mottaghitlab F, Samani S, Shokrgozar MA, Kundu SC, Reis RL, et al. Silk fibroin/hydroxyapatite composites for bone tissue engineering. *Biotechnology Advances*. 2018;36(1):68-91.
93. Singh BN, Pramanik K. Fabrication and evaluation of non-mulberry silk fibroin fiber reinforced chitosan based porous composite scaffold for cartilage tissue engineering. *Tissue and Cell*. 2018;55:83-90.
94. Du J, Zhu T, Yu H, Zhu J, Sun C, Wang J, et al. Potential applications of three-dimensional structure of silk fibroin/poly(ester-urethane) urea nanofibrous scaffold in heart valve tissue engineering. *Applied Surface Science*. 2018;447:269-78.
95. Yao D, Qian Z, Zhou J, Peng G, Zhou G, Liu H, et al. Facile incorporation of REDV into porous silk fibroin scaffolds for enhancing vascularization of thick tissues. *Materials Science and Engineering: C*. 2018;93:96-105.
96. Yan S, Wang Q, Tariq Z, You R, Li X, Li M, et al. Facile preparation of bioactive silk fibroin/hyaluronic acid hydrogels. *International journal of biological macromolecules*. 2018;118:775-82.
97. Afjeh-Dana E, Naserzadeh P, Nazari H, Mottaghitlab F, Shabani R, Aminii N, et al. Gold nanorods reinforced silk fibroin nanocomposite for peripheral nerve tissue engineering applications. *International journal of biological macromolecules*. 2019;129:1034-9.
98. Jindal SK, Kiamehr M, Sun W, Yang XB. 15 - Silk scaffolds for dental tissue engineering. In: Kundu SC, editor. *Silk Biomaterials for Tissue Engineering and Regenerative Medicine*: Woodhead Publishing; 2014. p. 403-28.
99. Crivelli B, Bari E, Perteghella S, Catenacci L, Sorrenti M, Mocchi M, et al. Silk fibroin nanoparticles for celecoxib and curcumin delivery: ROS-scavenging and anti-inflammatory activities in an in vitro model of osteoarthritis. *European Journal of Pharmaceutics and Biopharmaceutics*. 2019;137:37-45.
100. Costa JB, Silva-Correia J, Oliveira JM, Reis RL. Fast Setting Silk Fibroin Bioink for Bioprinting of Patient-Specific Memory-Shape Implants. *Advanced healthcare materials*. 2017;6(22).
101. Mauney JR, Cannon GM, Lovett ML, Gong EM, Di Vizio D, Gomez P, et al. Evaluation of gel spun silk-based biomaterials in a murine model of bladder augmentation. *Biomaterials*. 2011;32(3):808-18.
102. Nazarov R, Jin H-J, Kaplan DL. Porous 3-D scaffolds from regenerated silk fibroin. *Biomacromolecules*. 2004;5(3):718-26.
103. Silva SS, Popa EG, Gomes ME, Oliveira MB, Nayak S, Subia B, et al. Silk hydrogels from non-mulberry and mulberry silkworm cocoons processed with ionic liquids. *Acta biomaterialia*. 2013;9(11):8972-82.

104. Li M, Tao W, Lu S, Kuga S. Compliant film of regenerated *Antheraea pernyi* silk fibroin by chemical crosslinking. *International journal of biological macromolecules*. 2003;32(3):159-63.
105. Chen X, Shao Z, Knight DP, Vollrath F. Conformation transition kinetics of *Bombyx mori* silk protein. *Proteins: Structure, Function, and Bioinformatics*. 2007;68(1):223-31.
106. Yan L-P, Oliveira JM, Oliveira AL, Caridade SG, Mano JF, Reis RL. Macro/microporous silk fibroin scaffolds with potential for articular cartilage and meniscus tissue engineering applications. *Acta biomaterialia*. 2012;8(1):289-301.
107. Yan LP, Oliveira JM, Oliveira AL, Reis RL. Core-shell silk hydrogels with spatially tuned conformations as drug-delivery system. *Journal of tissue engineering and regenerative medicine*. 2016.
108. Fini M, Motta A, Torricelli P, Giavaresi G, Aldini NN, Tschon M, et al. The healing of confined critical size cancellous defects in the presence of silk fibroin hydrogel. *Biomaterials*. 2005;26(17):3527-36.
109. Wang X, Kluge JA, Leisk GG, Kaplan DL. Sonication-induced gelation of silk fibroin for cell encapsulation. *Biomaterials*. 2008;29(8):1054-64.
110. Yucel T, Cebe P, Kaplan DL. Vortex-induced injectable silk fibroin hydrogels. *Biophysical journal*. 2009;97(7):2044-50.
111. Karageorgiou V, Tomkins M, Fajardo R, Meinel L, Snyder B, Wade K, et al. Porous silk fibroin 3-D scaffolds for delivery of bone morphogenetic protein-2 in vitro and in vivo. *Journal of Biomedical Materials Research Part A*. 2006;78A(2):324-34.
112. Moll R, Divo M, Langbein L. The human keratins: biology and pathology. *Histochem Cell Biol*. 2008;129(6):705-33.
113. Sow WT, Lui YS, Ng KW. Electrospun human keratin matrices as templates for tissue regeneration. *Nanomedicine (London, England)*. 2013;8(4):531-41.
114. Rouse JG, Van Dyke ME. A Review of Keratin-Based Biomaterials for Biomedical Applications. *Materials*. 2010;3(2):999-1014.
115. Sharma S, Gupta A. Sustainable Management of Keratin Waste Biomass: Applications and Future Perspectives. *Brazilian Archives of Biology and Technology*. 2016;59.
116. Tachibana A, Furuta Y, Takeshima H, Tanabe T, Yamauchi K. Fabrication of wool keratin sponge scaffolds for long-term cell cultivation. *Journal of biotechnology*. 2002;93(2):165-70.
117. Strnad P, Usachov V, Debes C, Grater F, Parry DA, Omary MB. Unique amino acid signatures that are evolutionarily conserved distinguish simple-type, epidermal and hair keratins. *J Cell Sci*. 2011;124(Pt 24):4221-32.
118. Dhouailly D, Xu C, Manabe M, Schermer A, Sun TT. Expression of hair-related keratins in a soft epithelium: subpopulations of human and mouse dorsal tongue keratinocytes express keratin markers for hair-, skin- and esophageal-types of differentiation. *Exp Cell Res*. 1989;181(1):141-58.
119. Tan HB, Wang FY, Ding W, Zhang Y, Ding J, Cai DX, et al. Fabrication and Evaluation of Porous Keratin/chitosan (KCS) Scaffolds for Effectively Accelerating Wound Healing. *Biomedical and Environmental Sciences*. 2015;28(3):178-89.
120. Navarro J, Swayambunathan J, Lerman M, Santoro M, Fisher JP. Development of keratin-based membranes for potential use in skin repair. *Acta biomaterialia*. 2019;83:177-88.
121. Yue K, Liu Y, Byambaa B, Singh V, Liu W, Li X, et al. Visible light crosslinkable human hair keratin hydrogels. *Bioeng Transl Med*. 2018;3(1):37-48.
122. Goto H, Sawada K, Fujisato T. Preparation and evaluation of keratin scaffold derived from wool and human hair for cell culture and tissue engineering. *Frontiers in Bioengineering and Biotechnology*.
123. Rippa AL, Vorotelyak EA, Vasiliev AV, Terskikh VV. The role of integrins in the development and homeostasis of the epidermis and skin appendages. *Acta Naturae*. 2013;5(4):22-33.
124. Reichl S. Films based on human hair keratin as substrates for cell culture and tissue engineering. *Biomaterials*. 2009;30(36):6854-66.
125. Lee H, Noh K, Lee SC, Kwon I-K, Han D-W, Lee I-S, et al. Human hair keratin and its-based biomaterials for biomedical applications. *Tissue Engineering and Regenerative Medicine*. 2014;11(4):255-65.
126. Masukawa Y, Narita H, Imokawa G. Characterization of the lipid composition at the proximal root regions of human hair. *J Cosmet Sci*. 2005;56(1):1-16.
127. Hwang J, Mehrani T, Millar SE, Morasso MI. Dlx3 is a crucial regulator of hair follicle differentiation and cycling. *Development*. 2008;135(18):3149-59.
128. Sierpinski P, Garrett J, Ma J, Apel P, Klorig D, Smith T, et al. The use of keratin biomaterials derived from human hair for the promotion of rapid regeneration of peripheral nerves. *Biomaterials*. 2008;29(1):118-28.
129. Pace LA, Plate JF, Smith TL, Van Dyke ME. The effect of human hair keratin hydrogel on early cellular response to sciatic nerve injury in a rat model. *Biomaterials*. 2013;34(24):5907-14.
130. Hill PS, Apel PJ, Barnwell J, Smith T, Koman LA, Atala A, et al. Repair of peripheral nerve defects in rabbits using keratin hydrogel scaffolds. *Tissue Eng Part A*. 2011;17(11-12):1499-505.

131. Pace LA, Plate JF, Mannava S, Barnwell JC, Koman LA, Li Z, et al. A human hair keratin hydrogel scaffold enhances median nerve regeneration in nonhuman primates: an electrophysiological and histological study. *Tissue Eng Part A*. 2014;20(3-4):507-17.
132. Konop M, Sulejczak D, Czuwara J, Kosson P, Misicka A, Lipkowski AW, et al. The role of allogenic keratin-derived dressing in wound healing in a mouse model. *Wound Repair Regen*. 2017;25(1):62-74.
133. Zhao X, Lui YS, Choo KKC, Sow WT, Huang CL, Ng KW, et al. Calcium phosphate coated Keratin-PCL scaffolds for potential bone tissue regeneration. *Mater Sci Eng C Mater Biol Appl*. 2015;49:746-53.
134. Zabarsky Z, Marquez-Lara A, Luo TD, Dyke MV, Smith TL. The Effect of Keratin on Spinal Cord Injury Recovery. *The FASEB Journal*. 2016;30(1_supplement):993.10-10.
135. Lin YC, Ramadan M, Van Dyke M, Kokai LE, Philips BJ, Rubin JP, et al. Keratin gel filler for peripheral nerve repair in a rodent sciatic nerve injury model. *Plastic and reconstructive surgery*. 2012;129(1):67-78.
136. Cheng Z, Chen X, Zhai D, Gao F, Guo T, Li W, et al. Development of keratin nanoparticles for controlled gastric mucoadhesion and drug release. *Journal of Nanobiotechnology*. 2018;16(1):24.
137. Rahmany MB, Hantgan RR, Van Dyke M. A mechanistic investigation of the effect of keratin-based hemostatic agents on coagulation. *Biomaterials*. 2013;34(10):2492-500.
138. Borrelli M, Joepen N, Reichl S, Finis D, Schoppe M, Geerling G, et al. Keratin films for ocular surface reconstruction: evaluation of biocompatibility in an in-vivo model. *Biomaterials*. 2015;42:112-20.
139. Xu H, Cai S, Xu L, Yang Y. Water-stable three-dimensional ultrafine fibrous scaffolds from keratin for cartilage tissue engineering. *Langmuir*. 2014;30(28):8461-70.
140. Yen K-C, Chen C-Y, Huang J-Y, Kuo W-T, Lin F-H. Fabrication of keratin/fibroin membranes by electrospinning for vascular tissue engineering. *Journal of Materials Chemistry B*. 2016;4(2):237-44.
141. Ramburrin P, Kumar P, Choonara YE, Bijukumar D, du Toit LC, Pillay V. A review of bioactive release from nerve conduits as a neurotherapeutic strategy for neuronal growth in peripheral nerve injury. *Biomed Res Int*. 2014;2014:132350-.
142. Deister C, Schmidt CE. Optimizing neurotrophic factor combinations for neurite outgrowth. *Journal of neural engineering*. 2006;3(2):172-9.
143. Peleshok J, Saragovi HU. Functional mimetics of neurotrophins and their receptors. *Biochemical Society transactions*. 2006;34(Pt 4):612-7.
144. Rickert U, Grampp S, Wilms H, Spreu J, Knerlich-Lukoschus F, Held-Feindt J, et al. Glial Cell Line-Derived Neurotrophic Factor Family Members Reduce Microglial Activation via Inhibiting p38MAPKs-Mediated Inflammatory Responses. *Journal of neurodegenerative diseases*. 2014;2014:369468-.
145. Boyd JG, Gordon T. Neurotrophic factors and their receptors in axonal regeneration and functional recovery after peripheral nerve injury. *Molecular Neurobiology*. 2003;27(3):277-323.
146. Shakhbazov A, Kawasoe J, Hoyng SA, Kumar R, van Minnen J, Verhaagen J, et al. Early regenerative effects of NGF-transduced Schwann cells in peripheral nerve repair. *Molecular and Cellular Neuroscience*. 2012;50(1):103-12.
147. Cheng S, Tereshchenko J, Zimmer V, Vachey G, Pythoud C, Rey M, et al. Therapeutic efficacy of regulable GDNF expression for Huntington's and Parkinson's disease by a high-induction, background-free "GeneSwitch" vector. *Experimental neurology*. 2018;309:79-90.
148. Ding Z, Xu W, Zhang J, Zou W, Guo Q, Huang C, et al. Normalizing GDNF expression in the spinal cord alleviates cutaneous hyperalgesia but not ongoing pain in a rat model of bone cancer pain. *International journal of cancer*. 2017;140(2):411-22.
149. Höke A. Augmenting glial cell-line derived neurotrophic factor signaling to treat painful neuropathies. *Proceedings of the National Academy of Sciences of the United States of America*. 2014;111(6):2060-1.
150. Tajdaran K, Chan K, Gordon T, Borschel GH. Matrices, scaffolds, and carriers for protein and molecule delivery in peripheral nerve regeneration. *Experimental Neurology*. 2018.
151. Pfister LA, Papaloizos M, Merkle HP, Gander B. Nerve conduits and growth factor delivery in peripheral nerve repair. *Journal of the Peripheral Nervous System*. 2007;12(2):65-82.
152. Vince DG, Hunt JA, Williams DF. Quantitative assessment of the tissue response to implanted biomaterials. *Biomaterials*. 1991;12(8):731-6.
153. Nerem RM, Schutte SC. Chapter 2 - The Challenge of Imitating Nature. In: Lanza R, Langer R, Vacanti J, editors. *Principles of Tissue Engineering (Fourth Edition)*. Boston: Academic Press; 2014. p. 9-24.
154. Meek MF, Jansen K, Steendam R, van Oeveren W, van Wachem PB, van Luyn MJ. In vitro degradation and biocompatibility of poly(DL-lactide-epsilon-caprolactone) nerve guides. *Journal of biomedical materials research Part A*. 2004;68(1):43-51.
155. Rosenberg ES, Cytryn F, Guzman A, Maldonado B. The role of guided tissue regeneration and guided bone regeneration. *Annals of the Royal Australasian College of Dental Surgeons*. 1994;12:80-8.

156. Viateau V, Guillemin G, Calando Y, Logeart D, Oudina K, Sedel L, et al. Induction of a barrier membrane to facilitate reconstruction of massive segmental diaphyseal bone defects: an ovine model. *Veterinary surgery* : VS. 2006;35(5):445-52.
157. Dagum AB. Peripheral nerve regeneration, repair, and grafting. *Journal of Hand Therapy*. 1998;11(2):111-7.
158. Ruini F, Tonda-Turo C, Raimondo S, Tos P, Pugliese P, Geuna S, et al. Nerve guidance conduits based on bi-layer chitosan membranes for peripheral nerve regeneration 2016.
159. Hoffman AS. Hydrogels for biomedical applications. *Advanced drug delivery reviews*. 2012;64:18-23.
160. Bai X, Gao M, Syed S, Zhuang J, Xu X, Zhang X-Q. Bioactive hydrogels for bone regeneration. *Bioactive Materials*. 2018;3(4):401-17.
161. Tan H, Chu CR, Payne KA, Marra KG. Injectable in situ forming biodegradable chitosan–hyaluronic acid based hydrogels for cartilage tissue engineering. *Biomaterials*. 2009;30(13):2499-506.
162. Liu M, Zeng X, Ma C, Yi H, Ali Z, Mou X, et al. Injectable hydrogels for cartilage and bone tissue engineering. *Bone research*. 2017;5:17014-.
163. Kundu J, Poole-Warren LA, Martens P, Kundu SC. Silk fibroin/poly (vinyl alcohol) photocrosslinked hydrogels for delivery of macromolecular drugs. *Acta biomaterialia*. 2012;8(5):1720-9.
164. Liang H-F, Hong M-H, Ho R-M, Chung C-K, Lin Y-H, Chen C-H, et al. Novel method using a temperature-sensitive polymer (methylcellulose) to thermally gel aqueous alginate as a pH-sensitive hydrogel. *Biomacromolecules*. 2004;5(5):1917-25.
165. Teixeira LSM, Feijen J, van Blitterswijk CA, Dijkstra PJ, Karperien M. Enzyme-catalyzed crosslinkable hydrogels: emerging strategies for tissue engineering. *Biomaterials*. 2012;33(5):1281-90.
166. Wei YT, Tian WM, Yu X, Cui FZ, Hou SP, Xu QY, et al. Hyaluronic acid hydrogels with IKVAV peptides for tissue repair and axonal regeneration in an injured rat brain. *Biomedical Materials*. 2007;2(3):S142-S6.
167. Zusiak SP, Durbal R, Leach JB. Influence of cell-adhesive peptide ligands on poly(ethylene glycol) hydrogel physical, mechanical and transport properties. *Acta biomaterialia*. 2010;6(9):3404-14.
168. da Silva LP, Cerqueira MT, Sousa RA, Reis RL, Correlo VM, Marques AP. Engineering cell-adhesive gellan gum spongy-like hydrogels for regenerative medicine purposes. *Acta biomaterialia*. 2014;10(11):4787-97.
169. Kim MH, Kim BS, Lee J, Cho D, Kwon OH, Park WH. Silk fibroin/hydroxyapatite composite hydrogel induced by gamma-ray irradiation for bone tissue engineering. *Biomaterials research*. 2017;21:12-.
170. Hopkins AM, De Laporte L, Tortelli F, Spedden E, Staii C, Atherton TJ, et al. Silk Hydrogels as Soft Substrates for Neural Tissue Engineering. *Advanced Functional Materials*. 2013;23(41):5140-9.
171. Li X, Yang Y, Fan Y, Feng Q, Cui FZ, Watari F. Biocomposites reinforced by fibers or tubes as scaffolds for tissue engineering or regenerative medicine. *Journal of biomedical materials research Part A*. 2014;102(5):1580-94.
172. Mooney DJ, Breuer C, McNamara K, Vacanti JP, Langer R. Fabricating tubular devices from polymers of lactic and glycolic Acid for tissue engineering. *Tissue engineering*. 1995;1(2):107-18.
173. Jaspan VN, Hines GL. The Current Status of Tissue-Engineered Vascular Grafts. *Cardiology in review*. 2015;23(5):236-9.
174. Konofaos P, Ver Halen JP. Nerve repair by means of tubulization: past, present, future. *Journal of reconstructive microsurgery*. 2013;29(3):149-64.
175. Hiob MA, She S, Muiznieks LD, Weiss AS. Biomaterials and Modifications in the Development of Small-Diameter Vascular Grafts. *ACS Biomaterials Science & Engineering*. 2017;3(5):712-23.
176. Smith L, Xia Y, Galatz LM, Genin GM, Thomopoulos S. Tissue Engineering Strategies for the Tendon/Ligament-to-bone insertion. *Connective tissue research*. 2012;53(2):95-105.
177. Zhang C, Li Q, Tang X, Li J. [RESEARCH PROGRESS OF STRATEGIES TO AUGMENT TENDON-TO-BONE HEALING]. *Zhongguo xiu fu chong jian wai ke za zhi = Zhongguo xiufu chongjian waike zazhi = Chinese journal of reparative and reconstructive surgery*. 2015;29(7):912-6.
178. Sendul SY, Cagatay HH, Dirim B, Demir M, Yildiz AA, Acar Z, et al. Comparison of Medpor coated tear drainage tube versus silicon tear drainage tube in conjunctivodacryocystorhinostomy: problems and solutions. *TheScientificWorldJournal*. 2014;2014:164834.
179. Pushker N, Khurana S, Shrey D, Bajaj MS, Chawla B, Chandra M. Conjunctivodacryocystorhinostomy using a high-density porous polyethylene-coated tear drain tube. *International ophthalmology*. 2013;33(4):329-33.
180. Winter CC, Katiyar KS, Hernandez NS, Song YJ, Struzyna LA, Harris JP, et al. Transplantable living scaffolds comprised of micro-tissue engineered aligned astrocyte networks to facilitate central nervous system regeneration. *Acta biomaterialia*. 2016;38(Supplement C):44-58.
181. Caliar SR, Harley BA. The effect of anisotropic collagen-GAG scaffolds and growth factor supplementation on tendon cell recruitment, alignment, and metabolic activity. *Biomaterials*. 2011;32(23):5330-40.
182. Kojima K, Vacanti CA. Tissue engineering in the trachea. *Anatomical record (Hoboken, NJ : 2007)*. 2014;297(1):44-50.

183. Wang X, Zhang L, Chen Q, Hou Y, Hao Y, Wang C, et al. A Nanostructured Degradable Ureteral Stent Fabricated by Electrospinning for Upper Urinary Tract Reconstruction. *Journal of nanoscience and nanotechnology*. 2015;15(12):9899-904.
184. Widmer MS, Gupta PK, Lu L, Meszlenyi RK, Evans GR, Brandt K, et al. Manufacture of porous biodegradable polymer conduits by an extrusion process for guided tissue regeneration. *Biomaterials*. 1998;19(21):1945-55.
185. Yan LP, Silva-Correia J, Ribeiro VP, Miranda-Goncalves V, Correia C, da Silva Morais A, et al. Tumor Growth Suppression Induced by Biomimetic Silk Fibroin Hydrogels. *Scientific reports*. 2016;6:31037.
186. Yan LP, Oliveira JM, Oliveira AL, Reis RL. Core-shell silk hydrogels with spatially tuned conformations as drug-delivery system. *Journal of tissue engineering and regenerative medicine*. 2017;11(11):3168-77.
187. Chirila TV, Suzuki S, Papolla C. A comparative investigation of Bombyx mori silk fibroin hydrogels generated by chemical and enzymatic cross-linking. *Biotechnology and applied biochemistry*. 2017;64(6):771-81.
188. Qi Y, Wang H, Wei K, Yang Y, Zheng RY, Kim IS, et al. A Review of Structure Construction of Silk Fibroin Biomaterials from Single Structures to Multi-Level Structures. *Int J Mol Sci*. 2017;18(3).
189. McGill M, Coburn JM, Partlow BP, Mu X, Kaplan DL. Molecular and macro-scale analysis of enzyme-crosslinked silk hydrogels for rational biomaterial design. *Acta biomaterialia*. 2017.
190. Franca R, Mbeh DA, Samani TD, Le Tien C, Mateescu MA, Yahia L, et al. The effect of ethylene oxide sterilization on the surface chemistry and in vitro cytotoxicity of several kinds of chitosan. *Journal of biomedical materials research Part B, Applied biomaterials*. 2013;101(8):1444-55.
191. Hartrianti P, Nguyen LTH, Johaness J, Chou SM, Zhu P, Tan NS, et al. Fabrication and characterization of a novel crosslinked human keratin-alginate sponge. *Journal of tissue engineering and regenerative medicine*. 2017;11(9):2590-602.
192. Taraballi F, Wang S, Li J, Lee FY, Venkatraman SS, Birch WR, et al. Understanding the nano-topography changes and cellular influences resulting from the surface adsorption of human hair keratins. *Advanced healthcare materials*. 2012;1(4):513-9.
193. Wang S, Taraballi F, Tan LP, Ng KW. Human keratin hydrogels support fibroblast attachment and proliferation in vitro. *Cell and tissue research*. 2012;347(3):795-802.
194. Gao CH. Unique rheology of high acyl gellan gum and its potential applications in enhancement of petroleum production. *Journal of Petroleum Exploration and Production Technology*. 2016;6(4):743-7.
195. Sofia S, McCarthy MB, Gronowicz G, Kaplan DL. Functionalized silk-based biomaterials for bone formation. *Journal of Biomedical Materials Research Part A*. 2001;54(1):139-48.
196. Jin H-J, Kaplan DL. Mechanism of silk processing in insects and spiders. *Nature*. 2003;424(6952):1057-61.
197. Reichelt R. Scanning electron microscopy. *Science of microscopy*: Springer; 2007. p. 133-272.
198. Oliveira A, Malafaya P, Costa S, Sousa R, Reis R. Micro-computed tomography (μ -CT) as a potential tool to assess the effect of dynamic coating routes on the formation of biomimetic apatite layers on 3D-plotted biodegradable polymeric scaffolds. *Journal of Materials Science: Materials in Medicine*. 2007;18(2):211-23.
199. Desplentere F, Lomov SV, Woerdeman DL, Verpoest I, Wevers M, Bogdanovich A. Micro-CT characterization of variability in 3D textile architecture. *Composites Science and Technology*. 2005;65(13):1920-30.
200. Rugar D, Hansma P. Atomic force microscopy. *Physics today*. 1990;43(10):23-30.
201. Eaton P, West P. Atomic force microscopy: Oxford University Press; 2010.
202. Cwikel D, Zhao Q, Liu C, Su X, Marmur A. Comparing Contact Angle Measurements and Surface Tension Assessments of Solid Surfaces. *Langmuir*. 2010;26(19):15289-94.
203. Harnett EM, Alderman J, Wood T. The surface energy of various biomaterials coated with adhesion molecules used in cell culture. *Colloids and Surfaces B: Biointerfaces*. 2007;55(1):90-7.
204. Lai HC, Zhuang LF, Liu X, Wieland M, Zhang ZY, Zhang ZY. The influence of surface energy on early adherent events of osteoblast on titanium substrates. *Journal of biomedical materials research Part A*. 2010;93(1):289-96.
205. Owens DK, Wendt R. Estimation of the surface free energy of polymers. *Journal of applied polymer science*. 1969;13(8):1741-7.
206. Kaelble D. Dispersion-polar surface tension properties of organic solids. *The Journal of Adhesion*. 1970;2(2):66-81.
207. Thibault P, Dierolf M, Menzel A, Bunk O, David C, Pfeiffer F. High-resolution scanning x-ray diffraction microscopy. *Science*. 2008;321(5887):379-82.
208. Theophanides T. Introduction to infrared spectroscopy. *Infrared Spectroscopy-Materials Science, Engineering and Technology*: InTech; 2012.
209. Barreneche C, Solé A, Miró L, Martorell I, Fernández AI, Cabeza LF. Study on differential scanning calorimetry analysis with two operation modes and organic and inorganic phase change material (PCM). *Thermochimica Acta*. 2013;553:23-6.
210. Czichos H. Materials and Their Characteristics: Overview. *Springer Handbook of Materials Measurement Methods*: Springer; 2006. p. 95-102.

211. Clements BA, Bushman J, Murthy NS, Ezra M, Pastore CM, Kohn J. Design of barrier coatings on kink-resistant peripheral nerve conduits. *Journal of tissue engineering*. 2016;7:2041731416629471-.
212. Manoukian OS, Arul MR, Rudraiah S, Kalajic I, Kumbar SG. Aligned microchannel polymer-nanotube composites for peripheral nerve regeneration: Small molecule drug delivery. *Journal of controlled release : official journal of the Controlled Release Society*. 2019;296:54-67.
213. Nectow AR, Marra KG, Kaplan DL. Biomaterials for the Development of Peripheral Nerve Guidance Conduits. *Tissue Engineering Part B: Reviews*. 2012;18(1):40-50.
214. Yan L-P, Salgado AJ, Oliveira JM, Oliveira AL, Reis RL. De novo bone formation on macro/microporous silk and silk/nano-sized calcium phosphate scaffolds. *Journal of Bioactive and Compatible Polymers*. 2013;28(5):439-52.
215. Steed MB, Mukhatyar V, Valmikinathan C, Bellamkonda RV. Advances in Bioengineered Conduits for Peripheral Nerve Regeneration. *Atlas of the Oral and Maxillofacial Surgery Clinics*. 2011;19(1):119-30.
216. Yomota C, Komuro T, Kimura T. [Studies on the degradation of chitosan films by lysozyme and release of loaded chemicals]. *Yakugaku zasshi : Journal of the Pharmaceutical Society of Japan*. 1990;110(6):442-8.
217. Kennedy L, Sutherland IW. Gellan lyases–novel polysaccharide lyases. *Microbiology (Reading, England)*. 1994;140 (Pt 11):3007-13.
218. Li M, Ogiso M, Minoura N. Enzymatic degradation behavior of porous silk fibroin sheets. *Biomaterials*. 2003;24(2):357-65.
219. Tas AC. Synthesis of biomimetic Ca-hydroxyapatite powders at 37 C in synthetic body fluids. *Biomaterials*. 2000;21(14):1429-38.
220. Kokubo T, Takadama H. How useful is SBF in predicting in vivo bone bioactivity? *Biomaterials*. 2006;27(15):2907-15.
221. Wang W, Itoh S, Matsuda A, Ichinose S, Shinomiya K, Hata Y, et al. Influences of mechanical properties and permeability on chitosan nano/microfiber mesh tubes as a scaffold for nerve regeneration. *Journal of biomedical materials research Part A*. 2008;84(2):557-66.
222. Kaur G, Dufour JM. Cell lines: Valuable tools or useless artifacts. *Spermatogenesis*. 2012;2(1):1-5.
223. Grothe C, Heese K, Meisinger C, Wewetzer K, Kunz D, Cattini P, et al. Expression of interleukin-6 and its receptor in the sciatic nerve and cultured Schwann cells: relation to 18-kD fibroblast growth factor-2. *Brain Research*. 2000;885(2):172-81.
224. Krump-Konvalinkova V, Bittinger F, Unger RE, Peters K, Lehr HA, Kirkpatrick CJ. Generation of human pulmonary microvascular endothelial cell lines. *Laboratory investigation; a journal of technical methods and pathology*. 2001;81(12):1717-27.
225. Mao Q, Yuan J, Ming X, Wu S, Chen L, Bekker A, et al. Role of dorsal root ganglion K2p1.1 in peripheral nerve injury-induced neuropathic pain. *Molecular pain*. 2017;13:1744806917701135-.
226. Amirikia M, Shariatzadeh SMA, Jorsaraei SGA, Mehraniani MS. Auto-fluorescence of a silk fibroin-based scaffold and its interference with fluorophores in labeled cells. *European biophysics journal : EBJ*. 2018;47(5):573-81.
227. Wang ML, Rivlin M, Graham JG, Beredjikian PK. Peripheral nerve injury, scarring, and recovery. *Connective Tissue Research*. 2019;60(1):3-9.
228. O'brien J, Wilson I, Orton T, Pognan F. Investigation of the Alamar Blue (resazurin) fluorescent dye for the assessment of mammalian cell cytotoxicity. *The FEBS Journal*. 2000;267(17):5421-6.
229. Stiefel P, Schmidt-Emrich S, Maniura-Weber K, Ren Q. Critical aspects of using bacterial cell viability assays with the fluorophores SYTO9 and propidium iodide. *BMC Microbiol*. 2015;15:36-.
230. Rudge TL, Jr., Sankovich KA, Niemuth NA, Anderson MS, Badorrek CS, Skomrock ND, et al. Development, qualification, and validation of the Filovirus Animal Nonclinical Group anti-Ebola virus glycoprotein immunoglobulin G enzyme-linked immunosorbent assay for human serum samples. *PLoS One*. 2019;14(4):e0215457-e.
231. Molnár E. Immunocytochemistry and immunohistochemistry. *Essential Guide to Reading Biomedical Papers: Recognising and Interpreting Best Practice*. 2013:117-27.
232. Moreno-Jimenez I, Kanczler JM, Hulsart-Billstrom G, Inglis S, Oreffo ROC. (*) The Chorioallantoic Membrane Assay for Biomaterial Testing in Tissue Engineering: A Short-Term In Vivo Preclinical Model. *Tissue engineering Part C, Methods*. 2017;23(12):938-52.
233. Lokman NA, Elder AS, Ricciardelli C, Oehler MK. Chick chorioallantoic membrane (CAM) assay as an in vivo model to study the effect of newly identified molecules on ovarian cancer invasion and metastasis. *International journal of molecular sciences*. 2012;13(8):9959-70.
234. Modulevsky DJ, Cuerrier CM, Pelling AE. Biocompatibility of Subcutaneously Implanted Plant-Derived Cellulose Biomaterials. *PLoS one*. 2016;11(6):e0157894-e.
235. Haastert-Talini K, Geuna S, Dahlin LB, Meyer C, Stenberg L, Freier T, et al. Chitosan tubes of varying degrees of acetylation for bridging peripheral nerve defects. *Biomaterials*. 2013;34(38):9886-904.

236. Ribatti D, Nico B, Vacca A, Presta M. The gelatin sponge-chorioallantoic membrane assay. *Nature protocols*. 2006;1(1):85.
237. Silva-Correia J, Miranda-Gonçalves V, Salgado AJ, Sousa N, Oliveira JM, Reis RM, et al. Angiogenic potential of gellan-gum-based hydrogels for application in nucleus pulposus regeneration: in vivo study. *Tissue Engineering Part A*. 2012;18(11-12):1203-12.
238. Nowak-Sliwinska P, Ballini J-P, Wagnières G, Van Den Bergh H. Processing of fluorescence angiograms for the quantification of vascular effects induced by anti-angiogenic agents in the CAM model. *Microvascular research*. 2010;79(1):21-8.
239. Huelsenbeck SC, Rohrbeck A, Handreck A, Hellmich G, Kiaei E, Roettinger I, et al. C3 peptide promotes axonal regeneration and functional motor recovery after peripheral nerve injury. *Neurotherapeutics : the journal of the American Society for Experimental NeuroTherapeutics*. 2012;9(1):185-98.
240. Chang W, Shah MB, Lee P, Yu X. Tissue-engineered spiral nerve guidance conduit for peripheral nerve regeneration. *Acta biomaterialia*. 2018;73:302-11.

SECTION 3

EXPERIMENTAL STUDIES

Chapter V

Investigation of cell adhesion in chitosan membranes for peripheral nerve regeneration

Chapter V

Investigation of cell adhesion in chitosan membranes for peripheral nerve regeneration¹

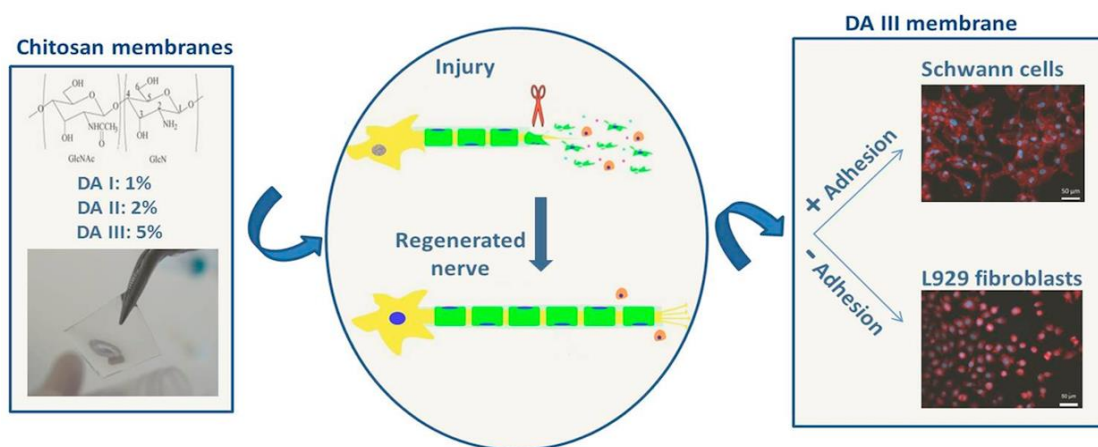
ABSTRACT

Peripheral nerve injuries have produced major concerns in regenerative medicine for several years, as the recovery of normal nerve function continues to be a significant clinical challenge. Chitosan (CHT), because of its good biocompatibility, biodegradability and physicochemical properties, has been widely used as a biomaterial in tissue engineering scaffolding. In this study, CHT membranes were produced with three different Degrees of Acetylation (DA), envisioning its application in peripheral nerve regeneration. The three CHT membranes (DA I: 1%, DA II: 2%, DA III: 5%) were extensively characterized and were found to have a smooth and flat surface, with DA III membrane having slightly higher roughness and surface energy. All the membranes presented suitable mechanical properties and did not show any signs of calcification after SBF test. Biodegradability was similar for all samples, and adequate to physically support neurite outgrowth. The *in vitro* cell culture results indicate selective cell adhesion. The CHT membranes favored Schwann cells invasion and proliferation. At the same time, they presented low fibroblast infiltration. This fact may be greatly beneficial for the prevention of fibrotic tissue formation, a common phenomenon impairing peripheral nerve regeneration. The great deal of results obtained during this work permitted to select the formulation with the greatest potential for further biological tests.

Keywords: Peripheral nerve injuries, biomaterials, chitosan, degree of acetylation, Schwann cells

¹This chapter is based on the following publication: [Carvalho CR, López-Cebal R, Silva-Correia J, Silva JM, Mano JF, Silva TH, Freier T, Reis RL, Oliveira JM](#). Investigation of cell adhesion in chitosan membranes for peripheral nerve regeneration. *Materials Science and Engineering: C*. 2017;71:1122-3. doi: 10.1016/j.msec.2016.11.100.

V-1. GRAPHICAL ABSTRACT



V-2. INTRODUCTION

Peripheral nerves transmit information from the central nervous system to the remaining body parts, also transferring sensory information the other way around. Accordingly, lesions at this level can be highly harmful, causing life-long disabilities, commonly accompanied by pain. Peripheral nerve injuries (PNI) arise from different situations and pathologies, such as trauma, congenital birth defects or surgical complications (1). Indeed, it has been reported that about 3 % of trauma patients are affected by PNI (2) and these statistics are underestimated, as only traumatic injuries that reach the health care system are included (3). Overall, more than half a million peripheral nerve injury cases are annually reported worldwide (4).

At present, nerve autografting is the most effective technique for nerve repair. Still, the outcomes are not satisfactory, often leading to incomplete functional recovery accompanied by tissue fibrosis formation and painful conditions. In addition, autografts have many drawbacks such as donor site morbidity and limited availability (5). To improve PNI therapeutics, the production of bio-engineered scaffolds combining the knowledge about regeneration mechanisms, biomaterials and the novel biotechnological approximations, seem the only possible option leading to a successful outcome (6). In previous works (7), it was asserted that the pathway leading to the development of successful neuronal scaffolds should start by the selection of the appropriate material, followed by its synthesis and characterization, and continued by *in*

in vitro testing. These analyses will reveal whether the material has the appropriate characteristics to be further studied. It is also desired for the implantable scaffolds not only to hinder a fibrotic response, but to stop the formation of scar tissue. This will be mainly achieved by avoiding fibroblast adhesion (8). Scar formation is important for avoiding wound extension, but excessive proliferation of this tissue as a response to nerve injury will result in inhibition of axon elongation (9). On the other hand, it is essential for a peripheral nervous repair material to present good Schwann cell adhesion, as these cells are of fundamental importance for the nerve regeneration process to take place (10-12).

During the last decade, scientists have been looking for the production of effective biodegradable artificial nerve guidance conduits (NGCs), without any significant success (13). In this regard, increasing attention has been paid to chitosan (CHT) (14-17), due to the undisputable biomedical potential of this material, namely its polyelectrolyte properties (18), the presence of reactive functional groups, gel-forming ability (19), high adsorption capacity, complete biodegradability (20), bacteriostatic (21) and fungistatic properties (22) or anti-tumour influence (23, 24).

The degree of acetylation (DA) represents the proportion of N-acetyl-D-glucosamine units in the chitosan chain (25, 26) and has an important impact on several physicochemical properties (*i.e.* viscosity, hydrophilicity, crystallinity, tensile strength, brittleness and degradation), as well as other important characteristics such as biocompatibility, biodegradation and cell interaction properties (25, 27-29). According to the literature, there are a few studies proving that, considering a wide range of DAs, lower acetylated materials lead to better results in terms of increased cell adhesion for PNR (26, 30). This statement has also been proved true in other regenerative medicine fields (20, 25, 29, 31-33). However, it has never been reported before how minor changes in the DAs would have a visible effect in cell adhesion, since a wider range and greater differences in the DAs are commonly studied. Also, it was verified that in the above-mentioned previous studies, the lowest DA analysed varied greatly, from 0.5 % to 10 %. Therefore, the statement found in the literature “DA close to zero leads to better results” is imprecise. Taking the previous information into account, the niche of DAs close to zero should be further investigated in order to shed light on their real suitability for peripheral nerve regeneration purposes.

In this work, we hypothesize that even very small differences in low DAs might affect cellular behaviour and their regenerative potential. Therefore, we produced three different membranes using very low and similar DA CHTs as raw materials, DA I: 1 % DA; DA II: 2 % DA and DA III: 5 % DA, and thoroughly investigated their surface and physicochemical properties. The biological performance of the developed CHT membranes was investigated using mouse lung L929 fibroblasts and human immortalized Schwann cells. This extensive characterization proved the potential of the membranes for PNR applications, leading to the revelation of the DA III membrane as the formulation with the highest PNR potential, consequently being this system the one selected for the future continuation of the present experimental work.

V-3. EXPERIMENTAL SECTION

V-3.1. Materials

Highly purified chitosan powder (*Ki2Med*® LO₈₀₊) with 5 % DA was provided by Altakitin S.A. (Lisboa, Portugal). Chitosan powder with 2 % and 1 % DA, respectively, was produced from 5 % DA chitosan by one or two hydrolysis steps in 40 % sodium hydroxide for 2 hours at 80 °C. Chitosan membranes with different degrees of acetylation (DAI: 1 %, DAII: 2 %, DAIII: 5 %) were produced and supplied by Medovent GmbH (Mainz, Germany) (**Table V-1**). All chemicals for SBF preparation were obtained from Sigma-Aldrich, (Germany); Alamar Blue (AB) was purchased to Invitrogen™; CyQUANT® Cell Proliferation Assay Kit and Sodium Pyruvate 100 mM were obtained from ALFAGENE; Calcein AM and propidium iodide were obtained from Life Technologies, (CA, USA).

V-3.2. Methods

V-3.2.1. Membranes production

Briefly, highly purified chitosan powder with 1 %, 2 %, or 5 % DA, respectively, was dissolved in 0.75 % (v/v) acetic acid to obtain a 1.5 %wt. solution, which was filtered and poured into Petri dishes, followed by drying at room temperature (RT) for 72 hours. The resulting

membranes were treated with a solution of ammonia in methanol/water [25], washed once with distilled water and dried for another 24 hours. The membranes were cut into the required size and sterilized by electron beam. The DA of the chitosan samples was determined using $^1\text{H-NMR}$ spectroscopy, as previously described (26). Briefly, samples were dissolved in a mixture of 0.25 % (v/v) DCI in D_2O . The $^1\text{H-NMR}$ spectra were recorded on Avance III HD 300 NMR-spectrometer (Bruker). The DA was calculated by comparing the integrated area of the H2-H6 group signal with that corresponding to the signal of the methyl group (26).

V-3.2.2. Physicochemical and Surface Characterization of Membranes

V-3.2.2.1 *Scanning Electron Microscopy (SEM)*

The studied membranes were sputter coated with gold for the analyses of their surface morphology by means of SEM (model S360, Leica, Cambridge, England).

V-3.2.2.2 *Atomic Force Microscopy (AFM)*

The membranes surface roughness was analyzed using a Dimension 3000 Atomic Force Microscope (Digital Instruments, Santa Barbara, CA), on a $5\ \mu\text{m} \times 5\ \mu\text{m}$ scan area. Contact mode was used with a Multimode (Veeco, USA) connected to a NanoScopelll (Veeco, USA) having a contacting silicon nitride nanoprobe (model DNP, Bruker). For this analysis, the membranes were tested under ambient conditions (dry) and after being immersed in Phosphate Buffer Saline (PBS) for 2 hours to mimic physiological conditions (wet). The average surface roughness (R_a , nm) corresponding to the membranes in both dry and wet state was measured.

V-3.2.2.3 *Contact angle measurements: Wettability and Surface Energy determination*

Differences in the wettability and surface free energy of the membranes were evaluated by means of contact angle measurements. Static contact angle measurements were carried out by the sessile drop method, using a contact angle meter (Goinometer OCA 15+, Germany) in association with a high-performance image processing system (DataPhysics Instruments,

Filderstadt, Germany). During every determination, a motor driven syringe was used to deposit a drop of liquid over the membrane surface. The images corresponding to these drops were properly recorded and analysed. The different determinations were performed at RT and in triplicate.

For the wettability determination, water was used. For the surface energy quantification, two different test liquids were required, one apolar (diiodomethane) and one polar (water). The surface energy and its polar and dispersive components were calculated by means of the Owens, Wendt, Rabel and Kaeble (OWRK) method (34).

V-3.2.2.4 *Fourier Transform Infrared Spectroscopy (FTIR)*

The FTIR spectrum was obtained using Shimadzu IRPrestige 21 spectrometer (Shimadzu, Europe). Samples were prepared as potassium bromide pellets at room temperature. The spectrum was collected by averaging 32 scans with a resolution of 4 cm⁻¹, corresponding to the 4000-400 cm⁻¹ spectra region.

V-3.2.2.5 *X-Ray Diffraction (XRD)*

X-ray diffraction was used to determine the crystal structure of chitosan membranes. The diffraction pattern was measured using grazing incidence X-ray diffraction (GIXRD) with a diffractometer (Bruker D8 Discover) operated with accelerating voltage of 40 kV and a current of 40 mA. The GIXRD scans were performed using Cu K α radiation (wavelength = 0.154 nm), keeping a fixed incidence angle of 1° between the incident X-rays and specimen plane, while the detector was revolved between 5° and 40° with respect to the specimen, at a speed of 0.04°/1 second. The analyses were performed at room temperature.

V-3.2.2.6 *Differential Scanning Calorimetry (DSC)*

DSC analysis was performed on a DSC Q100 apparatus (TA Instruments Inc, USA). Samples were packed in a TA aluminum pan (3.5 - 4 mg sample weight), which was covered with a suitable aluminum cover. Both temperature and heat flux were previously calibrated with Indium.

All samples were subjected to a first heating cycle, ranging from 0 °C to 200 °C at a rate of 10 °C/minute, an isothermal step of 2 minutes followed by cooling to 0 °C and a second heating cycle, ranging from 0 °C to 350 °C at a rate of 1 °C/minute. The measurements were performed under dry nitrogen atmosphere, at a flow rate of 50 mL/minute. Only the behaviour showed by the membranes during the second heating cycle is presented.

V-3.2.2.7 *Weight loss and water uptake*

Weight loss and water uptake studies were performed by means of soaking 1 cm² chitosan membranes in PBS (pH 7.4) or PBS enriched with 13 mg/L of lysozyme for 30 days, at 37 °C. In the weight loss assay, to distinguish weight loss related to enzymatic degradation or simple hydrolysis, samples were also put in PBS without lysozyme for degradation assessment. At predefined time points (1 day, 15 days, 30 days) the swollen or degraded samples were extracted, and the excess of water removed with filter paper. To minimize both enzyme loss of activity and possible changes in the pH, enzyme solution was changed every 3 days. To determine the degradation behavior over time the samples were dried at RT and **Equation 1** was applied. The water uptake ability of the formulations was calculated according to **Equation 2**.

Equation V-1 - Equation for the determination of weight loss

$$\text{Weight loss (\%)} = \frac{m_i - m_f}{m_i} \times 100$$

where, m_i is initial mass (before immersion in solution) and m_f is final mass (after drying).

Equation V-2 - Equation for the determination of water uptake

$$\text{Water uptake (\%)} = \frac{m_w - m_i}{m_i} \times 100$$

where, m_w is the wet mass (wet, but after excessive water removal) and m_i is initial mass. Three replicates of each sample were studied, and the average values considered.

V-3.2.2.8 *Bioactivity*

The aim of the bioactivity assays was to assess the possibility of the *in vitro* biomineralization of the produced membranes. For the *in vitro* bioactivity tests an acellular Simulated Body Fluid (SBF) (1.0 X) was prepared as described elsewhere (35), containing the same ions as human blood plasma, at a nearly equal concentration. Sample membranes of 1 cm² were cut from the original processed membranes and immersed in freshly prepared SBF for 1, 15 and 30 days at 37 °C. Upon removal from SBF the samples were rinsed with distilled water and left to dry at RT. Finally, the presence/absence of a calcium-phosphate layer on their surface was determined using Scanning Electron Microscopy and Energy-Dispersive Spectroscopy (SEM/EDS) (Leica Cambridge S 360) at an accelerated voltage of 15 kV. Before SEM analyses, the membranes were gold coated at 6 mA, by using a Hitachi coater, in contraposition to dry membranes, that did not undergo this assay (controls).

V-3.2.2.9 *Mechanical Properties*

The viscoelastic measurements were performed using a Triton 2000B DMA (Triton Technology, UK). For this purpose, 5 mm width membrane samples were cut out and immersed in PBS overnight, at 37 °C. During the DMA analysis the samples were also immersed in PBS, in order to keep the physiological-like-state. Experiments were carried out under the tensile mode, following cycles of increasing frequency, from 0.1 to 20 Hz, with constant strain amplitude of 30 µm. A static pre-load of 1N was applied before the tests to keep the sample tight. Three samples were tested under each of the studied conditions.

V-3.2.3. Biological Evaluation

For these experiments, membrane samples of 1 cm² were obtained and the behaviour of L929 mouse lung fibroblasts on passage 31 and human immortalized Schwann cells on passage 20 were studied. These cells were seeded separately in 24-well cell culture plates, at a density of 3000 cells/cm² for metabolic activity assay and 6,000 cells/cm² for proliferation assay, due to the different sensibility of each kit. L929 fibroblasts were incubated with Low Glucose DMEM

medium, supplemented with 10 % (v/v) FBS and 1 % (v/v) penicillin/streptomycin, at 37 °C in 5 % CO₂. Immortalized Schwann cells were cultured under the same conditions, but the culture medium was High Glucose DMEM and was also supplemented with 1 % (v/v) Sodium Pyruvate. In all the following experiments, samples were appropriately washed with PBS and correspondingly analysed after 1, 3 and 7 days in culture.

V-3.2.3.1 *Live/Dead viability assay*

The viability of L929 fibroblasts and immortalized Schwann cells seeded over the studied membranes was evaluated using Calcein AM and PI staining. After 1, 3 and 7 days of culture, each seeded membranes was washed with PBS and immersed in 1 mL of culture medium supplemented with 1 µg Calcein AM and 2 µg propidium iodide. These immersions lasted for 15 minutes, after which the samples were washed with PBS and analyzed using a transmitted and reflected light microscope (Axio Imager Z1m, Zeiss, Jena, Germany).

V-3.2.3.2 *Metabolic Activity quantification in 2D cultures*

L929 fibroblasts and immortalized Schwann cells metabolic activity was followed with Alamar Blue (AB), a dye that yields a fluorescent signal and a colorimetric change when incubated with metabolically-active cells. Cell culture medium containing 10 % (v/v) AB was added to the different culture wells and the systems were left for incubation for 4 hours, after which 100 µl of each solution were transferred to white opaque 96-well plates, in triplicates. Fluorescence was monitored at 590 nm emission wavelength (excitation wavelength 530 nm), using a microplate reader (FL 600, Bio-Tek Instruments). PBS was used for removing the AB reagent and fresh medium was added in its place after each AB determination. The metabolic activity values were calculated by normalization with the mean fluorescence value obtained for the controls (Tissue culture polystyrene; TCPs) with and without cells.

V-3.2.3.3 *Cell Proliferation quantification in 2D cultures*

In order to assess L929 fibroblasts and immortalized Schwann cells proliferation CyQUANT® Cell Proliferation Assay Kit was used. After 1, 3 and 7 days the culture medium was removed from the wells, the samples were washed with PBS, placed in new wells and culture medium incorporating 0.4 % (v/v) of CyQUANT® Direct nucleic acid stain and 2 % (v/v) of CyQUANT® Direct background suppressor was added to the wells. The samples were incubated for 2 hours at 37 °C, in 5 % CO₂ atmosphere. The fluorescence intensity of each sample was measured using a fluorescence microplate reader (FL 600, Bio-Tek Instruments). The excitation wavelength was 485 nm and the emission detection was performed at 528 nm. All measurements were done in triplicate and the number of cells present in the different samples was calculated by using a calibration curve.

V-3.2.3.4 *Cells morphology and cytoskeletal organization*

For determining the morphology and cytoskeletal organization of L929 fibroblasts and immortalized Schwann cells DAPI (4,6-Diaminidino-2-phenylindole-dilactate fluorescent dye)-phalloidin (phalloidin tetramethyl rhodamine B isothiocyanate fluorescent dye) assay was performed. At each timepoint (1, 3 and 7 days of culture) the corresponding samples were washed with PBS after culture media removal and fixed in 10 % formalin for 1 hour. Afterwards, formalin was removed by PBS washing and 1 mL of PBS containing 2 µL of phalloidin (10 mg/mL) was added to the systems, leaving them to react for 40 min at RT. After extensively washing with PBS, 1 mL of PBS containing 1 µL of DAPI (20 mg/mL) was incorporated to the systems and left to react for 10 minutes. The dye was removed by washing with PBS. Finally, the samples were analyzed using a transmitted and reflected light microscope (Axio Imager Z1m, Zeiss, Jena, Germany).

V-3.3. Statistical analyses

All the performed tests were conducted in triplicate and the obtained data points are presented as mean ± standard deviation. The statistical results in the biological characterization

were analyzed using GraphPad Prism software. One-way analysis of variance (ANOVA) was used to establish statistical differences between the different materials ($n = 6$). $p < 0.05$ was considered statistically significant.

V-4. RESULTS

V-4.1. Physicochemical and Surface Characterization of Membranes

Three types of chitosan membranes, differing on the degree of acetylation (DAI: 1 %, DAII: 2 % and DAIII: 5 %), were produced and analyzed (**Table V-1**). All of them were almost transparent, with DA I and DA II having average thickness of 30 μm , while DA III was around 100 μm thick.

V-4.1.1. SEM Micrographs

SEM pictures (Figure V-1A) show very smooth and flat surfaces for the three samples.

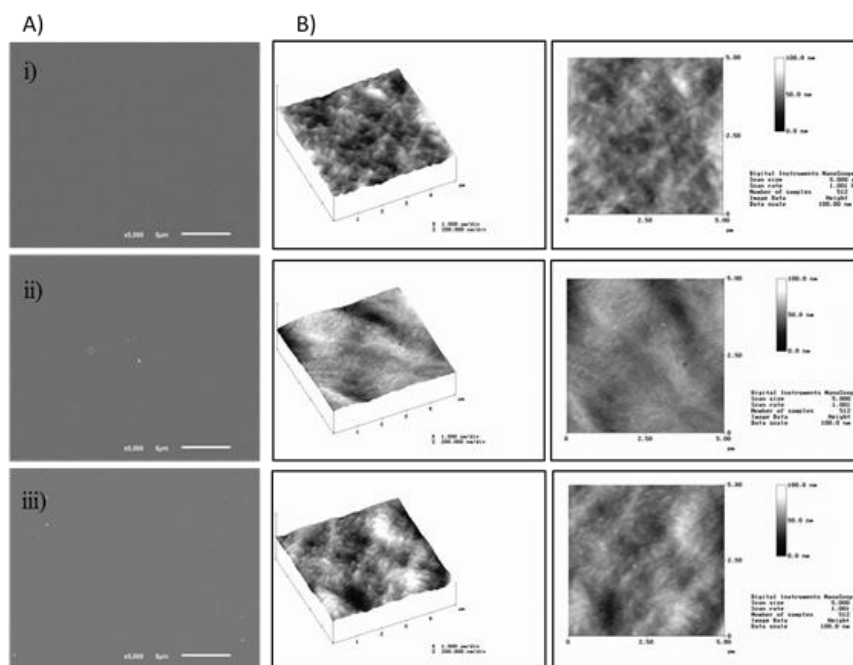


Figure V-1 - Surface characterization of chitosan membranes (i – DAI; ii – DA II; iii – DA III). A) Scanning Electron Microscopy micrographs. Scale bar 5 μm ; Magnification 5,000 \times ; B) Atomic Force Microscope three dimensional images of chitosan membranes under simulated physiological conditions by previous 2 hours immersion of samples in PBS. 5 $\mu\text{m} \times 5 \mu\text{m}$ scan area; Contact mode.

Table V-1 - General characteristics of the chitosan used on the preparation of each one of the studied membranes. Surface characterization of the chitosan membranes: Mean Roughness (\pm standard deviation) in dry and wet state measured by Atomic Force Microscope analysis and water contact angle, surface energy and its components calculated by the OWRK method.

| Sample | Concentration of chitosan | DA | Average Molecular Weight | Mean Roughness in dry state (Ra, nm) | Mean Roughness in wet state (Ra, nm) | θ water ($^{\circ}$) | SE (γ) mN m ⁻¹ | Disp (γ_d) mN m ⁻¹ | Polar (γ_p) mN m ⁻¹ |
|--------|---------------------------|-----|--------------------------|--------------------------------------|--------------------------------------|-------------------------------|------------------------------------|--|---|
| DAI | 1.5 % | 1 % | 260 kDa | 6.3 \pm 0.48 | 7.3 \pm 0.043 | 107.1 \pm 0.33 | 32.07 \pm 0.00 | 32.07 \pm 0.01 | 0.00 |
| DAII | 1.5 % | 2 % | 300 kDa | 3.7 \pm 0.82 | 5.1 \pm 0.64 | 95.6 \pm 4.49 | 31.53 \pm 0.01 | 30.27 \pm 0.00 | 1.26 \pm 0.00 |
| DAIII | 1.5 % | 5 % | 312 kDa | 7.2 \pm 0.24 | 7.5 \pm 0.35 | 115.2 \pm 1.96 | 35.22 \pm 0.01 | 34.61 \pm 0.01 | 0.61 \pm 0.00 |

V-4.1.2. AFM

It was determined that the mean roughness (Ra) in dry state was 6.3 ± 0.48 nm, 3.7 ± 0.82 nm and 7.2 ± 0.24 nm and after two hours in PBS the mean roughness was 7.3 ± 0.043 nm, 5.1 ± 0.64 nm and 7.5 ± 0.35 nm, for DA I, DA II and DA III membranes, respectively (**Table V-1**). Representative micrographs of membranes in simulated physiological conditions can be seen in **Figure V-1B** (AFM micrographs of the dry membranes are not shown). DA II film has a smoother surface, indicated by the lowest mean value of Ra, when compared to DA I and DA III.

V-4.1.3. Contact angle and surface energy

The water contact angles and the calculated surface energy for the three chitosan membranes can be seen in **Table V-1**. Water contact angles are $107.1^\circ \pm 0.33$, $95.6^\circ \pm 4.49$ and $115.2^\circ \pm 1.96$ for DA I, DA II and DA III, respectively. Regarding surface energy, values of 32.07 ± 0.00 mN m⁻¹ (DA I), 31.53 ± 0.01 mN m⁻¹ (DA II) and 35.22 ± 0.01 mN m⁻¹ (DA III) were obtained.

V-4.1.4. FTIR

FTIR spectroscopy can be seen in **Figure V-2A**. As expected, the transmission infrared spectra of all chitosan membranes exhibited a broad peak in a range from 3450 to 3390 cm⁻¹, assigned to OH stretching, representing intermolecular hydrogen bonding of chitosan molecules. In the same region, a peak corresponding to N-H stretching would also be visible, but it is overlapped with that of the OH stretching. The more acetylated form of the membranes (DA III) has a new peak at 1655 cm⁻¹, related to secondary amides. This peak is not visible in the two less acetylated membranes. On the other hand, DA I and DA II membranes display one peak at 1596 cm⁻¹, relative to N-H deformation. This means that during the N-deacetylation that took place for the obtaining of chitosan, the band at 1655 cm⁻¹ gradually decreased, while that at 1590 cm⁻¹ increased, thus indicating the prevalence of NH₂ groups.

V-4.1.5. XRD

After all the processing, only a diffuse peak is visible near 20° (2 Theta) (Figure V-2B), indicating that the studied chitosan samples lost their crystallinity and remain in an amorphous state.

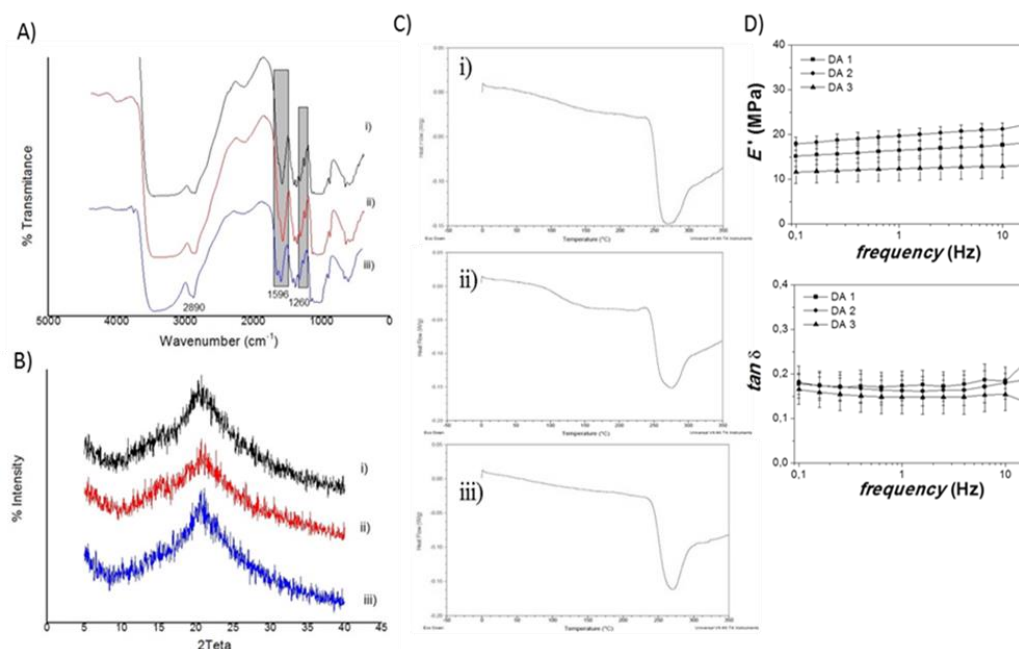


Figure V-2 - Physicochemical characterization of chitosan membranes (i – DA I; ii – DA II; iii – DA III). A) Fourier Transforming Infrared Spectroscopy analysis. 32 scans with resolution of 4 cm^{-1} , corresponding to the $4000\text{--}400\text{ cm}^{-1}$ spectra region. B) X-ray diffraction patterns of the studied chitosan membranes. Fixed incidence angle of 1° between the incident X-rays and specimen plane. C) Differential Scanning Calorimetry thermograms of chitosan membranes. Second heating cycle, ranging from $0\text{ }^\circ\text{C}$ to $350\text{ }^\circ\text{C}$ at a rate of $1\text{ }^\circ\text{C}/\text{minute}$. D) Mechanical properties analysis of chitosan membranes. Storage modulus (E') and loss factor ($\tan \delta$) of the three studied chitosan membranes measured as a function of frequency. Studies performed at room temperature.

V-4.1.6. DSC

There were no differences in the DSC thermograms regardless of their DA. A broad endothermic peak appearing during the first heating cycle is attributable to water evaporation at approximately $80\text{--}110\text{ }^\circ\text{C}$ (data not shown). The second heating spectra (Figure V-2C) revealed that all chitosan membranes have mainly one reaction zone, represented by an exothermic peak, which is related to the decomposition of the polymer (onset at $250\text{--}300\text{ }^\circ\text{C}$). In our studies, it was not detected the presence of any glass transition.

V-4.1.7. Weight loss and water uptake

The results of weight loss and water uptake can be seen in **Figure V-3**. After PBS immersion there was a weight loss of around 4 % after 30 days for all the membranes (**Figure V-3A**), indicating negligible hydrolysis phenomena. The membranes immersion in PBS with 13 mg/L of lysozyme also reveals reduced weight loss for all the membranes (**Figure V-3B**), indicating minor enzymatic degradation. To visually evaluate the degradation of the chitosan membranes in the presence of lysozyme, SEM micrographs of degraded membranes (DA I, DA II and DA III) can be seen in **Figure V-4B**, in comparison with the original aspect of dry membranes (**Figure V-4A**). Differences in the surface morphology can be clearly appreciated, since it is visible the flat and smooth aspect of the original membranes, in contrast to the wrinkled and rough features in the surface of the lysozyme treated ones. Thus, despite in terms of weight loss percentage there are not stand out variations, the degrading effects of the lysozyme can be appreciated in all chitosan membranes, regardless of the DA.

Regarding the water uptake (**Figure V-3C**), the studied membranes absorbed water progressively for one day, losing some of this gained weight during the following 15 days, to finally reach a stabilization in the water content between 15 and 30 days. In this last period the swelling was near 40 %wt of the membranes original weight for DA I and DA II and 50 % for DA III. All along the time of the study (30 days) the membrane with the higher DA (DA III) showed greater water uptake capability than those with the lower DA (DA I and DA II).

V-4.1.8. Bioactivity

For all the studied samples, SEM images (**Figure V-5**) revealed crystal or apatite free membranes after 1, 15 and 30 days of immersion in SBF (see the examples of the first and last timepoints evaluated, 1 and 30 days). The absence of peaks corresponding to Ca and P ions after EDS analysis confirmed these previous results.

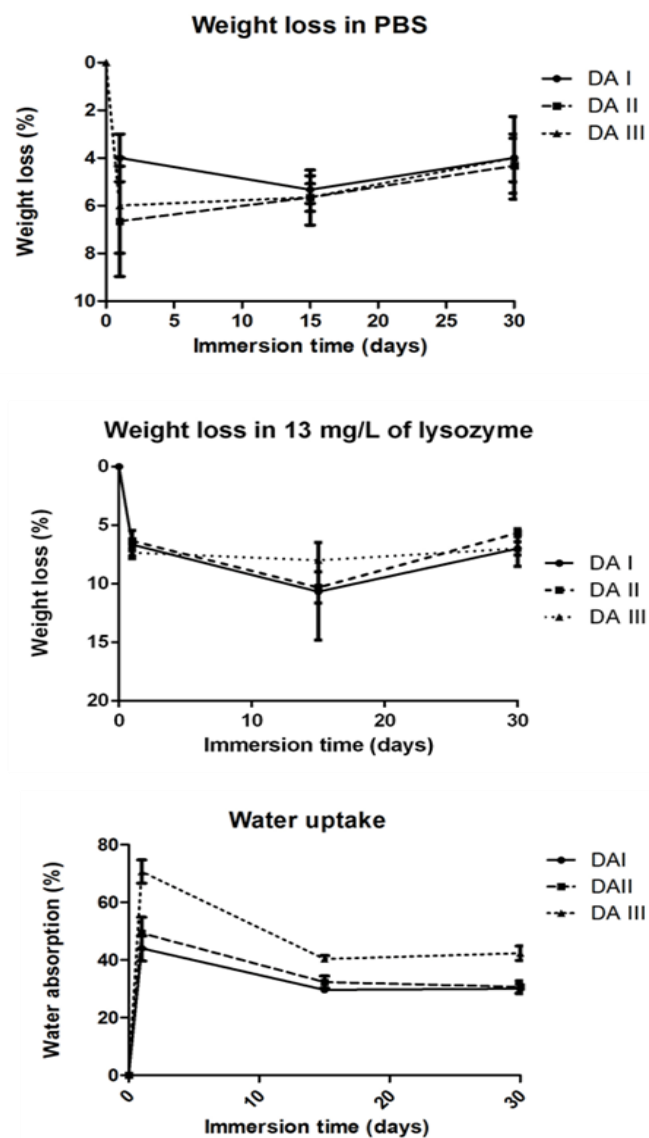


Figure V-3 - Weight loss and water uptake of chitosan membranes at 37 °C for different time periods; A) Weight loss of studied chitosan membrane formulations after storage in PBS; B) Weight loss of studied chitosan membrane formulations after storage in PBS with 13 mg/L of lysozyme; C) Water uptake of samples after storage in PBS. The data represents the mean for each timepoint \pm standard deviation.

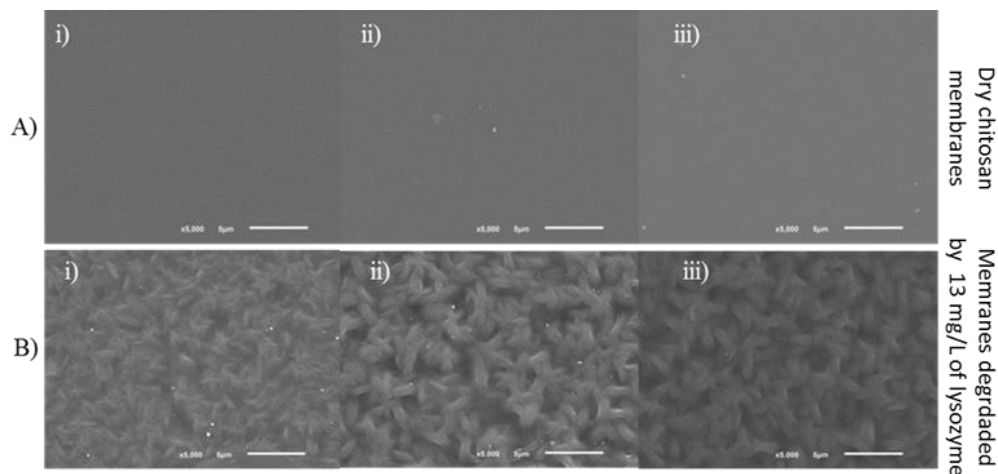


Figure V-4 - Scanning Electron Microscopy micrographs of chitosan membranes (i – DA I; ii – DA II; iii – DA III). A) Micrographs of dry unmodified surface; and B) Micrographs of dry membranes after 30 days in PBS in the presence of 13 mg/L of lysozyme. Scale bar: 5 μm .

V-4.1.9. Mechanical properties

The mechanical analysis results are presented in **Figure V-2D**. Comparing the membranes DA I and DA II the difference between the modulus (E') are almost imperceptible. However, for the higher degree of acetylation studied (DA III), a slight decrease of storage modulus (E') can be observed. It was found that for all the studied membranes, E' did not suffer variations with increasing frequency. The second graph shows the frequency influence on the loss factor ($\tan \delta$). Values of $\tan \delta$ between 0.15 and 0.2 were obtained for all the three membranes, all along the contemplated frequency range. As in the previous case, $\tan \delta$ values for DA I and DA II membranes were quite similar, while membrane DA III presented modest difference with respect to them, having slightly lower $\tan \delta$ values.

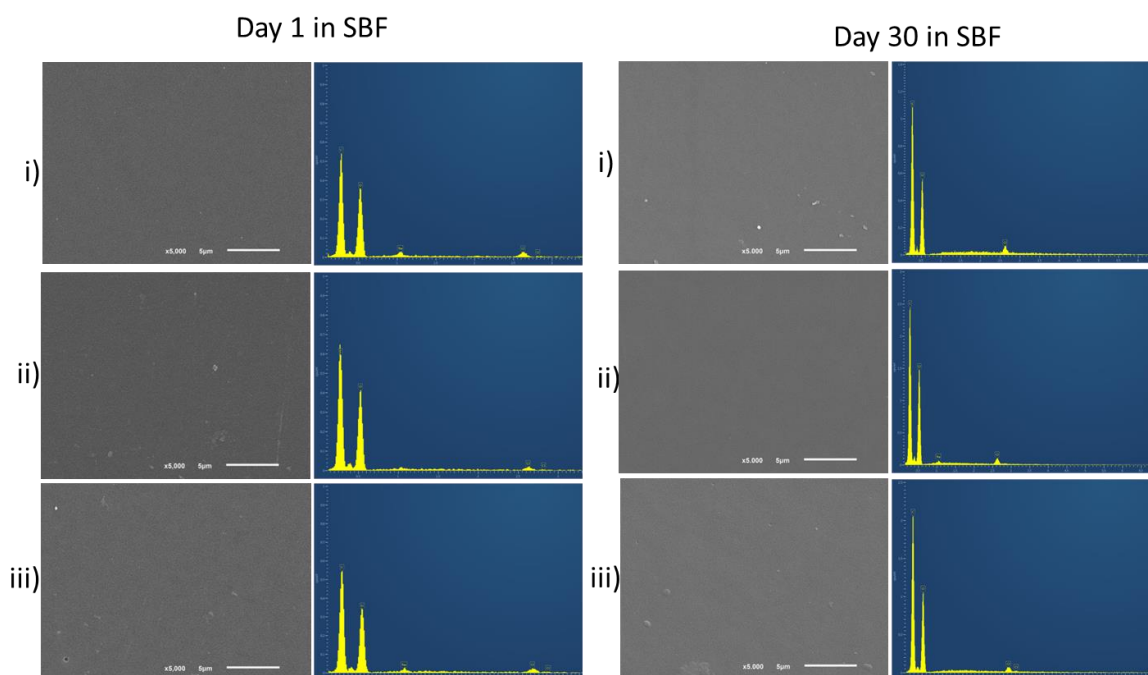


Figure V-5 - Scanning Electron Microscopy and EDS analysis of chitosan membranes after 1 and 30 days in SBF: A) DA I after 1 day in SBF; B) DA II after 1 day in SBF; C) DA III after 1 day in SBF; D) DA I after 30 days in SBF; E) DA II after 30 days in SBF; and F) DA III after 30 days in SBF. Scale bar: 5 μ m.

V-4.2. Biological characterization

In the Live/Dead assay of L929 fibroblasts very few green cells can be observed, regardless of the timepoint or DA (**Figure V-6A**). Concerning the SCs (**Figure V-6B**), spread green cells can be seen, their number increasing with time and with the degree of acetylation of the CHT in the membranes. **Figures V-7A** and **V-7B** show the metabolic activity of L929 Fibroblasts and Schwann cells, respectively, determined by means of AB analysis.

At all timepoints considered, the relative fluorescence units (RFU) corresponding to L929 fibroblasts were under 100 for all three membranes, diminishing with time from the first timepoint studied. On the contrary, in the case of the SCs, the RFU values increased progressively along the time of the study, being this tendency more pronounced in the case of the film with the higher degree of acetylation (DA III). For this cell line RFU values were between 50 and 100 in the case of DA I and DA II membranes, which showed a marked difference with membrane DA III, which showed an increase from 50 RFU in the first timepoint (1 day) to 400 RFU in the seventh day of the study. These results were supported by cell proliferation analysis, showing values around 19 RFU for L929 fibroblasts at the

seventh day of study (**Figure V-7C**), while in the case of the SC they were near 26 RFU (**Figure V-7D**) at that same timepoint.

Phalloidin/DAPI staining proves that L929 cells (**Figure V-8A**) present a round, non- typical fibroblasts morphology, clearly indicating a lack of adhesion of these cells to the membranes. Nevertheless, after SCs Phalloidin/DAPI staining (**Figure V-8B**) a characteristic spindle shaped and elongated morphology of the cells can be clearly appreciated, thus proving their good adhesion to the studied systems.

V-5. DISCUSSION

Chitosan has been described as an interesting biomaterial to be used in peripheral nerve engineering, as it promotes cells adhesion and proliferation (17, 26, 36, 37). Chitosan with a wide range of degrees of acetylation has been tested before for several regenerative applications. The results indicate that regardless of the cell type, the general rule is that lower DA chitosan's promote higher cell adhesion (20, 25, 26, 29-33). However, the gaps between the analyzed DA values are relatively large and, in most cases, while the lowest DA value analyzed is essentially from 1 % to 10 %. For instance, Chatelet *et al.* (25) evaluated a range of DA varying from 2.5 % to 47 % and the lowest presented the best cell adhesion results. Also, Freier *et al.* (26), studied a range that went from 0.5 % to 99 %, also concluding that the lowest DA % presented the best biological outcome. However, in this work, the authors did not perform an extensive physicochemical characterization. In a third study (31), Amaral *et al.* undoubtedly disclosed that for a range of DA varying from 4.23 % to 49.1 %, the lowest presented the most promising results for bone regeneration. Considering these particular results, we believe that values from 0 % to 5 % acetylated would be the most suited for tissue engineering and regeneration and worth studying in detail. Therefore, in the present investigation, chitosan powders with three different low DAs (DAI: 1 %, DAII: 2 %, DAIII: 5 %) were employed in the production of membranes for peripheral nerve regeneration purposes. The differences at a physicochemical and biological level among the different membranes were examined, with the ultimate objective to discern which one of them will be the most appropriate for its application in peripheral nerve regeneration.

In any scaffold to be implanted, the role played by the surface morphology and topography is a major parameter influencing cell adhesion and proliferation, and, eventually, the scaffold rejection or acceptance (38).

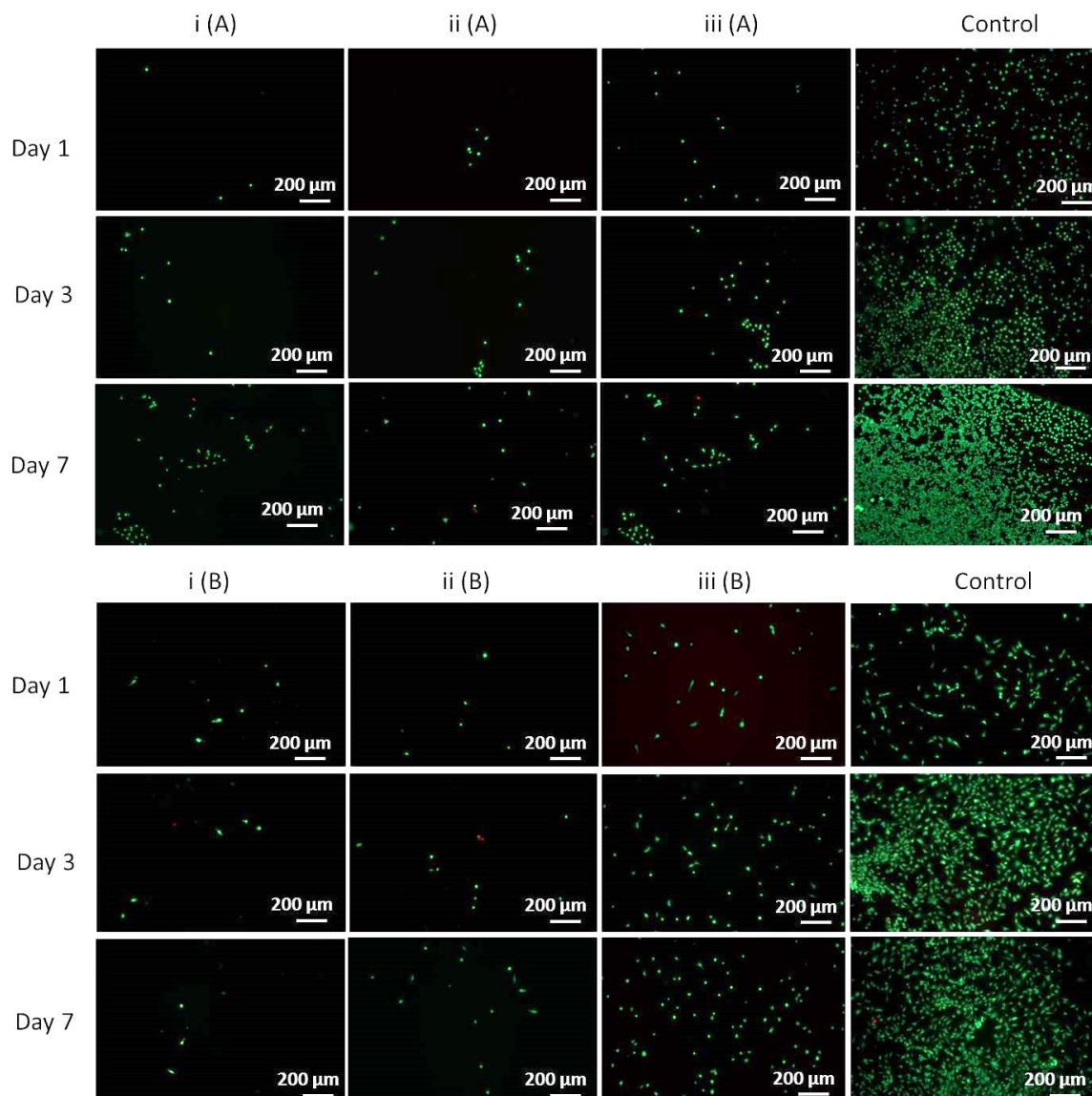


Figure V-6 - Viability live/dead assay of cell lines after 1, 3 and 7 days after direct seeding on chitosan membranes. Live cells stained with Calcein (green color) and dead cells stained with propidium iodide (red color). A) L929 cell line viability on chitosan films; and B) Schwann cell line viability on chitosan films. Scale bar: 200 μm.

SEM and AFM characterization showed very smooth and flat surfaces for all the studied membranes, with higher roughness for more elevated DA values. This is in concordance with the literature, where it is described that the parameter increases with the DA, due to an increment of acetyl groups, which will originate the formation of fibrillary aggregates. The increase in molecular weight as the DA does has also been related to roughness increments (31). During the SEM and AFM characterization it was observed that the membrane DA II did not follow the expected tendency. Consequently, it was postulated that preparation and processing procedures should give rise to some

sort of unexpected superficial modification. This premise should be confirmed after further analysis of the membranes surface.

Non-covalent forces established between liquids and the first monolayer belonging to the studied materials can be measured by contact angle. It is well-known that a smaller water contact angle is linked to better surface wettability, which will ultimately be more favourable for cell adhesion than a hydrophobic surface (31, 39). The water contact angle of DA III is higher with respect to that of DA I, which is within the expected, as it has been stated that contact angle changes with the DA, following a direct proportion. Also as expected, an inverse tendency is observed regarding the wettability. One possible reason for this is that the lower the DA, the more free amine functionalities at the surface. These amino groups may become protonated at neutral pH, resulting in a high positive surface charge that promotes the ability of the membranes to interact with water (40, 41). The obtained results related to surface energy (SE) proved the Dispersive component as the main parameter contributing to the surface energy, consequently showing a slight increase in the SE for DA III, with respect to DA I. These results are in concordance with what has been said in the preceding paragraphs.

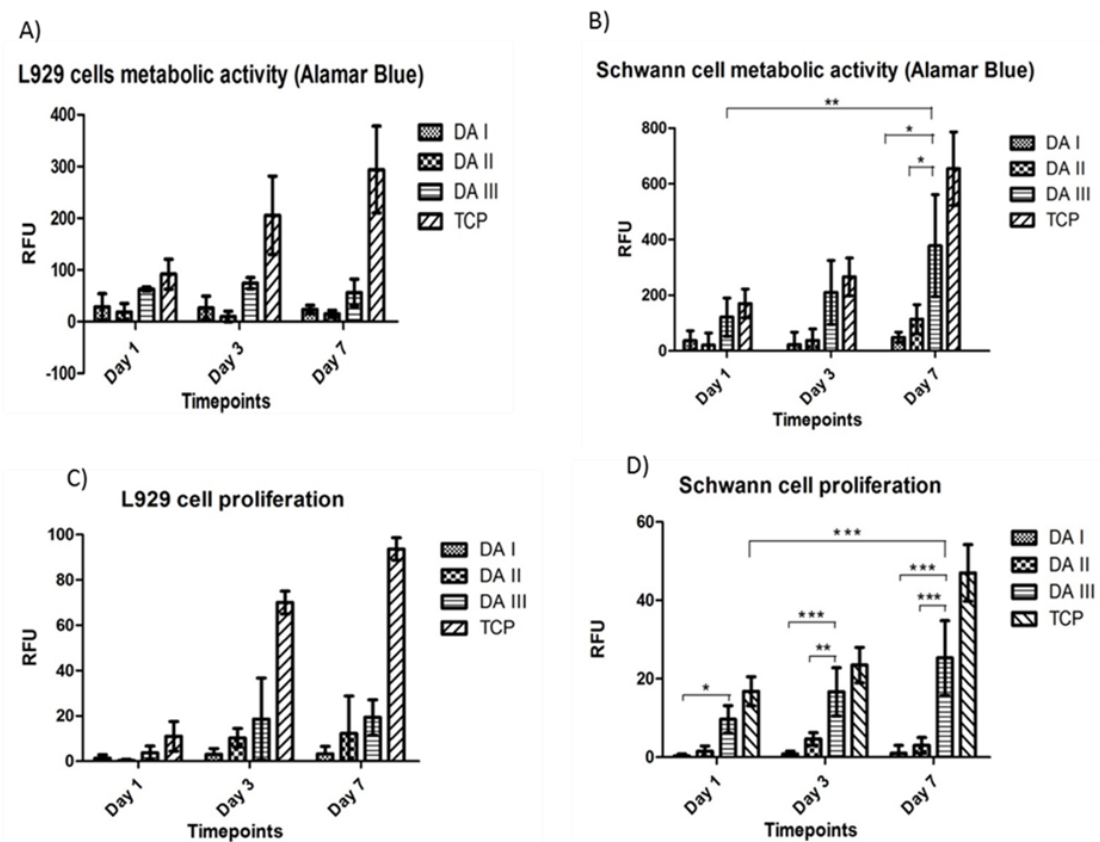


Figure V-7 - *In vitro* cell culture studies: A) Metabolic activity of L929 cells seeded on chitosan films determined by Alamar Blue after 1, 3 and 7 days; B) Metabolic activity of Schwann cells seeded on chitosan films determined by

Alamar Blue after 1, 3 and 7 days; C) Proliferation of L929 cells seeded on chitosan films determined by CyQUANT® Cell Proliferation Assay Kit after 1, 3 and 7 days; and D) Proliferation of Schwann cells seeded on chitosan films determined by CyQUANT® Cell Proliferation Assay Kit after 1, 3 and 7 days.

As it has been postulated before (42), higher surface energy enhances cell adhesion in the early stage of cell response, possibly inducing the expression of adhesion-associated molecules. The previous surface analyses confirm the existence of some sort of superficial abnormality for DA II membrane, possible consequence of its production/processing.

FTIR spectroscopy was used to obtain information about the molecular state and bulk properties of chitosan membranes. The results showed the typical spectra usually obtained for low acetylated chitosan's, where some of the typical glucosamine peaks were identified. The spectra corresponding to the three studied membranes were very similar between them, as expected, due to the similar DAs of the raw chitosan's. Indeed, more distant DAs would give rise to more noticeable variations in the FTIR spectra, particularly, the band associated with the vibration of C=O bond from secondary amide (amide I), barely observed on DA III membrane, but clearly described in other works (30, 43). These spectra made also possible to confirm that no contamination or any other kind of impurities were present in our formulations.

XRD analyses were carried out to determine the structural nature of the studied formulations, more specifically, whether the membranes are amorphous or crystalline. Up to date, there are contradictory results regarding this parameter, as some authors (30, 44) found that the lower the DA, the higher the degree of crystallinity. However, others (45, 46) observed that the crystallinity decreased with the decrease in DA. What is clear is that besides by the DA, the crystallinity of chitosan membranes can be also highly influenced by the source of the material, the preparation or dissolving conditions and the drying procedure (47). Indeed, in the case of the membranes analysed in this experimental work, no structural differences were found as a function of the DA, as all formulations were in an amorphous state, proved by the presence of a diffuse XRD peak near 20° (2 Theta) and the absence of two intense peaks at 10° and 20° (48). These results are in concordance with the literature, where it is described for chitosan membranes prepared by the solvent-casting technique, starting from an aqueous acetic acid solution, to be in an amorphous state. This may be caused by residues of the acetic acid solvent, which may impede the creation of inter and intramolecular hydrogen bonds between chitosan chains, resulting in a more irregular structural organization and thus a distancing from crystallinity (28, 49).

Differential scanning calorimetry is a powerful technique for studying the thermodynamics of polymers. It can provide a basic understanding of its behaviour with different temperatures. In a first heating cycle where temperature was raised to 200 °C, an endothermic peak corresponding to water evaporation appears in the obtained thermograms (data not shown). This evaporation was performed to avoid the water present in the chitosan membranes (chitosan is prone to absorb moisture) to act as a plasticizer, lowering the T_g (Glass Transition) temperature and giving rise to erroneous results (50). The second heating cycle of the experiment (0-350 °C) proved that there is no glass transition for the studied chitosan membranes. These materials do not melt, but degrade at elevated temperatures, as indicated by the exothermic peak near 300 °C present in all the thermograms (51).

Degradation is an important parameter to take into account when the use of a scaffold for peripheral nerve regeneration is envisioned. The ideal device should remain intact during axon regeneration, and then progressively degrade (52). In this experimental work the degradation will be referred to as weight loss (WL).

Weight loss of the membranes in PBS was negligible, proving that they were stable in aqueous solutions at a physiological pH during the period of study (30 days) and did not suffer significant hydrolysis. In addition, weight loss studies were also performed in PBS containing the enzyme lysozyme, the principal endogen enzyme responsible for chitosan degradation. Lysozyme transforms chitosan's from high molecular weight polymers to oligomers, and it is found in various human body fluids and tissues, including serum and tears (53). It should be pointed out that no accelerating conditions, as low pH or high enzyme concentrations, were used.

The WL values obtained were similar to the ones obtained in the absence of the enzyme. The lack of consecutive N-acetyl-D-glucosamine residues in low DA materials is responsible for the poor chain cleavage of chitosan, because their degradation kinetics are inversely related to the degree of acetylation. This can be explained by the fact that molecules consisting primarily of β -1,4-linked D-glucosamine residues are not accessible to the lysozyme active site. Indeed, the lysozyme can only access and act on sites where more than three N-acetyl-D-glucosamine sequences are present. A more extensive explanation for this phenomenon can be found elsewhere (26, 53).

One of the key aspects influencing the effectiveness of chitosan conduits in nerve repair is the swelling ability. It is critical to guarantee that swelling will not cause compression phenomena in the implanted scaffold, pressing the nerve or occluding the lumen, which could lead to ineffective nerve

functioning and regeneration (6). Still, it is important that the material swells to a certain extent *in vitro*, to be able to integrate the culture medium needed for cell survival, and *in vivo*, to mimic endogenous tissues, which are mainly composed by water ($\approx 60\%$ of the total weight). In this experimental work the swelling will be referred to as water uptake (WU).

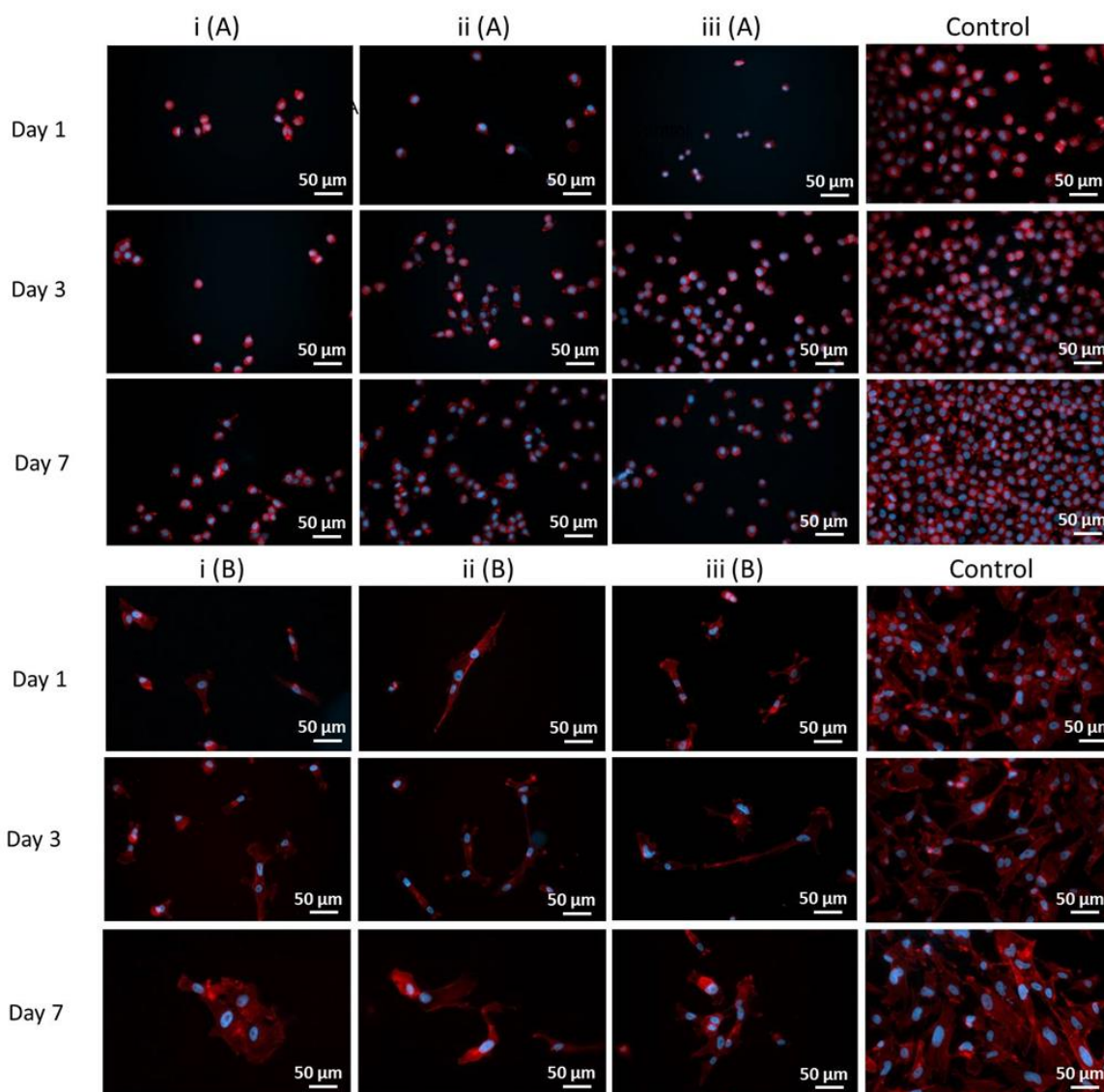


Figure V-8 - Phalloidin/DAPI staining of cell lines after 1 (i), 3 (ii) and 7 (iii) days after direct seeding on chitosan membranes. A) L929 cell line morphology on chitosan films; and B) Schwann cell line morphology on chitosan films. Scale bar: 50 μm .

Chemically, the swelling performance of a material is a balance between the presence of hydrophilic groups able to interact with water and the amount and strength of intramolecular bonds. Despite having the lower surface wettability, the membrane DA III is the one having the higher water uptake (inversely to what occurs for the membrane DA I). This is attributed to the fact that

intramolecular hydrogen bonds established between hydroxyl groups and amino groups are stronger than that formed between these same groups and water molecules (44). The bonding strength can result in more rigid structures, unable to efficiently incorporate, or even prone to extrude water. The membranes composed by the chitosan's with the higher degrees of acetylation have less amine groups available, with respect to the ones with the lowest DA, thus favouring the entering of water.

In vitro biomineralization of the produced membranes would be an undesired phenomenon for peripheral nerve regeneration applications, since the appearance of calcification around the implanted material will have negative effects over the regenerative process. Although chitosan itself usually does not have the capacity to calcify, it should be assured that our membranes would not mineralize under conditions similar to human body. Since no traces of Ca and P were detected in the surface of the membranes after 30 days in SBF, it can be asserted that no mineralization occurred.

When speaking about implanted materials it is important to take into account that, to a higher or lower extent, they will have to withstand mechanical stress. Indeed, a nerve is under tensile load *in situ*, as evidenced by the fact that it retracts when severed. The biological mechanical parameters of tissues comprehend a wide spectrum of values. In the specific case of artificial nerve grafts, they will have to endure the *in situ* stress to which peripheral nerves are submitted, while suture holding ability will also be needed. In addition, it is well-known that cells have a specific behaviour in response to mechanical stress. The structural organization of peripheral nerves enables them to function while tolerating and adapting to stresses placed upon them by postures and movements of the trunk, head and limbs. They are exposed to combinations of tensile, shear, and compressive stresses that result in nerve excursion, strain and transverse contraction. Thus, the tolerance of nerve guidance conduits to stiffness and strength should be enough to cope with the *in vivo* developed stresses, without collapsing or losing shape. For this reason, a proper mechanical characterization makes part of the most important physical tests to be performed over an implantable PNR system (54, 55).

Dynamic mechanical analysis (DMA) is a non-destructive technique that permits to characterize the mechanical and viscoelastic features of biomaterials, given an idea about which will be their mechanical behaviour after *in vivo* implantation (56). Taken into account the high moisture conditions of the physiological environment, it is expected for the membranes to be hydrated once implanted in the human body, and for this reason they were immersed in PBS before the DMA measurements. The membranes DA I and DA II have a similar E' . However, a more pronounced difference is observed for DA III, presenting the lower E' , which is synonymous of a lower stiffness. An occurrence of a slight

decrease of storage modulus (E'), and also loss factor ($\tan \delta$), with the increase in the DA is confirmed by literature (30). This behavior is consistent with the water uptake ability of the membranes and the plasticization effect of water molecules in such kind of polysaccharides, increasing their molecular mobility and decreasing the stiffness of the material. A similar loss of the stiffness due to the effect of water interacting with chitosan molecules was previously reported in pure chitosan membranes (57). It should also be pointed out that in all the membrane formulations no evident variations of E' along the frequency axis were seen, indicating that no relaxation phenomena took place in the membranes within the time scale covered by the experiments, and confirming their structural stability along the studied frequency range. The $\tan \delta$ provides information about the damping properties of the material (58, 59). In this case, DA III was the membrane with the lower $\tan \delta$, indicating a higher elastic character.

In a general manner, the developed membranes presented ≈ 10 to 20 MPa in Young Modulus, allowing the cell attachment and spreading, favoring Schwann cell proliferation when compared to L929 fibroblasts. As expected and previously reported in the literature, in a general way, nervous system cells prefer softer and more flexible membranes (60-62), which was the case of DA III, with ≈ 10 MPa in Young Modulus. The values of healthy peripheral nerves vary greatly in the literature. Related to fresh healthy nerves, the values of Young Modulus in mice and rats are very low (63) when compared to pigs (64) creating a range that goes from 0.5 MPa (in mice) to 7.75 MPa (in pigs). In this respect, comparing our data with the values of mechanical properties to fresh healthy *in vivo* nerves in pigs (64, 65) the values were similar and in the same range of the ones reported in the literature for porcine peroneal and tibial nerves (≈ 7.43 - 7.75 MPa).

Although it is a general concept in tissue engineering that mechanical strength of nerve guidance conduits should not outperform the peripheral nerve mechanical properties (6), there is a large variability in mechanical properties of biomaterials envisioned for peripheral nerve regeneration. Indeed, little research has been performed to find the standard reference value for ideal materials to be used with this goal. Hydrogels normally present a low value of Young Modulus, up to 1MPa (66-68).

Fabricated membranes planned for peripheral nerve regeneration usually show higher values of Young Modulus. For instance, PCL/PLA films revealed values ranging from 60 MPa in one study (69) to 175.52 in other report (70). When we consider poly- ϵ -caprolactone membranes, they have Young Modulus values ranging from 108.90 ± 7.13 to 69.60 ± 13.83 (71). All the references cited above display much higher values than the ones presented by the studied low acetylated chitosan membranes

(\approx 10 to 19 MPa). These results were also compared to other values obtained for chitosan membranes, with similar conclusions (30).

After damage in peripheral nerves, a series of physiological events take place, named Wallerian degeneration. As part of the process, Schwann cells dedifferentiate and proliferate to participate in the removal of myelin and axon debris, to secrete a series of neurotrophic factors and to form the bands of Bungner, which will act as guide for the regenerating axons. Ultimately, Schwann cells (SCs) will help in axon re-myelination. Consequently, for an implant to mediate a successful guided regeneration, it should promote SCs adhesion and proliferation (72). Simultaneously, the formation of fibrotic tissue is started. This process has the purpose to avoid the extension of the damage but supposes one of the main causes of regeneration failure. This appearance of fibrotic tissue is mediated by excessive fibroblasts infiltration and excessive collagen production (73, 74). Fibroblasts are the primary cell type participating in collagen synthesis and the build-up of connective tissue, as these cells are responsible for normal tissue homeostatic processes, such as tissue repair in response to injury. For this reason, the obtaining of a PNR scaffold able to avoid excessive fibroblast adherence will be of fundamental importance, although it is a clear technological challenge.

At the seventh day of the study the control of fibroblasts showed a much higher number of cells when compared to that corresponding to SCs. Nevertheless, the high proliferation of fibroblasts in the controls contrasts with the one in the membranes, thus indicating an inefficient capacity of these systems to support fibroblasts growth. Regarding SCs, the ability of the studied formulations to support the proliferation of this cell line was evidenced, with a much positive outcome in the case of DA III. The results obtained for L929 fibroblasts proved a low metabolic activity of the cells seeded in the DA membranes when compared to the controls. In the case of SCs, clearly smaller differences can be appreciated between the controls and the studied formulations. The DA III membranes were the ones giving rise to higher metabolic activity values, with significant differences regarding DA I and DA II and the initial and final time-points of study. The proliferation of fibroblasts in the three membranes was much lower than in the controls, while the formulation inducing higher proliferation of SCs was the DA III, with significant differences with respect to DA I and DA II. Although the value of RFU for Schwann cells also seem low, it should be kept in mind that this specific cell line presents low values of RFU when submitted to this type of studies. In accordance, these results confirmed the ones obtained in the cell metabolic activity studies.

In the case of L929 cells, Phalloidin/DAPI revealed that these cells are not expressing their habitual phenotype, an indicative of the absence of adherence to the membranes. Nevertheless, SCs seeded in the DA III membranes presented their characteristic functional phenotype, spread and elongated. The biological tests also confirmed a much better adherence and proliferation of SCs, including typical phenotypic differentiation, than fibroblasts to the analyzed membranes, above all noticeable in the case of the DA III one. One possible explanation for that is related to the mechanical properties. Cells are known to apply tension on their substrate, particularly during adhesion and migration processes, and have the ability to sense the underlying elasticity through their cellular receptors, primarily integrins, which then act as mechanotransducers. Well-described mechanotransducers include stretch-mediated ion channels (75), primary cilia (76) and integrins (77). Stiffness sensing has been demonstrated in a variety of cell types including endothelial cells (78), smooth muscle cells (79) transformed cells (80) and, specifically relate to PNR, Schwann cells (62) and fibroblasts (81).

Fibroblasts are known to have a superior adhesion in rigid substrates, and this apparent preference for a stiff substrates is known as "durotaxis" (81). On the other hand, nervous system cells and components such as scwhann cells and neurons, have a preference for softer matrix (60-62). Therefore, mechanics are an essential parameter for regenerative medicine and have to be controlled in detail, so they can influence specific cell adhesion. In relation to the studied samples, the native mechanical environment of DA III membrane was able to elicit a favorable Schwann cell response, since it presented itself as less stiff and more elastic, when compared to DA I and DA II. This not only explains why Schwann cells adhere in a higher extent to this matrix when compared to fibroblasts, but also sheds light on why DA III membrane was remarkably better in relation to less acetylated membranes. This modulated and preferential cellular adhesion is a good preliminary indicator for potential SC colonization and low fibroblastic infiltration once the systems are implanted *in vivo*. It is important to take into account though, that the presence of a certain number of fibroblasts will be necessary to sustain the healing process. Another possible explanation is an interaction based on non-specific electrostatic forces occurring between protonated amine groups from glucosamine units and negatively charged carboxylate and sulphate groups found onto the specific cell surface (31). DA III revealed itself as the membrane with higher potential for PNR purposes, thus being the one selected for further studies.

Although the general conclusion from most studies is that the lowest DA value possible is normally the best in terms of cell adhesion, our findings were different after the extensive characterization of these membranes, having the best result for the 5 % DA membrane. However, our results are in agreement with another report focused on chitosan targeted for PNR, in which the optimal DA was also 5 % (16). The physicochemical characterization played a crucial role in the understanding of the obtained results, also shedding light on how and why such particular biological performance was displayed. To the superior performance of DA III membrane contributed its increased roughness and surface energy as well as adequate mechanical properties.

We fundamentally studied in detail this niche of low DA values for tissue regeneration and effectively found significant differences between them, which was our initial hypothesis.

The physicochemical and biological features of DA III membrane revealed it as a very versatile and promising biomaterial to be explored in PNR, with different possible applications. This membrane may be suitable as internal guiding cue inside tubular nerve conduits, to function as an adherent platform for Schwann cells and growing axons, while prevents excessive fibroblast infiltration (**Supplementary Figure V-1**). This kind of guidance has been described to be of fundamental importance when treating large gap defects. The DA III membrane material presents the right characteristics to be used straightaway with this purpose. Other possible application of the membrane may be as a basis for the construction of the tubular nerve guidance conduit itself, since the material can be easily rolled or wrapped (**Supplementary Figure V-2**). However, for this specific purpose, slight production modifications and further characterization would be required.

V-6. CONCLUSION

This extensive study aimed at providing a broad view on the suitability of chitosan membranes with three different degrees of acetylation (DAI: 1 %, DAII: 2 %, DAIII: 5 %) to support peripheral nerve regeneration. The surface and bulk properties of the three membranes are similar, indicating good suitability for peripheral nerve purposes, above all in the case the DA III formulation. The superior potential of the DA III membrane regarding PNR was confirmed by the biological studies, which showed higher proliferation and phenotypic expression of SCs cells when compared with DA I and DA II membranes. Interestingly, all the three formulations presented resistance to fibroblast adhesion and proliferation. In summary, this experimental work has led to the conclusion that DA III membrane

should be the one considered for further PNR applications, since it will not induce calcification of the implant, excessive swelling or fibroblasts infiltration and it will allow a guided regeneration of the nerves mediated by preferential Schwann cell adhesion and proliferation.

V-7. ACKNOWLEDGMENTS

This work has received funding from the European Community's Seventh Framework Programme (FP7-HEALTH-2011) under grant agreement n° 278612 (BIOHYBRID). This study was also funded by European Union's FP7 Programme under grant agreement no REGPOT-CT2012-316331-POLARIS. The authors thank the chitosan raw material provided by Altakitin S.A. (Lisboa, Portugal).

V-8. REFERENCES

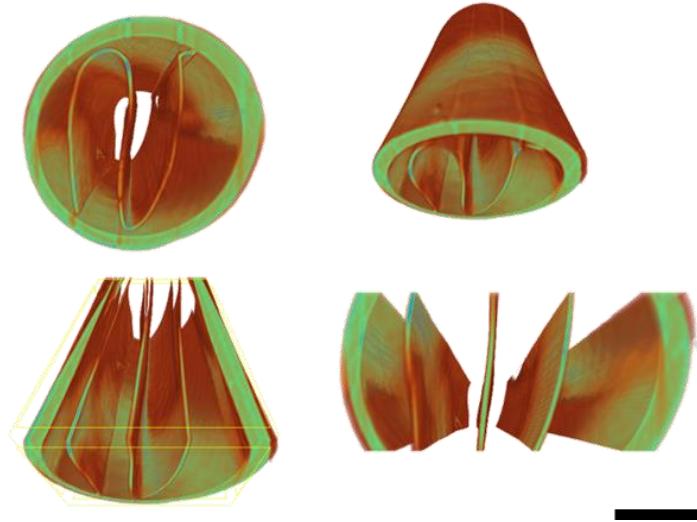
1. Robinson LR. Traumatic injury to peripheral nerves. *Muscle Nerve*. 2000;23(6):863-73.
2. Noble J, Munro CA, Prasad VS, Midha R. Analysis of upper and lower extremity peripheral nerve injuries in a population of patients with multiple injuries. *J Trauma*. 1998;45(1):116-22.
3. Taylor CA, Braza D, Rice JB, Dillingham T. The incidence of peripheral nerve injury in extremity trauma. *American journal of physical medicine & rehabilitation / Association of Academic Physiatrists*. 2008;87(5):381-5.
4. Daly W, Yao L, Zeugolis D, Windebank A, Pandit A. A biomaterials approach to peripheral nerve regeneration: bridging the peripheral nerve gap and enhancing functional recovery. *J R Soc Interface*. 2012;9(67):202-21.
5. Ray WZ, Mackinnon SE. Clinical outcomes following median to radial nerve transfers. *J Hand Surg Am*. 2011;36(2):201-8.
6. Nectow AR, Marra KG, Kaplan DL. Biomaterials for the development of peripheral nerve guidance conduits. *Tissue engineering Part B, Reviews*. 2012;18(1):40-50.
7. Saracino GAA, Cigognini D, Silva D, Caprini A, Gelain F. Nanomaterials design and tests for neural tissue engineering. *Chem Soc Rev*. 2013;42(1):225-62.
8. Que J, Cao Q, Sui T, Du S, Kong D, Cao X. Effect of FK506 in reducing scar formation by inducing fibroblast apoptosis after sciatic nerve injury in rats. *Cell Death Dis*. 2013;4:e526.
9. Ngeow WC. Scar less: a review of methods of scar reduction at sites of peripheral nerve repair. *Oral Surg Oral Med Oral Pathol Oral Radiol Endod*. 2010;109(3):357-66.
10. Ceci ML, Mardones-Krsulovic C, Sanchez M, Valdivia LE, Allende ML. Axon-Schwann cell interactions during peripheral nerve regeneration in zebrafish larvae. *Neural Dev*. 2014;9:22.
11. Bunge RP. The role of the Schwann cell in trophic support and regeneration. *J Neurol*. 1994;242(1 Suppl 1):S19-21.
12. Madduri S, Gander B. Schwann cell delivery of neurotrophic factors for peripheral nerve regeneration. *Journal of the peripheral nervous system : JPNS*. 2010;15(2):93-103.
13. Agrawal AM, Manek RV, Kolling WM, Neau SH. Water distribution studies within microcrystalline cellulose and chitosan using differential scanning calorimetry and dynamic vapor sorption analysis. *J Pharm Sci*. 2004;93(7):1766-79.
14. Gnani S, Barwig C, Freier T, Haastert-Talini K, Grothe C, Geuna S. Chapter One - The Use of Chitosan-Based Scaffolds to Enhance Regeneration in the Nervous System. In: Stefano Geuna IPPT, Bruno B, editors. *Int Rev Neurobiol*. Volume 109: Academic Press; 2013. p. 1-62.
15. Gonzalez-Perez F, Cobianchi S, Geuna S, Barwig C, Freier T, Udina E, et al. Tubulization with chitosan guides for the repair of long gap peripheral nerve injury in the rat. *Microsurgery*. 2015;35(4):300-8.
16. Haastert-Talini K, Geuna S, Dahlin LB, Meyer C, Stenberg L, Freier T, et al. Chitosan tubes of varying degrees of acetylation for bridging peripheral nerve defects. *Biomaterials*. 2013;34(38):9886-904.

17. Wrobel S, Serra SC, Ribeiro-Samy S, Sousa N, Heimann C, Barwig C, et al. In vitro evaluation of cell-seeded chitosan films for peripheral nerve tissue engineering. *Tissue engineering Part A*. 2014;20(17-18):2339-49.
18. Luo Y, Wang Q. Recent development of chitosan-based polyelectrolyte complexes with natural polysaccharides for drug delivery. *Int J Biol Macromol*. 2014;64C:353-67.
19. Cho MH, Kim KS, Ahn HH, Kim MS, Kim SH, Khang G, et al. Chitosan gel as an in situ-forming scaffold for rat bone marrow mesenchymal stem cells in vivo. *Tissue engineering Part A*. 2008;14(6):1099-108.
20. Ren D, Yi H, Wang W, Ma X. The enzymatic degradation and swelling properties of chitosan matrices with different degrees of N-acetylation. *Carbohydr Res*. 2005;340(15):2403-10.
21. Zheng L-Y, Zhu J-F. Study on antimicrobial activity of chitosan with different molecular weights. *Carbohydr Polym*. 2003;54(4):527-30.
22. Chatterjee S, Guha AK. A study on biochemical changes during cultivation of *Rhizopus oryzae* in deproteinized whey medium in relation to chitosan production. *Lett Appl Microbiol*. 2014;59(2):155-60.
23. Ignatova M, Kalinov K, Manolova N, Toshkova R, Rashkov I, Alexandrov M. Quaternized chitosan-coated nanofibrous implants loaded with gossypol prepared by electrospinning and their efficacy against Graffi myeloid tumor. *Journal of biomaterials science Polymer edition*. 2014;25(3):287-306.
24. Xu X, Li Y, Shen Y, Guo S. Synthesis and in vitro cellular evaluation of novel anti-tumor norcantharidin-conjugated chitosan derivatives. *Int J Biol Macromol*. 2013;62:418-25.
25. Chatelet C, Damour O, Domard A. Influence of the degree of acetylation on some biological properties of chitosan films. *Biomaterials*. 2001;22(3):261-8.
26. Freier T, Koh HS, Kazazian K, Shoichet MS. Controlling cell adhesion and degradation of chitosan films by N-acetylation. *Biomaterials*. 2005;26(29):5872-8.
27. Lieder R, Darai M, Thor MB, Ng CH, Einarsson JM, Gudmundsson S, et al. In vitro bioactivity of different degree of deacetylation chitosan, a potential coating material for titanium implants. *J Biomed Mater Res A*. 2012;100(12):3392-9.
28. Mogilevskaya EL, Akopova TA, Zelenetskii AN, Ozerin AN. The crystal structure of chitin and chitosan. *Polym Sci Ser A*. 2005;48(2):216-26.
29. Prasitsilp M, Jenwithisuk R, Kongsuwan K, Damrongchai N, Watts P. Cellular responses to chitosan in vitro: the importance of deacetylation. *J Mater Sci Mater Med*. 2000;11(12):773-8.
30. Wenling C, Duohui J, Jiamou L, Yandao G, Nanming Z, Xiufang Z. Effects of the degree of deacetylation on the physicochemical properties and Schwann cell affinity of chitosan films. *Journal of biomaterials applications*. 2005;20(2):157-77.
31. Amaral IF, Lamghari M, Sousa SR, Sampaio P, Barbosa MA. Rat bone marrow stromal cell osteogenic differentiation and fibronectin adsorption on chitosan membranes: the effect of the degree of acetylation. *J Biomed Mater Res A*. 2005;75(2):387-97.
32. Amaral IF, Cordeiro AL, Sampaio P, Barbosa MA. Attachment, spreading and short-term proliferation of human osteoblastic cells cultured on chitosan films with different degrees of acetylation. *Journal of Biomaterials Science, Polymer Edition*. 2007;18(4).
33. Lim SM, Song DK, Cho KJ, Oh SH, Lee-Yoon DS, Bae EH, et al. Cell Adhesion and Degradation Behaviors of Acetylated Chitosan Films. In: Ibrahim F, Osman NAA, Usman J, Kadri NA, editors. 3rd Kuala Lumpur International Conference on Biomedical Engineering 2006: Biomed 2006, 11 – 14 December 2006 Kuala Lumpur, Malaysia. Berlin, Heidelberg: Springer Berlin Heidelberg; 2007. p. 94-7.
34. Owens DK, Wendt RC. Estimation of the surface free energy of polymers. *J Appl Polym Sci*. 1969;13(8):1741-7.
35. Kokubo T, Takadama H. How useful is SBF in predicting in vivo bone bioactivity? *Biomaterials*. 2006;27(15):2907-15.
36. Baniyadi H, Ramazani SAA, Mashayekhan S. Fabrication and characterization of conductive chitosan/gelatin-based scaffolds for nerve tissue engineering. *Int J Biol Macromol*. 2015;74:360-6.
37. Wang Y, Zhao Y, Sun C, Hu W, Zhao J, Li G, et al. Chitosan Degradation Products Promote Nerve Regeneration by Stimulating Schwann Cell Proliferation via miR-27a/FOXO1 Axis. *Mol Neurobiol*. 2014.
38. Chang H-I. Cell Responses to Surface and Architecture of Tissue Engineering Scaffolds. Yiwei W, editor: InTech; 2011.
39. Kubiak KJ, Wilson MC, Mathia TG, Carras S. Dynamics of contact line motion during the wetting of rough surfaces and correlation with topographical surface parameters. *Scanning*. 2011;33(5):370-7.
40. Choe JH, Lee SJ, Lee YM, Rhee JM, Lee HB, Khang G. Proliferation rate of fibroblast cells on polyethylene surfaces with wettability gradient. *J Appl Polym Sci*. 2004;92(1):599-606.
41. Sethuraman A, Han M, Kane RS, Belfort G. Effect of surface wettability on the adhesion of proteins. *Langmuir*. 2004;20(18):7779-88.
42. Lai H-C, Zhuang L-F, Liu X, Wieland M, Zhang Z-Y, Zhang Z-Y. The influence of surface energy on early adherent events of osteoblast on titanium substrates. *Journal of Biomedical Materials Research Part A*. 2010;93A(1):289-96.

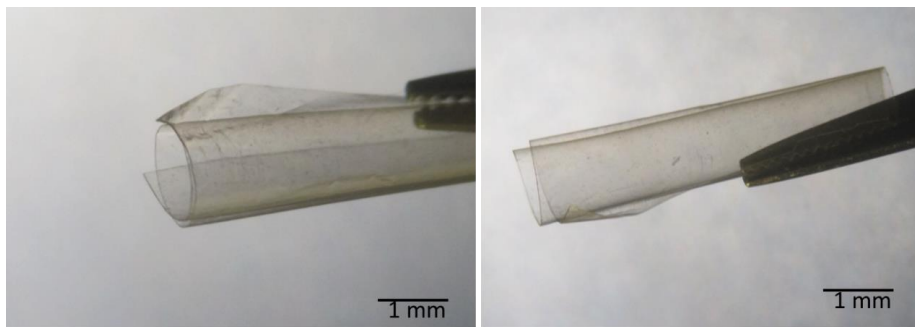
43. Dhiman HK, Ray AR, Panda AK. Characterization and evaluation of chitosan matrix for in vitro growth of MCF-7 breast cancer cell lines. *Biomaterials*. 2004;25(21):5147-54.
44. Wan Y, Creber KAM, Peppley B, Bui VT. Ionic conductivity of chitosan membranes. *Polymer*. 2003;44(4):1057-65.
45. Cho YW, Jang J, Park CR, Ko SW. Preparation and solubility in acid and water of partially deacetylated chitins. *Biomacromolecules*. 2000;1(4):609-14.
46. Li J, Revol J, Marchessault RH. Effect of N-Sulfonation on the Colloidal and Liquid Crystal Behavior of Chitin Crystallites. *J Colloid Interface Sci*. 1997;192(2):447-57.
47. Younes I, Rinaudo M. Chitin and chitosan preparation from marine sources. Structure, properties and applications. *Mar Drugs*. 2015;13(3):1133-74.
48. Gamiz-Gonzalez MA, Piskin AE, Pandis C, Chatzimanolis-Moustakas C, Kyritsis A, Mari B, et al. Determining the influence of N-acetylation on water sorption in chitosan films. *Carbohydr Polym*. 2015;133:110-6.
49. Wang SF, Shen L, Tong YJ, Chen L, Phang IY, Lim PQ, et al. Biopolymer chitosan/montmorillonite nanocomposites: Preparation and characterization. *Polym Degrad Stabil*. 2005;90(1):123-31.
50. Dhawade PP, Jagtap RN. Characterization of the glass transition temperature of chitosan and its oligomers by temperature modulated differential scanning calorimetry. *Adv Appl Sci Res*. 2012;3(3):1372-82.
51. Guinesi LS, Cavalheiro ÉTG. The use of DSC curves to determine the acetylation degree of chitin/chitosan samples. *Thermochim Acta*. 2006;444(2):128-33.
52. Steed MB, Mukhatyar V, Valmikinathan C, Bellamkonda RV. Advances in bioengineered conduits for peripheral nerve regeneration. *Atlas of the oral and maxillofacial surgery clinics of North America*. 2011;19(1):119-30.
53. Nordtveit RJ, Vårum KM, Smidsrød O. Degradation of partially N-acetylated chitosans with hen egg white and human lysozyme. *Carbohydr Polym*. 1996;29(2):163-7.
54. Millesi H, Zoch G, Reihnsner R. Mechanical properties of peripheral nerves. *Clin Orthop Relat Res*. 1995(314):76-83.
55. Meaney DF. Mechanical properties of implantable biomaterials. *Clin Podiatr Med Surg*. 1995;12(3):363-84.
56. Sobral JM, Caridade SG, Sousa RA, Mano JF, Reis RL. Three-dimensional plotted scaffolds with controlled pore size gradients: Effect of scaffold geometry on mechanical performance and cell seeding efficiency. *Acta Biomater*. 2011;7(3):1009-18.
57. Mano JF. Viscoelastic Properties of Chitosan with Different Hydration Degrees as Studied by Dynamic Mechanical Analysis. *Macromol Biosci*. 2008;8(1):69-76.
58. Ghosh S, Gutierrez V, Fernández C, Rodriguez-Perez MA, Viana JC, Reis RL, et al. Dynamic mechanical behavior of starch-based scaffolds in dry and physiologically simulated conditions: Effect of porosity and pore size. *Acta Biomater*. 2008;4(4):950-9.
59. Yan L-P, Wang Y-J, Ren L, Wu G, Caridade SG, Fan J-B, et al. Genipin-cross-linked collagen/chitosan biomimetic scaffolds for articular cartilage tissue engineering applications. *J Biomed Mater Res A*. 2010;95A(2):465-75.
60. Teixeira AI, Ilkhanizadeh S, Wigenius JA, Duckworth JK, Inganas O, Hermanson O. The promotion of neuronal maturation on soft substrates. *Biomaterials*. 2009;30(27):4567-72.
61. Flanagan LA, Ju YE, Marg B, Osterfield M, Janmey PA. Neurite branching on deformable substrates. *Neuroreport*. 2002;13(18):2411-5.
62. Ning L, Xu Y, Chen X, Schreyer DJ. Influence of mechanical properties of alginate-based substrates on the performance of Schwann cells in culture. *Journal of biomaterials science Polymer edition*. 2016;27(9):898-915.
63. Borschel GH, Kia KF, Kuzon Jr WM, Dennis RG. Mechanical properties of acellular peripheral nerve. *Journal of Surgical Research*. 2003;114(2):133-9.
64. Zilic L, Garner PE, Yu T, Roman S, Haycock JW, Wilshaw S-P. An anatomical study of porcine peripheral nerve and its potential use in nerve tissue engineering. *Journal of Anatomy*. 2015;227(3):302-14.
65. Zilic L, Wilshaw S-P, Haycock JW. Decellularisation and histological characterisation of porcine peripheral nerves. *Biotechnology and Bioengineering*. 2016;113(9):2041-53.
66. Kulshrestha AS, Mahapatro A, Henderson LA, editors. *Biomaterials: American Chemical Society*; 2010.
67. Wong JPF, Baptista D, Brown RA. Pre-crosslinked polymeric collagen in 3-D models of mechanically stiff tissues: Blended collagen polymer hydrogels for rapid layer fabrication. *Acta Biomaterialia*. 2014;10(12):5005-11.
68. Gunn JW, Turner SD, Mann BK. Adhesive and mechanical properties of hydrogels influence neurite extension. *J Biomed Mater Res A*. 2005;72(1):91-7.
69. Mobasser SA, Terenghi G, Downes S. Micro-structural geometry of thin films intended for the inner lumen of nerve conduits affects nerve repair. *Journal of Materials Science: Materials in Medicine*. 2013;24(7):1639-47.
70. Sun M, Downes S. Physicochemical characterisation of novel ultra-thin biodegradable scaffolds for peripheral nerve repair. *Journal of Materials Science: Materials in Medicine*. 2009;20(5):1181-92.
71. de Luca AC, Terenghi G, Downes S. Chemical surface modification of poly- ϵ -caprolactone improves Schwann cell proliferation for peripheral nerve repair. *Journal of tissue engineering and regenerative medicine*. 2014;8(2):153-63.

72. Namgung U. The role of Schwann cell-axon interaction in peripheral nerve regeneration. *Cells Tissues Organs*. 2014;200(1):6-12.
73. Atkins S, Smith KG, Loescher AR, Boissonade FM, O'Kane S, Ferguson MW, et al. Scarring impedes regeneration at sites of peripheral nerve repair. *Neuroreport*. 2006;17(12):1245-9.
74. Park JS, Lee JH, Han CS, Chung DW, Kim GY. Effect of hyaluronic acid-carboxymethylcellulose solution on perineural scar formation after sciatic nerve repair in rats. *Clin Orthop Surg*. 2011;3(4):315-24.
75. Martinac B. Mechanosensitive ion channels: molecules of mechanotransduction. *Journal of cell science*. 2004;117(Pt 12):2449-60.
76. Berbari NF, O'Connor AK, Haycraft CJ, Yoder BK. The primary cilium as a complex signaling center. *Current biology : CB*. 2009;19(13):R526-35.
77. Galbraith CG, Yamada KM, Sheetz MP. The relationship between force and focal complex development. *The Journal of cell biology*. 2002;159(4):695-705.
78. Reinhart-King CA, Dembo M, Hammer DA. The dynamics and mechanics of endothelial cell spreading. *Biophys J*. 2005;89(1):676-89.
79. Isenberg BC, Dimilla PA, Walker M, Kim S, Wong JY. Vascular smooth muscle cell durotaxis depends on substrate stiffness gradient strength. *Biophys J*. 2009;97(5):1313-22.
80. Levental KR, Yu H, Kass L, Lakins JN, Egeblad M, Ertler JT, et al. Matrix crosslinking forces tumor progression by enhancing integrin signaling. *Cell*. 2009;139(5):891-906.
81. Lo CM, Wang HB, Dembo M, Wang YL. Cell movement is guided by the rigidity of the substrate. *Biophysical Journal*. 2000;79(1):144-52.

V-9. SUPPLEMENTARY DATA



Supplementary Figure V-1 - 3D micro-CT reconstruction of the membrane serving as a guiding luminal filler. In this specific reconstruction, the chitosan tube is composed of DA III membrane and there is a Z shaped DA I membrane inside the tube, showing its flexibility. Scale bar: 2 mm.



Supplementary Figure V-2 - Stereomicroscope image of the DA III membranes wrapped to easily form a tubular device. Scale bar: 1 mm.

Chapter VI

Enhanced biological performance of chitosan/keratin membranes for peripheral nerve applications

Chapter VI

Enhanced biological performance of chitosan/keratin membranes for peripheral nerve applications¹

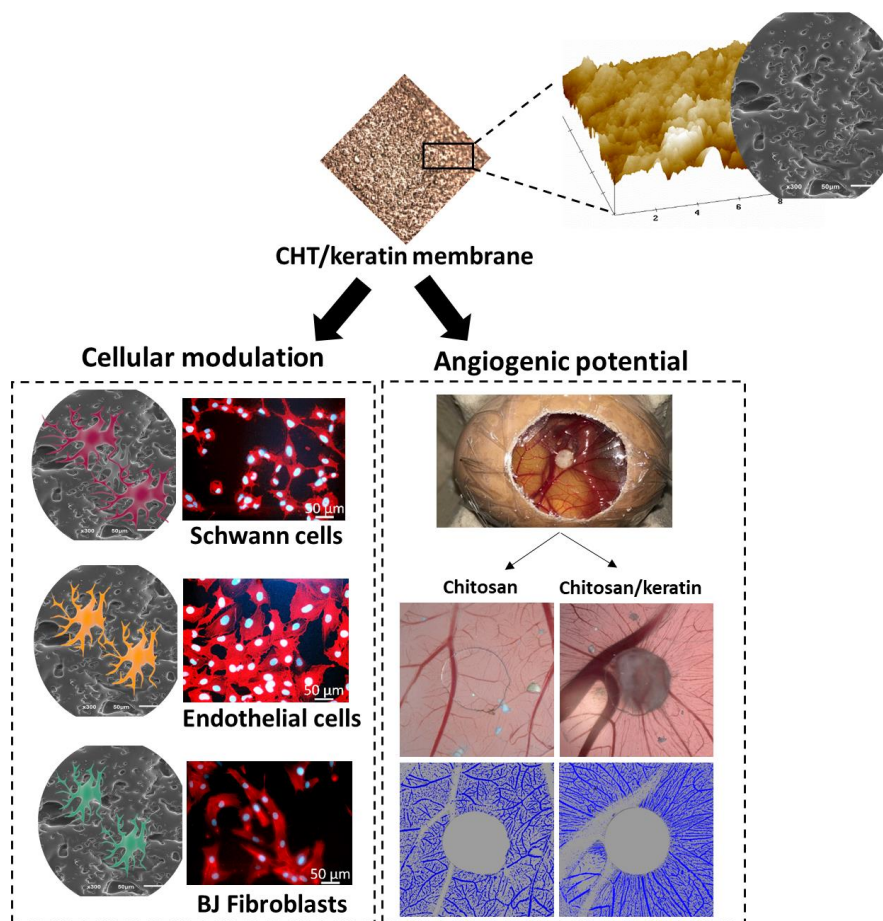
ABSTRACT

Although surgical management of peripheral nerve injuries (PNI) has improved over time, autografts are still the current “gold standard” treatment for PNIs, which still present numerous limitations. In an attempt to improve natural biomaterial-based nerve guidance conduits (NGC), chitosan (CHT), a derivative of the naturally occurring biopolymer chitin, has been explored for peripheral nerve regeneration (PNR). In addition to CHT, keratin has gained enormous attention as a biomaterial and tissue engineering scaffolding. In this study, biomimetic CHT/keratin membranes were produced using solvent casting technique. These membranes were broadly characterized in terms of surface topography and physicochemical properties, with techniques such as Fourier Transform Infrared Spectroscopy (FTIR), Differential scanning calorimetry (DSC), contact angle measurements, weight loss and water uptake, as well as Scanning Electron Microscopy (SEM) and Atomic force microscopy (AFM). Biological *in vitro* assays were also performed, where a preliminary cytotoxicity screening with L929 fibroblast cell line revealed that the membranes and respective materials are suitable for cell culture. In addition, Schwann cells, fibroblast, and endothelial cells, were directly seeded in the membranes. Quantitative and qualitative assays revealed that the addition of keratin enhanced cell viability and adhesion. Based on *in vitro* encouraging results, the *in vivo* angiogenic/antiangiogenic potential of CHT and CHT/keratin membranes was assessed, using an optimized chick embryo chorioallantoic membrane assay, where higher angiogenic responses were seen in keratin-enriched materials. Overall, the obtained results indicate the higher potential of CHT/keratin membranes for guided tissue regeneration applications in the field of PNR.

Keywords: Chitosan, keratin, peripheral nerve, biomaterials

¹This chapter is based on the following publication: **Carvalho CR, Costa JB, Costa L, Silva-Correia J, Moay ZK, NG KW, Reis RL, Oliveira JM.** Enhanced biological performance of chitosan/keratin membranes for peripheral nerve applications. (Submitted)

VI-1. GRAPHICAL ABSTRACT



VI-2. INTRODUCTION

Peripheral nerve injuries (PNI) affect a vast number of the world population (1). It has been estimated that approximately 2 % - 3 % of all patients admitted to a Level I trauma centers suffer from PNIs (2). However, these injuries can result from traumatic or non-traumatic causes, where the correct diagnosis might not be performed. Therefore, it is difficult to estimate the real number of affected people. Still being one of the great challenges in the regenerative medicine field, PNIs cause significant sensorimotor impairment, disabling neuropathic pain and allodynia, which can last for a lifetime (3). Furthermore, numerous studies suggest that functional and structural changes in the patient's brain are caused by PNIs and by its devastating life-long consequences (4).

After a nerve injury, peripheral nerve regeneration is frequently and mistakenly believed to occur entirely. That is especially true when compared with nerve regeneration in the central nervous system

(CNS), which is extremely limited. However, even with appropriate surgical treatment, severe incapacity often prevails after PNI. In order to improve the limited functional outcomes, strategies focused on increasing the speed of axonal growth, maintaining Schwann cells in a healthy, repair-capable state and keeping target tissues receptive to reinnervation are required (5).

Nowadays, nerve autografting, which consists in the implantation of patient's own healthy nerves into the injured site, remains the gold standard treatment for peripheral nerve gaps longer than 5 mm (6). To date, autografts have offered the best results in nerve regeneration under tension (7). However, nerve autografts present several limitations such as donor tissue availability, loss of donor nerve function or formation of neuromas (8). Consequently, there is an important need for the development of new and improved solutions for the treatment of PNIs (9). In this context, artificial nerve guidance conduits (NGCs) and protectant nerve wraps (PNW) can create a favorable microenvironment by mimicking the structure and composition of peripheral nerve (10). Membranes have also been used in guided tissue regeneration (GTR) to regulate tissue growth (11). This method is based on the principle that a physical barrier is needed to stop the invasion of fast proliferating cells, such as collagen-depositing fibroblasts, while protecting the injury site (12). This barrier will also provide an opportunity for more specific cells, such as Schwann cells and endothelial cells to migrate and participate in the regenerative process.

Until now, a variety of biomaterials have been studied for the repair of PNIs, including several natural and synthetic polymers (13). Over the last few decades, a greater importance has been given to naturally-derived materials used in NGCs, PNW and membranes development, which must be biologically active and show adequate biocompatibility and biodegradability (7). These materials should also form systems as similar as possible to the extracellular matrix (ECM) and provide an increased rate of growth for the regenerating tissue (6).

Chitosan (CHT), as a natural polysaccharide, has attracted increasing attention due to its biocompatibility, biodegradability, non-toxicity, ready availability and unique physicochemical properties (14). Recent reports revealed the suitability of CHT materials as a substrate for peripheral nerve regeneration (PNR) (15). Briefly, *in vitro* biological evaluation revealed that chitosan membranes sustained the survival, growth and alignment of different neuronal cells, such as neurons and Schwann cells, being suggestive of the potential use of chitosan in neural Tissue Engineering (TE) (16). It has also been demonstrated *in vivo* that CHT NGCs could induce a notable motor and sensory functional recovery in rat sciatic nerve defects (17). Furthermore, CHT constructs applied to long distance peripheral nerve defects performed comparably to autologous nerve grafting in rats (18, 19).

Recently, keratin extracted from human hair has emerged as a captivating biomaterial, which as a human-derived protein, exhibits excellent biocompatibility, does not elicit an immune reaction upon transplantation, presents appropriate cellular-material interactions and, biodegradability (20). Progresses in extraction, purification and characterization methods have boosted keratin as a potential scaffold material for biomedical applications (21, 22). Furthermore, it has been reported that the keratin molecule consists of approximately 400-600 amino acids and contains various cell-binding sites such as LDV (Leu-Asp-Val) and RGD (Arg-Gly-Asp), strongly supporting cell adhesion (23, 24). In addition to integrin-mediated cellular binding, it has been shown that a non-integrin receptor can mediate cell-keratin interactions. These molecular findings allowed keratin to be successfully used as coating material for cell culture, resulting in an improvement of cell adhesion and proliferation (20). Furthermore, the interest in keratin also arises from the fact that the hair follicle from which keratin is extracted, is a remarkably proliferative organelle that represents a highly arranged regenerative process. However, keratin alone gives origin to very fragile materials or scaffolds, with poor strength and flexibility. Hence, polymer blending is an attractive method which is commonly used for providing polymeric materials with combined properties suitable for a specific application. Also, the addition of keratin to other biomaterials has been shown to modulate the viscoelastic and the microstructural properties.

In the field of PNR, several studies with human hair keratin have been conducted in different animal models, from mice (25) and rats (26), to rabbits (27) and non-human primates (28). Due to the visible success of a keratin hydrogel in promoting nerve repair, a phase I prospective, randomized trial is currently ongoing, entitled “Multicenter Clinical Trial of Keratin Biomaterial for Peripheral Nerve Regeneration” (ADA613738).

In this experimental work, we hypothesized the reinforcement of the biological and mechanical potential of CHT membranes by blending them with keratin, envisioning its use in PNR. The resulting membranes were physico-chemically characterized in terms of surface topography by SEM and AFM, as well as their chemical features, by FTIR, DSC, degradation and swelling and contact angles, in order to confirm if the blending was successfully achieved. Afterwards, *in vitro* culture studies for cell behavior analysis were carried out using three human cell types that play key roles in the nerve regenerative process: skin fibroblasts, Schwann cells and endothelial cells. Since vascularization is a vital and limiting process in PNR, the chick embryo chorioallantoic membrane (CAM) assay was carried out to investigate the angiogenic potential of the developed materials.

VI-3. EXPERIMENTAL SECTION

VI-3.1. Materials

Alamar Blue was purchased from Invitrogen™; Phosphate buffer saline, Acetic acid, Sodium hydroxide, Sodium sulphide, Phalloidin, M199 medium, 4',6-diamidino-2-phenylindole (DAPI), Formalin, Haematoxylin and Eosin and Heparin were purchased from Sigma-Aldrich; MTS kit and filter paper were purchased from Promega. Glutamax and Penicillin/Streptomycin (100 U/100 g/mL) were purchased from Life Technologies; Endothelial cell growth supplement (ECGS - 25 µg/mL) was acquired from Becton Dickinson; Fertilized chicken eggs were acquired from Pintobar, Portugal; UltraVision Large Volume Detection System Anti-Polyvalent was acquired from LabVision Corporation; Citrate buffer was purchased from Merck; Hydrogen peroxide was brought from Panreac; SNA-lectin and 3,3'-diaminobenzidine (DAB) solution were purchased from Vector Laboratories.

VI-3.2. Manufacturing of CHT powder

Medical grade CHT powder supplied by Altakitin S.A. (Ki2Med® LO80+, Lisbon, Portugal) with a molecular weight (MW) of 260 kDa and degree of acetylation (DA) of 5 % was obtained from *Pandalus borealis* shrimp shells using standard conditions for chitin extraction and deacetylation, following ISO 13485 requirements and specifications. The purification method consisted in homogeneous washing (liquid/liquid extraction) of CHT with EDTA and SDS for heavy metals and protein removal. After the extractions, the product was washed with deionized water and neutralized prior to lyophilization. The product was provided after analyses using several methods and techniques to attest compliance with internal standards for degree of acetylation, molecular weight, heavy metal content, protein content, endotoxins, bioburden, pH, ash content and apparent viscosity.

VI-3.3. Extraction of keratin from human hair

Random human hair samples were obtained from hair salons in Singapore and processed as previously described (29), with minor modifications. Briefly, after washing the hair samples with soap and ethanol, delipidization was done with a mixture of chloroform and methanol at a ratio of 2:1, for 24 hours. The delipidized hair was thoroughly air-dried to remove the organic solvents and snipped into

fragments as small as 1-2 mm for keratin extraction. Hair fragments (45 g) were immersed in 1 L of 0.125 M sodium sulphide solution in deionized water and incubated at 40 °C for 4 hours. The resulting solution was filtered and extensively dialyzed against deionized water using membranes of 10 kDa molecular mass cut-off to remove residual sodium sulphide. The dialyzed solution was subsequently freeze-dried to obtain keratin powder and stored at -20 °C until use. To ensure sterility, the whole process was conducted in a class II biosafety cabinet and all solutions were sterile-filtered. Typical yields were calculated to be between 20 and 40 % by weight percentage. Based on this extraction protocol, the protein fraction obtained was previously shown to contain both monomers of Types 1 and 2 hair keratins in the molecular weight range of 45-60 kDa (30), which retain the typical peptide bond profiles expected for intact proteins (31).

VI-3.4. Preparation of CHT and CHT/keratin membranes

Ki2Med® CHT powder with 5 % DA was dissolved in 0.25 M acetic acid aqueous solution to attain a final concentration of 2 %wt. For the samples containing keratin, the freeze-dried powder was added to the previous solution to achieve a 2 %wt. CHT/1 %wt. keratin solution. The solutions were stirred overnight and filtered to remove impurities. After casting onto petri dishes, samples were dried for at least 5 days at room temperature (RT). The dried membranes were neutralized in 0.25 N sodium hydroxide and washed every 30 minutes until reaching neutral pH, and further dried at room temperature in the respective molds. All membranes were sterilized with ethylene oxide (EO) gas, considered by some authors the most suitable method of sterilization for CHT membranes (32).

VI-3.5. Physicochemical characterization of CHT and CHT/keratin membranes

VI-3.5.1. Membranes thickness measurement

Membranes thickness was measured with a digital micrometer (Mitutoyo, Japan). Five membranes were used. The results are expressed as mean \pm standard deviation.

VI-3.5.2. Surface evaluation by Stereomicroscope, Scanning Electron Microscopy (SEM) and Atomic force microscopy (AFM)

Three CHT and CHT/keratin membranes were cut into 1 cm² samples. The developed membranes were examined under the Stereomicroscope + Lamp (Schott KL 200, model Stemi 1000, Zeiss) for a macroscopic inspection of their topography and general aspect. For SEM, membranes were sputter coated with gold for the analyses of their surface morphology (model S360, Leica, Cambridge, England). For surface roughness analysis, membranes were analyzed on five spots using TappingMode™ with a MultiMode connected to a NanoScope III (Veeco, USA) and non-contacting silicon nanoprobe (TESP model, Bruker). The images (10 μm x 10 μm wide) were fitted to a plane using the first-degree flatten procedure included in the NanoScope software version 4.43r8. The surface roughness was calculated as Rq (root mean square from average flat surface) and Ra (average absolute distance from average flat surface).

VI-3.5.3. Fourier Transform Infrared Spectroscopy (FTIR)

FTIR spectra of keratin powders, as well as CHT and CHT/keratin membranes, were obtained in Shimadzu IRPrestige 21 spectrometer (IRPrestige-21, Shimadzu, Japan). All spectra were acquired at room temperature by averaging 32 scans at a resolution of 4 cm⁻¹ and wavelength range 400-4000 cm⁻¹.

VI-3.5.4. X-ray diffraction (XRD)

X-ray diffraction patterns of keratin powder, CHT and CHT/keratin membranes were used to determine their crystalline structure. Measurements were performed in a Bruker D8 Advance Davinci diffractometer equipped with Cu K α radiation ($\lambda = 1.547 \text{ \AA}$), produced at 40 kV and 40 mA. The data was collected at room temperature, increment of 0.02°, 2 θ range of 5-40° and increment's acquisition time of 1 second.

VI-3.5.5. Contact angle measurements: wettability and surface energy determination

CHT and CHT/keratin membranes surface properties were studied through static contact angle (θ) measurements using the sessile drop method (33) with ultra-pure distilled water (as polar liquid) and diiodomethane (as non-polar liquid) (OCA equipment, Germany and SCA-20 software). Five measurements were carried out for each sample. Considering contact angle measurements, the surface energy was calculated using the Owens, Wendt, Rabel and Kaelble (OWRK) equation (34). During every determination, a motor-driven syringe was used to deposit a drop of liquid over the membrane surface. The images corresponding to these drops were properly recorded and analyzed. The different determinations were performed at RT and in triplicate.

VI-3.5.6. Dynamic mechanical analysis (DMA)

The viscoelastic measurements of the CHT and CHT/keratin membranes were performed using a TRITEC8000B DMA (Triton Technology, UK), equipped with the tensile mode. All samples were immersed in phosphate buffer saline (PBS) solution before measurement and left overnight at 37 °C. DMA spectra were acquired in a frequency scan ranging between 0.1 and 15 Hz for all time points. The experiments were performed under constant strain amplitude, corresponding to approximately 2 % of the original height of the sample. Five samples were tested under physiological conditions.

VI-3.5.7. Differential scanning calorimetry (DSC)

DSC analysis was performed on a DSC Q100 apparatus (TA Instruments Inc, USA). Samples were packed in a TA aluminum pan (3 - 6 mg sample weight), which was covered with a suitable aluminum cover. Both temperature and heat flux were previously calibrated with Indium. Both samples were subjected to ramp heating ranging from 0 °C to 350 °C at a rate of 5 °C/minute. The measurements were performed under dry nitrogen atmosphere, at a flow rate of 50 mL/minute.

VI-3.5.8. In vitro weight loss and water uptake

In vitro weight loss by hydrolysis and water uptake profiles of CHT and CHT/keratin membranes were evaluated through immersion in PBS, in dynamic conditions (60 rpm) in a water bath at 37 °C, for a period up to 30 days. After determined timepoints (*i.e.* 0, 7, 14, 21 and 30 days) the excess of surface water was removed with filter paper. Afterwards, the membranes were let to dry completely at 60 °C and the weight of the sample was measured. The weight loss percentage of the membranes was calculated using **Equation VI-1**:

Equation VI-1 - Equation for the determination of weight loss.

$$\text{Weight loss (\%)} = \left[\frac{(m_i - m_f)}{(m_i)} \right] \times 100\%$$

where, m_i is the sample weight at the end of the assay, and m_i is the initial weight of the dry sample. For water uptake determination, at each timepoint, the excess of surface water was removed with filter paper and the weight of the sample was measured. The water uptake percentage was calculated using **Equation VI-2**.

Equation VI-2 - Equation for the determination of water uptake.

$$\text{Water uptake (\%)} = \left[\frac{(m_w - m_i)}{(m_i)} \right] \times 100\%$$

where, m_i corresponds to the initial weight of the dry sample and m_w to the wet weight after removal from solution at each timepoint. The average value of three measurements was considered for each assay.

VI-3.6. *In vitro* biological studies

VI-3.6.1. Cell culture

L929 mouse lung fibroblast (from the European Collection of Cell Cultures (ECCC)), human skin fibroblasts (BJ, CRL-2522, ATCC), immortalized human Schwann cells (iSCs, sNF96.2, ATCC) and human pulmonary microvascular endothelial cells (HPMEC-ST1.6R cell line) were cultured as monolayers at 37 °C in a humidified 5 % CO₂ atmosphere. L929 fibroblasts were incubated with Low

Glucose Dulbecco's Modified Eagle Medium (DMEM), supplemented with 10 % (v/v) FBS and 1 % (v/v) penicillin/streptomycin. Human skin fibroblasts were incubated with Eagle's Minimum Essential Medium (EMEM), supplemented with 10 % (v/v) FBS, 1 % (v/v) penicillin/streptomycin and 1 % (v/v) sodium pyruvate. Immortalized Schwann cells were cultured under the same conditions but incubated with High Glucose DMEM supplemented with 1 % (v/v) sodium pyruvate. HPMEC-ST1.6R endothelial cells were cultured in M199 medium supplemented with 20 % (v/v) FBS, 2 mM Glutamax, 2 % (v/v) penicillin/streptomycin, 50 µg/mL of heparin and 25 µg/mL of endothelial cell growth supplement (ECGS). Cellular expansion medium was exchanged every 2-3 days until confluency was achieved.

VI-3.6.2. Cytotoxicity screening and qualitative adhesion study

L929 fibroblasts were used in these preliminary cellular assays. To assess the short-term cytotoxicity of the developed membranes, a previously described protocol was used (35), that makes use of MEM extraction followed by MTS assay. This assay is particularly effective in determining possible toxic effects of leachables released from medical polymers during extraction, following ISO 10993-5. For such, CHT and CHT/keratin membranes were incubated with complete DMEM medium for 24 hours, at 37 °C and 60 RPM, where the ratio of material weight to extract fluid was constant and equal to 0.2 g/mL. At the same time, L929 fibroblasts were seeded in a 24-well plate at the density of 5×10^4 per well and cultured with complete DMEM medium for 24 hours at 37 °C in an atmosphere with 5 % CO₂. After 24 hours of incubation, the CHT and CHT/keratin extracts were filtered through a 0.45 mm pore size filter. Culture medium was removed from the wells and an identical volume of extraction fluid (1 mL) was added. The metabolic cell activity (an indirect measure of cytotoxicity) was measured by the conversion of MTS to formazan, which can be photometrically detected. Cell response in terms of metabolic viability was evaluated after 24, 48, and 72 hours of incubation time. At each timepoint, the extraction fluid was removed and 500 µL of a mixture of serum-free culture medium without phenol red and MTS reagent (5:1 ratio) was added to each well. Culture medium was used as positive control, since it represents the ideal situation for cell proliferation. Latex was used as a negative control (for cell death). All conditions were performed in triplicate and left to incubate for 3 hours at 37 °C in a humidified 5 % CO₂ atmosphere. Thereafter, the absorbance of each sample was measured in triplicate at 490 nm using a microplate reader (Synergy HT, Bio-TEK). The MTS assay was repeated 3 times.

A preliminary qualitative study of cellular adhesion was performed 3, 6, 8 and 24 hours after seeding of L929 fibroblasts in CHT and CHT/keratin membranes by using fluorescence microscopy. At each timepoint, cells were fixed with a 10 % (v/v) formalin solution and dyed with DAPI (4'-6 diamidine-2-phenylindole) to visualize the nuclei (blue color) and phalloidin, which binds to the cell cytoplasm F-actin (red color).

VI-3.6.3. Cellular viability quantification in 2D cultures of relevant cell types

For the Alamar Blue (AB) assay, BJ fibroblasts, immortalized Schwann cells and endothelial cells were seeded separately in 1 cm² CHT and CHT/keratin membranes, placed in the bottom of 24-well cell culture plates, at a density of 1.5 x10⁴ cells/membrane. Samples were analysed after 1, 3 and 7 days of culturing at 37 °C in a humidified 5 % CO₂ atmosphere using the corresponding culture medium. At each timepoint, the respective cell culture medium containing 10 % AB was added to the different culture wells and the systems were incubated for 3 hours. Afterwards, 100 µL of each solution were transferred in triplicate to white opaque 96-well plates. Fluorescence was read at 590 nm emission wavelength (excitation wavelength 530 nm), using a microplate reader (FL 600, Bio-Tek Instruments). Since AB is non-cytotoxic, the cells and membranes were maintained during all the 7 days of study. PBS was used for removing the AB reagent from the samples and was replaced by fresh medium after each AB determination. Normalization was performed by using the mean fluorescence value obtained for the controls (TCPs), with and without cells.

VI-3.6.4. Cellular cytoskeleton morphology study of relevant cell lines

Cell morphology was studied through fluorescence microscopy after fixing the samples used in the AB assay with 10 % (v/v) formalin solution. Staining with phalloidin and DAPI (4,6-diamidino-2-phenylindole dilactate) was performed following suppliers' protocol. The dye was removed by washing with PBS and the samples were analysed by means of using a transmitted and reflected light microscope (Axio Imager Z1m, Zeiss, Jena, Germany).

VI-3.7. *In vivo* angiogenesis evaluation

VI-3.7.1. Chick embryo chorioallantoic membrane (CAM) assay

CAM assay was performed according to the procedure described by Silva-Correia *et al.* (36) in a laminar-flow hood. White fertilized chicken eggs (n = 90 - 120) were incubated at 37 °C for 3 days. Afterwards, a small hole was created in the endpoints of the egg to permit detachment of the CAM from the shell membrane. Additionally, a spherical hole was made into the eggshell, in order to evaluate embryo viability and access the CAM. Shell window was then sealed with tape to prevent dehydration and the eggs were returned to the incubator until implantation of the CHT and CHT/keratin membranes (cut in 4 mm-diameter circles). A total of three experimental groups were tested. CHT and CHT/keratin sterile membranes were implanted on the CAM at day 10 of embryonic development. At the same time, a positive control group was also implanted on the CAM, which was based on filter paper (FP). The shell windows were protected with tape and the eggs returned to the incubator until day 14 of embryonic development. At the end of the assay, the embryos and their membranes were fixed *in ovo* by using freshly prepared formalin solution at 4 % (v/v) followed by incubation at -80 °C for 10 minutes. The implanted materials and the adjacent CAM portions were cut and transferred to 6-well plates containing 4 % (v/v) formalin solution. *Ex ovo* images were acquired using the AxioVision imaging software (release 4.8; Zeiss) connected to an AxioCAM ICc1 digital camera (Zeiss) attached to a stereomicroscope (Stemi 2000-C; Zeiss). The excised membranes were transferred to histological cassettes, embedded in paraffin and cut into sections of 4 mm thickness using a microtome (Spencer 820, American Optical Company, NY, USA). Three independent CAM assays were performed.

VI-3.7.2. Analysis of blood vessel convergence

To evaluate the total number of macroscopic blood vessels converging toward the implanted materials (CHT and CHT/keratin membranes and FP), a semi-quantitative method was used, as previously described by Ribatti *et al.* (37). The number of convergent blood vessels were counted in the *ex ovo* images obtained at day 14 of embryonic development, after image processing using the WCIF ImageJ software program (US National Institutes of Health). The mean number of blood vessels results from the counts performed by three independent observers of a minimum of 19 discs per implant.

VI-3.7.3. Hematoxylin & eosin (H&E) staining

The CAM sections were stained with H&E and observed under transmitted microscopy using an Axio Imager Z1m light microscope (Zeiss, Jena, Germany). Images were acquired using the Zen microscope processing software (Zeiss, Jena, Germany) connected to a digital camera AxioCam MRc5 (Zeiss, Jena, Germany).

VI-3.7.4. Immunohistochemical detection

Regular immunohistochemical protocol was used as described: after paraffin removal, sections were rehydrated and submitted to heat-induced antigen retrieval using 10 mM citrate buffer (pH 6.0) for 20 minutes at 98 °C. To inactivate endogenous peroxidases, the samples were incubated in 3 % (v/v) hydrogen peroxide solution for 10 minutes and then soaked in PBS. Sections were incubated in protein blocking solution for 10 minutes, followed by incubation with lectin (SNA, EBL) for 1 hour at room temperature. To conclude, sections were consecutively washed with PBS and incubated with the streptavidin-peroxidase complex for 10 minutes. DAB solution was used as chromogen. All sections were counterstained with H&E (Modified Mayer's). The histological sections were analyzed, and images acquired as described in VI-3.7.3.

VI-3.8. Statistical analysis

All the numerical results were presented as mean \pm standard deviation. At least 3 specimens were used in each condition. Statistical analysis of the data was conducted using the GraphPad Prism Software version 5.00 for Windows (GraphPad Software, Inc., La Jolla, USA). For AFM data analysis, Two-tailed Mann Whitney Test was used ($p < 0.05$). Results from *in vitro* tests were analysed for normality of data distribution by the Shapiro-Wilk normality test, followed by Kruskal Wallis test in order to compare the results from the different groups. The quantitative study of the convergent blood vessels was analysed first by Shapiro-Wilk test to access the normal distribution of data, followed by one-way analysis of variance (ANOVA) and a Tukey's multiple comparisons test. The significance level was set to * $p < 0.05$, ** $p < 0.01$, *** $p < 0.001$, **** $p < 0.0001$.

VI-4. RESULTS

VI-4.1. Physicochemical Characterization

VI-4.1.1. Membranes thickness

In order to assess if the addition of keratin would lead to any changes in membranes' thickness, five samples of each formulation were tested. CHT and CHT/keratin membranes thickness was $505.8 \pm 5.34 \mu\text{m}$ and $506.2 \pm 5.98 \mu\text{m}$, respectively. Therefore, no quantifiable effect of the addition of keratin was found regarding membranes' thickness.

VI-4.1.2. Microstructure evaluation

Stereomicroscope photographs revealing the surface macrostructure of the CHT-based membranes can be seen in **Figure VI-1A**. In **Figure VI-1Ai**, CHT membranes surface appears to be smooth, while the incorporation of freeze-dried keratin powder gave origin to an irregular and rough surface (**Figure IV-1Aii**). When comparing both surfaces (**Figure VI-1Aiii**), it is clear the increase of roughness when in the presence of keratin. That contrasts with the smooth surface of the CHT membrane. SEM microphotographs of CHT (**Figure VI-1Bi-ii**) and CHT/keratin (**Figure VI-1Biii-iv**) membranes confirmed the stereomicroscopy observation, revealing that the incorporation of keratin induced the formation of a rough area with grooves, ridges and heterogeneous porous microstructures with a pore size in the range of 3–100 μm . Conversely, CHT membranes are flat and smooth. The detailed surface structure of the membranes can be seen in the magnification images on the right (**Figure VI-1Bii and 1Biv**). Surface topography of CHT and CHT/keratin membranes was qualitatively and quantitatively studied by AFM (**Figure VI -C and 1D**, respectively). Visually and qualitatively, the difference between both membranes is striking. These results confirm the findings obtained from SEM. Quantitatively, for CHT/keratin membranes, the average roughness (Ra) was calculated to be $86.04 \pm 8.31 \text{ nm}$, whereas a significant lower value was obtained for the CHT membrane ($38.58 \pm 9.4 \text{ nm}$) (**Figure VI-1Di**). Similarly, a higher value of root mean square roughness (Rq) was obtained for CHT/keratin membrane ($113.5 \pm 24.4 \text{ nm}$), as compared to CHT membrane ($38.3 \pm 7.4 \text{ nm}$) (**Figure VI-1Dii**). Therefore, the results demonstrate that a significant higher roughness of the CHT/keratin membranes (both Ra and Rq) was observed at the nanoscale level.

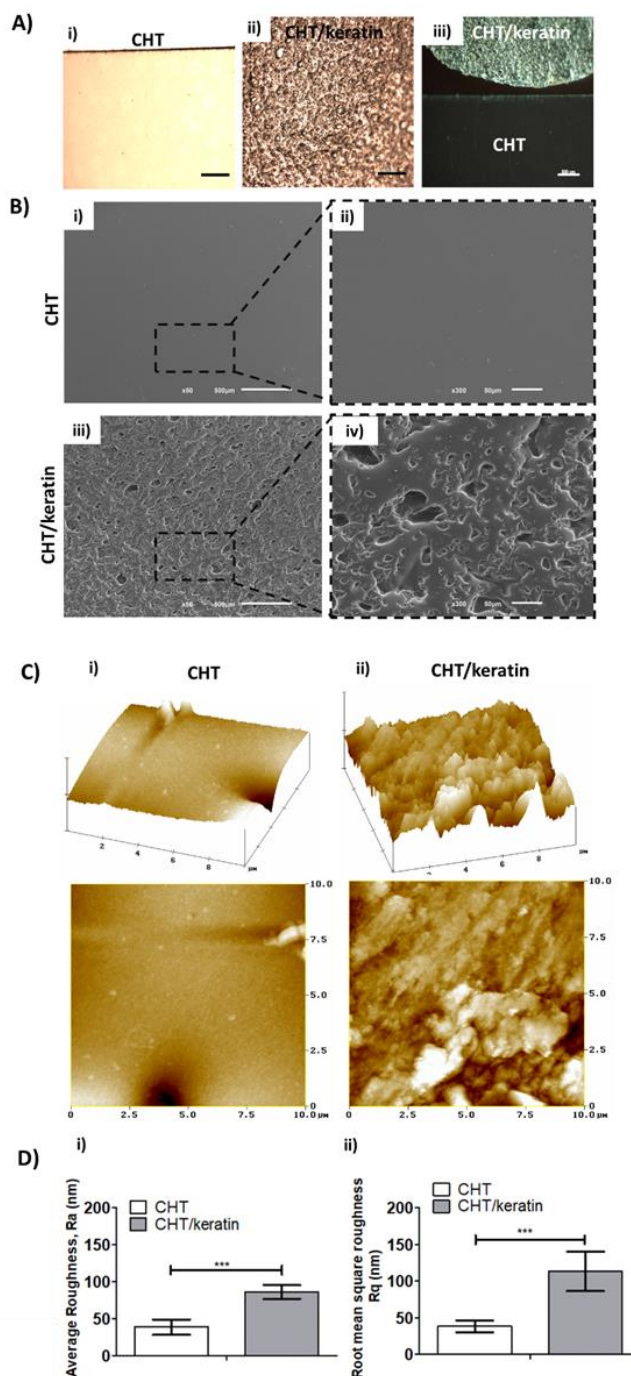


Figure VI-1 - Macro and microphotographs of the developed CHT and CHT/keratin membranes revealing its surface topography. A) Photographs of the membranes taken by stereomicroscope: i) smooth surface of CHT membrane, ii) rough surface of CHT/keratin membrane, iii) comparison between CHT and CHT/keratin membranes; B) SEM microphotographs of the developed membranes: i-ii) CHT membrane, iii-iv) CHT/keratin membrane; C) AFM three dimensional images of developed membranes, 10 $\mu\text{m} \times 10 \mu\text{m}$ scan area, contact mode of the i) CHT and ii) CHT/keratin; D) Quantitative information regarding the average roughness (Ra) and root mean square roughness (Rq) of the i) CHT and ii) CHT/keratin membranes. Two-tailed Mann Whitney Test was used ($p < 0.05$) and statistically significant differences were represented by *** ($p < 0.001$). Scale bars: A) 500 μm ; B) 500 μm (i and iii) and 50 μm (ii and iv).

VI-4.1.3. FTIR results

FTIR was used to confirm the presence of functional groups of both components, *i.e.* CHT and keratin, after the blending and to exclude any possible chemical modification induced by the blending and manufacturing processes. FTIR spectra is represented in **Figure VI-2A**. In one hand, keratin powder spectrum showed its fundamental characteristic peaks, *i.e.* the band in the range of 1600 cm^{-1} , which corresponds to amide I and is mainly related to the C=O stretching, and the band in the range of 1500 cm^{-1} , which suggest the presence of amide II and result from the phase combination of C-N stretching and C=O bending vibration. On the other hand, chitosan spectrum of pure CHT membrane has a band at 3441 cm^{-1} , which corresponds to the combined peaks of the NH_2 and OH group stretching vibration. The band at 1640 cm^{-1} and 1380 cm^{-1} correspond to the C=O and C-O stretching of amide group. The characteristic features of chitosan spectrum in this study are similar to that of previous reports (38, 39). As expected, in the spectra of the CHT/keratin membrane an increase of the intensity of the amide I and amide II bands (1600 and 1500 cm^{-1} , respectively) was observed, due to the presence of keratin in CHT membranes.

VI-4.1.4. XRD results

The XRD profile of CHT and CHT/keratin membranes and keratin powder is reported in **Figure VI-2B**. Characteristic peaks of CHT membrane appear at around 15° and 20° (40). Huang *et al.* (41) reported that the reflection at $2\theta = 15^\circ$ is assigned to the crystal form I and attributed to the hydrated crystals with low crystallinity. That study also reported that this peak may shift from 9° to 15° . The peak at $2\theta = 20^\circ$ represents the crystallinity of the crystal form II in the CHT structure. In the keratin powder spectrum presented in **Figure VI-2B** (superior right corner), two intense peaks can be visualized at $2\theta = 10^\circ$ and $2\theta = 20^\circ$, which are assigned to both α -helix and β -sheet structures of keratin, respectively, pointing towards the crystalline properties of the protein. After the blending, instead of an intense peak at $2\theta = 10^\circ$, there is only a small peak which indicates that final CHT/keratin membrane has relatively lower α -helix and crystallinity than the freeze-dried keratin powder. Overall, the addition of keratin to the chitosan membrane leads to a decrease in crystallinity, due to a lower degree of molecular order.

VI-4.1.5. Contact angle and surface energy measurements

The hydrophobic/hydrophilic nature of CHT and CHT/keratin membranes were assessed by means of performing contact angle measurements (Table VI-1). The results indicated that CHT/keratin membrane has higher polar component and surface energy, which corresponds to a lower water contact angle when compared to CHT membranes. CHT/Keratin membrane revealed to be slightly more hydrophilic, presenting a value of $101.06 \pm 5.35^\circ$ of water contact angle and 29.04 ± 0.01 mN/m of surface energy. By its turn, CHT membrane presented a value of $115.2 \pm 1.96^\circ$ of water contact angle and 25.22 ± 0.01 mN/m of surface energy.

Table VI-1 - Contact angles (θ), dispersive (γ_d) and polar (γ_p) components and surface energy (γ) of the CHT-based membranes calculated by the OWRK equation.

| Material | $\theta_{\text{water}}(^{\circ})$ | γ_d (mN/m) | γ_p (mN/m) | γ (mN/m) |
|----------------------|-----------------------------------|-------------------|-------------------|------------------|
| CHT membrane | 115.2 ± 1.96 | 34.61 ± 0.01 | 0.61 ± 0.00 | 25.22 ± 0.01 |
| CHT/keratin membrane | 101.06 ± 5.35 | 18.60 ± 0.01 | 0.93 ± 0.00 | 29.04 ± 0.01 |

VI-4.1.6. DMA analysis

Experiments were performed in a hydrated environment at 37°C , in an array of biologically relevant frequencies, in order to assess the samples behaviour in physiological-like setting. Both storage (elastic) modulus, E' , and the loss factor, $\tan \delta$, were obtained at different frequencies. The E' is a measure of the materials' stiffness. The loss factor corresponds to the ratio of the amount of energy dissipated (viscous component) relative to the energy stored (elastic component); $\tan \delta = E''/E'$. CHT and CHT/keratin properties are shown in Figure VI-2C. Comparing both membranes, it can be observed that the presence of keratin affected the viscoelastic properties. The values of storage modulus (E') for CHT membranes presented a slightly increase from 68.8 ± 5.8 MPa to 77.7 ± 9.8 MPa, as frequency increased from 0.1 to 10 Hz. Looking at the same range of frequencies, CHT/keratin membranes revealed lower storage modulus values. For this sample, the storage modulus remained relatively constant in the range of frequencies tested, presenting values from 40.1 ± 6.7 MPa to 41.7 ± 4.2 MPa. Regarding the loss factor results ($\tan \delta$), CHT/keratin presented higher values comparing to

simple CHT membranes. A slightly decrease from 0.74 ± 0.07 to 0.66 ± 0.09 and from 0.48 ± 0.05 to 0.41 ± 0.07 was observed for CHT/keratin and CHT membranes, respectively, as the frequency increased.

VI-4.1.7. DSC analysis

DSC thermogram of CHT and CHT/keratin membranes, as well as keratin powder, is shown in **Figure VI-2D**. The intense endothermic peak verified at 50 °C is the keratin powder thermogram is related to the evaporation of water of the freeze-dried powder. It is worth noting that in the keratin powder, water evaporation occurs at lower temperature as compared to CHT and CHT/keratin membranes (50 °C in the keratin powder and 70-100 °C in the CHT/keratin membranes). This can be related to the high tendency of water absorption from the freeze-dried powder, which promotes its evaporation at lower temperatures. In the keratin powder thermogram, it is also visible an endothermic peak around 240 °C, which occurs due to protein denaturation, more specifically, denaturation of the α -helix of keratin. This same peak is visible in the CHT/keratin blend, although with less intensity. In both CHT and CHT/keratin membranes, the presence of intense peaks at 300 °C was observed, which are associated to the decomposition of the amine units in the chitosan structure.

VI-4.1.8. Weight loss and water uptake profiles

Weight loss of the developed membranes was evaluated in PBS (at pH 7.4). From **Figure VI-2E**, it can be observed that CHT and CHT/keratin follow a similar pattern of degradation with time. The weight loss was minimum after 1 day, with values of 0.70 ± 0.53 % and 0.9 ± 0.3 % for CHT and CHT/keratin, respectively. The weight loss gradually increased from 2.54 ± 0.16 % to 4.19 ± 0.75 % in the CHT sample, from day 7 to day 30. In the same time period, the CHT/keratin sample degraded from 2.9 ± 1.2 % to 6.0 ± 0.7 %.

The water uptake of the membranes is represented in **Figure VI-2F**. The swelling of both samples was found to reach its maximum and stabilize after 5 days of immersion, with values of 131.2 ± 2.5 % and 139.2 ± 9.7 % for CHT and CHT/keratin samples, respectively.

VI-4.2. *Biological In vitro* studies

VI-4.2.1. Cytotoxicity screening and qualitative adhesion study

Leachables obtained from CHT and CHT/keratin membranes did not demonstrate any cytotoxic effect to L929 cells after 24, 48 and 72 hours of incubation, as shown in **Figure VI-3A**. There are no significant differences in the MTS results regarding both membranes and the positive control, despite the timepoint analysed. The qualitative adhesion assay suggests a relatively higher adhesion of L929 cells to keratin-containing membranes, during several timepoints (3, 6, 8 and 24 hours) throughout the first day (**Figure VI-3B**). Although there is a differential adhesion to the membranes, L929 fibroblasts remained in a circular shape, not showing their typical elongated shape, when comparing to the positive control.

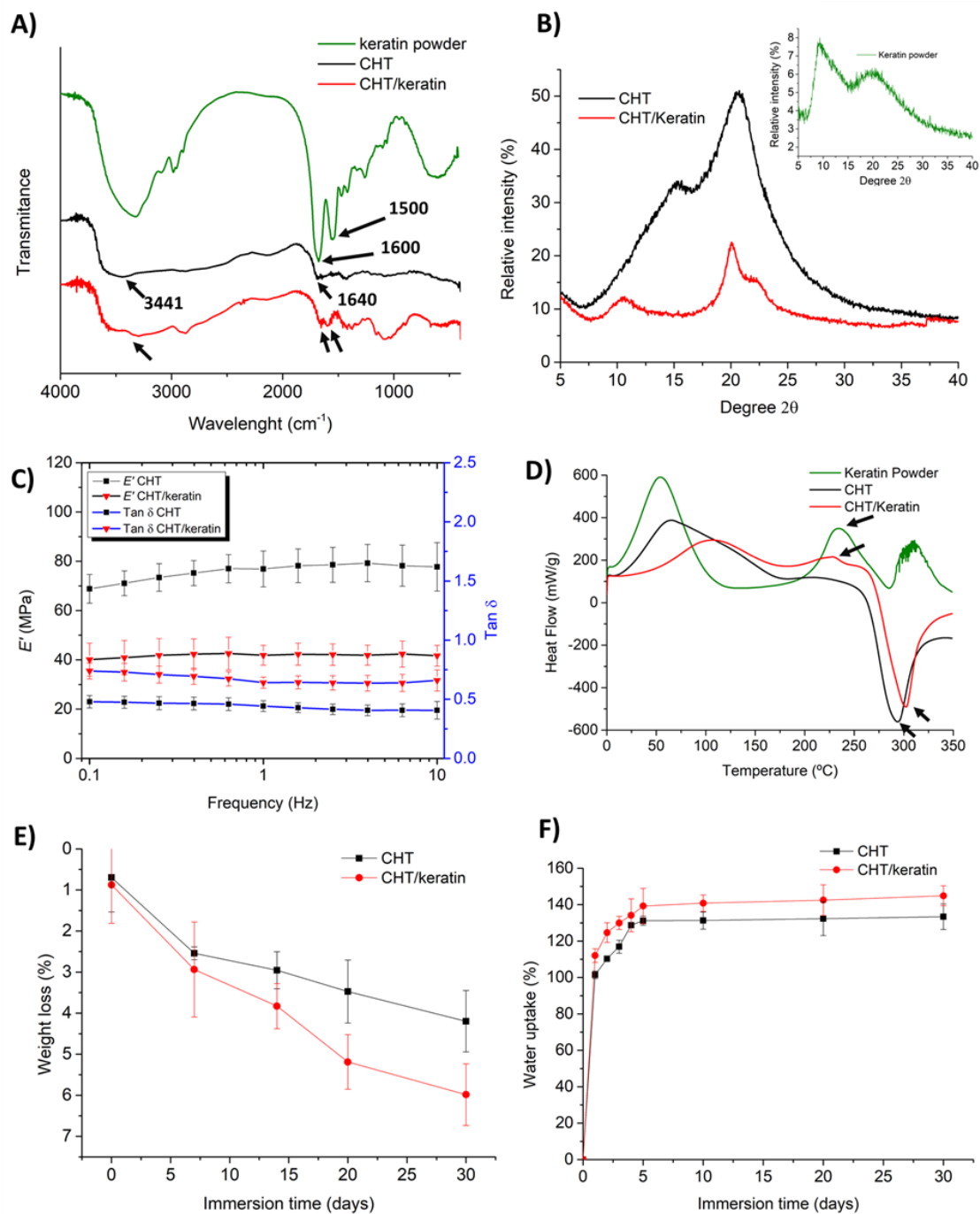


Figure VI-2 - Physicochemical characterization of CHT and CHT/keratin membranes. A) FTIR spectra of the produced membranes and keratin powder. Arrows point to specific and characteristic peaks of each component, which are also visible in the final blending membrane; B) XRD pattern of the produced membranes. In the upper right side (green line), at a different scale, is the XRD pattern of keratin powder; C) Dynamic mechanical analysis of the membranes. Storage modulus (E' ; black lines) and loss factor ($\tan \delta$, blue lines) of samples measured as a function of frequency; D) Differential Scanning Calorimetry thermograms of developed membranes. Arrows point to specific and characteristic peaks of each component, which are also visible in the final blending membrane; E) Percentage of weight loss of the developed membranes after incubation in PBS for different periods of time. The data represents the mean for each timepoint \pm standard deviation; F)

Percentage of water uptake of the developed membranes after incubation in PBS for different periods of time. The data represents the mean for each timepoint \pm standard deviation.

VI-4.2.2. Viability of relevant cell types in 2D cultures

Metabolic viability of several cell lines seeded in the CHT and CHT/keratin membranes was quantitatively determined by AB assay, as can be seen in **Figure VI-4** (left panels). For all cellular lines tested, there was an increase of fluorescence values in terms of relative fluorescence units (RFUs) with time, from day 1 to day 7, suggesting that the cells remained viable and an overall cellular proliferation occurred in both CHT and CHT/keratin samples. More specifically, BJ fibroblasts' metabolic activity was significantly higher when seeded on keratin-based materials, both at day 3 and day 7, when compared to cells seeded in CHT membranes. Schwann cells' metabolic activity was significantly higher in CHT/keratin membranes in all the timepoints analysed (1, 3 and 7 days). Regarding endothelial cells, the determined metabolic activity was significantly higher in CHT/keratin materials after 3 and 7 days *in vitro*.

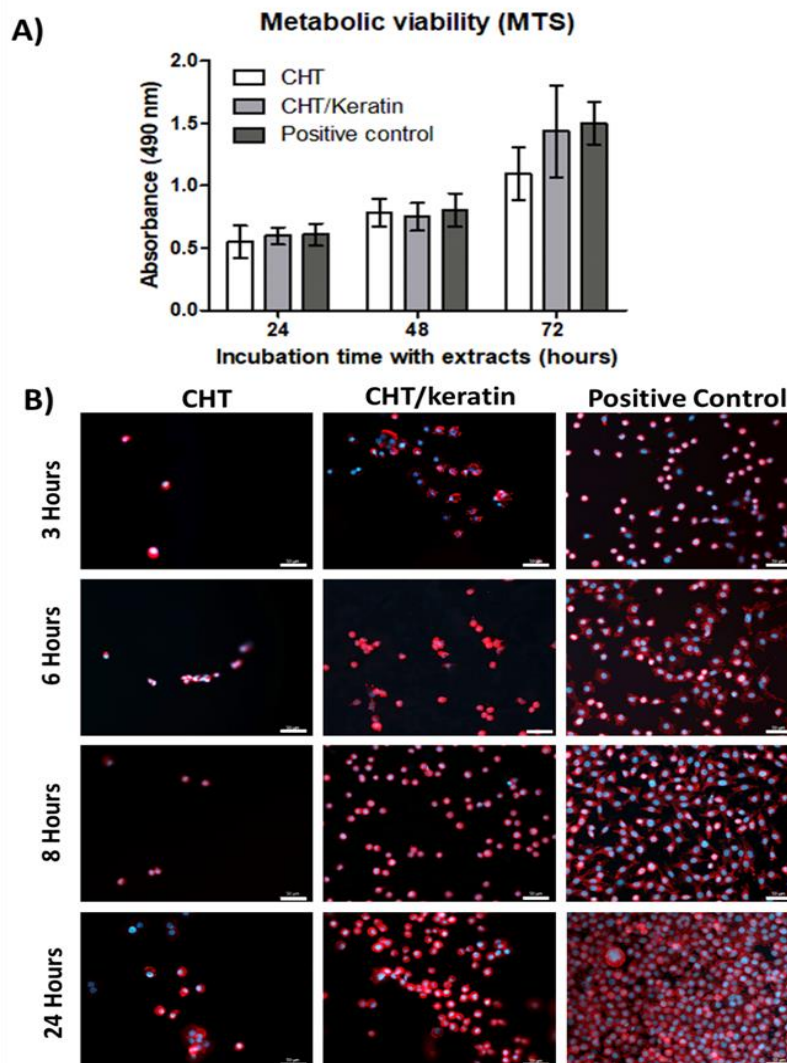


Figure VI-3 - Short term cytotoxicity and qualitative adhesion study of L929 fibroblasts. A) Metabolic activity of L929 fibroblasts incubated with leachables from CHT and CHT/keratin developed membranes. Kruskal-Wallis test was performed followed by Dunn's multiple comparison test, $p < 0.05$; B) Fluorescence photomicrographs of qualitative adhesion study where L929 fibroblasts were seeded on CHT and CHT/keratin membranes and compared to the positive control (TCPs). Cells were subjected to DAPI/phalloidin staining after fixation. Scale bar: 50 μm .

VI-4.2.3. Cellular cytoskeleton morphology study of relevant cell lines

Cell morphology of the different cell types was qualitatively analysed after DAPI/phalloidin staining at 1, 3 and 7 days of culturing (Figure VI-4, right panels). The representative qualitative images are in accordance to metabolic activity determination, where an increased number of cells in CHT/keratin materials was observed when compared to CHT materials. Also, all cell types appeared to have their native morphology

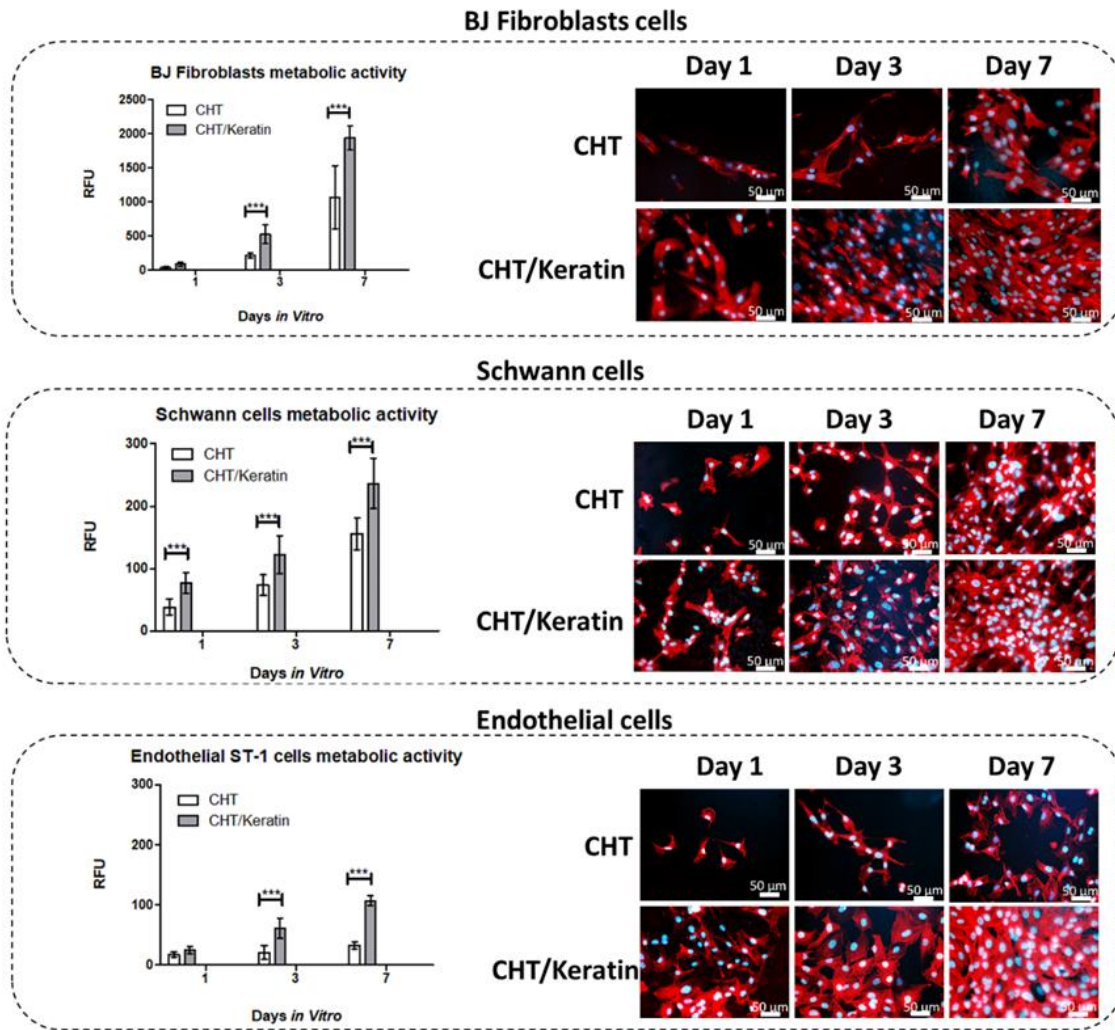


Figure VI-4 - Metabolic viability and cellular cytoskeleton morphology of BJ fibroblasts, Schwann cells and endothelial cells when seeded on CHT and CHT/keratin membranes, at 1, 3 and 7 days of culturing. At left, graphical representation of the quantification of metabolic activity of each cell type up to 7 days of culturing. On the right, fluorescence micrographs of DAPI/Phalloidin stained cells, up to 7 days of culturing. Scale bar: 50 μm .

VI-4.3. *In vivo* angiogenic assay

Following the superior biological performance demonstrated by CHT/keratin membranes on the *in vitro* studies, particularly on the significant higher metabolic activity of the cultured endothelial cells, a CAM assay was performed to access the effect of keratin addition on CHT membranes and make an association to their angiogenic response. After 4 days of implantation, the macroscopic assessment of the angiogenic response, based on the quantification of the convergent blood vessels toward the implanted materials, showed significant differences between the CHT/keratin and the simple CHT membranes. These findings can be appreciated

in **Figure VI-5A**, where it is clear the statistically significant higher number of blood vessels converging to the CHT/keratin membranes comparing to the CHT membranes (** $p < 0.01$ CHT/keratin vs. CHT). Both membranes exhibited a statistically significant lower number of convergent blood vessels when compared to the positive control, filter paper, being this difference less prominent for the CHT/keratin membranes. The microscopic study of the angiogenic response was performed by the histological characterization of representative CAM sections through H&E and lectin staining, the later for the detection of chick origin-endothelial cells. The light microscopy images of the 4 μm -sagittal CAM sections depicted in the **Figure VI-5B** showed that both membranes were well integrated on the CAM. However, it is noticeable a slightly stronger adhesion of the CHT/keratin membranes to the CAM. In such membranes, it was more often perceptible the presence of a morphologically related cellular interface that can be attributed to a normal immune response to the implanted CHT/keratin membranes. However, no acute inflammatory response was noticed, confirming the non-immunogenicity of the CHT-based membranes. Nevertheless, the presence of a noticeable number of micro-vessels in the proximity of the CHT membranes could be observed, being this more pronounced on the CAM implanted with the keratin enriched membranes. Moreover, this tendential preference of these newly formed micro-vessels on the proximity of the CHT/keratin membranes could be noticed by the migration of erythrocytes that seems to be arranging in new micro-vessels (marked by white arrows).

The integrity of both membranes was maintained during the implantation period. However, it is possible to microscopically see that the CHT/keratin membranes present a more striated structure than the CHT, which could retain its structure, after 4 days of implantation. These results are in agreement with the degradation studies. From staining's observation, it can be stated that the membranes were impermeable to cellular infiltration.

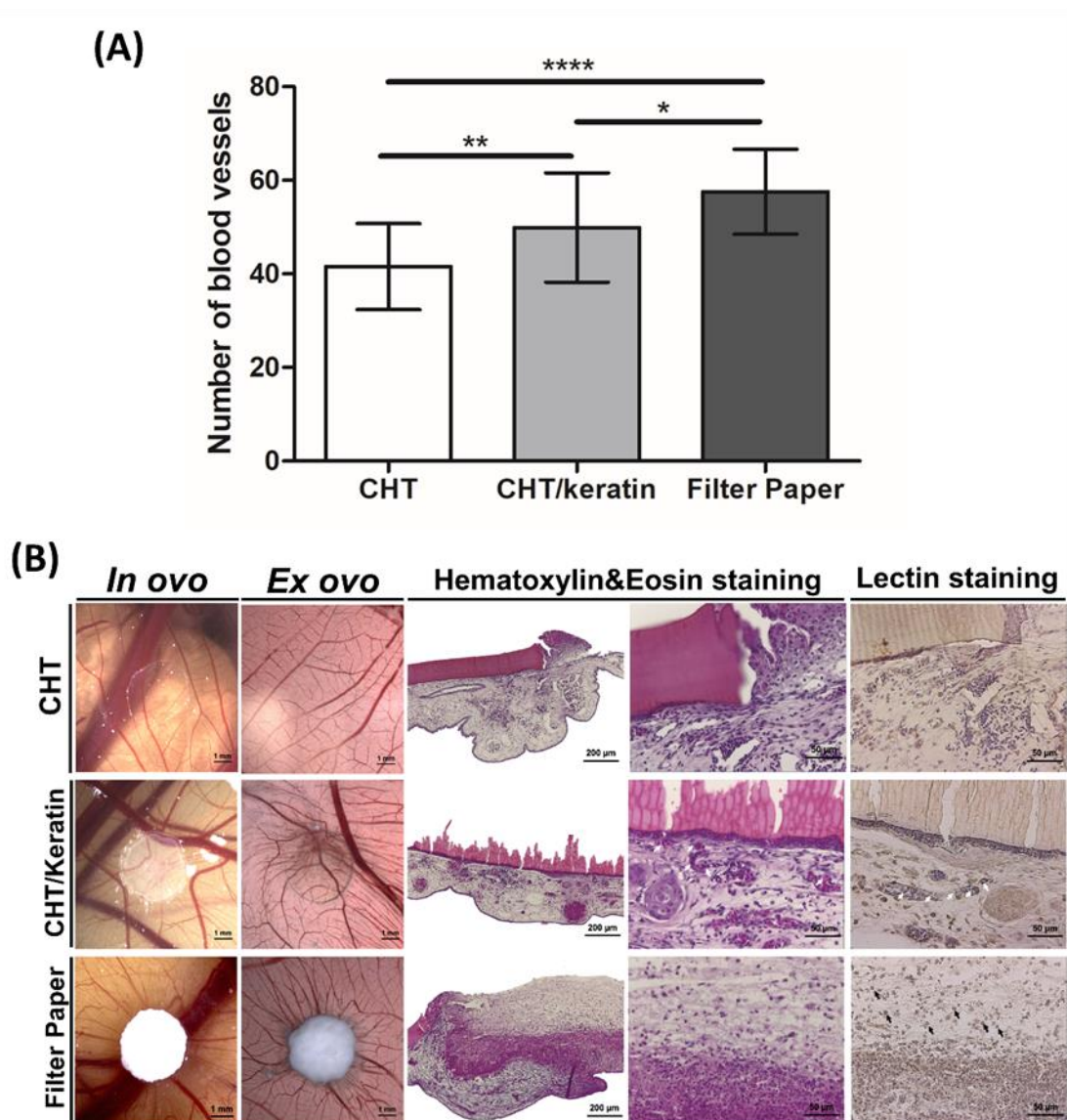


Figure VI-5 - Angiogenic response of the CHT-based membranes evaluated in the CAM assay. (A) Ex ovo quantification of the macroscopic blood vessels converging to the implanted CHT and CHT/Keratin membranes and to the positive control Filter paper, after 4 days of implantation. The mean number of convergent blood vessels results from the counts of three independent observers of a minimum of 19 discs per implant. Statistical analysis was performed using one-way analysis of variance followed by Tukey's post-test. Symbols denote significant differences for * $p < 0.05$, ** $p < 0.01$ and **** $p < 0.0001$. (B) *In ovo* and *ex ovo* stereomicroscopy photographs of the CAM with the implanted materials after 4 days of implantation and light microscopy representative images of the respective 4 μm -sagittal CAM sections stained with H&E and lectin. The black arrows indicate infiltrated chick endothelial cells and the white arrows indicate the tendential migration of the erythrocytes and micro-vessels to the proximity of the CHT/keratin membranes.

VI-5. DISCUSSION

GTR is a surgical technique developed for bone-related procedures in which a physical barrier is used to regulate tissue growth (42). However, this same principal is one of the most effective methods used for PNR. NGC and PNW are the most common strategies applied to stop fast-proliferating and collagen depositing fibroblasts from filling the injury site, while protecting it (16, 43).

An ideal NGC or PNW intended for PNR needs to feature a combination of optimal material, size, architecture and surface properties to be fully effective (44). These features must allow the formation of new ECM consisting of endothelial cells and subsequently blood vessels, Schwann cells and the correct type and amount of fibroblasts, which collectively create favorable circumstances for nerve regeneration to occur (45). In this study we propose the use of solvent casted CHT/keratin membranes as possible tools to aid in the repair of damaged nerves.

Keratin has been recently extracted from human hair and has emerged as a captivating biomaterial (46). This is because keratin is a human-derived protein, exhibits excellent biocompatibility, no immune reaction upon transplantation, good cellular interaction activity and biodegradability (47). In this case, the aim was to provide new desirable and improved characteristics to CHT membranes (16). Making use of the previously developed 5 % DA CHT membrane (16), which was found to be optimal for PNR, we intended to study of the effect related to the addition of 1 % of freeze-dried hair keratin. The surface topography evaluated by SEM and AFM revealed a significantly higher surface roughness in the presence of keratin, which might contribute to the advantageous characteristics of keratin containing membranes, since rougher materials have been linked to improved cellular behavior (48). Techniques such as FTIR, XRD and DSC were useful for confirming the success of the blending and proved that CHT and keratin are miscible polymers. The good miscibility between keratin and CHT may be attributed to intermolecular hydrogen bonding between CHT carbonyl groups and keratin amine groups. The hydrophilicity of the ECM is one of the most noteworthy factors that directly affect cell adhesion in TE and is usually characterized by contact angle testing. The presence of keratin containing rich amino and carboxylic groups demonstrated to improve the hydrophilicity and wettability of the CHT membrane, which has been reported before (49). This is linked to the fact that keratin is a naturally hydrophilic protein (47). The capacity to react with water is also visible in the weight loss and water uptake properties of the CHT/keratin membranes. In agreement with other reports (50), the presence of keratin in the polymer blending makes it more prone to react with water molecules, achieving higher

swelling and degradation rates due to hydrolysis. However, despite a slightly higher degradation rate, only 6 % of mass loss was verified after 30 days.

Mechanical properties of devices to be used in PNR, whether they are NGC or PNW, are of great importance for the repair to be successful. It is of special interest that the matrix is not only mechanically strong enough to withstand the pressures after implantation, but also deformable enough (51). In one hand, the presence of keratin decreased the stiffness related to CHT membranes. On the other hand, its presence increased the capacity to disperse energy when subjected to a tensile force, by increasing the damping properties. To summarize, the incorporation of keratin changes the membrane's mechanical properties, which might be due to the presence of keratin protein interfering with the crosslinking of the CHT solution, consequently decreasing its stiffness. This result is in accordance with previous reports.(52) Since different cells types respond differently based on the substrate stiffness, it is known that cell behavior can be improved if cultured in a mechanically favorable microenvironment (53). Opposite to hard tissues, soft tissues present high flexibility and low mechanical, generally viscoelastic properties. As expected and previously reported in the literature, in a general way, nervous system cells prefer softer membranes (53), which was the case of CHT/keratin membranes. In this sense, it is expected that the presence of hair keratin will be beneficial in future PNR systems. Knowing that different cell types play central roles in PNR, their interaction with the developed membrane was assessed in this experimental work, namely with fibroblasts, Schwann cells and endothelial cells.

The role of fibroblasts in the process of PNR has been controversial, with different opinions whether their presence is beneficial or harmful for nerve regeneration (54). To achieve an effective regeneration, an equilibrium must occur so that nerve fibroblasts proliferate and contribute to tissue remodeling, but not over-proliferating and creating excessive scar tissue.

Schwann cells, which myelinate and ensheath nerve fibers in the peripheral nervous system, also secrete neurotrophins and produce ECM molecules, which facilitates nerve regeneration (55). Furthermore, the basal lamina produced by Schwann cells after an injury is thought to be one of the main effector parts in PNR. For the role of endothelial cells, increasing attention has been given to the close relationship between tissue regeneration and angiogenesis, as the lack of blood supply is one of important constraint factors hindering nerve regeneration (56). Overall, the biological *in vitro* results indicate that cellular behavior was significantly improved when cells were seeded on CHT/keratin membranes, as opposed to CHT membranes. The improvement in the attachment and proliferation of

neuronal cells in the presence of keratin has already been demonstrated (50). One explanation for such phenomena might be the existence of cell binding motifs in hair extracted keratin, such as leucine-aspartic acid-valine (LDV) and glutamic acid-aspartic acid-serine (EDS) binding residues. These motifs are capable of supporting cellular attachment since they create a favorable matrix that permits cellular infiltration, attachment, proliferation and differentiation (57). However, not only the cell binding motifs play a role in increased cellular attachment, but the increased surface roughness may be associated with maximal cell adhesion. Mechanical and hydrophilicity properties, which were critically modified in the presence of keratin, will also have a direct effect on the ability of cellular adhesion, proliferation and differentiation (58).

Since a significant higher metabolic activity was found when endothelial cells were seeded in CHT/keratin membranes, it was relevant to perform a CAM assay investigating if the presence of keratin in the materials would elicit a superior angiogenic response. The quantification of the macroscopic blood vessels converging toward the implanted membranes and the histological characterization of the explants suggest that the presence of keratin can have a chemotactic effect on the endothelial cells, promoting their tendential migration to the proximity of the CHT/keratin membranes. The positive effect of the keratin on the angiogenic response of the CHT/keratin membranes was also reinforced by the statically significant higher number of convergent blood vessels on the CAM implanted with CHT/keratin membranes when compared to the free keratin CHT membranes. The hair-derived keratin effect on promoting angiogenesis has been reported in previous studies, for peripheral nerve regeneration and cardiac regeneration after myocardial infarct (57). In fact, the expression of some epithelial keratins in pathological conditions, such as, the cytokeratin 19 and 17 have been identified as stimulators of tumor angiogenesis development by interfering or activating some signaling pathways involved in cancer progression and metastasis (59, 60). These findings could unveil an underexplored potential of the hair-derived keratin for the development of new biomaterials for applications where angiogenesis is a crucial factor.

Given all the benefits found after the extensive characterization of CHT/keratin membranes, their use as GTR tools in PNR can be envisioned using different strategies, as can be seen in Figure 6. This membrane has a potential use as: (i) PNW around the damaged nerve (61), protecting the site of nerve crush or repair by end-to-end surgery and avoiding post-operative nerve adhesions; (ii) bridging, as a NGC, the two nerve stumps after a severe peripheral nerve lesion with substance loss (62); and (iii) as a luminal filler, where simple NGC are enhanced by introduction of a longitudinal membrane to

reconstruct critical length injuries (19). The choice of which strategy to use in the clinics regarding the CHT/keratin membrane will mainly be dependent on the severity of the nerve injury. Regarding the first option, the PNW, its use requires the nerve cable to be complete and the desirable qualities of a barrier nerve wrap include a substance that decreases nerve scarring, does not constrict the nerve and improves nerve gliding. The NGC is necessary when the nerve is severed and there is a gap that needs to be protected from the remaining environment (63). Finally, the CHT/keratin membrane could be used as a guiding luminal filler inside a NGC for when the gap is critical, and the nerve cannot regenerate without further support (19).

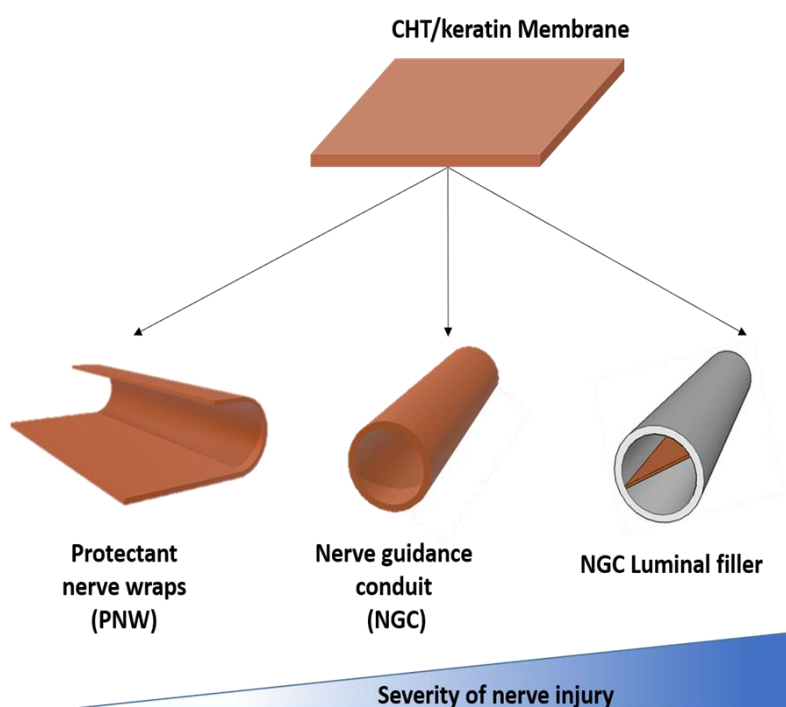


Figure VI-6 - The developed CHT/keratin membrane exhibited superior characteristics when compared to simple CHT membranes, both on a physico-chemical as well as on a biological level. When envisioned to be applied in Peripheral Nerve Regeneration, different strategies can be used according to the severity of nerve injury. PNW should be used when the nerve is injured but the cable is intact. NGC must be used the nerve is severed and the result is a non-suturable gap. At last, a luminal filler must be added to a NGC when the nerve cable cannot regenerate on its own due to the excessive long gap formed, and an extra guiding path is necessary for the nerve to reach the proximal side.

VI-6. CONCLUSIONS

In this work, the physicochemical and biological effect of incorporating human hair extracted keratin in 5 % DA CHT membranes and its possible use as a GTR-based membrane were investigated.

Surface and chemical characterization confirmed increased roughness and hydrophilicity with the addition of keratin, which pointed to an improved cellular behavior. Furthermore, mechanical tests confirmed the suitability of the membrane to be applied in soft tissues regeneration. *In vitro* biological assays established the membranes as non-cytotoxic, as well as being an appropriate matrix for several cellular types pertinent to nerve regeneration, such as fibroblasts, Schwann cells and endothelial cells. The CAM assay further proved the angiogenic potential of the developed blending CHT/keratin membrane and pointed to its beneficial effect in nerve repair. These results indicate the superior performance of CHT/keratin membranes, which features perfectly fit the demands of a guiding device to be applied in peripheral nerve regeneration.

VI-7. ACKNOWLEDGEMENTS

The authors thank the chitosan raw material provided by Altakitin S.A. (Lisboa, Portugal). This study was also supported by the European Community's Seventh Framework Programme (FP7-HEALTH-2011) under grant agreement n° 278612 (BIOHYBRID). The authors acknowledge the Portuguese Foundation for Science and Technology (FCT) for the financial support provided to Joaquim M. Oliveira (IF/00423/2012 and IF/01285/2015) and Joana Silva-Correia (IF/00115/2015) under the program “Investigador FCT”. The authors would also like to acknowledge the contribution of Elsa Ribeiro for the SEM images acquisition; Sandra Pina for the acquisition of XRD diffractograms; and Teresa Oliveira for histology samples processing.

VI-8. REFERENCES

1. Rodrigues MC, Rodrigues AA, Jr., Glover LE, Voltarelli J, Borlongan CV. Peripheral nerve repair with cultured schwann cells: getting closer to the clinics. *TheScientificWorldJournal*. 2012;2012:413091.
2. Noble J, Munro CA, Prasad VSSV, Midha R. Analysis of Upper and Lower Extremity Peripheral Nerve Injuries in a Population of Patients with Multiple Injuries. *Journal of Trauma and Acute Care Surgery*. 1998;45(1):116-22.
3. Taylor KS, Anastakis DJ, Davis KD. Chronic pain and sensorimotor deficits following peripheral nerve injury. *Pain*. 2010;151(3):582-91.
4. Goswami R, Anastakis DJ, Katz J, Davis KD. A longitudinal study of pain, personality, and brain plasticity following peripheral nerve injury. *Pain*. 2016;157(3):729-39.
5. Scheib J, Höke A. Advances in peripheral nerve regeneration. *Nature Reviews Neurology*. 2013;9:668.
6. Li R, Liu Z, Pan Y, Chen L, Zhang Z, Lu L. Peripheral nerve injuries treatment: a systematic review. *Cell biochemistry and biophysics*. 2014;68(3):449-54.
7. Jiang X, Lim SH, Mao HQ, Chew SY. Current applications and future perspectives of artificial nerve conduits. *Experimental neurology*. 2010;223(1):86-101.

8. Dodla MC, Alvarado-Velez M, Mukhatyar VJ, Bellamkonda RV. Chapter 69 - Peripheral Nerve Regeneration. In: Atala A, Lanza R, Mikos AG, Nerem R, editors. *Principles of Regenerative Medicine (Third Edition)*. Boston: Academic Press; 2019. p. 1223-36.
9. Yi S, Xu L, Gu X. Scaffolds for peripheral nerve repair and reconstruction. *Experimental neurology*. 2018.
10. Haastert-Talini K, Geuna S, Dahlin LB, Meyer C, Stenberg L, Freier T, et al. Chitosan tubes of varying degrees of acetylation for bridging peripheral nerve defects. *Biomaterials*. 2013;34(38):9886-904.
11. Mali R, Lele P, Vishakha. Guided tissue regeneration in communicating periodontal and endodontic lesions - A hope for the hopeless! *Journal of Indian Society of Periodontology*. 2011;15(4):410-3.
12. Belanger K, Dinis TM, Taourirt S, Vidal G, Kaplan DL, Egles C. Recent Strategies in Tissue Engineering for Guided Peripheral Nerve Regeneration. *Macromolecular bioscience*. 2016;16(4):472-81.
13. Nectow AR, Marra KG, Kaplan DL. Biomaterials for the development of peripheral nerve guidance conduits. *Tissue engineering Part B, Reviews*. 2012;18(1):40-50.
14. Gnani S, Barwig C, Freier T, Haastert-Talini K, Grothe C, Geuna S. The use of chitosan-based scaffolds to enhance regeneration in the nervous system. *International review of neurobiology*. 2013;109:1-62.
15. Boecker A, Daeschler SC, Kneser U, Harhaus L. Relevance and Recent Developments of Chitosan in Peripheral Nerve Surgery. *Frontiers in Cellular Neuroscience*. 2019;13(104).
16. Carvalho CR, Lopez-Cebral R, Silva-Correia J, Silva JM, Mano JF, Silva TH, et al. Investigation of cell adhesion in chitosan membranes for peripheral nerve regeneration. *Materials science & engineering C, Materials for biological applications*. 2017;71:1122-34.
17. Haastert-Talini K, Geuna S, Dahlin LB, Meyer C, Stenberg L, Freier T, et al. Chitosan tubes of varying degrees of acetylation for bridging peripheral nerve defects. *Biomaterials*. 2013;34(38):9886-904.
18. Stenberg L, Stossel M, Ronchi G, Geuna S, Yin Y, Mommert S, et al. Regeneration of long-distance peripheral nerve defects after delayed reconstruction in healthy and diabetic rats is supported by immunomodulatory chitosan nerve guides. 2017;18(1):53.
19. Meyer C, Stenberg L, Gonzalez-Perez F, Wrobel S, Ronchi G, Udina E, et al. Chitosan-film enhanced chitosan nerve guides for long-distance regeneration of peripheral nerves. *Biomaterials*. 2016;76:33-51.
20. Reichl S. Films based on human hair keratin as substrates for cell culture and tissue engineering. *Biomaterials*. 2009;30(36):6854-66.
21. Singaravelu S, Ramanathan G, Raja MD, Nagiah N, Padmapriya P, Kaveri K, et al. Biomimetic interconnected porous keratin-fibrin-gelatin 3D sponge for tissue engineering application. *International journal of biological macromolecules*. 2016;86:810-9.
22. Placone JK, Navarro J, Laslo GW, Lerman MJ, Gabard AR, Herendeen GJ, et al. Development and Characterization of a 3D Printed, Keratin-Based Hydrogel. *Annals of biomedical engineering*. 2016.
23. Tachibana A, Furuta Y, Takeshima H, Tanabe T, Yamauchi K. Fabrication of wool keratin sponge scaffolds for long-term cell cultivation. *Journal of biotechnology*. 2002;93(2):165-70.
24. Goto H, Sawada K, Fujisato T. Preparation and evaluation of keratin scaffold derived from wool and human hair for cell culture and tissue engineering. *Frontiers in Bioengineering and Biotechnology*.
25. Sierpinski P, Garrett J, Ma J, Apel P, Klorig D, Smith T, et al. The use of keratin biomaterials derived from human hair for the promotion of rapid regeneration of peripheral nerves. *Biomaterials*. 2008;29(1):118-28.
26. Pace LA, Plate JF, Smith TL, Van Dyke ME. The effect of human hair keratin hydrogel on early cellular response to sciatic nerve injury in a rat model. *Biomaterials*. 2013;34(24):5907-14.
27. Hill PS, Apel PJ, Barnwell J, Smith T, Koman LA, Atala A, et al. Repair of peripheral nerve defects in rabbits using keratin hydrogel scaffolds. *Tissue engineering Part A*. 2011;17(11-12):1499-505.
28. Pace LA, Plate JF, Mannava S, Barnwell JC, Koman LA, Li Z, et al. A human hair keratin hydrogel scaffold enhances median nerve regeneration in nonhuman primates: an electrophysiological and histological study. *Tissue engineering Part A*. 2014;20(3-4):507-17.
29. Hartrianti P, Nguyen LTH, Johanes J, Chou SM, Zhu P, Tan NS, et al. Fabrication and characterization of a novel crosslinked human keratin-alginate sponge. *Journal of tissue engineering and regenerative medicine*. 2017;11(9):2590-602.
30. Taraballi F, Wang S, Li J, Lee FY, Venkatraman SS, Birch WR, et al. Understanding the nano-topography changes and cellular influences resulting from the surface adsorption of human hair keratins. *Advanced healthcare materials*. 2012;1(4):513-9.
31. Wang S, Taraballi F, Tan LP, Ng KW. Human keratin hydrogels support fibroblast attachment and proliferation in vitro. *Cell and tissue research*. 2012;347(3):795-802.
32. França R, Mbeh DA, Samani TD, Tien C, Mateescu MA, Yahia LH, et al. The effect of ethylene oxide sterilization on the surface chemistry and in vitro cytotoxicity of several kinds of chitosan. *Journal of Biomedical Materials Research Part B: Applied Biomaterials*. 2013;101(8):1444-55.

33. Nizhenko VI, Eremenko VN, Sklyarenko LI. Application of the sessile drop method to the determination of the surface energy and density of liquids wetting the backing material. *Powder Metall Met Ceram*. 1965;4(6):463-6.
34. Owens DK, Wendt RC. Estimation of the surface free energy of polymers. *Journal of Applied Polymer Science*. 1969;13(8):1741-7.
35. Salgado AJ, Coutinho OP, Reis RL. Novel starch-based scaffolds for bone tissue engineering: cytotoxicity, cell culture, and protein expression. *Tissue engineering*. 2004;10(3-4):465-74.
36. Silva-Correia J, Miranda-Gonçalves V, Salgado AJ, Sousa N, Oliveira JM, Reis RM, et al. Angiogenic Potential of Gellan-Gum-Based Hydrogels for Application in Nucleus Pulposus Regeneration: In Vivo Study. *Tissue Engineering Part A*. 2012;18(11-12):1203-12.
37. Ribatti D, Nico B, Vacca A, Presta M. The gelatin sponge-chorioallantoic membrane assay. *Nature protocols*. 2006;1(1):85-91.
38. Zheng H, Du Y, Yu J, Huang R, Zhang L. Preparation and characterization of chitosan/poly(vinyl alcohol) blend fibers. *Journal of Applied Polymer Science*. 2001;80(13):2558-65.
39. Zheng X-F, Lian Q, Yang H, Wang X. Surface Molecularly Imprinted Polymer of Chitosan Grafted Poly(methyl methacrylate) for 5-Fluorouracil and Controlled Release. *Scientific Reports*. 2016;6:21409.
40. Dhawade PP, Jagtap RN. Characterization of the glass transition temperature of chitosan and its oligomer by temperature modulated differential scanning calorimetry. *Adv Appl Sci Res*. 2012;3(3):1372-82.
41. Fahmy HM, Fouda MM. Crosslinking of alginic acid/chitosan matrices using polycarboxylic acids and their utilization for sodium diclofenac release. *Carbohydrate polymers*. 2008;73(4):606-11.
42. Caffesse RG, Nasjleti CE, Plotzke AE, Anderson GB, Morrison EC. Guided tissue regeneration and bone grafts in the treatment of furcation defects. *Journal of periodontology*. 1993;64(11 Suppl):1145-53.
43. Wrobel S, Serra SC, Ribeiro-Samy S, Sousa N, Heimann C, Barwig C, et al. In vitro evaluation of cell-seeded chitosan films for peripheral nerve tissue engineering. *Tissue engineering Part A*. 2014;20(17-18):2339-49.
44. Carvalho CR, Costa JB, da Silva Morais A, López-Cebral R, Silva-Correia J, Reis RL, et al. Tunable Enzymatically Cross-Linked Silk Fibroin Tubular Conduits for Guided Tissue Regeneration. *Advanced healthcare materials*. 2018;7(17):1800186.
45. de Luca AC, Lacour SP, Raffoul W, di Summa PG. Extracellular matrix components in peripheral nerve repair: how to affect neural cellular response and nerve regeneration? *Neural regeneration research*. 2014;9(22):1943-8.
46. Mogosanu GD, Grumezescu AM, Chifiriuc MC. Keratin-based biomaterials for biomedical applications. *Current drug targets*. 2014;15(5):518-30.
47. Ham TR, Lee RT, Han S, Haque S, Vodovotz Y, Gu J, et al. Tunable Keratin Hydrogels for Controlled Erosion and Growth Factor Delivery. *Biomacromolecules*. 2016;17(1):225-36.
48. Zhang Z, Gupte MJ, Ma PX. Biomaterials and stem cells for tissue engineering. *Expert opinion on biological therapy*. 2013;13(4):527-40.
49. Zhu H, Li R, Wu X, Chen K, Che J. Controllable fabrication and characterization of hydrophilic PCL/wool keratin nanonets by electronnetting. *European Polymer Journal*. 2017;86:154-61.
50. Wu P, Dai X, Chen K, Li R, Xing Y. Fabrication of regenerated wool keratin/polycaprolactone nanofiber membranes for cell culture. *International journal of biological macromolecules*. 2018;114:1168-73.
51. Cangellaris OV, Gillette MU. Biomaterials for Enhancing Neuronal Repair. *Frontiers in Materials*. 2018;5(21).
52. Tanabe T, Okitsu N, Tachibana A, Yamauchi K. Preparation and characterization of keratin–chitosan composite film. *Biomaterials*. 2002;23(3):817-25.
53. Ning L, Xu Y, Chen X, Schreyer DJ. Influence of mechanical properties of alginate-based substrates on the performance of Schwann cells in culture. *Journal of Biomaterials Science, Polymer Edition*. 2016;27(9):898-915.
54. Dreesmann L, Mitnacht U, Lietz M, Schlosshauer B. Nerve fibroblast impact on Schwann cell behavior. *European Journal of Cell Biology*. 2009;88(5):285-300.
55. Jessen KR, Mirsky R, Lloyd AC. Schwann Cells: Development and Role in Nerve Repair. *Cold Spring Harbor perspectives in biology*. 7(7):a020487-a.
56. Wang H, Zhu H, Guo Q, Qian T, Zhang P, Li S, et al. Overlapping Mechanisms of Peripheral Nerve Regeneration and Angiogenesis Following Sciatic Nerve Transection. *Frontiers in cellular neuroscience*. 2017;11:323-.
57. Shen D, Wang X, Zhang L, Zhao X, Li J, Cheng K, et al. The amelioration of cardiac dysfunction after myocardial infarction by the injection of keratin biomaterials derived from human hair. *Biomaterials*. 2011;32(35):9290-9.
58. Nectow AR, Marra KG, Kaplan DL. Biomaterials for the development of peripheral nerve guidance conduits. *Tissue engineering Part B, Reviews*. 2012;18(1):40-50.
59. Xu Y, Zhang SZ, Huang CH, Liu XY, Zhong ZH, Hou WL, et al. Keratin 17 identified by proteomic analysis may be involved in tumor angiogenesis. *BMB reports*. 2009;42(6):344-9.
60. Takano M, Shimada K, Fujii T, Morita K, Takeda M, Nakajima Y, et al. Keratin 19 as a key molecule in progression of human hepatocellular carcinomas through invasion and angiogenesis. *BMC cancer*. 2016;16(1):903.

61. Hasturk AE, Yilmaz ER, Hayirli N, Kayalar AE, Akyildiz S, Gökce EC, et al. Stereologic and ultrastructural comparison of human and rat amniotic membrane wrapping for rat sciatic nerve repair. *Journal of Clinical Neuroscience*. 2018;57:157-61.
62. Peng S-W, Li C-W, Chiu I-M, Wang G-J. Nerve guidance conduit with a hybrid structure of a PLGA microfibrillar bundle wrapped in a micro/nanostructured membrane. *International journal of nanomedicine*. 2017;12:421-32.
63. Sarker M, Naghieh S, McInnes AD, Schreyer DJ, Chen X. Strategic Design and Fabrication of Nerve Guidance Conduits for Peripheral Nerve Regeneration. *Biotechnology journal*. 2018;13(7):e1700635.

Chapter VII

Gellan gum-based luminal fillers for peripheral nerve regeneration. An in vivo study in the rat sciatic nerve repair model

Chapter VII

Gellan gum-based luminal fillers for peripheral nerve regeneration. An *in vivo* study in the rat sciatic nerve repair model¹

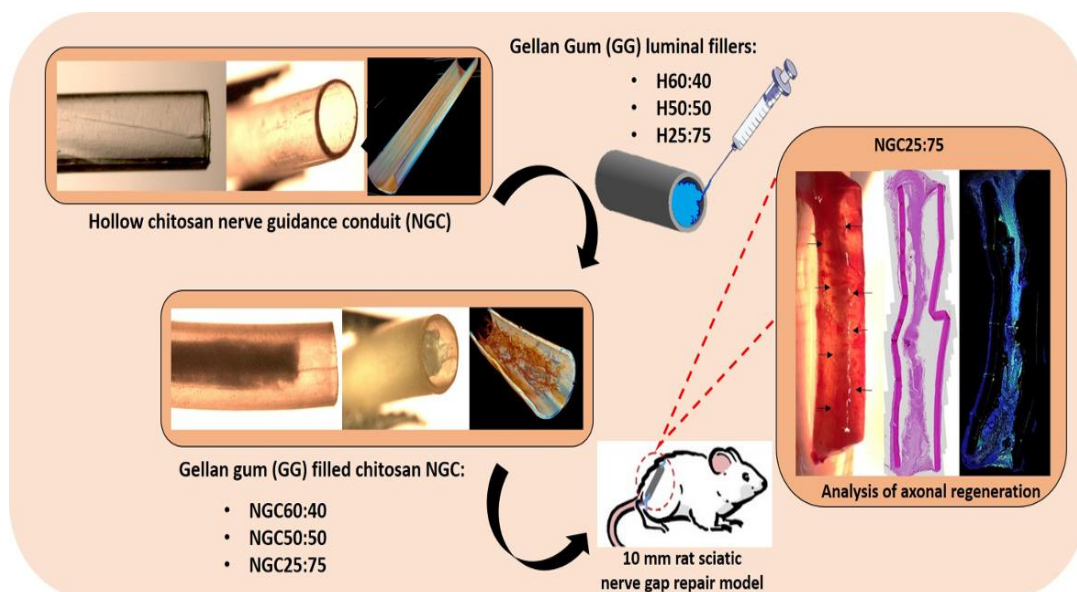
ABSTRACT

Peripheral nerve injuries (PNI) resulting in a gap to be bridged between the transected nerve ends are commonly reconstructed with autologous nerve tissue, but there is a need for valuable alternatives. This experimental work considers the innovative use of the biomaterial Gellan Gum (GG) as luminal filler for nerve guidance channels made from chitosan with a 5 % degree of acetylation. The engineered constructs should remodel the structural support given to regenerating axons by the so-called bands of Büngner. Four different GG formulations were produced, by combining varying amounts of High-Acyl GG (HA-GG) and Methacrylated GG (MA-GG). The effective porosity of the freeze-dried networks was analyzed by SEM and Micro-CT 3D reconstructions, while the degradation and swelling abilities were characterized *in vitro* for up to 30 days. The metabolic activity and viability of immortalized Schwann cells seeded onto the freeze-dried networks were also evaluated. Finally, the developed hydrogel formulations were freeze-dried within the chitosan nerve guides and implanted in a 10 mm rat sciatic nerve defect. Functional and histomorphological analyses after 3, 6, and 12 weeks *in vivo* revealed that although it did not result in improved nerve regeneration, the NGC25:75 formulations could provide a basis for further development of GG scaffolds as luminal fillers for hollow nerve guidance channels.

Keywords: Gellan gum, chitosan, biomaterials, peripheral nerve regeneration

¹This chapter is based on the following publication: [Carvalho CR, Wrobel S, Meyer C, Brandenberger C, Cengiz IF, López-Cebral R, Silva-Correia J, Ronchi G, Reis RL, Grothe C, Oliveira JM, Haastert-Talini K. The potential of gellan gum-based luminal fillers for peripheral nerve regeneration: An *in vivo* study in rat sciatic nerve repair model. Biomaterials Science. 2018; 1059-1075. doi: 10.1039/c7bm01101f.](#)

VII-1. GRAPHICAL ABSTRACT



VII-2. INTRODUCTION

Peripheral nerves originate with their motor and sensory roots from the spinal cord or the brain stem, sending efferent signals from the Central Nervous System (CNS) to all organs and tissues, where they also collect afferent information and transmit it back to the CNS. Their widespread presence and lack of protection against transection or injuries make them vulnerable to diverse types of lesions, *i.e.* car accidents, military and sports injuries or metabolic damage. Indeed, peripheral nerve injuries (PNIs) affect over one million people across the world every year (1). Although the peripheral nervous system (PNS) has a superior capacity to regenerate when compared to the CNS, this ability is not as efficient as desired and surgical intervention is often required. However, even if skilled microsurgical reconstruction is performed, inefficient recovery is common, leading to motor and sensory perception impairments, as well as too painful conditions (2).

For PNIs that require surgical intervention, like all complete transection injuries, end-to-end suturing is applicable in the case of gaps shorter than 5 mm. For longer gap injuries autologous nerve grafts (AUTOGs) have been considered the gold standard for decades (3). However, they are associated with several drawbacks, for instance, donor site morbidity and limited availability of donor tissue. Nerve mismatches are frequent, both in terms of size and alignment. Additionally, complete recovery of nerve function is rare. Meanwhile, immune rejection dismisses primary allografts and xenografts (4). Nerve guidance conduits (NGCs), with base on the natural biology of regeneration, seem a potentially outstanding alternative to overcome this public health problem (1, 5, 6).

Up to date, several NGCs have been developed, using many different strategies, from simple hollow tubes (7, 8) to subdivided or filled tubes (9, 10), also comprising the addition of neurotrophic factors (11, 12) or stem cells (13, 14). Also, their combinations were explored (15). FDA approved NGCs consist in hollow tubular structures, made from cross-linked collagen, resorbable biopolymers or non-resorbable hydrogels.(16) The absence of luminal structures to guide axons and Schwann cells, the peripheral glia cells, was pointed as one possible cause for their failure in long gap PNIs (17, 18).

Chitosan is a polysaccharide extracted mainly from crab shells and has been widely studied for its application in nerve regeneration (19). Recently, Reaxon® (Medovent GmbH, Germany), a nerve guide made out of chitosan with a 5 % degree of acetylation (20), received CE and FDA approval for reconstruction of up to 26 mm in length peripheral nerve defects in humans. Current research attempts focus on the design of more refined chitosan nerve guides, able to support the reconstruction of nerve defects exceeding 3-5 cm in length. Consequently, luminal enrichment should be further engineered to optimize axonal guidance. The strategies already explored go from simply inserting a central longitudinal chitosan film (9) to adding regenerative hydrogel matrices, like a hyaluronic acid and laminin based hydrogel (21).

Gellan Gum (GG) is a linear anionic polysaccharide composed of tetrasaccharide (1,3-b-D-glucose, 1,4-b-D-glucuronic acid, 1,4-b-D-glucose, 1,4-a-L-rhamnose) repeating units. This biomaterial exists in nature in two forms: high-acyl (HA-GG) and a low-acyl (LA-GG) form. The side groups in the LA-GG polymeric chain are susceptible to chemical modification, such as the incorporation of methacrylate groups (MA-GG). The methacrylation process allows harsh reagents-free hydrogels preparation, with temperatures and pH resembling that of the human body (22).

This experimental work proposes the utilization of different HA-GG and MA-GG blending hydrogels as luminal fillers of tubular chitosan nerve guidance conduits (NGC). Since HA-GG and MA-GG behave differently, these blends are expected to affect hydrogel degradation rate and cellular adhesion, thus permitting to evaluate the influence of these parameters on the peripheral nerve regeneration process. To our knowledge, it is the first time that the biomaterial GG was studied with regard to PNR purposes. However, GG has already shown great potential for other regenerative applications, such as dentistry (23), fibrocartilage tissue engineering (24), wound healing (25) or bone regeneration (26), as well as in the area of drug delivery (27, 28). After the production of different GG formulations, the hydrogels were subjected to a physicochemical characterization and *in vitro* preliminary assessment using immortalized Schwann cells. Subsequently, the formulations were injected into chitosan nerve guidance conduits,

freeze-dried and implanted *in vivo* for different periods of observation time. Immunohistochemical studies were carried out to assess nerve regeneration and re-vascularization, allied to macroscopic evaluation of the explants, evaluation of functional motor recovery and nerve morphometry. The evaluation of their characteristics was performed in a 10 mm sciatic nerve defect in order to select the most promising as luminal filler for NGCs, for future studies in longer gaps.

VII-3. MATERIALS AND METHODS

VII-3.1. Production of biomedical systems

VII-3.1.1. Production of Gellan-Gum freeze-dried hydrogels

Four different GG-based formulations were obtained by combining 0.7 %wt. HA-GG (KelcoGelW LT100 with MW=1–2 x 10⁶ Da, CP Kelco, Atlanta, GA, USA) and 0.7 %wt. MA-GG (Mimsys G[®] with MW=62.4 kDa, Stematters, Irisbiosciences, Guimarães, Portugal) aqueous solutions. The studied ratios were, 60:40 %, 50:50 %, 25:75 % 0:100 % (v/v) of HA-GG:MA-GG (see **Table VII-1**). These preparations were heated at 37 °C for 30 minutes and transferred into silicone disc moulds (diameter and height were 6 mm and 10 mm, respectively), self-made from silicon tubing (purchased from Deltalab, Spain), which were ultimately immersed into PBS solutions (pH = 7.4) overnight. Gelation occurred by ionic crosslinking at room temperature (RT). These hydrogels were punched with a branched (200 µm of diameter linear branches) metallic self-made device (stainless steel), in order to create interior linear porous channels. The obtained hydrogels were frozen (-80 °C) and freeze-dried. The polymeric networks obtained will be transformed into hydrogels after re-hydration.

VII-3.1.2. Production of chitosan nerve guidance conduits (NGCs) filled with freeze-dried Gellan Gum hydrogels

Chitosan hollow tubes, kindly supplied by Medovent GmbH (Mainz, Germany), were manufactured under ISO 13485 conditions, using Medical grade chitosan (Ki2Med[®] LO₃₀₊ extracted from *Pandalus borealis* shrimp shells, Mw=260 kDa, supplied by Altakitin S. A.,

Lisbon, Portugal). More specifically, an extrusion process was applied for their obtaining, followed by distinctive washing and hydrolysis steps to set the Degree of Acetylation at a 5 % value. The formulations were finally cut into fragments presenting the required length (14 mm) and sterilized by ethylene oxide. The mixtures mentioned in section 2.1.1. (60:40 %, 50:50 % and 25:75 % (v/v) HA-GG:MA-GG) were injected inside the tubes with the help of a syringe. During this step, it was important to keep 2 mm hydrogel-free segments at each extreme of the tube, for nerve insertion and suture purposes. The filled tubes were then immersed in PBS overnight for gelation by ionic crosslink, frozen at -80 °C and freeze-dried (see **Table VII-1**).

Table VII-1 - Gellan Gum formulations and designations. This table presents the nomenclature utilized to designate the different formulations studied during this experimental work.

| Composition | Freeze-dried hydrogel formulation | Nerve guidance conduit, NGC (Freeze-dried hydrogel filling chitosan tube) |
|-----------------------------------|-----------------------------------|---|
| 60:40 % (v/v) HA-GG : MA-GG | H60:40 | NGC60:40 |
| 50:50 % (v/v) HA-GG : MA-GG | H50:50 | NGC50:50 |
| 25:75 % (v/v) HA-GG : MA-GG | H25:75 | NGC25:75 |
| 0:100 % MA-GG (v/v) HA-GG : MA-GG | H0:100 | x |

VII-3.2. Physicochemical characterization

VII-3.2.1. Microstructure evaluation

The microstructure evaluation was performed by means of observation in a stereomicroscope, Scanning Electron Microscope (SEM) and X-ray micro-computed tomography (micro-CT) analysis. The freeze-dried HA-GG:MA-GG hydrogel formulations and HA-GG:MA-GG hydrogel filled chitosan NGCs (**Table VII-1**) were examined under the Stereo Microscope + Lamp (Schott KL 200, model Stemi 1000, Zeiss). For SEM, the formulations described were sputter coated with gold, in order to facilitate the analyses of their surface morphology (model S360, Leica, Cambridge, England). The microstructure of the formulations was also qualitatively and quantitatively evaluated by micro-CT analysis (n = 3). The detailed structure of the samples was acquired by X-ray scanning and 3D-reconstructed. Morphometric parameters, such as porosity, mean pore size and trabecular thickness, were determined. Data acquisition was carried out using a SkyScan 1072 scanner with a pixel size of 2 µm and an integration time of 1182 ms.

The X-ray source was set at 39.4 kV and 244 μ A. A total of 500 projections were acquired over a rotation range of 180°, with a rotation step of 0.23°. Datasets were reconstructed using standardized cone-beam reconstruction software (NRecon v. 1.6.6.0, SkyScan). The output format for each sample was bitmap images. The set of images was orientated with DataViewer software (v. 1.4.4, SkyScan) to obtain all the samples in the same axis. A representative dataset of the slices was segmented into binary images with a dynamic threshold of 40–120, which were used for morphometric analysis (CT Analyser, v. 1.12.0.0, SkyScan) and to obtain the 3D models (CT Vox, v. 2.3.0 r810, SkyScan).

VII-3.2.2. Water uptake and weight loss

Water uptake and weight loss studies concerning the GG freeze-dried hydrogels were performed by means of PBS (pH 7.4 at 37 °C) soaking. At predefined time points (1, 7, 14 and 30 days) the swollen or degraded samples were extracted, and the excess of water removed with filter paper. The water uptake ability of the formulations was calculated according to **Equation VII-1**. To determine the degradation profile over time the samples were dried at RT and **Equation VII-2** was applied.

Equation VII-1 - Equation for the determination of percentage of water uptake

$$\text{Water uptake (\%)} = \frac{mw - mi}{mi} \times 100$$

where, mw is the wet mass (after excessive water removal) and mi is initial mass.

Equation VII-2 - Equation for the determination of percentage of weight loss

$$\text{Weight loss (\%)} = \frac{mi - mf}{mi} \times 100$$

where, mi is initial mass (before immersion in solution) and mf is final mass (after drying). Three replicates of each sample were studied, and the average values considered.

VII-3.3. Biological *in vitro* assays

Rat immortalized Schwann cell (rat iSCs) (29) were taken from a stock and cultured in non-coated cell culture flasks. The culture medium was DMEM supplemented with 10 % fetal calf serum, 1 % (v/v) Penicillin/Streptomycin, 1 % (v/v) sodium pyruvate, and 1% (v/v) L-glutamine (all from PAA Laboratories, GmbH).

VII-3.3.1. Metabolic activity evaluation

iSCs metabolic activity was followed with Alamar Blue (AB), a dye that yields a fluorescent signal and a colorimetric change when incubated with metabolically-active cells. The cells were directly seeded (500,000 cells/scaffold) over the GG freeze-dried hydrogels. After 1, 5 and 7 days *in vitro* (DIV), specific cell culture medium containing 20 % (v/v) AB was added to the different culture wells. The systems were left for incubation for 3 hours, after which fluorescence was monitored at 590 nm emission wavelength (excitation wavelength 530 nm), using a microplate reader (FL 600, Bio-Tek Instruments). AB reagent was removed using PBS and fresh culture medium was added in its place after each AB determination. The metabolic activity values were calculated by normalization with the mean fluorescence value obtained for the negative controls (different formulations without cells that undergo the exact same processing. The positive control refers to the same cellular density seeded on Tissue culture polystyrene (TCPs).

VII-3.3.2. Live/dead viability assay

iSCs viability was qualitatively assessed using Calcein AM (for living cells) and propidium iodide staining (for dead cells). The cells were seeded (500,000 cells/scaffold) over the dry network's formulations. After 1, 5 and 7 days *in vitro*, each scaffold was washed with PBS and immersed in 1 mL of culture medium supplemented with 2 μ g Calcein AM and 4 μ g propidium iodide (Life Technologies, CA, USA). These immersions lasted for 2 hours, after which the samples were thoroughly washed with PBS. The samples were analyzed using a transmitted and reflected light microscope (Axio Imager Z1m, Zeiss, Jena, Germany).

VII-3.4. *In vivo* study

VII-3.4.1. Experimental design

The effectiveness of the developed chitosan tubes filled with freeze-dried hydrogels as PNR guidance conduits (see **Table VII-1**; NGC60:40, NGC50:50 and NGC25:75) was tested in a 10 mm rat sciatic nerve defect. Samples for histological analysis were collected after both short-term (ST, 3 and 6 weeks) and long-term (LT, 12 weeks) observation periods. For the ST studies, 4 animals were selected for the implantation of each NGC formulation. Hollow chitosan tubes served as positive controls (20). For LT studies, 7 animals were studied per NGC formulation and 7 animals receiving an autologous nerve graft (AUTOG) served as controls. The majority of the *in vivo* studies described in this experimental work were performed in Hannover Medical School (MHH, Hannover, Germany), except for the micro-CT analysis of the explants and vascularization detection studies, which were performed in 3B's Research Group (Guimarães, Portugal). Histomorphometry was completed at University of Turin (UNITO, Italy).

VII-3.4.2. Surgical procedure

All animal experiments followed the rules of the EU Directive 2010/63/EU for animal experiments and were permitted by the animal care committee of Lower-Saxony, Germany: Nds. Landesamt für Verbraucherschutz und Lebensmittelsicherheit Dezernat 33/Tierschutz, reference number 33.12 42502-04-12/0816.

Female Wistar rats (225 to 250 g) were kept in groups of four animals under standard conditions (room temperature 22 ± 2 °C; humidity 55 ± 5 %; light-dark cycle 14 hours/10 hours), with food and water *ad libitum*. For surgical procedures, animals were anesthetized by an intraperitoneal injection of chloral hydrate (370 mg/kg of body weight, Sigma-Aldrich). NGCs with a length of 14 mm were saturated for 30 minutes in 0.9 % (v/v) NaCl prior to implantation. Animals were placed on a thermostatic blanket throughout the surgical procedures and postoperative periods. Aseptic conditions were observed.

After exposure of the sciatic nerve, it was transected at a constant point (6 mm from the exit of the gluteus muscle) for the removal of 5 mm of the distal end. Once the PNI was caused, NGCs were

implanted to bridge a 10 mm nerve defect. NGCs were connected by a single 9-0 suture (9-0, EH7981G, Ethilon, Ethicon, Scotland) to the respective nerve end. Alternatively, autologous nerve grafts were implanted. Therefore, a 10 mm nerve segment was excised from the same nerve (proximal transection again at 6 mm from the exit of the gluteus muscle), reversed and 180° turned along its longitudinal axis) and sutured back into the nerve with three 9-0 sutures at each end. Postoperative analgesia was guaranteed by intramuscular injection of buprenorphine (0.045 mg/kg of body weight, Buprenovet®; Bayer Pharmaceuticals, Lerverkusen, Germany).

VII-3.4.3. Evaluation of functional motor recovery

Electrodiagnostical recordings of evoked compound muscle action potentials (CMAPs) from the anterior tibial muscles (TA) and the plantar muscles (PL) were performed. During the 12 weeks study period two sessions of non-invasive (week 4 and week 8 post-surgery) measurements and one final session of invasive (12 weeks post-surgery) measurements were carried out. The investigators performing the tests were blinded for the general implantation condition and the formulation type of the implanted tubes.

In brief, a portable electrodiagnostic device (Keypoint Portable; Medtronic Functional Diagnostics A/S, Denmark) was used to stimulate the sciatic nerve and to record the evoked CMAPs. In the non-invasive setting, the sciatic nerve was stimulated with single electrical pulses (100 µs duration and supramaximal intensity) delivered by monopolar needles (30G, diameter 0.3 mm, length 10 mm; Natus Europe GmbH, Planegg, Germany), percutaneously placed at the sciatic notch (proximal stimulation) or at the popliteal fossa (distal stimulation). The active recording electrode was located in the respective muscle belly, the reference electrode in the tip of the second toe and the ground needle electrode was inserted in the skin at the flank. In the invasive setting, the sciatic nerves at both the injured and non-injured side were consecutively exposed. With the help of a bipolar steel hook electrode, the sciatic nerves were directly stimulated proximal and distal to the transplants. Single electrical pulses (100 ms duration) with gradually increased intensity (not exceeding 8 mA) were applied in order to evaluate the threshold and maximal CMAP. The recording electrodes were placed as described before. Whenever a CMAP could be evoked, the signal was recorded and the signal amplitude of the negative CMAP peak analyzed. Amplitude ratio values were obtained using CMAP signals evoked and recorded from the

contralateral healthy side of the animal. If no evoked CMAP was detected, a 0.00 value was noted down.

VII-3.4.4. Macroscopic inspection of the reconstructed nerves upon explantation

At the end of the ST or LT observation periods, animals were sacrificed under deep general anesthesia, following the animal protection rules. The regenerated sciatic nerves were exposed and inspected with the help of a microsurgery microscope.

VII-3.4.5. Micro-CT evaluation of the explants

This technique was performed in 3B's Research Group, (Guimarães, Portugal) after shipment of the entire LT study (12 weeks) explants from MHH (Hannover, Germany) which were preserved in ethanol solutions. The explants were scanned using a high-resolution micro-CT device, VivaCT 80 (Scanco Medical AG, Brüttisellen, Switzerland). 250 projections with a resolution of 1024 x 1024 pixels were obtained in each scan with an integration time of 200 ms. Images with an isotropic pixel size of 31.2 μm were obtained at 45 kV, 177 μA and 8 W. The acquired images were reconstructed to obtain 2D image datasets in μCT Evaluation Program V6.5 (Scanco Medical AG, Brüttisellen, Switzerland). Using the CT Analyzer software V1.15.4.0 (Bruker Micro-CT, Belgium) the region of interests were defined on the 2D images of the explants that were viewed in 3D and 2D all planes on DataViewer V1.5.3.6 (Bruker Micro-CT, Belgium).

VII-3.4.6. Nerve histology for detection of axonal regeneration and immunological reaction*

After the corresponding period of study, the animals were sacrificed and the nerve implants, together with the respective controls, were harvested for further analysis. The entire samples were fixed in 4 % (v/v) PFA overnight (4 °C), transferred to 70 % (v/v) ethanol and subsequently embedded in paraffin \ddagger .

For both, 6 weeks and 12 weeks' time point samples, longitudinal sections were produced in order to harvest the complete length of the GG material and eventually regrown tissue along the 10 mm nerve

gap. As soon as the complete length of the material was visible in one section a series of 24 sections (7 µm thickness) was produced and two sections per slide were collected. Again, the sections on one slide were harvested in 84 µm distance from each other. Once the first section series was completed a similar, the second one was collected without discarding any tissue. In the end, a total distance of 336 µm was longitudinally cut from the middle of the NGC content.

Selected slides were subjected to hematoxylin-eosin (H&E) staining. Briefly, samples were deparaffinized in xylol, hydrated through decreasing ethanol series (100 %, 96 %, 70 % and 50 % (v/v) alcohol) and finally washed in distilled water. After immersion in Hematoxylin, samples were rinsed in running soft tap water. Samples were then immersed in 80 % (v/v) alcohol solution and briefly in the Eosin staining. Slides were dehydrated through 96 % (v/v) ethanol, absolute ethanol and finally cleared in xylol and mounted with Moviol (Calbiochem, Germany, N° 475904).

Immunohistology was performed over sections that were consecutive to the ones processed for H&E staining. A double-staining was performed to detect neurofilaments (NF-200) and activated macrophages (ED-1). Nuclear counterstaining was obtained with DAPI. For such, slides were deparaffinized and immersed in an antigen retrieval solution (citrate buffer 10 mM pH 6.0 + 0.05 % (v/v) tween 20), heated at 90 °C for 30 minutes and left to cool down for another 30 minutes in distilled water. Afterwards, they were incubated in a blocking solution (PBS + 5 %wt. milk powder + 0.5 % (v/v) Triton X-100), prior to incubation with primary mouse anti-rat ED-1 antibody (1:1000 diluted in blocking solution, MCA 275R Serotec, UK) at 4 °C overnight. The next day the sections were washed with PBS (3x) before being incubated with Alexa 555-conjugated secondary goat-anti-mouse antibody (1:1000 diluted in blocking solution, Invitrogen, Germany) for 1 hour at room temperature (RT). After incubation with the secondary antibody, sections were further washed with PBS (3x) and a second blocking step was performed for 20 minutes.

Overnight incubation (4 °C) with primary rabbit anti-rat NF-200 antibody (1:200 diluted in blocking solution, N4142, Sigma Aldrich, Germany) followed the previously described steps. The samples were washed with PBS (3x) and incubated with Alexa 488-conjugated secondary goat-anti rabbit antibody (1:1000 diluted in blocking solution, Invitrogen, Germany) for 1 hour at RT. The double-labelled sections were afterwards counterstained with the nuclear dye (DAPI, 1:2000 diluted in PBS, Sigma, Germany) for 5 minutes at RT, and finally mounted with Moviol.

For qualitative analysis, representative photomicrographs of H&E stained sections were taken with the help of BX53 and BX51 microscopes, as well as analyzed with the help of the programs CellSense Dimension and CellSense Entry (all Olympus, Germany). Immunohistochemistry images were digitized by means of a fluorescence microscope (BX60, Olympus, Germany), operated by cellP software (Olympus, Germany) and qualitatively analyzed.

VII-3.4.7. Nerve histology for detection of neovascularization*

Immunohistology for neovascularization (CD31 and CD34) was performed in 3B's Research Group (Guimarães, Portugal), after shipment of paraffinized slides. Slides sections consecutive to the ones processed for H&E and double immunostaining staining were used for this purpose. Blind-coded sections from each segment were deparaffinized and immersed in an antigen retrieval solution (citrate buffer 10 mM pH 6.0 + 0.05 % (v/v) tween 20), heated at 90 °C for 30 minutes and left to cool down for another 30 minutes in distilled water. Slides were posteriorly immersed in a blocking solution (PBS + 3 %wt. BSA), prior to incubation with primary goat anti Mouse/Rat CD31/PECAM-1 antibody (AF3628, R&D Systems, UK) (15 µg/mL diluted in PBS + 1 %wt. BSA) at 4 °C overnight. The next day the corresponding sections were washed with PBS (3x), before being incubated with Alexa 488-conjugated secondary rabbit anti-goat antibody (1:500 in PBS + 1 %wt. BSA) for 1 hour at RT. After incubation with the secondary antibody, sections were further washed with PBS (3x) and a second blocking step was done for 20 minutes. This was followed by overnight incubation (4 °C) with primary rabbit anti-mouse CD34 (1:2500 diluted in PBS + 1 %wt. BSA, Abcam, Cambridge, UK). After washing with PBS (3x), incubation with Alexa Fluor 594 donkey anti-rabbit IgG secondary antibody (1:500 diluted in PBS + 1 %wt. BSA, Molecular Probes, Oregon, United States) was performed for 1 hour at RT. Sections were finally counterstained with the nuclear dye (DAPI, 1:2000 diluted in PBS, Sigma, Germany) for 5 minutes at RT and then mounted with PermaFluor (Thermo Fisher Scientific, UK). Since for the 3 weeks' time point the samples were cut in cross-section, the example photo belongs to an area around 5 mm after the proximal nerve end. Results were qualitatively analyzed using a transmitted and reflected light microscope (Axio Imager Z1m, Zeiss, Jena, Germany).

VII-3.4.8. Nerve morphometry

In the LT study, upon explanation 12 weeks after nerve reconstruction, nerve tissue segments 5 mm in length, were harvested directly distal to the sutures connecting the implants with the distal nerve end and processed for nerve morphometry. Segments taken from the contralateral healthy nerve at similar height served as controls. Therefore, fixation was performed in Karnovsky fixans (2 % (v/v) PFA, 2.5 % (v/v) glutaraldehyde in 0.2 M sodium cacodylate buffer, pH 7.3 for 24 hours) (30, 31), prior to rinsing the samples 3 times with 0.1 M sodium cacodylate buffer containing 7.5 %wt. sucrose. Post-fixation was performed in 1 %wt. OsO₄ for 1.5 hours and followed by myelin staining for 24 hours in 1 %wt. potassium dichromate, 24 hours in 25 % (v/v) ethanol and 24 hours in hematoxylin (0.5 % in 70 % (v/v) ethanol), according to a modified Schultze protocol (32), After dehydration, the samples were embedded in EPON (SERVA Electrophoresis GmbH, Heidelberg, Germany). Semi-thin (1 μm) cross-sections were cut with glass knives (Ultramikrotome System, 2128 Ultratome®, LKB, Bromma, Sweden) and mounted on uncoated glass slides. Toluidine blue staining followed, to further enhance the myelin staining (33). For quantitative analysis those samples were chosen that were derived from animals with electrodiagnostically proven reinnervation of the tibialis anterior muscle 12 weeks after surgery (LT). Morphometrical analysis revealed the total myelinated fiber number, cross sectional area, nerve fiber density, axon diameter, fiber diameter, g-ratio, and myelin thickness. All histomorphometry was performed with the help of systematic random sampling (20), at the University of Turin (UNITO, Italy) after shipping the finalized slides/sections from MHH.

VII-3.5. Statistical analysis

All quantitative physicochemical and biological *in vitro* experiments were run in triplicates, and results are expressed as mean ± standard deviation. Statistical analysis of the data was conducted using the GraphPad Prism Software for Windows, version 5.00 (GraphPad Software, Inc., La Jolla, USA). Regarding Alamar Blue assay, normality of data distribution was tested by the Shapiro-Wilk normality test. Afterwards, a Kruskal Wallis test was performed in order to compare the different groups, followed by Dunn's multiple comparison test. The significance level was set to *p < 0.05, **p < 0.01, ***p < 0.001.

No statistical analysis was performed on the data obtained during functional evaluation of nerve recovery since n ≤ 3 of the NGCs groups demonstrated functional recovery and the numbers were too

few for statistical analysis. Results of the morphometrical analysis are given in mean \pm SD for healthy nerve samples, AUTOG, and NGC25:75, while for less than 3 animals per group (NGC50:50) the single values are presented. * $p < 0.05$ after Dunn's multiple comparison test.

VII-4. RESULTS

VII-4.1. Physicochemical characterization

VII-4.1.1. Microstructure evaluation

All GG freeze-dried hydrogels (H60:40, H50:50, H25:75, H0:100, **Table VII-1**) were analyzed according to the techniques mentioned above. However, due to the similar aspect of the different formulations, only the images corresponding to formulation H25:75 are presented.

In **Figure VII-1**, the first row of images shows the different representative aspects displayed by GG formulations along the preparation process. **Figure VII-1A** represents the outline of the network with the intended microstructure. **Figure VII-1B** shows the hydrogels obtained after the ionic PBS crosslinking. These hydrogels were punched with branched wires (**Figure VII-1C**), to produce vertical aligned porous channels within their structure. **Figure VII-1D** shows the aspect of the freeze-dried networks obtained. Once rehydrated with cell culture medium, the formulations become hydrogels that maintain the conferred porous structure (**Figure VII-1E**). **Figure VII-1F** shows the SEM microphotographs corresponding to the surfaces of the cross-sections. High diameter pores (around 200 μm) can be seen, which originated from both, metallic punching and freeze-drying. Meanwhile, **Figure VII-1G** represents the longitudinal cut of a scaffold. The aligned channels made by the metallic device (indicated by arrows) are clearly discernible from the random pores obtained by freeze-drying. **Figure VII-1H** and **Figure VII-1I** show the longitudinal and transversal sections, respectively, of the chitosan tubes (arrows pointing to their walls) filled with the GG freeze-dried hydrogels. Micro-CT studies were performed to obtain 3D reconstructions of the studied formulations at the micrometric level. **Figure VII-1J** and **Figure VII-1K** show the 3D reconstructed structures of the freeze-dried GG hydrogels and the final NGC constructs, respectively.

Micro-computed tomography technology was also used to define the mean pore size (μm), the mean trabecular thickness (μm) and the % of porosity of all developed formulations. Regarding the

freeze-dried GG formulations, detailed results can be found in the supplementary material supplied (**Supplementary Table VII-1**). The mean pore size varied from 230.6 ± 3.2 to 339.0 ± 75.9 μm , trabecular thickness from 58.1 ± 2.1 to 65.8 ± 4.7 μm and the % of porosity from 79.2 ± 1.7 to 81.5 ± 8.2 %. For hydrogels freeze-dried within NGCs (**Supplementary Table VII-2**) the mean pore sizes varied from 321.6 ± 89.4 to 377.8 ± 50.8 μm , trabecular thickness from 98.0 ± 13.5 to 121.4 ± 13.4 μm and the % of porosity from 73.8 ± 7.3 to 82.8 ± 5.2 %.

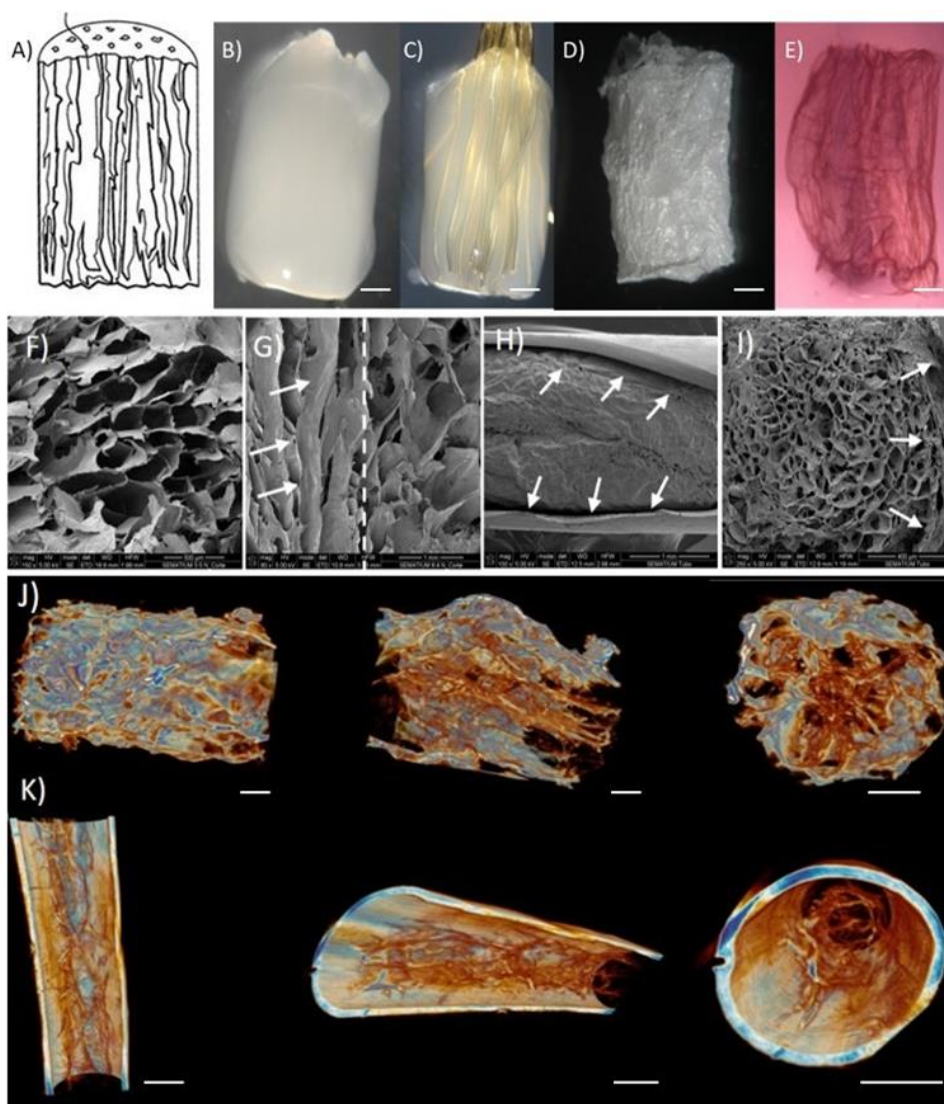


Figure VII-1 - Macro- and microstructure evaluation of the developed formulations. The first row of images corresponds to the different aspects of the formulations throughout the production process: A) Scheme of a scaffold with the intended microstructure of vertically aligned channels; B) Hydrogel obtained after the ionic PBS crosslinking; C) Hydrogel punched with branched wires to display longitudinal porous channels; D) Freeze-dried hydrogel; E) Re-hydrated freeze-dried hydrogel resembling the initial scheme. The second row of images corresponds to SEM micrographs of the freeze-dried formulations: F) Surface cross-section of the scaffold; G) Longitudinal

cut of the scaffold. White arrows point to the aligned channels made by the punching (right), which differ from the random network porosity (left); H) Longitudinal section of a chitosan NGC (arrows pointing to the wall of it) filled with GG freeze-dried hydrogel and I) Cross-section of the chitosan NGC (arrows pointing to its wall) filled with GG freeze-dried hydrogels. The third row of images reveals the structure of the biomaterials after Micro-CT 3D reconstructions: J) 3D reconstructions of freeze-dried GG networks; K) 3D reconstructions of final NGCs constructs. As the aspect of all the studied formulations was very similar, the previously presented images are representative of all of them. Scale bars: 1 mm.

VII-4.1.2. Water uptake and weight loss

The results of water uptake (WU) and weight loss (WL) can be seen in **Figure VII-2**. With respect to WU, all the studied formulations reached maximum swelling stability after 1 day of immersion.

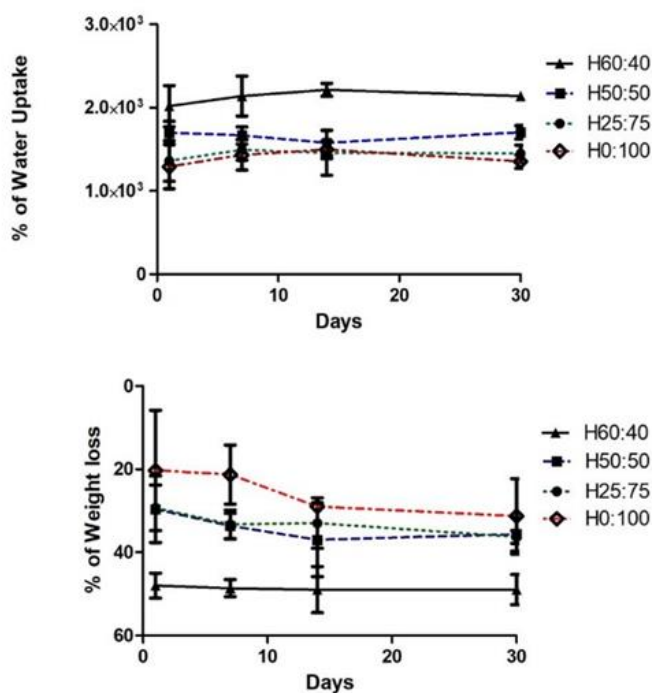


Figure VII-2 - Percentage of water uptake and weight loss of the developed GG freeze-dried hydrogels. The graphics represent the water uptake and weight loss values corresponding to all the studied formulations along the 30 days of study. The evaluations were performed at 37 °C.

From that day to day 30, the percentages of swelling were constant. H60:40 is the formulation with higher WU, presenting values slightly above 2,000 %. On the opposite, H0:100 % is the system having lower WU, with values rounding 1,000 %. The H60:40 formulation showed a higher mass loss around 45 %wt.) when compared to the other formulations. On the contrary, H0:100 % formulations underwent the lowest WL, as the loss reached averages of 20 to 30 % of mass after 30 days.

VII-4.2. Biological *in vitro* assays

VII-4.2.1. Metabolic activity of immortalized Schwann cells

The results (**Figure VII-3A**) show a general increase in the metabolic activity increasing amounts of MA-GG in the formulations, regardless of the time point analyzed, the highest values were obtained for H0:100. However, in general, the metabolic activity values did not increase significantly over time. The only exception was formulation H0:100, with a significant increase in metabolic activity both from day 1 to 5 and 1 to 7. Indeed, both at 5 and 7 days the metabolic activity of iSCs seeded onto the H0:100 formulation was significantly higher than that obtained from iSCs on H60:40 and H50:50.

VII-4.2.2. Live/dead viability assay

In **Figure VII-3B** it can be seen that, in accordance with the metabolic activity quantification, a higher number of living cells are present in the formulations with increasing amount of methacrylated GG, from H60:40 to H0:100. As expected, the number of living cells also increases progressively along the time (days *in vitro*). Importantly, the number of dead cells is negligible, as reflected by the presence of very few red-stained spots.

VII-4.3. *In vivo* studies

A concise summary of all results presented in the following for the GG filled NGCs can be found in the supplementary data. Whenever appropriate the reader will be referred to see **Supplementary Tables VII-4, VII-5** or **VII-6** that summarize the results of the evaluation performed on samples retrieved 3 weeks, 6 weeks and 12 weeks after reconstruction, respectively. For the ST studies, hollow chitosan tubes served as positive controls (20) and 4 animals per group were selected for implantation of each NGC formulation. or LT studies, autologous nerve graft (AUTOG) served as controls and 7 animals were subjected each to implantation of either NGC formulation or of an AUTOG.

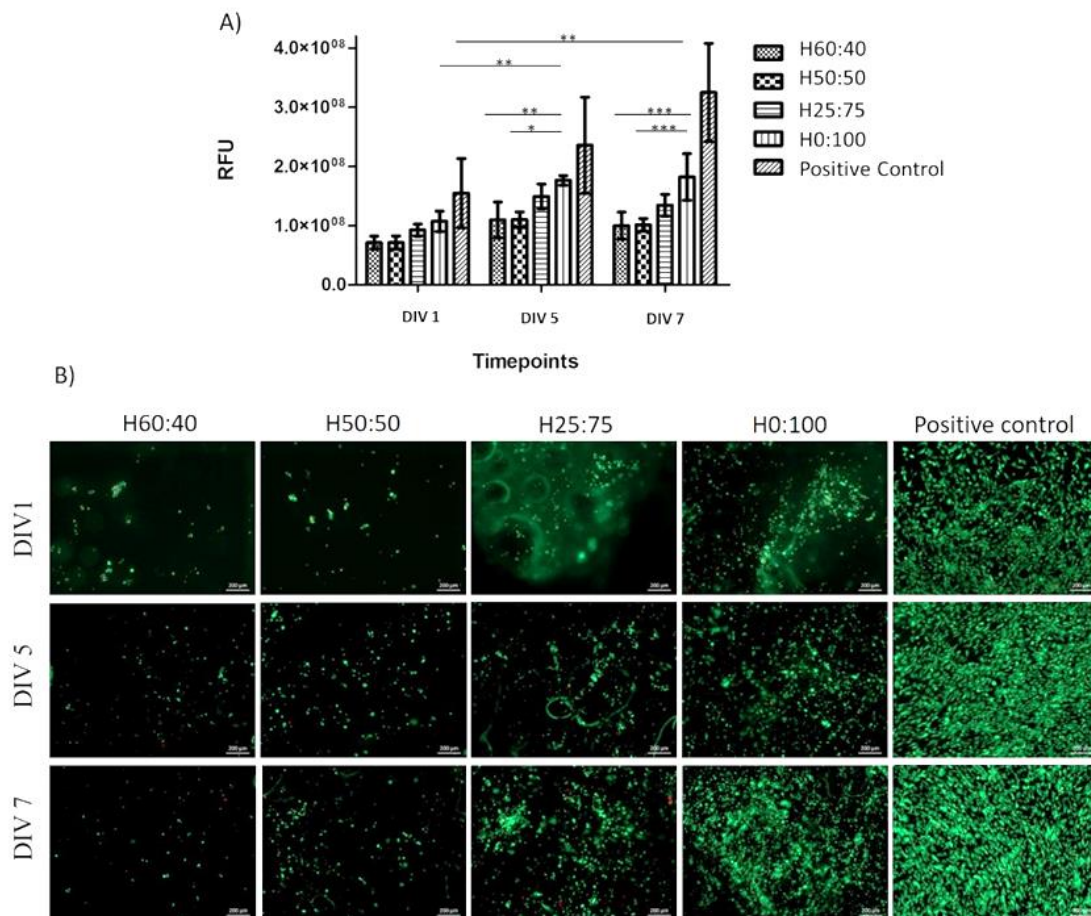


Figure VII-3 - Biocompatibility of GG formulations with immortalized Schwann cells (iSCs) *in vitro*. A) Metabolic activity of iSCs seeded on freeze-dried hydrogels formulations after up to 7 days; determination by Alamar Blue; n =3. B) Representative Live/Dead qualitative assay images after direct iSC seeding on freeze-dried hydrogels formulations after up to 7 days; determination by Calcein AM (green fluorescence) and propidium iodide (red fluorescence). Scale bars: 200 μ m.

Table VII-2 - Evaluation of functional motor recovery. This table presents the percentages, as well as animals per group, with evocable compound muscle action potentials (CMAPs) recordable from the tibialis anterior muscle or plantar interosseous muscle. The measurements were performed 4, 6 and 12 weeks after nerve reconstruction surgery. Varying animal numbers displayed for CMAP recording from tibialis anterior and plantar muscles, respectively, are related to eventual temporary suspension of animals from plantar recordings upon occurrence of signs of minimal autotomy.

| | 8 weeks | | 12 weeks (invasive) | |
|---------------------------------|---------------|----------------|---------------------|----------------|
| | Animals/group | Percentage (%) | Animals/group | Percentage (%) |
| <i>Tibialis anterior muscle</i> | | | | |
| <i>AUTOG</i> | 6/7 | 86 | 7/7 | 100 |
| <i>NGC60:40</i> | 0/7 | 0 | 0/7 | 0 |
| <i>NGC50:50</i> | 0/7 | 0 | 2/7 | 29 |
| <i>NGC25:75</i> | 0/5 | 0 | 3/5 | 60 |
| <i>Plantar Muscle</i> | | | | |
| <i>AUTOG</i> | 3/7 | 43 | 5/7 | 71 |
| <i>NGC60:40</i> | 0/7 | 0 | 0/7 | 0 |
| <i>NGC50:50</i> | 0/3 | 0 | 0/6 | 0 |
| <i>NGC25:75</i> | 0/4 | 0 | 0/5 | 0 |

VII-4.3.1. Evaluation of functional motor recovery

Functional nerve regeneration was only examined during the LT experiment (at 4, 8 and 12 weeks). Here, recovery after implantation of NGCs filled with different freeze-dried GG formulations (n=7 NGC60:40, n=7 NGC50:50, n=5 NGC25:75) was compared to that observed after implantation of AUTOGs (n=7). In the following weeks, however, the number of animals in the NGC25:75 group was reduced by two in comparison to the other groups, because the animals had to be removed from the study after showing massive autotomy behavior. The results of electrodiagnostical measurements are presented in **Table VII-2**. After 4 weeks of implantation there was no functional recovery. Consequently, the presented results correspond to 8- and 12-weeks post-implantation. After 8 weeks, only animals from the AUTOG group showed nerve recovery, represented by CMAPs recorded from the tibialis anterior (86 %) or plantar muscles (43 %) upon stimulation of the reconstructed sciatic nerve. At 12 weeks post-surgery, the control group (AUTOG) demonstrated an increased degree of recovery with 100 % and 71 % evocable CMAPs recorded from the tibialis anterior and plantar muscles, respectively. Recovery in animals transplanted with GG filled NGCs was less frequent. At that time point, nerve reconstruction with NGC60:40 did not result in any detectable muscle reinnervation. Only two animals

from the NGC50:50 (29 %) group and three animals from the NGC25:75 group (60 %) displayed evocable CMAPs, which were also only recordable from the more proximal tibialis anterior muscle. The small number of animals displaying motor recovery detectable by electrodiagnostic procedures did not justify any statistical analysis. However, as depicted in **Supplementary Figure VII-1**, a closer look into the CMAP amplitude ratios ($mV_{\text{ipsilateral}}/mV_{\text{contralateral}}$) revealed that the quality of regeneration in one animal of the NGC25:75 group ranged among the values also detected in AUTOG group animals. **Supplementary Table VII-5** indicates for all animals of the NGC transplanted groups, if a positive or negative evaluation was performed regarding the presence of evocable CMAPs.

VII-4.3.2. Macroscopic inspection of nerve implants

Since the chitosan NGC is transparent, macroscopic inspection of its content can be performed with the help of a microsurgery microscope. At 3 weeks post-surgery a tissue bridge connecting the nerve ends through the hollow NGCs of the control group were detectable in 4/4 cases, as expected from the positive control. At the same time, NGCs from the NGC60:40 group did not contain any visible tissue (0/4), while 1/4 NGC50:50 samples and 2/4 NGC25:75 samples displayed some (nerve) tissue infiltration of the GG scaffolds. **Supplementary Figure VII-2** shows photographs of representative samples harvested at 3 weeks post-surgery and **Supplementary Table VII-4** summarizes the results of the macroscopic inspection of all samples.

At 6 weeks after surgery 3/4 NGCs from the control group (hollow chitosan NGCs) contained a visible tissue bridge connecting the nerve ends, while the last specimen from this group only contained a hairy connection, as it was not much thicker than a hair when inspected by naked eye. Again, NGCs from the NGC60:40 group did not display visible nerve tissue ingrowth into the GG scaffolds. However, the scaffolds appeared infiltrated by cells. At the same time 1/4 NGC50:50 sample and 3/4 NGC25:75 samples appeared to contain more organized (nerve) tissue. Residues of GG s could be clearly identified in the latter two groups as well. Noteworthy, some of the samples demonstrated a clear vascularization of the NGC contents. **Supplementary Figure VII-3** shows photographs of representative samples harvested at 6 weeks post-surgery and **Supplementary Table VII-5** summarizes the results of the macroscopic inspection of all samples.

At 12 weeks after surgery, all NGCs contained either residues of the freeze-dried GG hydrogel material or the same together with tissue infiltration. NGC contents frequently displayed a

vascularization by small vessels grown longitudinally through the NGC. Compact nerve tissue, however, could not be clearly identified macroscopically. Implants were more closely inspected for which a content of regenerated nerve tissue could be expected after positive evaluation with electrodiagnostic procedures. This was the case for two samples from the NGC50:50 group and three samples from the NGC25:75. The NGC50:50 samples indicated from macroscopic inspection that the regrown tissue had used the GG scaffolds as guidance structures. From macroscopic inspection of the NGC25:75 samples it appeared that regenerated tissue was more grown around or along the central GG scaffold instead of having the axons using the longitudinal channels within them as guidance structure. However, these impressions were put into another perspective after histological evaluation of the samples as described below. **Supplementary Figure VII-4** shows photographs of representative samples harvested at 12 weeks post-surgery and **Supplementary Table VII-6** summarizes the results of the macroscopic inspection of all samples.

VII-4.3.3. Micro-computed tomography (micro-CT) evaluation of the explants

The samples harvested at the end of the LT study (12 weeks after implantation) were subjected to micro-CT evaluation in order to analyse the 3D and 2D dimensions of the residual GG hydrogel matrices and eventually ingrown nerve tissue. **Figure VII-4** illustrates representative findings from the micro-CT evaluation of the explants, namely the explants' 3D and 2D images and the histograms that complement the histological images, plus a correlating histological section after H&E staining. In the AUTOG sample (positive control), the nerve tissue was clearly visible in the 3D image (enclosed in parafilm so the samples would not dry) and corroborated by the histogram (**Figure VII-6A**). No signs of new tissue formation were found in the NGC60:40 (**Figure VII-6B**). NGC50:50 sample's micro-CT images apparently showed some new tissue formation pointed by the black arrow (**Figure VII-6C**). In the NC25:75 sample, the brighter spots (white arrows) correspond to newly formed tissue, also making the histogram more similar to the autologous graft (**Figure VII 6D**). Despite the fact that NGC50:50 samples revealed the presence of some tissue; it did not appear as mature as compared with the tissue detected in AUTOG and the NC25:75 samples.

VII-4.3.4. Nerve histology for the detection of axonal regeneration and immunological reaction

The samples harvested 3 weeks after reconstruction were cut in cross-sections, at certain distances from the proximal nerve end as exemplified in **Figure VII-5** (top row). H&E and NF200 (data not shown) staining attested the findings from macroscopic evaluation: only 1 of the 4 NGC60:40 samples and 2 of the 4 NGC50:50 samples presented a certain degree of regrown tissue all along the conduit. The same was verified for 3 of the 4 NGC25:75 samples. HE representative microscopic pictures can be seen in **Figure VII-5**, where black arrows point to regenerated tissue in every cross-section analyzed (A, B, C and D). Histological images show that, regardless of the formulation, GG was still present inside the conduits (marked by asterisks and stained in soft pink). Most of residual GG material was detected in the NGC60:40 group samples. In general, re-growing tissue followed the longitudinal channels as guidance structures in NGC25:75 samples, where tissue regeneration was observed across the whole conduit.

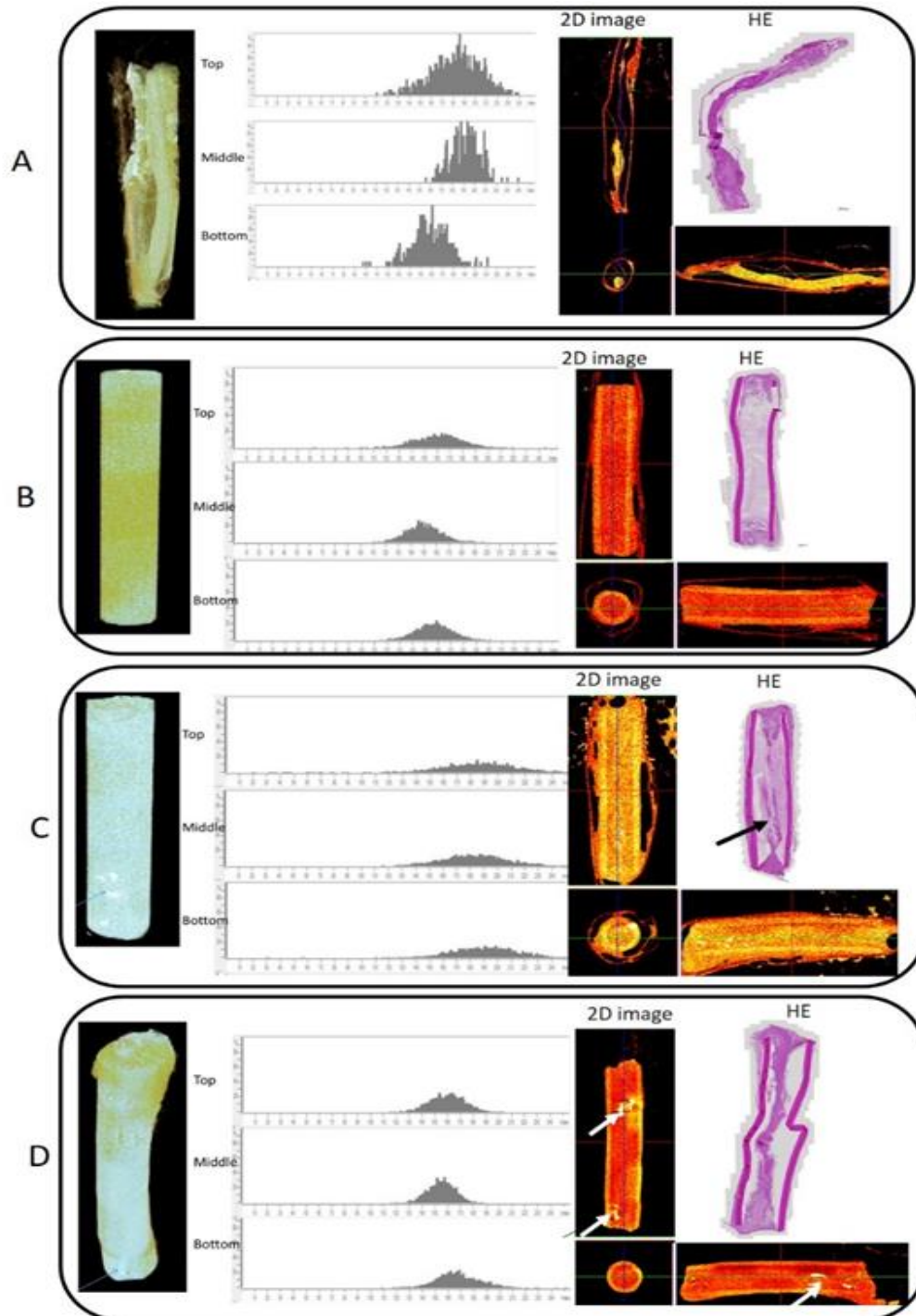


Figure VII-4 - Micro-computed tomography (micro-CT) evaluation of the explants 12 weeks after surgery and correlation to a corresponding H&E stained histological section. For each sample, different characterization images are displayed in a panel, from left to right: 3D micro-CT reconstruction image, corresponding histograms concerning three areas of the conduit (top, middle and bottom), 2D micro-CT reconstructions (longitudinal sections in vertical and horizontal images and cross section in quadratic box image) and histological sections (H&E staining) in the upper left part of each panel. Notice that in the case of the NGCs just lumen area was selected as a Region of Interest (ROI) for the 3D reconstruction, thus excluding the chitosan tubes from the analysis. All samples were covered with parafilm to avoid water evaporation. A) Positive control where the autologous nerve graft is visible involved by parafilm. B) The representative NGC60:40 sample shows no

signs of cellular or tissue ingrowth the NGC or the central GG matrix; C) The representative NGC50:50 sample shows some tissue inside the NGC/ the GG matrix (indicated by the black arrows); D) The representative NGC25:75 shows some tissue ingrowth (indicated by the white arrows). Scale bar: 500 μ m.

Supplementary Table VII-3 summarizes the results of the histological evaluation of tissue regrowth and axonal regeneration of all NGC samples harvested 3 weeks after reconstruction.

The samples explanted 6 and 12 weeks after the reconstruction were cut longitudinally, in order to display entire regeneration distance and tissue extension along the conduit. Representative pictures of such slides can be seen in **Figure VII-6**. In all samples varying amounts of GG were still visible inside the NGC (marked by asterisks and stained in light pink). During analysis of both H&E and anti-NF200 staining of sections corresponding to the 6 weeks' time point (upper row of **Figure VII-6**), the impressions from the macroscopic evaluation were confirmed. **Figure VII-6A**, corresponding to the positive control (hollow NGC), indicates the formation of a complete nerve bridge linking the two extremes of the lesion. In samples belonging to NGC60:40 group, almost no cellular tissue nor axons were detectable in the inner part of the conduit. Instead, NF-200 immuno-positive axons were located along the tube wall, avoiding the GG as growth substrate (see an example in **Figure VII-6B**). The appearance of samples belonging to the NGC50:50 group was inconsistent. In general, less residual GG was present than in NGC60:40 samples, (see an example in **Figure VII-6C**) as 3/4 of the NGC25:75 presented an organized and almost intact tissue cable that almost extends to the distal nerve end. In these 3 encouraging samples, anti-NF200 stained regenerating axons (green fluorescence) were elongating from proximal to distal through the NGCs. An example of a NGC25:75 sample is shown in **Figure VII-6D**. **Supplementary Table VII-4** summarizes the results of the histological evaluation of tissue regrowth and axonal regeneration of all NGC samples harvested 6 weeks after reconstruction.

Histological findings corresponding to 12 weeks after nerve reconstruction (lower row of **Figure VII-6**) match the ones from previous time points. The positive control in this case, an auto-transplant, displayed a thick and complete nerve bridge between the original nerve ends that is mainly composed of NF200 immunopositive axons (**Figure VII-6A**). In the NGC60:40 group the formation of new nerve tissue was scarce, and it showed pronounced fragmentation, indicating a complete absence of linearity (**Figure VII-6B**). Samples from NGC50:50 displayed nerve trunk fragments irregularly found all along the nerve gap. This indicates the absence of a continuous nerve bridge with a consistent linear trajectory.

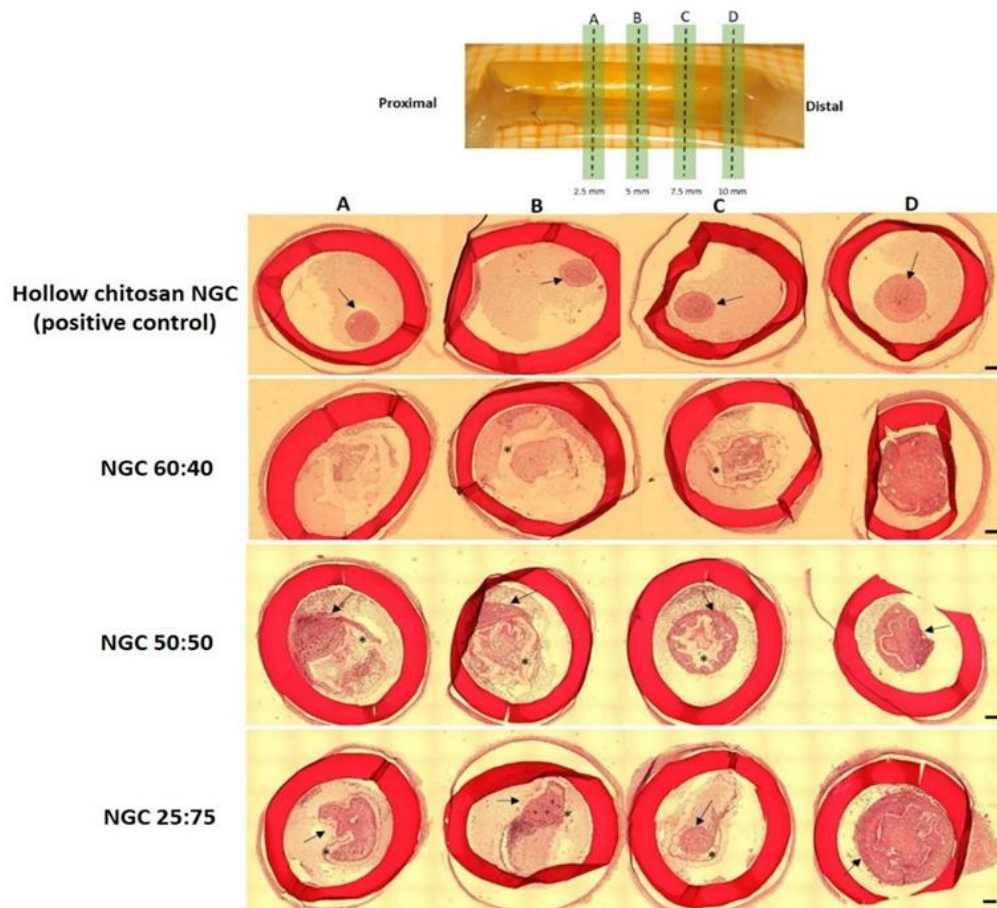


Figure VII-5 - Representative photomicrographs of the studied formulations after hematoxylin-eosin (H&E) staining. Schematic representation of the cross-sections positioning (top row, example NGC is placed on scale paper with 1mm intersections). Row 2-4: H&E stained cross-sections corresponding to chitosan hollow NGCs (positive control for the ST study) and NGCs filled with different GG freeze-dried formulations (NGC60:40, NGC50:50, NGC25:75) explanted 3 weeks after reconstruction. Black arrows point to regenerated tissue in the respective cross-sections. Asterisks are placed where residual GG is visible inside the NGCs. Scale bars: 200 μ m.

Even in the samples that presented positive results in the electrodiagnostic recordings, the regenerated axons were not found to be aligned along the longitudinal histological sections analyzed (Figure VII-6C). Almost all samples belonging to NGC25:75, namely the ones that presented positive results in the electrodiagnostic evaluation, display a thin but continuous nerve cable nearly connecting the two nerve ends along the histological sections analyzed. Immunohistochemistry of these samples shows oriented axons along the conduit, invading the GG, which serves as a guiding cue. Thus, differing with the previous case. **Supplementary Table VII 5** summarizes the results of the histological evaluation of tissue regrowth and axonal regeneration of all NGC samples harvested 12 weeks after reconstruction

VII-4.3.5. Nerve histology for the detection of neovascularization

Neo-vascularization was qualitatively evaluated by positive expression of two endothelial markers: CD31 (expressed on platelet and endothelial cell adhesion molecules, detected by green fluorescence) and CD34 (expressed on hematopoietic progenitor cells and the small vessels endothelium, detected in red fluorescence). Samples were collected from both, the ST and the LT, studies. The results of the immunohistochemical analysis show both, blood vessel growth and blood cells proliferation. The presence of these vascular components is incremented as the amount of MA-GG in the formulations increases. Accordingly, NGC50:50 and NGC25:75 samples present an increasing neovascularization and it was perceptible that newly formed blood vessels accompany the newly formed tissue throughout the conduit. This tendency was verified at all the studied time points (see **Figure VII-7** and **Supplementary Tables VII-3, VII-4, and VII-5**).

VII-4.3.6. Nerve morphometry of distal nerve segments

Nerve morphometry was performed on samples harvested in the LT study. For these analyses, only distal nerve segments originating from reconstructed nerves that have demonstrated muscle re-innervation during the final electrodiagnostic measurements were considered. More specifically, samples from the NGC50:50 and NGC25:75 groups were assessed, besides samples from the AUTOG positive control group. Further control values were obtained from uninjured contralateral nerve segments. Although not significantly, it is obvious from **Figure VII-8** that the total number and density of NGC50:50 and NGC25:75 axons were decreased with respect to the values obtained from AUTOGs and increased with respect to healthy nerve values. However, AUTOGs, NGC50:50s, and NGC25:75 axon and fiber diameters, as well as myelin thickness, were reduced in distal segments from reconstructed nerves when compared to healthy nerves. Significantly reduced values were detected for axon diameter, fiber diameter and myelin thickness between healthy and NGC25:75 distal nerve segments. **Figure VII-8** illustrates the previous quantitative results. It shows high resolution images of representative nerve semithin sections, stained with Toluidine blue, from a healthy sciatic nerve (A), an AUTOG (B), a NGC50:50 conduit (C+D) and NGC25:75 conduit (E+F).

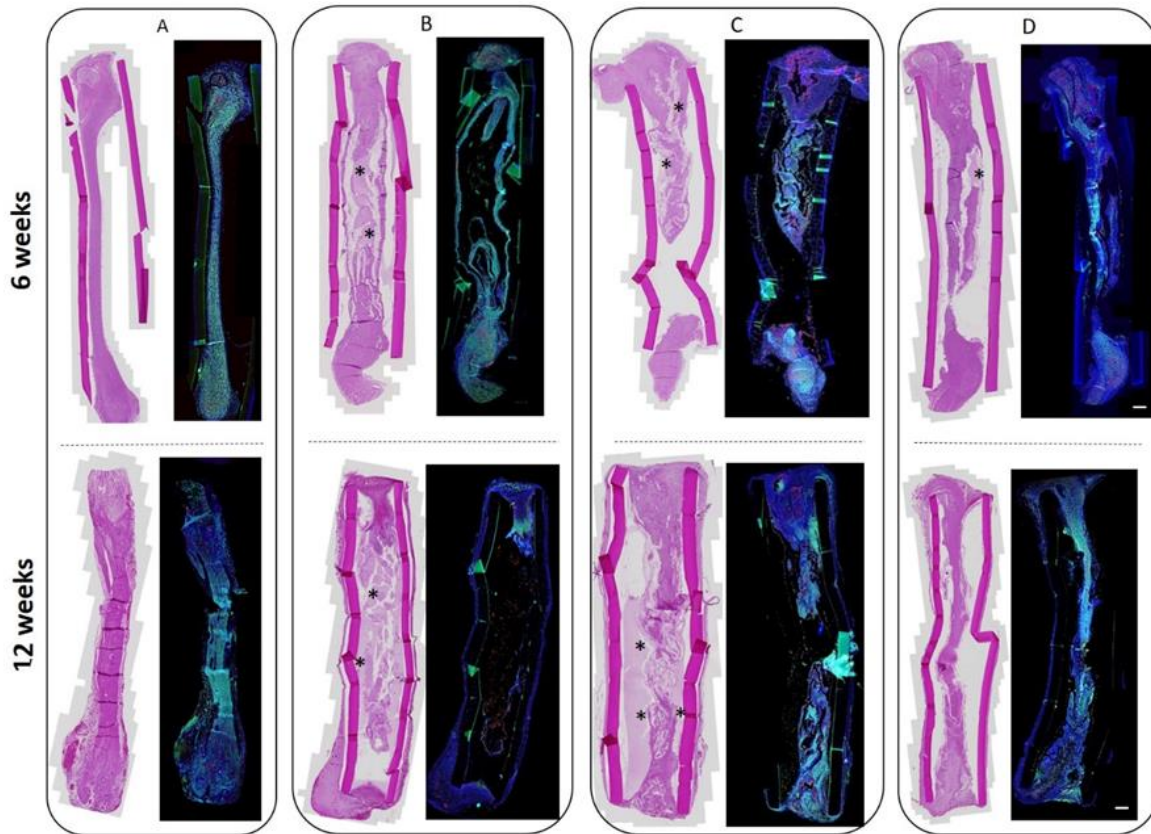


Figure VII-6 - Representative photomicrographs of histologically stained NGCs with GG fillings 6 and 12 weeks after reconstruction. Longitudinal sections for each sample after H&E staining can be seen at left and respective immunohistochemistry staining's for NF200, ED1 and DAPI at right. A) Positive control (Hollow conduit at 6 weeks (ST study) and autologous nerve graft (LT study) at 12 weeks. B) NGC60:40 sample; C) NGC50:50; D) NGC25:75. Proximal nerve end is on the top and distal nerve end is on the bottom. Asterisks mark the visible GG in light pink. Scale bars: 500 μ m.

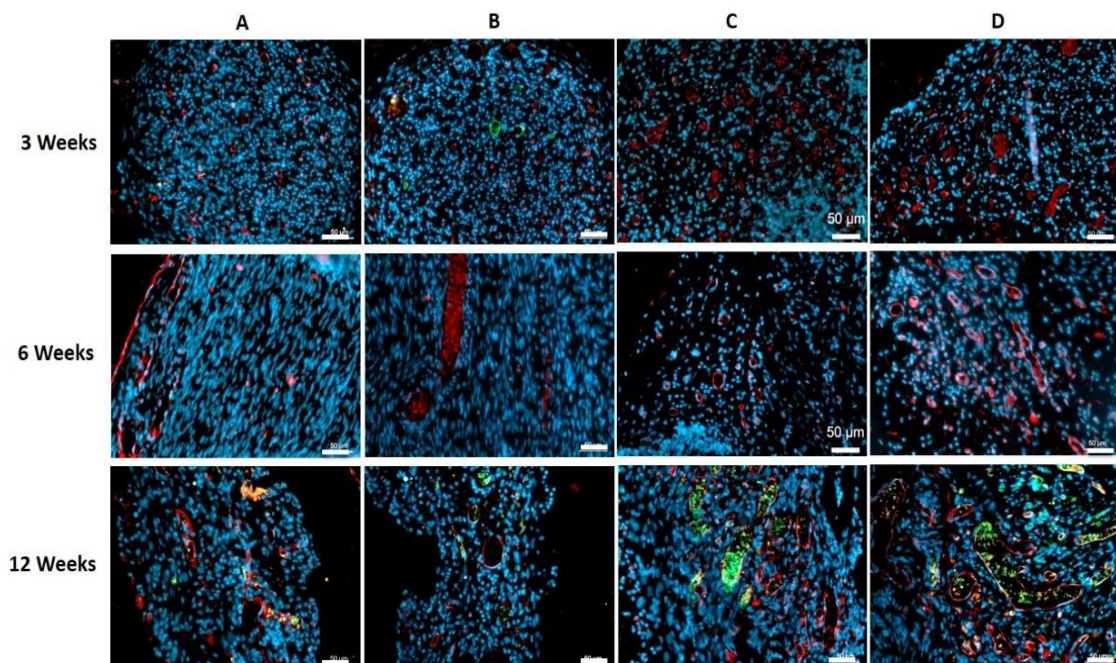


Figure VII-7 - Detection of neovascularization in the implanted formulations. Representative photomicrographs of immunohistologically stained sections correspondent to the studied formulations. Stains were performed for the detection of CD31 (green) and CD34 (red) after 3, 6- and 12-weeks post-reconstruction. Photomicrographs correspond to the central zone of the conduits. A) Positive control (at 3 and 6 weeks is a hollow NGC and at 12 weeks is an ANG; B) NGC60:40; C) NGC50:50; D) NGC25:75; Scale bars: 50 μ m.

VII-5. DISCUSSION

Experimental approaches developing novel nerve guidance conduits (NGCs) lay an emerging focus on creation of a three-dimensional endoneurial structure (resembling the Bands of Büngner) (34). The internal structures of luminal fillers of otherwise hollow NGCs should contribute to the regeneration process in different manners: i) increase the intraluminal surface area, ii) serve as supportive platforms to facilitate the extension of the regenerating axons, iii) promote endogenous Schwann cell function, and iv) eventually act as drug delivery vehicle of pro-regenerative substances (34, 35). However, it should be kept in mind that the intraluminal structures may also negatively influence the regeneration process, for instance, by compromising the luminal permeability and penetrability or by affecting the NGC flexibility (36). Gellan Gum was the material chosen as luminal filler in this peripheral nerve repair (PNR) oriented study, because of its biocompatibility, adequate physical properties, simply tunable features (37) and the fact that it has been largely explored within our group, in the context of other regenerative areas, with encouraging results (38, 39). The NGC shielding tube is made of chitosan with approximately 5 % degree of acetylation, which has already proven its PNR supporting properties (9, 20, 40).

The rationale behind this experimental work is based on the fact that the hollow chitosan nerve guides approved as Reaxon® Nerve Guides fail to reconstruct peripheral nerve defects larger than 2.6 cm. Indeed, it is very difficult to bridge larger defects with bioartificial nerve grafts without the help of any type of cues, either physical or chemical, like the use of luminal fillers or growth factors, respectively.(41) In fact, allografts are the best option for longer gaps since they naturally provide the needed cues, like the native extracellular matrix present in the grafts but access to it is extremely difficult.(42) A luminal filler providing a valuable milieu for invading Schwann cells, good axonal guidance and induction of vascularization is suggested to lead to the development of such an implant. GG freeze-dried hydrogel was chosen as luminal filler in this study because of the ability to easily tune GG formulations and thereby to influence its polymeric behavior. Accordingly, different HA-GG:MA-GG blends gave rise to the diverse luminal fillers studied.(43) The evaluation of their characteristics was

performed in a 10 mm sciatic nerve defect in order to select the most promising as luminal filler for NGCs, for future studies in longer gaps.

The first part of the study was dedicated to the production, physicochemical and *in vitro* testing of HA-GG:MA-GG freeze-dried hydrogels. The second part focused on the *in vivo* evaluation of diverse regeneration-associated parameters after the implantation of the developed NGCs.

A major restraint of traditional hydrogels as cell-instructive biomaterials for tissue engineering applications concerns the absence of cell adhesion motifs. For that reason, an intermediate step of freeze-drying was included in the process to obtain the final materials. This process transforms the specific spatial disposition of the hydrogel network. When the dry matrices are rehydrated with a cell suspension, cells become entrapped and are able to adhere and proliferate. This methodology offers the possibility of producing cell supporting matrices off-the-shelf that can be stored and quickly used.

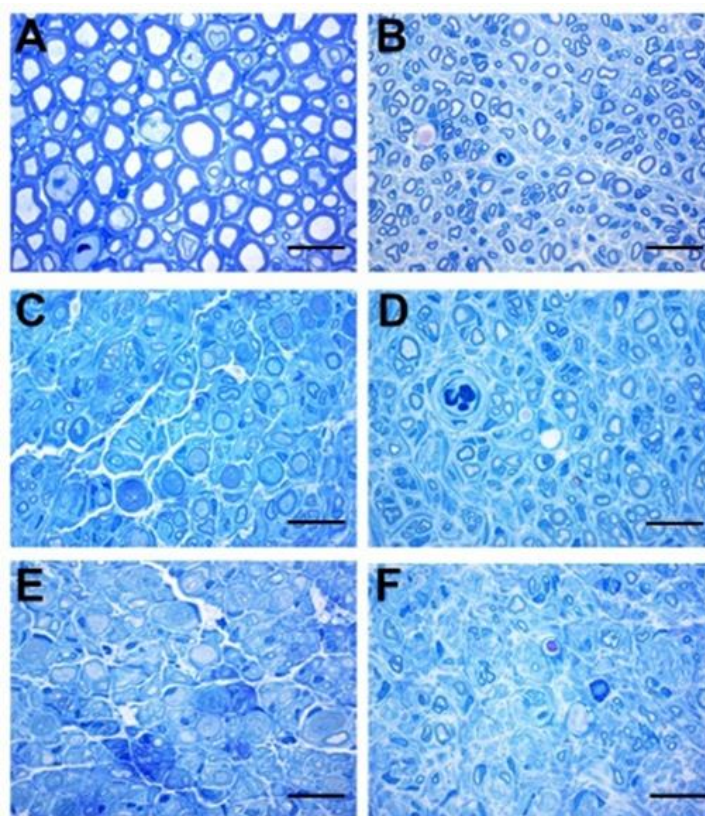


Figure VII-8 - Representative photomicrographs of myelinated axons visualized in distal peripheral nerve segments 12 weeks after reconstruction. High resolution images of representative semithin sections, stained with Toluidine blue, of nerve samples from a (A) healthy sciatic nerve and (B) regenerated through an ANG; (C+D) NGC50:50 conduit, and (E+F) NGC25:75 conduit. Scale bars: 20 μ m.

Increasing attention is also being paid to the micro- and nanostructure of tissue engineering scaffolds for PNR (35). Indeed, different strategies have been explored in this respect, *i.e.* the use of

aligned fibers (44), channels (45), patterned surfaces (46) or electrical and magnetic fields (47). In this respect, longitudinal channels were physically induced within our hydrogels by punching with a stainless-steel device. SEM analysis demonstrated the micro-structure obtained in the final networks, where the freeze-drying induced porosity contrasts with the punched aligned porosity.

X-ray micro-computed tomography provided insight into how the GG scaffolds are oriented within the NGC. This technique captures images with spatial resolution in the micron domain, using X-ray beams to probe interiors of opaque solid objects. Large pores and high % of porosity lead to minor trabecular thickness, which translated into fragile and brittle systems in the dry state. Comparing the results, there seems to be no relation between the mean pore size or the % of porosity and the amount of HA-GG or MA-GG in the formulations. These results were within the expected range, as we envisioned a highly porous and interconnected matrix inside the chitosan conduit, which would allow the growth of regenerating fibers, as well as guide them. Indeed, the method of production, freezing at -80 °C and subsequent freeze-drying, was selected because it allows great pores to be formed (21). However, despite the identically rigorous processing of freeze-dried hydrogels and NGCs, higher mean pore sizes and trabecular thickness were obtained in the second case. This indicates that the protector layer of the chitosan tube influences the formation of water crystals, probably by lowering the speed of freezing, ultimately altering the microstructure of the GG network inside the conduit. As a result, fewer pores are created, with reduced % of porosity and increased trabecular thickness. This effect can be also appreciated in the SEM images.

Concerning water uptake (WU), this parameter is related to the exchange of metabolic products and nutrients. Meanwhile, the weight loss (WL) is a parameter related to the biodegradation of the biomaterial. An optimized device for peripheral nerve reconstruction should remain intact until a proper invasion of repair Schwann cells occur, as these cells, together with invading perineurial cells, build the forefront of a regenerating nerve (48), and then progressively degrade as the re-growing axons occupy new space (49). Our *in vitro* results confirm that the formulations containing more MA-GG suffer from less swelling and degradation over time, as higher WU and WL were verified in H60:40, while the lowest values occurred for H0:100. On the one hand, this is probably because of the tighter matrix granted by the MA-GG, when compared to native GG. In addition, methacrylate groups are hydrophobic in nature, thus impairing the interaction with water molecules (50). On the other hand, higher percentages of HA-GG have been linked to faster degradation, due to the acyl group in its structure, which interferes with the gelling process. The resultant gels are weaker. Our results indicate that a relation exists between the

swelling ability and the degradation of the freeze-dried hydrogel materials. The formulations that uptake more water, are the ones that suffer more hydrolysis. This leads to the hypothesis that as water is taken up, it starts to break the trabeculae in the formulation's microstructure.

Since to our knowledge GG systems have not been previously explored for PNR purposes, an immortalized Schwann cell line was used to evaluate the effect of the studied formulations on the performance of peripheral glial cells. The results indicate that a higher portion of MA-GG in the formulations is related to higher cell metabolic activity. This tendency has been previously observed for diverse cell types (38, 51), and is probably related to the stability and micro-structure of the matrices that MA-GG forms. An increased metabolic activity of invading Schwann cells is expected to be beneficial for the peripheral nerve regeneration process *in vivo*. In fact, nerve reconstruction with formulations containing higher amounts of MA-GG, such as NGC25:75 resulted in better functional recovery than reconstruction with the other GG containing NGCs.

Summarizing the characterization results up to this point, the formulations containing higher amounts of HA-GG are likely to have a higher swelling rate, which is also likely to be accompanied by a faster degradation. Meanwhile, formulations with higher amounts of MA-GG offer the advantage of having a more positive influence over the cells in contact with them. *In vivo* experiments were designed in order to investigate how these characteristics balance each other once the formulations have been implanted into a peripheral nerve defect. Although the H0:100 formulation induced the highest cell metabolic activity, its low degradation rate seems inappropriate for PNR purposes. Accordingly, it was excluded from the *in vivo* tests in order to avoid unnecessary animal sacrifices.

In vivo results did not match the degradation rates of the isolated GG formulations *in vitro*. The *in vivo* tests showed that only small amounts of GG hydrogel residues were present in NGC25:75 (higher amounts of MA-GG) samples 6 and 12 weeks after nerve reconstruction. Vice versa, formulations containing higher amounts of HA-GG (NGC60:40) displayed higher residual amounts of non-degraded GG, which seemingly impaired regenerative tissue growth. Although isolated HA-GG formulations have higher degradation rate *in vitro*, certainly by hydrolysis mechanisms, it seems that other biological parameters influence the *in vivo* biodegradation of the studied formulations (*i.e.* specific enzymes such as amylase and lysozyme, cellular interaction or fluid infiltration) (50), leading to a faster clearance as the amount of MA-GG increases. The specific GG degradation mechanisms *in vivo* have not yet been identified yet (24). WU also played an important role in the *in vivo* outcomes, as an excessive WU of the formulations containing increasing quantities of HA-GG has likely led to lumen-occlusion phenomena.

The complete failure of nerve regeneration through NGC60:40 grafts could be a consequence of this phenomenon, allied to lower peripheral glial cell adhesion and axonal ingrowth. Following nerve transection, the process of regeneration is largely dependent on the activity of non-neuronal cells, such as macrophages or Schwann cells (52). In fact, macrophages that are attracted to the injury site secrete substances that increase Schwann cell migration (53). Beyond that, invading macrophages play a key role in eliminating both myelin and axonal debris, as well as in releasing a large number of axonal regeneration-related substances, including extracellular matrix (ECM) proteins, growth factors, cytokines and chemokines (53). Consequently, the presence of such immune cells in the distal nerve segments following injury is important for the remodeling of the nerve. Nevertheless, an excessive and persistent amount of activated macrophages induced by the transplanted nerve guide material may lead to a progressive inflammatory response, which will have a detrimental effect on regeneration (53). Both after 3, 6 and 12 weeks, NGC25:75 demonstrated a presence of activated ED1-immunopositive macrophages qualitatively comparable to that in the positive control. These macrophages probably contributed to myelin and axonal clearance, a process that may be prolonged during weeks. In addition, macrophages were detected all along the lumen of NGC60:40 and NGC50:50 after 6 and 12 weeks of implantation. The fact that the formulations with higher HA-GG amount present more macrophages might suggest that this polymer is recognized as a foreign body by the host organism. Despite the good biocompatibility results shown by GG in other regenerative applications (54), a foreign body reaction might originate due to the fact that these formulations were not degrading during the observation time. This finding points to the need of a faster degrading luminal filler material. Also, the authors hypothesize that the same formulations with higher HA-GG amount present great values of WU that impaired regeneration and that may also arouse some type of vigilante response by the host organism (55).

The vascular net supplying peripheral nerves is very complex (56). Furthermore, it is long known that angiogenesis is a crucial factor for a successful peripheral nerve regeneration across a critical length nerve gap and required for cell survival (57). CD31 (PECAM-1; platelet/endothelial cell adhesion molecule-1) is a single chain type-1 transmembrane protein present in endothelial cells, which plays a key role in the interaction with adjacent CD34 (a single-chain transmembrane glycoprotein) expressing hematopoietic precursor cells or capillary endothelial cells. Both proteins are related to microvasculature formation (58). After qualitative analysis, it seems that regardless of the GG formulation implanted within the NGCs, there was angiogenesis taking place. However, the presence of blood vessels (as well as the presence of erythrocytes within capillaries) seems to increase as the

amount of MA-GG also increases within the formulations. This improved neo-angiogenesis verified in NGC50:50 and NGC27:75 at all timepoints studied could have positively influenced the extent of functional recovery.

Interestingly, after 3 and 6 weeks, CD31 positive endothelial cells were not detected in any of the analyzed sections, in contrast to CD34 that marked both blood vessels and red blood cells. However, by 12 weeks, both markers have been perceived, with CD34 marking mainly the endothelial cells in the walls of the newly generated blood vessels and CD31 identifying red blood cells. One possible explanation for this is that CD31 only identifies differentiated and mature cells, while CD34 already detects precursors of endothelial cells or not completely differentiated cells (59).

The previously described micro-CT methodology is also a popular method to evaluate tissue engineering constructs (60), human tissues (61) and animal tissues (62), In a typical micro-CT image, relatively higher density structures appear brighter than structures with lower density. Soft tissues usually have a uniform density, and their internal structure cannot be discriminated with a conventional micro-CT method (63), During the analysis of the explanted formulations, water, GG, and regenerated nerve tissue could not be discriminated properly in the wet explants since the densities of the soaked polymer and soft-tissue like nervous tissue are identical. The results of the current study indicate that NGC25:75 has better biological performance than others, however, still not as good as the autologous graft. This information could not be retrieved from the 3D images reconstructions, but from the 2D cross and longitudinal sections and the histograms related to these images, in which density differences were detected pointing to the previous affirmation.

The initial macroscopic inspection of the explants after the in vivo observation time, matched the histological findings, such as the lumen-blocking properties of NGC60:40 and the pronounced induction of vascularization by NGC25:75. This, in turn, finds functional correlation with the results obtained from electrophysiological measurements, micro-CT analysis and nerve morphometry assessments in the distal nerve segments after 12 weeks post-surgery. Overall, the regeneration promoting properties of chitosan NGCs filled with the freeze-dried hydrogel GG scaffolds is significantly reduced in comparison to hollow chitosan NGCs for which in the same model in 69 % of animals evocable CMAP signals were recorded from the tibialis anterior muscle 12 weeks after nerve reconstruction (20). Muscle reinnervation detectable by electrodiagnostic procedures was, however, still found in some animals investigated throughout the current study. Nerve reconstruction with NGC60:40 completely prevented proper muscle reinnervation, while occurred to an increasing percentage in the NGC50:50 group and in

the NGC25:75 group. Reinnervation of distal plantar interosseous muscles did, in the current study, only occur in the AUTOG group and was demonstrated, although to a lesser extent, also after implantation of hollow chitosan NGCs (20). Morphometric analysis performed on nerve cross sections obtained distal to the grafts that resulted in functional recovery, confirmed the presence of regenerated myelinated axons. The fact that the overall results of the nerve morphometry indicate NGC50:50 as the eventually most promising formulation might be misleading, since despite two animals out of seven showed outstanding functional recovery, the remaining five showed no functional recovery at all. Consequently, it is probable that these outstanding results were due to any inter-individual variability between the groups of rats.

All together, these findings indicate that filling the lumen of chitosan NGCs with freeze-dried hydrogel GG scaffolds could not increase their peripheral nerve regeneration promoting properties, with results that do not outperform the positive controls used in both ST and LT studies (hollow chitosan tube and AUTOG, respectively). The concept of providing additional guidance structures inside the lumen of the NGCs is however still promising (9). Indeed, the NGC25:75 implants showed a better performance than 5 % degree of acetylation chitosan conduits containing NVR-Gel (composed of high molecular weight hyaluronic acid and laminin) as luminal filler. This study was performed by some of the authors of the present work, and proved that the previously indicated non-freeze dried hydrogels dramatically impaired nerve regeneration (21). However, both of these studies demonstrate that a luminal filler such as an hydrogel or hydrogel-like structure present in the lumen might have detrimental effects in terms of nerve regeneration, since some obstruction is observed.

However, these results concerning the NGC25:75 highlight the potential of the GG presented during this experimental work, indicating the interest in continuing our research in this direction, further improving our NGC systems with methacrylated biomaterial.

VII-6. CONCLUSIONS

This work demonstrates for the first time the innovative use of gellan gum freeze-dried hydrogels as luminal fillers for nerve guidance conduits intended for peripheral nerve reconstruction. The biomaterials have been evaluated *in vitro* before *in vivo* trials were initiated to define their short- and long-term potential to support peripheral nerve regeneration through chitosan nerve guides. The outcome of our studies demonstrates that the use of GG fillers did not result in improved nerve

regeneration and that our system still has to be optimized. So far, the presence of such biomaterial in the lumen of the chitosan tubes might have negative effects in terms of nerve regeneration. The best results, however, have been achieved in the presence of higher amounts of MA-GG in the blending systems. The methacrylated material better supported axonal regeneration and increased vascularization, ultimately resulting in a certain degree of muscle re-innervation. Future attempts need to be focused on MA-GG formulations or peptide-modified GG for luminal fillers that are presented with lower concentrations of polymer or supplemented with supporting cells and/or regeneration promoting cues.

VII-7. ACKNOWLEDGMENTS

This study was supported by the European Community's Seventh Framework Programme (FP7-HEALTH-2011) under grant agreement n° 278612 (BIOHYBRID). Medical grade chitosan for manufacturing the chitosan films and nerve guides was supplied by Altakitin SA (Lisbon, Portugal). The chitosan materials were supplied by Medovent GmbH (Mainz, Germany). This study was also funded by European Union's FP7 Programme under grant agreement no REGPOT-CT2012-316331-POLARIS. The authors thank Silke Fischer, Natascha Heidrich, Jennifer Metzen, Maike Wesemann (all Institute of Neuroanatomy and Cell Biology, Hannover Medical School) for their excellent technical support. The authors also acknowledge the Portuguese Foundation for Science and Technology (FCT) for the financial support provided to Joana Silva-Correia (IF/00115/2015) and Joaquim M. Oliveira (IF/00423/2012 and IF/01285/2015) under the program "Investigador FCT".

NOTES

‡ During the ST study, explanted samples were immediately processed for histological evaluation. In contrast, samples obtained after the LT observation period, were sent back from the 3B's Research Group, (Guimaraes, Portugal) to MHH (Hannover, Germany) after the micro-CT scanning in order to have them processed for histology.

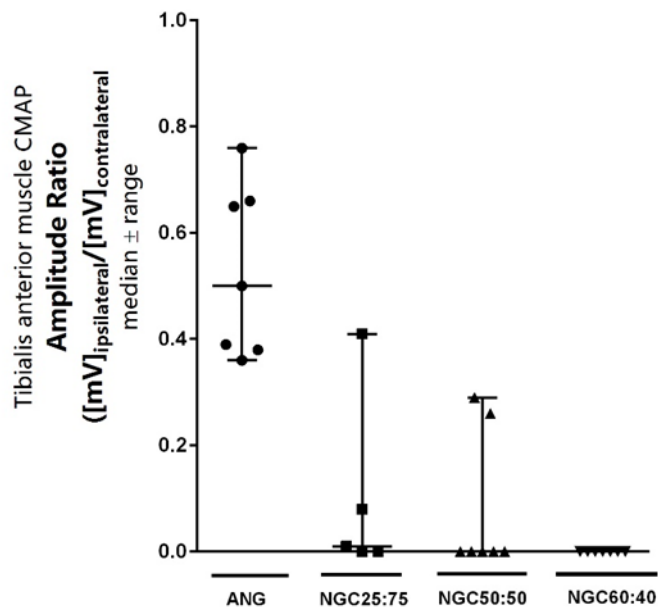
VII-8. REFERENCES

1. Daly W, Yao L, Zeugolis D, Windebank A, Pandit A. A biomaterials approach to peripheral nerve regeneration: bridging the peripheral nerve gap and enhancing functional recovery. *Journal of the Royal Society, Interface / the Royal Society*. 2012;9(67):202-21.
2. Mukhatyar V, Karumbaiah L, Yeh J, Bellamkonda R. Tissue engineering strategies designed to realize the endogenous regenerative potential of peripheral nerves. *Advanced Materials*. 2009;21(46):4670-9.
3. Siemionow M, Bozkurt M, Zor F. Regeneration and repair of peripheral nerves with different biomaterials: Review. *Microsurgery*. 2010;30(7):574-88.
4. Trumble TE, Shon FG. The physiology of nerve transplantation. *Hand Clinics*. 2000;16(1):105-22.
5. Korus L, Ross DC, Doherty CD, Miller TA. Nerve transfers and neurotization in peripheral nerve injury, from surgery to rehabilitation. *Journal of neurology, neurosurgery, and psychiatry*. 2016;87(2):188-97.
6. Grinsell D, Keating CP. Peripheral nerve reconstruction after injury: a review of clinical and experimental therapies. *BioMed Research International*. 2014;2014:698256.
7. Haastert-Talini K, Mauritz C, Chaturvedi S, Grothe C. Human and rat adult Schwann cell cultures: fast and efficient enrichment and highly effective non-viral transfection protocol. *Nature protocols*. 2007;2(1):99-104.
8. Gonzalez-Perez F, Cobianchi S, Geuna S, Barwig C, Freier T, Udina E, et al. Tubulization with chitosan guides for the repair of long gap peripheral nerve injury in the rat. *Microsurgery*. 2015;35(4):300-8.
9. Meyer C, Stenberg L, Gonzalez-Perez F, Wrobel S, Ronchi G, Udina E, et al. Chitosan-film enhanced chitosan nerve guides for long-distance regeneration of peripheral nerves. *Biomaterials*. 2016;76:33-51.
10. Dinis TM, Elia R, Vidal G, Dermigny Q, Denoed C, Kaplan DL, et al. 3D multi-channel bi-functionalized silk electrospun conduits for peripheral nerve regeneration. *Journal of the mechanical behavior of biomedical materials*. 2015;41:43-55.
11. Santos D, Giudetti G, Micera S, Navarro X, del Valle J. Focal release of neurotrophic factors by biodegradable microspheres enhance motor and sensory axonal regeneration in vitro and in vivo. *Brain research*. 2016;1636:93-106.
12. Marquardt LM, Ee X, Iyer N, Hunter D, Mackinnon SE, Wood MD, et al. Finely Tuned Temporal and Spatial Delivery of GDNF Promotes Enhanced Nerve Regeneration in a Long Nerve Defect Model. *Tissue Engineering Part A*. 2015;21(23-24):2852-64.
13. Klein SM, Vykoukal J, Li DP, Pan HL, Zeitler K, Alt E, et al. Peripheral Motor and Sensory Nerve Conduction following Transplantation of Undifferentiated Autologous Adipose Tissue-Derived Stem Cells in a Biodegradable U.S. Food and Drug Administration-Approved Nerve Conduit. *Plastic and Reconstructive Surgery*. 2016;138(1):132-9.
14. Sowa Y, Kishida T, Imura T, Numajiri T, Nishino K, Tabata Y, et al. Adipose-Derived Stem Cells Promote Peripheral Nerve Regeneration In Vivo without Differentiation into Schwann-Like Lineage. *Plast Reconstr Surg*. 2016;137(2):318e-30e.
15. Gu X, Ding F, Williams DF. Neural tissue engineering options for peripheral nerve regeneration. *Biomaterials*. 2014;35(24):6143-56.
16. Kehoe S, Zhang XF, Boyd D. FDA approved guidance conduits and wraps for peripheral nerve injury: A review of materials and efficacy. *Injury*. 2012;43(5):553-72.
17. Dinis TM, Elia R, Vidal G, Dermigny Q, Denoed C, Kaplan DL, et al. 3D multi-channel bi-functionalized silk electrospun conduits for peripheral nerve regeneration. *Journal of the mechanical behavior of biomedical materials*. 2015;41(Supplement C):43-55.
18. Ao Q, Wang A, Cao W, Zhang L, Kong L, He Q, et al. Manufacture of multimicrotubule chitosan nerve conduits with novel molds and characterization in vitro. *J Biomed Mater Res A*. 2006;77(1):11-8.
19. Gnani S, Barwig C, Freier T, Haastert-Talini K, Grothe C, Geuna S. The use of chitosan-based scaffolds to enhance regeneration in the nervous system. *International Review of Neurobiology*. 2013;109:1-62.
20. Haastert-Talini K, Geuna S, Dahlin LB, Meyer C, Stenberg L, Freier T, et al. Chitosan tubes of varying degrees of acetylation for bridging peripheral nerve defects. *Biomaterials*. 2013;34(38):9886-904.
21. Meyer C, Wrobel S, Raimondo S, Rochkind S, Heimann C, Shahar A, et al. Peripheral Nerve Regeneration Through Hydrogel-Enriched Chitosan Conduits Containing Engineered Schwann Cells for Drug Delivery. *Cell Transplantation*. 2016;25(1):159-82.
22. Silva-Correia J, Gloria A, Oliveira MB, Mano JF, Oliveira JM, Ambrosio L, et al. Rheological and mechanical properties of acellular and cell-laden methacrylated gellan gum hydrogels. *Journal of Biomedical Materials Research Part A*. 2013;101(12):3438-46.
23. Chang SJ, Huang Y-T, Yang S-C, Kuo S-M, Lee M-W. In vitro properties of gellan gum sponge as the dental filling to maintain alveolar space. *Carbohydrate Polymers*. 2012;88(2):684-9.

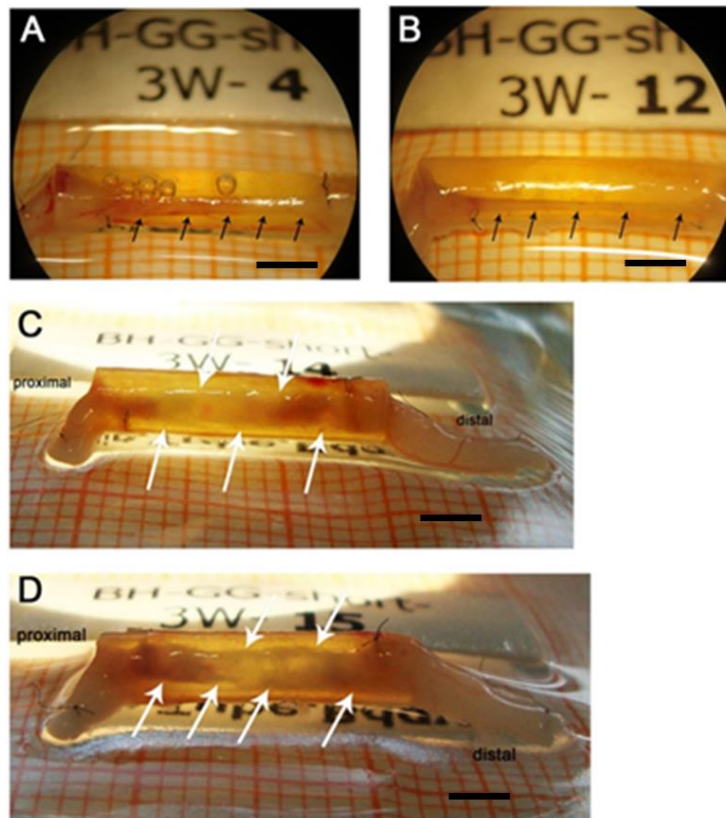
24. Lee H, Fisher S, Kallos MS, Hunter CJ. Optimizing gelling parameters of gellan gum for fibrocartilage tissue engineering. *Journal of biomedical materials research Part B, Applied biomaterials*. 2011;98(2):238-45.
25. Cerqueira MT, da Silva LP, Santos TC, Pirraco RP, Correlo VM, Marques AP, et al. Human skin cell fractions fail to self-organize within a gellan gum/hyaluronic acid matrix but positively influence early wound healing. *Tissue Eng Part A*. 2014;20(9-10):1369-78.
26. Douglas TEL, Pilarz M, Lopez-Heredia M, Brackman G, Schaubroeck D, Balcaen L, et al. Composites of gellan gum hydrogel enzymatically mineralized with calcium-zinc phosphate for bone regeneration with antibacterial activity. *Journal of Tissue Engineering and Regenerative Medicine*. 2017;11(5):1610-8.
27. Carmona-Moran CA, Zavgorodnya O, Penman AD, Kharlampieva E, Bridges SL, Jr., Hergenrother RW, et al. Development of gellan gum containing formulations for transdermal drug delivery: Component evaluation and controlled drug release using temperature responsive nanogels. *International journal of pharmaceutics*. 2016;509(1-2):465-76.
28. Boni FI, Prezotti FG, Cury BS. Gellan gum microspheres crosslinked with trivalent ion: effect of polymer and crosslinker concentrations on drug release and mucoadhesive properties. *Drug development and industrial pharmacy*. 2016;42(8):1283-90.
29. Grothe C, Meisinger C, Holzschuh J, Wewetzer K, Cattini P. Over-expression of the 18 kD and 21/23 kD fibroblast growth factor-2 isoforms in PC12 cells and Schwann cells results in altered cell morphology and growth. *Brain research Molecular brain research*. 1998;57(1):97-105.
30. Karnovsky M. A formaldehyde-glutaraldehyde fixative of high osmolality for use in electron microscopy. *Journal of Cell Biology*. 1965;27:137-8.
31. Feria-Velasco A, Karnovsky MJ. Optimal central nervous system preservation with glutaraldehyde perfusion for ultrastructural study. *Archivos de investigacion medica*. 1970;1(3):201-20.
32. Schultze O. Über die Anwendung von Aminosäure und eine neue Osmiumhämatoxylinmethode. *Z Wiss Mikrosk*. 1910;27:465–75.
33. Huelsenbeck SC, Rohrbeck A, Handreck A, Hellmich G, Kiaei E, Roettinger I, et al. C3 peptide promotes axonal regeneration and functional motor recovery after peripheral nerve injury. *Neurotherapeutics : the journal of the American Society for Experimental NeuroTherapeutics*. 2012;9(1):185-98.
34. Faroni A, Mobasseri SA, Kingham PJ, Reid AJ. Peripheral nerve regeneration: experimental strategies and future perspectives. *Advanced drug delivery reviews*. 2015;82-83:160-7.
35. Bellamkonda RV. Peripheral nerve regeneration: an opinion on channels, scaffolds and anisotropy. *Biomaterials*. 2006;27(19):3515-8.
36. Carballo-Molina OA, Velasco I. Hydrogels as scaffolds and delivery systems to enhance axonal regeneration after injuries. *Frontiers in Cellular Neuroscience*. 2015;9:13.
37. Stevens LR, Gilmore KJ, Wallace GG, in het Panhuis M. Tissue engineering with gellan gum. *Biomaterials Science*. 2016;4(9):1276-90.
38. Silva-Correia J, Oliveira JM, Caridade SG, Oliveira JT, Sousa RA, Mano JF, et al. Gellan gum-based hydrogels for intervertebral disc tissue-engineering applications. *Journal of tissue engineering and regenerative medicine*. 2011;5(6):e97-107.
39. da Silva LP, Cerqueira MT, Sousa RA, Reis RL, Correlo VM, Marques AP. Engineering cell-adhesive gellan gum spongy-like hydrogels for regenerative medicine purposes. *Acta biomaterialia*. 2014;10(11):4787-97.
40. Wrobel S, Serra SC, Ribeiro-Samy S, Sousa N, Heimann C, Barwig C, et al. In vitro evaluation of cell-seeded chitosan films for peripheral nerve tissue engineering. *Tissue engineering Part A*. 2014;20(17-18):2339-49.
41. Mobini S, Spearman BS, Lacko CS, Schmidt CE. Recent advances in strategies for peripheral nerve tissue engineering. *Current Opinion in Biomedical Engineering*. 2017;4:134-42.
42. Brooks DN, Weber RV, Chao JD, Rinker BD, Zoldos J, Robichaux MR, et al. Processed nerve allografts for peripheral nerve reconstruction: A multicenter study of utilization and outcomes in sensory, mixed, and motor nerve reconstructions. *Microsurgery*. 2012;32(1):1-14.
43. Khang G, Lee SK, Kim HN, Silva-Correia J, Gomes ME, Viegas CA, et al. Biological evaluation of intervertebral disc cells in different formulations of gellan gum-based hydrogels. *Journal of tissue engineering and regenerative medicine*. 2015;9(3):265-75.
44. Vimal SK, Ahamad N, Katti DS. A simple method for fabrication of electrospun fibers with controlled degree of alignment having potential for nerve regeneration applications. *Materials science & engineering C, Materials for biological applications*. 2016;63:616-27.
45. Sridharan R, Reilly RB, Buckley CT. Decellularized grafts with axially aligned channels for peripheral nerve regeneration. *Journal of the mechanical behavior of biomedical materials*. 2015;41:124-35.
46. Mobasseri A, Faroni A, Minogue BM, Downes S, Terenghi G, Reid AJ. Polymer scaffolds with preferential parallel grooves enhance nerve regeneration. *Tissue engineering Part A*. 2015;21(5-6):1152-62.

47. Li Y, Wang PS, Lucas G, Li R, Yao L. ARP2/3 complex is required for directional migration of neural stem cell-derived oligodendrocyte precursors in electric fields. *Stem cell research & therapy*. 2015;6:41.
48. Belkas JS, Shoichet MS, Midha R. Peripheral nerve regeneration through guidance tubes. *Neurological research*. 2004;26(2):151-60.
49. Steed MB, Mukhatyar V, Valmikinathan C, Bellamkonda RV. Advances in bioengineered conduits for peripheral nerve regeneration. *Atlas of the oral and maxillofacial surgery clinics of North America*. 2011;19(1):119-30.
50. Coutinho DF, Sant SV, Shin H, Oliveira JT, Gomes ME, Neves NM, et al. Modified Gellan Gum hydrogels with tunable physical and mechanical properties. *Biomaterials*. 2010;31(29):7494-502.
51. Nichol JW, Koshy S, Bae H, Hwang CM, Yamanlar S, Khademhosseini A. Cell-laden microengineered gelatin methacrylate hydrogels. *Biomaterials*. 2010;31(21):5536-44.
52. Chen P, Piao X, Bonaldo P. Role of macrophages in Wallerian degeneration and axonal regeneration after peripheral nerve injury. *Acta Neuropathol*. 2015;130(5):605-18.
53. Gaudet AD, Popovich PG, Ramer MS. Wallerian degeneration: gaining perspective on inflammatory events after peripheral nerve injury. *Journal of Neuroinflammation*. 2011;8:110-.
54. Silva-Correia J, Zavan B, Vindigni V, Silva TH, Oliveira JM, Abatangelo G, et al. Biocompatibility evaluation of ionic- and photo-crosslinked methacrylated gellan gum hydrogels: in vitro and in vivo study. *Advanced healthcare materials*. 2013;2(4):568-75.
55. Anderson JM, Rodriguez A, Chang DT. Foreign body reaction to biomaterials. *Seminars in immunology*. 2008;20(2):86-100.
56. Lehmann M, Konerding MA, Blank M. Vascularization of the peripheral nerve after epineural suture. In: Samii M, editor. *Peripheral Nerve Lesions*. Berlin, Heidelberg: Springer Berlin Heidelberg; 1990. p. 149-53.
57. Penkert G, Bini W, Samii M. Revascularization of nerve grafts: an experimental study. *Journal of reconstructive microsurgery*. 1988;4(4):319-25.
58. Pisacane AM, Picciotto F, Risio M. CD31 and CD34 expression as immunohistochemical markers of endothelial transdifferentiation in human cutaneous melanoma. *Cellular oncology : the official journal of the International Society for Cellular Oncology*. 2007;29(1):59-66.
59. Nagatsuka H, Hibi K, Gunduz M, Tsujigiwa H, Tamamura R, Sugahara T, et al. Various immunostaining patterns of CD31, CD34 and endoglin and their relationship with lymph node metastasis in oral squamous cell carcinomas. *Journal of Oral Pathology and Medicine*. 2005;34(2):70-6.
60. Cengiz IF, Oliveira JM, Reis RL. Micro-computed tomography characterization of tissue engineering scaffolds: effects of pixel size and rotation step. *Journal of Materials Science: Materials in Medicine*. 2017;28(8):129.
61. Pereira H, Caridade SG, Frias AM, Silva-Correia J, Pereira DR, Cengiz IF, et al. Biomechanical and cellular segmental characterization of human meniscus: building the basis for tissue engineering therapies. *Osteoarthritis and cartilage*. 2014;22(9):1271-81.
62. Cardeira J, Gavaia PJ, Fernandez I, Cengiz IF, Moreira-Silva J, Oliveira JM, et al. Quantitative assessment of the regenerative and mineralogenic performances of the zebrafish caudal fin. *Scientific reports*. 2016;6:39191.
63. Mizutani R, Suzuki Y. X-ray microtomography in biology. *Micron (Oxford, England : 1993)*. 2012;43(2-3):104-15.

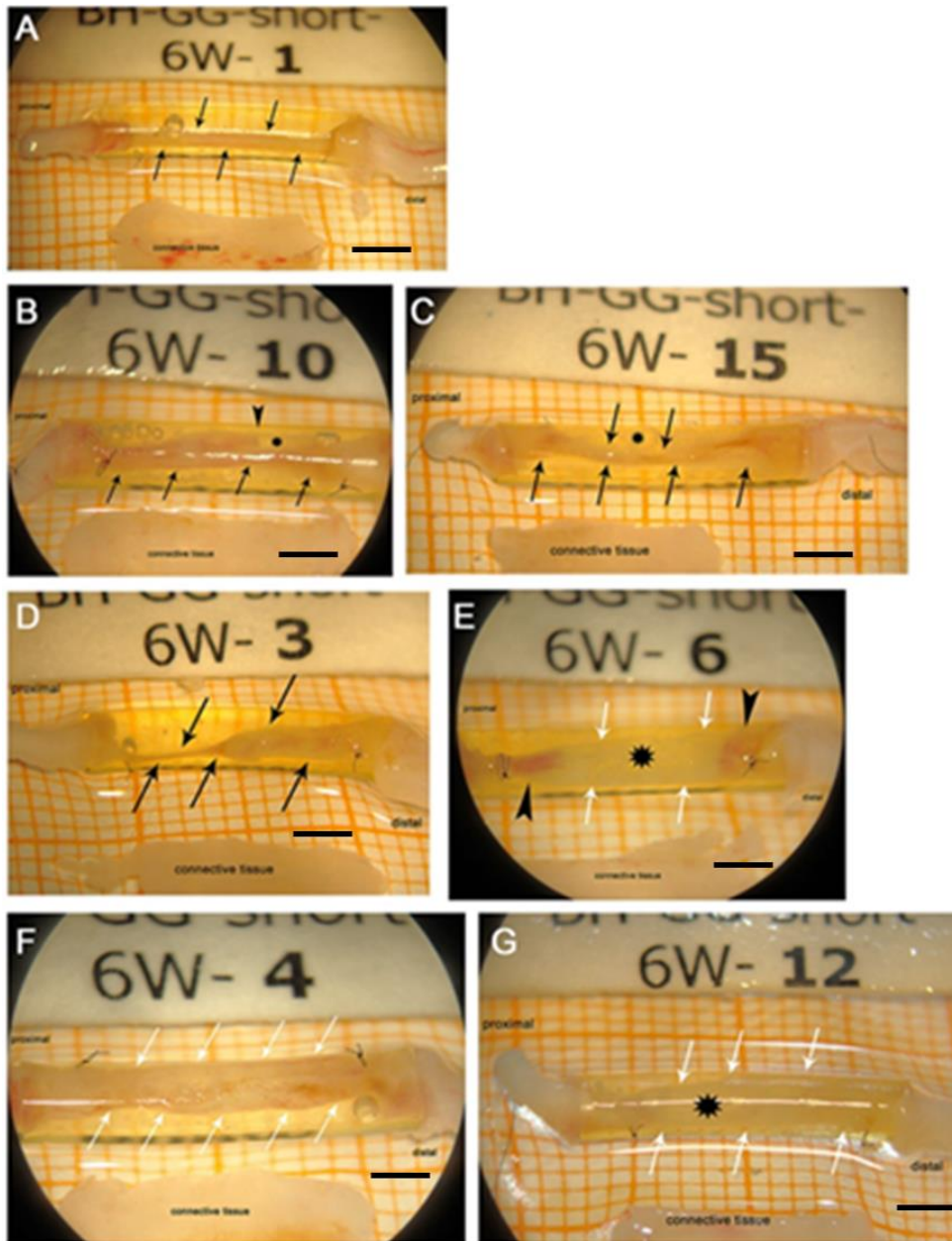
VII-9. SUPPLEMENTARY DATA



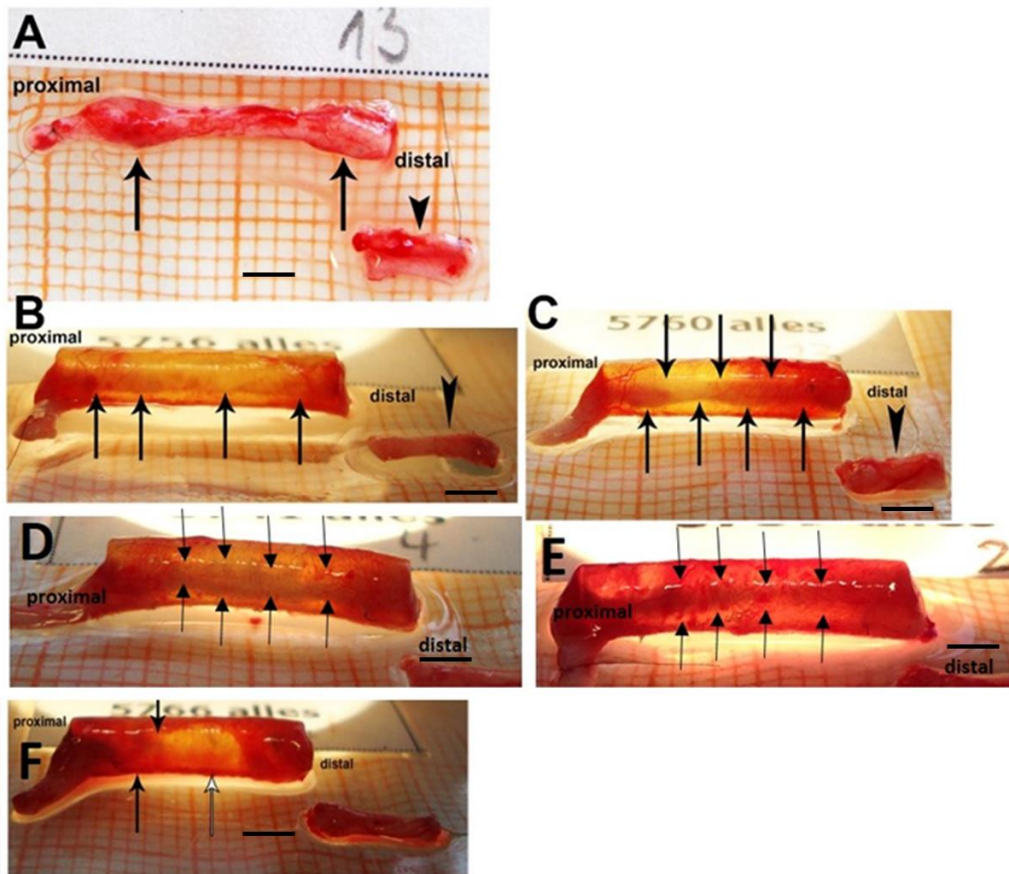
Supplementary Figure VII-1 - Scatter plot depicting the median and range of the amplitude ratios of evocable compound action potentials recorded 12 weeks after nerve reconstruction in the tibialis anterior muscle of control group (AUTOG) and experimental groups (NGC25:75, NGC50:50, NGC60:40) animals. While all animal of the control group displayed motor recovery, only single animals of the experimental groups did so. Nerve reconstruction with NGC60:40 did not allow for recordable muscle reinnervation in any case.



Supplementary Figure VII-2 - Appearance of the studied formulations 3 weeks after reconstruction. A+B) Regenerated tissue bridge grown through hollow control NGCs. Black arrows point to the tissue cables located inside the NGC. C) Sample from the NGC50:50 group. White arrows point to the border of the infiltrated GG freeze-dried hydrogel. D) Sample from the NGC25:75 group. White arrows point to the border of the infiltrated GG freeze-dried hydrogel. The NGCs are still enclosed by a thin layer of connective tissue that has formed around them. The specimens were placed on glass plates on top of scale-papers with 1 mm intersections. Scale bar: 3 mm.

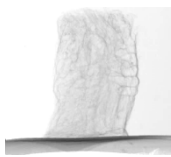
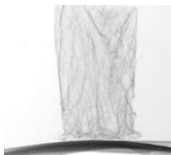

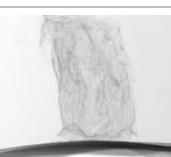


Supplementary Figure VII-3 - Appearance of the studied formulations through the microsurgery microscope 6 weeks after reconstruction. A) Regenerated nerve tissue grown through an hollow control NGC. Black arrows delineate the tissue bridge that has formed between the nerve ends. B+C) Samples from the NGC60:40 group. There is no presence of ingrown tissue within the GG residues indicated by the asterisk and delineated by white arrows. D+E) Samples from the NGC50:50 group. Black arrows in D) delineate ingrown tissue in the proximal part of the NGC, which is thin and free of surrounding GG residues. White arrows in E) point to the border of an empty GG freeze-dried hydrogel scaffold. The asterisk marks the GG material, while the black arrows signal the infiltrated blood supply in close vicinity to the nerve ends. F+G) Samples from the NGC25:75 group. Black arrows indicate the presence of ingrown tissue. Arrow heads point to a border of the tissue and asterisks indicate residues of freeze-dried GG hydrogel scaffold. Eventually small vessels can be seen along or inside the GG freeze-dried hydrogel scaffolds. The connective tissue that has formed around the NGCs has been removed. The specimens were placed on glass plates on top of scale-papers with 1mm intersections. Scale bar: 3 mm.

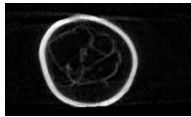
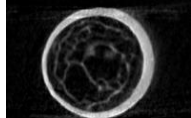
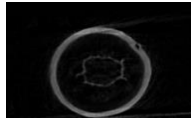


Supplementary Figure VII-4 - Aspects of nerve implants with electrodiagnostically proven muscle reinnervation at the moment of explantation after 12 weeks in vivo (view through the microsurgery microscope). The connective tissue that has formed around the NGCs has not been removed. Black arrow heads point to the distal nerve segment further processed for nerve morphometry. The specimens have been placed on a glass plate on top of scale-paper with 1mm intersections. A) Autologous nerve graft, black arrows point to the suture line. B-C) Samples from the NGC50:50 group. Black arrows indicate the presence of tissue most likely grown through Gellan Gum scaffolds. Both specimens were affiliated with a positive evaluation for functional recovery. D-F) Samples from the NGC25:75 group: Black arrows indicate the presence of tissue most likely grown partially through and partially along the Gellan Gum hydrogel matrix. White arrow in F) points to a whitish area not clearly indicating if the GG scaffolds contains ingrown tissue or not. Samples shown in D and F were affiliated with positive evaluation for functional recovery while sample shown in E was not. Scale bar: 3 cm.

Supplementary Table VII-1 - Micro-CT analysis of freeze-dried hydrogels for *in vitro* assays: Quantification of mean pore size, trabecular thickness and % of porosity from n=3 samples each.

| Freeze-dried hydrogel formulation | Mean Pore Size (μm) | Trabecular Thickness (μm) | Porosity (%) | Image $\mu\text{-CT}$ |
|-----------------------------------|----------------------------------|--|----------------|---|
| H60:40 | 265.5 \pm 2.9 | 58.1 \pm 2.1 | 80.5 \pm 2.5 |  |
| H50:50 | 339.0 \pm 75.9 | 65.8 \pm 4.7 | 81.5 \pm 8.2 |  |
| H25:75 | 299.2 \pm 25.5 | 65.4 \pm 2.5 | 81.2 \pm 1.4 |  |
| H100 | 230.6 \pm 3.2 | 61.8 \pm 0.78 | 79.2 \pm 1.7 |  |

Supplementary Table VII-2 - Micro-CT analysis of nerve guidance conduits with different gellan gum freeze-dried hydrogels as fillers, similar to those prepared for evaluation *in vivo*. Quantification of mean pore size, trabecular thickness and % of porosity from n=3 samples each.

| Nerve guidance conduit, NGC (Freeze-dried hydrogel filling chitosan tube) | Mean Pore Size (μm) | Trabecular Thickness (μm) | Porosity (%) | Image $\mu\text{-CT}$ |
|---|----------------------------------|--|----------------|---|
| NGC60:40 | 377.8 \pm 50.8 | 98.0 \pm 13.5 | 82.8 \pm 5.2 |  |
| NGC 50:50 | 321.6 \pm 89.4 | 109.0 \pm 4.9 | 73.8 \pm 7.3 |  |
| NGC 25:75 | 360.7 \pm 36.0 | 121.4 \pm 13.4 | 79.4 \pm 3.3 |  |

Supplementary Table VII-3 - 3 weeks' time point general evaluation.

| Formulation | Animals (Code number) | Macroscopic evaluation ^(a) | H&E ^(b) | NF200 | ED1 ^(c) | Neo-vascularization ^(d) |
|-------------|-----------------------|---------------------------------------|--------------------|-------|--------------------|------------------------------------|
| NGC60:40 | 1 | + | - | - | - | x |
| | 8 | + | + | - | + | x |
| | 9 | - | + | - | - | - |
| | 16 | + | x | x | x | + |
| NGC50:50 | 2 | + | + | + | - | x |
| | 7 | + | - | - | - | x |
| | 10 | ++ | + | - | + | + |
| | 15 | + | x | x | x | - |
| NGC25:75 | 3 | ++ | ++ | ++ | + | x |
| | 6 | - | - | - | - | x |
| | 11 | ++ | x | x | x | ++ |
| | 14 | + | x | x | x | + |

^(a)(-) No tissue within the NGC; (+) Strips of tissue mainly between the NGC wall and the GG; (++) Tissue along the entire NGC, but fragmented; (+++) complete nerve bridge.

^(b)In the case of ED1-immunopositive activated macrophages, (-) indicates very few visible red fluorescent cells, (+) indicates an intermediate and (++) a more intense immune response with increasing numbers of red fluorescent cells detected.

^(c)For neovascularization, (-) indicates no visible blood vessels and (+) refers to visible blood vessels.

^(d)(x) Samples not analyzed since NGCs were macroscopically looking totally empty or purulent.

Supplementary Table VII-4 - 6 weeks' time point general evaluation.

| Formulation | Animals (Code number) | Macroscopic evaluation | H&E | NF200 | ED1 | Neo-vascularization (when applicable, (when applicable, + or - only) |
|-------------|-----------------------|------------------------|-----|-------|-----|--|
| NGC60:40 | 4 | ++ | + | + | - | + |
| | 5 | - | x | x | X | x |
| | 12 | + | + | + | - | + |
| | 13 | - | x | x | x | x |
| NGC50:50 | 3 | + | ++ | + | + | + |
| | 6 | + | - | - | - | + |
| | 11 | - | x | x | X | x |
| | 14 | - | x | x | x | x |
| NGC25:75 | 2 | ++ | +++ | ++ | - | + |
| | 7 | ++ | - | - | - | + |
| | 10 | +++ | +++ | +++ | + | x |
| | 15 | +++ | ++ | + | - | x |

¹(-) No tissue within the NGC; (+) Strips of tissue mainly between the NGC wall and the GG; (++) Tissue along the entire NGC, but fragmented; (+++) complete nerve bridge

²In the case of ED1-immunopositive activated macrophages, (-) indicates very few visible red fluorescent cells, (+) indicates an intermediate and (++) a more intense immune response with increasing numbers of red fluorescent cells detected.

³For neovascularization, (-) indicates no visible blood vessels and (+) refers to visible blood vessels.

⁴(x) Samples not analyzed since NGCs were macroscopically looking totally empty or purulent.

Supplementary Table VII-5 - 12 weeks' time point general evaluation. NGC25:75 only present 5 samples because 2 animals from this group had to be sacrificed due to severe autotomy.

| Formulation | Animals (Code number) | Macroscopic evaluation | H&E | NF200 | ED1 | Electrodiagnostic recordings (+ or - only) | Neo-vascularization (when applicable, + or - only) |
|-------------|-----------------------|------------------------|-----|-------|-----|--|--|
| NGC25:75 | 5739 | +++ | +++ | ++ | - | - | X |
| | 5741 | +++ | ++ | ++ | + | + | + |
| | 5755 | - | X | X | X | - | X |
| | 5763 | + | ++ | ++ | - | + | + |
| | 5766 | - | X | X | X | + | X |
| NGC50:50 | 5740 | + | ++ | + | + | - | + |
| | 5743 | - | X | X | X | - | X |
| | 5748 | ++ | ++ | + | - | - | X |
| | 5752 | + | + | + | - | - | + |
| | 5756 | +++ | X | X | X | + | X |
| | 5760 | +++ | + | ++ | + | + | X |
| | 5764 | ++ | X | X | X | - | X |
| NGC60:40 | 5742 | - | - | - | - | - | X |
| | 5745 | + | - | - | - | - | X |
| | 5749 | ++ | + | + | + | - | + |
| | 5753 | - | | | | - | X |
| | 5757 | +++ | + | + | + | - | + |
| | 5761 | - | | | | - | X |
| | 5765 | - | - | - | - | - | X |

¹(-) No tissue within the tube; (+) Strips of tissue mainly between the tube and GG; (++) Tissue along the tube, but fragmented; (+++) complete nerve bridge.

²In the case of ED1 positive activated macrophages, (-) indicates very few visible red cells, (+) intermediate and (++) more intense immune response.

³For neovascularization, (-) indicates no visible blood vessels and (+) refers to visible blood vessels.

⁴All positive controls consisting of autotransplant had a positive electrodiagnostic recording and a complete nerve bridge.

⁵(x) Animals not analyzed since they were macroscopically looking totally empty or purulent.

Chapter VIII

Patent - Nerve guidance conduits derived from silk fibroin hydrogels: Methods of production and uses thereof

Chapter VIII

Patent - Nerve Guidance Conduits Derived from Silk Fibroin Hydrogels: Methods of Production and Uses Thereof¹

ABSTRACT

The present disclosure relates to a silk fibroin tubular conduit, a new methodology for obtaining said silk fibroin tubular conduit, and respective uses. The tubular conduit may be used in the treatment of diseases that involve the repair and/or regeneration of tissues, nerves and bones. However, this patent focuses on the particular use for peripheral nerve regeneration.

¹This chapter is based on the following publication: Carvalho CR, Costa JB, Ribeiro V, Silva-Correia J, Olivera JM, Reis RL. Nerve guidance conduits derived from silk fibroin hydrogels: methods of production and uses thereof.

Request N.: PCT/IB2017/054708,

Priorities: PT 109562 (01.08.2016)

WIPO N°: WO18025186

VIII-1. TECHNICAL FIELD

The present disclosure relates to a silk fibroin tubular conduit, a new methodology for obtaining said silk fibroin tubular conduit, and respective uses.

The tubular conduit of the present disclosure may be use in treatment of diseases that involve the repair and/or regeneration of tissues, nerves or bone. In particular, the use for peripheral nerve regeneration.

VIII-2. BACKGROUND

Document CA 2580349 described methods and apparatus for enhanced growth of peripheral nerves and nervous tissue. The device has a matrix is silk fibroin protein, the matrix was cross-linked using formaldehyde gas, citrate ions, ribose, glyoxal or genipin. However, CA 2580349 does not describe an enzymatic cross-linking that allows obtaining a hydrogel as an intermediate step of the process of fabrication of the tubular conduit that confers advantages. In addition, by the methodology now disclosed, it is obtained a uniform device, in comparison to the composite material comprising different components that is achieved in the patent CA 2580349.

Document WO 2009023615 A1 describes a tubular silk fibroin composition that can be used in the repair or replacement of damaged or diseased blood vessels. However, the WO 2009023615 A1 does not disclose the use of tubular silk compositions for other applications other than that of repair or replacement of damaged or diseased blood vessels. The present disclosure is intended for peripheral nerve regeneration. In addition, the methodology described in the patent referred above consists in a technique called dipping or spraying. Therefore, the result of this process is a layer-by-layer obtained device. In contrast, the present disclosure produces a uniform and one layered device. Furthermore, with the present disclosure, it is possible to control and fine-tune the porosity of tubular device by adjusting parameters in the process and in the referred patent the authors have to add different compounds such as polyethylene oxide (PEO).

Document CN 101879330 B discloses a small-caliber silk fibroin tubular material. The document uses the fibroin solution impregnation, drying, curing and other methods can close integration of three layers of material, and the use of heparin and other anti-clotting drugs for its inner processed material has anticoagulant properties, it can be used to repair blood vessels, nerves, and other tissues.

Nevertheless, this document does not disclose the attainment of a hydrogel during the process, due to an enzymatic cross-linking obtained with horseradish peroxidase. Furthermore, the method of production now disclosed is related to mold casting, as the one mentioned in the patent refers to the electrospinning technique, in which is mandatory to use aggressive and not biocompatible reagents such as formic acid and hexafluoroisopropanol. The mentioned device implicates the presence of three layers, mimicking the natural structure of blood vessels and the use of high temperatures, none of which is present in our methodology since it is green and cell-friendly.

US 9068282 B2 described a system and method for making biomaterial structures that can be used as tubular vessels for tissue engineering. However, US 9068282 B2 does not disclose a mold casting technique that makes use of a hydrogel as an intermediate component of the process to produce a tubular device.

A bibliographic research revealed many publications related to the production of silk nerve guidance conduits, but mainly by electrospinning and dipping in silk aqueous solutions.

Unsatisfying functional recovery after peripheral nerve injury (PNI) is still a significant clinical challenge faced today, even after decades of research in the field (1). PNIs only are related to 8.5 million restricted activity days and almost 5 million “bed days” each year around the world (2). Consequently, over 200,000 peripheral nerve repair procedures are performed annually in the US alone (3). A variety of reasons may lead to PNI, such as car accidents, military and sport injuries as well as degenerative diseases. Although peripheral nervous system (PNS) has a superior capacity to regenerate when compared to CNS, they repeatedly result in painful neuropathies owing to reduction in motor function and sensory perception. Surgical interventions such as neurorrhaphy, which is the direct suture repair without the use of grafted materials – may be used in cases where a short (<5 mm) nerve gap must be overcome. However, larger defects repaired by neurorrhaphy, exhibit excessive tension over the suture line and offer poor surgical results (4). To this day, the typical choice in this situation is a nerve autograft that is harvested from another site in the body. However, this recognized “gold standard” technique for peripheral nerve repair is limited by tissue availability, donor-site morbidity, secondary deformities, as well as potential differences in tissue structure and size. In the last 30 years, FDA has approved a few devices based on natural and synthetic biomaterials to repair nerve defects arising from PNI, since autograft is not always an option (**Table VIII-1**). The effort of the scientific community to tackle this issue is visible when one considers the 732 publications in 2015 alone

concerning peripheral nerve regeneration. Still, despite all this research and effort, not many alternatives reach the market or when they do, they do not outperform the autograft.

The first materials used in nerve guidance conduits were synthetic, such as PCL, PLGA and polyurethane. Among the natural and biodegradable materials, agarose, chitosan, collagen, fibrin, gelatin, keratin and silk have been used.

These facts are disclosed in order to illustrate the technical problem addressed by the present disclosure.

VIII-3. GENERAL DESCRIPTION

The present disclosure relates to a silk fibroin tubular conduit, a new methodology for obtaining said silk fibroin tubular conduit, and respective uses. In particular, the use for peripheral nerve regeneration.

Materials used for peripheral nerve regeneration, requires not only to have good biocompatibility, but must also have a controllable biodegradability, certain mechanical strength, and performance can be related to the release of drugs or other factors.

There are three methods for producing silk tubular structures: mold casting, dipping and electrospinning. The method now disclosed is included in the mold casting. However, the process now disclosed is different from the ones of the state of the art. In the process of the state of the art, an aqueous silk solution is made and injected in the mold and β -sheet is induced, using a standardized method comprising a methanol solution for induction of β -sheet crystalline structure, transforming a transparent solution into opaque and solid final material.

The present disclosure comprises the transformation of an initially produced aqueous silk solution into an amorphous and transparent hydrogel, through a peroxidase-mediated cross-link reaction.

In an embodiment, surprisingly a temporary β -sheet is induced with liquid nitrogen facilitating the removal of the outer mold and a posterior permanent semi-crystalline structure is induced with an ethanol solution. Alternatively, the induction of β -sheet conformation can be made by freezing at $-80\text{ }^{\circ}\text{C}$ and freeze-drying may be performed to avoid the use of organic solvents.

In an embodiment, silk fibroin may contain around 5 mol% tyrosine groups, which are oxidized by peroxidase/hydrogen peroxide and subsequently cross-linked to form a three-dimensional network. Silk fibroin hydrogels are achieved by the cross-linking of tyrosine groups in silk fibroin. This cross-link leads to a stronger and more stable three-dimensional network, thus conferring the scaffold higher mechanical properties, more elasticity and a lower degradation rate, when compared to tubes that did not undergo this cross-link before turning in β -sheet conformation.

In an embodiment, by transforming the aqueous solution in a hydrogel in the middle of the process, increasing its viscosity without having to increase silk concentration, it is easier to incorporate and make gradients of bioactive molecules. Therefore, the present disclosure relates to a more stable three-dimensional network after the formation of the hydrogel, as the swelling shall not be as intense as a tube produced without the formation of the hydrogel, which is an advantage for PNR. With this methodology, it is possible to produce tubular conduits/tubes with variable length, variable wall thickness and variable intraluminal diameter.

The tubular conduit according to the present disclosure provides a fibroin silk tubular conduit with improved mechanical properties. This allows implanting the products obtainable by the present process *in vivo* into regions where they are exposed to specific mechanical influences, such as sciatic nerve or hand, wrist and forearms regions.

In an embodiment, *in vivo* implants of a nerve conduit may be exposed to pressure forces, which may cause collapse of said implants. In such a case, a tube of silk fibroin would collapse and hinder a growing nerve covered by such tube.

In an embodiment, the fibroin silk tubular conduit obtainable by the process disclosed in the present subject matter allows provision of transplants resisting such forces causing crush or contusion.

In an embodiment, the process now disclosed for obtaining a fibroin silk tubular conduit, results in a tubular conduit with improved properties, since as the hydrogel is obtained during said process, which will comprise a more stable and stronger three-dimensional network. This step provides advantages in terms of mechanical features, more elasticity, kinking-resistance ability, adjustable permeability and a more controlled degradation and swelling rate (**Figure VIII-1 and VIII-2**).

The tubular conduit described in the present subject-matter has improved elastic properties, kinking resistant and shape recovery as shown in **Figure VIII-4 and VIII-13**.

Thus, the tubular conduit discloses in the present disclosure advantageously regenerates nerve cells and blood vessels in peripheral nerve tissues and thus rehabilitates the injured nerve tissues, improve nerve conduction velocity, and relief of pain induced by traumatic peripheral nerve injury.

An aspect of the present disclosure is related to a tubular conduit comprising an enzymatically cross-linked silk fibroin hydrogel wherein said tube is predominantly β -sheet conformation and, comprises a porosity up to 70 % and a pore size up to 30 μm , optionally the pore may be interconnected.

In an embodiment, the tubular conduit may comprise porosity up to 70 % and a pore size up to 7 μm , optionally the pore may be interconnected.

In an embodiment for better results, the porosity may be up to 70 %, preferably 0.5 – 50 %, more preferably 3-25 %, even more preferably 5-10 %.

In an embodiment for better results, the pore size may be up to 10, preferably up to 7 μm , preferably 0.5-7 μm , even more preferably 1-7 μm .

In an embodiment for better results, the porosity may be up to 70 %, preferably 0 – 50 %, more preferably 3-25 %, even more preferably 5-10 %.

In an embodiment for better results, the tubular conduit may have a wall with a thickness of 0.2 mm - 2 mm, preferably 0.3 mm – 1 mm, more preferably 0.3 mm – 0.7 mm.

In an embodiment for better results, the cross-linked silk fibroin hydrogel may be enzymatically cross-linked with horseradish peroxidase and hydrogen peroxide.

In an embodiment for better results, the hydrogel now disclosed may comprise between 5-25 %wt. of silk fibroin, preferably between 12-18 %wt. of silk fibroin, more preferably between 15-16%wt of silk fibroin.

In an embodiment for better results, the tubular conduit may comprise an internal diameter of 1 mm - 10 mm, preferably 2 mm - 4 mm.

In an embodiment for better results, the tubular conduit may have a wall with a thickness of 0.3 mm - 2 mm, preferably 0.3 mm - 1 mm.

In an embodiment for better results, the tubular conduit may have a length of 5 mm – 100 mm, preferably 10 mm - 50 mm.

In an embodiment for better results, the tubular conduit of the present disclosure may further comprise a conductive agent, preferably selected from a list consisting of gold, silver, polypyrrole, or mixtures thereof.

In an embodiment for better results, the tubular conduit may further comprise hyaluronic acid, alginate, casein, polyethylene oxide, polyethylene glycol, collagen, fibronectin, keratin, polyaspartic acid, polylysine, chitosan, pectin, polylactic acid, polycaprolactone, polyglycolic acid, polyhydroxyalkanoate, polyanhydride, and mixtures thereof.

In an embodiment for better results, the tubular conduit may further comprise a biological active agent, a therapeutic agent, an additive, a pharmaceutically acceptable excipient, a pharmaceutically acceptable carrier, and mixtures thereof.

In an embodiment for better results, the biologically active agent may be selected from the following list: a peptide, a protein, a nucleic acid, an antibody, an aptamer, an anticoagulant agent, a growth factor, a cytokine, an antibiotic, an immunosuppressor, a steroid, non-steroidal anti-inflammatory drug, and mixtures thereof. It is understood that other drugs or factors to promote nerve regeneration or to suppress the formation of glioma or fibrosis can be added.

In an embodiment for better results, the thickness of the walls of the final conduits can be modified by changing the specific sizes of the molds used. For more permeable conduits, thin wall conduits must be chosen.

In an embodiment for better results, the tubular conduit may comprise of dorsal root ganglia, Schwann cells and/or stem cells. Other cell types could also be added as required.

The present disclosure also relates to of silk fibroin hydrogel enzymatically cross-linked, in particular with horseradish peroxidase and hydrogen peroxide,

- for use in use in medicine or in veterinary;
- wherein said composition is administered in a tubular conduit;
- wherein said tubular conduit comprises a β -sheet conformation obtainable by an enzymatically cross-linked of silk fibroin hydrogel; comprising a porosity up to 70 % and a pore size up to 30 μm .

In an embodiment for better results, the tubular conduit may be use in treatment of diseases that involve the repair and/or regeneration of tissues, nerves or bone.

In an embodiment for better results, the tubular conduit may be use in treatment of a peripheral nerve injury, a spinal cord injury, regeneration of peripheral nerve cells.

In an embodiment for better results, the tubular conduit may be for use in bone regeneration and several tissues-bone interfaces.

In an embodiment for better results, the tubular conduit may be for use in regeneration of peripheral nerve cells in the spinal cord and/or in a peripheral nerve.

In an embodiment for better results, the tubular conduit may be for use in the treatment of traumatic peripheral nerve injury.

In an embodiment for better results, the tubular conduit may comprise dorsal root ganglia and/or Schwann cells.

This disclosure also relates to a kit comprising the tubular conduit now disclosed.

Furthermore, an aspect of the present disclosure also relates to a method for producing said tubular conduit of silk fibroin comprising the steps of:

- preparing an aqueous silk fibroin solution with a concentration of 5-25 %wt.;
- adding of horseradish peroxidase and hydrogen peroxide to the aqueous silk fibroin solution to form an enzymatically cross-linked silk fibroin hydrogel;
- injecting said silk fibroin hydrogel into a mould;
- wherein said mould comprises an outer wall and an inter wall;
- incubating the mould at 37 °C for 0.5-5 hours, for the complete formation of the hydrogel;
- placing the silk fibroin hydrogel in liquid nitrogen for at least 30 seconds, until temporary development of β -sheet;
- removing of polymeric outer wall of the mould;
- induction of β -sheet conformation by placing the obtainable hydrogel in ethanol absolute solution, in particular for least 30 minutes or by freezing the obtainable hydrogel at -80 °C.

In an embodiment for better results, the drying step may be carried out by freeze dry for obtaining a pore size of 0.5 μm – 3 μm , preferably a pore size of 0.5 μm – 2 μm .

In an embodiment for better results, the drying step may be carried out at 25 °C – 70 °C for obtaining a porosity that varies from non-porous up to 3 μm pores.

In an embodiment for better results the aqueous silk fibroin solution concentration may be between 12-18 %wt.

In an embodiment for better results, the incubating step may be carried out for 2 hours.

In an embodiment for better results, the placing step of the silk fibroin hydrogel in liquid nitrogen may be carried out for 30-45 seconds.

In an embodiment for better results, the placing step in ethanol absolute solution may be carried out for 1 hour.

In an embodiment for better results, the placing step in ethanol absolute may be carried out overnight.

In an embodiment for better results, the induction of β -sheet conformation by freezing at between -80 °C to -20 °C and free-drying may be performed to avoid the use of organic solvents, preferably -80 °C.

In an embodiment for better results, the method may further comprise a step of freezing the obtained tubular conduits at -80 °C overnight and freeze-drying for 4 days.

In an embodiment for better results, the mold made has stainless steel as interior rod and a polymeric outer wall.

In an embodiment, final β -sheet conformation may be determined by FTIR, NanoIR and XRD techniques, to assess the presence of functional groups and the crystallinity of final material.

In an embodiment, the porosity of the tubular conduit may be determined by Micro-CT 3D reconstructions in which morphometric parameters such as total % of porosity, mean pore size and trabecular thickness will be quantified.

In an embodiment, the permeability according to the pore sizes may be assessed with fluorescent dyed molecules quantification or O₂ permeability studies.

In an embodiment, the pore size distribution of the conduit may be determined by Micro-CT 3D analysis and SEM micrographs.

In an embodiment, the pores may be interconnected.

VIII-4. DETAILED DESCRIPTION

The present disclosure relates to a silk fibroin tubular conduit, a new methodology for obtaining said silk fibroin tubular conduit, and respective uses. In particular, the use for peripheral nerve regeneration.

In an embodiment, by changing the method of solvent extraction, diverse conduits can be obtained, that will implicate changes in all features of the conduits (see **Figure VIII-6**).

In an embodiment, the mold used to inject the silk polymeric solution has a crucial impact on the size specifications of the final conduit, which in other hand, it has an impact on the conduit's characteristics. Several different wall thicknesses may be obtained, as seen in **Figure VIII-7**.

In an embodiment, tubular/nerve conduit of the present disclosure may have different drugs/bioactive/conductive molecules and/or a random drug distribution in the tube sections. In particular (see **Figure VIII-8**):

- (I) Growth factors gradient: Growth factors relevant to regeneration, such as GDNF, NGF, BDNF, FGF or VEGF can be incorporated. Since the lack of vascularization and nutrients supply in the distal site of injuries is a major complication leading to cell death and there is the need to guide proximal growing axons to the distal site, one of the objectives is to have higher amounts of growth factors in this distal area. Since in a middle step of forming the NGC we will be handling a viscous silk hydrogel, it is possible to make gradients of several molecules, increasing its concentration from proximal to the distal site, where it is most needed
- (II) Conductive conduits: An important aspect of synthetic nerve grafts is their ability to conduct electricity. Studies have showed that electrical stimulation can significantly promote the regeneration of peripheral nerve injuries.
- (III) Incorporation of proteins, in particular: as a method to increase biological properties, the inclusion of human hair keratin is very feasible and already proved to be effective,

increasing cellular viability in the conduits containing only 1 % of keratin in the polymeric solution.

In an embodiment, simple conduits are composed only of silk. However, since the main purpose of these biomaterials is for peripheral nerve regeneration applications, many different molecules can be added to the conduits, for varying purposes.

In an embodiment, different drying methods or simply not drying the silk conduits after the fabrication method affects all properties of the conduits. Degradation is one of these parameters that is largely affected. The conduits that are not dried, or used directly from ethanol, degrade much faster than the others (after 21 days) and tend to disaggregate in blocks in both thin and thick wall tubes (see **Figure VIII-11B**). The freeze-dried formulations have an intermediate degradation, while the air-dried formulations last for longer periods of time (only degrades 5 % after 30 days). With these results is possible to verify that using the exact same methodology and concentration, and changing only the method of drying, we can tune the degradation from total degradation to almost not degrading after 30 days, according to needs.

In an embodiment, the drying of the conduits in different manners has implications in the physico-chemical characteristics of silk conduits. After 30 days in Simulated Body Fluid (SBF), the only formulation that presented bioactivity capabilities or that allowed the formation of calcified crystals, was the air-dried formulation. That was proved by EDS technique, which detected a high concentration of calcium phosphates (ions phosphor and calcium) and by SEM, which detected these crystals in the surface of the conduit. For peripheral nerve regeneration purposes, calcification is not desired. However, this feature can be of high importance in hard tissue regeneration applications, such as bone regeneration.

In an embodiment, nerve conduits must not collapse and retain mechanical stability to withstand the traction of moving joints. Peripheral nerves are under tensile loads in situ and experience ≈ 11 % strain in resting position. Concerning this strain, thick tubes tolerate a higher tensile stress when compared to thinner tubes. Among the thick, FDMP and AD present higher tensile stress for the same % of strain. Regarding the tensile modulus, corroborating the previous results, thick tubes present higher modulus. Again, the FDMP and air dried revealed higher stiffness when compared to others.

Corroborating the previous results, the air-dried formulation, due to bioactivity and stiffness could easily find application in hard tissue regeneration applications.

In an embodiment, depending on the application of silk conduits, more or less permeability is an important feature to consider. In the case of peripheral nerve regeneration, it is important to keep permeability to oxygen and nutrients for the regenerating nerve, however maintaining a close and protective environment. Therefore, permeability assays are of outmost importance. By simply changing the method of drying or the thickness of the conduit walls, different permeability is obtained. In a 48 hours assay, a fluorescent molecule (FITC-dextran with 4 kDa of weight) was injected in the lumen of the conduits and the ends were sealed. The release of this molecule through the conduit walls was evaluated. In thick wall conduits, only ethanol formulation allows 80 % passage of molecule. On the other hand, all thin wall tubes allow the 4 kDa molecule to cross through the walls, regardless of the formulation, reaching 100 % of release after 48 hours. The microscopic images of the conduits after the assay suggest some molecules are entrapped in the thick wall conduits.

In an embodiment, the wall conduits varied from $\pm 700 \mu\text{m}$ in thick wall conduits to $\pm 300 \mu\text{m}$ in thin wall conduits, which made a significant difference in terms of permeability. For instance, in the air-dried formulation, the release went from 20 % to 100 %, due to the wall thickness alone.

In an embodiment, the cytocompatibility and *in vitro* biological performance was carried out by means of using different cell types relevant for peripheral nerve regeneration, namely Human Schwann cells and human skin fibroblasts (BJ). All formulations of conduits were tested. Quantitative results of cellular density after 7 days in culture are shown (Alamar Blue assay) and corroborated by qualitative images (Live/Dead assay).

In an embodiment, the silk conduits formulations of the present disclosure were implanted in male CD1 mice, in four subcutaneous pockets on the animals' backs. Animals were sacrificed 4 weeks after implantation, and conduits were explanted with the surrounding connective tissue for analysis. Sections were prepared and stained with hematoxylin and eosin (H&E). It is possible to see the expected formation of a fibrous capsule around the conduits. However, that tissue does not show a high concentration of inflammatory cells, indicating that the host response to the silk conduit was negligible and in agreement with prior findings on the host response to silk fibroin biomaterials. It is also possible to see that there is no infiltration or migration of cells through the conduits walls, proving the conduits impermeability to undesired cells such as fibroblasts and consequent formation of scar tissue.

Table VIII-1 - Commercially available nerve guides and wraps. Apart from Avance, Qigel and RevolNerve, all other listed nerve devices are FDA approved.

| Commercial name | Company | Material |
|---|----------------------|---|
| Neuragen®/Neurawrap™ | Integra | Type I collagen |
| Neurolac® | Polyganics | PDLLA/CL |
| Neurotube® | Synovis | PGA |
| Neuromatrix/Neuroflex™ conduits and NeuroMend™ wrap | Collagen matrix Inc. | Type I collagen |
| Salubridge™/Salutunnel™ | Salumedica | Polyvinyl alcohol hydrogel |
| Surgisis®/Axoguard™ | AxoGenInc | Porcine small intestine submucosa |
| Avance® | AxoGenInc | Decellularized nerve |
| QiGel™, Re-Axon® | Medovent | Chitosan |
| RevolNerve® | Orthomed | Collagen type I and III from porcine skin |

In an embodiment, silk fibroin from the silk worm *Bombyx mori*, has often been used as a textile material, yet, more and more attention has been given to silk lately due to its appropriate processing, biodegradability and the presence of easily accessible chemical groups for functional modifications. Studies suggest that silk is not only biodegradable but also bioresorbable, characteristics for tissue engineering and regenerative medicine. The major advantage of silk compared to other natural biopolymers is its excellent mechanical property. Other important advantages include good biocompatibility, water-based processing, biodegradability and the presence of easy accessible chemical groups for functional modifications. Studies suggest that silk is not only biodegradable but also bioresorbable.

In an embodiment, regarding the application of this biomaterial in peripheral nerve regeneration, it is known that silk fibroin supports the viability of dorsal root ganglia and Schwann cells without affecting their normal phenotype or functionality.

The present disclosure refers to the development of a nerve guidance conduit derived from silk fibroin, using a different methodology than the ones referred to in the literature, intended for bridging nerve defects, for peripheral nerve regeneration.

In an embodiment, the porosity of the tube wall may be defined by the drying method. For peripheral nerve regeneration, it is necessary to have some porosity that allows the exchange of oxygen and nutrients from the outside to the region of the lesion. However, such porosity must block the

infiltration of cells, such as fibroblasts that will induce fibrosis and scar tissue formation. In addition, tubes frozen with liquid nitrogen presented cracks and are more brittle, for which they were excluded.

In an embodiment, the tubes that were not dried and were used directly after being soaked in ethanol cannot be observed by SEM.

In an embodiment, the kink resistance ability was determined by bending the conduits 180 ° on a flexible wire. The thick wall formulations that were produced by inducing β -sheet conformation with ethanol present kink resistance ability, with no occlusion of the lumen whatsoever. This feature is important, since nerves are close to articulations and might be subjected to forces. The device used must be capable of bending during patient movement without kinking and compression.

In an embodiment, the tubular conduit can be obtainable by the following steps:

- preparing an aqueous silk fibroin (SF) solution - concentration to be defined according to final intended features;
- adding of horseradish peroxidase (100 μ L/mL of SF solution) and hydrogen peroxide (65 μ L/mL of silk solution) - quantity to be defined according to final intended features;
- injecting the enzymatically cross-linked SF hydrogel into the mould (with the preferred dimensions);
- incubating the whole system at 37 °C for 2 hours for the complete formation of the hydrogel;
- placing the whole system in liquid nitrogen (-190 °C) for 30 - 45 seconds, until temporary development of β -sheet (with low temperature);
- the induction of β -sheet conformation by freezing at -80 °C and freeze-drying may be performed to avoid the use of organic solvents;
- For the methodology involving the β -sheet conformation using organic solvents such as ethanol, after placing the whole system in liquid nitrogen (-190 °C) for 30 - 45 seconds
 - removing outer mould;
 - placing in ethanol absolute for 1 hour for induction of β -sheet conformation;
 - removing the inner mould;
 - placing in water (**Figure VIII-2**);
- proceed with most suitable method of drying according to the final requirements.

Aqueous solutions of silk fibroin with different concentrations work as precursors for the formation of the hydrogel. The silk fibroin solutions are capable of forming hydrogels in the presence of

horseradish peroxidase and hydrogen peroxide (oxidizer) at mild temperatures and within physiological pH range. During the gelation procedure, it is allowed the combination of bioactive reagents, detecting reagents and any combination thereof. At this stage and in order to tackle peripheral nerve regeneration difficulties such as excessive fibrosis and scar tissue formation or to stimulate vascularization, we can include anti-fibrotic substances, angiogenic growth factors such as VEGF or even neurotrophic growth factors such as NGF and GDNF. The blending of silk with other polymers to enhance mechanical properties or cell adhesion such as keratin is also feasible. Later on this process, and its innovation, resides in the rest of the process and the additional steps necessary until the obtainment of the final nerve guidance conduit. We also envision the incorporation of conductive and drug-delivery nanoparticles, as gold nanoparticles. These have the capability of delivering agents of interest in the case of peripheral nerve regeneration and guide electrical impulses, since electrical stimulation is a proved method to improve regeneration, so by this approach we can have two advantages in the addition of one component.

The physicochemical and biological performances of the silk nerve guidance conduit (*e.g.*, compressive modulus, storage modulus, stiffness, swelling behavior, durability, degradation profile, porosity, permeability, suture ability) can be tuned for specific uses, by means of using different drying methods, different sized molds and concentrations of silk fibroin in the same process. Furthermore, the inner diameter, thickness of the wall and length of the nerve guidance conduit can be tuned according to the final needs of the user and depends solely on the molds used. According to the final objectives (animal model and size of nerve defect), different sizes are needed and can easily be obtained.

In an embodiment, with this methodology, it is possible to fine-tune the permeability of the nerve guidance conduit, in particular, by controlling the porosity of the tube wall.

Table VIII-2 - Relation between drying method and pore size.

| Freezing/drying method | Pore size (μm) |
|---|-----------------------------|
| Dried at 50 °C (passage in ethanol) | 0 ± 3 |
| Frozen at -80 °C and freeze dried (passage in ethanol) | 1.5 ± 0.5 |
| Frozen with liquid N ₂ and freeze dried (passage in ethanol) | 0.9 ± 0.3 |
| Frozen at -80 °C and freeze dried (no passage in ethanol) | 2 ± 0.5 |

The simplicity of a regular mold casting or dipping technique does not allow for fine control over conduits wall thickness, uniformity and pore size or distribution. We were able to refine this mold

casting method by introducing an extra step in the process: the formation of a hydrogel. This additional cross-linking step leads to a stronger and more stable three-dimensional network, thus conferring the scaffold higher mechanical properties, more elasticity and a lower degradation rate, when compared to tubes that did not undergo this step before turning in β -sheet conformation.

The term "comprising" whenever used in this document is intended to indicate the presence of stated features, integers, steps, components, but not to preclude the presence or addition of one or more other features, integers, steps, components or groups thereof.

It will be appreciated by those of ordinary skill in the art that unless otherwise indicated herein, the particular sequence of steps described is illustrative only and can be varied without departing from the disclosure. Thus, unless otherwise stated the steps described are so unordered meaning that, when possible, the steps can be performed in any convenient or desirable order.

The disclosure should not be seen in any way restricted to the embodiments described and a person with ordinary skill in the art will foresee many possibilities to modifications thereof.

The above-described embodiments are combinable.

The following claims further set out particular embodiments of the disclosure.

The following references, should be considered herewith incorporated in their entirety:

1. Oh SH, Kim JH, Song KS, Jeon BH, Yoon JH, Seo TB, *et al.* Peripheral nerve regeneration within an asymmetrically porous PLGA/Pluronic F127 nerve guide conduit. *Biomaterials*. 2008 Apr;29(11):1601-9. PubMed PMID: 18155135.
2. Belkas JS, Shoichet MS, Midha R. Peripheral nerve regeneration through guidance tubes. *Neurological research*. 2004 Mar;26(2):151-60. PubMed PMID: 15072634
3. Ichihara S, Inada Y, Nakamura T. Artificial nerve tubes and their application for repair of peripheral nerve injury: an update of current concepts. *Injury*. 2008 Oct;39 Suppl 4:29-39. PubMed PMID: 18804584.
4. Johnson EO, Soucacos PN. Nerve repair: experimental and clinical evaluation of biodegradable artificial nerve guides. *Injury*. 2008 Sep;39 Suppl 3:S30-6. PubMed PMID: 18722612.
5. Yang Y, Chen X, Ding F, Zhang P, Liu J, Gu X. Biocompatibility evaluation of silk fibroin with peripheral nerve tissues and cells in vitro. *Biomaterials*. 2007 Mar;28(9):1643-52. PubMed PMID: 17188747-

VIII-5. CLAIMS

1. Tubular conduit comprising an enzymatically cross-linked silk fibroin hydrogel wherein said tube is predominantly β -sheet conformation and comprises a porosity up to 70 % and a pore size up to 30 μm .
2. Tubular conduit according to the previous claim comprising a pore size up to 10 μm .
3. Tubular conduit according to the previous claim comprising a pore size up to 7 μm , preferably a pore size between 1-7 μm .
4. Tubular conduit according to any of the previous claims wherein the tubular conduit has a wall with a thickness of 0.2 mm - 2 mm, preferably 0.3 mm – 1 mm, more preferably 0.3 mm – 0.7 mm.
5. Tubular conduit according to any one of the previous claims further comprising a conductive agent, preferably selected from a list consisting of: gold, silver, polypyrrole, or mixtures thereof.
6. Tubular conduit according to any one of the previous claims wherein the cross-linked silk fibroin hydrogel is enzymatically cross-linked with horseradish peroxidase and hydrogen peroxide.
7. Tubular conduit according to any one of the previous claims wherein said hydrogel comprises between 5-25 %wt. of silk fibroin.
8. Tubular conduit according to any one of the previous claims wherein said hydrogel comprises between 12-18 %wt. of silk fibroin, preferably 15-16 % of silk fibroin.
9. Tubular conduit according to any one of the previous claims wherein the porosity is of 1 – 50 %, preferably 3-25 %, more preferably 5-10 %.
10. Tubular conduit according to any one of the previous claims wherein the pore size is of 0.5-7 μm .

11. Tubular conduit according to any one of the previous claims wherein the tubular conduit has an internal diameter of 1 mm - 10 mm, preferably 2 mm - 4 mm.
12. Tubular conduit according to any one of the previous claims wherein the tubular conduit has a length of 5 mm – 100 mm, preferably 10 mm - 50 mm.
13. Tubular conduit according to any one of the previous claims wherein the tubular conduit further comprises hyaluronic acid, alginate, casein, polyethylene oxide, polyethylene glycol, collagen, fibronectin, keratin, polyaspartic acid, polylysine, chitosan, pectin, polylactic acid, polycaprolactone, polyglycolic acid, polyhydroxyalkanoate, polyanhydride, and mixtures thereof.
14. Tubular conduit according to any one of the previous claims wherein the tubular conduit further comprises a biological active agent, a therapeutic agent, an additive, a pharmaceutically acceptable excipient, a pharmaceutically acceptable carrier, and mixtures thereof.
15. Tubular conduit according to any one of the previous claims wherein the biologically active agent is selected from the following list: a peptide, a protein, a nucleic acid, an antibody, an aptamer, an anticoagulant agent, a growth factor, a cytokine, an antibiotic, an immunosuppressor, a steroid, non-steroidal anti-inflammatory drug, and mixtures thereof.
16. Tubular conduit according to any one of the previous claims wherein the tubular conduit comprises of dorsal root ganglia, Schwann cells and/or stem cells.
17. A composition of silk fibroin hydrogel enzymatically cross-linked, in particular with horseradish peroxidase and hydrogen peroxide, for use in use in medicine or in veterinary;
18. wherein said composition is administrated in a tubular conduit;
wherein said tubular conduit comprises a β -sheet conformation obtainable by an enzymatically cross-linked of silk fibroin hydrogel; comprising a porosity up to 70 % and a pore size up to 30 μm (**Table VIII-2**).
19. Composition according to the previous claim for use in the treatment of diseases that involve the repair and/or regeneration of tissues, nerves or bone.

20. Composition for use according to any the previous claims 17 - 18 for the treatment peripheral nerve injury, a spinal cord injury, regeneration of peripheral nerve cells, brain diseases or nerve degenerative diseases.
21. Composition for use according to any of the previous claims 17 - 19 for use in regeneration of peripheral nerve cells in the spinal cord and/or in a peripheral nerve.
22. Composition according to any of the previous claims 17 - 20 for use in the treatment of traumatic peripheral nerve injury.
23. Composition according to any of the previous claims 17 - 21 wherein the tubular conduit comprises of dorsal root ganglia and/or Schwann cells.
24. Kit comprising the tubular conduit described in any of the previous claims or the composition described in any of the previous claims.
25. Method for producing the tubular conduit of silk fibroin described in any one of the previous claims comprising the steps of:
 - preparing an aqueous silk fibroin solution with a concentration of 5 - 25 %wt.,
 - adding of horseradish peroxidase and hydrogen peroxide to the aqueous silk fibroin solution to form an enzymatically cross-linked silk fibroin hydrogel;
 - injecting said silk fibroin hydrogel into a mould with desired dimensions, wherein said mould comprises an outer wall and an inter wall;
 - incubating the mould at 37 °C for 0.5 - 5 hours, for the complete formation of the hydrogel;
 - placing the silk fibroin hydrogel in liquid nitrogen for at least 30 seconds, until temporary development of β -sheet;
 - removing of polymeric outer wall of the mould;
 - induction of β -sheet conformation by placing in the obtainable hydrogel ethanol absolute solution, in particular for least 30 minutes or by freezing the obtainable hydrogel.

26. Method according to the previous claim wherein the drying step is carried out by freeze dry for obtaining a pore size of 0.5 μm - 2 μm .

VIII-6. LIST OF FIGURES

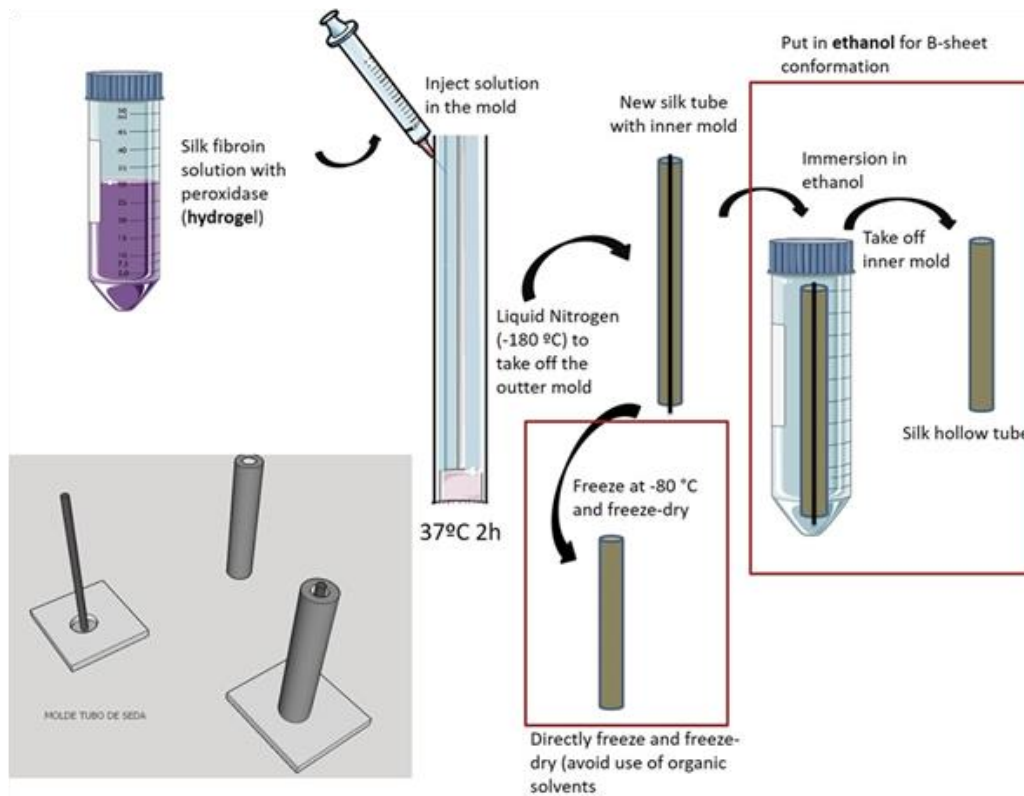


Figure VIII-1 - Schematic representation of the processing method of a tubular conduit/ nerve guidance conduit of silk fibroin.

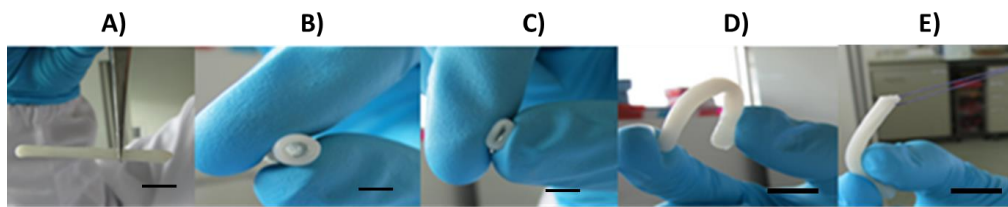


Figure VIII-2 - Schematic representation of embodiment of a tubular conduit/nerve guidance conduit of silk fibroin after production. Scale bar of A), B) and C): 5 mm; Scale bar of D) and E): 3 mm.

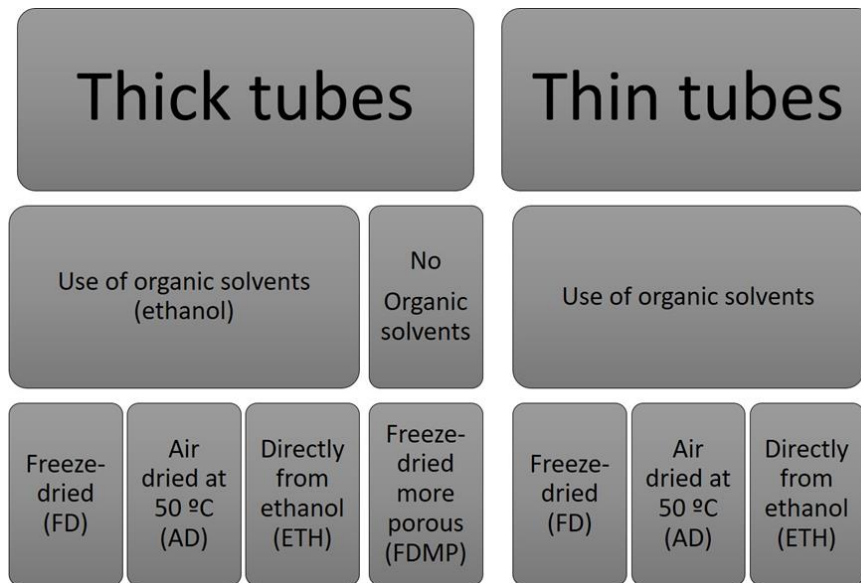


Figure VIII-3 - Schematic representation of possible methods for obtain the tubular conduit described in the present disclosure.

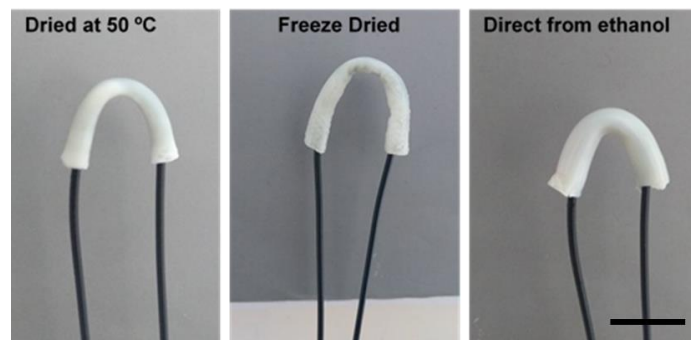


Figure VIII-4 - Schematic representation of kinking resistance ability of thick wall conduits. Scale bar: 7mm.

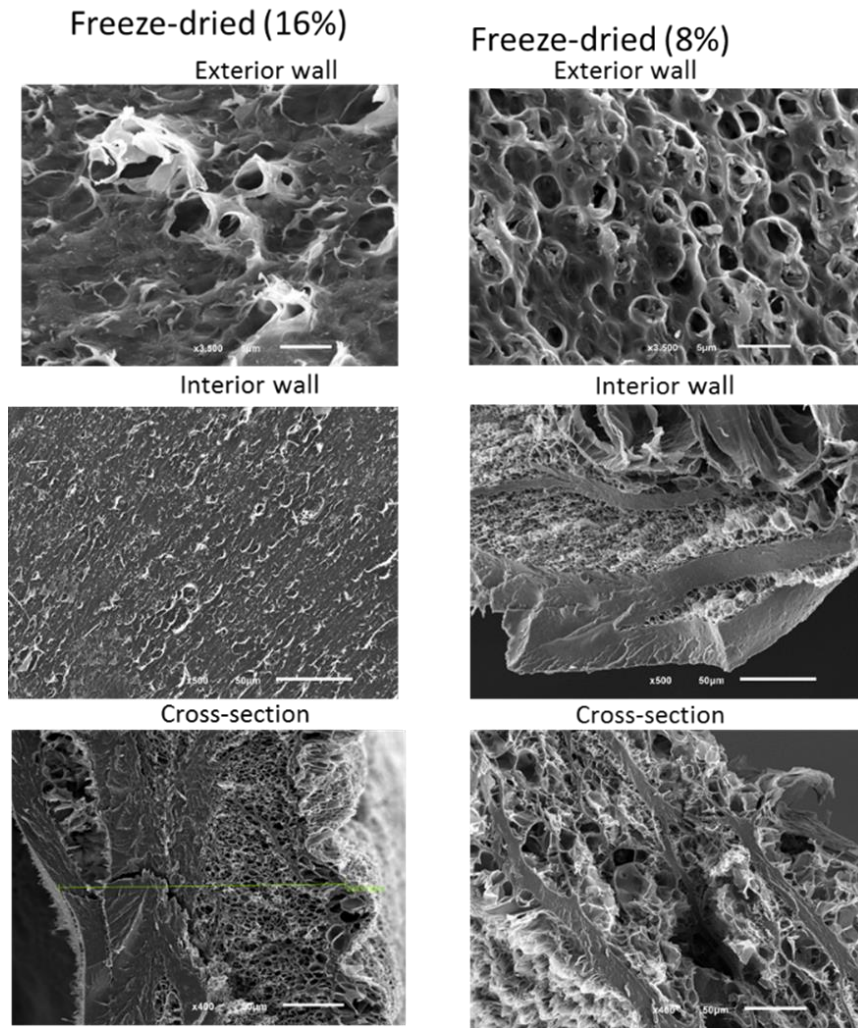


Figure VIII-5 - Schematic representation of SEM micrographs revealing the increased porosity achieved by reducing silk concentration from 16 % to 8 %. The cross-section is specially affected, with high interconnectivity from the inner to the outer walls of the conduit. Scale bar: 5 μm (top micrographs) and 50 μm (bottom micrographs).

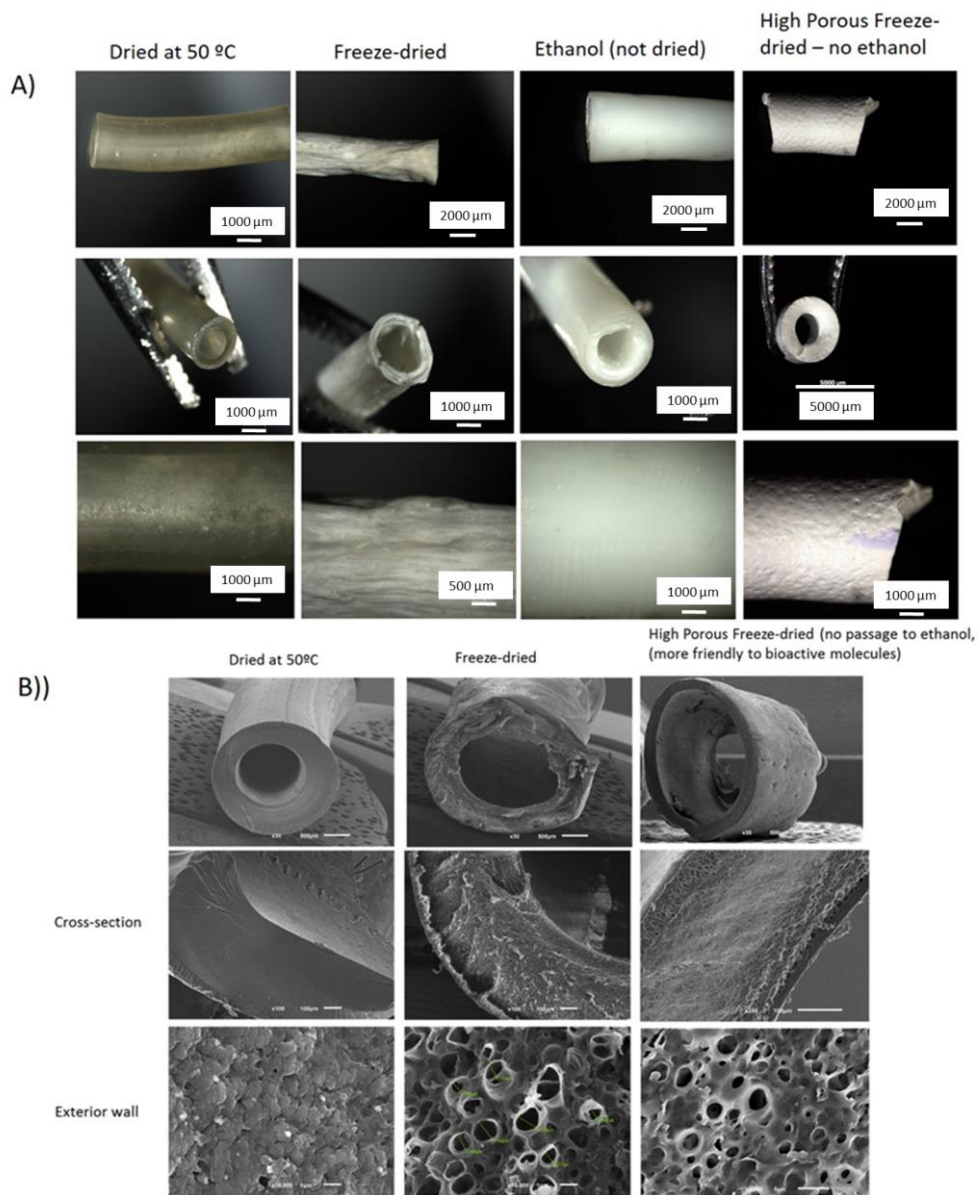


Figure VIII-6 - Schematic representation of: A) Stereomicroscope pictures of the different silk conduits obtained with different drying methods; B) SEM micrographs of the different silk conduits obtained with different drying methods that lead to different micro-structure and porosity. Scale bar: 500 μm (first row); 100 μm (second row); 5 μm (third row).

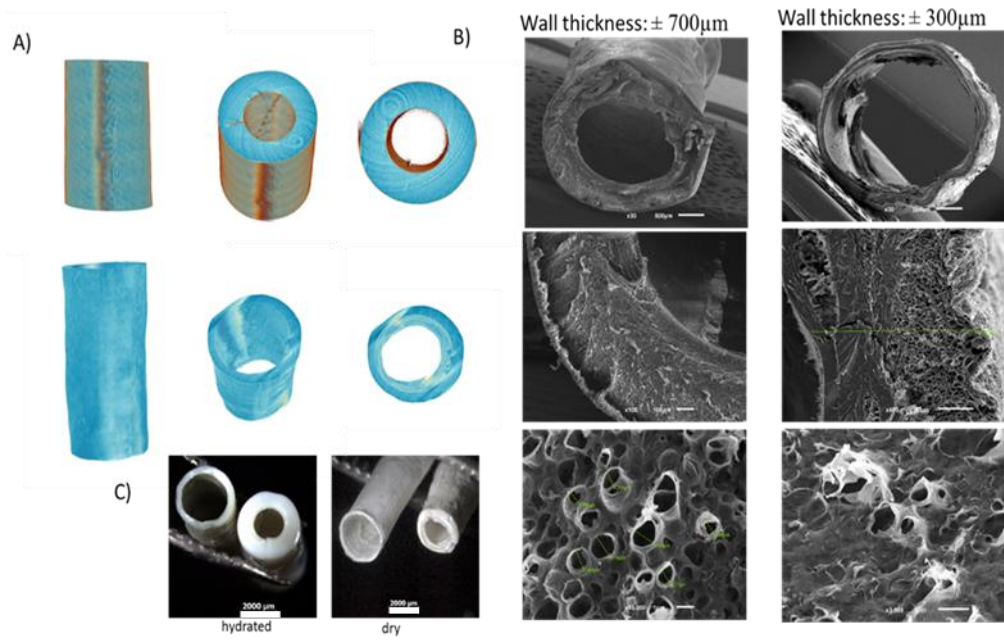


Figure VIII-7 - Schematic representation of: A) 3D micro-CT reconstruction of thick and thin wall conduits obtained used different sized molds; B) SEM micrographs of the mentioned conduits, where wall thickness varies; C) Stereomicroscope images of thick and thin wall conduits, in hydrated and dry state. Scale bar: B) top row: $500\mu\text{m}$; B) middle row: $100\mu\text{m}$; B) bottom row: $5\mu\text{m}$.

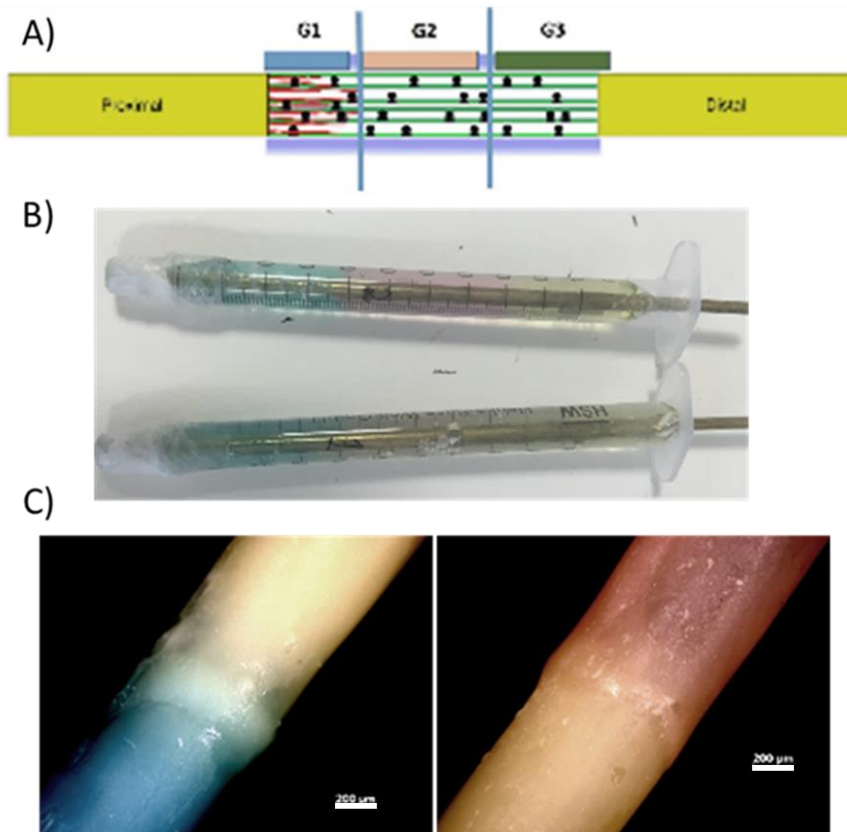


Figure VIII-8 - Schematic representation of silk conduits containing gradients of bioactive molecules. A) Scheme of desired prototypes containing three different and increasing concentrations, from proximal to distal sites; B) Fabrication of a silk conduit (hydrogel step) with three different zones, that correspond to different growth factor concentrations; C) Different concentrations interface of obtained silk conduit. Scale bar: 200 µm.



Figure VIII-9 - Schematic representation of a simple hydrated silk conduit (white) when compared to a conductive silk/polypyrrole conduit (black). Scale bar: 500 µm.

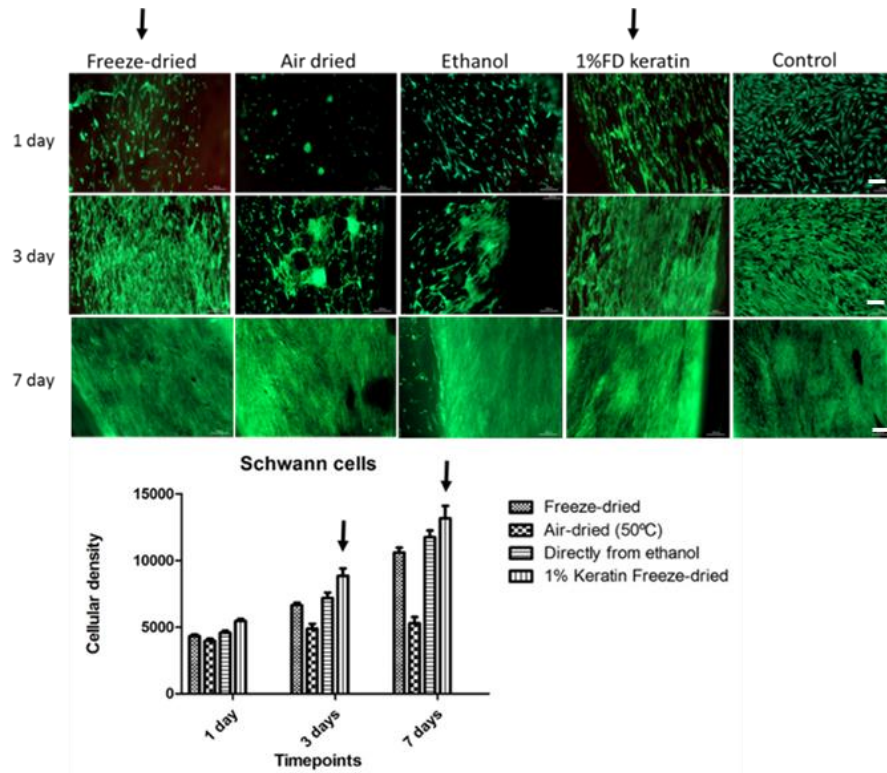


Figure VIII-10 - Schematic representation of a silk conduit when incorporating just 1% of hair keratin in the silk polymeric solution, cellular adhesion increased, which is proved qualitatively by Live/dead assay as well as quantitatively, by Alamar blue assay; (1 % FD Keratin = freeze-dried conduit containing 1 % keratin). Scale bar: 50 μ m.

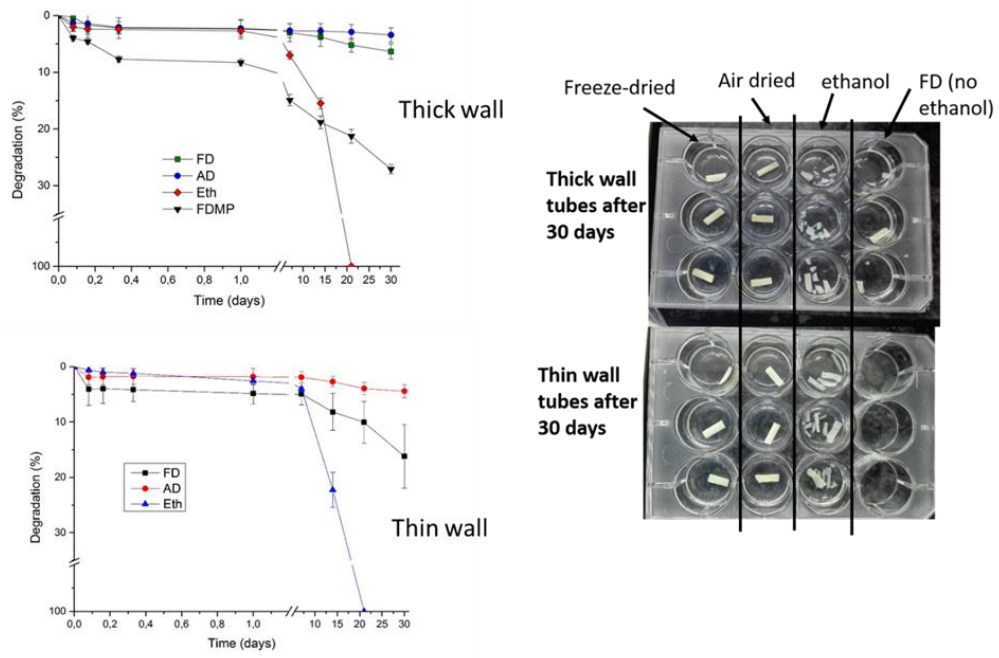


Figure VIII-11 - Schematic representation of the degradation profiles of several silk fibroin conduits formulations in the presence of 0.2 U/mL of protease for 30 days. By varying only the method of drying, weight loss *in vivo* and *in vitro* will be modified; (FD = freeze-dried; AD = air dried at 50 °C; Eth = Directly from ethanol; FDMP= Freeze-dried more porous).

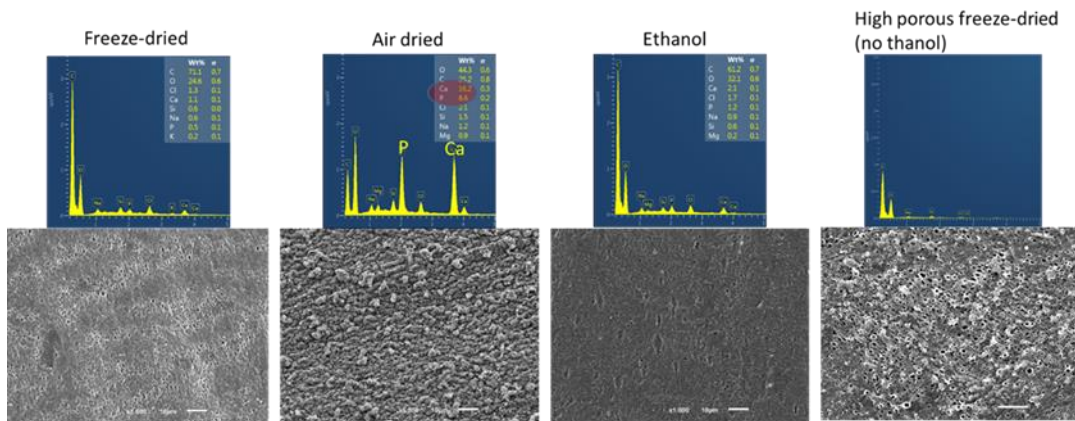


Figure VIII-12 - SEM micrographs and respective EDS spectra of the silk conduits after 30 days in Simulated Body Fluid. Scale bar: 10 μm .

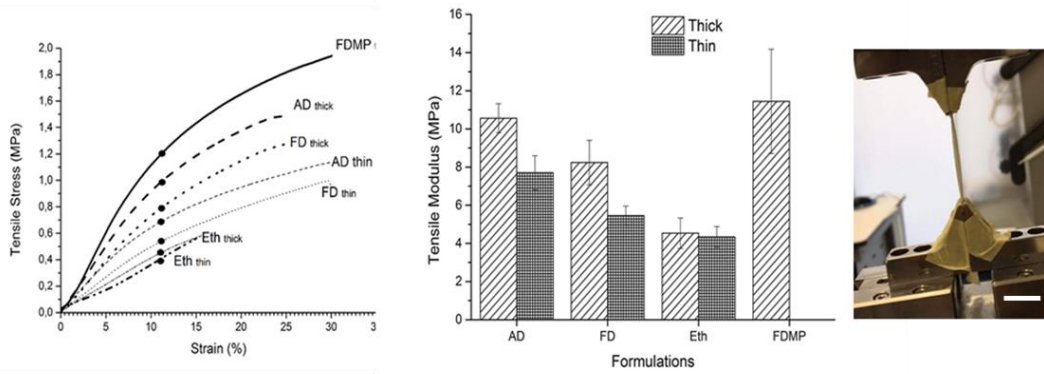


Figure VIII-13 - Schematic representation of mechanical properties of some embodiment of the silk conduits: Tensile stress and Tensile modulus; (FD = freeze dried; AD = air dried at 50 °C; Eth = Directly from ethanol; FDMP= Freeze dried more porous). Scale bar: 1 cm.

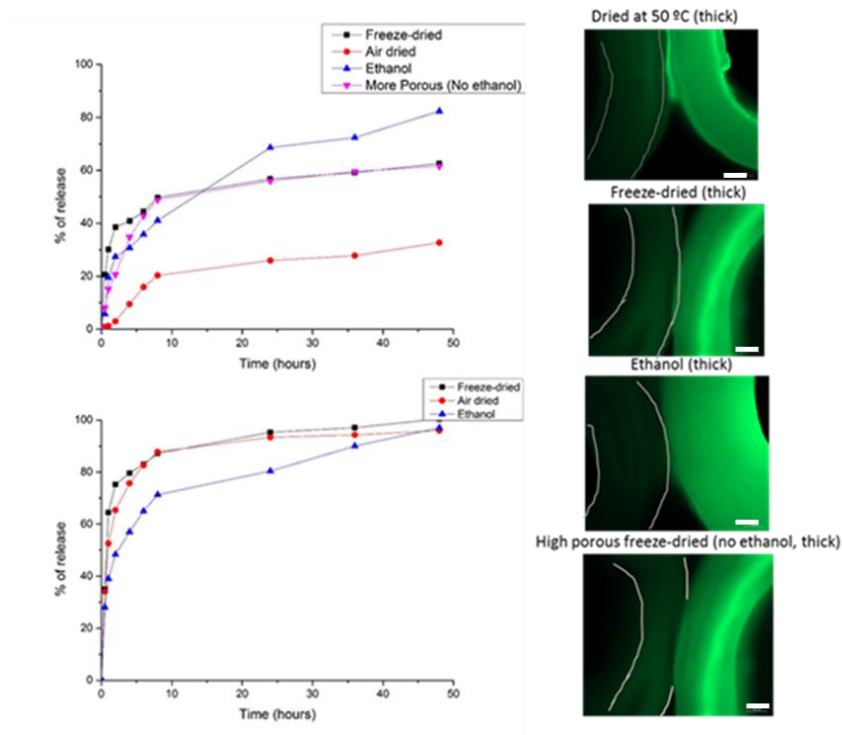


Figure VIII-14 - Differences in the silk fibroin conduits permeability of a 4 kDa molecule due to the method of drying and due to the thickness of the conduit's wall. Scale bar: 1 mm.

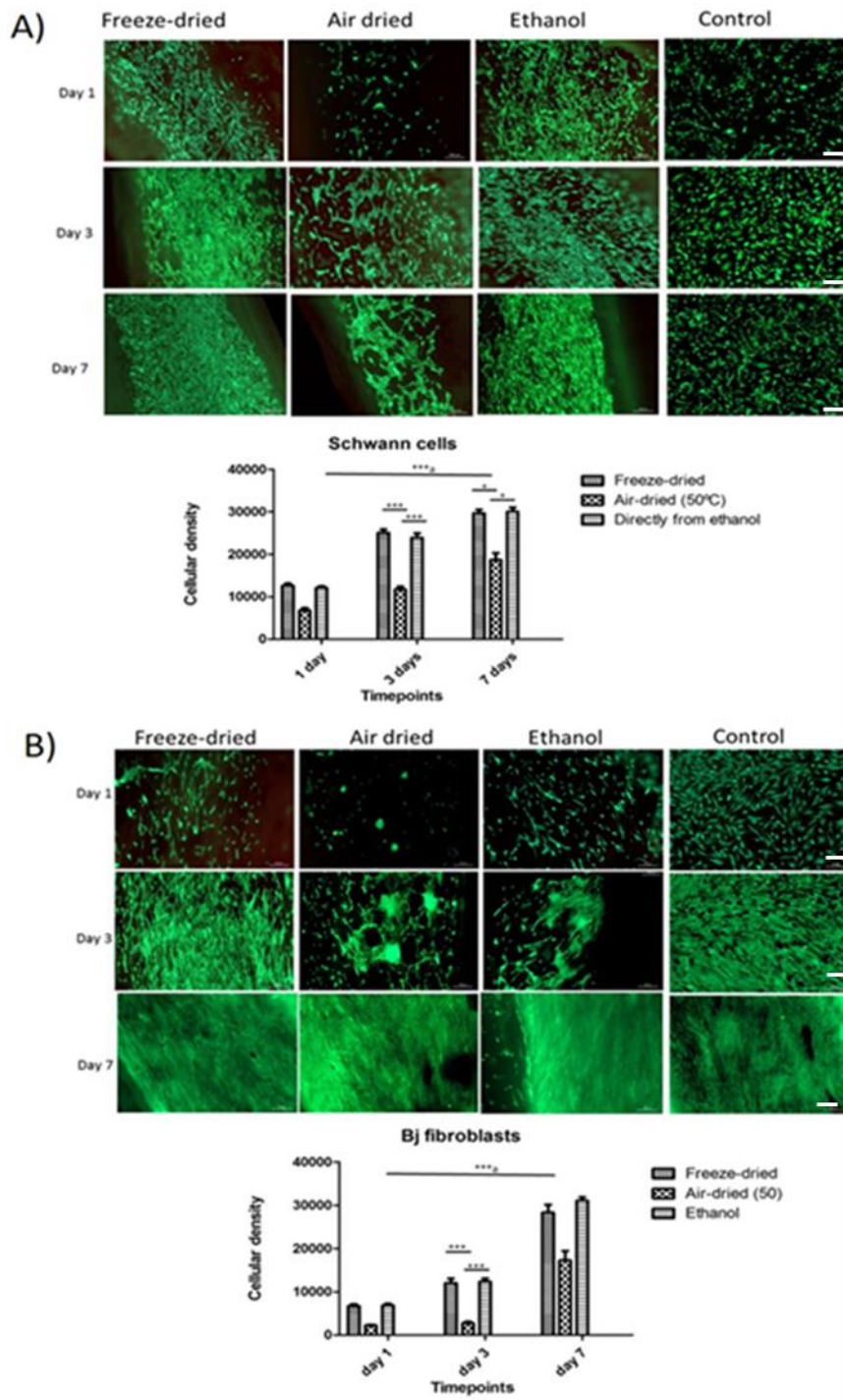


Figure VIII-15 - Schematic representation of: A) Results of Alamar Blue cellular density quantification and Live/dead qualitative assay after Schwann cells were seeded in all formulations of thick wall tubes after 7 days. B) Results of Alamar Blue cellular density quantification and Live/dead qualitative assay after BJ skin fibroblasts were seeded in all formulations of thick wall tubes after 7 days. Scale bar: 50 μ m.

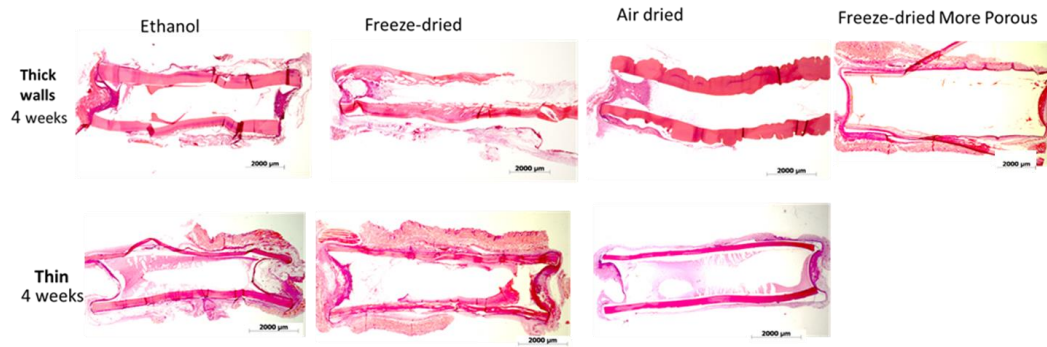


Figure VIII-16 - Schematic representation of: Longitudinal view of thick and thin wall conduits after 4 weeks *in vivo* subcutaneous implantation in mice. Scale bar: 2000 μm.

Chapter IX

Tunable enzymatically crosslinked silk fibroin tubular conduits for guided tissue regeneration

Tunable enzymatically cross-linked silk fibroin tubular conduits for guided tissue regeneration¹

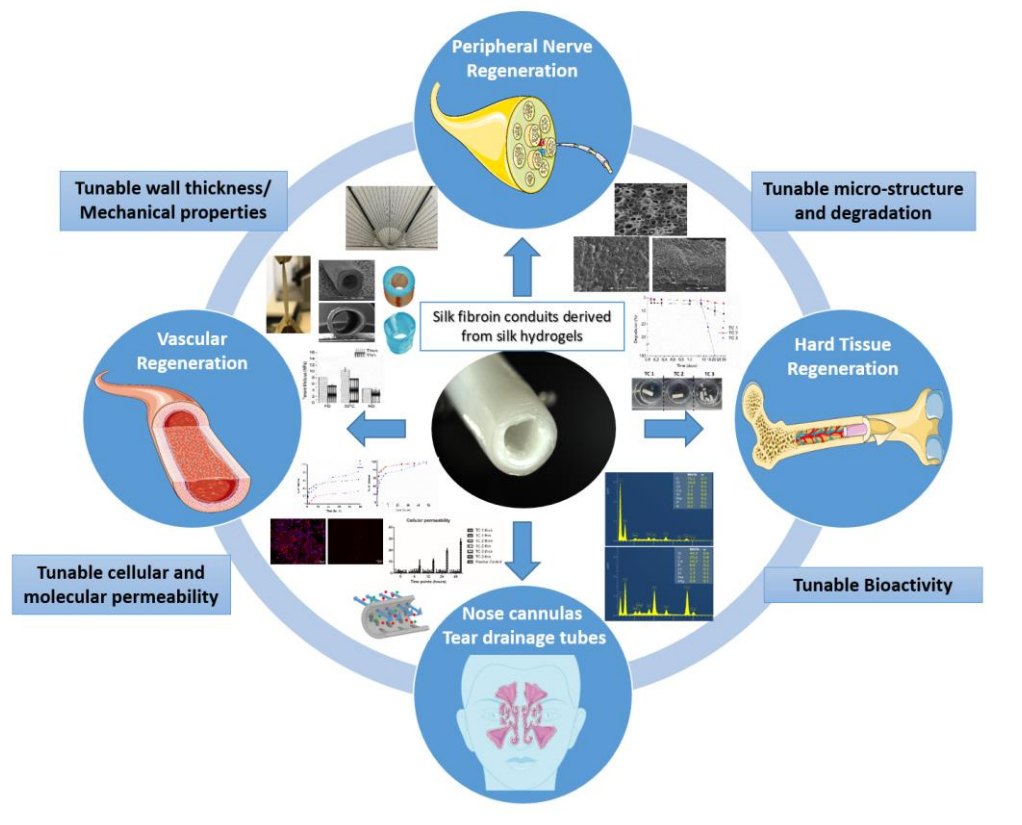
ABSTRACT

Hollow tubular conduits (TCs) with tunable architecture and biological properties are in great need for modulating cells functions and drug delivery in guided tissue regeneration. Herein, a new methodology to produce enzymatically-crosslinked silk fibroin TCs is described, which takes advantage of the tyrosine groups present in the structure of silk fibroin that are known to form a covalently-crosslinked hydrogel. Three different processing methods were used as a final step to modulate the properties of the silk-based TCs. This approach allows to virtually adjust any characteristic of the final TCs. The final microstructure ranged from a non-porous to a highly porous network, allowing the TCs to be selectively porous to 4 kDa molecules, but not to human skin fibroblasts. Mechanical properties were dependent both on the processing method and thickness of the TCs. Bioactivity was observed after 30 days of immersion in Simulated Body Fluid only for the TCs submitted to a drying processing method (50 °C). The *in vivo* study performed in mice demonstrated the good biocompatibility of the TCs. The results demonstrate that the enzymatically-crosslinked silk fibroin TCs are highly versatile and have adjustable characteristics that can be exploited in a variety of biomedical applications, particularly in guidance of peripheral nerve regeneration

Keywords: Tubular conduits, silk fibroin, enzymatic crosslink

¹This chapter is based on the following publication: [Carvalho CR, Costa JB, Morais AS, López-Cebal R, Silva-Correia J, Reis RL and Oliveira JM. Tunable Enzymatically Cross-linked Silk Fibroin Tubular Conduits for Guided Tissue Regeneration. Advanced Healthcare Materials. 2018. e1800186. doi: 10.1002](#)

IX-1. GRAPHICAL ABSTRACT



IX-2. INTRODUCTION

The development of tubular conduits (TCs) in the biomedical field is in rapid expansion due to the growing medical need for viable supports that can aid in the guidance of soft and hard tissues regeneration (1).

Soft tissue regeneration includes, among others, vascular regeneration (2) and peripheral nerve regeneration (PNR) (3). For PNR tissue regeneration, there is currently a significant clinical need for the development of an alternative substitute to autologous grafts, especially in terms of small diameter conduits. Indeed, no clinically viable small-diameter grafts, synthetic or natural, have been successfully developed so far (4), at least to a point where the outcomes are better than autografts. Although some biomaterials and techniques have demonstrated promising results, they usually have some type of drawback associated, as for example, the use of harsh reagents, lack of size precision or inadequate

mechanics (5). The preferred treatment for complete nerve transections is end-to-end repair. However, the suture must be done without creating excessive tension in the nerve ends. When the nerve gap length makes end-to-end suture unfeasible, peripheral nerve grafts are the gold standard treatment for nerve restoration. However, the limited availability of autografts, as well as the immunological drawbacks of allografts and xenografts, forced the researchers to investigate and develop other approaches (6).

Hard tissue regeneration includes bone or ligament-to-bone tissue regeneration. In the latter, a graded material system exhibiting a gradual transition from non-mineralized tissue (*e.g.*, tendon or ligament) to mineralized tissue (*e.g.*, bone) is necessary, which is extremely difficult to achieve (7). Thus, several soft-to-hard tissues would benefit from advances in the field of TCs development and fine-tuning, including the central nervous system (8), tendon (9), tracheas (10), and ureters (11). Currently, there is a lack of biomanufacturing approaches that can produce reproducible TCs with the desired characteristics for a specific application (12). In the particular case of PNR, customized TCs that can offer guidance for the regenerating axons, while the influence of external cellular and humoral factors is minimized would be the ideal solution for tackling short- and long-gap nerve defects. In this way, the effect of the elements that stimulate regeneration and normally occur at the injury site will be fully preserved, and even strengthened (13). However, up-to-date there are no engineered TCs that can outperform the fallouts obtained by autografts and provide fully sensory and motor recovery (14).

Various “bridging” strategies for peripheral nerve gaps have been explored in the last years. Engineered TCs rely on the use of both synthetic and natural-origin materials processed using different fabrication techniques (15). Synthetic materials are still considered very promising. Most of the FDA-approved nerve guidance conduits are composed of materials such as polyglycolic acid (PGA), polylactic-co-glycolic (PLGA), and polycaprolactone (PCL) (16).

Among the natural-based biomaterials, polysaccharides such as chitosan (17) and alginates (18) are have been considered as TCs. Still among the natural-origin biomaterials, extracellular matrix (ECM) endogenous proteins such as collagen (19), fibrin (20), laminin (21) and hyaluronic acid (22) have been highly investigated, both alone or in formulations. Recently, other proteins such as silk fibroin (SF) (23) or keratin (24) have also attracted great deal of attention.

Interestingly, SF obtained from *Bombyx mori* (silk worm) can be regarded as an exceptional biomaterial, which has historically been greatly recognized for its strength, both in textile and surgical

suture applications (25). Large-scale worldwide cultivation of silkworms makes this natural polymer extremely abundant. Therefore, it can be obtained daily at a reasonable cost, which is an important factor for technology transfer, as sustainability is a crucial issue that engineers face with every product or process (26). According to the literature, silk-based tubular structures have been produced using four main methods: mold casting (27), dipping (28), electrospinning (29) and membrane rolling (30). The mold casting or dipping methods, followed by demolding through freeze-drying, results in very brittle conduits, although with a good shape, with poor mechanical properties, especially in terms of compression and tensile strength. The conduits prepared by electrospinning, despite presenting appropriate tensile strength, are easily crushed, and consequently become flat. In addition, harsh organic and halogenated solvents are usually involved in their processing (31). The conduits produced by membrane rolling display low reproducibility and their large-scale fabrication is extremely time-consuming.

Due to the shortcomings shown by the conventional methodologies, it was hypothesized to produce tunable silk fibroin-based TCs using an enzymatically-mediated crosslinking method. Our research group (32) as well as others (33), have been previously exploiting the presence of tyrosine groups in silk to obtain enzymatically-crosslinked hydrogels, by using horseradish peroxidase (HRP) as enzyme and hydrogen peroxide (H_2O_2) as substrate. By means of using the HRP/ H_2O_2 crosslinking method, the initially produced aqueous silk solution can be rapidly transformed into an amorphous and transparent hydrogel with superior stability (34), which can undergo conformational changes under specific conditions. Therefore, the potential of the developed work to produce innovative TCs is based on this recently developed class of enzymatically-crosslinked silk fibroin hydrogels. Our strategy to develop tube-shape scaffolds with customized properties relies solely on using different final processing steps, which include different methods of solvent extraction and the use of molds with diverse diameters of the inner cylinder. The TCs developed following these processing methods can be modulated in virtually any of its intrinsic characteristics, which cannot be achieved using the previously described conventional methodologies. By altering the final processing method for production of the conduits, different surface properties can be achieved, in a way that TCs with the same composition can display surface characteristics adequate either for soft or hard tissue engineering. Despite being possible the application of such TCs in several applications, due to the versatility of the processing method and easy tunability, we mainly envision its use in PNR, where functional recovery after peripheral nerve injury (PNI) is still a significant clinical challenge faced today (35).

This study presents for the first time an innovative and reliable methodology to reproducibly produce highly tunable silk fibroin conduits intended for clinical use and guide tissue regeneration, particularly for PNR. By simply altering the final processing method applied, we were able to modify the surface properties of the developed TCs and obtain different conduits that can be either used for soft or hard tissue regeneration. Silk-based TCs were obtained from enzymatically-crosslinked silk hydrogel using three different final processing methods: freeze-drying, oven drying and no drying. The microstructure of the developed TCs was carefully assessed by using stereomicroscopy and scanning electron microscopy (SEM), revealing a porosity that may vary from non-porous to highly porous TCs. This methodology allowed producing TCs with varying mechanical properties, kinking resistance and suturability. Accordingly, the *in vitro* assays exposed variable results in terms of degradation and swelling, as well as selective biomineralization, subsequent to the different processing methods used. Regarding TCs' molecular and cellular permeability, results demonstrate the ability of the conduits to deliver and exchange molecules, although being impermeable to scar tissue-forming fibroblasts, being at the same time an appropriate substrate material for Schwann cells proliferation. An *in vivo* subcutaneous assay was performed in CD-1 Albino mice to evaluate the TCs biocompatibility. The results showed a normative host response and revealed well-tolerated, integrated and vascularized implants.

The methodology and TCs presented herein provide not only a very promising alternative to already developed TCs intended for nerve regeneration, but also opens the door for further investigation in many other fields, where tubulization strategies are required.

IX-3. EXPERIMENTAL SECTION

IX-3.1. Materials

Bombyx mori cocoons were supplied by the Portuguese Association of Parents and Friends of Mentally Disabled Citizens (APPACDM, Castelo Branco, Portugal). Other materials and reagents were purchased from Sigma–Aldrich (St Louis, MO, USA), unless mentioned otherwise.

IX-3.2. SF Purification

The purified silk fibroin (SF) was prepared as previously described by Yan *et al.* [32a] Briefly, SF was first separated from the other main protein present in the cocoons, sericin. For this purpose, the cocoons were immersed in a 0.02 M boiling sodium carbonate solution for 1 hour, followed by rinsing with abundant distilled water [61]. The obtained SF was then immersed in a 9.3 M lithium bromide solution at 70 °C until its complete dissolution (1 hour) and dialyzed (benzoylated dialysis tubing, MWCO: 2 kDa) against distilled water during 48 hours to remove impurities. The purified SF was concentrated against a 20 %wt. poly(ethylene glycol) solution for at least 6 hours, and the final concentration was determined by weighting the dry product after a sample of this solution was left at 70 °C overnight. Meanwhile, the rest of the SF solution was stored at 4 °C until further use, for a maximum of 5 days.

IX-3.3. Preparation of SF Conduits

SF solution was diluted to 16 wt.% with distilled water, after which it was mixed with horseradish peroxidase solution (HRP type VI, 0.84 mg/mL, 100 μ L) and hydrogen peroxide solution (H_2O_2 , 0.36 wt.%, 65 μ L; Panreac, Barcelona, Spain) [32a]. The previous mixture was then injected within the space between two concentric cylinder molds, where the outer cylinder had a constant diameter of 4 mm. Meanwhile, variations in the diameter of the inner cylinder, 2 mm and 3 mm, lead to thick-wall-conduits and thin-wall-conduits, respectively. The outer mold was made of polypropylene, whereas the inner mold was a brass cylinder. The system was incubated at 37 °C in order to induce gelation for the period of 30 minutes. After gelation, a quick immersion in liquid nitrogen is needed to remove the outer mold, followed by an immersion in ethanol to induce permanent β -sheet conformation and to remove the inner mold. The obtained hollow tubes were subjected to three different final processing steps [37], which gave origin to three different conduits: (1) freeze-dried after freezing at -80 °C (TC 1), (2) dried in an oven at 50 °C for 3 days (TC 2) and (3) kept in a permanent hydrated state (TC 3), as specified in **Table IX-1**.

IX-3.4. Structure Evaluation by Stereomicroscope

The developed TCs were examined under the Stereo Microscope + Lamp (Schott KL 200, model Stemi 1000, Zeiss, Germany) for a macroscopic inspection.

IX-3.5. Micro-computed tomography

The 3D reconstruction of the developed silk TCs was performed using a high-resolution Micro-CT Skyscan 1072 scanner (Skyscan, Kontich, Belgium) with a pixel size of 10 μm . Data sets were reconstructed using standardized cone-beam reconstruction software (NRecon v1.4.3, SkyScan). Representative dataset of the slices was segmented into binary images with a dynamic threshold of 22-40 (grey values). Then, the binary images were used for morphometric analysis (CT Analyser, v1.5.1.5, SkyScan) and to build the three-dimensional models (ANT 3D creator, v2.4, SkyScan).

IX-3.6. Microstructure evaluation by scanning electron microscopy (SEM)

The silk fibroin TCs were sputter coated with gold, prior the analysis of surface morphology and microstructure by SEM (model S360, Leica, Cambridge, England).

IX-3.7. Fourier transform infrared (FTIR) spectroscopy

The chemical composition and conformation of the TCs were analyzed by FTIR spectroscopy under an attenuated total reflectance (ATR) model (IRPrestige-21, Shimadzu, Japan). All spectra were obtained between 4600 cm^{-1} and 800 cm^{-1} , at a 4 cm^{-1} resolution for an average of 50 scans.

IX-3.8. Mechanical properties

The mechanical properties of SF conduits were studied with a universal mechanical testing machine (Instron model 5540, USA), according to the ASTM C749-08 standard method. A load cell of 1kn was used. All the samples were fixed in each extremity by using a grip. A cross-head speed of 2 mm/min was employed and the samples were stressed until enough force was applied to trigger their rupture. Strain-stress curves were obtained from each experiment. The initial linear region of stress-

strain curves was used to determine the Tensile Young's Modulus by the tangent method. Five hydrated samples with 3 cm of length were tested per condition.

Kinking tests were done with 3 cm length conduits by bending them up to 50 ° in a metallic flexible 0.5 mm wire and assessing macroscopically the bending point.

The suturability was assessed by means of inserting a 4 - 0 suture at the place where peripheral nerve suturing would be performed, which is 2 mm from the end of the conduit, considering its long axis and strain to the rupture point.

IX-3.9. *In vitro* weight loss and water uptake profiles

The weight loss of the TCs was evaluated by an enzymatic degradation assay. For this purpose, the conduits were immersed in PBS and kept at 37 °C for 24 hours, to reach the maximum swelling. Then, filter paper was used to remove the excess of liquid prior to initial weighing (m_i). The conduits were then immersed in 5 mL of PBS containing protease XIV solution (0.2 U/mL), which was changed every 24 hours. After 0.08 (2 hours), 0.16 (4 hours), 0.33 (8 hours), 1, 3, 7, 14, 21 and 30 days, the specimens were removed, the excess of liquid eliminated, and final mass determined (m_f). The weight loss ratio was determined using **Equation IX-1**:

Equation IX-1 - Equation for the determination of percentage of water uptake

$$\text{Water uptake (\%)} = \frac{m_w - m_i}{m_i} \times 100$$

For the assessment of the water uptake profile, dry samples of TC 1 and TC 2 were weighed (m_i) and immersed in PBS at 37 °C during the same intervals mentioned in the weight loss assay. For TC 3, m_i was considered right after the sample was removed from ethanol. The specimens were removed from the solution and weighted (m_w) after eliminating the excess of liquid with paper. Water uptake ratio was determined by using **Equation IX-2**:

Equation IX-2 - Equation for the determination of percentage of weight loss

$$\text{Weight loss (\%)} = \frac{m_i - m_f}{m_i} \times 100$$

Three replicates of each sample were measured, and the average values were considered.

IX-3.10. Bioactivity test in Simulated Body Fluid (SBF)

For the *in vitro* bioactivity tests, an acellular SBF (1.0x) was prepared as described elsewhere [62]. The SBF contains the same ions as human blood plasma, at nearly equal concentrations. Silk conduits with 14 mm of length were immersed in freshly prepared SBF for 1, 15 and 30 days at 37 °C. Upon removal, the samples were rinsed with distilled water and left to dry at RT. Finally, the presence/absence of a calcium-phosphate layer on their surface was determined using SEM/EDS, at an accelerated voltage of 15 kV. Before SEM analysis the membranes were gold-coated at 6 mA, by using a Hitachi coater.

IX-3.11. *In vitro* molecular permeability assay

In order to assess the molecular permeability of the SF conduits walls, an assay based on the fluorometric properties of fluorescein isothiocyanate–dextran (FITC-labeled Dextran, 4 kDa) molecule was designed. More specifically, conduits of 14 mm in length were immersed in a PBS solution for 24 hours to reach the maximum swelling, and then the excess of liquid was rapidly removed with filter paper. Each conduit was filled with 10 µL of FITC-labeled Dextran solution (1 mg/mL in PBS) and both conduit ends were sealed. Each loaded conduit was kept in individual vials with 1 mL of PBS at 37 °C for up to 48 hours. Aliquots of 300 µL were withdrawn from the vial at predetermined time periods and replenished by fresh PBS. The amount of FITC-labeled Dextran that got to the PBS release medium after crossing the conduit wall was determined with the help of a microplate reader (FL 600, Bio-Tek Instruments, USA) at a 520 nm emission wavelength (480 nm excitation wavelength), and independent calibration curves. A total of 5 replicates per condition were studied. Data is presented as average ± standard deviation of the cumulative percentage of dextran release.

IX-3.12. Cell culture of immortalized human Schwann cells and immortalized human skin fibroblasts (BJ)

Immortalized Schwann cells (iSCs, sNF96.2, ATCC) were used in passage 11 and cultured at 37 °C and 5 % CO₂ in High Glucose Dulbecco's Modified Eagle's Medium (DMEM) supplemented with 10 % (v/v) fetal bovine serum (FBS), 1 % (v/v) penicillin/streptomycin and 1 % (v/v) sodium pyruvate, in non-coated cell culture flasks. BJ fibroblasts (BJ, CRL-2522, ATCC) were used in passage 9 and incubated

in Eagle's Minimum Essential Medium (EMEM), supplemented with 10 % (v/v) FBS and 1 % (v/v) penicillin/streptomycin and 1 % (v/v) sodium pyruvate at 37 °C and 5% CO₂. For both cell types, cellular expansion medium was exchanged every 2 - 3 days.

IX-3.13. Cellular direct seeding in SF conduits and quantitative and qualitative viability evaluations

For cellular seeding, conduits with 14 mm of length were cut longitudinally and used in halves. Both cell types were separately seeded in the internal and concave surface of the dry conduits, at a density of 1×10^4 cells/conduit. The quantitative viability of iSC and BJ fibroblasts was followed with Alamar Blue (AB), a dye that yields a fluorescent signal when incubated with metabolically-active cells. After 1, 3 and 7 days in culture, specific cell culture medium containing 20 % (v/v) AB was added to the different culture wells. The system was incubated for 4 hours, after which fluorescence was monitored at 590 nm emission wavelength (excitation wavelength 530 nm), using a microplate reader (FL 600, Bio-Tek Instruments). PBS was used to remove the excess of AB reagent and fresh culture medium was added in its place after each AB determination.

Cell viability was calculated in terms of cell number per conduit and time point. A calibration curve relating the fluorescence values to a specific cellular density was performed for each cell type. Normalization with the mean fluorescence value obtained for the controls was also performed (using tissue culture polystyrene; TCPs), with and without cells.

The qualitative evaluation of viability of iSC and BJ fibroblasts within silk conduits was followed with a Live/Dead assay, at the time points described previously. Briefly, cell-laden conduits were washed three times with PBS and incubated for 30 minutes, at 37 °C in the dark with Calcein AM (1 μ M) and propidium iodide (PI, 1.5 μ M). Before observation, the samples were washed with PBS to eliminate excessive background. Samples were imaged using a transmitted and reflected light microscope (Axio Imager Z1m, Zeiss, Jena, Germany).

IX-3.14. *In vitro* cellular permeability assay (using a modified Boyden chamber)

A cell migration assay was designed to verify the cellular permeability of the SF conduits to BJ fibroblasts, using HTS Corning FluoroBlok™ Cell Culture Inserts (24 well) with an 8 μ m pore size (Becton Dickinson, USA). For direct cellular seeding, conduits with 4 mm in length were cut

longitudinally (to fit the insert) and used in halves. First, BJ fibroblasts were pre-labelled with Cell Tracker Red (Invitrogen, CA, USA) for 30 minutes (5 mM), and then seeded directly in the internal and concave surface of the conduit (cell density: 8×10^3 cells/conduit). Briefly, Cell Tracker probes freely pass through cell membranes and once inside the cell they are transformed into cell-impermeable reaction products well retained in living cells through several generations, but not transferred to adjacent cells in a population.

Cellular adhesion was allowed to occur in a normal non-adherent 24 well plate for 3 hours, using a serum free medium. Cell-laden constructs were then moved to the upper chamber of the HTS Corning FluoroBlok Cell Culture Inserts, making sure the external and convex surface of the conduit was in contact with the insert surface. In the upper chamber where the construct was placed, MEM serum-free medium was added (500 μ L). In the lower chamber, MEM medium supplemented with 40 % (v/v) FBS was added (500 μ l), in order to serve as a chemoattractant gradient. As a positive control, the same cellular density was directly seeded in the upper chamber. At different time points (0, 6, 24 and 48 hours), fluorescence intensity from the bottom (basal side) was measured using a microplate spectrofluorometer (FL 600, Bio-Tek Instruments) in area-scan bottom-reading mode, at excitation/emission wavelengths of 553/570 nm. Results are presented as the increment in fluorescence values (RFU) in relation to the time point 0 hours (when cell-laden constructs were put in the FluoroBlok Cell Culture Inserts). Fluorescence images of cells that migrated through the conduit wall were collected using an inverted fluorescence microscope (model TCS SP8, Leica, Germany). After the last time point (48 hours), cells that migrated through the conduit wall were fixed with formalin (10 % (v/v)) (Sigma, Germany) and stained with phalloidin (Molecular Probes, Invitrogen, USA) and 4,6-diamidino-2-phenylindole dilactate (DAPI blue, Molecular Probes), following suppliers' protocol. To evaluate if cells were viable and capable of migrating throughout the assay, the cells in the conduit were subjected to Calcein AM staining after the last time point (48 hours).

IX-3.15. *In vivo* implantation of SF conduits

In order to evaluate the biocompatibility of the SF conduits, as well as their general behavior *in vivo*, conduits with 14 mm in length were subcutaneously implanted in mice. The maintenance and study of animals were carried out in accordance to the Ethics Committee of University of Minho and approved by the Portuguese Licensing Authority (DGV-DSSPA). Six 5-weeks old mice Hsd:ICR (CD-1®)

with an average weight of 25-30 g (Charles River Laboratories, Massachusetts, USA) were used in this study. Each mouse was anesthetized by intraperitoneal injection of ketamine (25 mg/kg) and medetomidine (0.15 mL/kg) for anesthesia; cephalexin (15 mg/kg) as antibiotic; and bupivacaine, pethidine (5-10 mg/kg) as analgesic. removed at the implantation area by shaving, followed by disinfection with iodine. In each mouse, two skin incisions (1 cm length) were made in the dorsal midline, one close from the head (CH) and the other far from the head (FH). Afterwards, sterile conduits were implanted subcutaneously into the four different positioned pockets and then the skin was sutured. Four replicates of each condition (thick and thin TC 1, TC 2 and TC 3) were implanted. Four- and eight-weeks post-surgery, the mice were euthanized by injection of overdose of pentobarbital sodium. The implanted materials, together with the surrounding tissue, were then retrieved. For histological analysis, the explants were fixed with 10 % (v/v) formalin solution (Sigma-Aldrich, Germany) for at least 2 days at RT, dehydrated through increasing series of ethanol concentrations (from 30 % up to 100 % (v/v)) and transferred to histological cassettes for immersion in paraffin. Samples were then serially sectioned using a microtome (5 μ m thick) for hematoxylin & eosin (H&E) staining.

IX-3.16. Statistical analyses

All the numerical results (mechanical analysis and molecular permeability assay) were presented as mean \pm standard deviation. At least 3 specimens were used in each condition. For biological assays (quantitative and qualitative viability evaluation and *in vitro* cellular permeability assay), three independent experiments were performed, and three samples were analyzed per group in each culturing time. Statistical analysis was performed using the GraphPad Prism 5.0 (GraphPad Software, La Jolla, CA, USA). First, a Shapiro-Wilk test was used to ascertain about the data normality. Subsequently, a Kruskal-Wallis test was performed followed by Dunn's multiple comparison test, where the significance level was set to $p < 0.05$. For the analysis of Tensile Modulus results, a Two-tailed Mann Whitney Test was used ($p < 0.05$).

IX-4. RESULTS AND DISCUSSION

IX-4.1. Production of TCs using an enzymatically cross-linking approach

The application of tubulization approaches in the field of tissue regeneration are based on the biomedical implantation of engineered conduits for repairing defects, which are able to mimic important biological features, of both soft and hard tissues (36). The production parameters of TCs must be carefully regulated and controlled, in order to engineer reproducible tubes with specific relevant properties. The strategy presented herein takes advantage of the presence of 5 mol% tyrosine groups in silk fibroin, which can be covalently crosslinked throughout a peroxidase/hydrogen peroxide-mediated reaction to obtain elastomeric, optically transparent and biocompatible hydrogels. These hydrogels are in reality a middle step of fundamental importance, as they will lead to stronger and more stable three-dimensional networks when compared to conventional methods (34). The HRP-mediated covalent crosslink leads to a stronger and more stable three-dimensional network, thus conferring superior mechanical properties and elasticity to the final conduit, when compared to the tubes in amorphous conformation. Therefore, to produce the conduits, a SF solution was diluted to 16 wt.%, after which it was mixed with HRP and H₂O₂. The previous blend was then introduced within the space between two concentric cylinder molds, with different diameters, leading to the formation of thick-wall-conduits and thin-wall-conduits. The system was posteriorly incubated at 37 °C for 30 minutes to achieve the gelation of the solution. After hydrogel crosslinking, a temporary β -sheet is induced with liquid nitrogen, which gives rise to a permanent semi-crystalline structure and facilitates the removal from the outer mold. Afterwards, the conduits were immersed in ethanol to induce permanent β -sheet conformation and remove the inner mold. Although most of the research published so far mentions the use of methanol to induce such conformational change in the SF structure, this is a toxic and harmful substance for the nervous system and thus should be avoided (31). As final stage of the processing, the obtained hollow tubes were subjected to three different methodologies (37), namely: (1) freeze-drying after freezing at -80 °C (TC 1), (2) drying in an oven at 50 °C for 3 days (TC 2), and (3) kept in a permanent hydrated state without ever extracting the solvent (TC 3), as specified in **Table IX-1**. A scheme representing the above-mentioned steps is shown in **Figure IX-1**.

Table IX-1 - Silk fibroin conduits according to the processing method used as final step. The table presents the nomenclature utilized to designate the different TCs studied during this work.

| Processing method | Designation of the TC |
|--|-----------------------|
| Freeze-drying after freezing at -80 °C | TC 1 |
| Drying in oven at 50 °C | TC 2 |
| Kept in permanent hydrated state (no drying) | TC 3 |

IX-4.2. Macro- and micro-structure of the TCs

For assessing the macro- and micro-structure of TCs, stereomicroscopy and SEM techniques were used (**Figure IX-2**). In **Figure IX-2A** and **IX-2B**, it is possible to observe the macrostructure of the thick and thin wall conduits, with a wall thickness of $\approx 700 \mu\text{m}$ and $\approx 200 \mu\text{m}$, respectively. For this specific evaluation, the TC 3 was left to dry at room temperature (RT) prior analysis. One of the advantages of the hydrogel formation as an intermediate step in the preparation of the silk-based TCs is that the thickness of the walls remains constant and is only dependent on the dimensions of the molds utilized for the conduits preparation. Accordingly, the method used for conduit drying did not modified the wall thickness.

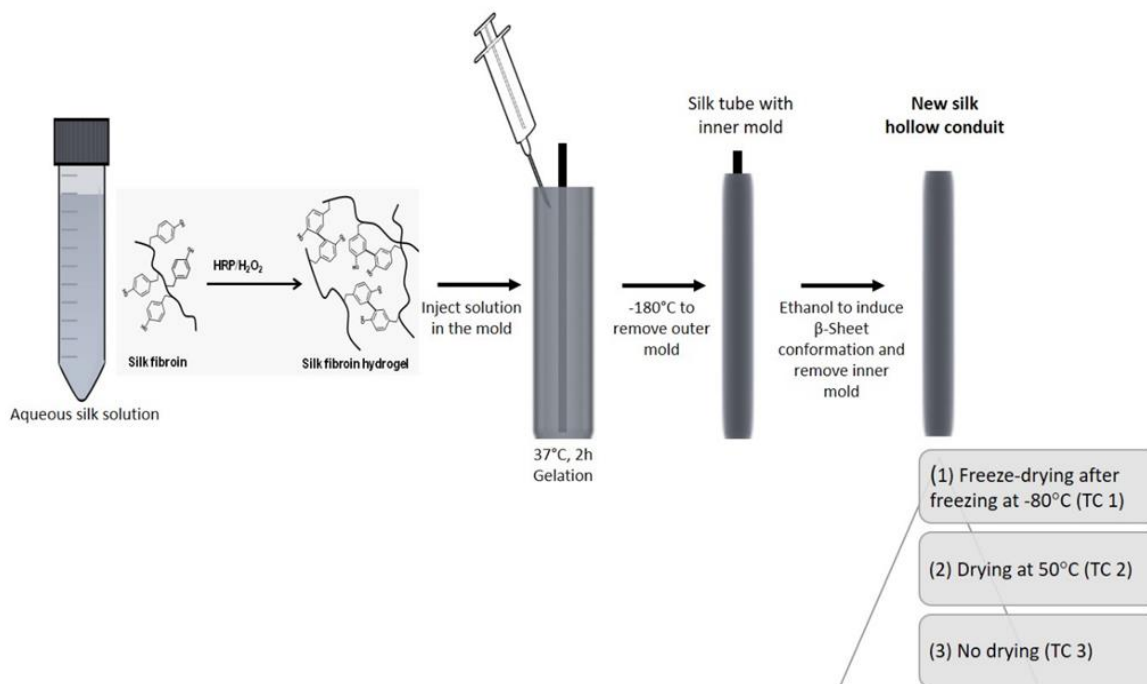


Figure IX-1 - Scheme of the steps involved in the methodology developed to produce silk fibroin TCs. An intermediate step mediated by enzymatic crosslink allows to obtain a silk fibroin hydrogel inside the mold. As a final step, three different processing methods were explored: freeze-drying after freezing at -80 °C (TC 1), drying in an oven at 50 °C (TC 2) or simply leaving them in a hydrated state without ever extracting the solvent (TC 3).

This is one of the advantages over a simple mold casting technique, where different wall thicknesses are obtained with different methods of drying (38). With the dipping technique, it is even harder to maintain a reproducible wall thickness, since in each immersion a random amount of polymer sticks to the mold.

In **Figure IX-2C**, the microstructure of the thick TCs is presented. The thick TC 1 displayed a porous morphology, with pores in the exterior wall between 5-6 μm , whereas smaller ($\approx 1 \mu\text{m}$) pores were observed in the interior wall (**Supplementary Figure IX-1**). The SEM images of the cross-section of the thick conduits also revealed some degree of porosity. This is an important property, since the level of porosity will influence nutrients and waste exchange. The thick TC 2 is essentially non-porous, as it can be observed in **Figure IX-2C**. Since the TC 3 was never in a dried state, the SEM analysis became impracticable. A similar pattern of porosity was observed for the thin conduits (data not shown).

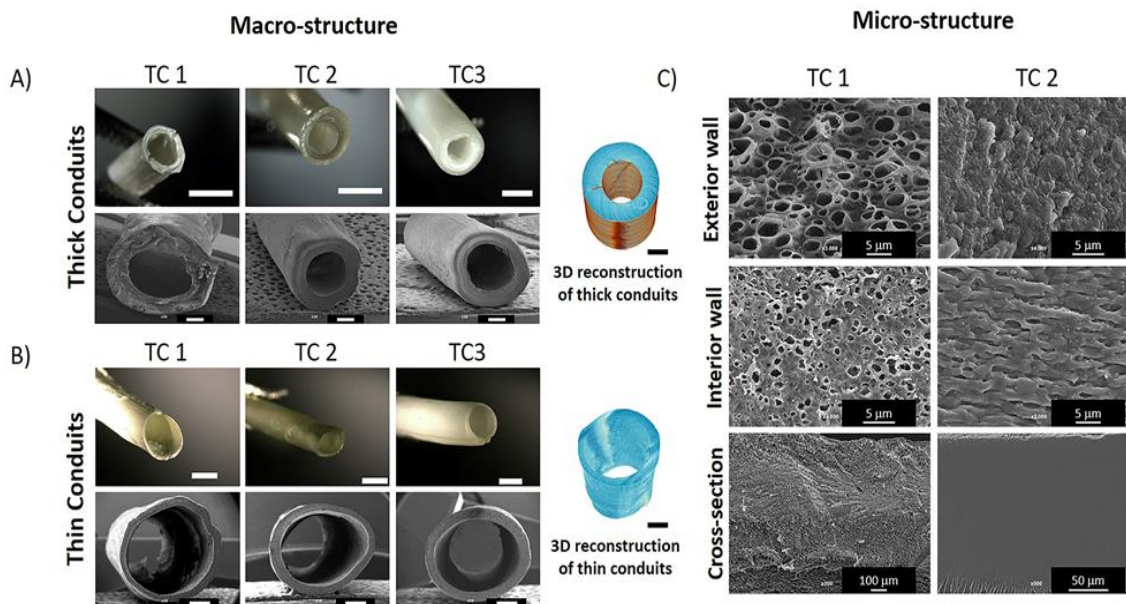


Figure IX-2 - Macro and microphotographs of the developed silk conduits. A and B) Macrophotographs taken by stereomicroscopy (top) and SEM microphotographs (bottom) of the thick and thin silk conduits, respectively. At right, micro-CT reconstruction of the conduits. For thickness comparison, the TC 3 was left to dry at room temperature (RT). C) Representative SEM microphotographs corresponding to the external, internal and cross-section microstructure of the thick conduits (TC 1 and TC 2). The TC 3 was not suitable for SEM microstructure evaluation. Scale bar: A and B) 2 mm (top), 500 μm (bottom). Micro-CT 3D reconstruction: 1 mm.

In PNR, a balance must be achieved between an adequate wall porosity to minimize the outward diffusion of growth factors and the need to prevent scar tissue infiltration. More specifically, it is known that larger pores allow the permeation of non-neural cells into the conduit lumen. These cells will promote the excessive formation of fibrous tissue, which will ultimately impair nerve regeneration (39). In the case of PNR, the optimal pores size ranging from 5-20 μm (40). Also, high porosity is an important feature of a vascular prosthesis, as it should allow early fixation of the graft and fibrous organization of the intima (41).

For PNR, it should also be taken into consideration that the porosity plays an increasingly important role as the nerve gap increases, since oxygen and nutrients cannot diffuse through long distances between the ends of the conduits, and the penetration of micro blood vessels will be needed to supply these elements (39). In this work, the freezing temperatures were raised (0 $^{\circ}\text{C}$ followed by -20 $^{\circ}\text{C}$) in order to obtain higher porosity of the TCs. The observation of the microstructure after freeze-drying have shown TCs with greater pores (10-15 μm) and superior interconnectivity (**Supplementary Figure IX-2**).

IX-4.3. Chemical structure of the TCs

Regarding the chemical structure, a β -sheet conformation is related to both semi-crystalline state and low water solubility. The conformation of the developed conduits was evaluated by ATR-FTIR. Although the intermediate structure in the form of hydrogel is characterized by an amorphous state, all final TCs displayed the same strong absorbance peaks at 1627 cm^{-1} and 1520 cm^{-1} , characteristic of a β -sheet conformation (amide I and II band) (42). Also, the appearance of an additional shoulder is perceptible at 1262 cm^{-1} , which corresponds to the amide III band (**Supplementary Figure IX-3**), (38) confirming a successful transition from amorphous to crystalline state.

IX-4.4. Mechanical properties of the TCs

Mechanical properties are of extreme importance for the success of any biomaterial to be applied in tissue regeneration (43). In the case of PNR, it has been established for over two decades that mechanical properties are an imperative regulator of axonal regeneration and elongation (44). In their mission to conduct action potentials, nerves have to endure mechanical loads exerted by the surrounding musculoskeletal system (45). Peripheral nerves are under strong tensile loads and experience $\approx 12\%$ of mechanical strains when they are in resting positions (46).

Indeed, it is known that a TC for nerve regeneration must be able to not only bear, but also to elongate under this specific strain. All TCs were previously incubated in PBS at $37\text{ }^{\circ}\text{C}$, to mimic physiologic conditions. Regarding the thick TCs, a Tensile Stress of 0.8 ± 0.05 , 1 ± 0.04 , and 0.3 ± 0.03 MPa was required to achieve 12% of strain for TC 1, TC 2 and TC 3, respectively (**Figure IX-3A**). Slightly lower values were necessary in the case of thin conduits, where TC 1, TC 2 and TC 3 required 0.5 ± 0.03 , 0.7 ± 0.04 and 0.3 ± 0.02 MPa, respectively (**Figure IX-3B**). These values indicate that the TC 2 displayed the higher resistance to the applied load. **Figure IX-3C** displays the Tensile Modulus, *i.e.* the ability to withstand changes in length when submitted to lengthwise tension, of all the studied TCs. The method used to produce TC 2 enables to obtain the stiffest conduits (10.5 ± 0.7 MPa and 7.7 ± 0.8 MPa, for the thick and thin TCs, respectively), whereas less rigid conduits are attained with the methodology used to produce TC 3 (4.5 ± 0.8 MPa and 4.3 ± 0.5 MPa, for the thick and thin TCs, respectively). In fact, statistically significant differences were found between the Tensile Modulus values of TC 2 and TC 3, both for thick and thin conduits. Intermediate stiffness values were observed for TC 1 (8.2 ± 1.2 MPa and 5.5 ± 0.5 MPa, for the thick and thin TCs, respectively). However, no statistically

significant differences were observed between TC 1 and the other two TCs. The thickness of the walls influenced the mechanical properties of TC 1 and TC 2, with values of Tensile Modulus statistically higher for the thick wall conduits, as compared to the thin wall tubes. **Supplementary Figure IX-4** shows the apparatus used for universal mechanical testing machine.

It has been pointed out that nerve guidance conduits should not outperform peripheral nerve in terms of mechanical properties, at least not in a large scale (47), since it will cause a loss of elastic continuity between the nerve guide and the growing tissue itself (48). Accordingly, the values obtained for the mechanical properties of the silk-based conduits were similar to the ones reported in the literature for porcine peroneal and tibial nerves (≈ 7 MPa) (49, 50).

An engineered conduit must hold structural integrity and stability when a surgeon manipulates and grafts it. More specifically, the resistance of the TCs to sutures is of capital importance when grafting purposes are considered. Suturability tests showed that the developed TCs can withstand a suture thread being pulled in and out of them, thus indicating its appropriateness in terms of suturability.

Since TCs are often placed near flexible body parts such as knees, hips or fingers, it is clinically relevant that they resist to lumen occlusion when subjected to bending forces. Collagen tubes developed by Yoshii *et al.* (51) were shown to lack adequate kinking resistance, as these tubes collapsed after implantation in a rat sciatic nerve defect. The kinking resistance of the silk-based thick and thin TCs was verified by bending to 50° , as it can be seen in **Figure IX-3D** and **IX-3E**, respectively. As the FDA-approved conduit NeuraGen[®] occludes its lumen after bending to 50° (52), the silk-based conduits were tested after bending to this angle for comparison with a relevant clinical example. The thick TCs curved 50° when forced to, without any occlusion of the lumen, and recovered their original diameter when the force has ceased to be exerted. On other hand, thin wall conduits tend to kink, occluding the lumen as the wires are bended up to 50° . The results demonstrate that the kinking resistance of the TCs is highly dependent on wall thickness and is not related to the method of drying.

IX-4.5. Physico-chemical *in vitro* characterization of the TCs

The degradation of the thick and thin wall TCs was evaluated *in vitro* by weight loss analysis, performed in an enzymatic solution containing protease XIV. The potential of protease XIV to cleave silk at multiple and non-discriminated places has been previously reported (53, 54). Overall, a similar degradation profile for the thick and thin conduits was observed (**Figure IX-4A** and **IX-4B**). For both types

of conduits, the TC 3 degraded completely after 21 days, but started to lose its integrity after only 7 days ($6.9 \pm 0.7 \%$ and $4.0 \pm 0.3 \%$ for thick and thin conduits, respectively). On the other hand, the results demonstrated that TC 2 produced the more stable TCs, with a weight loss of about $3.4 \pm 1.3 \%$ and $4.4 \pm 1.2 \%$ for the thick and thin conduits, respectively, by the end of the assay (30 days). These values were doubled in the case of the TC 1, with a weight loss of $6.3 \pm 1.3 \%$ and $12.2 \pm 5.8 \%$ for the thick and thin conduits, respectively, by the end of the assay. After 30 days in a proteolytic solution, the effect of degradation on the silk-based TCs can also be observed macroscopically (**Supplementary Figure IX-5A and IX-S5B**). TC 1 and TC 2 remained with thin and fragile walls, but the integrity of the conduits was maintained both for thick and thin conduits. Unlike the previous methods, thick and thin TC 3 disintegrated into fragments, which represents a hindrance for *in vivo* implantation.

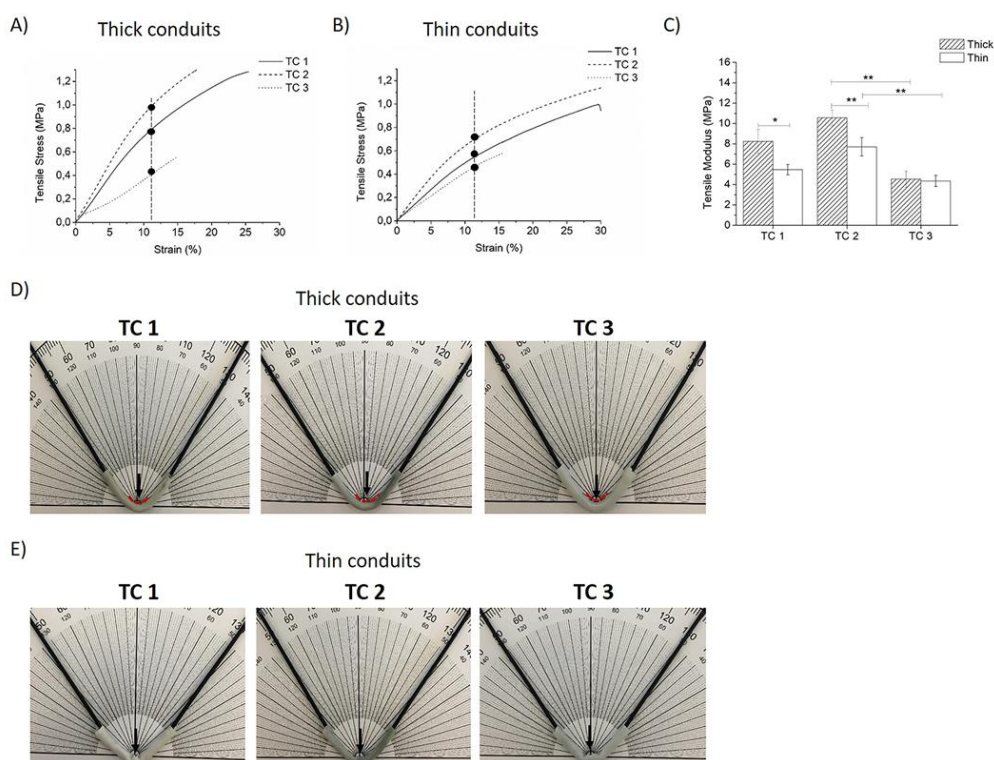


Figure IX-3 - Mechanical properties and kinking resistance of the developed silk-based conduits. A and B) Strain (%) as a function of Tensile Stress (MPa) applied in thick and thin conduits. C) Tensile Modulus of thin and thick conduits, according to the methodology (TC 1, TC 2 and TC 3). Quantitative data is presented as mean \pm sd (n=5), where *p < 0.05, **p < 0.01. D and E) Kinking tests performed on thick and thin conduits after bending to 50°. Thick conduit revealed to resist bending, with no occlusion of the lumen at this degree, whereas thin conduits did not resist, showing occlusion of the lumen.

The water uptake profile is an important parameter when envisioning the use of TCs in PNR, since an excessive swelling can block the nerve growth and trigger an inflammatory response (47) The water uptake profile of the conduits is presented in **Figure XI-4C** and **IX-4D**. The thick wall conduits presented a slightly higher percentage of swelling. The TC 3 reached a swelling rate of 28.0 ± 2.0 % and 28.0 ± 4.3 % for the thick and thin wall conduits, respectively, after 1 hour, when they were moved from ethanol to phosphate buffered saline (PBS) solution. It is hypothesized that when the conduits are immersed in ethanol, molecules become ordered and tight together, since ethanol causes crystalline structures' formation and tightens the polymer structure, turning it more hydrophobic. However, many amorphous groups are still present in the β -sheet crystalline conformation of silk. When moved to PBS or water, the H₂O molecules will interact mainly with the amorphous unordered regions that are still present in the polymer, since these are more hydrophilic, which promotes an overall swelling of the material.(32)

The TC 1 displayed the higher swelling ratio of all the conditions tested, which can be related to their porosity and ability to uptake water molecules. A swelling ratio of 166.0 ± 7.6 % and 123.0 ± 2.9 % was observed for the thick and thin wall conduits, respectively, after 30 days in PBS. The TC 2 presented an intermediate swelling behavior, with values of 128.0 ± 21.0 % and 115.0 ± 9.1 % for the thick and thin wall conduits, respectively, at the end of the assay (30 days). The TC 3 presented the lowest degree of swelling, with values of 28.0 ± 2.0 % and 28.0 ± 4.3 % for the thick and thin TCs, respectively. Despite the relatively high swelling ratios verified for the TC 1, the swelling does not occur towards the lumen of the conduit, as can be seen in **Supplementary Figure IX-5C** and **IX-5D**. This means that there is no risk of occlusion for the regenerating tissue that grows inside the conduit.

It is crucial that an engineered nerve conduit does not calcify once implanted. The apatite-forming ability of the developed conduits was evaluated *in vitro* by soaking in a Simulated Body Fluid (SBF) solution. In **Figure IX-4E**, the Energy-dispersive spectroscopy (EDS) and SEM images of the thick conduits prepared by different methods is presented. The results showed that the deposition of calcium and phosphorus ions in the surface of thick SF conduits is dependent on the final processing step. After 30 days in solution, only the TC 2 developed an apatite layer (**Figure IX-4E**). Indeed, SEM images showed cauliflower crystals on the surface of the thick TC 2, whereas higher weight percentage of calcium and phosphorus ions were detected by EDS, as compared to the TC 1 and TC 3 (**Table IX-2**). Similar results were obtained for the thin conduits (data not shown). The apatite-forming capacity of the TC 2 is a significant drawback and an exclusion factor considering their application in PNR. However, it

can be considered an advantage if other applications are envisioned, such as hard tissue regeneration, where calcification is desirable. To our knowledge, the ability of mineralization was never achieved in scaffolds with the same composition by simply modifying the processing methods and consequently the surface microstructure. It is noteworthy that this difference in bioactivity can be due to the surface topography and mechanical properties of TC 2 formulation. Indeed, a correlation between biomaterials stiffness and its mineralization ability has been previously described (55).

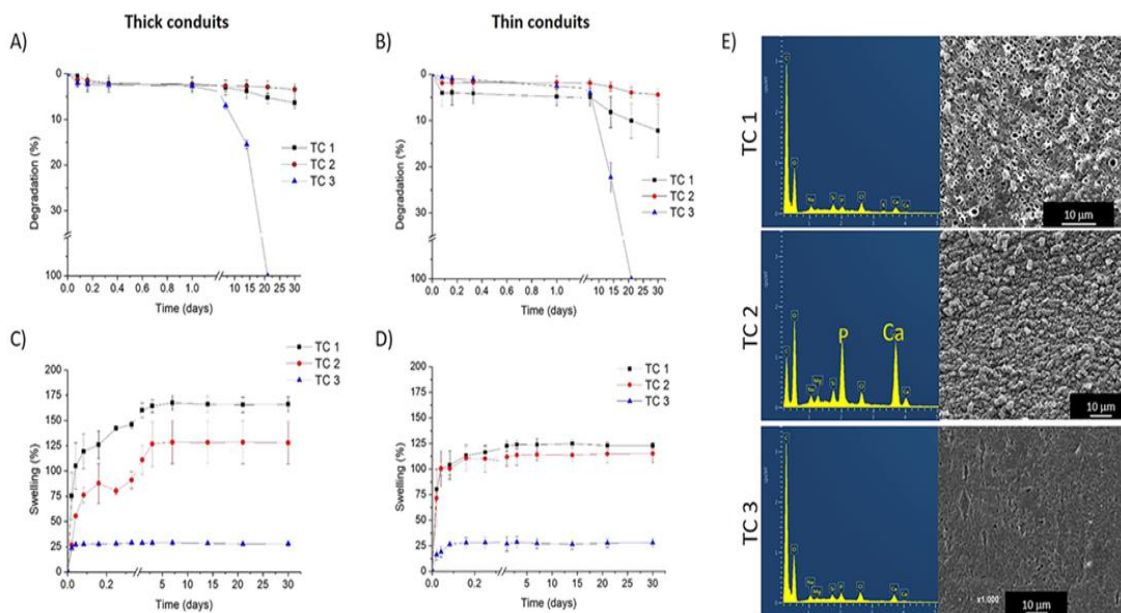


Figure IX-4 - *In vitro* weight loss, water uptake and bioactivity evaluation of the developed silk fibroin-based conduits. A and B) Weight loss of the different thick and thin conduits, respectively, performed by immersion in a PBS protease XIV solution (0.2 U/mL) up to 30 days. C and D) Water uptake profile of the thick and thin conduits, respectively, in a PBS solution up to 30 days. E) Bioactivity assay for the thick silk conduits where results are shown as EDS spectra and SEM microphotographs. The SEM images of the conduits external surface revealed the presence or absence of cauliflower crystals. The results show the absence of an apatite layer in TC 1 and TC 3 but revealed the presence of such crystals in the surface of TC 2. Quantitative data is presented as mean \pm sd (n=3).

Table IX-2 - EDS results revealing the elemental composition and their relative abundance present in the surface of TC 1, TC 2 and TC 3. The bioactivity assay was performed in Simulated Body Fluid. %Wt. stands for percentage by weight and σ stands for standard deviation.

| | TC 1 | | TC 2 | | TC 3 | |
|---|------|----------|------|----------|------|----------|
| | %Wt. | σ | %Wt. | σ | %Wt. | σ |
| C | 71.1 | 0.7 | 25.2 | 0.8 | 61.2 | 0.7 |

| | | | | | | |
|-----------|------|-----|-------------|-----|------|-----|
| O | 24.6 | 0.6 | 44.3 | 0.6 | 32.1 | 0.6 |
| Cl | 1.3 | 0.1 | 2.1 | 0.1 | 1.7 | 0.1 |
| Ca | 1.1 | 0.1 | 16.2 | 0.3 | 2.1 | 0.1 |
| Si | 0.6 | 0.0 | 1.5 | 0.1 | 0.6 | 0.1 |
| Na | 0.6 | 0.1 | 1.2 | 0.1 | 0.9 | 0.1 |
| P | 0.5 | 0.1 | 8.6 | 0.2 | 1.2 | 0.1 |

IX-4.6. Molecular and cellular permeability of the TCs

As previously discussed, the permeability of the conduit wall plays a key role in the regenerative process (56). More specifically, a conduit should be protein permeable but not cell permeable (**Figure IX-5A**). In this sense, molecular and cellular permeability assays of the conduit wall were designed and performed. In **Figure IX-5B** and **IX-5C**, it is possible to observe the cumulative release of FITC-labeled Dextran (4 kDa) from the thick and thin conduits, respectively. The principle behind this assay is that if the wall is permeable to FITC-labeled Dextran, it will also allow the exchange of nutrients (glucose \approx 180 Da) and oxygen. The results showed that the release is highly dependent, not only on the wall thickness, but also on the method of drying. For the thick wall conduits, the permeability reached 82.3 ± 6.5 % in the TC 3 after 48 hours of study. However, these values dropped to 62.6 ± 0.5 % and 32.7 ± 2.6 % for TC 1 and TC 2, respectively. In fact, statistically significant differences can be verified between TC 1 and TC 2 in the first hours of the study (at 0.5, 2, 4, 6 and 8 hours), and between TC 2 and TC 3 at the end of the assay (48 hours). The percentage of release increased dramatically, when the same assay was performed using thin wall conduits. TC 1 and TC 3 reached 100.4 ± 5.7 % and 99.0 ± 3.9 % of release after 48 hours, respectively, whereas TC 2 reached 95.9 ± 5.0 % of FITC-labeled Dextran release. For the thin conduits, no statistically significant differences were observed between the release values of the different TCs. The release values are comparable to those obtained from conduits made of other biomaterials, namely chitosan and silk fibroin conduits (57, 58).

A modified Boyed chamber assay was employed to evaluate cellular permeability, as graphically represented in **Figure IX-5D**. The test was based on the chemotactic properties of fetal bovine serum (FBS). Fibroblasts were selected to perform these studies, since an excessive fibroblast infiltration will

lead to uncontrolled collagen deposition and scar tissue formation (39). For these experiments, the studied conduits were cut in half longitudinally and BJ fibroblasts were seeded in the interior wall and allowed to adhere. Subsequently, the half-sectioned conduits were placed with their exterior wall over a permeable insert. At the same time, the permeable insert served as frontier between two chambers: a superior chamber with culture medium without FBS, and an inferior chamber with culture medium supplemented with 40 % (v/v) FBS (59). The positive control was composed of marked fibroblasts seeded at similar density directly in the insert, without the developed TCs. Half-sectioned TCs without cells served as negative control. Fluorescence quantification (**Figure IX-5E and IX-5F**) and DAPI/phalloidin staining of migrated cells performed after 48 hours (**Figure IX-5G**), revealed that both thick and thin-wall TCs have a cellular impermeable surface, as no fibroblasts were detected in the inferior chamber. Statistically significant differences were observed to the positive control for all the studied TCs. The results were similar regardless of the method of drying, thickness of the wall and elapsed time period. Viable fibroblasts were observed attached to the interior wall of both thick and thin TCs, after 48 hours of culturing (**Supplementary Figure IX-6**). The non-permeability of the developed TCs observed *in vitro*, is expected to be reproduced also *in vivo*, thus avoiding the infiltration of undesirable cells to the regeneration environment.

After the physico-chemical characterization, it can be noticed that TC 3 behaved differently from the TC 1 and TC 2. It all points out to the fact that somehow, not drying the silk materials when they are in a β -sheet conformation affects its core structure. Not only TC 3 had degraded faster, but it was also highly permeable to molecules. Furthermore, it presented lower mechanical properties as compared to the other formulations. This leads the authors to believe that the structure of TC 3 is softer and in some way more fragile as compared to the TC 1 and TC 2.

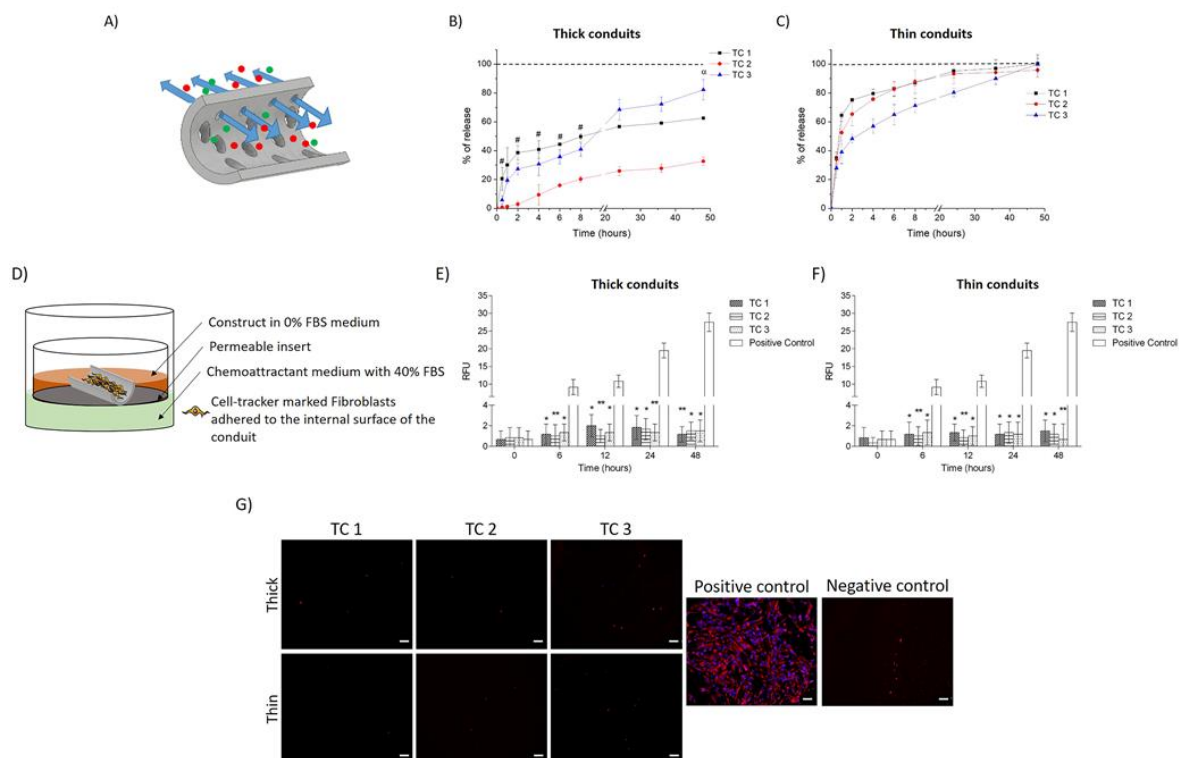


Figure IX-5 - Molecular and cellular permeability evaluation of the developed silk-based conduits. A) Graphical representation of the desirable permeability behavior: the conduit wall should allow molecular exchange but not non-neuronal cellular infiltration; B and C) Cumulative release percentage of FITC-labeled Dextran (4 kDa) across the thick and thin conduit walls, respectively, up to 48 hours of study; D) Graphical representation of the Modified Boyden chamber, where the cell-laden conduits were placed on top of an insert, which was immersed in a 0 % FBS medium. Meanwhile, a 40 % FBS-containing medium acts as a chemo-attractant in the bottom; E and F) Fluorescence quantification of BJ fibroblasts (labelled with Cell Tracker) that were able to migrate through the thick and thin conduits wall, respectively, in the modified Boyden chamber, and comparison with the positive control; G) DAPI/Phalloidin staining performed in the bottom of the chamber reveals that cells were not able to migrate through the conduit wall. Quantitative data is presented as mean \pm sd ((B-C) $n=3$ and (E-F) $n=9$). # indicates significant differences ($p < 0.05$) comparing TC 1 with TC 2; indicates significant differences ($p < 0.05$) comparing TC 2 with TC 3; * and ** indicates significant differences ($p < 0.05$ and $p < 0.01$) comparing to the positive control. Scale bar: 100 μm .

IX-4.7. *In vitro* and *in vivo* biological properties of the TCs

It is also crucial to investigate whether TCs would provide a supportive luminal surface for proliferation of Schwann cells (SC) after an injury, as these cells have key roles in the regeneration process.(60) For this purpose, SC were directly seeded in the interior surface of the studied conduits and their viability was evaluated (**Figure IX-6**). Regarding the thick conduits (**Figure IX-6A**), the TC 1 and TC 3 presented a significantly higher number of cells when compared to the TC 2. This difference was observed after 3 days and 7 days of *in vitro* culturing, but not after 1 day, where statistically significant

differences were verified only between TC 2 and TC 3. Cellular proliferation is progressive along the study, up to 7 days of culturing. Live/Dead staining permitted to qualitatively confirm the previous results. Accordingly, very few live cells were observed in the TC 2 when compared to the TC 1 and TC 3, where a higher number of cells can be clearly detected. In the case of the thin conduits (Figure IX-6B), the results were similar to the ones observed for the thick conduits, where cell number was significantly lower in the TC 2 when compared to others. The fact that fewer live cells can be found in TC 2 can be related to the conduit's surface properties such as surface roughness and surface energy, but further atomic force microscopy and wettability studies should be conducted to further clarify these observations. In tissue engineering applications, it is well known that cellular attachment is favored when cells are presented to rough and porous surfaces (61, 62). Although Schwann cells revealed affinity for both thick and thin conduits, interestingly, a significantly higher cellular density and proliferation was observed in the thin conduits. More specifically, cellular density values in the thin conduits almost doubled the thick ones, being statistically different for all the studied time points and all the methodologies used (Figure IX-6C).

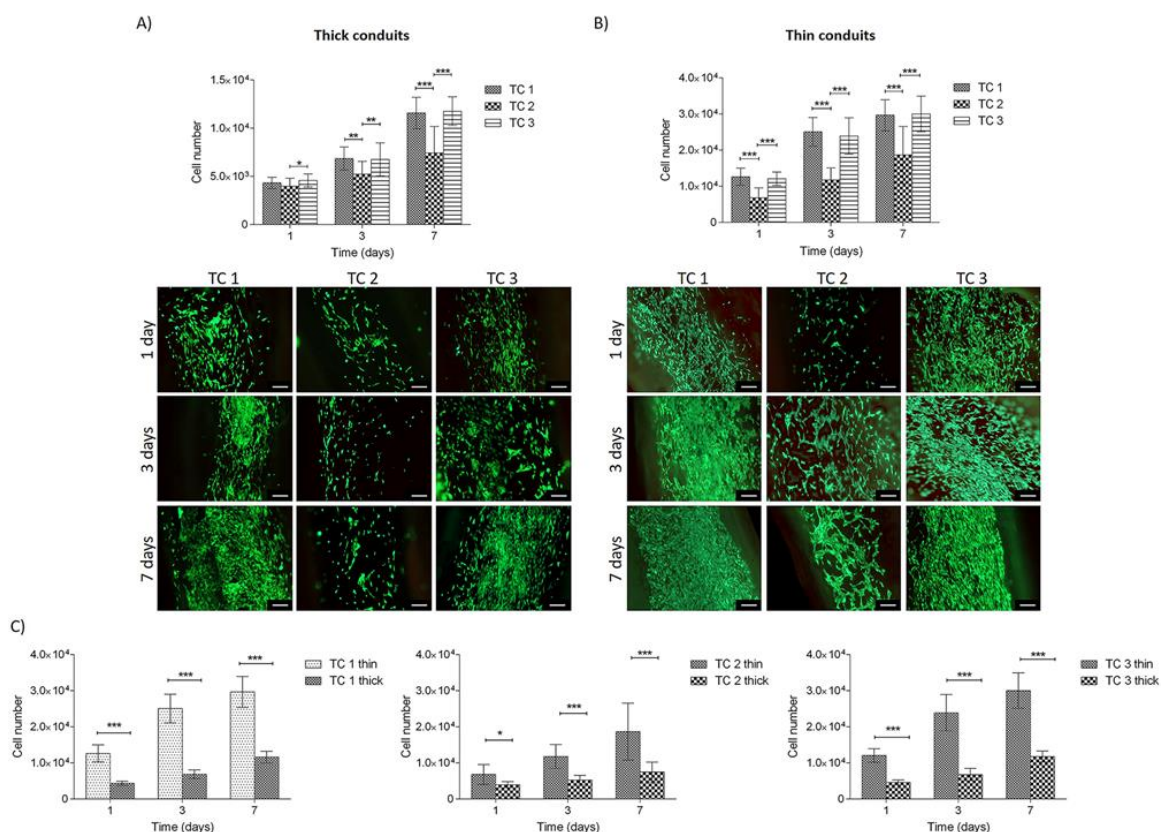


Figure IX-6 - Quantitative and qualitative evaluation of Schwann cells viability when cultured *in vitro* in the surface of the silk-based conduits. A and B) Determination of cell number by Alamar Blue assay in thick and thin conduits, respectively, after 1, 3 and 7 days of culturing (top) and respective Live/Dead staining (bottom). C)

Quantitative determination of the effect of the wall thickness on Schwann cell proliferation, after 1, 3 and 7 days of culturing in the different conduits (TC 1, TC 2, TC 3). Quantitative data is presented as mean \pm sd (n=3), where *p < 0.05, **p < 0.01, ***p < 0.001. Scale bar: 200 μ m.

The biocompatibility of the developed TCs was also evaluated *in vivo* (Figure IX-7), by subcutaneous implantation in Hsd:ICR CD-1 Albino mice. After 4- and 8-weeks post-implantation, the implants were collected, and a macroscopic analysis was then performed. All the TCs conserved their shape, thus confirming the adequate mechanical properties, which prevented them from collapsing under the pressures exerted by the surrounding connective tissue. The maintenance of the shape also indicates that the conduits did not face severe degradation, suggesting their adequacy for long gap PNR, where complete regeneration of the nerve can take several months. Finally, no signs of necrosis or suppuration were observed, thus revealing a good acceptance of the conduits by the host tissue. Indeed, a robust vascularization can be seen around all conduits (Figure IX-7A). Histological observation after hematoxylin-eosin (H&E) staining showed the formation of a thin fibrotic capsule around all TCs in the samples collected 4 weeks after implantation (Figure IX-7B). This fibrotic capsule made of collagen fiber bundles was still present in the samples retrieved 8 weeks after implantation. However, there were no signs of inflammation after 8 weeks, as no multinucleated foreign body giant cells were detected in any of the samples. The *in vivo* studies also permitted to confirm the *in vitro* permeability results, showing no external cell penetration through the TCs walls. Accordingly, the microstructure of all the wall conduits, whether thick or thin, prevented fibroblast infiltration into the lumen, and subsequent fibrotic tissue formation. Indeed, fibrotic tissue formed by fibroblast infiltration is only visible through the conduit ends, up to the place where anastomosis would be made (marked in Figure IX-7B with asterisks). Cell invasion at this point will undoubtedly be beneficial for peripheral nerve regeneration (39). The H&E staining also permitted to confirm the maintenance of the TCs cylindrical shape, as well as the empty luminal space, after 8 weeks of implantation. The mechanical properties of the TCs were suitable to resist the circumferential contraction provoked by the connective tissue formed around the conduits (63). However, the *in vitro* degradation results do not match with the *in vivo*.

The fastest degrading samples *in vitro* were the TC 3. Nevertheless, in the *in vivo* experiments, the TC 3 and TC 2 remained intact. Meanwhile, the TC 1, although it appeared macroscopically intact *in vitro*, showed signs of *in vivo* degradation as depicted in the histological visualization (pointed by the arrows in Figure IX-7B). This is probably related either with the enzyme concentration used *in vitro*, that does not mimic *in vivo* conditions, or with the fact that more enzymes are interplaying *in vivo*, thus leading to a mismatch in the results. Up to date, there is no agreement in which enzymatic

concentration to use, with several published reports using different enzymatic concentrations, more specifically, ranging from 0.001 U/mL to 2U/mL (64-67). However, the concentration of protease XIV in mammals has not been determined yet.

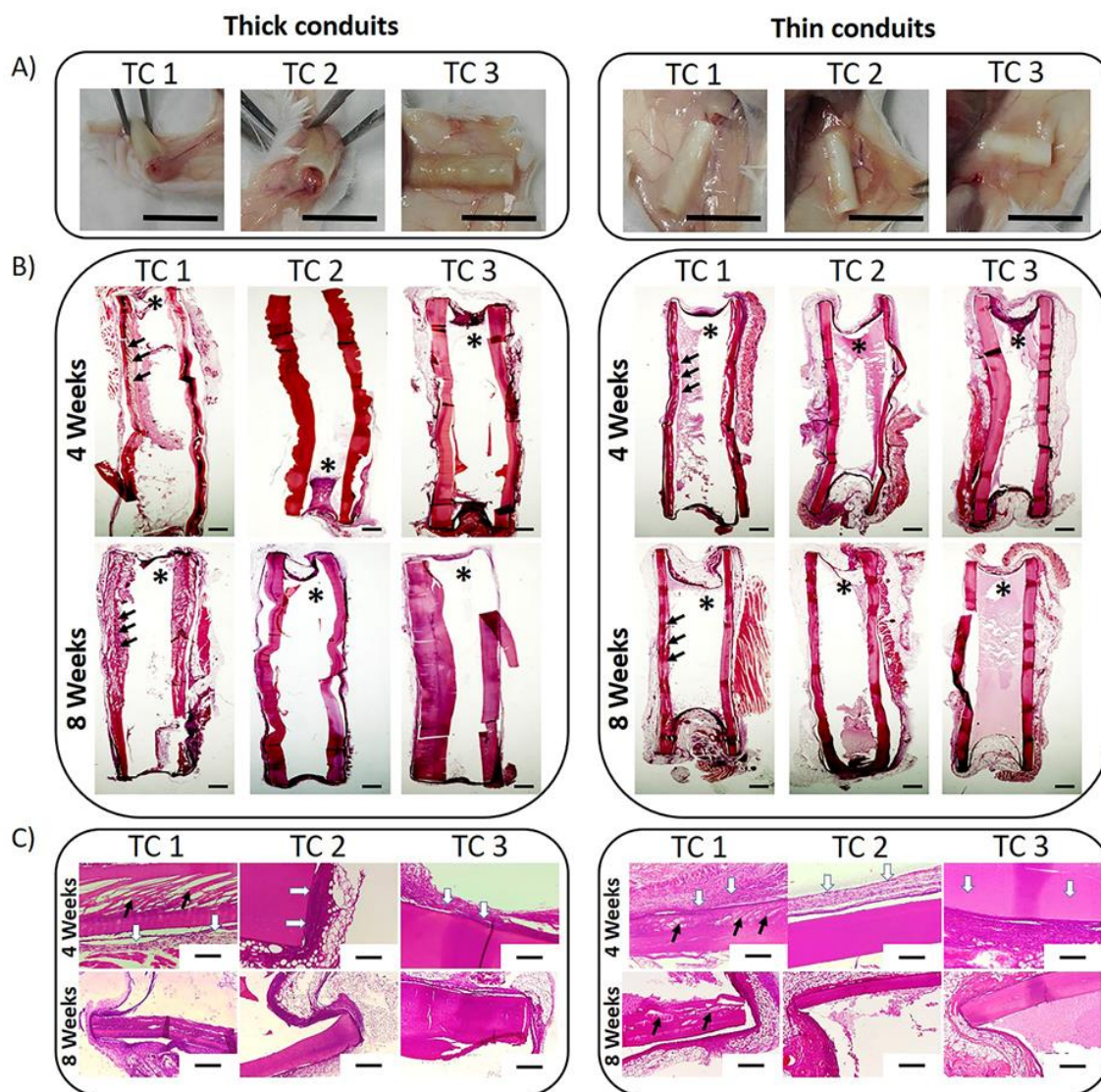


Figure IX-7 - Biocompatibility evaluation for the developed silk-based conduits. The results were obtained after subcutaneous implantation in CD-1 Albino mice. A) Macroscopic aspect of the conduits at the moment of explantation (after 8 weeks), revealing high vascularization and no signs of material rejection. B) H&E-stained longitudinal sections after 4 and 8 weeks of implantation. Asterisks show cellular infiltration only until the point of anastomosis and not through the conduits walls. Black arrows point to fissures verified in the freeze-dried conduits' structure, which reveal the beginning of the degradation process. C) Higher magnification of the H&E-stained longitudinal sections, where black arrows point to fissures in the freeze-dried conduits' structure and white arrows point to the thin fibrotic capsule formed around the conduits. Scale bar: A) 1 cm, B) 1 mm, C) 200 μm (top), 500 μm (bottom).

The *in vivo* results demonstrated that they were well tolerated by the host as observed by the appearing of few immune cells at implantation site.

Additionally, considering this might be an off-the-shelf product used by surgeons and clinicians, the long-term stability of the conduits was evaluated, being the TC 1 and TC 2 kept in a dry vial and the TC 3 stored in ethanol for 6 months. No significant weight loss was observed and the TCs maintained their integrity after 6 months of storage (**Supplementary Figure IX-7**).

Comparing the results to what has been reported in the literature regarding biomaterials science for PNR applications, TC 1 shows the most promising performance for PNR purposes, after both physico-chemical and biological characterization. Not only the bioactivity test, but also the molecular permeability and Schwann cellular viability assays allowed to immediately exclude the formulation TC 2 as a future candidate for further studies. TC 2 intrinsic characteristics are far from the ones desired for a nerve medical device. TC 1 presents poor molecular permeability as compared to TC 2 and TC3. Also, when soaked in SBF, TC 1 induces the deposition of an apatite layer which might lead to the calcification of the implant, which is undesirable in PNR. On the other hand, the conduit must be considered a suitable matrix for Schwann cell adhesion and proliferation, which TC 2 revealed not to be, when compared to TC 1 and TC 3. Finally, the mechanical and degradation assays revealed that TC 3 is the weakest of all formulations, placing TC 1 as the most promising candidate for PNR applications.

Nevertheless, the obtained results also demonstrated that the characteristics of the different developed TCs varied depending on the final processing step applied, as well as the diameter of the inner cylinder used to vary the thickness of the wall. In this sense, minor adjustments in the production method will allow to obtain tuned conduits with different characteristics. Indeed, the TCs produced herein can greatly vary in terms of porosity, degradation and swelling. Also, molecular permeability as well as mechanical properties, cellular adhesion and bioactivity can be easily tuned, making these silk-based conduits exceptionally versatile and with an extended range of possible applications, as can be seen in Figure IX-8.

IX-5. CONCLUSION

In this work, novel silk-based tubular conduits were developed using an enzymatically-crosslinked silk fibroin hydrogel processed by three different methods as a final step. In the first method, the conduits were frozen and consequently freeze-dried after β -sheet conformation induction (TC 1). In the

second and third methodologies, conduits were dried at 50 °C or used directly from ethanol (TC 2 and TC 3, respectively).

That permitted tuning the conduits and obtaining different properties for each one of the formulations. Indeed, these methodologies allowed to obtain extremely versatile TCs by adjusting minor processing parameters, such as the method of drying or the diameter of the inner cylinder that permitted to obtain thick and thin-wall tubes. The TC 2 showed to induce mineralization *in vitro* opening up new application in the treatment of hard tissue defects, while TC 1 and TC 3 revealed higher biological properties, especially when it comes to peripheral nerve regeneration.

The fine-tuned tubular conduits can allow preventing fibroblasts' infiltration and reduce the risk of scar tissue formation *in vivo*, which is advantageous in tissue regeneration. Overall, the proposed enzymatically-crosslinked silk fibroin tubular conduits should have a significant impact in tissue regeneration field (and potentially in clinics) for the treatment of either soft and hard tissue defects, in particular in peripheral nerve guided tissue regeneration, where tubulization techniques are required.

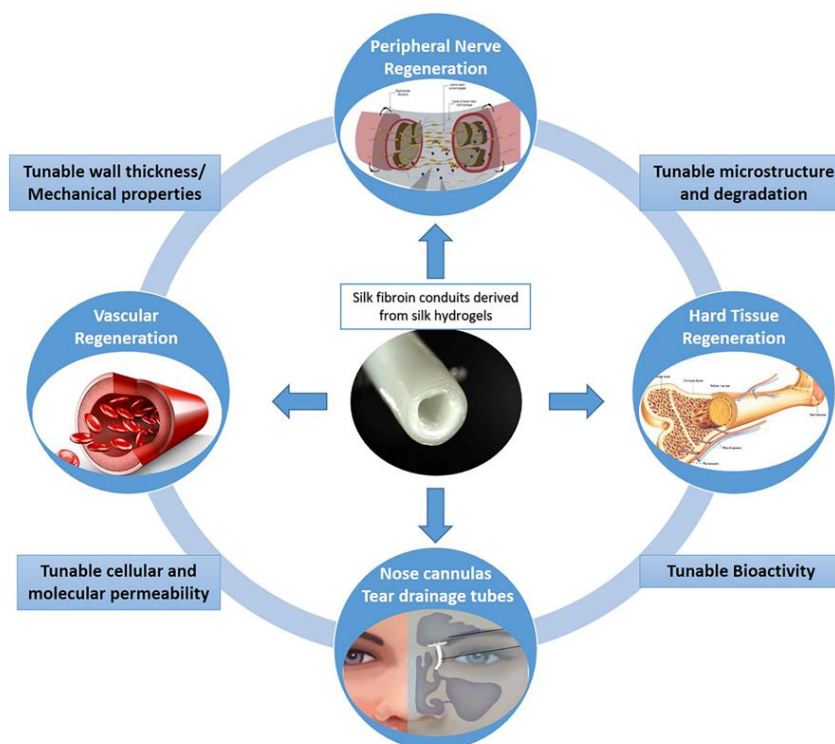


Figure IX-8 - Representative scheme of the easy tunability of the developed silk-based TCs. By simply changing the final processing step or the diameter of the inner mold, conduits with diverse characteristics are obtained. Therefore, apart from peripheral nerve regeneration, these conduits can be envisioned for many other clinical and guided tissue regeneration applications, where tubulization is also required.

IX-6. ACKNOWLEDGMENTS

The authors acknowledge the Portuguese Foundation for Science and Technology (FCT) for the financial support provided to Joaquim M. Oliveira (IF/01285/2015) and Joana Silva-Correia (IF/00115/2015) under the program “Investigador FCT”. Alain da Silva Morais acknowledges ERC-2012-ADG 20120216–321266 (ComplexiTE project) for his Postdoc scholarship.

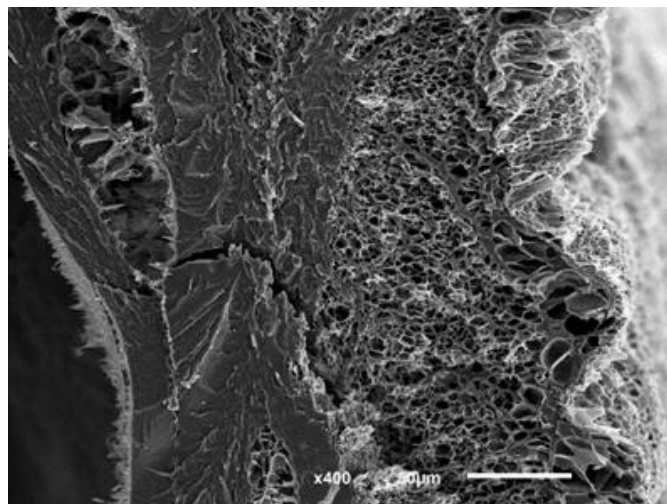
IX-7. REFERENCES

1. Li X, Yang Y, Fan Y, Feng Q, Cui FZ, Watari F. Biocomposites reinforced by fibers or tubes as scaffolds for tissue engineering or regenerative medicine. *Journal of biomedical materials research Part A*. 2014;102(5):1580-94.
2. Jaspan VN, Hines GL. The Current Status of Tissue-Engineered Vascular Grafts. *Cardiology in review*. 2015;23(5):236-9.
3. Konofaos P, Ver Halen JP. Nerve repair by means of tubulization: past, present, future. *Journal of reconstructive microsurgery*. 2013;29(3):149-64.
4. Hiob MA, She S, Muiznieks LD, Weiss AS. Biomaterials and Modifications in the Development of Small-Diameter Vascular Grafts. *ACS Biomaterials Science & Engineering*. 2017;3(5):712-23.
5. Lovett M, Eng G, Kluge JA, Cannizzaro C, Vunjak-Novakovic G, Kaplan DL. Tubular silk scaffolds for small diameter vascular grafts. *Organogenesis*. 2010;6(4):217-24.
6. Arslantunali D, Dursun T, Yucel D, Hasirci N, Hasirci V. Peripheral nerve conduits: technology update. *Medical Devices (Auckland, NZ)*. 2014;7:405-24.
7. Zhang C, Li Q, Tang X, Li J. [RESEARCH PROGRESS OF STRATEGIES TO AUGMENT TENDON-TO-BONE HEALING]. *Zhongguo xiu fu chong jian wai ke za zhi = Zhongguo xiu fu chongjian waike zazhi = Chinese journal of reparative and reconstructive surgery*. 2015;29(7):912-6.
8. Winter CC, Katiyar KS, Hernandez NS, Song YJ, Struzyna LA, Harris JP, et al. Transplantable living scaffolds comprised of micro-tissue engineered aligned astrocyte networks to facilitate central nervous system regeneration. *Acta biomaterialia*. 2016;38(Supplement C):44-58.
9. Caliarì SR, Harley BA. The effect of anisotropic collagen-GAG scaffolds and growth factor supplementation on tendon cell recruitment, alignment, and metabolic activity. *Biomaterials*. 2011;32(23):5330-40.
10. Kojima K, Vacanti CA. Tissue engineering in the trachea. *Anatomical record (Hoboken, NJ : 2007)*. 2014;297(1):44-50.
11. Wang X, Zhang L, Chen Q, Hou Y, Hao Y, Wang C, et al. A Nanostructured Degradable Ureteral Stent Fabricated by Electrospinning for Upper Urinary Tract Reconstruction. *Journal of nanoscience and nanotechnology*. 2015;15(12):9899-904.
12. Widmer MS, Gupta PK, Lu L, Meszlenyi RK, Evans GR, Brandt K, et al. Manufacture of porous biodegradable polymer conduits by an extrusion process for guided tissue regeneration. *Biomaterials*. 1998;19(21):1945-55.
13. Doolabh VB, Hertl MC, Mackinnon SE. The role of conduits in nerve repair: a review. *Reviews in the neurosciences*. 1996;7(1):47-84.
14. Gaudin R, Knipfer C, Henningsen A, Smeets R, Heiland M, Hadlock T. Approaches to Peripheral Nerve Repair: Generations of Biomaterial Conduits Yielding to Replacing Autologous Nerve Grafts in Craniomaxillofacial Surgery. *BioMed Research International*. 2016;2016:18.
15. López-Cebral R, Silva-Correia J, Reis RL, Silva TH, Oliveira JM. Peripheral Nerve Injury: Current Challenges, Conventional Treatment Approaches, and New Trends in Biomaterials-Based Regenerative Strategies. *ACS Biomaterials Science & Engineering*. 2017.
16. Kehoe S, Zhang XF, Boyd D. FDA approved guidance conduits and wraps for peripheral nerve injury: A review of materials and efficacy. *Injury*. 2012;43(5):553-72.
17. Carvalho CR, López-Cebral R, Silva-Correia J, Silva JM, Mano JF, Silva TH, et al. Investigation of cell adhesion in chitosan membranes for peripheral nerve regeneration. *Materials Science and Engineering: C*. 2017;71(Supplement C):1122-34.

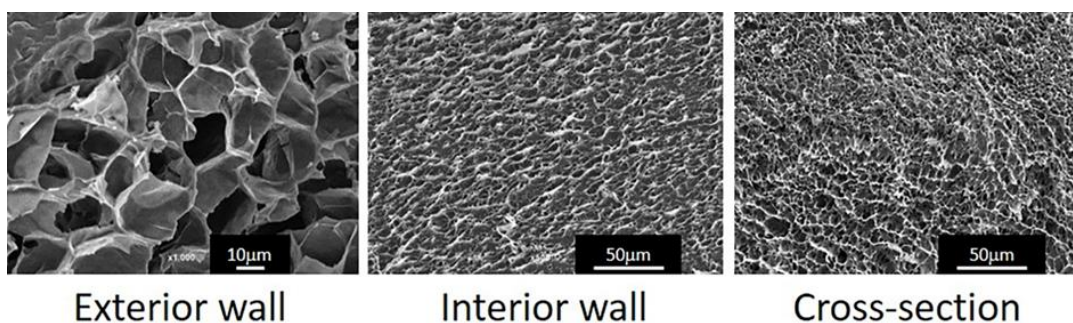
18. Lin SC-Y, Wang Y, Wertheim DF, Coombes AGA. Production and in vitro evaluation of macroporous, cell-encapsulating alginate fibres for nerve repair. *Materials Science and Engineering: C*. 2017;73(Supplement C):653-64.
19. Huang L, Zhu L, Shi X, Xia B, Liu Z, Zhu S, et al. A compound scaffold with uniform longitudinally oriented guidance cues and a porous sheath promotes peripheral nerve regeneration in vivo. *Acta biomaterialia*.
20. Reichenberger MA, Mueller W, Hartmann J, Diehm Y, Lass U, Koellensperger E, et al. ADSCs in a fibrin matrix enhance nerve regeneration after epineural suturing in a rat model. *Microsurgery*. 2016;36(6):491-500.
21. Zhang XF, Liu HX, Ortiz LS, Xiao ZD, Huang NP. Laminin-modified and aligned poly(3-hydroxybutyrate-co-3-hydroxyvalerate)/polyethylene oxide nanofibrous nerve conduits promote peripheral nerve regeneration. *Journal of tissue engineering and regenerative medicine*. 2016.
22. Zor F, Deveci M, Kilic A, Ozdag MF, Kurt B, Sengezer M, et al. Effect of VEGF gene therapy and hyaluronic acid film sheath on peripheral nerve regeneration. *Microsurgery*. 2014;34(3):209-16.
23. Zhao Y, Gong J, Niu C, Wei Z, Shi J, Li G, et al. A new electrospun graphene-silk fibroin composite scaffolds for guiding Schwann cells. *Journal of biomaterials science Polymer edition*. 2017;28(18):2171-85.
24. Pace LA, Plate JF, Mannava S, Barnwell JC, Koman LA, Li Z, et al. A human hair keratin hydrogel scaffold enhances median nerve regeneration in nonhuman primates: an electrophysiological and histological study. *Tissue engineering Part A*. 2014;20(3-4):507-17.
25. Omenetto FG, Kaplan DL. New opportunities for an ancient material. *Science (New York, NY)*. 2010;329(5991):528-31.
26. Kundu B, Rajkhowa R, Kundu SC, Wang X. Silk fibroin biomaterials for tissue regenerations. *Advanced drug delivery reviews*. 2013;65(4):457-70.
27. Yang Y, Zhao Y, Gu Y, Yan X, Liu J, Ding F, et al. Degradation behaviors of nerve guidance conduits made up of silk fibroin in vitro and in vivo. *Polymer Degradation and Stability*. 2009;94(12):2213-20.
28. Ghaznavi AM, Kokai LE, Lovett ML, Kaplan DL, Marra KG. Silk fibroin conduits: a cellular and functional assessment of peripheral nerve repair. *Annals of plastic surgery*. 2011;66(3):273-9.
29. Madduri S, Papaloizos M, Gander B. Trophically and topographically functionalized silk fibroin nerve conduits for guided peripheral nerve regeneration. *Biomaterials*. 2010;31(8):2323-34.
30. Ye C, Nikolov SV, Calabrese R, Dindar A, Alexeev A, Kippelen B, et al. Self-(Un)rolling Biopolymer Microstructures: Rings, Tubules, and Helical Tubules from the Same Material. *Angewandte Chemie (International ed in English)*. 2015;54(29):8490-3.
31. Wang Y-I, Gu X-m, Kong Y, Feng Q-I, Yang Y-m. Electrospun and woven silk fibroin/poly(lactic-co-glycolic acid) nerve guidance conduits for repairing peripheral nerve injury. *Neural Regeneration Research*. 2015;10(10):1635-42.
32. Yan LP, Oliveira JM, Oliveira AL, Reis RL. Core-shell silk hydrogels with spatially tuned conformations as drug-delivery system. *Journal of tissue engineering and regenerative medicine*. 2017;11(11):3168-77.
33. Qi Y, Wang H, Wei K, Yang Y, Zheng RY, Kim IS, et al. A Review of Structure Construction of Silk Fibroin Biomaterials from Single Structures to Multi-Level Structures. *Int J Mol Sci*. 2017;18(3).
34. McGill M, Coburn JM, Partlow BP, Mu X, Kaplan DL. Molecular and macro-scale analysis of enzyme-crosslinked silk hydrogels for rational biomaterial design. *Acta biomaterialia*. 2017.
35. Grinsell D, Keating CP. Peripheral Nerve Reconstruction after Injury: A Review of Clinical and Experimental Therapies. *BioMed Research International*. 2014;2014:13.
36. Daly W, Yao L, Zeugolis D, Windebank A, Pandit A. A biomaterials approach to peripheral nerve regeneration: bridging the peripheral nerve gap and enhancing functional recovery. *Journal of the Royal Society, Interface*. 2012;9(67):202-21.
37. Carvalho C, Costa J, Ribeiro V, Silva-Correia J, Oliveira J, Reis R. Nerve guidance conduits derived from silk fibroin hydrogels: methods of production and uses thereof. Patent P4061 PP, Priority: PT 109562 (01082016). 2016.
38. Uebersax L, Mattotti M, Papaloizos M, Merkle HP, Gander B, Meinel L. Silk fibroin matrices for the controlled release of nerve growth factor (NGF). *Biomaterials*. 2007;28(30):4449-60.
39. Ezra M, Bushman J, Shreiber D, Schachner M, Kohn J. Porous and Nonporous Nerve Conduits: The Effects of a Hydrogel Luminal Filler With and Without a Neurite-Promoting Moiety. *Tissue engineering Part A*. 2016;22(9-10):818-26.
40. Chiono V, Tonda-Turo C. Trends in the design of nerve guidance channels in peripheral nerve tissue engineering. *Progress in neurobiology*. 2015;131:87-104.
41. Bradham RR. The importance of porosity in vascular prostheses. *The American Journal of Surgery*. 100(4):557-60.
42. Jin HJ, Park J, Karageorgiou V, Kim UJ, Valluzzi R, Cebe P, et al. Water-Stable Silk Films with Reduced β -Sheet Content. *Advanced Functional Materials*. 2005;15(8):1241-7.
43. O'Brien FJ. Biomaterials & scaffolds for tissue engineering. *Materials Today*. 2011;14(3):88-95.
44. Heidemann SR, Buxbaum RE. Mechanical tension as a regulator of axonal development. *Neurotoxicology*. 1994;15(1):95-107.

45. Bueno FR, Shah SB. Implications of tensile loading for the tissue engineering of nerves. *Tissue Eng Part B Rev.* 2008;14(3):219-33.
46. Rydevik BL, Kwan MK, Myers RR, Brown RA, Triggs KJ, Woo SL, et al. An in vitro mechanical and histological study of acute stretching on rabbit tibial nerve. *Journal of orthopaedic research : official publication of the Orthopaedic Research Society.* 1990;8(5):694-701.
47. Nectow AR, Marra KG, Kaplan DL. Biomaterials for the Development of Peripheral Nerve Guidance Conduits. *Tissue Engineering Part B, Reviews.* 2012;18(1):40-50.
48. Luis AL, Rodrigues JM, Lobato JV, Lopes MA, Amado S, Veloso AP, et al. Evaluation of two biodegradable nerve guides for the reconstruction of the rat sciatic nerve. *Bio-medical materials and engineering.* 2007;17(1):39-52.
49. Zilic L, Garner PE, Yu T, Roman S, Haycock JW, Wilshaw S-P. An anatomical study of porcine peripheral nerve and its potential use in nerve tissue engineering. *Journal of Anatomy.* 2015;227(3):302-14.
50. Zilic L, Wilshaw S-P, Haycock JW. Decellularisation and histological characterisation of porcine peripheral nerves. *Biotechnology and Bioengineering.* 2016;113(9):2041-53.
51. Yoshii S, Oka M. Collagen filaments as a scaffold for nerve regeneration. *Journal of biomedical materials research.* 2001;56(3):400-5.
52. Clements BA, Bushman J, Murthy NS, Ezra M, Pastore CM, Kohn J. Design of barrier coatings on kink-resistant peripheral nerve conduits. *Journal of tissue engineering.* 2016;7:2041731416629471.
53. Li M, Ogiso M, Minoura N. Enzymatic degradation behavior of porous silk fibroin sheets. *Biomaterials.* 2003;24(2):357-65.
54. Horan RL, Antle K, Collette AL, Wang Y, Huang J, Moreau JE, et al. In vitro degradation of silk fibroin. *Biomaterials.* 2005;26(17):3385-93.
55. DeVolder RJ, Kim IW, Kim ES, Kong H. Modulating the rigidity and mineralization of collagen gels using poly(lactic-co-glycolic acid) microparticles. *Tissue engineering Part A.* 2012;18(15-16):1642-51.
56. Wang W, Itoh S, Matsuda A, Ichinose S, Shinomiya K, Hata Y, et al. Influences of mechanical properties and permeability on chitosan nano/microfiber mesh tubes as a scaffold for nerve regeneration. *Journal of biomedical materials research Part A.* 2008;84(2):557-66.
57. Yang Y, Ding F, Wu J, Hu W, Liu W, Liu J, et al. Development and evaluation of silk fibroin-based nerve grafts used for peripheral nerve regeneration. *Biomaterials.* 2007;28(36):5526-35.
58. Freier T, Montenegro R, Shan Koh H, Shoichet MS. Chitin-based tubes for tissue engineering in the nervous system. *Biomaterials.* 2005;26(22):4624-32.
59. Maia FR, Fonseca KB, Rodrigues G, Granja PL, Barrias CC. Matrix-driven formation of mesenchymal stem cell-extracellular matrix microtissues on soft alginate hydrogels. *Acta biomaterialia.* 2014;10(7):3197-208.
60. Yang Y, Chen X, Ding F, Zhang P, Liu J, Gu X. Biocompatibility evaluation of silk fibroin with peripheral nerve tissues and cells in vitro. *Biomaterials.* 2007;28(9):1643-52.
61. Zareidoost A, Yousefpour M, Ghaseme B, Amanzadeh A. The relationship of surface roughness and cell response of chemical surface modification of titanium. *Journal of materials science Materials in medicine.* 2012;23(6):1479-88.
62. Engineering surfaces to enhance cell adhesion: Surface engineering. *Materials Today.* 2003;6(11):19.
63. Huang X, Yang N, Fiore VF, Barker TH, Sun Y, Morris SW, et al. Matrix stiffness-induced myofibroblast differentiation is mediated by intrinsic mechanotransduction. *American journal of respiratory cell and molecular biology.* 2012;47(3):340-8.
64. Zhou J, Cao C, Ma X, Hu L, Chen L, Wang C. In vitro and in vivo degradation behavior of aqueous-derived electrospun silk fibroin scaffolds. *Polymer Degradation and Stability.* 2010;95(9):1679-85.
65. Raia NR, Partlow BP, McGill M, Kimmerling EP, Ghezzi CE, Kaplan DL. Enzymatically crosslinked silk-hyaluronic acid hydrogels. *Biomaterials.* 2017;131(Supplement C):58-67.
66. Numata K, Cebe P, Kaplan DL. Mechanism of enzymatic degradation of beta-sheet crystals. *Biomaterials.* 2010;31(10):2926-33.
67. Park SH, Gil ES, Kim HJ, Lee K, Kaplan DL. Relationships between degradability of silk scaffolds and osteogenesis. *Biomaterials.* 2010;31(24):6162-72.

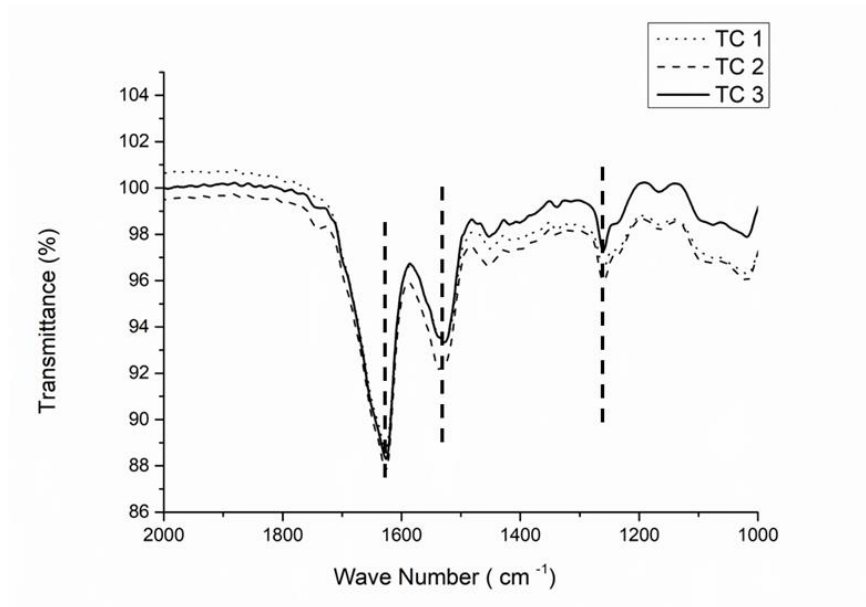
IX-8. SUPPLEMENTARY DATA



Supplementary Figure IX-1 - SEM analysis of the TC 1 formulation cross-section. The micrographs confirm the porosity obtained, where the exterior wall presents higher pore size when compared to the interior wall. Scale bar: 50 μm.



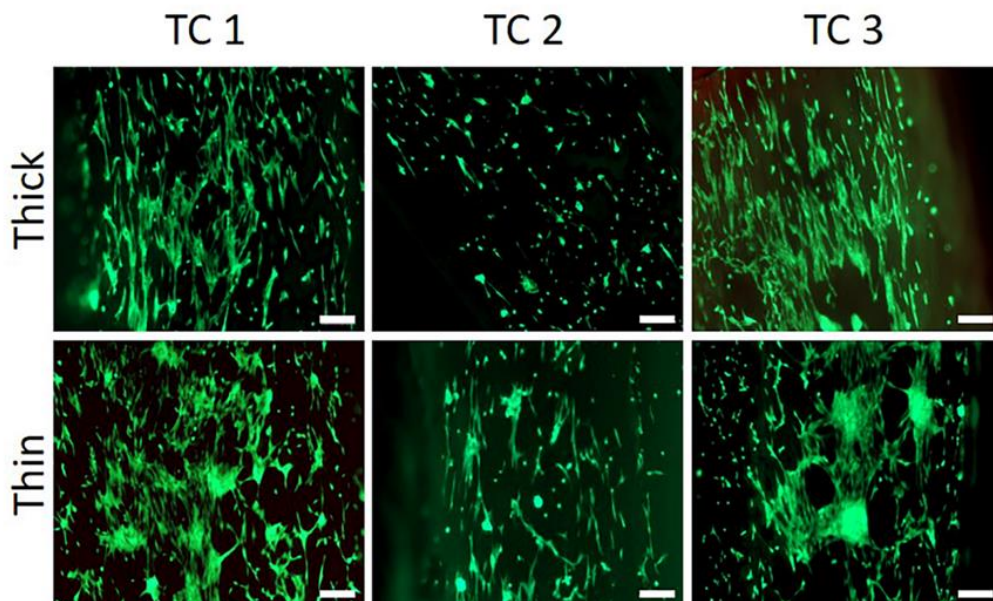
Supplementary Figure IX-2 - SEM analysis of the modified TC 1, *i.e.* conduit produced by freeze-drying after a slower freezing step. The micrographs reveal the exterior and interior walls, as well as the cross-section microstructure of the conduits obtained after a slower freezing process (0 °C followed by -20 °C), showing high porosity as compared to the conventional TC 1. The freezing was performed previously to the freeze-drying. This type of conduits would be required in the case of more severe injuries, where bigger gaps need to be treated. The modified treatment of the conduits was done merely as a proof-of-concept, to demonstrate the versatility of the developed tubes.



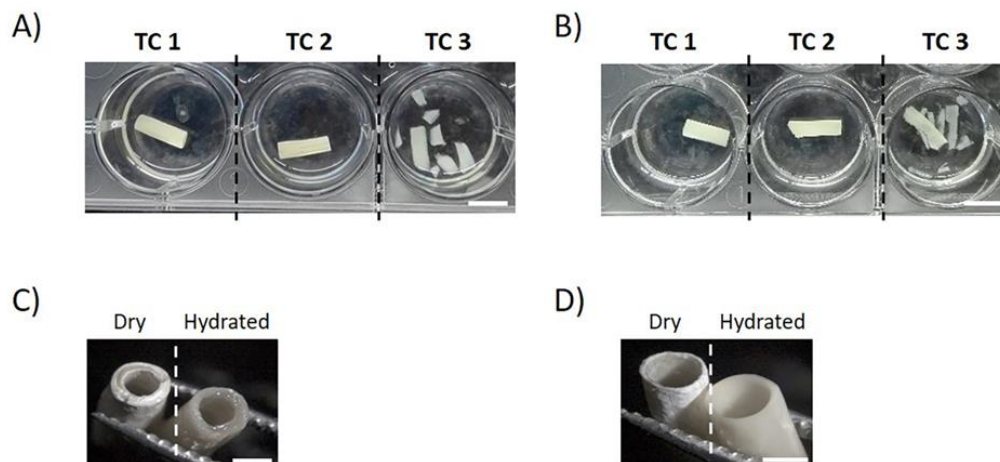
Supplementary Figure IX-3 - FTIR spectra of the different silk fibroin thick TCs (TC 1, TC 2 and TC 3). Similar spectra were obtained regardless of the thickness of the wall (thin conduits data not shown). The spectra show characteristic peaks at 1627 cm^{-1} (amide I), 1520 cm^{-1} (amide II) and 1262 cm^{-1} (amide III).



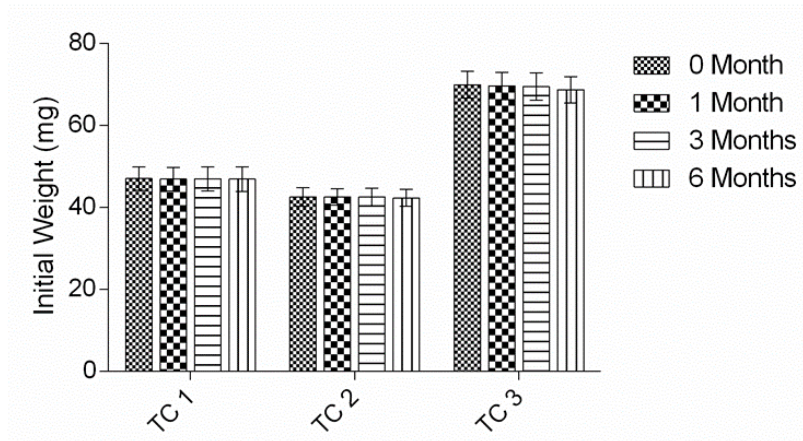
Supplementary Figure IX-4 - Apparatus used for universal mechanical testing machine (Instron) for tensile tests in the developed TCs. Both TC ends were hold with a grip.



Supplementary Figure IX-5 - Calcein-AM staining demonstrating the presence of viable cells (capable of migrating) adhered to the interior surface of both thick and thin conduits. The images were taken at the end of the cellular permeability assay (after 48 hours). Scale bar: 200 μ m.



Supplementary Figure IX-6 - Weight loss macroscopic observation of the TCs under the effect of Protease XIV solution after 30 days. A) Macroscopic degradation of thick conduits. B) Macroscopic degradation of thin conduits. The TC 1 and TC 2 remained with fragile walls, but the integrity of the conduits was maintained, whereas the TC 3 disintegrated into fragments. Scale bar: 10 mm.



Supplementary Figure IX-7 - Weight of the developed TCs measured from the moment of production to up to 6 months, revealing the weight stability, with no statistically significant differences along time. The TC 1 and TC 2 were kept in a dry state and the TC 3 was kept in ethanol. This assay demonstrated that the developed TCs are sustainable as off-the-shelf products, allowing storage for several months prior to their use.

Chapter X

Engineering a silk fibroin-based nerve conduit with neurotrophic factors for proximal protection and vascularization after peripheral nerve injury

Chapter X

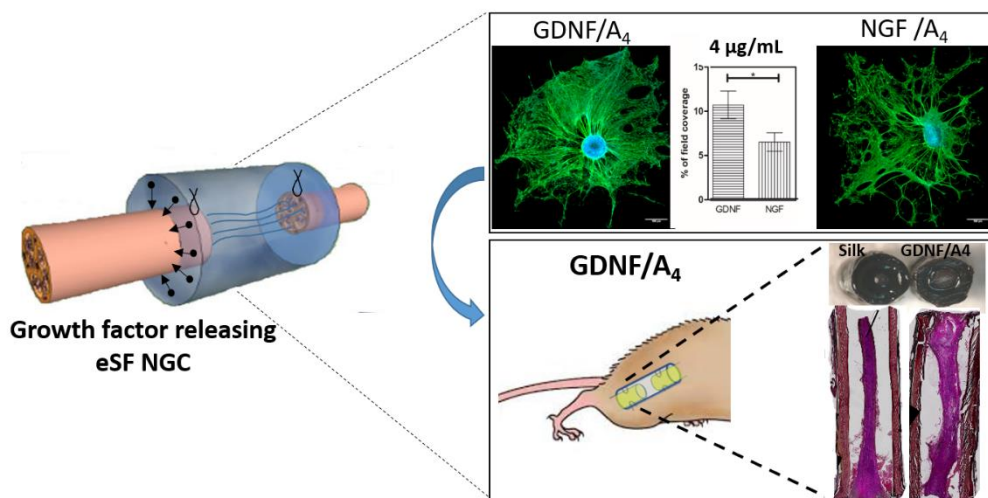
Engineering silk fibroin-based nerve conduit with neurotrophic factors for proximal protection and vascularization after peripheral nerve injury¹

ABSTRACT

As an alternative strategy to autologous nerve grafts, artificial nerve guidance conduits capable of adequately releasing neurotrophic factors have been extensively studied to bridge nerve defects and guide regeneration. However, the lack of neurotrophic factors (NTFs) in the proximal area and their visible effects in axonal retrograde transport following peripheral nerve injury is one of the factors causing an incomplete and deficient nerve regeneration. In this study, we aim at producing an advanced conduit made of silk fibroin, which can incorporate diverse growth factors and therefore promote an effective regeneration after injury. For that, enzymatically crosslinked silk fibroin-based (eSF) conduits, resorting to horseradish peroxidase, were developed with the objective of being used as a platform for the controlled delivery of neurotrophic factors. Two different concentrations (2 and 4 $\mu\text{g}/\text{mL}$) of Nerve growth factor (NGF) and Glial-cell line derived neurotrophic factor (GDNF) were incorporated using two different methodologies: (i) crosslinking method and (ii) absorption method. The release profile was measured by ELISA technique showing GDNF's suitable and sustained release using the absorption method. The bioactivity of the neurotrophic factors was evaluated *in vitro* by using primary dorsal root ganglia (DRGs) and evaluating them at pre-determined released time points. The results suggested that GDNF/A₄ formulation promoted a significant improvement in DRGs neurite density, with higher coverage area than NGF, *in vitro*. When implanted in a 10 mm sciatic nerve defect in rats, GDNF-loaded silk fibroin conduits revealed retrograde neuro-protection as compared to autografts and plain silk fibroin conduit. In addition, muscle atrophy was prevented at 6 weeks recovery. Therefore, our novel design presents a substantial improvement of retrograde trafficking, neurons' protection, and motor nerve reinnervation, which were all absent in our plain silk fibroin conduit that mimics the current marketed nerve conduits.

¹This chapter is based on the following publication: [Carvalho CR, Chang W, Silva-Correia J, Reis RL, Oliveira JM, Kohn J. Engineering silk fibroin-based nerve conduit with neurotrophic factors for proximal protection and vascularization after peripheral nerve injury \(Submitted\)](#)

X-1. GRAPHICAL ABSTRACT



X-2. INTRODUCTION

Peripheral nerve injuries (PNIs) are one of the most important burdens in public healthcare systems worldwide. They are considered intractable and a common disease with a high and gradually increasing incidence over the past decades (1). When surgically repairing PNIs, autologous nerve graft is the current gold standard option for bridging gaps that cannot be repaired by direct suturing. Despite that, the autograft is often associated with increased morbidity, painful neuroma formation and inappropriate match of nerves (2). To solve some of the problems related to biological grafts, artificial nerve guidance conduits (NGCs) have been developed as an alternative strategy (2). The properties of the biopolymer used to engineer NGCs and the features of the final conduit itself, such as pore size and degradation, play a crucial role in the nerve regeneration efficiency. The biomaterial must be biocompatible and support cellular growth, proliferation and migration (3). Furthermore, NGCs must allow the passage of nutrients and oxygen, but at the same time, inhibit the infiltration of fibroblasts, which may form scar tissue at the injury site (4). Mechanical properties that support nerve regeneration and flexibility are also a prerequisite (5). The previously developed SF conduits presented several advantages and overcame all these problems, showing features such as kinking resistance-ability and suturability.

However, even with the efforts and advances in the Tissue Engineering (TE) field and the fact that peripheral nervous system (PNS) has an intrinsic capacity to regenerate (6), poor outcomes are still a problem. They are mainly related to: (I) death of primary motor and sensory neurons; (II) absence of fiber regeneration over the gap area, and (III) target-organ incomplete reinnervation, limiting the full recovery of the patients at a functional and sensory level (7). In fact, even when injured nerves are surgically restored in the optimal timeframe after the injury, the period that axons take to regenerate is too extended, resulting in the lack of contact between neurons and target organs. The consequence is a state of chronic axotomy and end targets become chronically denervated (8). Such problem is not solved by the use of simple hollow NGCs, that are FDA-approved and used extensively in the clinics, but only provide regenerating nerves with poor guidance and protection (9). Several strategies have been used to enhance functional and sensory recovery, aiming to increase the number of suitable axons which correctly reach their targets. In this sense, one of the most promising and prominent possibilities to improve nerve regeneration is the inclusion of neurotrophic factors (NTFs) in the NGCs. NTFs are endogenous proteins capable of binding to cell receptors with the purpose of modulating and directing cellular activities (8). In relation to the PNS, NTFs are able to promote neuronal survival, axonal regeneration and Schwann cells' migration. Furthermore, it has been reported that NTFs have a very good efficiency in enhancing not only neurogenesis when applied concomitantly with scaffolds, but also angiogenesis (10).

With distinctive properties and functions, nerve growth factor (NGF) and glial cell line-derived neurotrophic factor (GDNF) were used. Briefly, NGF promotes survival and axonal outgrowth of sensory neurons both *in vitro* and *in vivo* (11), and has been proved to promote early axonal regeneration. However, the role of NGF in the recovery of motor neuron function is restricted (12). On the other hand, GDNF is one of the most protective factors for motor neurons and is abundantly expressed by skeletal muscle (13). Nevertheless, it has also marked activity on sensory neurons. Acting through different intrinsic mechanisms and different pathways, both NTFs will have various effects on neurons and respective neurites, such as neurite elongation or density increase. In the case of NGF, the trkA receptor is a 140 kDa glycoprotein which binds NGF. The NGF-activated trkA receptor undergoes dimerization and autophosphorylation at several tyrosine residues that selectively trigger activity in several intracellular signalling pathways, having direct action on sensory neurons (14). The GDNF, a neuronal survival factor, binds its co-receptor GDNF family receptor alpha1 (GFR alpha 1) and signals

through the receptor tyrosine kinase RET, showing its effects on both sensory and motor neurons. These were the NTFs chosen for this experimental work, due to their distinctive properties.

In addition to the selection of NTFs, it is recognized that the selection of a suitable delivery method for these molecules is crucial for an effective regenerative potential. The inclusion and consequent delivery of growth promoting biological molecules can be achieved by several ways, accounting for many different and adjustable delivery systems (8). When considering the delivery of NTFs from the conduit wall, methods such as conjugation (15), adsorption (16), and physical entrapment in the wall (17) are among the most used methods. Regardless of the delivery method, general complications related to loss of bioactivity, initial burst release or too low daily dose must be avoided in order to have a beneficial effect on nerve regeneration (18). Optimized delivery methods for NTFs eluted from SF conduits described in the literature are solely based in the simple blending of NTFs in SF solution without further entrapment or electrospinning technique (19).

In this work, we have tested two methods, (i) crosslinking and (ii) adsorption, and compared their efficacy for retention and controlled delivery of GDNF or NGF. The methods are based on and interrelated with the SF NGC production method. For such, a new methodology previously developed and patented by our group to produce enzymatically crosslinked SF (eSF) conduits was used (3). First, since this fabrication process involves the formation of an hydrogel as a middle step, due to crosslinking of tyrosine groups in its structure, it is hypothesized that the NTFs would be entrapped in a more complex and tight matrix after crosslinking the NTFs in the SF structure (20), creating a more appropriate condition for sustained release. Such method was compared to the absorbing process, where the eSF conduits are immersed in a NTFs solution, in which, processes like absorption and adsorption were expected to occur. Due to the porosity of the conduit and its high surface area for solution penetration, we envision that the NTFs would be greatly bounded to its surface in the second approach. Furthermore, the suitability of eSF to be processed in aqueous media, turns it a promising biomaterial for the fabrication of bioactive protein delivery systems (21).

Since the importance of NTFs to enhance PNR was noticed, it has been investigated the importance of their retrograde transport to the cell body (22, 23). A body of evidence proposes that the mechanism of NTF retrograde transport is essential for signal propagation, neuronal development and prevention of neuronal degeneration. In the case of PNIs, the retrograde transport of injury signals is one of the indispensable cellular instruments leading to regeneration (24). This mechanism can allow the coordination between the injury site and the cell body, therefore regulating the proper genes to

promote neuronal survival. Both NGF and GDNF have shown to be retrogradely transported (23), with beneficial effects in terms of nerve protection and regeneration, although with different mechanisms (25).

The aim of this investigation was to assess the feasibility of retrograde delivery of GDNF or NGF by eSF conduits, with distinct release kinetics after different incorporation methods. The GDNF and NGF biological activities were assessed *in vitro* with primary dorsal root ganglia explants (DRGs). The most promising formulation of NTF-loaded eSF conduit was then implanted in a 10 mm rat sciatic nerve injury model and compared to both autograph and eSF conduit. The 10 mm sciatic nerve injury model was used in order to create a gap to avoid the effect of distal neurotrophic factors, and in fact, assess the outcome of the NGCs delivered NTFs. The data was evaluated based on pinch test, muscle weight, and proximal nerve histology following sciatic nerve injury

X-3. MATERIALS AND METHODS

X-3.1. Materials

Bombyx mori cocoons were supplied by the Portuguese Association of Parents and Friends of Mentally Disabled Citizens (APPACDM, Portugal). Hydrogen peroxide was purchased from Panreac (Spain). Human recombinant GDNF (cat#450-10-10 µg) and Human recombinant NGF (cat#450-01-100 µg) were purchased from Peprotech (USA). Human GDNF DuoSet ELISA kit (cat#DY212) and Human β-NGF DuoSet ELISA kit (cat#DY256) were purchased from R&D Systems (USA). Corning Matrigel® phenol red-free was purchased from VWR (USA). Other materials and reagents were purchased from Sigma–Aldrich (USA).

X-3.2. Preparation of silk fibroin conduits

The purification of SF and consequent preparation of eSF NGCs was prepared as described elsewhere.(26) Briefly, SF was detached from the other main protein present in the cocoons, sericin. For this purpose, the cocoons were immersed in a 0.02 M boiling sodium carbonate solution for 1 hour, followed by rinsing with abundant distilled water. The obtained SF was then dissolved in a 9.3 M lithium bromide solution at 70 °C for 1 hour and dialyzed (benzoylated dialysis tubing, MWCO: 2 kDa) against

distilled water for 48 hours to remove contaminations. The purified SF was concentrated against a 20 %wt. poly(ethylene glycol) solution for at least 6 hours, and the final concentration was determined by weighting the dry product after drying at 70 °C overnight. After determining the concentration, the SF solution was diluted to 16 %wt. with distilled water, and mixed with horseradish peroxidase solution (HRP type VI, 0.84 mg/mL, 100 µL) and hydrogen peroxide solution (H₂O₂, 0.36 %wt., 65 µL) for enzymatic crosslinking following the procedure described by Yan *et al.*(27) In order to produce the conduits, the previous mixture was injected within the space between two concentric cylinder molds, where the outer cylinder had a diameter of 4 mm and the inner cylinder had a diameter of 2 mm. The system was incubated at 37 °C for the period of 1 hour in order to induce gelation. After gelation, a quick immersion in liquid nitrogen is needed to remove the outer mold, followed by an immersion in ethanol 100 % (v/v) to induce permanent crystalline β-sheet conformation and to remove the inner mold. The obtained hollow conduits were subjected to a process of lyophilization for 72 hours (26). Final conduits had a wall thickness of ≈ 700 µm, a lumen diameter of ≈ 5 mm and an external pore size in the range of 3-6 µm. Conduits were cut to a total length of 14 mm for all assays.

X-3.3. Physical characterization of the conduits

The morphology of the produced eSF conduits was assessed under a scanning electron microscope (model S360, Leica, Cambridge, England). The specimens were sputter coated with gold, prior to the analysis of surface morphology and microstructure

X-3.4. Incorporation of NTFs

The incorporation of NTFs was achieved via two different methods, which will be designated throughout the manuscript: (i) crosslinking method, and (ii) adsorption method. For the crosslinking method, a NTF solution of 4 µg/mL in PBS was added to 1 mL of aqueous SF solution. As described in the preparation of the conduits, the solution was mixed with HRP and H₂O₂, allowing the NTFs to be entrapped in the conduits' walls after crosslinking. The processing was then carried out as previously described. For the adsorption method, the conduits' preparation was carried normally and the final lyophilized conduits (made of 1 mL of silk fibroin solution) were immersed in 1 mL of a 4 µg/mL or 2 µg/mL of NTF solution in PBS for 3 hours at 37 °C. A second step of lyophilization was performed.

The NTFs incorporated in the eSF conduits by crosslinking and absorption were GDNF and NGF. A table identifying the six produced samples is shown below (**Table X-1**).

Table X-1 - Samples produced for *in vitro* assays by means of using the crosslinking and absorption methods, different NTFs (*i.e.*, GDNF and NGF), and different NTFs concentrations (*i.e.*, 2 and 4 µg/mL).

| | Crosslinking 4 µg/mL | Absorption 2 µg/mL | Absorption 4 µg/mL |
|------|-------------------------|-----------------------|-----------------------|
| GDNF | GDNF/C | GDNF/A ₂ | GDNF/A ₄ |
| NGF | NGF/C | NGF/A ₂ | NGF/A ₄ |

X-3.5. Determination of NTFs' loading efficiency in eSF conduits

After the production of the different samples indicated in **Table X-1**, the NTFs' loading efficiency in the eSF conduits was determined using the Enzyme-linked immunosorbent assay (ELISA) kits for GDNF and NGF, respectively. These experiments were only carried for the absorption method, since it can be predicted that 100 % of NTF was incorporated in the crosslinking method. Considering that the initial NTF solutions had the concentration of 2 and 4 µg/mL, the NTF solutions that remained after the absorption process were frozen at -20 °C, stored and later subjected to ELISA quantification. In order to determine the percentage of NTFs' loading efficiency, **Equation X-1** was applied, where C_i represents the initial NTF concentration in which the conduit was soaked, and x represents NTF quantification obtained by ELISA. A triplicate of samples was measured in 3 independent experiments, and the results were expressed as mean ± SD.

Equation X-1 - Equation for the determination the NTF loading efficiency.

$$NTF \text{ loading efficiency} = 100 - \frac{(x * 100)}{C_i}$$

X-3.6. *In vitro* release of NTFs from the nerve conduits

The amount of NTFs released from the eSF conduits was quantified by ELISA according to the manufacturer's instructions. Each eSF conduit, with the size of 14 mm in length, was incubated in 1 mL of release medium (1 %wt. BSA in PBS) at 37 °C, with shaking at 60 rpm, for 50 days. The supernatant was collected and substituted with 1 mL of fresh release medium every 24 hours. The absorbance was measured in the collected solutions at 450 nm using a plate reader (Tecan, Spark 10M, Switzerland). The NTFs concentration was determined by means of comparing the reading to the obtained standard curve after normalization.

X-3.7. *In vitro* isolation and culturing of DRGs for NTFs bioactivity assay

The biological activity of the NTFs released from the eSF conduits was assessed by determining the axonal outgrowth of DRGs. DRGs explants were isolated from neonatal rat pups (considered neonatal from day 1 to day 5). They were aseptically harvested and cleaned with dissecting forceps to remove the tails and excessive connective tissue. After cutting the DRGs in halves, they were immediately seeded on Matrigel® coated wells. The Matrigel® coating was done at least 3 hours before the DRGs seeding, using cold Matrigel (4 °C) and allowing it to polymerize at 37 °C. The DRGs were kept in regular Dulbecco's modified Eagle Medium (DMEM) supplemented with 10 % (v/v) fetal bovine serum and 1 % (v/v) Penicillin/Streptomycin for the first 24 hours, allowing cellular attachment. DRGs were plated at a density of two DRGs per well.

At the same time, the NTF loaded eSF conduits were immersed in 1 mL of complete DMEM and incubated at 37 °C and 60 rpm, producing a NTF enriched media, denominated as conditioned media. Every 24 hours, the conditioned media was transferred to the wells containing DRGs and replaced with fresh media. For this assay, the negative control consisted of DRGs treated with regular DMEM and the positive control comprised DMEM media supplemented with 50 ng/mL of GDNF or NGF. DRGs were cultured with this methodology for 5 days, at 37 °C and 5 % CO₂. This assay was performed 3 independent times, with 6 DRGs per condition each time.

X-3.8. Immunocytochemistry

After 5 days of incubation, DRGs and cells were fixed with 4 % (v/v) paraformaldehyde for 30 minutes. DRGs were washed and treated with Triton 0.2 % (v/v) in PBS for 10 minutes for permeabilization purposes. The next step consisted in adding blocking buffer comprising 3 %wt. BSA in PBS, at room temperature (RT), for 30 minutes. The primary antibody, diluted in 1 %wt. BSA in PBS, was then added, and the mixture incubated for 1 hour at RT (1:150, Monoclonal Anti-Neurofilament 200, produced in mouse). After washing with PBS, the secondary antibody was immediately added and incubated for 1 hour at RT, protected from light (1:500, Alexa Fluor® 488 goat anti-mouse). The last step consisted in nuclei staining, in which Hoechst staining was applied for 5 minutes (1:5000).

X-3.9. Image acquisition and data analysis

The stained DRGs were analyzed using the confocal laser microscope (Leica). Confocal images were acquired and mounted together to fit in a black square (with the exact same size in all images) so that it would be possible to do image analysis and comparable quantifications. Fluorescent images were imported to ImageJ software (Fiji) and three parameters were analyzed and quantified concerning the DRGs neurite outgrowth: neurite length, cellular migration and percentage of field coverage (28, 29). For neurite length and cellular migration quantifications, the average of the 20 longest neurites and the 20 furthest cells in each image were measured, in a total of 5 images per condition (30, 31). For percentage of field coverage, ImageJ was also used to convert the pictures to black and white (threshold of 58 for all images) and the % of white pixels in the black field was quantified. After statistical analysis, the group presenting the best performance was selected for the animal study and compared with autograft.

X-3.10. *In vivo* study using rat model of sciatic nerve defect

The regenerative potential of the developed conduits was investigated *in vivo* on a 10 mm rat sciatic nerve gap. In a total of fifteen animals, five animals were distributed in three experimental groups (n=5). More specifically, the experimental groups include the following: 1) autograft; 2) eSF and 3) GDNF/A₄. The reversed autograft was considered the positive control and the plain silk conduit was

considered the negative control, in order to assess the beneficial effects of NTF incorporation. The degree of regeneration was assessed 6 weeks after implantation surgery.

X-3.10.1. Surgical procedure

All experiments were conducted under an approved protocol of the Rutgers Animal Care and Facilities Committee and the Institutional Animal Care and Use Committee (IACUC). Male Lewis rats weighing 250–300 g (Charles River Labs, USA) were anesthetized with isoflurane inhalation (1-5 % isoflurane in 100 % O₂) via an appropriate face mask, which was kept throughout the surgical procedure for anesthesia maintenance. Animals were kept on a heated pad until they recovered from anesthesia.

Before the surgery, Buprenorphine (for analgesic purposes, 0.05 mg/kg) and Baytril (for antibiotic purposes, 5 mg/kg) were administered subcutaneously. After shaving the surgical site on the left limb, local anesthesia (Bupivacaine, diluted to 0.25%, 2.5 mg/kg) was also administered in the place of incision. The shaved area was then cleaned by alternating applications of chlorhexidine and 70 % (v/v) isopropyl alcohol in circular motions.

Nerve cutting tools were printed from poly(lactic acid) on a Monoprice fused deposition modeling printer. Tools were designed with a hook presenting an inner diameter of 2.5 mm and a scalpel alignment groove 700 µm in width. Tools had a beveled tip and specific dimensions to allow for minimal tissue damage while exposing and sectioning the nerve. Printed tools were cleaned in ethanol, individually packed and surgically sterilized with ethylene oxide. A scheme of a nerve cutting tool can be seen in **Supplementary Figure X-1**.

For the conduits' groups, a 5 mm section of the sciatic nerve was removed with the aid of the above-described nerve cutting tool, and the nerve stumps were allowed to retract to form a 10 mm gap. Sterile conduits (14 mm in length) were first hydrated for 10 minutes with sterile saline and then sutured to the nerve stumps using two 9-0 epineurial sutures on each end, maintaining the 10 mm gap between the stumps. In that process, nerve stumps were secured approximately 1 mm into each end of the conduit. In the case of autografts, a 10 mm segment of nerve was removed, reversed, and sutured back in the gap using 9-0 sutures on each end. Both muscular and skin tissues were sutured in layers using absorbable 5-0 sutures.

For post-operative analgesia, buprenorphine SR (1 mg/kg) was administered 8 hours after the surgery. Six weeks after surgery, rats were deeply anesthetized using the same method. The All

analyzed groups were harvested (SF conduits containing the regenerated nerves and the autografts were collected, on the experimental side), as well as a segment of uninjured nerve on the contralateral side, for comparison purposes. Still under general anesthesia, animals were euthanized by carbon dioxide asphyxiation.

X-3.10.2. Pinch Test

A pinch test was performed in a way to assess sensory functional recovery. The distal nerve segment was pinched with a pair of forceps to determine any reflex of the ipsilateral side. Every animal of every group was subjected to this test, repeated at least 3 times

X-3.10.3. Gastrocnemius muscle harvest and weight ratio

Upon nerve harvest and after animal sacrifice, the gastrocnemius muscle of both hind limbs (operated side and contralateral healthy side) were immediately harvested by exposing the musculature via a knee to ankle longitudinal skin incision. The muscles were harvested from origin to insertion and weighed with an electronic balance in order to be able to determine the muscle atrophy resultant from muscle denervation. Results were expressed as the percentage of the left side (reconstructed with eSF conduits) to the non-operated contralateral side, as a mean of five samples per condition (mean \pm SD).

X-3.10.4. Histological preparation

Immediately after harvesting, both reconstructed nerves and healthy contralateral nerves were subjected to in-situ fixation by immersing in 4 % (v/v) paraformaldehyde. Sections 3 mm into the NGC (after C1X area) were cut longitudinally and further processed for hematoxylin and eosin (H&E) staining. Briefly, samples were deparaffinized in xylol, hydrated through decreasing ethanol series (100 %, 96 %, 70 % and 50 % (v/v) alcohol) and finally washed in distilled water. After immersion in hematoxylin, samples were rinsed in running soft tap water. Samples were then immersed in an 80 % alcohol solution and briefly in the eosin staining. Slides were dehydrated through 96 % (v/v) ethanol, absolute ethanol and finally cleared in xylol and mounted.

X-3.10.5. Histomorphometric analysis of explanted nerves

Immediately after harvesting, both reconstructed nerves and healthy contralateral nerves were subjected to in-situ fixation by immersing in 4 % (v/v) paraformaldehyde. The nerve was then harvested and processed as previously described (32). Briefly, the explant was embedded in epoxy resin and 1 μ m thick sections were obtained and stained with osmium tetroxide followed by 1 % (v/v) toluidine blue. Cross-sections of the proximal nerve (3 mm from the conduit, PNX), conduit (3 mm into proximal side of the conduit, C1X) and longitudinal sections of the regenerated nerve were analyzed for axon count and assessment of regenerated nerve cable formation. Image analysis was performed using ImageJ software.

X-3.11. Statistical analysis

Numerical data was represented as mean \pm SD. At least 3 specimens were used in each condition. Statistical analysis was performed using the GraphPad Prism 5.0 (GraphPad Software, USA) For ELISA quantification analysis, a Shapiro-Wilk test was used to ascertain about the data normality. Subsequently, a Kruskal-Wallis test was performed followed by Dunn's Multiple comparison test, where the significance level was set to $p < 0.05$. The biological experiments were repeated three independent times. For *in vitro* and *in vivo* image analysis, a Two-tailed Mann Whitney test was used ($p < 0.05$). For percentage of muscle weight loss, results were expressed as the percentage of the left side (reconstructed with eSF conduits) to the non-operated contralateral side, as a mean of five samples per condition (mean \pm SD). Subsequently, a Kruskal-Wallis test was performed followed by Dunn's Multiple comparison test, where the significance level was set to $p < 0.05$.

X-4. RESULTS

X-4.1. Production and physical characterization of silk fibroin conduits

SF conduits were successfully produced according to a protocol previously developed by our group (26). **Figure X-1A** depicts a detailed scheme of the production steps, in which the different methods of NTFs incorporation are represented. The microstructure of the final conduits can be appreciated both in

Figure X-1B and **Supplementary Figure X-2**, which shows representative SEM micrographs of the eSF NGCs microstructure.

X-4.2. Neurotrophic factors loading efficiency

NTFs loading in the eSF conduits was attained by two different methods designated by crosslinking and absorption. For the crosslinking method, a 4 $\mu\text{g}/\text{mL}$ of each NTF was diluted in 1 mL of SF solution at 16 %, carrying the rest of process until obtaining a freeze-dried eSF NGC. For GDNF and NGF crosslinked formulations, the loading efficiency can be considered 100 %, as all the amount of growth factor that was added in the 4 $\mu\text{g}/\text{mL}$ solution got entrapped in SF structure. However, the loading efficiency in the absorption method needed to be determined. For that, ELISA quantification was performed on the remaining NTF solution after the absorption process, in order to calculate the amount of growth factor that was, in fact, absorbed. In **Table X-2**, the loading efficiency determined for the different formulations is presented. For GDNF/A₂ formulation, the loading efficiency reached 78.3 ± 1.25 %. A similar value (77.2 ± 0.85 %) was determined for GDNF/A₄ formulation. The retention of NGF by the eSF conduit was inferior when compared to GDNF, as the loading efficiency of 46.2 ± 0.43 % and 44.5 ± 1.02 % was observed for NGF/A₂ and NGF/A₄, respectively.

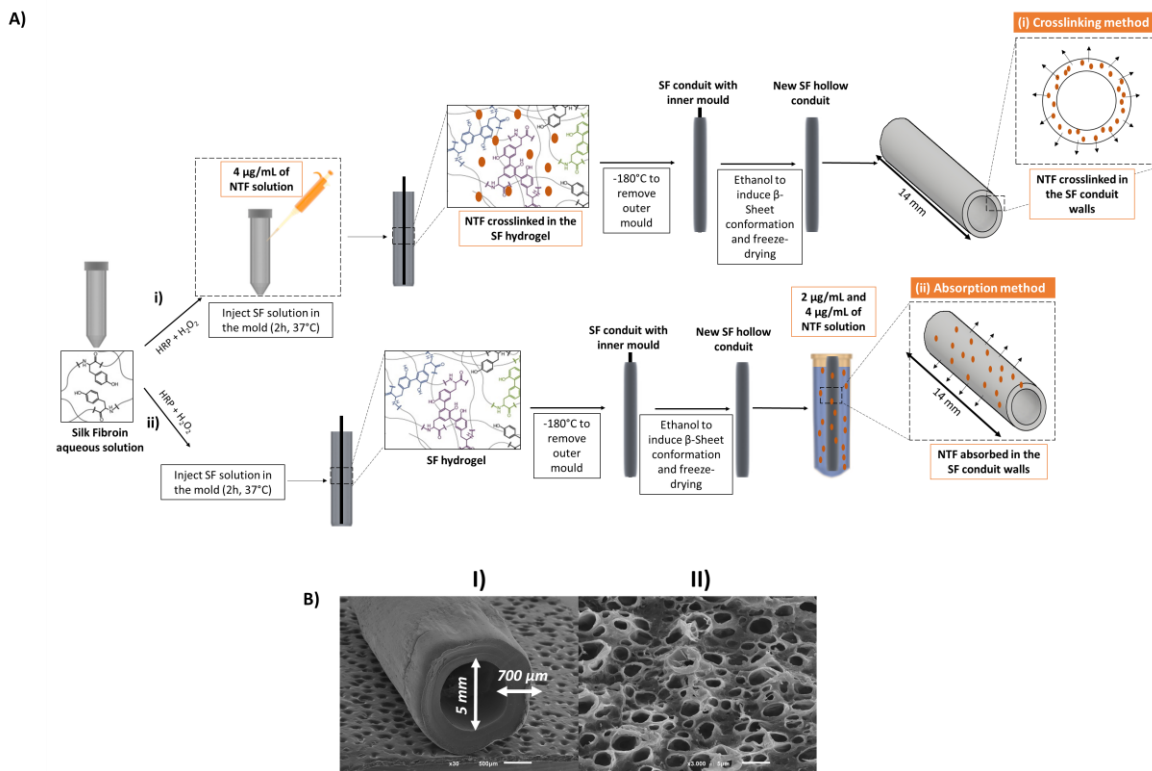


Figure X-1 - Schematic representation of the methodology used to produce the SF conduits. The methodology allows fabricating the enzymatically crosslinked SF NGCs following a method previously developed by Carvalho *et al.*(3, 33) which takes advantage of the presence of tyrosine groups in SF that are known to form a covalently-crosslinked hydrogel. The two different techniques used to incorporate NTFs into the eSF conduits are highlighted in: (i) Crosslinking method, and (ii) Absorption method.; BI) SEM micrographs of eSF conduit where the wall thickness is $\approx 700 \mu\text{m}$ and the lumen has a diameter of $\approx 5 \text{ mm}$; BII) SEM micrograph of eSF conduit surface where the external pore size is in the range of 3-6 μm . Conduits were cut to a total length of 14 mm for all assays. Scale bars: BI) 500 μm and BII) 5 μm .

Table X-2 - NTFs loading efficiency in the eSF conduits produced by crosslinking and adsorption methods.

| Formulation | Loading efficiency (%) |
|---------------------|------------------------|
| GDNF/A ₂ | 78.3 ± 1.25 |
| GDNF/A ₄ | 77.2 ± 0.85 |
| NGF/A ₂ | 46.2 ± 0.43 |
| NGF/A ₄ | 44.5 ± 1.02 |

X-4.3. *In vitro* release of NTFs from silk conduit

The amount of released GDNF or NGF from the eSF conduits was quantified daily within the first five days and in a cumulative manner up to fifty days, according to the different methods of loading and concentrations of NTFs (**Figure X-2**). The scheme of the methodology used in the NTF release study is depicted in **Figure X-2A**.

The daily GDNF release profile presented in **Figure X-2BI** reveals a significantly higher delivery of the NTF when the loading is done by means of performing the absorption method as compared to crosslinking method, in all the timepoints. In what concerns the absorption formulations, the higher amount released was verified in the first day, with a reduction of the delivery verified day by day, from 2.45 ± 0.42 ng/mL on day 1 to 1.06 ± 0.12 ng/mL on day 5 for GDNF/A₄ formulation. With a slightly overall lower release, there was also a reduction from 2.19 ± 0.15 ng/mL in day 1 to 1.04 ± 0.12 ng/mL in day 5 for GDNF/A₂ formulation. The cumulative release shown in **Figure X-2BII** reveals that the tendency to slowly decrease the amount of NTF released is kept throughout the timepoints, with GDNF/A₄ formulation releasing 36.8 ± 0.9 ng/mL and GDNF/A₂ releasing 32.3 ± 3.3 ng/mL after 50 days. The daily NGF releasing profile can be seen in **Figure X-2BIII** where, similarly to GDNF daily release, the higher amount released was verified in the first day, but with a more drastic reduction from day 1 to day 2, in a burst release manner. NGF/A₄ formulation reduced its release from 2.23 ± 0.14 ng/mL in day 1 to 0.24 ± 0.05 ng/mL in day 5, whereas NGF/A₂ formulation reduced its release from 1.42 ± 0.12 ng/mL on day 1 to 0.11 ± 0.06 ng/mL in day 5. The cumulative release of NGF depicted in **Figure X-2BIV** shows that the tendency to decrease NTF release is kept, with NGF/A₄ formulation releasing 8.9 ± 2.5 ng/mL and NGF/A₂ releasing 6.3 ± 2.3 ng/mL after 50 days. In all timepoints analyzed and for both GDNF and NGF, there is a significant statistical difference between the formulations produced using the absorption method in comparison to the crosslinked formulations.

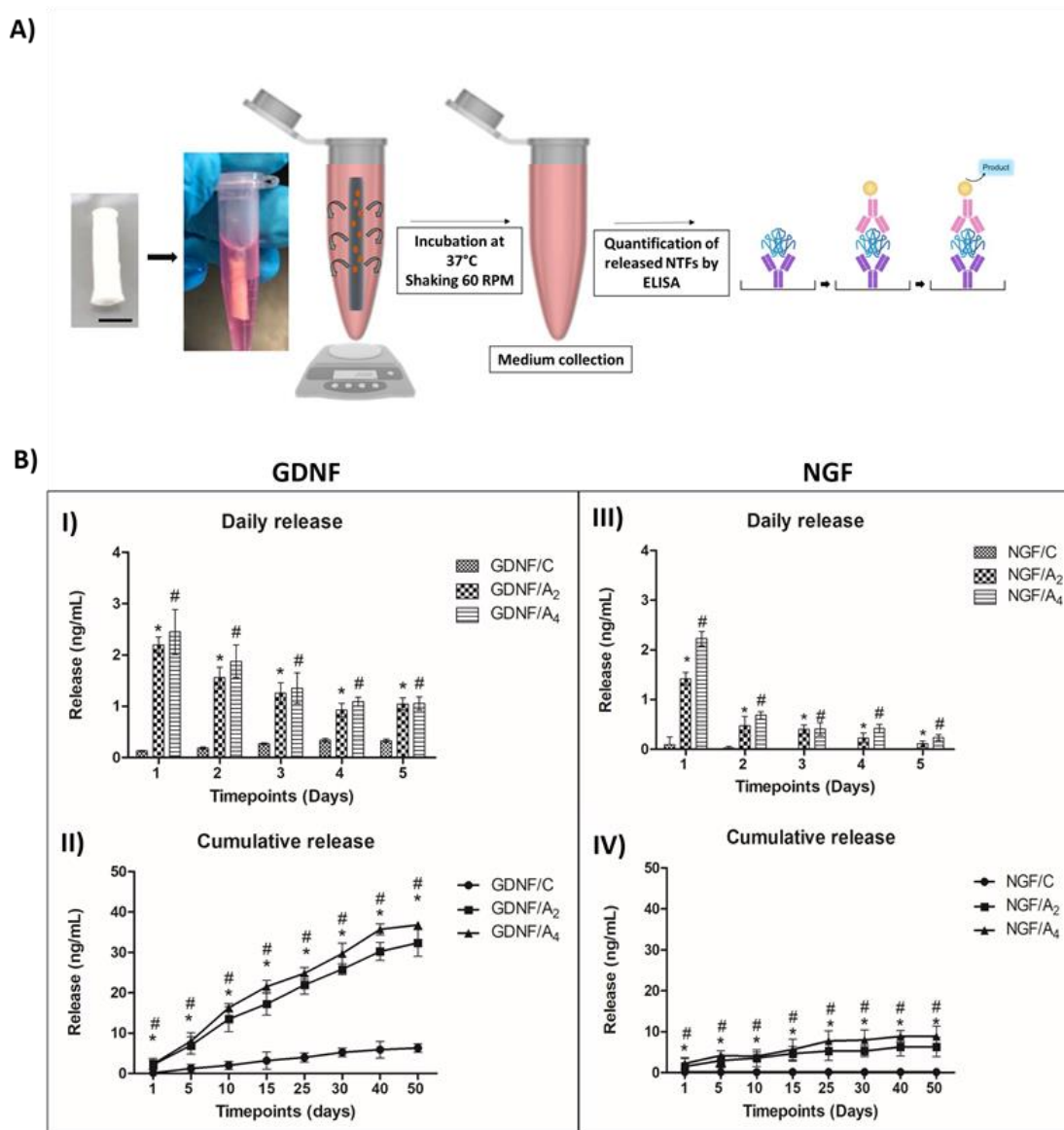


Figure X-2 - A) Scheme of the methodology used in the NTF release assay. Scale bar: 5 mm. B) ELISA quantification of the NTFs released from the eSF conduit, considering the different methods of incorporation, NTFs used and concentration. BI) Daily amount of GDNF released from eSF conduits within 5 days; BII) Cumulative amount of released GDNF within 50 days; BIII) Daily amount of NGF released from eSF conduits within 5 days; BIV) Cumulative amount of released NGF within 50 days. Results were represented as mean \pm SD (n=3). For multiple comparisons, * symbol indicates the comparison of GDNF/A2 or NGF/A2 and crosslinked formulations, # symbol regards comparison of GDNF/A4 or NGF/A4 and crosslinked formulations. Statistically significant differences were represented by */# (p < 0.5), **/## (p < 0.01), and ***/### (p < 0.001).

X-4.4. NTFs bioactivity assay with DRGs

The responses of the DRGs when subjected to the different conditions and different NTFs were evaluated in terms of neurite outgrowth (**Figure X-3**). The scheme of the methodology used in the bioactivity assay *in vitro* is presented in **Figure X-3A**. DRGs responses to GDNF can be observed qualitatively and quantitatively in **Figures X-3B** and **3C**, respectively. GDNF/A₄ formulation presented the highest values for all the parameters, whereas the crosslinked formulation presented the lowest, even lower than the negative control. More specifically, in terms of neurite length, there is a significant difference between the crosslinked samples (GDNF/C) and both absorption formulations (GDNF/A₂ and GDNF/A₄), where the longest neurites extended for an average of $122.8 \pm 119.3 \mu\text{m}$, $595.2 \pm 246.2 \mu\text{m}$ and $759.0 \pm 160.7 \mu\text{m}$, respectively. For the positive control and negative control, neurite length achieved values of $961.7 \pm 197.8 \mu\text{m}$ and $492.0 \pm 170.5 \mu\text{m}$, respectively. Regarding cellular migration from the DRG body, there was no significant differences between the values obtained for all the tested groups. The values obtained for the tested formulations (GDNF/C, GDNF/A₂ and GDNF/A₄), are $712.8 \pm 281.3 \mu\text{m}$, $1422.1 \pm 417.6 \mu\text{m}$, and $1525.8 \pm 384.9 \mu\text{m}$, respectively. For the positive and negative control, the values were $1307.3 \pm 266.9 \mu\text{m}$ and $854.7 \pm 282.9 \mu\text{m}$. In what concerns the percentage of field coverage, the values obtained were $1.3 \pm 0.8 \%$, $4.4 \pm 1.5 \%$ and $10.9 \pm 1.6 \%$ for GDNF/C, GDNF/A₂ and GDNF/A₄ formulations, respectively. In the positive and negative controls, values of $15.6 \pm 5.3 \%$ and $3.1 \pm 1.3 \%$ were obtained, respectively. For this parameter, a statistically significant difference was observed for GDNF/A₄ formulation when compared to GDNF/C and GDNF/A₂ samples. A summary of the above-mentioned information regarding GDNF treated DRGs can be found in **Supplementary Table X-1**.

DRGs responses to NGF can be seen qualitatively and quantitatively in **Figures X-3D** and **Figures X-3E**, respectively. The results obtained with NGF followed the same pattern as with GDNF. The NGF/A₄ formulation presented consistently higher values as compared to NGF/A₂ formulation, whereas lower neurite outgrowth was observed for NGF/C when compared to the negative control. More precisely, the neurite length reached values of $1072.6 \pm 227.4 \mu\text{m}$ for the positive control and $492.0 \pm 170.5 \mu\text{m}$ for the negative control. Regarding the formulations NGF/C, NGF/A₂ and NGF/A₄, the determined values were $220.5 \pm 116.6 \mu\text{m}$, $641.1 \pm 176.4 \mu\text{m}$ and $870.9 \pm 246.7 \mu\text{m}$, respectively. For this parameter, significant statistical differences were found between all the formulations containing NGF. For cellular migration, the media values were of $1464.8 \pm 262.9 \mu\text{m}$ for the positive control and $854.7 \pm 282.9 \mu\text{m}$

for the negative control. Regarding the formulations NGF/A₂ and NGF/A₄, the measured values were $1196.2 \pm 285.6 \mu\text{m}$ and $1560.4 \pm 403.6 \mu\text{m}$, respectively. In contrast, for NGF/C, no cellular migration was observed. A significant statistical difference was found between NGF/A₂ and NGF/A₄. For the percentage of field coverage obtained with NGF formulations, the values for the formulations NGF/C, NGF/A₂ and NGF/A₄ were $8 \pm 1.6 \%$, $4.2 \pm 1.0 \%$ and $7 \pm 1.4 \%$, respectively. On the other hand, values of $7.0 \pm 1.3 \%$ and $3.1 \pm 1.3 \%$ were determined for the positive control and negative control, respectively. Significant statistical differences were found between the two NGF absorption formulations and between NGF/A₄ and NGF/C formulation. A summary of above-mentioned information regarding NGF treated DRGs can be found in **Supplementary Table X-2**.

When comparing GDNF/A₄ with NGF/A₄ in terms of percentage of field coverage (**Figure X-4**), which reflects both the length and density of neurite outgrowth, it was observed a statistically significant difference between them, with values of $10.9 \pm 1.6 \%$ and $7 \pm 1.4 \%$, respectively. Due to the statistically significant different results obtained between both NTFs, GDNF/A₄ formulation was selected to proceed with further *in vivo* studies.

Taking a closer look at the confocal images, it is clear that the migratory stage of Schwann cells and the secretion of laminin cues closely interacts with axons (**Supplementary Figure X-5**) (34). It was also interesting to observe the whole axon physiology in the DRGs, where nucleated cells, assumed to be Schwann cells, were surrounding the growing neurites to form the myelin sheets,(35) as can be seen in **Supplementary Figure X-6**. From figure, it was also visible the terminal button, confirming the presence of growing axons.

X-4.5. *In vivo* study

Three different study groups were tested *in vivo*. The autograft, eSF and GDNF/A₄ were implanted in a 10 mm sciatic nerve defect in rats, by performing a sciatic nerve resection. The 3D printed tool allowed for a very clean and precise cut of the sciatic nerve, in the exact required position. All experimental animals tolerated the anesthesia and surgery and survived until the end of the observation period. Throughout the 6 weeks of *in vivo* experiment, animals were checked at least once a day and no complications were observed. All rats recovered well, without any sign of infection in the wounds, which healed completely approximately one week after surgery.

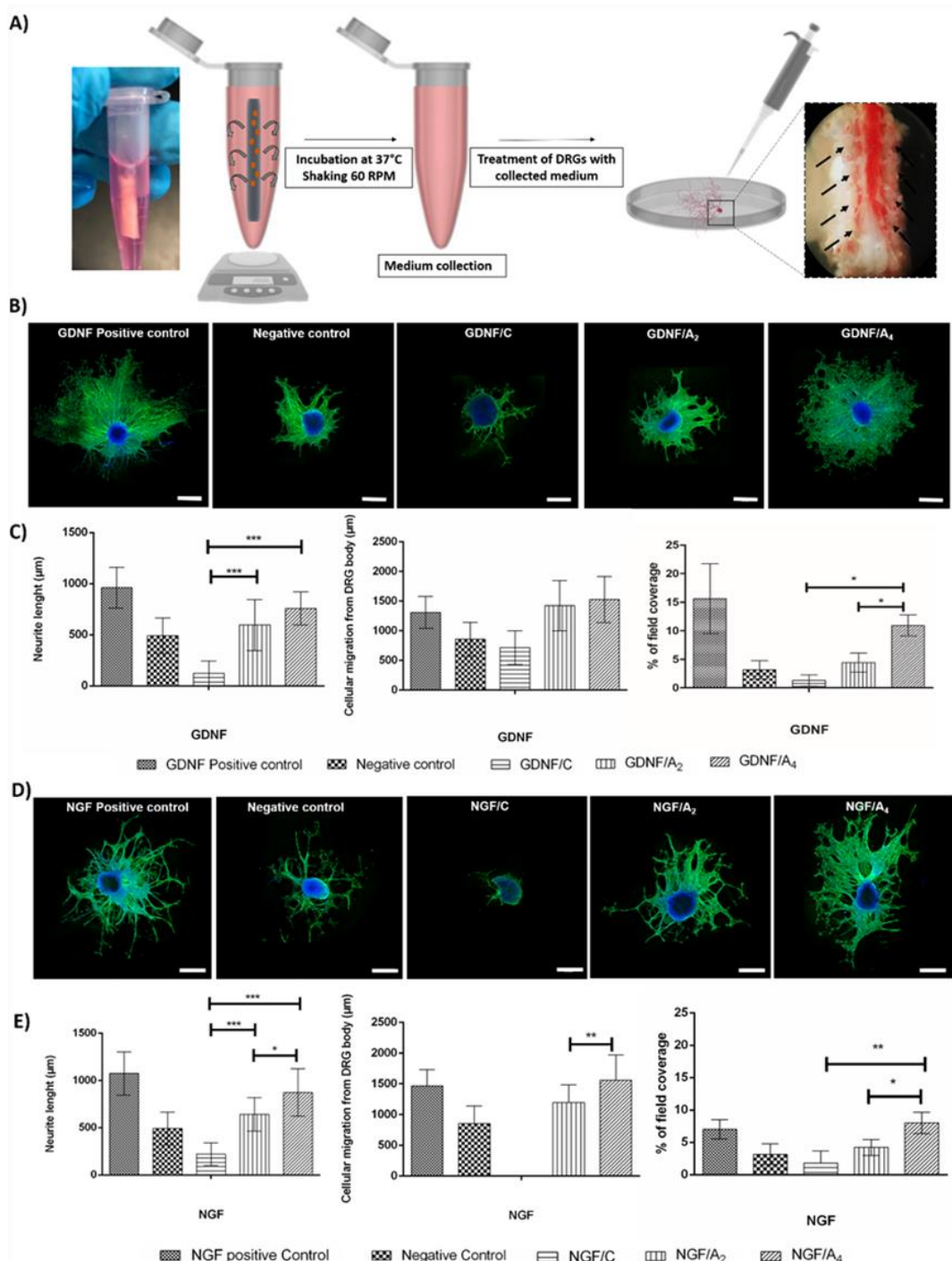


Figure X-3 - A) Scheme of the methodology used in the bioactivity assay *in vitro*, which is similar to the methodology used for ELISA quantification. B) Representative confocal fluorescent images of DRGs stained with Neurofilament 200 (in green) after being treated with GDNF released from eSF conduits. C) Quantification of different parameters related to the DRGs neurite outgrowth, such as neurite length, cellular migration from DRG body and percentage of field coverage after being in contact with GDNF releasing eSF conduits. D) Representative confocal fluorescent images of DRGs stained with Neurofilament 200 (in green) after being treated with NGF released from eSF conduits. E) Quantification of different parameters related to the DRGs neurite outgrowth, such as neurite length, cellular migration from DRG body and percentage of field coverage after being in

contact with NGF releasing eSF conduits. Statistically significant differences were represented by * ($p < 0.5$), ** ($p < 0.01$), and *** ($p < 0.001$). Scale bar: B and D) 500 μm .

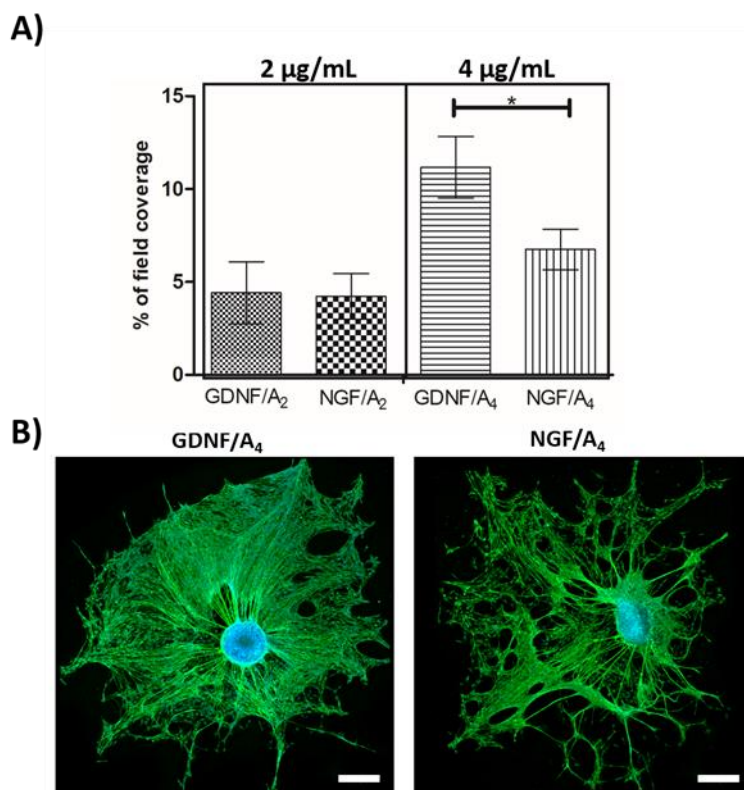


Figure X-4 - Impact of the different GDNF or NGF formulations on DRGs percentage of field coverage (which reflects both the length and density of neurite outgrowth). A) When considering the 4 $\mu\text{g/mL}$ concentration, there is a significant statistical difference between GDNF/A₄ and NGF/A₄ treated DRGs in terms of percentage of field coverage. Statistically significant differences were represented by * ($p < 0.5$), ** ($p < 0.01$), and *** ($p < 0.001$); **B)** Representative confocal fluorescent images of DRGs stained with Neurofilament 200 (in green) and Hoechst (in blue) after being treated with GDNF/A₄ or NGF/A₄ Scale bar: 500 μm .

No signs of ulcers or autophagy were verified in the paws of any of the 15 operated rats. Overall, no visible distress was detected in the animals after surgery. At the time of explantation, no signs of necrosis, acute inflammatory reaction, and calcifications were observed in the implant site and apparently, healthy connective tissue was observed surrounding all the explants.

The results of the pinch test can be seen in the **Table X-3**. At 6 weeks post-surgery, the distal segment of the nerve was isolated and stimulated with a pinch by forceps. Contraction of muscle on the back or retraction of the leg indicates the presence of regenerating sensory fibers in the pinched segment.

Table X-3 - Pinch test results indicating the level of regenerated nerves within the conduit.

| <i>In vivo</i> implanted formulations | Number of animals with positive result to pinch test |
|---------------------------------------|--|
| Autograft | 5/5 (100 %) |
| SF | 1/5 (20 %) |
| GDNF/A ₄ | 4/5 (80 %) |

In **Figure X-5A**, the different *in vivo* study groups: autograft, eSF and GDNF/A₄, implanted in the animals are shown. Nerve regeneration was further assessed through the percentage of muscle weight loss, which was determined to be $73.3 \pm 2.7 \%$, $79.8 \pm 1.3 \%$, and $76.6 \pm 2.6 \%$ for the autograft, eSF and GDNF/A₄ groups, respectively, as can be seen in **Figure X-5B**. The results illustrate that plain eSF NGC lead to a significant increase in terms of percentage of muscle weight loss ($p < 0.01$), when compared to the autograft. However, when using GDNF formulation, no significant differences were found. These results suggest that similar outcomes were obtained when autograft and GDNF/A₄ were used.

After analyzing the H&E stained longitudinal sections, a regeneration cable across the 10 mm nerve gap was observed in 100 % of the autografts (5/5), 80 % in the eSF conduits (4/5), and 100 % of the GDNF/A₄ (5/5). Furthermore, it was found that the longitudinal sectional nerve area was significantly higher in the GDNF/A₄ when compared to eSF (**Figure X-5C**), where the values obtained were $832.68 \pm 293.15 \mu\text{m}^2$, $390.55 \pm 130.18 \mu\text{m}^2$, and $950.99 \pm 239.58 \mu\text{m}^2$ for the autograft, eSF conduit and GDNF/A₄, respectively. This result can be seen qualitatively in **Figures X-5D**. The difference in the thickness of the nerve cable can evidently be seen in a cross-section of the NGCs, where the thickness of the cable roughly doubles from eSF to GDNF/A₄ as can be seen in **Figure X-5E**.

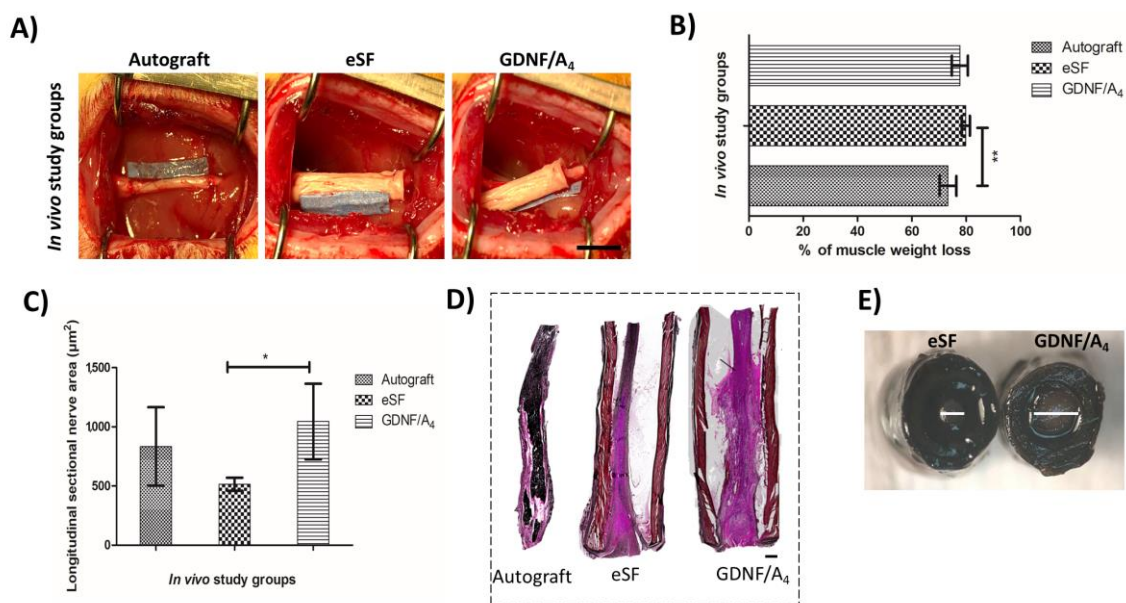


Figure X-5 - Assessment of the *in vivo* performance of the NTF-loaded eSF conduits in a sciatic defect model: A) Implantation of the different study groups: autograft, eSF and GDNF/A₄. B) Immediately after animal sacrifice, the percentage of muscle weight loss was determined. C) Quantitative measurements of the longitudinal sectional nerve area. Measurements were made in the middle of the conduit (since the proximal area was cut for histomorphometric analyses, the measurement was performed 7 mm from the distal stump). D) Representative photomicrographs of the longitudinal sections of implanted autograft, eSF and GDNF/A₄ after hematoxylin-eosin (H&E) staining. E) Representative photograph showing the difference in the regenerated nerve cable thickness. Statistically significant differences were represented by * ($p < 0.5$), ** ($p < 0.01$), and *** ($p < 0.001$). Scale bars: A) 500 μm; D): 500 μm; E) 250 μm (left) and 500 μm (right).

Explanted samples were cut for histological procedures according to the scheme in **Figure X-6A**. Semi-thin cross-sections were observed under a light microscope for a proximal area analysis (PNX section, view at the point of 3 mm outside the conduit), after osmium tetroxide staining. The number of regenerated myelinated nerve fibers detected (**Figure X-6B**) was similar in the case of the autograft ($5,443 \pm 985$) and the GDNF/A₄ formulation ($4,916 \pm 305$), but significantly higher in the eSF formulation ($9,281 \pm 2,957$). The healthy contralateral side contains an average of $6,110 \pm 745$ myelinated axons. Qualitatively, the nerve histological image from the GDNF/A₄ formulations resembles the one from the autograft, while the eSF formulation presented a distinct microstructure (**Figure X-6C**). Proximal myelinated nerves are larger and more uniform in the autograft and GDNF/A₄, as compared to the very irregular shape and size axons in the eSF formulation. In the same cross-section area (PNX), blood vessel quantification was performed, both qualitatively (**Supplementary Figure X-3**) and quantitatively (**Supplementary Figure X-4**). The results showed a significant difference between the autograft and the eSF conduits with and without GDNF. It was also observed a significant increase in

the blood vessel number in the presence of GDNF/A₄ reconstructed nerve as compared to the eSF conduit.

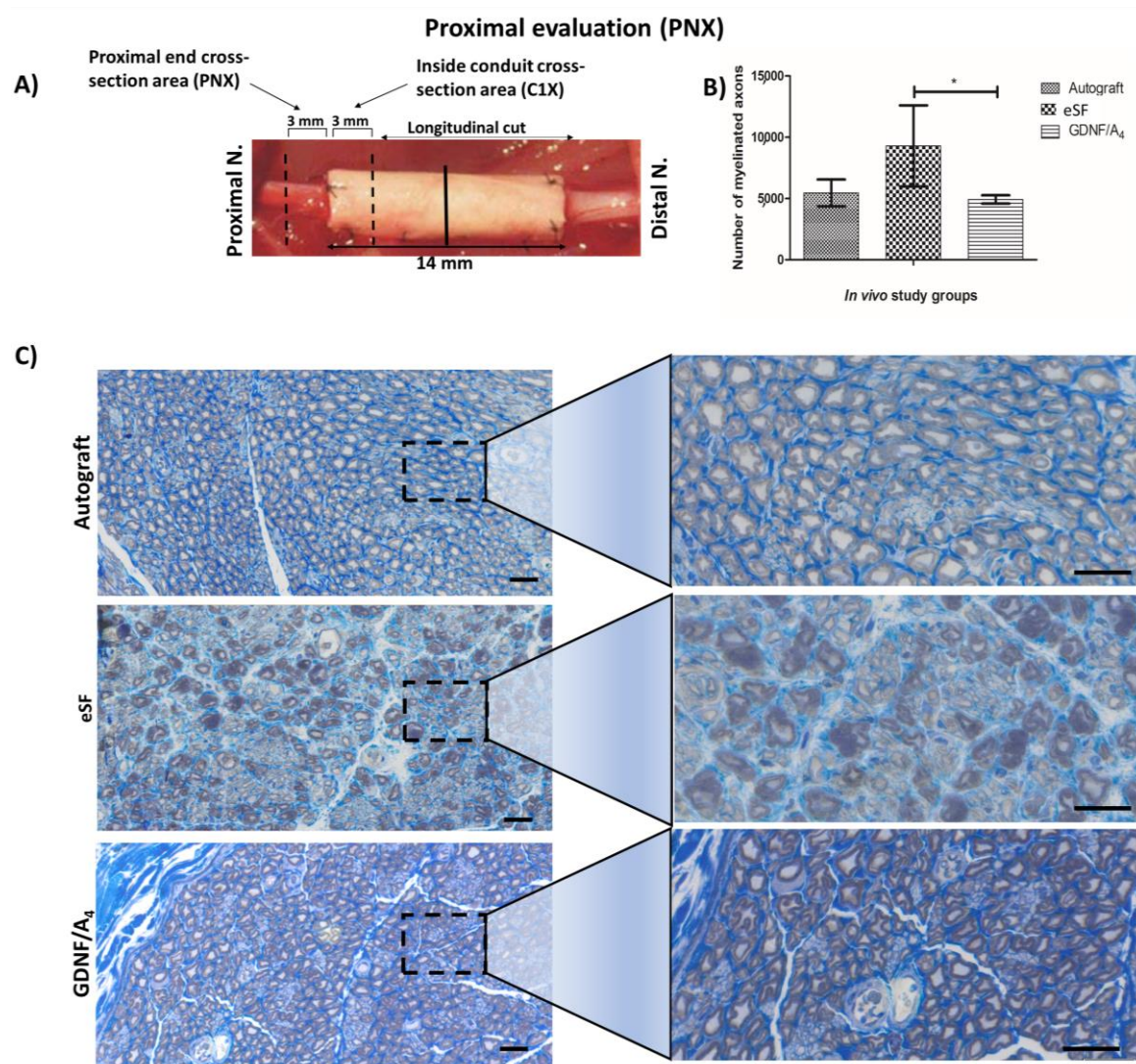


Figure X-6 - A) Schematic representation of the cross- and longitudinal sections positioning for histological analysis. B) Quantitative evaluation of myelinated axons in the proximal area (PNX), where statistically significant differences were represented by * ($p < 0.5$), ** ($p < 0.01$), and *** ($p < 0.001$). C) Light microscopy representative images of semi-thin nerve cross-sections in the PNX cross-section area, after osmium tetroxide and toluidine blue staining. On the right, close-up images of each *in vivo* study groups. Scale bar: 20 μm.

X-5. DISCUSSION

The lack of a pivotal breakthrough in PNR field is leading scientists and medical community to search for new and innovative ways to tackle the problem. As a consequence, TE is receiving increasing

attention in the treatment of PNI (36). As the classical FDA-approved NGCs do not provide sufficiently good results in terms of functional recovery, alternative strategies considering the mimicry of natural microenvironment and incorporation of physical and chemical cues for optimal axon guiding became crucial (37). Furthermore, several works confirmed that NGCs releasing NTFs can improve nerve regeneration across long nerve gaps (38). Including NTFs in a matrix is a required step since simple administration of NTFs is not sufficient to achieve an effective concentration over a suitable time period that would ultimately promote nerve repair. This is due to their rapid diffusion in the body fluids and destruction by proteolytic enzymes (39). In this context, the present study demonstrated the beneficial effects of controlled delivery of two PNS prominent growth factors, *i.e.* GDNF and NGF, in a way to reproduce the native NTF distribution during the nervous system development, therefore stimulating PNR (16). Moreover, different ways of immobilizing NTFs using a previously described production method of eSF conduits were investigated (20).

SF was selected for developing NGCs because of its well-known biocompatibility, good mechanical properties and friendly processing (40). The stability and bioactivity of NTFs during processing is enhanced when using mild processing conditions, which is the case of the eSF, where no organic solvents or harsh reagents were used.

For the crosslinking method, the loading efficiency can be considered as 100 %. In what concerns the absorption method, it has been hypothesized that the NTFs would be captured by the eSF conduit by two different manners. The first relates to the liquid absorption by the porous eSF wall, associated with the swelling capability of the material. The second regards the electrostatic interactions that occur between the negatively charged eSF and the positively charged NTFs,(41) which play a crucial role in this process. In this sense, the affinity of GDNF or NGF proteins to the eSF conduit can partially determine its loading efficiency and give rise to a differential absorption/adsorption. There is a difference of approximately 30 % between the absorption efficiency of GDNF to NGF, being GDNF more prone to bind to the eSF conduit. Without any other variables in the process, this differential absorption could be explained by the molecular/ionic affinity to eSF, which is higher in the case of GDNF, having a higher positive charge when compared to NGF. This is due to the fact that GDNF has an amino-acid rich sequence of 16 N-terminal residues (42). In this context, it can be predicted that higher NTFs loading implies higher release. The higher affinity binding of GDNF to the SF conduit was visible in its daily release profile, where GDNF has a more sustained release when compared to the burst release observed in the NGF loaded conduits. Similarly, the same principle of higher loading resulting in higher

release was verified for both GDNF and NGF, as the GDNF/A₄ and NGF/A₄ formulations released higher amounts of NTFs than GDNF/A₂ and NGF/A₂. When comparing the crosslinking to the absorption method, and given the fact that the same amounts of NTF were loaded in the crosslinked 4 µg/mL and absorption 4 µg/mL formulations, the minute amounts of NTFs released in the crosslinked formulation evidences the initial hypothesis of stronger molecular entrapment and difficulty to diffuse across the conduit wall. Furthermore, in addition to the expected entrapment of NTFs in the SF matrix, we hypothesize that NTFs could have been covalently linked to each other and to SF tyrosine groups.

Overall, the quantity of GDNF and NGF released by GDNF/A₄ and NGF/A₄ formulations, respectively, were similar and in the range of the release values reported in the literature, also demonstrating that the absorption/surface binding which occurs during the absorption process allowed the NTFs to maintain a relatively stable and adequate concentration (16, 43). Controlled release of GDNF and NGF in the range of 1-10 ng/mL from SF-based NGCs has been suggested to be optimal for nerve repair,(44) which was also verified in our experimental work.

We then investigated the effect of the different formulations on neurite outgrowth of freshly isolated DRGs *in vitro*, seeded on Matrigel®. Matrigel® was selected as substrate, since DRGs are highly mechanosensitive and its hydrogel-like stiffness represents the optimal surface for regeneration (34, 45). Furthermore, in the case of negative control, despite the absence of added NTFs, neurite outgrowth was observed since Matrigel® can be considered a permissive substrate,(46) very rich in extracellular matrix (ECM) proteins, namely laminin, which is optimal for neuronal cells attachment (47-49). Matrigel® has been routinely used in pre-clinical studies for neuronal cells' adhesion and proliferation and its effect in neurite extension has been studied.(49) DRG neurons are constituents of the peripheral sensory nervous system and one of the best models to study PNR (50). The parameters evaluated were the conventional neurite length, cellular migration from DRG body and percentage of field coverage. The pattern of the results was similar for GDNF- and NGF-treated ganglia, where neurite outgrowth reached its maximum in the GDNF/A₄ and NGF/A₄ formulations, followed by the intermediate values obtained by GDNF/A₂ and NGF/A₂. The crosslinked formulations, *i.e.* GDNF/C and NGF/C, presented the lowest values for neurite outgrowth. Such results are in accordance with their respective releasing profile, where higher amounts of released NTF led to increased neurite length, cellular migration, and percentage of field coverage. The results are also in accordance with other reports, where DRGs were shown to respond to concentrations of 1-2 ng/mL of GDNF or NGF (43). Although we initially predicted good outcomes from the crosslinking formulations by preventing NTF burst release,

the *in vitro* results showed otherwise. We can hypothesize that, when compared to the negative control, the poor performance of the crosslinked formulations can be explained by the fact that both NTFs are rich in tyrosine amino acid, possibly leading to an enzymatic crosslinking between SF and NTFs. This covalent binding can result in the slow release of the NTFs, which can be beneficial for long-term applications of the eSF conduits such as the case of the regeneration of long-gaps (51, 52). However, the low amounts released still seem to have an undesired effect on neurite outgrowth, possibly due to binding of the GF to the receptors, occupying or blocking them. In this scenario, the ECM molecules that have a favorable effect in the presence of Matrigel® (also present in the negative control) would not be able to act in the crosslinked formulation.

A strong correlation was found between cellular migration and neurite outgrowth (53, 54). It was evident in the confocal images that cellular components that were isolated with the DRGs, namely Schwann cells and fibroblasts, were paving the way for neurite growth. Only in the case of visible cellular proliferation and spreading, neurite outgrowth would be detected

Neurite length in the positive control is similar to what is found in the literature, with an average growth of 100-200 μm per day, validating our study (55). It has been shown that Schwann cell proliferation and migration play a crucial role during nerve regeneration (56). Therefore, it is possible to predict that which NTF is able to promote a higher Schwann cell migration, is also capable of further enhancing the *in vivo* outcomes. Together with the ELISA results, the *in vitro* biological tests allowed to exclude any crosslinked formulation for further studies and elect the GDNF/A₄ and NGF/A₄ as the most promising formulations. In our study, GDNF and NGF prompted similar neurite elongation, but GDNF increased the neurite density. In this context, GDNF/A₄ was selected for the *in vivo* evaluation since its percentage of field coverage was significantly higher than NGF/A₄.

Considering the results withdrew from the *in vivo* study, the presence of GDNF significantly promoted motor reinnervation and motor fibers survival, as the muscle weight loss or atrophy was significantly avoided in the gastrocnemius muscle, when compared to the SF samples, which was critical for functional recovery (57). On the other hand, in relation to the pinch test, the reflex shown by most of the animals in the GDNF/A₄ study group, proves that GDNF could act on sensory reinnervation. (58) These findings could be related to the *in vitro* biological observations, where sensory DRGs positively respond to GDNF.

Longitudinal H&E sections allowed to study the general nerve regeneration potential of the different formulations. A complete fibrin nerve cable formation is essential for obtaining a complete nerve regeneration with functional recovery. Longitudinal sectional nerve area and number of samples in which the nerve cable was able to cross the 10 mm gap, point to GDNF supplemented SF conduits to significantly outperform the SF formulation.

It has to be taken in consideration that the active retrograde transport of growth factors is crucial for the normal function of nerves, and disorders in this mechanism result in neurodegeneration, neuropathies and cell death (59). Signaling proteins frequently travel from the axon terminals to the cell body in order to trigger and stimulate their signaling pathways. In the case of an injury, NTFs released by the native tissue are transported to the cell bodies, in order to promote survival mechanisms (60). In this experimental work, a simple osmium tetroxide/toluidine blue staining allowed to assess that GDNF/A₄ formulation showed better retrograde nerve protection and nerve trunk protection when compared to the SF conduit (61). In the proximal area, without the GDNF being transported backwards, SF reconstructed nerves suffered from significant degeneration. Although it is noteworthy that many axons began sprouting from proximal site, this indicated that nerve was severely damaged and withdrew further back down from injury site. In this scenario, the regeneration may be delayed or failed.

Only recently the scientific community has realized the importance of vascularization in PNR. In fact, the lack of blood supply is one of the most important and limiting factors impairing regeneration (62). Although no specific vascularization staining was performed, blood vessels are well-identified in the toluidine blue staining because of the visible endothelial wall, shape and presence of erythrocytes (63). The significant increment on blood vessel number in the nerve regenerated within the GDNF/A₄ conduit demonstrated the beneficial environment provided by the developed NGC, while confirming the direct relationship between nerve regeneration and angiogenesis (64). It has been shown that not only the new vasculature reduces hypoxia in the regenerating nerve, but Schwann cells use the blood vessels present in the proximal nerve as “tracks” to cross and migrate through the bridge, taking re-growing axons with them (65). These results confirm other reports, where certain GDNF peptides are described as potent angiogenic factors (66). Thus, all evidence withdrew from this study points to the gainful effects of trophically functionalizing NGCs.

The advantageous effects of an NGC on nerve repair will difficultly achieve a similar performance than an autograft. Still, the developed GDNF loaded SF conduit performed similarly to the autograft in the variety of parameters evaluated, namely in what concerns the quality of the regenerated nerve cable

and recovery of nerve function (assessed by the pinch test). Although a 6-weeks period for nerve regeneration can be considered short and early for some assessments, such as electrophysiological evaluations, the fact that significant statistical differences were found between the studied formulations in some parameters, confirms that effective conclusions can be made from this study.

X-6. CONCLUSIONS

In this study, we have demonstrated that the enzymatically crosslinked silk fibroin conduits may be loaded with two different neurotrophic factors, via different methodologies. They presented distinctive releasing profiles, according to their affinity to silk fibroin. *In vitro*, the superior releasing profile of GDNF could be assessed when it was incorporated by the adsorption method at the concentration of 4 µg/mL. These results were confirmed when DRGs' neurite density was significantly enhanced in the presence of such formulation. Furthermore, the valuable effects of GDNF/A₄ on improving nerve regeneration *in vivo* resulted in a suitable environment for peripheral nerve regeneration. Implanting such formulation on a 10 mm rat sciatic nerve defect acted on both sensory and motor fibers, as was perceived by the specific assays of pinch test and percentage of muscle weight loss. Related to the histological and histomorphometrical evaluation, when using the adsorbed GDNF formulation, proximal nerve protection was found to be more robust when compared to plain silk fibroin conduit and comparable to the autograft, via retrograde transport of GDNF. Vascularization was also significantly increased by the addition of GDNF to silk fibroin, which represents another gain in terms of nerve regeneration.

Overall, the addition of GDNF to the silk fibroin conduit could be one possible treatment to prevent neurodegeneration. The findings from this experimental work could significantly contribute to TE field. It is our firm belief that the developed GDNF-incorporating silk fibroin conduit is a promising candidate for future studies, where cellular therapies and guiding luminal fillers might be included, creating new and multi-factorial therapeutic alternatives for the treatment of peripheral nerve injuries.

X-7. ACKNOWLEDGMENTS

This work was supported by Cristiana Carvalho PhD scholarship (Norte-08-5369-FSE-000037) and awarded FLAD scholarship (Proj. 29/2018). The FCT distinctions attributed to J. M. Oliveira

(IF/00423/2012 and IF/01285/2015) and J. Silva-Correia (IF/00115/2015) under the Investigador FCT program are also greatly acknowledged. The authors also would like to thank Ijaz Ahmed from the BME department and Joe Steel from NJCBM, both from Rutgers University, for their important contribution in this scientific paper. The New Jersey Center for Biomaterials at Rutgers University provided additional support for this study. The authors would also like to acknowledge the project: “Nano-accelerated nerve regeneration and optogenetic empowering of neuromuscular functionality” (ref. PTDC/NAN-MAT/29936/2017).

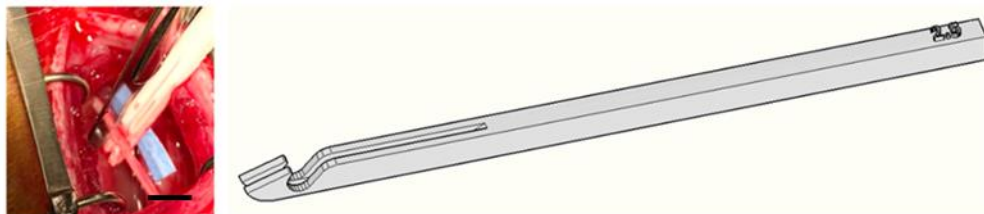
X-8. REFERENCES

1. Wiberg M, Terenghi G. Will it be possible to produce peripheral nerves? *Surgical technology international*. 2003;11:303-10.
2. Grinsell D, Keating CP. Peripheral Nerve Reconstruction after Injury: A Review of Clinical and Experimental Therapies. *BioMed Research International*. 2014;2014:13.
3. Carvalho CR, Costa JB, da Silva Morais A, López-Cebral R, Silva-Correia J, Reis RL, et al. Tunable Enzymatically Cross-Linked Silk Fibroin Tubular Conduits for Guided Tissue Regeneration. *Advanced Healthcare Materials*. 2018;7(17):1800186.
4. Deumens R, Bozkurt A, Meek MF, Marcus MA, Joosten EA, Weis J, et al. Repairing injured peripheral nerves: Bridging the gap. *Progress in neurobiology*. 2010;92(3):245-76.
5. Patel N, Lyon K, Huang J. An update on tissue engineered nerve grafts for the repair of peripheral nerve injuries. *Neural Regeneration Research*. 2018;13(5):764-74.
6. Horner PJ, Gage FH. Regenerating the damaged central nervous system. *Nature*. 2000;407(6807):963-70.
7. Kingham PJ, Terenghi G. Bioengineered nerve regeneration and muscle reinnervation. *Journal of anatomy*. 2006;209(4):511-26.
8. Tajdaran K, Chan K, Gordon T, Borschel GH. Matrices, scaffolds, and carriers for protein and molecule delivery in peripheral nerve regeneration. *Experimental Neurology*. 2018.
9. Meek MF, Coert JH. US Food and Drug Administration/Conformit Europe-approved absorbable nerve conduits for clinical repair of peripheral and cranial nerves. *Annals of plastic surgery*. 2008;60(1):110-6.
10. Blais M, Lévesque P, Bellenfant S, Berthod F. Nerve Growth Factor, Brain-Derived Neurotrophic Factor, Neurotrophin-3 and Glial-Derived Neurotrophic Factor Enhance Angiogenesis in a Tissue-Engineered In Vitro Model. *Tissue Engineering Part A*. 2013;19(15-16):1655-64.
11. Rich KM, Luszczynski JR, Osborne PA, Johnson EM, Jr. Nerve growth factor protects adult sensory neurons from cell death and atrophy caused by nerve injury. *Journal of neurocytology*. 1987;16(2):261-8.
12. Wong V, Arriaga R, Ip NY, Lindsay RM. The Neurotrophins BDNF, NT-3 and NT-4/5, But Not NGF, Up-regulate the Cholinergic Phenotype of Developing Motor Neurons. *European Journal of Neuroscience*. 1993;5(5):466-74.
13. Blesch A, Tuszynski MH. Cellular GDNF delivery promotes growth of motor and dorsal column sensory axons after partial and complete spinal cord transections and induces remyelination. *Journal of Comparative Neurology*. 2003;467(3):403-17.
14. Petruska JC, Mendell LM. Nerve Growth Factor. In: Squire LR, editor. *Encyclopedia of Neuroscience*. Oxford: Academic Press; 2009. p. 71-8.
15. Ho PR, Coan GM, Cheng ET, Niell C, Tarn DM, Zhou H, et al. Repair with collagen tubules linked with brain-derived neurotrophic factor and ciliary neurotrophic factor in a rat sciatic nerve injury model. *Archives of otolaryngology–head & neck surgery*. 1998;124(7):761-6.
16. Tang S, Zhu J, Xu Y, Xiang AP, Jiang MH, Quan D. The effects of gradients of nerve growth factor immobilized PCLA scaffolds on neurite outgrowth in vitro and peripheral nerve regeneration in rats. *Biomaterials*. 2013;34(29):7086-96.
17. Wang S, Cai Q, Hou J, Bei J, Zhang T, Yang J, et al. Acceleration effect of basic fibroblast growth factor on the regeneration of peripheral nerve through a 15-mm gap. *Journal of Biomedical Materials Research Part A*. 2003;66A(3):522-31.

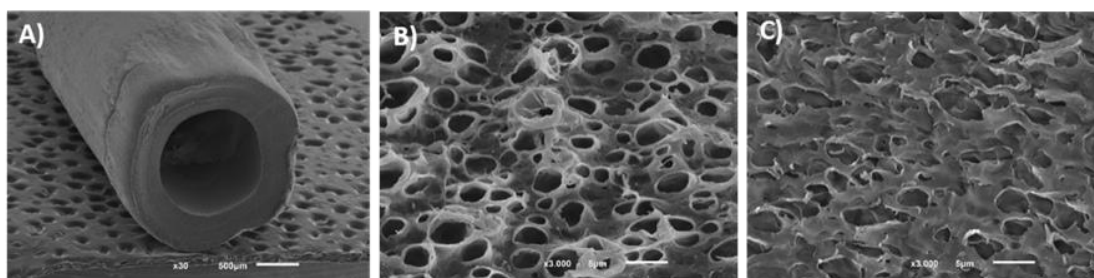
18. Tajdaran K, Chan K, Gordon T, Borschel GH. Matrices, scaffolds, and carriers for protein and molecule delivery in peripheral nerve regeneration. *Experimental neurology*. 2018.
19. Madduri S, Papaloizos M, Gander B. Trophically and topographically functionalized silk fibroin nerve conduits for guided peripheral nerve regeneration. *Biomaterials*. 2010;31(8):2323-34.
20. Carvalho CR, Costa JB, da Silva Morais A, Lopez-Cebral R, Silva-Correia J, Reis RL, et al. Tunable Enzymatically Cross-Linked Silk Fibroin Tubular Conduits for Guided Tissue Regeneration. 2018;7(17):e1800186.
21. Uebersax L, Mattotti M, Papaloizos M, Merkle HP, Gander B, Meinel L. Silk fibroin matrices for the controlled release of nerve growth factor (NGF). *Biomaterials*. 2007;28(30):4449-60.
22. Chowdary PD, Che DL, Zhang K, Cui B. Retrograde NGF axonal transport–motor coordination in the unidirectional motility regime. *Biophysical journal*. 2015;108(11):2691-703.
23. Ito K, Enomoto H. Retrograde transport of neurotrophic factor signaling: implications in neuronal development and pathogenesis. *The Journal of Biochemistry*. 2016;160(2):77-85.
24. Abe N, Cavalli V. Nerve injury signaling. *Current opinion in neurobiology*. 2008;18(3):276-83.
25. Paravicini U, Stoeckel K, Thoenen H. Biological importance of retrograde axonal transport of nerve growth factor in adrenergic neurons. *Brain research*. 1975;84(2):279-91.
26. Carvalho CR, Costa JB, da Silva Morais A, Lopez-Cebral R, Silva-Correia J, Reis RL, et al. Tunable Enzymatically Cross-Linked Silk Fibroin Tubular Conduits for Guided Tissue Regeneration. 2018:e1800186.
27. Yan LP, Silva-Correia J, Ribeiro VP, Miranda-Goncalves V, Correia C, da Silva Morais A, et al. Tumor Growth Suppression Induced by Biomimetic Silk Fibroin Hydrogels. *Scientific reports*. 2016;6:31037.
28. Balgude AP, Yu X, Szymanski A, Bellamkonda RV. Agarose gel stiffness determines rate of DRG neurite extension in 3D cultures. *Biomaterials*. 2001;22(10):1077-84.
29. Bilsland J, Rigby M, Young L, Harper S. A rapid method for semi-quantitative analysis of neurite outgrowth from chick DRG explants using image analysis. *Journal of Neuroscience Methods*. 1999;92(1):75-85.
30. Deister C, Schmidt CE. Optimizing neurotrophic factor combinations for neurite outgrowth. *Journal of neural engineering*. 2006;3(2):172-9.
31. Wang HB, Mullins ME, Cregg JM, Hurtado A, Oudega M, Trombley MT, et al. Creation of highly aligned electrospun poly-L-lactic acid fibers for nerve regeneration applications. *Journal of neural engineering*. 2009;6(1):016001.
32. Chang W, Shah MB, Lee P, Yu X. Tissue-engineered spiral nerve guidance conduit for peripheral nerve regeneration. *Acta biomaterialia*. 2018;73:302-11.
33. Carvalho CR, Costa JB, Ribeiro V, Silva-Correia J, Oliveira JM, Reis RL, inventors Nerve guidance conduits derived from silk fibroin hydrogels: methods of production and uses thereof patent P406.1 PP, WO18025186. 2016.
34. Rosso G, Young P, Shahin V. Mechanosensitivity of Embryonic Neurites Promotes Their Directional Extension and Schwann Cells Progenitors Migration. *Cellular physiology and biochemistry : international journal of experimental cellular physiology, biochemistry, and pharmacology*. 2017;44(4):1263-70.
35. Corfas G, Velardez MO, Ko C-P, Ratner N, Peles E. Mechanisms and Roles of Axon-Schwann Cell Interactions. *The Journal of Neuroscience*. 2004;24(42):9250-60.
36. Liu F, Lin H, Zhang C. Construction of Tissue-Engineered Nerve Conduits Seeded with Neurons Derived from Hair-Follicle Neural Crest Stem Cells. *Methods in molecular biology (Clifton, NJ)*. 2016;1453:33-8.
37. Liu C, Wang C, Zhao Q, Li X, Xu F, Yao X, et al. Incorporation and release of dual growth factors for nerve tissue engineering using nanofibrous bicomponent scaffolds. *Biomedical materials (Bristol, England)*. 2018;13(4):044107.
38. Xiao N, Le Q-T. Neurotrophic Factors and Their Potential Applications in Tissue Regeneration. *Archivum immunologiae et therapiae experimentalis*. 2016;64(2):89-99.
39. Wang B, Yuan J, Xu J, Chen X, Ying X, Dong P. Brain-derived and glial cell line-derived neurotrophic factor fusion protein immobilization to laminin. *Experimental and therapeutic medicine*. 2017;13(1):178-86.
40. Abbott RD, Kimmerling EP, Cairns DM, Kaplan DL. Silk as a Biomaterial to Support Long-Term Three-Dimensional Tissue Cultures. *ACS Applied Materials & Interfaces*. 2016;8(34):21861-8.
41. Madduri S, Gander B. Schwann cell delivery of neurotrophic factors for peripheral nerve regeneration. *Journal of the peripheral nervous system : JPNS*. 2010;15(2):93-103.
42. Alfano I, Vora P, Mummery RS, Mulloy B, Rider CC. The major determinant of the heparin binding of glial cell-line-derived neurotrophic factor is near the N-terminus and is dispensable for receptor binding. *The Biochemical journal*. 2007;404(1):131-40.
43. Madduri S, Papaloizos M, Gander B. Trophically and topographically functionalized silk fibroin nerve conduits for guided peripheral nerve regeneration. *Biomaterials*. 2010;31(8):2323-34.
44. Catrina S, Gander B, Madduri S. Nerve conduit scaffolds for discrete delivery of two neurotrophic factors. *European journal of pharmaceuticals and biopharmaceuticals : official journal of Arbeitsgemeinschaft fur Pharmazeutische Verfahrenstechnik eV*. 2013;85(1):139-42.

45. Rosso G, Liashkovich I, Young P, Rohr D, Shahin V. Schwann cells and neurite outgrowth from embryonic dorsal root ganglions are highly mechanosensitive. *Nanomedicine : nanotechnology, biology, and medicine*. 2017;13(2):493-501.
46. Novikova LN, Mosahebi A, Wiberg M, Terenghi G, Kellerth JO, Novikov LN. Alginate hydrogel and matrigel as potential cell carriers for neurotransplantation. *Journal of biomedical materials research Part A*. 2006;77(2):242-52.
47. Hughes CS, Postovit LM, Lajoie GA. Matrigel: a complex protein mixture required for optimal growth of cell culture. *Proteomics*. 2010;10(9):1886-90.
48. Lee SJ, Zhu W, Heyburn L, Nowicki M, Harris B, Zhang LG. Development of Novel 3-D Printed Scaffolds With Core-Shell Nanoparticles for Nerve Regeneration. *IEEE transactions on bio-medical engineering*. 2017;64(2):408-18.
49. Wu S, Chen MS, Maurel P, Lee YS, Bunge MB, Arinzeh TL. Aligned fibrous PVDF-TrFE scaffolds with Schwann cells support neurite extension and myelination in vitro. *Journal of neural engineering*. 2018;15(5):056010.
50. Sajjilafu, Zhou FQ. Genetic study of axon regeneration with cultured adult dorsal root ganglion neurons. *Journal of visualized experiments : JoVE*. 2012(66).
51. Xue C, Zhu H, Tan D, Ren H, Gu X, Zhao Y, et al. Electrospun silk fibroin-based neural scaffold for bridging a long sciatic nerve gap in dogs. *Journal of tissue engineering and regenerative medicine*. 2018;12(2):e1143-e53.
52. Lin YC, Ramadan M, Hronik-Tupaj M, Kaplan DL, Philips BJ, Sivak W, et al. Spatially controlled delivery of neurotrophic factors in silk fibroin-based nerve conduits for peripheral nerve repair. *Annals of plastic surgery*. 2011;67(2):147-55.
53. Thompson DM, Buettner HM. Neurite Outgrowth Is Directed by Schwann Cell Alignment in the Absence of Other Guidance Cues. *Annals of Biomedical Engineering*. 2006;34(1):161.
54. Bunge RP. Tissue culture observations relevant to the study of axon-Schwann cell interactions during peripheral nerve development and repair. *The Journal of experimental biology*. 1987;132:21-34.
55. Tonge DA, Golding JP, Edbladh M, Kroon M, Ekstrom PE, Edstrom A. Effects of extracellular matrix components on axonal outgrowth from peripheral nerves of adult animals in vitro. *Exp Neurol*. 1997;146(1):81-90.
56. Jessen KR, Mirsky R. The Success and Failure of the Schwann Cell Response to Nerve Injury. *Frontiers in Cellular Neuroscience*. 2019;13(33).
57. Mirzakhani N, Farshid AA, Tamaddonfard E, Imani M, Erfanparast A, Noroozina F. Carnosine improves functional recovery and structural regeneration after sciatic nerve crush injury in rats. *Life sciences*. 2018.
58. Lundborg G, Dahlin L, Dohi D, Kanje M, Terada N. A new type of “bioartificial” nerve graft for bridging extended defects in nerves. *The Journal of Hand Surgery: British & European Volume*. 1997;22(3):299-303.
59. Bisby MA. Functions of retrograde axonal transport. *Federation proceedings*. 1982;41(7):2307-11.
60. Zweifel LS, Kuruvilla R, Ginty DD. Functions and mechanisms of retrograde neurotrophin signalling. *Nature reviews Neuroscience*. 2005;6(8):615-25.
61. Ghnenis AB, Czaikowski RE, Zhang ZJ, Bushman JS. Toluidine Blue Staining of Resin-Embedded Sections for Evaluation of Peripheral Nerve Morphology. *Journal of visualized experiments : JoVE*. 2018(137).
62. Novosel EC, Kleinhans C, Kluger PJ. Vascularization is the key challenge in tissue engineering. *Advanced drug delivery reviews*. 2011;63(4-5):300-11.
63. Sierpinski P, Garrett J, Ma J, Apel P, Klorig D, Smith T, et al. The use of keratin biomaterials derived from human hair for the promotion of rapid regeneration of peripheral nerves. *Biomaterials*. 2008;29(1):118-28.
64. Wang HK, Wang YX, Xue CB, Li ZM, Huang J, Zhao YH, et al. Angiogenesis in tissue-engineered nerves evaluated objectively using MICROFIL perfusion and micro-CT scanning. 2016;11(1):168-73.
65. Wang H, Zhu H, Guo Q, Qian T, Zhang P, Li S, et al. Overlapping Mechanisms of Peripheral Nerve Regeneration and Angiogenesis Following Sciatic Nerve Transection. *Frontiers in cellular neuroscience*. 2017;11:323-.
66. Blais M, Levesque P, Bellenfant S, Berthod F. Nerve growth factor, brain-derived neurotrophic factor, neurotrophin-3 and glial-derived neurotrophic factor enhance angiogenesis in a tissue-engineered in vitro model. *Tissue engineering Part A*. 2013;19(15-16):1655-64.

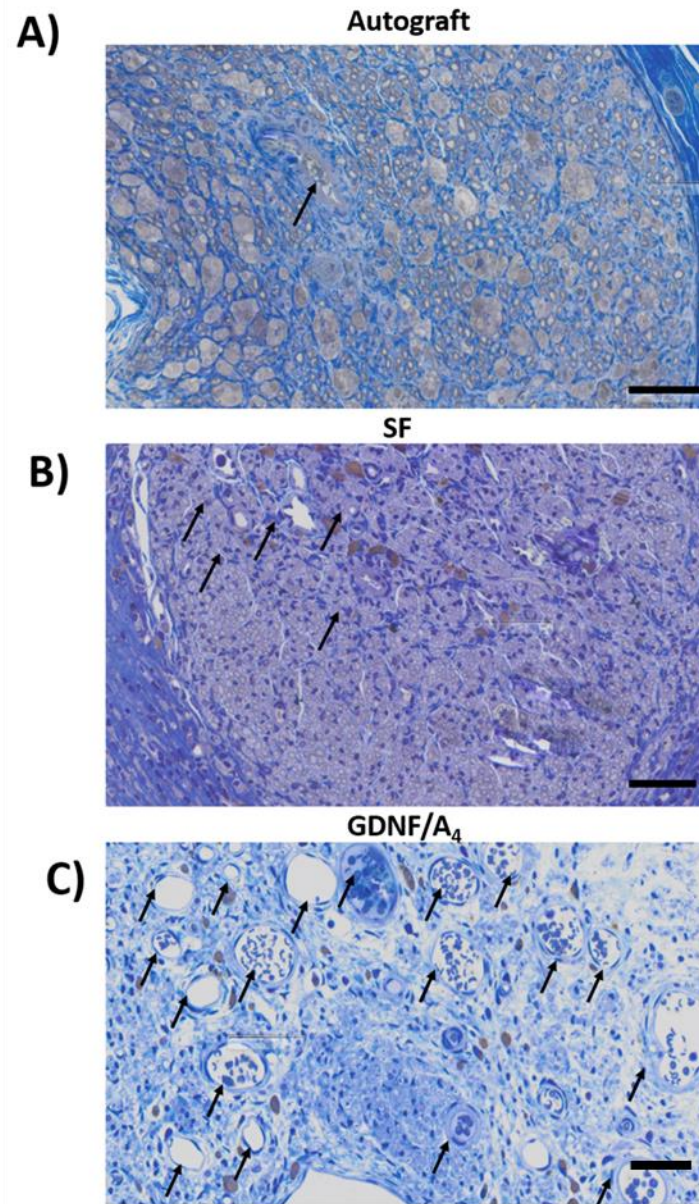
X-9. SUPPLEMENTARY DATA



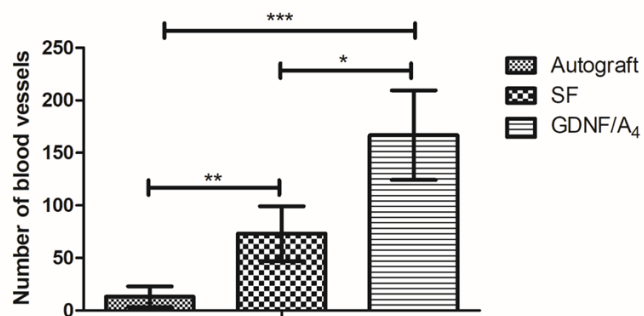
Supplementary Figure X-1 - Photograph and scheme of the nerve cutting tool used in the in vivo study, designed to precisely hold and cut the sciatic nerve during surgery. Tools were 3D-printed using poly(lactic acid) and consisted of a hook with an inner diameter of 2.5 mm and a scalpel alignment groove 700 µm in width. Scale bar: 5 mm.



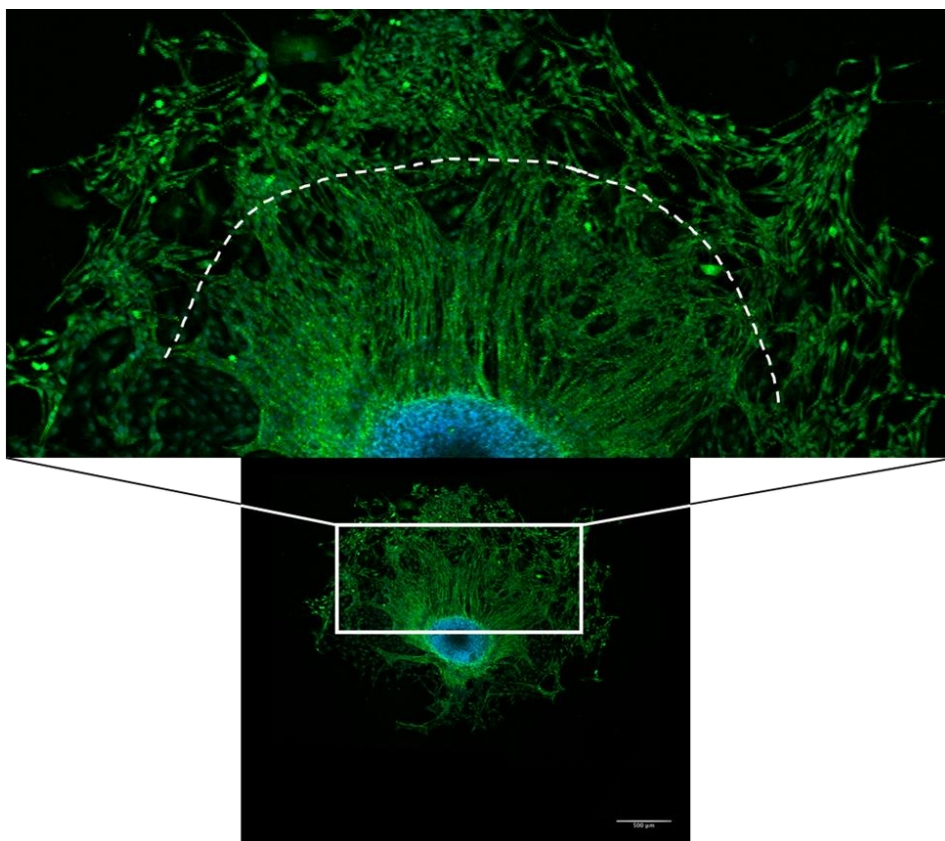
Supplementary Figure X-2 - Representative SEM micrographs of the SF NGCs microstructure: A) overall aspect of the conduit; B) outer surface of the conduit; C) inner surface of the conduit. Scale bars: A) 500 µm; B) 5 µm; C) 5 µm.



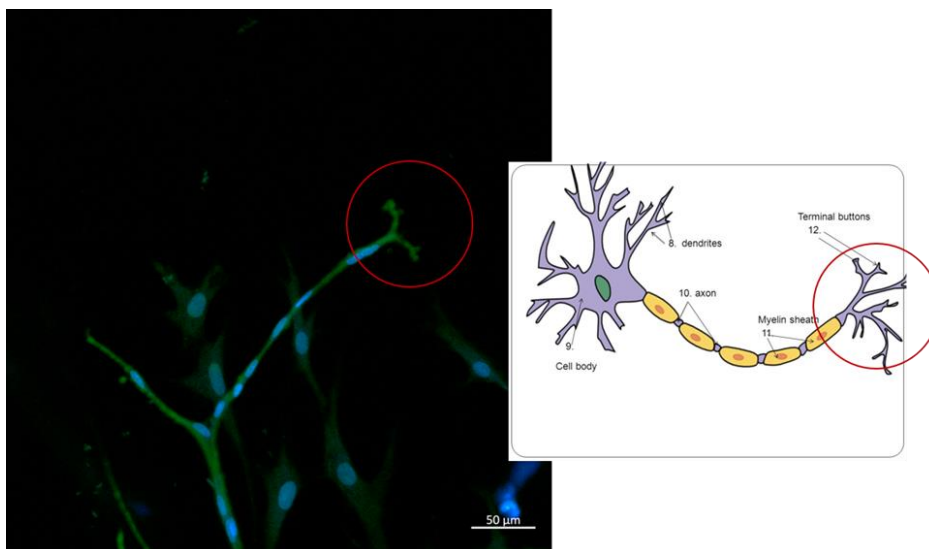
Supplementary Figure X-3 - Qualitative vascularization assessment in the *in vivo* study groups in the middle conduit section (C1X) after Toluidine Blue staining: A) Autograft; B) SF; C) GDNF/A₄. Scale bar: 20 μ m.



Supplementary Figure X-4 - Vascularization assessment by quantification of blood vessels in the middle conduit area (C1X). Statistically significant differences were represented by * ($p < 0.05$), ** ($p < 0.01$), and *** ($p < 0.001$).



Supplementary Figure X-5 - Influence of cellular components on neurite outgrowth. Representative confocal images of DRGs stained with Neurofilament 200 (green) and DAPI (blue). Cellular migration from the DRG body will influence neurite length, possibly due to biochemical cues formed by laminin secretion. Scale bar: 500 μm .



Supplementary Figure X-6 - Classical neuron structure found within confocal fluorescent images of DRGs after 5 days in culture. Nuclei of Schwann cells (DAPI staining, in blue) can be seen enwrapping long axon (Neurofilament 200 staining, green). In the end, marked by a red circle, a terminal bouton or axon terminal can be seen. Scale bar: 50 μm .

Supplementary Table X-1 - Quantification of DRGs neurite outgrowth parameters in the presence of GDNF releasing SF conduits and respective controls.

| | Neurite length (μm) | Cellular migration from DRG body (μm) | Field coverage (%) |
|-----------------------|-------------------------------------|---|-----------------------|
| GDNF positive control | 961.7 \pm 197.8 | 1,307.3 \pm 266.9 | 15.6 \pm 5.3 |
| Negative control | 492.0 \pm 170.5 | 854.7 \pm 282.9 | 3.1 \pm 1.3 |
| GDNF/C | 122.8 \pm 119.3 | 712.8 \pm 281.3 | 1.3 \pm 0.8 |
| GDNF/A ₂ | 595.2 \pm 246.2 | 1,422.1 \pm 417.6 | 4.4 \pm 1.5 |
| GDNF/A ₄ | 759.0 \pm 160.7 | 1,525.8 \pm 384.9 | 10.9 \pm 1.6 |

Supplementary Table X-2 - Quantification of DRGs neurite outgrowth parameters in the presence of NGF releasing SF conduits and respective controls.

| | Neurite length (μm) | Cellular migration from DRG body (μm) | Field coverage (%) |
|----------------------|----------------------------------|--|--------------------|
| NGF positive control | 1,072.6 \pm 227.4 | 1,464.8 \pm 262.9 | 7.0 \pm 1.3 |
| Negative control | 492.0 \pm 170.5 | 854.7 \pm 282.9 | 3.1 \pm 1.3 |
| NGF/C | 220.5 \pm 116.6 | 0 | 1.8 \pm 1.6 |
| NGF/A ₂ | 641.1 \pm 176.4 | 1,196.2 \pm 285.6 | 4.2 \pm 1.0 |
| NGF/A ₄ | 870.9 \pm 246.7 | 1,560.4 \pm 403.6 | 7 \pm 1.4 |

SECTION 4

CONCLUSIONS AND FUTURE PERSPECTIVES

Chapter XI

Conclusions and future perspectives

General conclusions and future perspectives

XI-1. GENERAL CONCLUSIONS

Peripheral nerve injuries may result in a damage without gaps, or where a part of the native nerve tissue disappears between nerve stumps, creating a gap. In the presence of a nerve defect where a gap exists, the placement of a nerve graft is mandatory for nerve restoration. The clinical employment of conduits as an alternative to autologous nerve grafts is mainly justified by the limited availability of donor tissue for nerve autografts and their related morbidity, as well as poor outcomes.

Not considered as a single disease, peripheral neuropathy is a nerve damage caused by several different causes such as trauma, Diabetes, certain medications, autoimmune diseases, alcoholism and tumor related surgeries. When affected by peripheral neuropathies, patients experience a different set of symptoms, which impedes them to carry a normal lifestyle. These vary from simple weakness to extreme sensitivity or total paralysis, according to the degree of the injury.

Tissue engineered nerve guidance conduits are useful, crucial and daily used medical devices used as autologous nerve graft substituents, in the management of numerous neurological disorders related to peripheral nerves. However, despite their extensive use in the clinical setting, contemporary nerve guide technology is far from the ideal and underperforms when compared to the autologous graft. A complete understanding of neurobiology, usual complications and past fails are required to find how nerve guidance conduit design can be further improved.

The major goal of the work developed under the scope of the present thesis was to develop new strategies to progress the state of the art in what regards nerve guidance conduits, based only on natural-origin polymers. To improve therapeutics, the production of bio-engineered scaffolds combining the knowledge about regeneration mechanisms, biomaterials and the novel biotechnological approximations, seem the only possible option leading to a successful outcome. All the technologies studied and proposed procured to match the main drawbacks identified in the literature and attempt to overcome them, recurring to innovative and more precise technologies.

In **Chapter V**, a thorough study of chitosan's degree of acetylation (DA) was carried on, for suitable application in nerve regeneration. According to the literature, there are many studies proving and experimentally demonstrating that, considering a wide range of DAs, lower acetylated materials lead to better results in terms of increased cell adhesion for nerve regeneration. This statement has also been proved true in other regenerative medicine fields, with other types of cells belonging to other physiological systems such, as bone or skin. However, it has never been reported before how minor changes in the DA would have a visible effect in cell adhesion, since a wider range and greater differences in the DA are commonly studied. Also, it was verified in the literature that the lowest DA analyzed varied greatly, from 0.5 % to 10 %. Therefore, the statement found in the literature "DA close to zero leads to better results" is imprecise. Taking the previous information into account, the niche of "proper DA close to zero" was further investigated in order to shed light on the real suitability of chitosan membranes and their DAs for peripheral nerve regeneration purposes.

After the extensive characterization performed, this experimental work led to the conclusion that a 5 % DA membrane should be the one considered for further PNR applications. It was shown not to induce calcification of the implant, excessive swelling or fibroblasts infiltration. It also allowed a guided regeneration of the nerves mediated by preferential Schwann cell adhesion and proliferation. The confidence in these results also arises from the fact that chitosan with 5 % DA was also found to be the most suitable for nerve regeneration by other authors in the scope of the Biohybrid project, with other *in vitro* and *in vivo* results that complement each other as a whole. Working as a team and at the same time in the biohybrid consortium, many authors reached the same conclusion. That gives abundant scientific support to state that we were able to determine the exact DA that must be applied when attempting nerve regeneration. This study, together with others, allowed to move with 5 % DA chitosan conduit to clinical trials and into the clinic.

Furthermore, even though mold casting membranes were the processing chosen for this specific study, their practical use goes beyond that, as the membranes can be easily transformed in conduits, nerve wraps or luminal fillers, according to the severity of the lesion or the patient needs.

In **Chapter VI**, the knowledge gained about chitosan and the most suitable DA for neural applications was taken in consideration, as the biomaterial with 5 % DA was used. However, it is known that chitosan itself lacks adhesion motifs to support direct cell anchorage. Consequently, it was decided that an upgrading needed to be done in this field. After literature research, keratin extracted from human hair seemed as a captivating biomaterial with the correct features: a human-derived protein,

excellent biocompatibility, no immune reaction upon transplantation, good cellular interaction activity and biodegradability. The fact that hair is found to be a waste and we could use in Tissue Engineering approaches with zero costs was also an attractive consideration. Other than that, the fact that the keratin molecule contains various cell-binding sites such as LDV and RGD, strongly supporting cell adhesion, led to the interesting possibility of blending it with chitosan. Since our main interest was related to studying the shift of biological properties when chitosan was blended with keratin, cell behavior analysis was carried out using three human cell types that play key roles in nerve regenerative process. For this purpose, fibroblasts, Schwann cells and endothelial cells were used. The results were in accordance with the hypothesis proposed, as cellular adhesion was significantly enhanced by the presence of as much as only 1 % of keratin in the membranes. Since vascularization is a vital, limiting and inter-related process associated with improved neuronal regeneration, an *ex ovo* CAM investigation was carried out to assess the angiogenic potential of the developed chitosan/keratin novel materials, with promising results. This experimental study clearly showed that the addition of human hair keratin elevated the biological properties of chitosan membranes, inclusively stimulating the so much desired process of angiogenesis.

However, not only the biological properties were greatly enhanced. Looking at the study as a whole, membranes become rougher in its surface and the mechanical properties became more attractive to neuronal cells, with the decrease of stiffness of materials with the incorporation of keratin.

Although this work was carried out with only 1% of keratin, it would be interesting to see the behavior of the membranes when lower or higher amounts of hair extracted keratin would be used.

For the conception of the experimental work described in **Chapter VII**, it was verified that all FDA-approved nerve guidance conduits consist in hollow tubular structures. The absence of luminal structures to guide growing axons and Schwann cells, the peripheral glia cells, has been pointed as the cause of their failure in nerve injuries with longer gaps. As such, we hypothesized the utilization of different HA-GG and MA-GG blending freeze-dried hydrogels as luminal fillers for chitosan conduits. Since HA-GG and MA-GG behave differently, these blends were expected to affect hydrogel degradation rate and cellular adhesion, thus permitting to evaluate the influence of these parameters on the peripheral nerve regeneration process. Once again using the knowledge taken from the previous work in **Chapter V**, nerve guides produced with chitosan with a 5 % DA were used to hold the GG luminal structures. Extensive *in vitro* and *in vivo* studies were initiated to define the potential of such combinatorial system for nerve regeneration. This experimental work demonstrated for the first time the

innovative use of gellan gum freeze-dried hydrogels as luminal fillers for nerve guidance conduits intended for peripheral nerve reconstruction. The outcome of our studies demonstrated that, although nerve regeneration occurred to some extent, our system still must be optimized and the presence of such a biomaterial in the lumen of the chitosan tubes might have negative effects in terms of nerve regeneration, due to excessive swelling. Our conclusions, however, matched some statements found in literature, where it was found that excessive material density and swelling in the lumen as a deleterious effect in the regenerative process. The best results, however, have been achieved in the presence of higher amounts of MA-GG in the blending systems, both *in vitro* and *in vivo*, giving consistency to this finding. The main conclusion that can be withdrawn from this chapter is that methacrylated GG supported axonal regeneration and increased vascularization, ultimately resulting in muscle re-innervation.

The previous work was extensive and could in fact contribute to the general knowledge about chitosan and keratin as a biomaterial and the use of luminal fillers for nerve repair and regeneration. However, at this stage, it was decided to move on to another strategy and test a new natural origin biomaterial that would be the focus of the future work: the silk fibroin.

Chapter VIII is focused on an international patent which discloses a new methodology to obtain enzymatically crosslinked silk fibroin nerve guidance conduits, as well as their possible applications in Tissue Engineering and biomedical field in general. The innovation of the method relied on the transformation of an initially produced aqueous silk fibroin solution into an amorphous and transparent hydrogel, through a horseradish peroxidase-mediated crosslink reaction. That is only possible due to the 5 mol % of tyrosine groups present in silk fibroin structure, which are oxidized by peroxidase/hydrogen peroxide and subsequently covalently crosslinked to form a three-dimensional network. After the preliminary laboratorial work performed in the scope of the patent, it can be concluded that through this crosslinking step, a stronger and more stable three-dimensional network is achieved. Consequently, it confers the conduits higher mechanical properties, more elasticity and a lower degradation rate, when compared to conduits that did not undergo this crosslink before turning in β -sheet conformation. Due to the versatility of such conduits, it was found that they could be adjusted in several ways, completely transforming their properties and becoming suitable for other different applications, other than peripheral nerve regeneration.

Regarding this patented method of producing enzymatically crosslinked silk fibroin nerve guidance conduits, further work was carried on in **Chapter IX**. The previously produced enzymatically crosslinked

silk fibroin nerve guidance conduits were subjected to three different processing methods as a final step (freeze-dry, dry at 50 °C or simply not removing the solvent) to modulate their physical and biological properties. The experimental work allowed to understand that we could virtually adjust any characteristic of the final conduits by changing the final step. After an extensive literature research, it was realized that several soft-to-hard tissues would benefit from the use of these conduits, as they can be fine-tuned and tailored to match the needs of several applications, including the central nervous system, tendon, tracheas, and ureters.

In one hand, it has been demonstrated that silk fibroin conduits which are dried at 50 °C are capable of inducing mineralization *in vitro*, opening up new application in the treatment of hard tissue defects. On the other hand, freeze-dried conduits or conduits which solvent was not removed revealed higher biological properties, especially when it comes to peripheral nerve regeneration. In peripheral nerve scope, we were able to prove the fine-tuned tubular conduits prevented fibroblasts' infiltration and reduced the risk of scar tissue formation *in vitro* and *in vivo*, which is advantageous in nerve regeneration. Still, they allowed the diffusion of crucial molecules such as oxygen, glucose or vitamin B12 (inferior to 4 kDa). In a general manner, the herein produced conduits can greatly vary in terms of thickness, porosity, degradation and swelling. Also, molecular permeability as well as mechanical properties, cellular adhesion and bioactivity can be easily tuned, making these silk-based conduits exceptionally versatile and with an extended range of possible applications. Globally, the proposed enzymatically crosslinked silk fibroin tubular conduits, which can be seen as an off-shelf product, should have a significant impact in tissue regeneration field and potentially in clinics, for the treatment of either soft and hard tissue defects, where tubulization techniques are required.

It must be mentioned that since there is the formation of an hydrogel as middle step in the fabrication process, it allows for a variety innovations. For instance, molecules of interest can be easily incorporated in the friendly processing. Neurotrophic factors, electrically conductive molecules such as polypyrrole or other therapeutic drugs can be easily incorporated in a water-based system and be released from the conduits in the lesion site. we envision this as an exciting world of possibilities.

In **Chapter X**, taking the previous statement in consideration, we further realized the potential of the in-house developed enzymatically crosslinked silk fibroin conduits to fill a gap that exists in the literature of nerve repair: the correct inclusion and timely fashion delivery of growth factors at the nerve injury site. The state of art in this subject indicated that optimized delivery methods for neurotrophic factors eluted from silk fibroin conduits have been solely based in two techniques: (i) simple blending of

neurotrophic factors in silk solution without further entrapment, and (ii) based in the electrospinning technique. After carefully observing and studying the developed fabrication method of silk fibroin nerve guidance conduits, we realized we had the opportunity of testing two different approaches, using only the proposed fabrication method that was previously patented and used in **Chapters VIII** and **IX**. As such, we have adopted and tested two different incorporation methods and compared their efficacy: (i) crosslinking method or (ii) adsorption method. These methods are solely based on and interrelated with the silk fibroin nerve guidance conduits production method, without further technology needed.

Succinctly, the purpose of this study was to upgrade the already developed silk conduits and direct the future design of conduits to better support and stimulate nerve regeneration through the incorporation and delivery of neurotrophic factors. Through this work, we have once again demonstrated that the previously described silk conduits manufacture method resorting to horseradish peroxidase and hydrogen peroxide is, in fact, versatile. It allowed to functionalize the conduits via different methodologies and deliver two different neurotrophic factors with diverse releasing profiles, according to their affinity to silk fibroin. With the obtained results, we can assume the valuable effects of GDNF, which enhanced regeneration in models both *in vitro* and *in vivo*. Moreover, its presence resulted in a suitable environment for peripheral nerve regeneration, acting on both sensory and motor fibers. Using the GDNF/A₄ formulation, proximal nerve protection was found to be more robust when compared to plain silk fibroin conduit and comparable to the autograft, via retrograde transport of GDNF. Overall, the addition of GDNF to the silk fibroin conduit via adsorption method could be one effective treatment to prevent neurodegeneration. We believe the findings from this experimental work could significantly contribute to TE field and support the use of the patented method of silk fibroin nerve guidance conduit production.

In the diverse Chapters, all of the above-mentioned results and subsequent conclusions add new expertise and information to the current knowledge in the field of biomaterials for peripheral nerve tissue engineering.

XI-2. FUTURE RESEARCH DIRECTIONS

Nerve guidance conduit design is an interesting and exciting field which has gained more attention, particularly in last years. To date, and despite impressive scientific effort achieved up to this day, none of the technological developments has led to the “ideal conduit”. However, much progress has been

made by improving the physical characteristics of the biomaterials and the application of recent technologies. Nevertheless, the fact that we have not found the perfect technology or biomaterial yet, opens the door for exciting and new investigation that may exceed imagination, with the new knowledge and information that arises every day.

It must be taken in consideration that despite some level of regenerative potential, peripheral nerve regeneration is much harder than commonly assumed. To be able to develop alternatives, one must be aware and fully understand the phenomena and concepts of peripheral nerve injury and regeneration, as well as the natural impairing biological challenges. Knowing that neuroinflammation, fibrosis, lack of vascularization and oxidative stress are some of the biological phenomena that contribute to the limited success of nerve regeneration, those phenomena give insight on what must be overcome to be more effective in the developed approaches.

The three pillars of Tissue Engineering and Regenerative Medicine: scaffolds, cellular components and growth factors, are crucial for success in nerve regeneration. The finest regeneration will not be achieved using single-factor strategies, since nerve regeneration is a multifaceted and complex evolution of events that entails the presence of numerous factors. Therefore, an appropriate combinatorial approach must be considered, considering the triad of Regenerative medicine.

In a personal point of view, the development of favorable and permissive luminal filler structures would be the focus of future research, since larger gaps simply cannot be overcome now-a-days. Anisotropic guiding cues would offer the best approach to topographically guide the cone of the axons. Apart from the use of suitable NGCs and fillers, the creation of a more conductive microenvironment is of high importance. Nerve growth factors are molecules that are naturally released in the process of injury and result in nerve regeneration. Therefore, it is important to mimic their release, which is vital for nerve growth and regeneration. In a third approach, cell-based therapy has become an important and evidenced practice which improves the functional clinical outcome in case of nerve injury. It is important to point out that these three strategies work by different mechanisms and distinct biochemical pathways, complementing each other, in a multi-factorial therapeutic alternative. Also, to truly progress in such a challenging field, experts of different areas must contribute, either physicians, surgeons, engineers, biologists and chemists, in a multi-disciplinary team of work.

In a more particular field, the influence of microRNAs has only recently been discovered and was discussed in **Chapter II**. However, the knowledge about the mechanisms involved and controlled by

miRNAs offer the opportunity to explore potential new therapies, at a molecular level, in terms of neuronal adhesion, proliferation, migration and myelination. This niche of molecular biology has extreme potential to provide possible therapeutic target for peripheral nerve injury or repair and should unquestionably be further explored. If phenomena such as myelination/demyelination, cellular apoptosis or neurite extension can be controlled at its very core, controlling the future events even before they have occurred.

A special note must be made regarding nanotechnology-based technologies in nerve repair. Although no specific work related to nanotechnology has been developed under this thesis, one must recognize its extreme potential. After having the great opportunity to learn and review all the nanotechnological approaches currently applied to peripheral nerve regeneration in **Chapter III**, it would be my personal desire to enter in this field, due to its exciting nature. Extraordinary nanotechnologies are now being considered for the repair and reconstruction of nerve injuries, having the power to deliver bioactive molecules in a controlled manner, to tune cellular behavior, and ultimately, guide tissue regeneration in an effective manner. It also offers opportunities in the imaging field, with a degree of precision never achieved before, which is useful for diagnosis, surgery and in the patient's follow-up, in a patient-specific manner. Exploring and practically working in this specialized field would certainly give a major contribution to the future neurological medicine.

In practical terms, another improvement that needs to be attained in the near future relies on the scientific rodent models of nerve injury. Considering the millions of research papers that exist with *in vivo* studies in rodent models, the nonexistence of significant breakthroughs in the clinical setting is shocking and disappointing. Slowly, scientific community is coming to the conclusion that there is a poor translation of the findings from rodent models to humans, making it tough for the translational medicine. However, the lack of alternatives is concerning. In attempts to solve that problem, a few of large animal studies and clinical trials have been carried out, from which new directions and novel scientific findings are continuously being learned. They are, however, scarce and investment needs to be made in this specific area. Although *in vivo* animal models mimic a living system, visualization of the distinct events is nearly impossible. In fact, recent studies suggest that the correspondence between animal models (regardless of their size) and successful clinical trials does not reach 10 %. On the other hand, two dimensional *in vitro* models have reduced physiological relevance, capturing only limited aspects of the respective microenvironment. Therefore, moving to 3D *in vitro* models, comprising the integration of tissue engineering strategies with microfluidic technologies can spark a breakthrough into

the design of nerve injury models. These better adapt to morphological changes in tissue structure and function over time, providing a level of precision control that could not be achieved before, being one possible way to move forward in the future of nerve regeneration. There is, however, very scarce literature on bioreactors or 3D models for nerve regeneration. This field would greatly benefit from advances in this area, also saving the lives of millions of animals.

In a final aspect, the future medical devices should, despite comprehending a combinatorial approach, remain simple in its conception. “Off the shelf” products are the ones both industries and clinicians seek for. Therefore, last generation and truly multi-approach nerve guidance conduits that have the skills to surpass the autografts and be considered in the clinical setting must feature simple manufacturing techniques, as well as simple storage requirements.

As a conclusion, although significant steps have been taken in what regards natural-origin biomaterials, future studies have to be performed to find the ideal combination of intraluminal scaffolds, incorporated cells and specific neurotrophic factor delivery for long gap peripheral nerve repair. However, new directions of research must also be trailed, as the traditional ones that have been used for the last decades do not have the capacity to render the results that patients really need after suffering from a debilitating peripheral nerve injury.